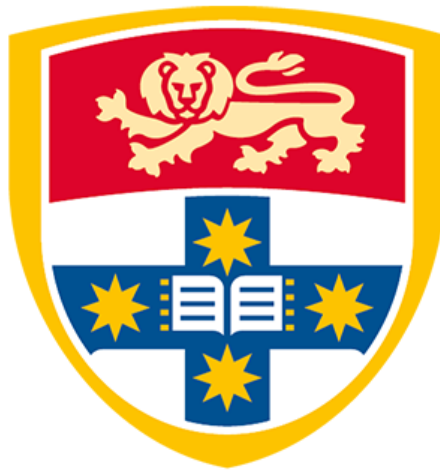


Targeting glioblastoma with microtubule-targeting agents and epigenetic modulators

Ramzi H. Abbassi

*A thesis submitted to fulfil requirements for the degree of
Doctor of Philosophy (Medicine)*



Discipline of Pathology
School of Medical Sciences
Faculty of Medicine and Health
The University of Sydney

2020

For Johny.

Originality statement

This is to certify that, to the best of my knowledge, the content of this thesis is my own work. This thesis has not been submitted for any degree or other purposes.

I certify that the intellectual content of this thesis is the product of my own work and that all assistance received, and sources used in preparing this thesis have been acknowledged.

Ramzi H. Abbassi

20th December 2020

Table of contents

Acknowledgements.....	v
Awards and scholarships	vii
Publications and presentations arising from this thesis.....	viii
Abstract.....	x
List of abbreviations.....	xii
List of figures.....	xiv
List of tables.....	xvi
Authorship contribution statement.....	xvii
CHAPTER 1. INTRODUCTION	1
1. 1. GLIOBLASTOMA TUMOURS	1
1. 1. 1. Diffuse gliomas.....	1
1. 1. 2. Glioblastoma prevalence and risk factors.....	4
1. 1. 3. Primary and secondary glioblastomas.....	5
1. 1. 4. Standard-of-care therapy	6
1. 2. MOLECULAR ALTERATIONS IN GLIOBLASTOMA	7
1. 2. 1. Up-regulation of proliferative signals	7
1. 2. 2. Dysregulation of the cell cycle.....	9
1. 2. 3. Evasion of antiproliferative and apoptotic signals.....	10
1. 2. 4. Kinase-targeted therapy.....	10
1. 3. CHALLENGES IN GLIOBLASTOMA THERAPY	14
1. 3. 1. Intertumour heterogeneity	14
1. 3. 2. Intratumour heterogeneity.....	15
1. 3. 3. Glioblastoma stem cells.....	16
1. 3. 4. The blood-brain barrier	20
1. 4. MICROTUBULES AND MICROTUBULE-TARGETING AGENTS.....	21
1. 4. 1. Microtubule formation and dynamics.....	22
1. 4. 2. Microtubule-targeting agent binding domains	25
1. 4. 3. Microtubule-targeting agents in cancer therapy	27
1. 4. 4. The tubulin code in cancer	31
1. 5. THESIS AIMS.....	37
CHAPTER 2. MATERIALS AND METHODS	40
2. 1. EXPERIMENTAL MODELS AND MATERIALS	40
2. 1. 1. Glioblastoma cell line models.....	40
2. 1. 2. Reagents and chemicals	42
2. 2. IMMUNOBLOTS	46
2. 2. 1. Tubulin code analysis.....	46
2. 2. 2. Histone code analysis	46
2. 3. CAPILLARY IMMUNOASSAY.....	47
2. 4. CELL-BASED ASSAYS.....	47
2. 4. 1. CellTitre-Blue viability assay	47
2. 4. 2. Proliferation rate assay	48
2. 4. 3. DTP generation and expansion.....	48
2. 4. 4. Nuclear-ID DNA Red staining	48
2. 4. 5. Immunofluorescence imaging.....	48
2. 4. 6. Clonogenic outgrowth assays	49
2. 5. QUANTITATIVE POLYMERISED CHAIN REACTION	49
2. 6. SEQUENTIAL WINDOW ACQUISITION OF ALL THEORETICAL FRAGMENT ION SPECTRA MASS SPECTROMETRY (SWATH-MS).....	50
2. 6. 1. Sample preparation	50
2. 6. 2. Nano-liquid chromatography and electrospray ionisation tandem mass spectrometry	52
2. 6. 3. Database search and spectral library generation	52
2. 6. 4. Histone PTM quantification using DDA and DIA	53
2. 6. 5. Data normalisation and statistical analysis.....	53
2. 7. KDM4 ALPHASCREEN ASSAY DEVELOPMENT.....	54
2. 7. 1. Peptide validation by dot blots.....	54
2. 7. 2. Peptide and enzyme assessment by RapidFire mass spectrometry.....	54
2. 7. 3. Optimised AlphaScreen assay.....	55
2. 8. STATISTICAL ANALYSIS.....	56
2. 8. 1. Correlations between the tubulin code and MTA metrics.....	56
2. 8. 2. Statistical tests of comparison.....	56

CHAPTER 3. LOWER TUBULIN EXPRESSION IN GLIOBLASTOMA STEM CELLS ATTENUATES EFFICACY OF MICROTUBULE-TARGETING AGENTS	58
3. 1. PREFACE	58
CHAPTER 4. QUANTIFICATION OF CMPD1-INDUCED CHANGES TO HISTONE MODIFICATIONS USING SWATH-MS.....	61
4. 1. INTRODUCTION.....	61
4. 1. 1. <i>Chromatin remodelling in drug-tolerant persisters</i>	61
4. 1. 2. <i>Sequential window acquisition of all theoretical mass spectra assays</i>	65
4. 2. RESULTS.....	69
4. 2. 1. <i>Glioblastoma cells are tolerant to CMPD1 and tivantinib</i>	69
4. 2. 2. <i>Histone extraction from cells</i>	72
4. 2. 3. <i>Mass spectrometry data acquisition and analysis</i>	73
4. 2. 4. <i>H3 variant and post-translational changes in CMPD1-tolerant cells</i>	76
4. 2. 5. <i>Confirmation of MS data by immunoblotting</i>	86
4. 3. DISCUSSION	89
CHAPTER 5. PHARMACOLOGICAL ASSESSMENT OF HISTONE-MODIFYING ENZYMES AS TARGETS IN CMPD1-TOLERANT PERSISTERS.....	93
5. 1. INTRODUCTION.....	93
5. 1. 1. <i>Histone H3 lysine methyltransferases and demethylases</i>	93
5. 1. 2. <i>Protein targets in drug-tolerant persister cells</i>	98
5. 2. RESULTS.....	100
5. 2. 1. <i>Gene expression of histone lysine modifiers in drug-tolerant persisters</i>	100
5. 2. 2. <i>Screening epigenetic probes against parental and persister cells</i>	106
5. 2. 3. <i>Combination studies of CMPD1 and epigenetic probes</i>	114
5. 2. 4. <i>Cathepsin L1 in drug tolerance</i>	119
5. 3. DISCUSSION	121
CHAPTER 6. DEVELOPMENT OF KDM4 ACTIVITY ASSAY USING ALPHASCREEN TECHNOLOGY	126
6. 1. INTRODUCTION.....	126
6. 1. 1. <i>KDM4 enzymes and inhibitors</i>	126
6. 1. 2. <i>The principle of AlphaScreen technology</i>	130
6. 2. RESULTS.....	131
6. 2. 1. <i>Peptide and antibody validation</i>	131
6. 2. 2. <i>KDM4 enzyme validation</i>	133
6. 2. 3. <i>AlphaScreen assay validation</i>	135
6. 2. 4. <i>Screening for hit molecules to develop KDM4 inhibitors</i>	137
6. 2. 5. <i>Establishing KDM4 potency of hit compounds</i>	144
6. 3. DISCUSSION	146
APPENDIX. <i>KDM4A Protein Expression and Purification</i>	149
CHAPTER 7. ADDITIONAL PUBLICATIONS.....	152
7. 1. PREFACE	152
CHAPTER 8. FINAL CONCLUSIONS	154
8. 1. <i>DRUG TOLERANCE VERSUS DRUG RESISTANCE</i>	154
8. 2. <i>TARGETING DRUG-TOLERANT GLIOBLASTOMA CELLS</i>	156
8. 3. <i>THE ROLE OF KDM4 IN GLIOBLASTOMA</i>	160
CHAPTER 9. REFERENCES.....	163

Acknowledgements

Undergoing a PhD candidature was a rollercoaster of challenges, failures and successes. I have had the pleasure of working with brilliant scientists and colleagues who have taught me, inspired me and helped get back on my feet whenever I felt overwhelmed by my project. Through dedication, hard work and encouragement, I overcame these challenges, and the outcome was more than rewarding.

My deepest gratitude goes, first and foremost, to my supervisor, A/Prof. Lenka Munoz, whose guidance, care and support throughout my candidature have been invaluable. I could not have asked for a better mentor and role model. Thank you for the excellent opportunities to learn new techniques, build networks both nationally and internationally and share my research with the scientific community. Your mentorship has made me a better scientist and I will never forget the incredible journey we have had over the last seven years. I hope that I have made you proud.

To the postdocs of the *Cell Signalling Group* (past and present) who have taught me and guided me – Dr. Monira Hoque, Dr. Sharleen Menezes, Dr. Ariadna Recasens and Dr. Dinesh Indurthi: I cannot thank you enough for all there help over the last four years. I will miss you all very dearly. To the only other long-standing member of the Munoz group, Athena Phoa: thank you for your friendship and support over the previous seven (!!!) years. We have both finally come out the other side! I cannot wait to see where the future takes us both. To all the past and present Honours and visiting students (Jayden Sterling, Alexander Cerroti, Kudzai Chinjekure, Sean Tan, Michael Ellis, Tara Betts, Brianna Chen and Dylan McCuaig-Walton) with whom I have had the pleasure of working, and in some cases, mentoring: Thank you for your friendship and support (and the laughs!). I wish all of you the best in the future. A special thank you goes to ex-lab members who have supported me at the beginning of my research career, Dr. Fadi Gurgis, Dr. Mia Åkerfeldt, Dr. Alexander Döbber and Mona Mokhatab.

To my auxiliary supervisor, Dr. Jason Low, I extend my gratitude to you for taking the time to train me in mass-spectrometry and histone proteomics, which is by no means the easiest methodology. I thank Dr. Pengyi Yang for his assistance with the statistical analysis of proteomic data. I also acknowledge the contribution of Dr. Chandrika Deshpande and Sydney Analytical for synthesising the KDM4 enzymes that I used in my AlphaScreen assays. On that note, I could not have developed the AlphaScreen assay without the expertise and guidance of Dr. Anthony Tumber (Prof. Christopher Schofield's laboratory, University of Oxford), who had mentored me during my visit to the UK. I

would also like to thank Prof. Paul Brennan (University of Oxford) for providing us with the KDM4A plasmid and selective KDM5/6 inhibitors used in this thesis, and Prof. Adam McClusky and Dr. Jennifer Baker (University of Newcastle) for synthesising the compound library that was used in the KDM4A AlphaScreen. I also acknowledge the Bosch Institute Molecular Biology Facility and Sydney Mass Spectrometry Facility for their great guidance and support in the use of the equipment needed to generate data for this thesis.

I would like to thank Dr. Josep Font and acknowledge his assistance with teaching me how to design and edit molecular models that are included in this thesis. To Dr. Johnathon David Teo: Thank you for all your help with microscopy over the years, and for the beautiful cover image that you created for my publication that was featured as *ACS Editors' Choice*. Also, thanks to all the Level 4W peeps at the Charles Perkins Centre for making the last four years memorable and enjoyable (Immanuel Green, Keely Tan, Reichelle Yeo, Cassandra Malecki, Natalia Pinello, Aster Pijning, Stef Portelli, Holly McEwen and Tim Couttas). I also extend my gratitude to Craig Jackson, Dr. Alice Brown and the rest of the Research Support Team for their constant support over the last 4 years. I will miss you all.

Last, but certainly not least, I thank all my family and friends who have showered me with unconditional love and support, especially my parents Hussam and Janet and my sisters Raimee and Reena. Thank you from the bottom of my heart. I love you.

Awards and scholarships

- 2017** **Reginald Maney Lake and Amy Laura Bonamy Scholarship**
Sydney Medical School, The University of Sydney
Awarded as a bridging scholarship; “High Flyer” programme
- Research Training Program (RTP) Scholarship**
Sydney Medical School, The University of Sydney
Awarded for the duration of PhD candidature
- Postgraduate Research Support Scheme (PRSS)**
Sydney Medical School, The University of Sydney
To attend and give an oral presentation at the Royal Australia
Chemical Institute’s (RACI) National Centenary Conference in
Melbourne, Australia
- 2018** **Postgraduate Research Support Scheme (PRSS)**
Sydney Medical School, The University of Sydney
Stipend for travel, conference registration and accommodation costs
RACI Medicinal Chemistry and Chemical Biology Conference 2018
- 2019** **Glioblastoma Research Scholarship**
Sydney Medical School, The University of Sydney
Awarded for the development of AlphaScreen assays
- Postgraduate Research Support Scheme (PRSS)**
Sydney Medical School, The University of Sydney
Stipend to cover travel and accommodation costs for partaking in a
laboratory exchange at the University of Oxford, UK

Publications and presentations arising from this thesis

Publications arising from this candidature

- Recasens, A.; Humphrey, S.; Ellis, M.; Hoque, M.; **Abbassi, R.**; Chen, B.; Longworth, M.; James, D.; Johns, T.; Day, B.; Kassiou, M.; Yang, P.; Munoz, L., Global phosphoproteomics reveal DYRK1A regulates CDK1 activity in glioblastoma cells. *Cell Death Discov* **2021**, *7*, 81.‡
- Hoque, M.; Wong, S. W.; Recasens, A.; **Abbassi, R.**; Nguyen, N.; Stashko, M. A.; Wang, X.; Frye, S.; Day, B. W.; Baell, J.; Munoz, L. MerTK is not necessary for the proliferation of glioblastoma stem cells. *Biochem Pharmacol* **2021**, *186*, 114437-114455.‡
- Sterling, J.; Menezes, S. V.; **Abbassi, R. H.**, Munoz, L. Histone lysine demethylases and their functions in cancer. *Int J Cancer* **2020**, *149*, 2375-2388.
- **Abbassi, R. H.**; Recasens, A.; Indurthi, D. C.; Johns, T. G.; Stringer, B. W.; Day, B. W.; Munoz, L., Lower tubulin expression in glioblastoma stem cells attenuates efficacy of microtubule-targeting agents. *ACS Pharmacol Transl Sci* **2019**, *2*, 402-413.†
- Hoque, M.; **Abbassi, R. H.**; Froio, D.; Man, J.; Johns, T. G.; Stringer, B. W.; Day, B. W.; Pajic, M.; Kassiou, M.; Munoz, L., Changes in cell morphology guide identification of tubulin as the off-target for protein kinase inhibitors. *Pharmacol Res* **2018**, *134*, 166-178.
- Zhou, Q; Reekie, T. A.; **Abbassi, R. H.**; Indurthi, D. C.; Font, J. S.; Ryan, R. M.; Munoz, L.; Kassiou, M., Synthesis and in vitro evaluation of diverse heterocyclic diphenolic compounds as inhibitors of DYRK1A. *Bioorg Med Chem* **2018**, *26* (22), 5852-5869.‡
- Zhou, Q; Reekie, T. A.; **Abbassi, R. H.**; Indurthi, D. C.; Font, J. S.; Ryan, R. M.; Rendina, L. M.; Munoz, L.; Kassiou, M., Flexible analogues of azaindole dyrk1a inhibitors elicit cytotoxicity in glioblastoma cells. *Aust J Chem* **2018**, *71* (10), 781-799.‡
- Döbber, A.; Phoa, A. F.; **Abbassi, R. H.**; Stringer, B. W.; Day, B. W.; Johns, T. G.; Abadleh, M.; Peifer, C.; Munoz, L. Development and biological evaluation of a photoactivatable small molecule microtubule-targeting agent. *ACS Med Chem Lett* **2017**, *8*, 395-400.

Publications arising from work prior to candidature

- Zhou, Q; Phoa, A. F.; **Abbassi, R. H.**; Hoque, M.; Reekie, T. A.; Font, J. S.; Ryan, R. M.; Stringer, B. W.; Day, B. W.; Johns, T. G.; Munoz, L., Structural optimization and pharmacological evaluation of inhibitors targeting dual-specificity tyrosine phosphorylation-regulated kinases (DYRK) and CDC-like kinases (CLK) in glioblastoma. *J Med Chem* **2017**, *60*, 2052-2070.‡
- **Abbassi, R. H.**; Johns, T. G.; Kassiou, M.; Munoz, L., DYRK1A in neurodegeneration and cancer: Molecular basis and clinical implications. *Pharmacol Ther* **2015**, *151*: 87-98.‡

† Featured in ACS Editors' Choice, sponsored for immediate, free open-access publication by ACS and featured on the cover of the issue.

‡ Articles investigated drug targets in glioblastoma which were not the focus of this dissertation.

Conference and Symposium Presentations

2017 **School of Medical Sciences HDR seminar, the University of Sydney, NSW, 29th June**

Abbassi, R. H., *Delineating the role of the tubulin code in glioblastoma (Research Proposal). Oral Presentation.*

RACI National Centennial Conference, Melbourne, VIC, 23rd–27th July

Abbassi, R. H., Döbber, A., Phoa, A., Stringer, B. W., Day, B. W., Johns, T. G., Abadleh, M., Peifer, C., Munoz, L. *Development and biological evaluation of photoactivatable small molecule microtubule-targeting agent. Oral Presentation.*

2018 **Discipline of Pathology, The University of Sydney, NSW, 3rd September**

Abbassi R. H., *The tubulin code of glioblastoma stem cells and its correlation with sensitivity to microtubule-targeting agents. Oral Presentation.*

RACI Medicinal Chemistry and Chemical Biology Conference, Brisbane, QLD, 18th–21th November

Abbassi R. H., Indurthi, D. C.; Recasens, A.; Johns, T. G.; Stringer, B. W.; Day, B. W.; Munoz, L *Quantification of the efficacy of microtubule-targeting agents in glioblastoma stem cells using GR metrics. Poster Presentation.*

2020 **Discipline of Pathology, The University of Sydney, NSW, 16th October**

Abbassi R. H., *Targeting glioblastoma with microtubule-targeting agents and epigenetic modulation (Completion Seminar). Oral Presentation.*

Abstract

Glioblastoma is one of the most lethal tumours. However, current standard of care therapy is ineffective at eradicating the entire tumour cell population. This fractional killing occurs as glioblastoma cells possess great intertumour (patient-to-patient) and intratumour (cell-to-cell) heterogeneities, leading to tumour recurrence.

Microtubules are required for proliferation and other integral cell processes, thus one proposed therapeutic approach to glioblastoma is the use of microtubule-targeting agents (MTAs). It is postulated that this 'non-targeted' approach would kill all tumour cells. However, while classical MTAs such as taxanes and *Vinca alkaloids* are clinically successful anti-cancer drugs and are effective at killing glioblastoma cells *in vitro*, the polarity and large molecular mass of these drugs render them useless for the treatment brain tumours, as they cannot cross the blood-brain barrier. Our laboratory has been developing small-molecule MTAs, based on the lead inhibitor CMPD1, which are able to cross the blood-brain barrier and effectively kill glioblastoma cells *in vivo*. While the drug development of small-molecule MTAs for glioblastoma therapy is commercial-in-confidence, the overarching aim of this PhD candidature was to assess the translational potential of microtubule-targeting agents for glioblastoma therapy.

We first questioned whether microtubule heterogeneity, resulting from numerous tubulin isoforms and their post-translational modifications impacts on sensitivity of glioblastoma cells to MTAs. Using a panel of 12 genetically diverse glioblastoma stem cell lines and per-division growth rate inhibition metrics, we established that total α - and β -tubulin levels impact on MTA sensitivity. The baseline levels of α - and β -tubulin were up to 40% lower in cells that were not effectively killed by MTAs. Further, low α/β -tubulin expression was associated with higher degree of stemness. Importantly, we discovered that in every glioblastoma cell line, regardless of tubulin expression levels and sensitivity to MTA, a small subpopulation of cells survived MTA treatment via reversible non-mutational dormancy.

The cells that survived the treatment, known as drug-tolerant persister (DTP) cells, resumed proliferation in 'drug holidays' and displayed the same sensitivity to MTAs as their treatment-naïve parental population. Hence, the drug-tolerant state is a survival mechanism mediated by reversible epigenetic processes, often via changes to the histone H3 subunit of the nucleosome. We used SWATH-MS, a technique emerging as a gold-standard in large-scale proteomics, to assess changes in histone H3 post-translational

modifications in DTP cells and compared these to modifications in treatment-naïve parental cells. The analysis revealed that DTP cells exhibit a global decrease in histone lysine acetylation and an increase in histone lysine methylation, which is consistent with a genetically repressive chromatin state. Assessment of transcript levels of histone lysine methyltransferases (KMTs) and demethylases (KDMs) demonstrated more increases in KMT than KDM transcripts in DTP cells relative to their treatment-naïve parental counterparts, supporting SWATH-MS findings.

A screen of a library of epigenetic probes and a series of pharmacological assays using disease-relevant cell models discovered that DTP cell recovery and return to a proliferative state was hampered when treated with CMPD1 in combination with inhibitors targeting KDM4 or KDM6. Taken together, the research presented in this thesis suggests that small-molecule MTA are promising drugs to treat glioblastoma patients. However, in order to achieve complete killing of all glioblastoma cells within a tumour population, MTAs must be combined with drugs targeting DTPs. It is hypothesised that KDM inhibitors prevent the demethylation of methylated lysine residues acquired in drug-tolerant cells, and hence, prevent recovery.

Further, we identified KDM4 as a potential novel target in treatment-naïve glioblastoma cells. Given the lack of orthogonal and cell-permeable KDM4 inhibitors to validate KDM4 as a target, we established a high-throughput AlphaScreen KDM4 inhibition assay to begin the drug discovery process. Using this assay, we screened a small chemical library and identified two hit molecules that offer excellent starting points for future hit-to-lead optimisation and the development of KDM4 inhibitors.

List of abbreviations

2-OG	2-oxoglutarate (a. k. a. α -ketoglutarate)
γ -TuRC	γ -tubulin Ring Complex
ATAT1	α -tubulin acetyltransferase 1
ATP	Adenosine triphosphate
ATRX	Alpha-Thalassemia/mental Retardation syndrome X-linked
BBB	Blood-Brain Barrier
BSA	Bovine Serum Albumin
CDK	Cyclin-Dependent Kinase
CHI3L1	chitinase-3-like 1
CIC	Capicua transcriptional repressor
CNS	Central Nervous System
DAPI	4',6-diamidino-2-phenylindole
DAXX	Death-associated protein
DDA	Data-Dependent Acquisition
DIA	Data-Independent Acquisition
DMEM	Dulbecco's Minimum Essential Medium
DNA	Deoxyribonucleic acid
DTP	Drug-Tolerant Persister
DTT	DL-Dithiothreitol
DYRK1A	Dual-specificity Tyrosine Regulated Kinase 1A
EED	Embryonic Ectoderm Development protein
EGF(R)	Epidermal Growth Factor (Receptor)
EZH	Enhancer of Zeste homolog
FBS	Foetal Bovine Serum
FGF(R)	Fibroblast Growth Factor (Receptor)
G-CIMP	Glioma CpG Island Methylator Phenotype
GDP	Guanosine Diphosphate
GSC	Glioblastoma Stem Cell
GTP	Guanosine Triphosphate
HDAC	Histone Deacetylase
HGF(R)	Hepatocyte Growth Factor (Receptor) (HGFR a. k. a. c-Met)
HIF	Hypoxia-Inducible Factor
IDH	Isocitrate Dehydrogenase
KDM	Histone lysine demethylase
KMT	Histone lysine methyltransferase
MAPK	Mitogen-Activated Protein Kinase
MDR1	Multi-Drug Resistant 1 (a. k. a. P-glycoprotein)
MGMT	O ₆ -methylguanine-DNA methyltransferase
MMP	Matrix Metalloprotease
MTA	Microtubule-Targeting Agent

NF1	Neurofibromin 1
OLIG2	Oligodendrocyte transcription factor 2
PBS	Phosphate Buffered Saline
PDGF(R)	Platelet-Derived Growth Factor (Receptor)
PI3K	Phosphatidylinositol-3-OH Kinase (PI3K) (Genes
PRC	Polycomb Repressive Complex
PRM-MS	Parallel Reaction Monitoring Mass Spectrometry
PTEN	Phosphatase and tensin homologue
PTM	Post-Translational Modification
Rb	Retinoblastoma (Gene: <i>RB1</i>)
RNA	Ribonucleic acid
RT-qPCR	Reverse-Transcription quantitative Polymerised Chain Reaction
SOX2	Sex-determining region Y (SRY)-box 2
SRM-MS	Selected Reaction Monitoring Mass Spectrometry
SWATH-MS	Sequential Window Acquisition of All Theoretical Fragment Ion Spectra Mass Spectrometry
TCEP	Tris (2-carboxyethyl) phosphine
TCGA	The Cancer Genome Atlas
TERT	Telomerase Reverse Transcriptase
TET	Ten-Eleven Translocation proteins
TTL	Tubulin Tyrosine Ligase
TLL	Tubulin Tyrosine Ligase-Like
VEGF(R)	Vascular Endothelial Growth Factor (Receptor)
WHO	World Health Organisation

List of figures

Figure 1.1 The WHO 2016 clinical classification system for adult diffuse gliomas.	2
Figure 1.2 Key molecular pathway alterations in glioblastoma.	8
Figure 1.3 GSCs adapt to stressful stimuli by occupying different attractor states.	17
Figure 1.4 Microtubule nucleation and elongation.	24
Figure 1.5 Microtubule dynamics.	25
Figure 1.6 Binding sites in tubulin and microtubules.	26
Figure 1.7 Small-molecule MTAs for the treatment of brain cancers.	30
Figure 1.8 Microtubule heterogeneity directs microtubule properties and functions.	34
Figure 2.1 Histone SWATH mass spectrometry workflow.	51
Figure 4.1 The role of the histone code in regulating gene expression.	63
Figure 4.2 Principle of SWATH-MS assays for large-scale proteomics.	67
Figure 4.3 RK11 and FPW1 cells are tolerant to CMPD1 and tivantinib.	70
Figure 4.4 RK11 and FPW1 cells are tolerant to CMPD1 and tivantinib.	71
Figure 4.5 Immunoblots confirming subcellular fractionation.	73
Figure 4.6 Experimental workflow for quantifying changes in histone PTMs in glioblastoma cells.	74
Figure 4.7 SWATH-MS data quality control.	75
Figure 4.8 Ratio of the H3.1/3.2 K27K36 to the H3.3 K27K36 peptide families.	76
Figure 4.9 Changes in histone H3 modifications in CMPD1-tolerant FPW1 persisters.	77
Figure 4.10 Changes in histone H3 modifications in CMPD1-tolerant RK11 persisters.	78
Figure 4.11 Changes in histone H3K4 modifications in DTPs.	79
Figure 4.12 Changes in histone H3K9K14 modifications in DTPs.	80
Figure 4.13 Changes in histone H3K18K23 modifications in DTPs.	81
Figure 4.14 Changes in histone H3.1/3.2K27K36 modifications in DTPs.	82
Figure 4.15 Changes in histone H3.3K27K36 modifications in DTPs.	84
Figure 4.16 Changes in histone H3K79 modifications in DTPs.	85
Figure 4.17 Immunoblot analysis of H3 variants in parental and CMPD1-tolerant persisters.	86
Figure 4.18 Immunoblot analysis of H3 methylation in parental and CMPD1-tolerant persisters.	87
Figure 4.19 Immunoblot analysis of H3 cleavage in parental and CMPD1-tolerant persisters.	88
Figure 5.1 histone H3 lysine methyltransferases and their sites of action.	95
Figure 5.2 histone H3 lysine demethylases and their sites of actions.	97
Figure 5.3 Transcript levels of histone lysine methyltransferases in CMPD1-tolerant FPW1 cells.	101
Figure 5.4 Transcript levels of histone lysine methyltransferases in CMPD1-tolerant RK11 cells.	102
Figure 5.5 Transcript levels of histone lysine demethylases in CMPD1-tolerant FPW1 cells.	104
Figure 5.6 Transcript levels of histone lysine demethylases in CMPD1-tolerant RK11 cells.	105
Figure 5.7 Confirmation of KDM4D and KDM4E transcript changes in drug-tolerant cells.	106
Figure 5.8 Effect of epigenetic probes on the viability of parental and drug-tolerant cells.	108
Figure 5.9 Assessment of FPW1 cell sensitivity to KMT and KDM inhibitors.	109
Figure 5.10 Assessment of RK11 cell sensitivity to KMT and KDM inhibitors.	110
Figure 5.11 Assessment of FPW1 cell sensitivity to orthogonal KMT6 inhibitors.	112
Figure 5.12 Assessment of RK11 cell sensitivity to orthogonal KMT6 inhibitors.	113

Figure 5.13 Chou-Talalay analysis of CMPD1 and epigenetic probes in combinations.	114
Figure 5.14 Long-term effect of KMT and KDM inhibition on glioblastoma cell proliferation.	116
Figure 5.15 Long-term effect of KMT and KDM inhibition on DTP survival.	117
Figure 5.16 Effect of KMT and KDM inhibition on CMPD1-tolerant FPW1 cell recovery.	118
Figure 5.17 Effect of KMT and KDM inhibition on CMPD1-tolerant RK11 cell recovery.	119
Figure 5.18 Levels of CTSL1 expression in parental and CMPD1-tolerant cells.	120
Figure 5.19 Effect of CTSL inhibition on DTP survival.	121
Figure 5.20 Structural comparison of KMT6 inhibitors.	122
Figure 6.1 Demethylation reaction by KDM4 enzymes.	127
Figure 6.2 Binding sites of KDM4 inhibitors.	129
Figure 6.3 Measuring KDM4A demethylase activity using AlphaScreen technology.	130
Figure 6.4 Validating H3(1-21) K9(Me3)-biotin peptide and antibody specificity.	132
Figure 6.5 Assessing the integrity of KDM4A preparations.	134
Figure 6.6 Assessing the activity of KDM4A enzymes by RapidFire mass spectrometry.	135
Figure 6.7 Determining the optimal H3K9(Me2) antibody concentration.	135
Figure 6.8 Effect of BSA on KDM4A inhibition by QC6352.	136
Figure 6.9 Heterocyclic core structures of compounds screened for KDM4 inhibition.	137
Figure 6.10 IC₅₀ values of identified KDM4A inhibitor hits.	145
Figure 6.11 Hypothetical molecular docking of benzothiazinone and benzoxazinone.	148
Figure 6.12 Coomassie Blue staining of SDS-PAGE gels of prepared protein samples.	150
Figure 8.1 Mechanisms of cancer cell resistance to therapy.	155
Figure 8.2 Summary of main findings.	157
Figure 8.3 Pharmacological approaches to targeting drug-tolerant persister cells.	160

List of tables

Table 1.1 Glioblastoma clinical trials of failed kinase-targeted therapeutics.	11
Table 1.2 The molecular subtypes of glioblastoma and their molecular signatures..	15
Table 1.3 Clinical uses and adverse effects of MTAs.	29
Table 1.4 Known functions of tubulin isoforms in normal tissue and cancer.....	32
Table 1.5 Known aberrations of tubulin PTMs in cancer.....	36
Table 2.1 Pathway alterations of GSC lines.....	41
Table 2.2 Key resources.....	42
Table 4.1 Comparison of antibody- and label-free MS-based techniques.....	68
Table 4.2 Summary of SWATH-MS results.	85
Table 5.1 Reported mechanisms of DTP survival in several cancers.	99
Table 6.1 IC₅₀ values of KDM4 inhibitors using AlphaScreen assays.	137
Table 6.2 Inhibition of KDM4A activity by benzothiazinone analogues 1-10.	139
Table 6.3 Inhibition of KDM4A activity by methyl-benzothiazinone analogues 11-19.	140
Table 6.4 Inhibition of KDM4A activity by benzoxazinone analogues 20-29.	141
Table 6.5 Inhibition of KDM4A activity by dimethylaminopropyl-benzoxazinone analogues 30-35.	142
Table 6.6 Inhibition of KDM4 activity of quinazolinone analogues 36-44.	143
Table 6.7 Inhibition of KDM4A activity by analogues 45-46.....	144
Table 8.1 Reported mechanisms of DTP survival in several cancers (addendum to Table 5.1).	159

Authorship contribution statement

This thesis contains material previously published by the author, Ramzi Abbassi.

Chapter 1: the author wrote the chapter and prepared all the figures.

Dr. Josep Font assisted with creating the molecular model in **Figure 1.6**.
Section 1.5 is being prepared for publication as a literature review.

Chapter 2: the author wrote the chapter and prepared the figure.

Chapter 3: Publication in *ACS Pharmacology & Translational Science* (Abbassi et al., 2019).¹

All experiments were completed by the author, unless otherwise specified, under the supervision of A/Prof. Lenka Munoz.

The author prepared the figures and performed statistical analysis on all data (including supplementary data) and contributed to writing of the manuscript.

Dr. Ariadna Recasens performed the Nuclear-ID Red DNA staining in **Figure 4d**.

Dr. Dinesh Indurthi performed the experiments in **Figure 6a-d** & **Suppl. Figure 6c**.

Dr. Brett Stringer and Profs. Terrance Johns and Bryan Day generated, characterised and provided the primary glioblastoma cell lines.

Chapter 4: the author performed the experiments, wrote the chapter and prepared all the figures.

Dr. Jason Low supervised the experimental design, data acquisition and data analysis of SWATH-MS studies and revised the final draft of this chapter.

Dr. Pengyi Yang performed statistical analysis on SWATH-MS data and generated the heatmaps in **Figure 4.9** & **Figure 4.10**.

An adaptation of **Figure 4.1d** is published in *International Journal of Cancer* (Sterling et al., 2020).²

Chapter 5: the author performed the experiments, wrote the chapter and prepared all the figures.

An adaptation of **Figure 5.2** is published in *International Journal of Cancer* (Sterling et al., 2020).²

Chapter 6: the author performed the experiments, wrote the chapter and prepared all the figures.

Dr. Anthony Tumber aided with AlphaScreen assay optimisation and performed RapidFire-MS experiments with the author.

Dr. Jennifer Baker and Prof. Adam McCluskey synthesised the compounds tested in AlphaScreen assays.

Dr. Jennifer Baker revised the final draft of this chapter.

Chapter 7: Published manuscripts to which the author has contributed. A preamble details the author's contribution to each publication.

Chapter 8: the author wrote the chapter and prepared all the figures.

A/Prof. Lenka Munoz supervised the PhD candidature and its projects, contributed to their conception and design, and revised drafts of this thesis.

PERMISSION

As primary supervisor for the candidature upon which this thesis is based, I can confirm that the authorship attribution statements above are correct.

As corresponding author for manuscripts used in this thesis, I give permission for their inclusion and confirm that appropriate acknowledgement of authorial contributions has been stated.

A/Prof. Lenka Munoz

Chapter 1

Introduction

CHAPTER 1. INTRODUCTION

1. 1. Glioblastoma tumours

1. 1. 1. Diffuse gliomas

In addition to neurons, the Central Nervous System (CNS) is composed of glial cells such as astrocytes and oligodendrocytes.³ These glial cells play an integral role in supporting neuronal function in the CNS. Astrocytes, for instance, are dendritic star-shaped glial cells that maintain the extracellular environment by removing excess neurotransmitters from synapses, directing neuronal development and maintaining the integrity of the blood-brain barrier (BBB).⁴ Oligodendrocytes, which are morphologically similar to astrocytes with fewer protuberances, myelinate neurons within the CNS and facilitate signal transduction.⁴ Glial cells, their progenitors or neural stem cells can give rise to a group of tumours known as gliomas, which are the most common primary CNS tumours. While many gliomas are benign brain tumours, diffuse gliomas are highly malignant and lethal.⁵

Diffuse gliomas account for 1% of all cancer incidents worldwide but are associated with high morbidity and fatality rates.⁶ In other words, approximately 100,000 people are diagnosed with diffuse glioma every year.⁷ Glioblastomas, the most aggressive diffuse gliomas, account for 78% of all diffuse glioma incidents.⁸ The World Health Organization (WHO) classifies diffuse gliomas into three grades of malignancy (WHO Grade II-IV), which are assigned based on proliferative potential, angiogenesis, necrosis, nuclear polyploidy and response to therapy.^{9, 10} Moreover, as of 2016, the WHO categorises adult diffuse gliomas of oligodendroglial or astrocytic origins into five principal molecular subtypes, each with a distinct clinical course. Whereas the preceding WHO 2007 classifications of diffuse gliomas were based on histopathological characteristics alone,⁹ the 2016 counterparts aim to eliminate the resulting interobserver variability within clinicians and oncologists by incorporating genotypic as well as phenotypic characteristics of tumours.¹⁰ This new classification system allows for a more rigorous, accurate and reproducible diagnostic process.

The five WHO 2016 clinical subtypes (**Figure 1.1**) of adult diffuse gliomas are based on whether the specific tumour morphology, *i.e.* oligodendroglial or astrocytic, exhibits: (i) mutations in isocitrate dehydrogenase (*IDH1 / IDH2*) genes, (ii) the co-deletion of chromosome arms 1p and 19q (1p19q), (iii) mutations in the telomerase reverse transcriptase (*TERT*) promoter, and (iv) mutations in tumour suppressor gene, *TP53*.¹⁰⁻¹³ In all diffuse gliomas, a mutation in *IDH* is associated with higher median survival.^{11, 14} *IDH* mutations are associated with 1p19q co-deletion in oligodendrogliomas, and with *TP53*

mutations in astrocytoma (including glioblastoma), suggesting that a mutation in *IDH* is the preceding event in both situations.^{14, 15} Additionally, more recent evidence suggests a clinical value in assessing the status of *TERT* and its functional paralogue Alpha-Thalassemia/mental Retardation syndrome X-linked (*ATRX*).¹⁶ Both *TERT* and *ATRX* are epigenetic enzymes that play a role in telomere length maintenance. Alterations in these two genes lead to a genetic lengthening of telomeres, which plays a central role in gliomagenesis¹⁷ and is associated with a five-fold increase in the risk of developing glioma.^{16, 18}

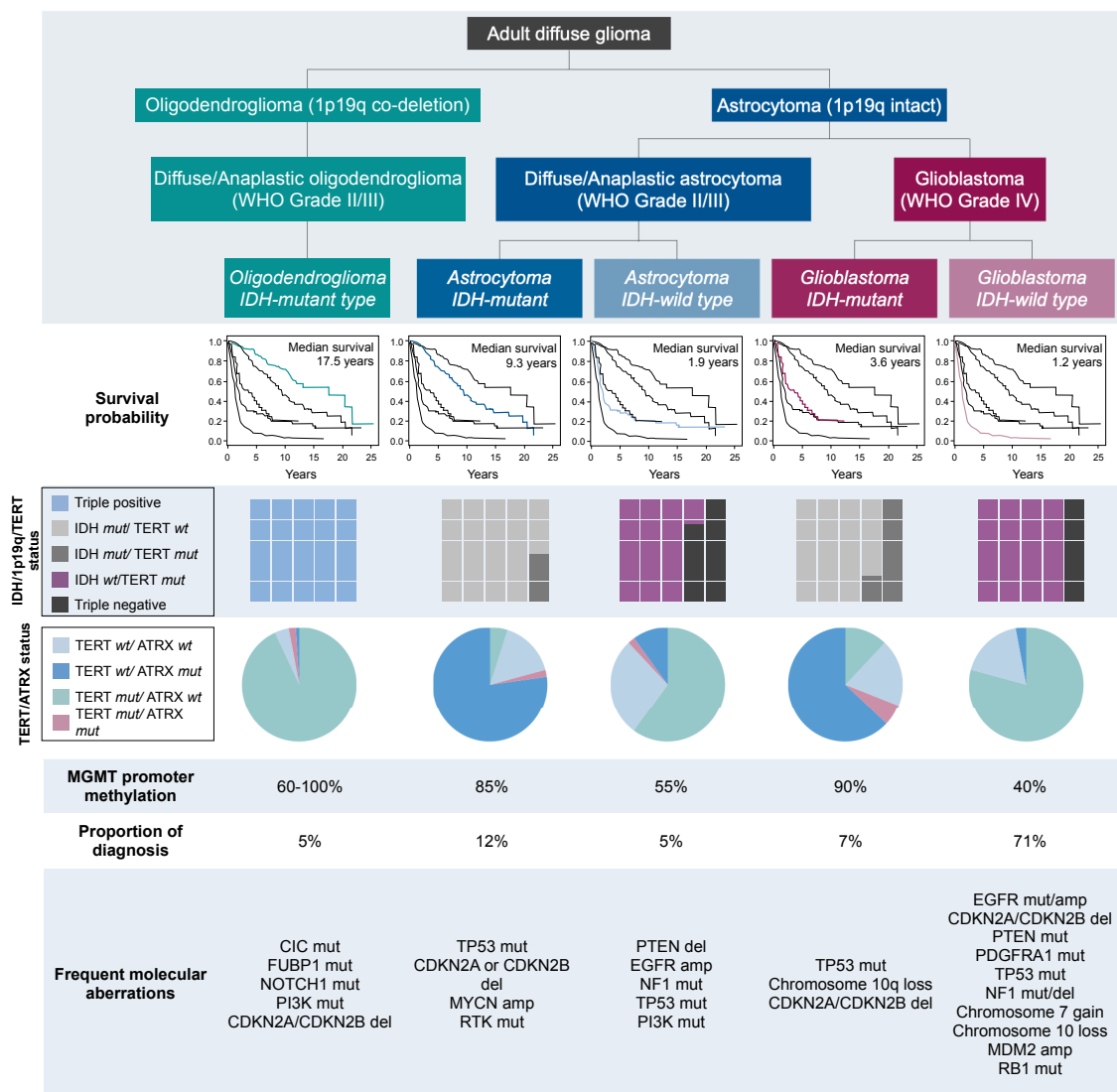


Figure 1.1 The WHO 2016 clinical classification system for adult diffuse gliomas.

Diffuse glioma can have astrocytic or oligodendroglial morphology. To increase the accuracy of diagnosis, the WHO developed a classification system based on molecular characteristics such as the deletion of chromosome arms 1p and 19q, and mutations in *IDH* and *TERT* among other molecular aberrations. These molecular markers (*IDH*/1p19q/*TERT*) can be used in diagnosis, predicting response to therapy and prognosis. Kaplan-Meier survival curves show data from 1989-2012.¹⁹ Figure adapted from REF¹² (*wt*: wild-type; *mut*: mutation, *amp*: amplification; *del*: deletion).

Oligodendrogliomas

The first subtype *Oligodendroglioma, IDH-mutant* includes both diffuse (WHO Grade II) and anaplastic oligodendroglioma (WHO Grade III), which tend to be the least aggressive, with a median survival of 17.5 years.²⁰ Up to 80% of oligodendroglioma possess a co-deletion of 1p19q, while more than 95% will possess a promoter mutation in *TERT*. In rare cases, oligodendroglioma can express *TERT* wild-type, but these have a significantly poorer prognosis.¹³ As such, oligodendrogliomas are generally triple-positive for the loss of *IDH/1p19q/TERT* promoter. The co-deletion of 1p19q, which is often accompanied by a mutation in *IDH*, is a unique diagnostic, therapy-predictive and prognostic biomarker used to distinguish oligodendroglioma from astrocytoma, and is associated with favourable prognosis.¹³ *ATRX* mutations are rare in oligodendroglioma (< 3%).¹⁶ *Oligodendroglioma, IDH-mutant* often harbour mutations in Capicua transcriptional repressor (*CIC*), Far Upstream element Binding Protein 1 (*FUBP1*) and *NOTCH* genes, which are all involved in regulating cell differentiation.^{21, 22} These molecular signatures are clinically useful when the morphological and genotypic observations are discordant, in which case, the molecular diagnosis takes precedence.

Astrocytomas

Diffuse (WHO Grade II) and anaplastic (WHO Grade III) astrocytomas are progressively more aggressive and are classified into *Astrocytoma, IDH-mutant* or *Astrocytoma, IDH-wildtype* subtypes, with median survivals of 9.3 and 1.9 years, respectively.²⁰ Glioblastoma is the most malignant type of astrocytic glioma and accounts for almost 80% of all diffuse glioma diagnoses.²³ Glioblastoma tumours (WHO grade IV) are classified into *Glioblastoma, IDH-mutant* and *Glioblastoma, IDH-wildtype*, with median survivals of 3.6 and 1.2 years, respectively.^{10, 24} Glioblastoma remains to be one of the most challenging and lethal cancers with a 5-year survival rate of 5%.^{20, 25}

The majority of *IDH* wild-type astrocytomas and glioblastomas are associated with *TERT* mutations, while *IDH*-mutant tumours are more likely to be associated with *ATRX* mutations (**Figure 1.1**).¹¹ There is, however, no clear association between *TERT/ATRX* status and survival in *Astrocytoma, IDH-mutant* and *Glioblastoma, IDH-mutant*.¹⁹ By contrast, *Glioblastoma, IDH-wildtype* tumours that have *ATRX* mutations and *Astrocytoma, IDH-wildtype* tumours that lack *TERT* mutations were associated with better survival.¹⁹ These results show that characterisation of *TERT* and *ATRX* genes may be warranted for a more individualised treatment, assessment of histological features and *IDH/1p19q* status. Other critical molecular aberrations are outlined in **Figure 1.1**.

Other diffuse gliomas

A sixth subtype, *Diffuse glioma, Not Otherwise Specified*, was added to allow for the classification of tumours for which *IDH* status cannot be thoroughly evaluated or if a diagnosis is inconclusive. This subtype also allows for the addition of other categories, if and when better diagnostic markers are implemented in the future.^{10, 12} Paediatric diffuse intrinsic pontine gliomas and adult diffuse gliomas occurring in midline locations, such as the spinal cord, brainstem, cerebellum and thalamus, are grouped into a seventh subtype, *Diffuse midline glioma, H3K27M-mutant*. Gain-of-function mutations in the histone H3 genes *HIST1H3B*, *HIST1H3C*, *HIST1H3I* and *H3F3I* resulting in a lysine-to-methionine substitution at position 27 (K27M) characterise these tumours.^{10, 12}

1. 1. 2. Glioblastoma prevalence and risk factors

The risk of glioblastoma increases with age, with peak incidences in people aged over 75 years.⁸ *Glioblastoma, IDH-wildtype* tumours tend to occur in older individuals with a median age at diagnosis 59 years, while *Glioblastoma, IDH-mutant* affect a younger demographic with a median age at diagnosis of 38 years (Figure 1.1).⁸

The prevalence of glioblastoma varies across the sexes. Men have a 1.6-fold increased risk of developing glioblastoma compared to women.⁸ Survival data analysis revealed higher responsiveness to standard-of-care therapy in females compared to males.²⁶ The molecular differences between males and females are not yet fully elucidated, but evidence suggests a sexually dimorphic inactivation of the retinoblastoma gene *RB1* could underly the increased risk of in a subset of glioblastoma male patients.²⁷ Furthermore, glioblastoma prevalence varies across racial groups. Non-Hispanic Caucasian populations were 30-50% more likely to develop glioblastoma and had a lower 5-year survival rate compared to African, Asian, Pacific Islander and Hispanic populations.²⁸

The majority of glioblastomas occur sporadically and with no known cause, but 5-10% are linked to familial history. In those cases, first-degree relatives of patients diagnosed with glioblastoma were twice as likely to develop the disease themselves.²⁹ Genome-wide association studies identified 11 heritable germline risk factors for glioblastoma. These risk alleles contain single nucleotide polymorphisms in several chromosome locations such as 5p15.33 *TERT*, 20q13.33 *RTEL1* (Regulator of Telomere Elongation helicase 1), 7p11.2 near *EGFR*, 7p11.2 *EGFR*, 9p21.3 *CDKN2A/CDKN2B* and

17p13.1 *TP53*.^{11, 30} Although the protein products of most of the genes in those locations are implicated in glioblastoma signalling pathways (discussed in **Section 1.2**), whether these single-nucleotide polymorphisms contribute to phenotypic consequences is yet to be confirmed. Other genetic diseases such as Li-Fraumeni syndrome and neurofibromatosis can increase the risk of glioblastoma.³¹

The only confirmed environmental risk factor is dose-dependent exposure to ionising radiation, such as that from atomic bombs³² or therapeutic irradiation during childhood used to treat infections or cancers.³³ Ionising radiation used in therapy can increase the risk by up to 3 to 7-fold.³⁴ The risk of glioblastoma is decreased in people with atopic diseases and allergies by up to 40%,³⁵ implicating the role of the immune system in glioblastoma pathology. In conclusion, while both genetic and environmental factors may play a role in disease formation, the majority of glioblastomas occur with no causalities identified.

1. 1. 3. Primary and secondary glioblastomas

Approximately 90-95% of glioblastomas are primary and arise *de novo* with no histological or clinical evidence of precursor lesions. The remaining 5-10% of glioblastomas are secondary, deriving from diffuse or anaplastic astrocytoma.³⁶ This germline-like progression occurs as a result of the accumulation of oncogenic mutations. Primary and secondary glioblastoma are genetically distinct in other ways. There is a strong correlation between the status of *IDH1/IDH2* and the origin of glioblastoma tumours with almost all primary tumours being *IDH*-wildtype, while most secondary tumours are *IDH* mutant. As such, secondary glioblastoma tumours are associated with a slightly better prognosis (**Figure 1.1**).¹⁰

IDH1 (cytoplasmic) and *IDH2* (mitochondrial) are proteins involved in the Krebs cycle, converting isocitrate into 2-oxoglutarate (2-OG). The reaction is coupled with the reduction of nicotinamide adenine dinucleotide phosphate (NADP⁺) to dihydronicotinamide adenine dinucleotide phosphate (NADPH). Mutations in *IDH1* or *IDH2* can disrupt these reactions, resulting in the conversion of isocitrate to R-2-hydroxyglutarate (2-HG) and a net reduction of the antioxidant NADPH.³⁷ *IDH* mutations can contribute to oncogenesis as 2-OG is a co-factor for many enzymes, including most of the histone lysine demethylases (KDMs) and Ten-Eleven Translocation proteins (TETs). KDMs and TETs play an essential role in epigenetic regulation as they demethylate histones and DNA, respectively. Further, 2-HG competes with 2-OG for binding sites on KDMs and TETs, inhibiting those proteins. These inhibitions contribute to global

hypermethylation of the genome and the formation of Glioma CpG Island Methylator (G-CIMP) phenotype, which can impact on glioblastoma response to standard-of-care therapy (discussed below).³⁸

While IDH-mutant oligodendrogliomas or astrocytomas can progress to secondary glioblastomas, *IDH* mutations are not sufficient to initiate gliomagenesis on their own. The acquired mutations past this point will determine the type and progression of the disease. While *PIK3CA/R1*, *CDK4/6*, *CDKN2A/B* and *RB1* gene alterations are typical of primary and secondary glioblastomas, the former is characterised by *EGFR* amplification, *PTEN* mutation and *MDM2* amplification and the latter is characterised by a higher frequency of *TP53* mutations as outlined in **Figure 1.1**.^{11, 14, 15, 30, 39} Moreover, while all glioblastomas exhibit loss of heterozygosity at chromosome 10, only primary glioblastomas exhibit gain of chromosome 7.¹⁰ In summary, primary and secondary glioblastomas have distinct pathologies and, therefore, require different treatment courses.

1. 1. 4. Standard-of-care therapy

Glioblastoma cells proliferate diffusely into the brain parenchyma, rendering complete surgical elimination impossible.⁴⁰ The current standard-of-care treatment post-surgery, known as the Stupp protocol, involves treatment with concomitant radiation and chemotherapy with temozolomide for six weeks, followed by six cycles of adjuvant temozolomide treatment.^{25, 41} This protocol increase the median survival from 12 to 15 months compared to radiotherapy alone.⁴¹ Recently, low-intensity tumour-treating fields, a new therapeutic modality applied to the entire scalp, has been shown to improve patient survival from 15 months to 21 months, in combination with the Stupp protocol.⁴² Low-intensity tumour-treating fields are approved for the treatment of both new and recurrent glioblastomas.⁴³

The G-CIMP phenotype is a result of an epigenetic reprogramming that impacts on overall patient survival and treatment outcomes. Hypermethylation of CpG islands containing the O₆-methylguanine-DNA methyltransferase (*MGMT*) promoter region causes repression of gene and decrease in protein expression. *MGMT* is a DNA-damage repair protein, and its inactivation has important implications in glioblastoma. The DNA-alkylating agent temozolomide is the standard-of-care therapeutic in glioblastoma; however, *MGMT* can repair temozolomide-induced DNA double-strand breaks. Thus, *MGMT* promoter methylation is associated with better prognosis, survival and increased sensitivity to temozolomide.^{41, 44} Studies have demonstrated a link between IDH mutation

and MGMT promoter methylation, though the two are not mutually inclusive and can independently have favourable outcomes on prognosis.⁴⁵ Approximately 40% of *Glioblastoma, IDH-wildtype* (primary) and 90% of *Glioblastoma, IDH-mutant* (secondary) express MGMT promoter methylation (**Figure 1.1**).^{46, 47} MGMT methylation status remains an important predictor of response to chemotherapy with temozolomide. In particular, patients aged over 65 with no MGMT promoter methylation do not show benefit from treatment with temozolomide and radiotherapy compared to radiotherapy alone. Therefore, these patients are treated with radiation only.^{41, 44, 48} MGMT status is one example that highlights the genetic and epigenetic heterogeneity of glioblastoma tumours and the need for personalised treatment regimens.

1. 2. Molecular alterations in glioblastoma

In 2008, glioblastoma was the first tumour to be systematically investigated by The Cancer Genome Atlas (TCGA) Research Network.⁴⁹ Extensive genetic sequence analyses of 91 glioblastoma tumours revealed three fundamental pathway alterations: (i) the over-activation of Receptor Tyrosine Kinase (RTK) pathways, (ii) the inactivation of the tumour suppressor p53 pathway and (iii) the inactivation of tumour suppressor retinoblastoma (Rb) pathways (**Figure 1.2**).^{49, 50}

1. 2. 1. Up-regulation of proliferative signals

RTKs control proliferation, invasion, angiogenesis and survival. Consequentially, RTK signalling dysregulation is a common hallmark of all human cancers, including glioblastomas.⁵¹ Up to 90% of all glioblastomas exhibit up-regulation of RTK signalling.^{49, 50} When RTKs are activated by growth factors, they dimerise and auto-phosphorylate, leading to the activation of the small G-protein RAS. RAS, in turn, activates BRAF and the Mitogen-Activated Protein Kinase (MAPK) pathways, which control the cell cycle by regulating Cyclin-Dependent Kinases (CDKs) (**Figure 1.2**). Moreover, RAS activates protein kinase B (Akt1), which in turn stimulates cell proliferation and survival pathways. Neurofibromin 1 (NF1) and phosphatase and tensin homologue (PTEN), regulate these pathways by inhibiting RAS and PI3K, respectively.⁵²

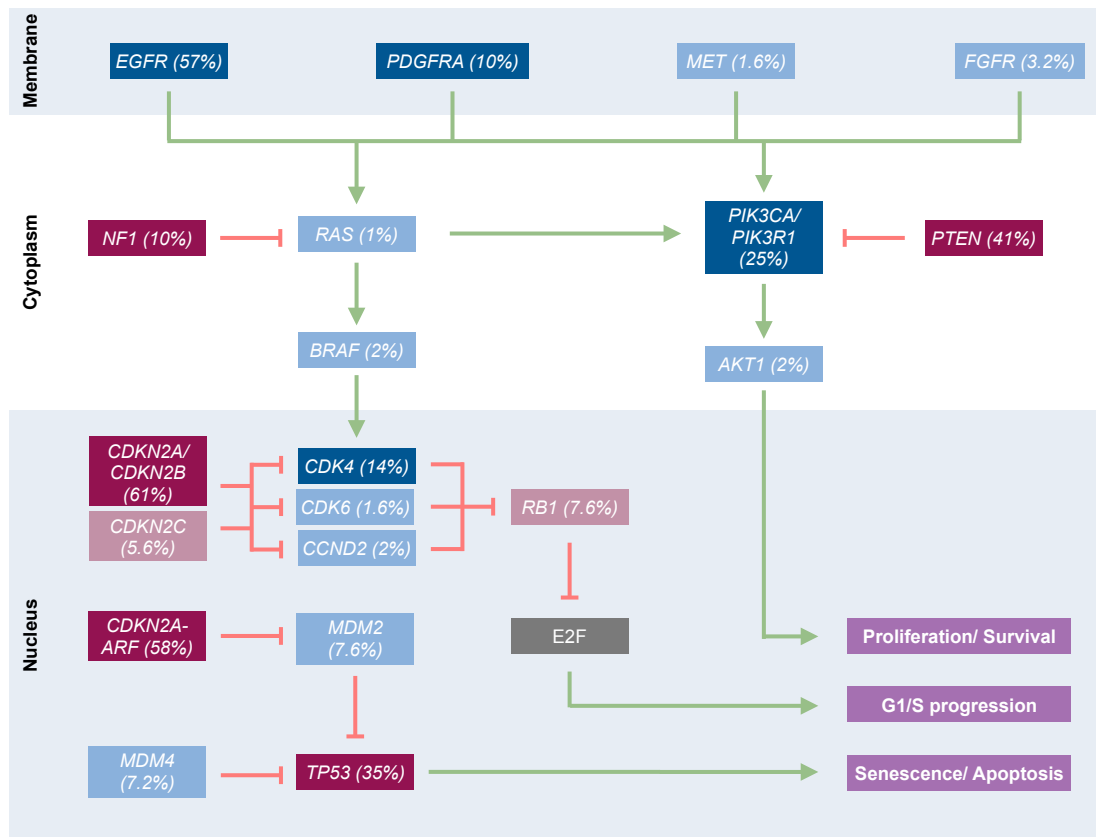


Figure 1.2 Key molecular pathway alterations in glioblastoma.

Next-generation sequencing and genome-wide association studies identified fundamental molecular pathway aberrations that initiate and drive glioblastoma pathology.^{49, 50} These include the up-regulation of proliferative RTK–PI3K–AKT and RTK–RAS–BRAF pathways and the downregulation of tumour-suppressing Rb and p53 pathways. The percentages shown reflect the proportion of glioblastomas that exhibit alterations in these genes. Activating genetic alterations are shown in blue while inactivating alterations are shown in maroon. Deeper shades indicate more frequent alterations than lighter shades.

Gain-of-function mutations or amplifications in RTKs such as Epidermal Growth Factor Receptor (EGFR), Platelet-Derived Growth Factor Receptor (PDGFR), Hepatocyte Growth Factor Receptor (HGFR or c-MET) and Fibroblast Growth Factor Receptor (FGFR) contribute to glioblastoma pathology. The *EGFR* gene exhibits rearrangements, focal-amplification or activating mutations in 57% of all glioblastomas (**Figure 1.2**).^{49, 50} In nearly half of those cases, the EGFRvIII mutant is expressed. EGFRvIII is a result of an in-frame deletion of exons 2-7, which code for the extracellular domain. The lack of the extracellular domain makes the receptor constitutively active and, in turn, results in the overactivation of RAS and PI3K.⁵³ As such, EGFRvIII-positive tumours are associated with poorer clinical outcomes than EGFR wild-type tumours.⁵⁴ This could be in part due to the ability of EGFRvIII to stimulate the growth of EGFR wild-type cells through paracrine signalling, further propagating the tumour.⁵³ EGFRvIII aids in the transformation of neural stem cells and astrocytes into malignant cells.^{55, 56} These findings stimulated research interest in EGFR- and EGFRvIII-targeted therapies for glioblastoma and other gliomas.

Alterations in other RTKs may also contribute to glioblastoma pathology but occur at much lower frequencies (**Figure 1.2**). Up to 10% of glioblastomas exhibit focal amplification of *PDGFRA* gene.⁵⁰ A small percentage of glioblastomas display alterations in *FGFR* (3.2%) and *MET* (1.6%), which encode for FGFR and c-Met, respectively.^{49, 50} Furthermore, the negative regulators of RTK pathways, PTEN and NF1, exhibit gene deletion, gene mutation or epigenetic inhibition in up to 25% and 10% in glioblastomas respectively.³⁸ Loss-of-function in PTEN plays a significant role in PI3K-pathway up-regulation and resistance to RTK inhibitors, as cells expressing this phenotype can bypass RTK-mediated activation of the pathway.⁵⁷ Likewise, NF1 negatively regulates RAS. Hence, alterations in the *NF1* gene can contribute to aberrant activation of the MAPK pathway.⁵⁸ PI3K gain-of-function is a result of alterations in *PIK3CA* and *PIK3R1* which encode for p110 α subunit and p85 α subunit of PI3K, respectively. These alterations in PI3K transpire in 25% of glioblastomas.^{50, 59} RAS or *BRAF* gain-of-function mutations are much less common and occur in 1-2% glioblastomas.^{50, 59} RAS or *BRAF* gain-of-function mutations are much less common and occur in 1-2% glioblastomas.⁵⁰

1. 2. 2. Dysregulation of the cell cycle

Intricate control over the cell cycle is orchestrated by regulatory proteins that mediate proliferation and quiescence. The loss or gain of these regulatory proteins may render the cell cycle vulnerable to over-stimulation by RTK signalling pathways (**Figure 1.2**). The protein retinoblastoma (Rb), a negative regulator of the cell cycle, prevents the transition from G₀/G₁ phases to S-phase by binding to E2F transcription factors.⁶⁰ In normal physiology, Rb is hyperphosphorylated and inhibited by cyclin D-CDK4/6 complexes to allow for cell cycle progression. Inactivating alterations to the encoding *RB1* gene occasionally occur in glioblastomas (7.8%), promoting uncontrolled progression through the cell cycle.^{50, 60} Likewise, gain-of-function alterations in *CDK4* (14%), *CDK6* (1.6%) and *CCND2* (2%), the genes encoding for CDK4, CDK6 and Cyclin-D, respectively, lead to the hyperphosphorylation of Rb, allowing the release of E2F transcription factors and cell cycle progression. Rb hyperphosphorylation can also occur due to loss-of-function alterations in CDK-inhibitor proteins p16^{INK4a}, p14^{INK4b} and p18^{INK4c}. Alteration in the encoding genes *CDK2NA* and *CDKN2B* are present 61% of glioblastomas, while alterations in *CDKN2C* are far less common and occur in 6% of glioblastomas.⁵⁰ Although Rb mutations are not common in and of themselves, dysregulation of the Rb pathways occurs in 79% of all glioblastomas.^{49, 50}

1. 2. 3. Evasion of antiproliferative and apoptotic signals

The tumour suppressor protein p53 is considered as 'the guardian of the genome'.⁶¹ P53 is expressed during cellular stress to control G_0/G_1 arrest, senescence, DNA repair and apoptosis in cells displaying genomic instability.^{62, 63} TP53 loss-of-function occurs in 35% of glioblastomas; it is an early event in gliomagenesis, and particularly in secondary glioblastomas.⁶⁴ One of the most well-characterised targets of p53 is the *CDKN1A* gene, which encodes for the protein p21^{Cip1}, an important CDK2 inhibitor.⁶⁵ While *CDKN1A* mutations do not occur in glioblastoma, p53 loss-of-function alterations undermine p21^{Cip1}, preventing G_0/G_1 arrest and allowing progression through the cell cycle.

The Mouse Double Minute homologs 2 and 4 genes (*MDM2* and *MDM4*) encode for Mdm2 and Mdm4, two proteins which regulate p53. Both proteins bind to and inactivate p53. Mdm2 also possesses E3 ubiquitin ligase activity and can tag p53 for proteasomal degradation, whereas Mdm4 lacks this intrinsic activity.⁶⁶ Hence, gain-of-function alterations in *MDM2* and *MDM4* result in a decrease in p53 activity or p53 levels, making cells susceptible to cell cycle aberration. Amplification of *MDM2* and *MDM4* occur in 7% of glioblastomas.⁵⁰ Furthermore, the alternate reading frame product of the *CDKN2A* gene, p14^{ARF}, is a negative regulator of Mdm2. Deletions of this gene are frequent in glioblastoma (58%), ultimately leading to p53 loss (**Figure 1.2**).⁵⁰ Approximately 86% of all glioblastomas exhibit dysregulation in the proteins involved in p53 pathways.^{49, 50}

1. 2. 4. Kinase-targeted therapy

Since abnormalities in kinase signalling largely contribute to glioblastoma pathology (**Figure 1.2**), and as kinases are druggable protein targets, numerous kinase inhibitors were developed and trialled for the treatment of glioblastoma. Despite the numerous clinical trials, the Stupp protocol remains as the standard-of-care therapy since 2005. The repeated failure of kinase therapy in improving survival outcomes emphasises the urgent need for more efficacious therapeutics. Selected kinase therapies trialled for the treatment of glioblastoma are summarised in **Table 1.1**.

Table 1.1 Glioblastoma clinical trials of failed kinase-targeted therapeutics.

TMZ: temozolomide; RT: radiotherapy.

Target	Drug	Stage	Study Design	Results	REF
EGFR	Erlotinib	Phase II	Non-progressive glioblastoma (n = 43); treatment following RT	Marginal benefit, particularly in patients who developed a rash as an adverse effect	67
		Phase II	Newly diagnosed glioblastoma (n = 65); treatment + TMZ/RT, followed by treatment dose-escalation	Longer survival compared to historical controls	68
	Gefitinib	Phase II	Newly diagnosed glioblastoma (n = 96); treatment following RT	No survival benefit compared to historical controls	69
	Afatinib	Phase II	Recurrent glioblastoma (n = 112); treatment ± TMZ/RT or TMZ alone	Longer median progression-free survival in EGFRvIII+ tumours vs. EGFRvIII- tumours, but limited overall efficacy	70
	Cetuximab	Phase II	Recurrent high-grade glioma (n = 55), monotherapy	Limited anti-tumour activity	71
VEGF	Bevacizumab	Meta-analysis	4 glioblastoma clinical trials (n = 607)	Moderate increase in progression-free survival in combination with chemotherapy compared to monotherapy; no change in overall survival	72
RTKs	Imatinib	Phase II	Recurrent glioblastoma (n = 51), monotherapy	Limited anti-tumour activity	73
		Phase III	Progressive glioblastoma pre-treated with TMZ (n = 240); hydroxyurea ± treatment	Treatment did not increase in progression-free survival	74
	Sunitinib	Phase II	Recurrent glioblastoma (n = 6); monotherapy	Low overall response rate: trial terminated due to lack of efficacy	75
	Dasatinib	Phase II	Recurrent glioblastoma (n = 187); TMZ/RT ± treatment	Treatment did not improve radio-sensitivity, trial terminated before progressing to Phase II	76
		Phase I/II	Newly diagnosed glioblastoma (n = 50); RT ± treatment	Treatment did not improve radio-sensitivity compared to RT only: trial terminated before progressing to Phase II	77
c-MET	Cabozantinib	Phase II	Refractory or recurrent glioblastoma patients (n = 152); monotherapy	Limited anti-tumour activity in recurrent glioblastoma patients naïve to antiangiogenic therapy	78
PI3K	Buparlisib	Phase II	Recurrent glioblastoma (n = 50); monotherapy	Minimal effect of progression-free and overall survival	79
	Sonolisib	Phase II	Recurrent glioblastoma (n = 33); monotherapy	Low overall response rate	59

Since approximately 57% of glioblastomas exhibit gain-of-function alterations in EGFR signalling, small-molecule EGFR inhibitors were extensively investigated in preclinical and clinical trials. Erlotinib and gefitinib are first-generation EGFR inhibitors that reversibly bind to the adenosine triphosphate (ATP) binding pocket, preventing receptor autophosphorylation. Erlotinib and gefitinib both inhibited proliferation of glioblastoma cells *in vitro* and the extent of inhibition positively correlated with levels of

EGFR expression.⁸⁰⁻⁸² Tumour-initiating glioblastoma stem cells were sensitive to erlotinib *in vitro*, but only in *PTEN* and *PIK3CA/PIK3R1* wild-type tumours.⁸² Furthermore, patient-derived xenografts showed a reduction of tumour burden in mouse models,⁸³ expressing *PTEN* wild-type.⁸⁴ In agreement with patient xenograft efficacy, Phase II trials of erlotinib monotherapy following irradiation showed only a marginal benefit for non-progressive recurrent glioblastoma.⁶⁷ Treatment of primary glioblastoma patients with erlotinib in combination with temozolomide and radiotherapy (Phase II) showed an increase in median survival.⁶⁸ The authors of the study proposed that erlotinib may be beneficial only in patients that lack *PTEN* and *PI3K* mutations, and only in combination with the Stupp protocol. However, these findings were not clinically translatable. Likewise, gefitinib inhibited glioblastoma cell proliferation and migration *in vitro*,^{81, 82} and enhanced median survival *in vivo* in intracranial glioblastoma xenograft mouse models. However, Phase II clinical trials demonstrated no benefit for glioblastoma patient survival when treated with gefitinib following radiotherapy.⁶⁹

Afatinib, a second-generation pan-EGFR inhibitor, blocks EGFR isoforms and the EGFRvIII mutant. Unlike the aforementioned EGFR inhibitors, afatinib irreversibly binds to the adenosine triphosphate (ATP) pocket and is, therefore, much more potent. Afatinib inhibited glioblastoma proliferation and migration *in vitro* predominantly via the inhibition of EGFRvIII-cMET heterodimerisation, resulting in a decrease in stem cell markers like the octamer-binding transcription factor 4 (OCT4).⁸⁵ Moreover, co-administration of afatinib and temozolomide decreased tumour growth and progression in mouse models *in vivo* compared to monotherapy with either drug.⁸⁵ However, Phase I/II clinical trials of afatinib showed no improvement in recurrent glioblastoma patients. Nonetheless, afatinib prolonged the median progression-free survival for patients with EGFRvIII-positive tumours compared to patients with EGFRvIII-negative tumours.⁷⁰

In addition to small-molecule inhibitors, monoclonal antibody therapy targeting RTKs have been developed and trialled. Cetuximab is a monoclonal antibody binds to EGFR, which prevents binding of the ligand EGF to its receptor. Cetuximab demonstrated *in vitro* and *in vivo* efficacy. However, it had limited anti-tumour activity in patients with recurrent glioblastoma in Phase II trials.^{71, 86} Bevacizumab, a monoclonal antibody that sequesters Vascular Endothelial Growth Factor (VEGF), is approved for the treatment of recurrent glioblastoma in combination with the DNA-alkylating nitrosourea drug lomustine.^{87, 88} By sequestering VEGF, bevacizumab prevents it from binding to its receptor VEGFR, an RTK that stimulates angiogenesis. Nonetheless, bevacizumab has limited efficacy, partly due to glioblastoma cells adapting to relying on proangiogenic signalling pathways that circumvent VEGF-targeted therapy (Table 1.1).^{72, 89}

Given the redundancy of RTK signalling, several non-selective RTK inhibitors were also trialled. Imatinib inhibits PDGFR and other kinases such as Abelson Murine Leukaemia viral oncogene homologue 1 (c-Abl). Imatinib increased radio-sensitivity of glioblastoma cells both *in vitro* and *in vivo*;^{90, 91} however, it exhibited limited anti-tumour activity as a monotherapy in Phase II recurrent glioblastoma trials.⁷³ Phase III trials testing the efficacy of imatinib in combination with hydroxyurea or alone found no improvement in glioblastoma progression-free survival.⁷⁴ Sunitinib, a dual PDGFR and VEGFR inhibitor, induced apoptosis in glioblastoma cell *in vitro*,⁹² and increased survival in glioblastoma mouse models both as monotherapy and in combination with radiotherapy.⁹³ However, Phase II trials on recurrent glioblastoma demonstrated that sunitinib exhibits limited efficacy both as monotherapy, or in combination with temozolomide and irradiation.^{75, 94} Dasatinib inhibits PDGFR and other RTKs such as the sarcoma proto-oncogene kinases (c-Src). Dasatinib repressed glioblastoma cell viability and motility *in vitro* and tumour growth *in vivo*.⁹⁵ In Phase II trials for newly diagnosed and recurrent glioblastomas, treatment with dasatinib following temozolomide and irradiation had no improvement in clinical outcomes compared to temozolomide and irradiation alone.^{76, 77} Cabozantinib is a c-Met and VEGFR dual-inhibitor, shown to induce apoptosis in endothelial and glioblastoma cells *in vivo*.⁹⁶ A recent Phase II trial indicated that cabozantinib has limited activity in the treatment of recurrent glioblastoma in patients naïve to bevacizumab.⁹⁶

As inhibition of RTKs has seen limited success in glioblastoma, inhibitors of downstream kinases such as PI3K have also been trialled. Buparlisib is a PI3K inhibitor that reduced glioblastoma cell growth both *in vitro* and *in vivo*.^{97, 98} However, buparlisib only showed minimal effect on progression-free survival and clinical outcome in a Phase II trial, which was reasoned to be a result of the incomplete inhibition of PI3K within tumour tissues.⁷⁹ Sonolisib is a more potent inhibitor of PI3K and also inhibited angiogenesis and invasion of glioblastoma cells *in vitro* and extended survival of glioblastoma mice models *in vivo*.^{99, 100} Despite these encouraging results, a Phase II trial of sonolisib demonstrated that the drug is inefficacious in recurrent glioblastoma.¹⁰¹

In conclusion, although EGFR and other kinases are crucial for glioblastoma proliferation and survival, kinase-targeted therapies have repeatedly seen a limited improvement of patient survival at best, and only within specific subgroups of patients. This failure is, in part, attributed to the ability of tumour cells to maintain RTK-signalling through reliance on other redundant RTKs not inhibited by the drug, the up-regulation of downstream signal-transduction proteins, or the downregulation of tumour suppressors that negatively regulate RTK signalling.¹⁰²⁻¹⁰⁵ RTK-targeted therapy has also failed due

to the functional redundancy and compensatory capacity of several RTKs, the expression of constitutively active EGFRvIII-mutants which circumvents EGFR inhibition, or the presence of dormant cells that do not rely on RTK signalling for survival.¹⁰⁶

1. 3. Challenges in glioblastoma therapy

As a result of the mutations that occur at different frequencies in glioblastomas (**Figure 1.2**), the molecular signatures of glioblastoma tumours vary significantly across patients (intertumour heterogeneity).¹⁰⁷ The existence of subpopulations of cells that acquire distinct molecular aberrations and varying degrees of stemness and differentiation (intratumour heterogeneity) further complicates treatment standardisation.¹⁰⁸ This tumour heterogeneity poses significant challenges to molecularly-targeted treatment of glioblastoma as some populations may possess innate resistance or develop adaptive resistance to therapy.^{109, 110}

1. 3. 1. Intertumour heterogeneity

Integrated genomic analysis of glioblastoma tumours by the TCGA identified three clinically relevant transcriptomic subtypes of glioblastoma characterised by unique molecular signatures: *proneural*, *classical* and *mesenchymal* subtypes. These signatures are supported on a transcript and protein levels (**Table 1.2**).^{39, 111, 112} The glioblastoma molecular subtypes are not to be confused with the clinical classification system used in diagnosing diffuse gliomas (**Figure 1.1**).

Proneural glioblastoma is typified by *PDGFRA* gene amplification, *TP53* inactivating mutations and *PI3KCA/PIK3R1* activating mutations, as well as the expression of oligodendroglial and proneuronal markers oligodendrocyte transcription factor 2 (*OLIG2*) and sex-determining region Y-box 2 (*SOX2*). Tumours of this subtype tend to occur in a younger demographic and resemble secondary glioblastoma.³⁹ The classical subtype carries the most common aberrations in glioblastoma such as *EGFR* amplification or truncation (*EGFRvIII*), chromosome 7 amplification, chromosome 10 loss, and *CDKN2A* deletions while lacking alterations in *TP53*, *NF1* and *IDH1*. Finally, the mesenchymal subtype is typified by the expression of epithelial-to-mesenchymal transition marker chitinase-3-like 1 glycoprotein (*CHI3L1*), as well as mutations/deletions in *NF1* and *MET* overexpression. This subtype is associated with higher levels of inflammation and necrosis.³⁹ Other common aberrations in each subtype are listed in **Table 1.2**.^{39, 111, 112}

Glioblastoma subtypes are predictive of clinical outcomes. The proneural subtype is associated with better overall survival compared to the other two subtypes.³⁹ However, in terms of response to standard-of-care therapy, glioblastomas of the classical and mesenchymal subtypes had favourable clinical outcome while the proneural subtype did not benefit from treatment.³⁹ Importantly, MGMT promoter methylation was a favourable prognostic and therapeutic marker regardless of glioblastoma subtype, particularly in older patients.^{39, 48, 111, 112}

Table 1.2 The molecular subtypes of glioblastoma and their molecular signatures.

mut: mutation; amp: amplification; del: deletion.

Subtype	Proneural	Classical	Mesenchymal
Signature	OLIG2 SOX2	EGFR, EGFRvIII AKT1	CHI3L1 MET
Mutations	IDH1 mut TP53 mut PIK3CA/PIK3R1 mut PDGFRA amp	PTEN mut/loss CDKN2A/CDKN2B del Chromosome 7 gain Chromosome 10 loss	NF1 mut/del TP53 mut/loss PTEN mut/loss
Clinical features	Treatment non-responsive	Clinical outcome improved with TMZ + radiation	Clinical outcome improved with TMZ + radiation

1. 3. 2. Intratumour heterogeneity

Although the three transcriptional subtypes have aided understanding of the disease, this classification was based on average gene expression within each patient biopsy sample. Realistically, however, a single glioblastoma tumour consists of several cell types, such as differentiated cancer cells, cancer stem cells, tumour-associated macrophages, endothelial cells and will include varying subpopulations of cells that represent each of the three different subtypes.¹⁰⁷ Tumours with higher degrees of heterogeneity are associated with poorer prognosis and resistance to chemo- and radiotherapy.^{113, 114} Cell subpopulations expressing the EGFRvIII mutant are present in 50% of patients,¹⁰⁸ and mediate resistance to EGFR inhibitors and upregulation of DNA double-strand break repair machinery. Thus, these subpopulations making tumours resistant to targeted RTK therapy and chemotherapeutic DNA damaging agents like temozolomide.^{102, 115} Furthermore, varying RTK types and expression levels across cell subpopulations contribute to the continuous failure of selective RTK-targeted therapy in clinical trials.¹⁰² Cancer cell phenotypes also vary depending on the spatial location of the cells within the tumour and the local microenvironment and tumour cells subvert the activity of neighbouring healthy cells to potentiate disease progression.¹¹⁶ Moreover,

subpopulations within the same tumour possess varying levels of stem cell and differentiation markers, hence, varying sensitivity to therapy across the entire cell population.¹¹⁷

1. 3. 3. Glioblastoma stem cells

Intertumour heterogeneity is potentiated and maintained by cancer stem cells. Glioblastoma stem cells (GSCs) arise from neural stem cells or from differentiated neoplastic cells that, through genetic perturbations, acquire stem-like developmental and survival programs.¹¹⁸ GSCs are characterised by a high expression of stem cell markers, tumour-initiating potential, self-renewal capacity and genetic instability.¹¹⁸⁻¹²⁰ GSCs initiate tumours and recapitulate tumour heterogeneity in mice models,¹¹⁹ and evidence suggests they initiate glioblastoma tumours in patients.¹²¹ GSCs differentiate into several cell types while maintaining their stem cell pool through asymmetric division.^{122, 123}

GSCs maintain a permissive epigenetic landscape that results in the low and fluctuating expression of a large number of genes. The epigenetic permissiveness of GSCs makes them highly adaptable and enhance intratumour heterogeneity.^{114, 117} As a result of this epigenetic plasticity, GSCs drive angiogenesis,^{124, 125} invasion,¹²⁶ chemoresistance,^{127, 128} radio-resistance,¹²⁹ and tumour recurrence.¹²⁸ In other words, the multipotency of GSCs allows them to undergo constant, non-hierarchical and reversible transcriptional fluctuations, which equip them with the ability to adapt to an array of stimuli or stressors such as cell-to-cell interactions, endocrine and paracrine signals, genetic mutations, microenvironmental niches or therapeutic intervention.¹⁰⁸

The adaptability of GSCs gave rise to the theory of 'attractor states.' Attractor states are defined as forces or events that drive GSCs in a constant dynamic flux towards a specific lineage of differentiation (**Figure 1.3**).^{110, 117} Such forces or events include genetic mutations, changes in the microenvironment or exposure to radiation and anti-cancer drugs. As GSCs differentiate, they lose their transcriptional diversity and start expressing fewer genes.¹³⁰ Within each microenvironmental niche, GSCs give rise to diverse subpopulations of progenitor and differentiated cells.¹¹⁷ These populations respond differently to treatment interventions, with some cells being less sensitive than others. The limited efficacy of kinase therapy is attributed to the differences in sensitivity to treatment across the whole cell population.¹³¹

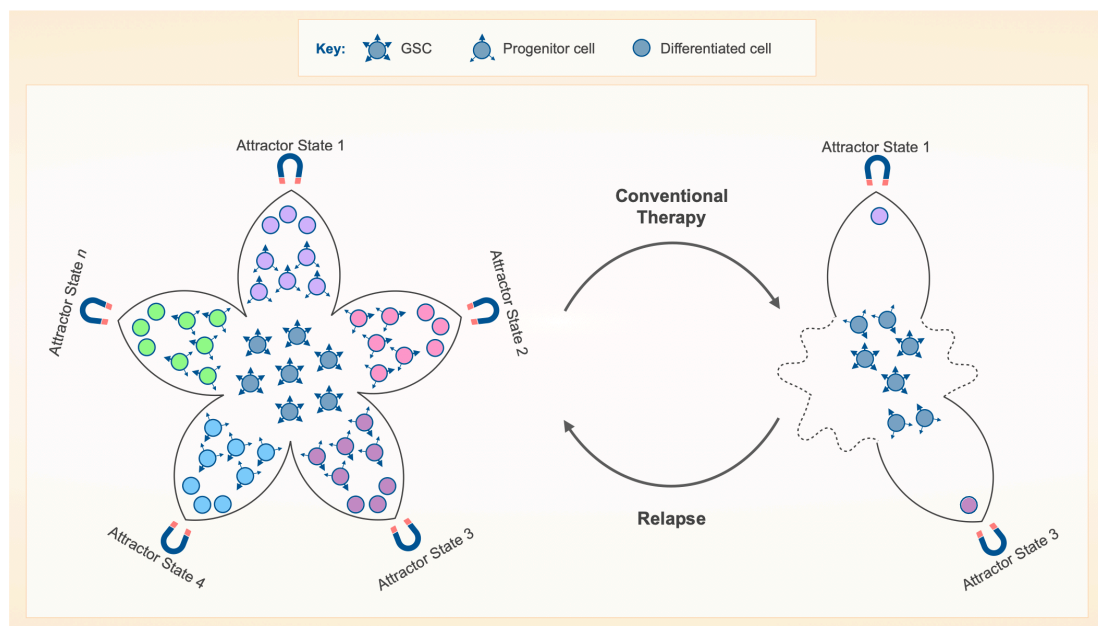


Figure 1.3 GSCs adapt to stressful stimuli by occupying different attractor states.

GSCs sit atop a cellular hierarchy, are epigenetically unstable and adapt to different attractor states, such as hypoxia or the presence of endothelial cells. Therefore, GSCs will differentiate into cell types adapted to suit a microenvironmental niche. GSCs also reconstruct their microenvironment to support and propagate the tumour. This plasticity results in a redundant tumour network that can endure failure due to irradiation or single-agent therapy, like temozolomide or EGFR inhibitors. Current treatments eliminate cells in some, but not all, attractor states. The surviving cells drive the formation of refractory tumours. Figure adapted from REF¹¹⁰.

Microenvironmental niches as drivers of attractor states

Attractor states are exemplified in the three major tumour microenvironments in glioblastoma tumours: the perivascular niche, the necrotic core and the invasive edge.¹³² The perivascular niche is a rich source of nutrients and oxygen for the tumour and is remodelled by the interplay of tumour-associated macrophages, endothelial cells and glioblastoma cells. The tumour core is necrotic, hypoxic and isolated from microvasculature. The invasive edge of the tumour penetrates the brain parenchyma as the tumour grows.^{110, 132} Each microenvironmental niche provides attractor states that promote GSC survival. In turn, GSCs influence other stromal cells within each niche to promote tumour propagation.

The perivascular niche provides attractor states that promote GSC proliferation, stemness, invasion and secretion of proangiogenic factors. Tumour-associated macrophages secrete cytokines that promote the proliferation of GSCs in the perivascular niche.^{133, 134} Endothelial cells maintain GSC stemness via the developmental NOTCH signalling pathway,^{133, 134} and promote GSC invasion by inducing the expression of matrix metalloproteases (MMPs) – proteins that break down the extracellular matrix.¹³⁴ The presence of endothelial cells stimulates the secretion of the proangiogenic VEGF from

GSCs. VEGF, in turn, stimulates endothelial cell proliferation, migration and permeability.¹³⁵ Moreover, GSCs in the perivascular region differentiate into pericyte-like cells, which form and stabilise vasculature for the tumour mass.¹²⁴

The core of the tumour generates attractor states that drive GSC dormancy, survival and stemness. Hypoxia drives the epigenetic reprogramming of GSCs, enhancing survival in oxygen-low and nutrient-deprived environments and the switch to energy-efficient mesenchymal pathways.¹³² The hypoxia-inducible factors HIF-1 α and HIF-2 α primarily drive the mesenchymal switch.¹³⁶ HIF-1 α stimulates VEGF gene transcription in hypoxic cells, driving angiogenesis and recapitulating a new perivascular niche.¹³⁷ On the other hand, HIF-2 α is constitutively activated in hypoxia to maintain cancer cell stemness, by inducing the expression of OCT4 and SOX2.^{138, 139} Furthermore, hypoxia supports radio-resistance as low oxygen levels result in less free radicals, and a failure of radiation to induce double-strand DNA breaks.¹⁴⁰

The invasive edge of the tumour offers attractor states that drive GSC migration, invasion and stemness. GSCs in this niche maintain stemness upregulating Akt signalling.¹⁴¹ They also express a range of MMPs and have enhanced migratory and invasive capacities.¹⁴² Extracellular vesicles released by tumour cells stimulate the secretion of MMP14 from normal microglia; MMP14, in turn, activates MMP2 released from tumour cells, enabling tumour cells to degrade the extracellular matrix and invade other brain regions.¹¹⁶ Complete surgical resection of the tumour is impossible, as GSCs and other tumour cells migrate along vasculature and into the brain parenchyma.⁴⁰

Glioblastoma stem cell dormancy and tolerance to therapy

Even after the multimodal standard-of-care therapy, some glioblastoma cells will lay dormant in one or several attractor states that make them less susceptible to treatment, thereby increasing the potential for tumour relapse (**Figure 1.3**). Cell dormancy describes a period in which a cell remains in a quiescent state, also known as G₀ cell cycle arrest.¹⁴³ Controversy existed surrounding whether dormant cells pre-exist within the tumour population or if their emergence is treatment-induced, with evidence supporting both arguments.

Dormant GSCs have been shown to exist within treatment-naïve tumours and contribute to treatment failure. Dormant and slow-cycling cancer cell populations with stem-like properties predominantly exist within the cores of growing, treatment-naïve tumours, where contextual cues on which cells initially depended, such as oxygen or

growth factors (e.g. EGF, FGF), are absent.^{106, 144, 145} The hypoxic, nutrient- and growth factor-deficient attractor states induce cell dormancy and enable cells to evade the immune system. Dormant cells within the tumour core also contribute to the failure of irradiation and treatment with temozolomide, both of which target rapidly dividing cells.^{131, 138, 146} This type of clonal selection of cells in response to therapy is Darwinian in nature.

On the other hand, in response to stressful stimuli, such as chemo- or radiotherapy, cancer cells may phenotypically switch to a dormant state using non-Darwinian epigenetic mechanisms.¹⁴³ The DNA-damage induced by radiation instigates a proneural-to-mesenchymal switch in GSCs, making them dormant and allowing them to escape therapy. This phenomenon is known as radiation-tolerance.¹⁴⁷ Likewise, treatment with temozolomide induces the expression of stem cell markers in GSCs, resulting in de-differentiation and a phenotypic switch to slow-cycling or quiescence states. This phenomenon is a form 'drug tolerance', wherein cells use non-mutational mechanisms to induce a phenotypic switch that allows them to survive anti-cancer therapy.¹⁴³ Bioinformatic analysis of 136 biopsies of glioblastoma patient treated with radiation and temozolomide revealed a differential expression of 383 genes correlating to overall patient survival. Glioblastoma tumours enriched for genes involved in dormancy and stemness were associated with shorter patient survival.¹⁴⁸ Therefore, understanding the mechanisms by which these cells survive and enter dormancy is integral to developing a cure for glioblastoma.

Hence, both radiotherapy and chemotherapy not only select for cells with a high apoptotic threshold within one or several attractor states but can also act as attractor states themselves, prompting a compensatory phenotypic shift in tumour subpopulations.¹¹⁰ In any case, dormant cells pose a significant threat for tumour reawakening, metastasis and recurrence.¹⁴⁹

Epigenetic mechanisms regulate glioblastoma stem cell dormancy

The remodelling of chromatin coordinates the phenotypic oscillation between quiescence and proliferation amongst tumour cells in response to contextual environmental cues. Chromatin remodelling is a form of epigenetic control of gene expression. Patient biopsies revealed that cells in the perivascular niche possess proneural features and remodel their chromatin using the gene-repressive Polycomb Repressive Complex 2 (PRC2).¹⁵⁰ As a result, the perivascular niche contains fast-cycling proliferative GSCs that depend on anaerobic glycolysis.¹⁴⁶ By contrast, GSCs in the tumour core are

mesenchymal and remodel their chromatin employing PRC1, a Polycomb complex involved in DNA repair and survival.¹⁵⁰ Phenotypically, this makes GSCs slow-cycling and dormant and dependent on non-anaerobic metabolism (lipid oxidation and oxidative phosphorylation).¹⁴⁶ Dual inhibition of the upregulated components of PRC1 and PRC2 eradicated GSCs and prevented tumour sphere formation *in vitro*, suggesting the need for novel therapeutic approaches that target both proliferative and dormant cells.¹⁵⁰

As aforementioned, cell dormancy is temozolomide-induced.¹²⁸ Tolerance to other drugs is also mediated by a phenotypic switch to a dormant state. For example, upon surviving prolonged treatment with the PDGFR/c-Src dual-inhibitor dasatinib, GSCs exhibited the downregulation of the histone lysine demethylase KMT6A, which is part of the PRC2 complex, and the upregulation of the histone lysine demethylases KDM6A/B. These enzymes methylate and demethylate the gene-repressive lysine 27 on histone H3, respectively, thereby remodelling chromatin.¹⁰⁶ This results in a phenotypic switch to a reliance on quiescent NOTCH-signalling proteins compared to their untreated counterparts, which predominantly expressed proliferative RTK-signalling proteins.¹⁰⁶ These cells are examples of drug-tolerant persisters (DTPs), a name given to a subpopulation of cells able to survive high selective pressures created by anti-cancer drugs. Upon drug removal, these dormant cells begin to recover and return to a proliferative state.¹⁵¹ Recovered cells repopulate the tumour and exhibit similar sensitivity to treatment as the primary tumour upon re-exposure.^{106, 144} Hence, the reversibility of dormancy and drug-tolerant states suggest that epigenetic mechanisms, and not irreversible genetic mutations, promote survival and treatment evasion.¹⁴³

In summary, GSCs can use epigenetic mechanisms to induce cell dormancy in response to internal or external stressors and this property is attributed to their permissive epigenetic landscape. The chromatin-remodelling mechanisms conferring drug-tolerant phenotypes vary in response to different treatments and in different cancers.^{106, 144, 145, 152-155} Hence, complete pharmacological eradication of glioblastoma tumours requires elucidation of the drug-specific epigenetic mechanisms that mediate cell dormancy. In this dissertation, epigenetic mechanisms in the context of GSC drug tolerance are investigated (**Chapters 4-5**)

1. 3. 4. The blood-brain barrier

Treatment of glioblastoma is challenged by the presence of highly adaptable stem cells and by the heterogeneity of cellular phenotypes to which they give rise. While cancer stem cells and tumour heterogeneity pose similar challenges in many tumour types, the

drugs used for the treatment of glioblastoma and other brain tumours face another 'barrier' for efficacy. The blood-brain barrier (BBB) is a specialised tight-junction neurovascular unit, formed by endothelial cells, pericytes and astrocytes. The BBB regulates the homeostasis in the CNS while protecting the brain from toxins and other harmful molecules in the systemic circulation. As well as pertaining physical properties that obstruct large and polar compounds, the BBB is equipped with efflux transporters, such as the Multi-Drug Resistant 1 (MDR1) protein, that reduce the bioavailability of drugs within the brain. While glioblastoma tumours increase the permeability in some regions of the BBB, the changes in permeability are heterogeneous, resulting in varying and suboptimal drug delivery to the tumour site.¹⁵⁶ Moreover, both glioblastoma cells and the supporting endothelial cells express higher levels of efflux transporters than their healthy counterparts, further reducing drug bioavailability at the tumour site.¹⁵⁷

In conclusion, intertumour and intratumour heterogeneity, the presence of highly versatile cancer stem cells and the blood-brain barrier all contribute to the limited efficacy of kinase targeted therapy seen in clinical trials. The identification of therapeutics that can cross the BBB, while maintaining therapeutic concentrations, remains a challenge. As a result, increased research interest is directed towards the development of BBB-permeable non-targeted chemotherapeutics for the treatment of glioblastoma.¹⁵⁸ While targeted therapy relies on the inhibition of oncoproteins, non-targeted therapy aims to inhibit critical cellular functions in cancer cells, namely cell division, angiogenesis and invasion, regardless of their genetic background. Non-targeted chemotherapeutic drugs include DNA-alkylating agents like temozolomide or Microtubule Targeting Agents (MTAs) like vinblastine and paclitaxel. MTAs were the first class of drugs developed for anti-cancer therapy and yet remain as some of the most clinically successful drugs to date for the treatment of a variety of cancers.^{159, 160} However, most MTAs have high molecular masses and low lipophilicity and are, therefore, examples of drugs rendered useless for the treatment of brain tumours as they cannot permeate the BBB.^{156, 158, 161} This dissertation assesses small-molecule brain permeable MTAs in patient-derived glioblastoma cell models. Therefore, subsequent sections will discuss microtubule biology and the clinical potential of MTAs for the treatment of glioblastoma.

1. 4. Microtubules and microtubule-targeting agents

Microtubules are polymers of α/β -tubulin heterodimers and are a vital component of the eukaryotic cytoskeleton. Microtubules are essential for cell viability as they are involved in fundamental functions such as signal transduction, motility, cargo transport, cellular

architecture and cell division.¹⁶² MTAs are generally more toxic to cancer cells than normal cells, and microtubules are, therefore, attractive targets for anti-cancer drug development. Particularly, anti-cancer MTAs disrupt the dynamics of spindle microtubules during mitosis, resulting in the cell's inability to separate duplicated chromosomes and ultimately leading to cell death by the activation of apoptotic pathways.^{163, 164} Microtubules carry out their functions by relying on their highly dynamic nature, which enables them to depolymerise and repolymerise rapidly, and an understanding of this property is needed for studying MTA mechanisms of action.

1. 4. 1. Microtubule formation and dynamics

In cells, microtubule formation begins with the *de novo* nucleation of α/β -tubulin heterodimers in Microtubule Organising Centres (MTOCs) – cellular structures responsible for the spatial and temporal control of microtubule assembly. The most well-characterised MTOC is known as the centrosome, which is an organelle that initiates and controls cell division. Additional MTOCs are present in other parts of the cell, such as the Golgi apparatus and in the basal bodies of epithelial cells that possess cilia and flagella.¹⁶⁵ MTOCs contain hundreds of γ -tubulin Ring Complex (γ -TuRC), each consisting of γ -tubulin and other capping proteins.^{162, 166} The γ -TuRCs initiate the process of microtubule nucleation and support microtubule elongation, thereby allowing MTOCs to radiate numerous microtubules within the cytoplasm and perform different functions. For example, the microtubule network growing out of centrosomes during mitosis aid in bipolar spindle formation and coordinate alignment and separation of duplicated chromosomes.¹⁶²

The γ -TuRC stabilises microtubule nucleation and elongation (**Figure 1.4**). Within each γ -TuRC, thirteen γ -tubulin molecules are bound to capping proteins and are arranged to form a single-turn helix to constitute a structural base for the microtubule lattice.¹⁶⁷ The γ -tubulins then bind to incoming α/β -tubulin heterodimers or protofilaments (single-chains of α/β -tubulin dimers) in the cytoplasm. The γ -TuRC stabilises lateral interactions between tubulin heterodimers, which are not otherwise thermodynamically favoured. At critical concentrations of soluble heterodimers, at which soluble tubulin heterodimers are in equilibrium with the growing microtubule ends, elongation of the microtubule rapidly ensues.^{162, 168} The 'minimal stable microtubule seed' is the short tubular structure that can exhibit rapid and thermodynamically favourable polymerisation.¹⁶⁷ The final microtubule lattice is hollow, consists of thirteen protofilaments and spans a diameter of approximately 25 nm.¹⁶⁹ The protofilaments within the microtubule exhibit homotypic interactions, with the exception of the two

protofilaments at the microtubule lattice seam, where β -tubulin from one protofilament binds to α -tubulin on the neighbouring protofilament (**Figure 1.4**).¹⁷⁰

The γ -TuRC plays another role in stabilising microtubules. By binding to and anchoring α -tubulin subunits, the γ -TuRC subjects the highly dynamic β -tubulin subunits to the cytoplasm. As such, microtubules are structurally polar, with the ends exposing β -tubulin growing at much faster rates than the ends that are bound to γ -TuRCs or (if released from the γ -TuRC) expose α -tubulin. The fast-growing end is known as the 'plus-end' while the slow-growing end is the 'minus-end'.¹⁷¹ The polarity of microtubules is integral for the functions of kinesins and dyneins, families of proteins that generally transport cargo towards the plus-end and minus-end of the microtubule, respectively.^{172,}
173

Tubulin polymerisation is GTP-dependent (**Figure 1.5a**). Both the α -tubulin and β -tubulin subunits within soluble heterodimers can bind to GTP. However, only β -tubulin can hydrolyse its GTP molecule to generate guanosine diphosphate (GDP), while GTP bound to α -tubulin is unexchangeable and non-hydrolysable. β -tubulin-mediated GTP hydrolysis occurs after the heterodimer joins a growing protofilament. The time lag between docking and hydrolysis induces a conformational change, resulting in the heterodimer to slightly curve as it joins the microtubule shaft.^{174, 175} The GTP molecules on 'curved' β -tubulin subunits stabilise the growing plus-end, creating what is known as the 'GTP cap' and as β -tubulin hydrolyses GTP, the dimer undergoes a 'curved-to-straight' conformational transition and incorporates into the growing shaft of the microtubule. Consequently, GDP-bound α/β -tubulin heterodimers compose the microtubule shaft.^{174, 175}

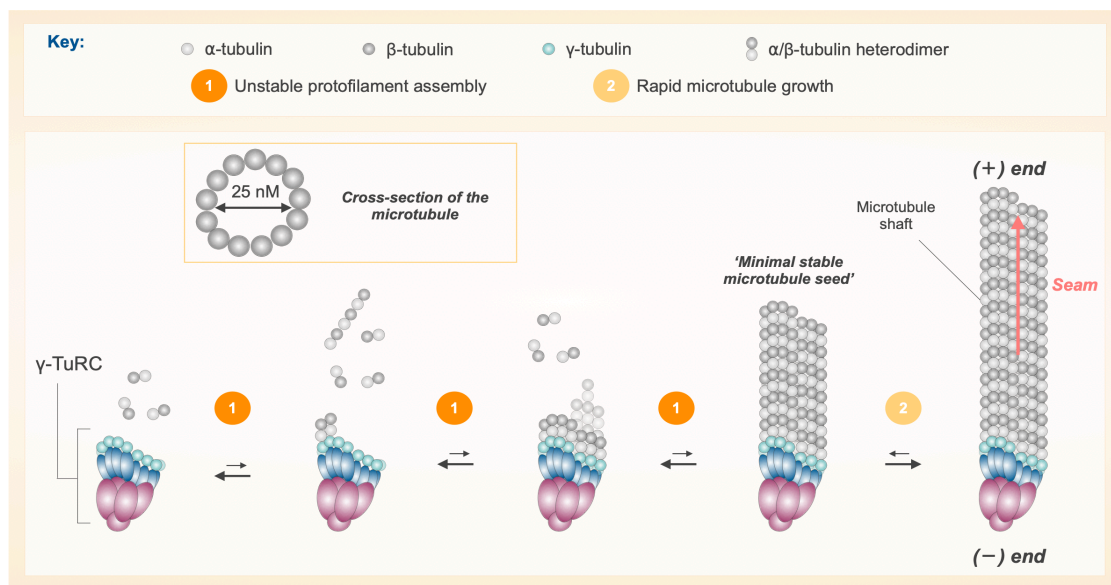


Figure 1.4 Microtubule nucleation and elongation.

The γ -TuRC stabilises the thermodynamically unfavourable nucleation of microtubules. Heterodimers and protofilaments of α/β -tubulin bind to γ -tubulin, gradually forming the shaft of a 13-protofilament microtubule lattice, approximately 25 nm in diameter. Once a minimal stable microtubule seed is formed, rapid elongation ensues. The protofilaments exhibit homotypic interactions within the microtubule, except for the two protofilaments joining at the seam, where heterotypic interactions between α -tubulin and β -tubulin occur.

Microtubules undergo a complex, dynamic chain of reactions and utilise two non-equilibrium dynamic processes known as ‘treadmilling’ and ‘dynamic instability’. Following elongation, the microtubule exhibits phases of net growth (growing phase), no net growth (stationary phase) or net loss (shrinking phase) of α/β -tubulin heterodimers. The term ‘dynamic instability’ refers to the ability of microtubules to oscillate between periods of shrinkage (catastrophe) and growth (rescue) (Figure 1.5a).¹⁶⁰ A stochastic loss of the GTP cap causes catastrophe events, with protofilaments peeling off the microtubule shaft and dissociating into GDP-bound oligomers and dimers.^{134, 143} Recent studies suggest that rescue events may be regulated by remnant ‘GTP-islands’ that were preserved during microtubule growth and not converted to GDP. As the microtubule depolymerises during a catastrophe event, GTP-bound dimers in those islands can instigate re-polymerisation.¹⁷⁶ Treadmilling occurs after the release of the formed microtubule from γ -TuRC and results from a net growth of the plus-end that is greater than or equal than the net shrinkage at the minus-end (Figure 1.5b).¹⁷⁷ This is regulated by microtubule-associated proteins.¹⁷⁸ Both treadmilling and dynamic instability are essential for microtubules to carry out their various functions and MTAs act by inhibiting those properties.

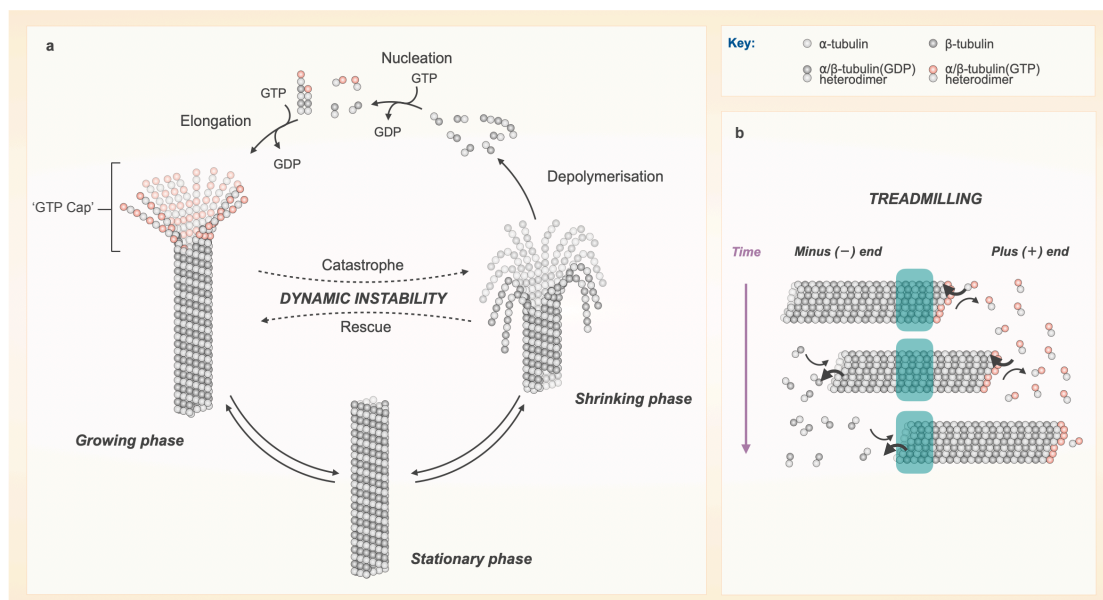


Figure 1.5 Microtubule dynamics.

(a) The α/β -tubulin heterodimer non-covalently polymerise into microtubules with fast-growing (plus) and slow-growing (minus) ends. This polymerisation reaction is dependent on β -tubulin's ability to hydrolyse GTP to GDP, shortly after the heterodimer docks on the growing protofilament. The GTP molecules on α -tubulin act as a stabilising cap (GTP cap). Moreover, microtubules exhibit two modes of polymerisation dynamics. The first mode is dynamic instability, which probably occurs due to a loss or gain of the GTP cap, enabling the microtubule to oscillate between periods of shrinkage (catastrophe) and growth (rescue). (b) In contrast, the second mode is treadmilling, where a net gain of heterodimers at the plus end and a net loss of heterodimers at the minus end enables the microtubule to grow in one direction.¹⁶⁰

1. 4. 2. Microtubule-targeting agent binding domains

A plethora of MTA compounds can inhibit microtubule function. At lower concentrations, all MTAs inhibit microtubule dynamics (namely, dynamic instability and treadmilling), thereby inhibiting mitosis in proliferative cells, without affecting the microtubule mass within cells.^{163, 164} Following MTA treatment, microtubules spend more time in the stationary phase and less time in the growing and shrinking phases (Figure 1.5).¹⁷⁹ However, at higher concentrations, MTAs act via one of two distinct mechanisms: either by stabilising or by destabilising microtubules, resulting in the increase or decrease of total microtubule mass, respectively. As such, MTAs are broadly classified as destabilising agents or stabilising agents.

There are six MTA-binding sites on the tubulin heterodimer. Stabilisers bind to the taxanes- or laulimalide-binding sites, while destabilisers bind to the colchicine-, vinc- , maytansine- or pironetin-binding sites (Figure 1.6a).¹⁶⁹ Ultimately, both stabilising and destabilising MTAs lead to mitotic arrest as cells fail to form mitotic spindle microtubules, resulting in apoptosis in proliferating cells.¹⁶⁰

Stabilising agents such as taxanes (e.g., paclitaxel, docetaxel) and epothilones (e.g., ixabepilone) bind to the taxane-binding site in β -tubulin (**Figure 1.6b**). As the tubulin heterodimer polymerises, the M-loops motifs of both α - and β -tubulin proteins become more structured and stable, facilitating incorporation in the microtubule shaft. However, taxane site agents restructure this disordered M-loop on β -tubulin of soluble dimers into a stable short helix, facilitating premature heterodimer incorporation into the microtubule. Taxane site MTAs are then incorporated into the microtubule lumen, stabilising the microtubule and preventing depolymerisation.¹⁸⁰ In contrast, laulimalide site stabilisers bind to β -tubulin on the outer surface of polymerised microtubules. The laulimalide-domain is situated near the protofilament lateral interface, and so, stabilisers binding to this site act as a clamp that strengthens inter-protofilament interactions.¹⁸¹

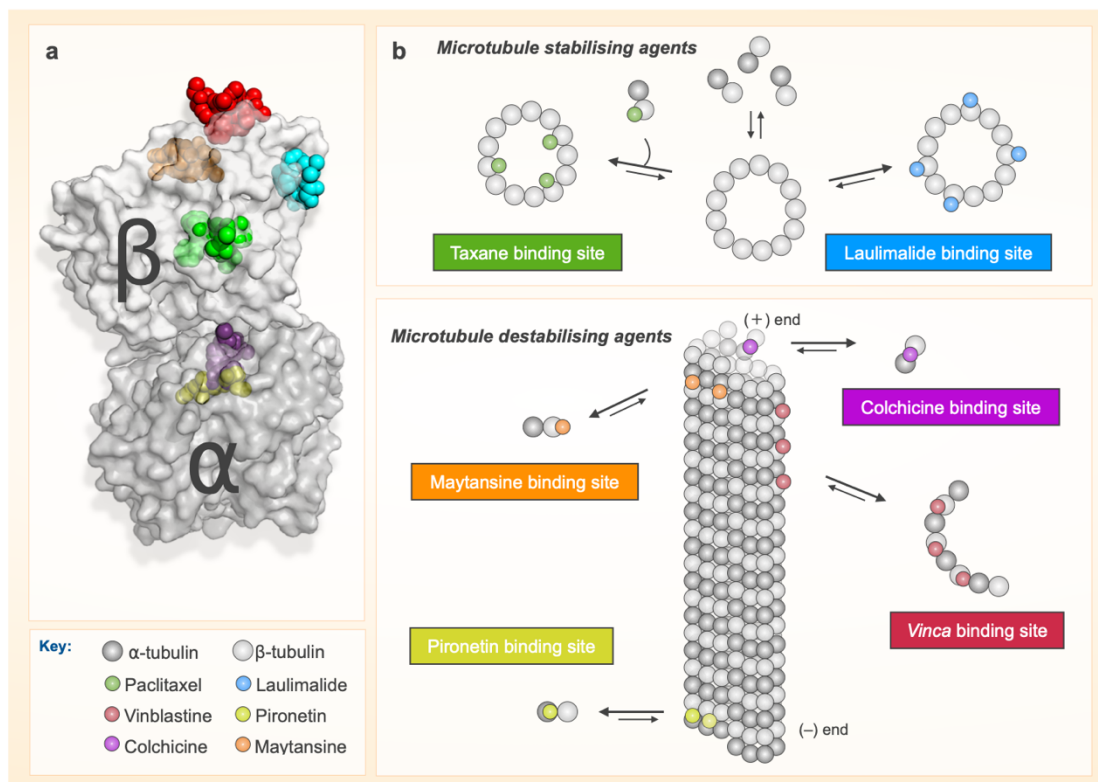


Figure 1.6 Binding sites in tubulin and microtubules.

(a) Molecular model of tubulin binding sites for 6 major MTA drug classes. Data from PDB files: 1SA0 (colchicine), 1Z2B (colchicine/vinblastine), 1JFF (paclitaxel), 4O4H (laulimalide), 4TV8 (maytansine) and 5FNV (pironetin). Model was created using PyMOL (Schrödinger). (b) A cross-sectional view of microtubule showing taxanes- and laulimalide-binding sites of stabilising agents, which occur on the lumen and outer surface of microtubules, respectively. (c) Simplified schematic of binding sites of destabilising agents on soluble tubulin and microtubules.

Colchicine-site destabilising agents that bind on β -tubulin near the intradimer interface, preventing the curved-to-straight conformational transition and decelerating microtubule polymerisation.¹⁸² Pironetin-site MTAs similarly impede microtubule

polymerisation by binding to α -tubulin on soluble heterodimers. Alternatively, they inhibit polymerisation at the minus-end of the microtubule by binding to polymerised α -tubulin.¹⁸³ *Vinca*-site MTAs bind to β -tubulin on the plus-ends of the microtubule between two longitudinal heterodimers, creating a 'wedge' between them. Moreover, they can create the same wedge in protofilaments and oligomers, creating assembly-incompetent ring-like complexes.¹⁸⁴ Lastly, maytansine-site MTAs bind to β -tubulin on both soluble heterodimers and microtubules, inhibiting longitudinal interactions at the inter-dimer interface (**Figure 1.6c**).¹⁸⁵

1. 4. 3. Microtubule-targeting agents in cancer therapy

MTAs have various clinical applications, mainly in the treatment of cancers (**Table 1.3**). In addition to having antimitotic effects on tumour cells, many MTAs are also antiangiogenic, making them cytotoxic to cancer cells.^{160, 164} However, the large molecular mass and polarity of those drugs render them unable to permeate the BBB. Thus, clinically used MTAs are unrealistic candidates for CNS tumour therapy. The immunosuppression and neurotoxicity of MTAs and the acquired resistance in recurrent tumours have limited the success of these drugs.¹⁸⁶ Therefore, hundreds of naturally-occurring and semi-synthetically compounds are tested each year to reduce toxicity and drug resistance.

Taxanes are efficacious in the treatment of numerous tumours (**Table 1.3**).¹⁶⁰ Paclitaxel, a naturally occurring compound in Pacific yew trees, is approved in the treatment of breast, lung and ovarian cancers and off-label for many other tumours.¹⁸⁷ Docetaxel, a semisynthetic analogue, is approved for the treatment of breast and lung cancer. Both paclitaxel and docetaxel are associated with high levels of resistance and toxicity. Taxanes are generally potent substrates for efflux proteins, and their polarity further exacerbates their low bioavailability. Neutropenia (low neutrophil counts in the blood) and neuropathy are the principal adverse effects of paclitaxel and docetaxel.¹⁸⁷⁻¹⁸⁹ Cabazitaxel is a second-generation taxane approved for the treatment of prostate cancers. Neutropenia is common with cabazitaxel treatment, but neuropathy is rare, and other side effects are relatively mild to moderate.¹⁸⁷ Ixabepilone is the only epothilone-derived compound approved for the treatment of refractory cancers that have become resistant to taxanes.^{190, 191} Ixabepilone is associated with less severe side-effects, and efflux proteins do not significantly reduce its bioavailability.¹⁹² Taxane-site MTAs retain their place as the first-line treatment for a variety of tumours.

Vinca alkaloids are highly effective against lymphatic and haematological cancers as well as solid tumours like breast and lung cancers and account for 60% of all cancer drugs currently in use (Table 1.3).¹⁹³ The first-generation *Vinca* alkaloids vinblastine and vincristine, isolated from the Madagascar periwinkle plant, *Catharanthus roseus*, are associated with peripheral neuropathy, neutropenia and myelosuppression.¹⁶⁰ The second-generation vinorelbine is used in the treatment of a wide variety of tumours due to its potent antiproliferative activity and lower toxicity than first-generation *Vinca* alkaloids.¹⁹⁴ A third-generation drug, vinflunine, is used for the treatment of metastatic or advanced urethral cancers and exhibits superior anti-tumour activity than other *Vinca* alkaloids. As such, vinflunine is currently being trialled for a variety of other tumours.¹⁹⁵ Eribulin mesylate, a macrolide that binds to the *Vinca*-site, is approved for the treatment of advanced and metastatic breast cancers and liposarcomas.^{196, 197}

Only one maytansine site MTA drug-conjugate, trastuzumab emtansine, is approved for the treatment of metastatic breast cancer.¹⁹⁸ Trastuzumab is a monoclonal antibody that targets a member of the EGFR family of RTKs, ERBB2. In addition to inhibiting MAPK and PI3K pathways, trastuzumab stimulates the endocytosis of antibody-bound ERBB2, localising the MTA emtansine (or mertansine in its free form) in ERBB2-positive cancer cells and increases median survival by 5 months compared with standard-of-care therapy.^{199, 200} The principal adverse effects associated with trastuzumab emtansine are neutropenia, anaemia and peripheral neuropathy, although they are less frequent and severe in comparison with other MTAs.^{198, 200}

Almost all small-molecule MTAs bind to the colchicine binding pocket on β -tubulin. Small-molecule MTAs such as colchicine and nocodazole have had limited clinical success owing to their severe toxicity. Colchicine is occasionally used in the treatment of gout.²⁰¹ Tivantinib, a well-tolerated and orally bioavailable small-molecule, was initially thought to be a selective c-Met inhibitor. However, further characterisation found that tivantinib exerts its cytotoxic effect mainly by destabilising microtubule dynamics.²⁰² Tivantinib failed as a second-line of treatment for hepatocellular carcinoma overexpressing c-Met in Phase III clinical trials, despite showing promise in Phase II.^{203, 204} As newer generation MTAs have exhibited better anti-cancer activity and less toxicity, research interest is directed towards the development of novel, less toxic MTAs, including BBB-permeable small-molecule MTAs for the treatment of CNS tumours.^{205, 206}

Table 1.3 Clinical uses and adverse effects of MTAs.

Binding domain	Drug	Clinical applications	Possible adverse effects	REFs
Taxane	Paclitaxel	Breast, ovarian, lung and many other cancers	Peripheral neuropathy, myelosuppression, neutropoenia, fatal urinary tract infections, myalgia	187
	Docetaxel	Breast, lung, prostate, stomach, head and neck cancers	Neutropoenia, leucopoenia, thrombocytopenia, anaemia, neuropathy, life-threatening allergic reactions	187, 188
	Cabazitaxel	Hormone-resistant prostate cancer	Neutropoenia, leucopoenia, thrombocytopenia, anaemia, myelosuppression	187, 207
	Ixabepilone	Paclitaxel-resistant breast and endometrial cancers	Neutropoenia, leucopoenia, thrombocytopenia, anaemia, myelosuppression	190-192
Vinca	Vinblastine	Lymphoma, breast, testicular, bladder, prostate cancers	Myelosuppression, neutropoenia, bone pain	193
	Vincristine	Lymphoma, leukaemia, testicular cancer	Myelosuppression, neuropathy, severe constipation	193
	Vinorelbine	Breast and lung cancers	Neutropoenia, anaemia, leucopoenia, thrombocytopenia, neuromyopathy	193
	Vinflunine	Urethral cancer	Neutropoenia, anaemia, leucopoenia, thrombocytopenia, myalgia	193
	Eribulin mesylate	Metastatic breast cancer, liposarcoma	Neutropoenia, anaemia, peripheral neuropathy	196, 197
Maytansine	Trastuzumab emtansine	Metastatic breast cancer	Peripheral neuropathy, thrombocytopenia, anaemia	198
Colchicine	Colchicine	Gout, Familial Mediterranean Fever	Myelosuppression, high toxicity in normal cells	160

Microtubule-targeting agents trialled in glioblastoma therapy

Several MTA compounds were trialled for the treatment of glioblastoma and other brain tumours. In Phase I/II trials patupilone, an epothilone analogue, was well-tolerated and had minimal side-effects in recurrent glioblastoma patients. Furthermore, patupilone accumulated in tumour cells and benefited the progression-free survival of two out of nine patients.²⁰⁸ Another BBB-permeable epothilone analogue, sagopilone, inhibited tumour growth and metastasis in glioblastoma mouse models.²⁰⁹ However, in Phase II trials, sagopilone had no anti-cancer activity and did not improve progression-free survival. Further, it has caused severe neuropathy in almost half of the patients in the trial.²¹⁰ Some of the most promising MTAs currently in clinical development are combretastatin A-4 derivatives – colchicine-site binders that are activated upon exposure to light. This property can be utilised to mediate spatiotemporal control over the activation of these drugs within the tumour and, therefore, limit the adverse side-effects

associated with MTAs.²¹¹ Verubulin, which also binds to the colchicine site, was trialled in combination with carboplatin for the treatment of new and recurrent glioblastoma in Phase I trials.²¹² Phase II trials demonstrated that it is well-tolerated with moderate activity and acceptable toxicity in patients with recurrent glioblastoma.²¹³

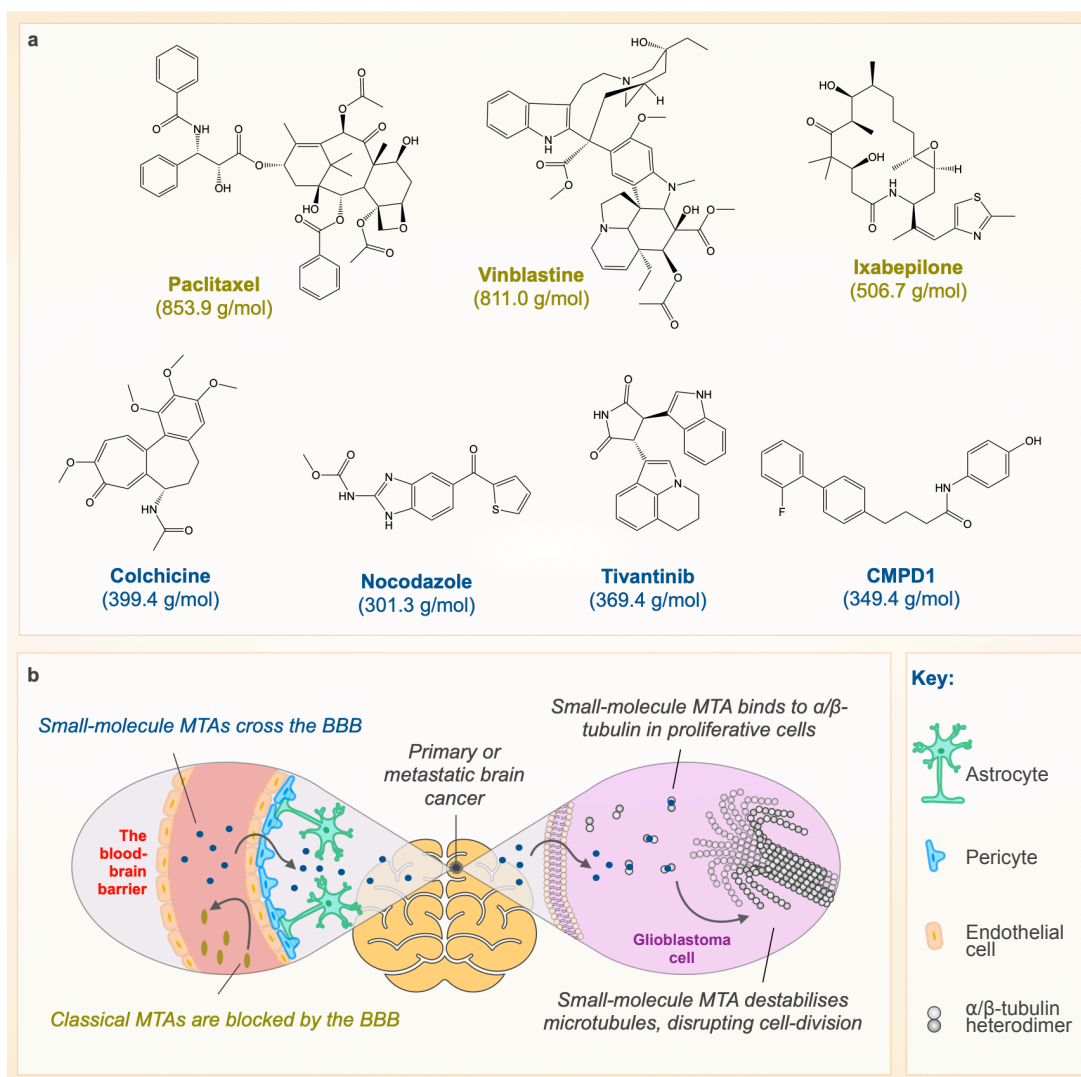


Figure 1.7 Small-molecule MTAs for the treatment of brain cancers.

(a) MTAs come in a range of molecular sizes, and this can alter their ability to cross membranes. CNS active drugs generally have a molecular weight < 400 g/mol. (b) Small-molecule inhibitors such as CMPD1, which can cross the BBB (formed by endothelial cells, pericytes and astrocytic end-feet), are currently being investigated for their potential treatment of gliomas and other CNS tumours.

Preclinical studies for the BBB-permeable CMPD1 and its analogues are underway in our laboratory (Figure 1.7). CMPD1 exhibited selective toxicity to glioblastoma cell lines over normal human astrocytes *in vitro*.²¹⁴ Furthermore, we have shown that CMPD1 and its analogues can be caged with photolabile protecting groups. These chemical groups are cleaved after irradiation.²¹⁵ Hence, we provide a proof-of-concept that small-molecule MTAs can be localised to the tumour site, in a fashion

analogous to combretastatin derivatives. Intriguingly, GSCs of the classical and mesenchymal subtype were more sensitive to CMPD1 treatment than the proneural subtypes,²¹⁶ raising the possibility of the pre-existence or emergence of MTA-tolerant cells to varying degrees in different tumours. Therefore, elucidation of MTA mechanisms of action and resistance in preclinical studies is necessary prior to progressing with clinical trials.

1. 4. 4. The tubulin code in cancer

Microtubular structures and functions are intricately coordinated by various molecular signatures present on tubulin dimers known as the 'tubulin code'. The tubulin code arises from the presence of eight α - and nine β -tubulin isoforms and a multitude of post-translational modifications (PTMs) that can occur on them and controls microtubule dynamics, physical properties and binding-affinity to microtubule-associated proteins.²¹⁷ Different elements of the tubulin code crosstalk to optimise microtubule dynamics in a cell type-dependent and function-dependent manner. Indeed, the tubulin code plays a vital role in fine-tuning cilia and flagella function, muscular function, neural function and cell-cycle control.²¹⁷ In diseases such as cancer, the tubulin code may modulate oncogenic signals, tumour aggressiveness, response to chemotherapy and anti-cancer MTA efficacy.²¹⁸ However, the role of the tubulin code in cancer and other diseases pathologies is yet to be completely elucidated.

Tubulin isoforms

While the tubulin isoforms have highly structured and conserved cores, their C-terminal tails are exceedingly variable (**Figure 1.8a, Table 1.4**).^{217, 219} These differences in tubulin tails impart distinct functions within the isoforms, as evident by cells possessing isoform-dependent specialised microtubule structures and by differential isoform expression throughout developmental stages.²²⁰ For example, the normal marginal band in mammalian platelets, which is essential for platelet structure and function, is made of microtubules constituting of α IV- and β I-tubulins. Deletions of or mutations in either of the genes encoding these isoforms results in a dysfunctional marginal band and hence, bleeding disorders.^{221, 222}

Tubulin isoforms can also regulate microtubule dynamics. Microtubules containing β II-tubulin were more resistant to depolymerisation and less dynamic than those containing β III-tubulin.^{223, 224} In addition, isoforms are tissue-specific. For instance, β III-

tubulin and β IVa-tubulin are predominantly found in the CNS and β III-tubulin is a well-established marker of neural differentiation.^{201, 225} Functionally, β III-tubulin is thought to increase the dynamic instability of neural microtubules, which is necessary for axonal regeneration.²²³

Table 1.4 Known functions of tubulin isoforms in normal tissue and cancer.

Tubulin isoform	Gene Name	Tissue-specific expression	Aberrations in cancer	REFs
α Ia, α Ib, α Ic	TUBA1A, TUBA1B, TUBA1C	All tissue-types	High α Ia associated with paclitaxel-resistance and poorer prognosis in hepatocellular carcinoma and mantle cell lymphoma	226-228
α IIc, α IIId, α IIle	TUBA3C, TUBA3D, TUBA3E	Testis	-	229, 230
α IVa	TUBA4A	All tissue-types	-	230
α VIII	TUBA8	Mainly cardiac and skeletal muscle; low expression in testis and brain	-	231
β I	TUBB	Spleen, thymus and developing brain	Higher β I linked with taxane-resistance in ovarian and breast cancers	232-234
β IIa, β IIb	TUBB2A, TUBB2B	Central and peripheral nervous system	Lower β IIa/b linked with taxane-resistance and correlates with advanced-stage ovarian and breast cancer	232, 235, 236
β III	TUBB3	Neurons	Higher β III linked with taxane-resistance in ovarian, breast, gastric, prostate, uterine and lung cancers; Higher β III linked with better cabazitaxel efficacy in breast cancer cell line	189, 232, 233, 237-242
β IVa	TUBB4	Central nervous system	Higher β IVa linked with taxane-resistance in ovarian cancers	232, 233
β IVb	TUBB2C	Ciliated cells	Lower β IVb linked with taxane-resistance in breast cancer cell line but correlated with increased sensitivity to <i>vinca</i> alkaloids in pancreatic and lung cancer cell lines	232, 243-245
β V	TUBB6	Breast, lung, skin, all muscle cells and secretory epithelial cells	Higher β V linked with better response to taxanes in lung cancers but correlated with malignancy grade of serous ovarian sarcomas	232, 246-249
β VI	TUBB1	Hematopoietic cells	-	232
β VIII	TUBB8	Oocytes and embryos	-	250

Tubulin isotypes may mediate response to microenvironmental stressors. Comparative structural analysis of β -tubulin isoforms demonstrated that the cysteine C239 residue present in β III-, β V- and β VI-tubulin is more readily oxidised than the serine

S239 residue found in other β -isoforms. Oxidation of cysteine C239 inhibits microtubule polymerisation and stability, suggesting that these isoforms may mediate cellular response to stimuli such oxidative stress and hypoxia.²⁵¹ Indeed, hypoxic cores of glioblastoma tumours are marked for higher expression of β III-tubulin.²⁵² However, the mechanisms through which β III-tubulin might contribute to cancer pathology are not entirely elucidated. Several studies propose β III-tubulin as a downstream target of RTK signalling arms (**Figure 1.2**) that may mediate oncogenic signal transduction.²⁵³⁻²⁵⁵

A growing body of evidence suggests that specific tubulin isoforms may be involved in disease pathology and metastasis within specific cancers.^{227, 233, 237, 246, 247} In some cancers, the extent of increase in tubulin isoform expression correlates with tumour aggressiveness and poor clinical outcomes.^{201, 233} In particular, β III-tubulin expression increases in a range of ovarian, lung, uterine, prostate and brain tumours (including glioblastoma) and as such, is the most well-characterised isoform.²¹⁸ Numerous studies have reported that increased β III-tubulin expression is associated with poorer clinical outcomes in breast, ovarian and gastric cancers.^{233, 237, 238, 240} Additionally, β I, β II and β IV-tubulin have altered expression in ovarian, breast and lung tumours (**Table 1.4**).^{233-238, 240, 243} β V-tubulin is highly upregulated in serous ovarian sarcoma, even though it is generally not expressed in normal fallopian tube epithelia.^{248, 249}

Tubulin isoforms may confer resistance to various MTAs (**Table 1.4**). In this context, the less dynamic α -tubulin isoforms are not well-characterised, as only one study suggests that α I-tubulin may confer resistance to paclitaxel.²²⁷ High expression of β III-tubulin is associated with paclitaxel-resistant ovarian cancer, with subsequent studies showing β III-tubulin-mediated resistance to taxanes and *vinca* alkaloids in a wide range of cancers.²¹⁸ *In vitro* studies found that microtubules from heterogenous tubulin fractions were seven-fold more sensitive to paclitaxel treatment than microtubules from containing only β III-tubulin isoform.²⁵⁶ This points to the dynamic nature of β III-tubulin and suggests that it impedes the effect of the stabilising agent paclitaxel on microtubules. In contrast, β III-tubulin protein expression more than doubled in a colchicine-resistant breast cancer cell line, which was paradoxically more sensitive to paclitaxel.²⁵⁷ Another study showed that both β II- and β III-tubulin confer resistance to laulimalide but not paclitaxel or vinblastine in human ovarian carcinoma cell lines.²⁵⁸ β V-tubulin expression positively correlated with response to taxane treatment in non-small cell lung cancers.^{246, 247} These contradictory findings and widely variable tubulin profiles across different cancers suggest that tubulin isoforms modulate sensitivity to various MTAs in a differential manner.

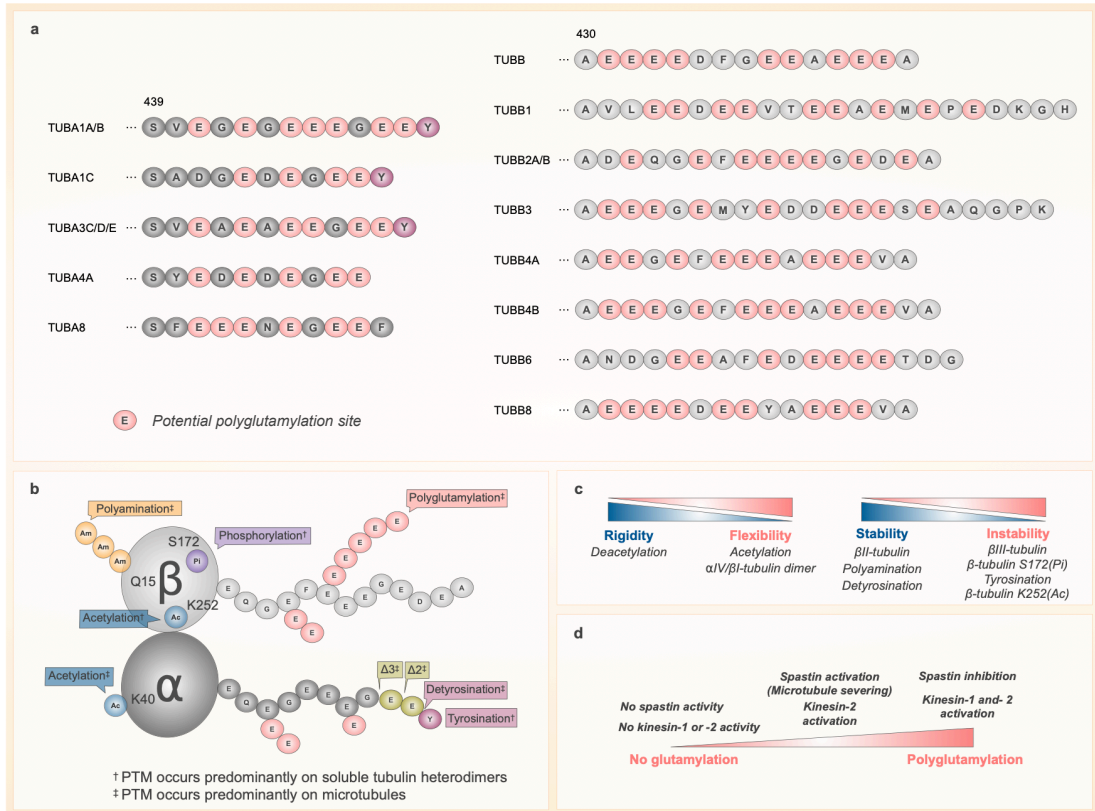


Figure 1.8 Microtubule heterogeneity directs microtubule properties and functions.

The tubulin heterodimer exhibits high levels of molecular diversity. In addition to the presence of (a) 8 α - and 9 β -tubulin isoforms,²⁵⁹ (b) several post-translational modifications (PTMs) can occur on the cores or tails of tubulin subunits and together, these form the tubulin code. (c) Tubulin isoforms and PTMs control microtubule dynamics (stability/instability) and mechanical properties (flexibility/rigidity). (d) Polyglutamylation levels exert differential control on the activity of microtubule-associated proteins such as spastin, kinesin-1 and kinesin-2.

Tubulin post-translational modifications

Both the unstructured tubulin C-terminal tails and the structured tubulin code are susceptible to PTMs (Figure 1.8b). PTMs can regulate microtubule dynamics and overall mechanical structure. For instance, acetylation on lysine residue K40 in α -tubulin in the inner lumen of microtubule protofilaments prevents the interaction between K40 and histidine H238 α -tubulin on adjacent protofilaments.²⁶⁰ Consequently, K40 acetylation facilitates inter-protofilament sliding, making the microtubules more flexible and less resistant to breakage.²¹⁷ K40 is acetylated on microtubules by α -tubulin acetyltransferase 1 (ATAT1)²⁶¹ and deacetylated on soluble tubulin heterodimers by histone deacetylase 6 (HDAC6)²⁶² and Sirtuin 2.²⁶³ Additionally, polyamination of glutamine side chains, by transglutaminases on both α - and β -tubulin incorporated into microtubules, stabilises microtubules, making them more resistant to depolymerisation.^{260,}
²⁶⁴ Other modifications that occur on soluble tubulin heterodimers can conversely slow

down tubulin incorporation and thus favour depolymerisation. These include phosphorylation of serine S172 on β -tubulin by CDK1²⁶⁵ or dual-specificity tyrosine-regulated kinase 1A (DYRK1A)²⁶⁶ or acetylation of K252 on β -tubulin by San acetyltransferase.²⁶⁷ No deaminases, phosphatases or deacetylases are known to reverse these PTMs.²¹⁷

Other PTMs regulate binding to microtubule-associated proteins and can, therefore, indirectly influence microtubule dynamics or mechanical properties. The C-terminal tyrosine of α -tubulin in microtubules is cleaved by the enzymes vasohibin 1 and 2.^{268, 269} This detyrosination is reversed by the enzyme Tubulin Tyrosine Ligase (TTL), which acts predominantly on soluble heterodimers.²⁷⁰ Cytosolic carboxypeptidases irreversibly detyrosinate microtubules by cleaving the penultimate and antepenultimate glutamates, yielding $\Delta 2$ and $\Delta 3$ α -tubulin, respectively.^{271, 272} Detyrosination may indirectly slow down microtubule dynamics by reducing the binding of dynactin subunit 1 or cytoplasmic linker protein 170 (CLIP170), two proteins that localise to and track the plus-ends of the microtubule, inhibiting microtubule catastrophe.²⁷³ Conversely, the KIF2A and mitotic centromere-associated kinesin (MCAK), two proteins of the kinesin-13 subfamily of enzymes that catalyse microtubule depolymerisation and are integral for mitosis, require tyrosinated tubulin to function. Therefore, detyrosination also renders microtubules less susceptible to depolymerisation by kinesin-13 proteins, stabilising microtubules.²⁷⁴ A summary of the components of the tubulin code known to influence microtubular properties is shown in **Figure 1.8c**.

Polyglutamylation (polyE) can occur on both α - and β -tubulin. Addition of glutamyl groups is catalysed by TTL-like enzymes (TTLL), acting preferentially on microtubules.²⁷⁵⁻²⁷⁷ Cytosolic carboxypeptidases deglutamylate both soluble and polymerised tubulin, offering constant control of polyE patterns on polymerised microtubules.²⁷⁸⁻²⁸⁰ Tubulin polyglutamylation, much like polyamination, provides gradual control over microtubules, with chain lengths mediating distinct functions. However, unlike polyamination chains, the length of which correlates to the degree of induced microtubule stability, polyE chains exert biphasic control over microtubules. Spastin, a microtubule-severing enzyme, is initially activated by moderate levels of polyglutamylation.^{281, 282} Nevertheless, past a certain threshold, polyE begins to inhibit spastin activity, and hence, microtubule severing. This mechanism enables cells to control total microtubule mass.²⁸² Similarly, polyE patterns offer differential control over the motor proteins kinesin-1 and kinesin-2, two families of proteins that transport cargo towards the plus-ends of

microtubules. Moderate polyE levels are needed to activate kinesin-2, whereas higher levels are needed for kinesin-1 activity (Figure 1.8d).^{283, 284}

The effects of tubulin PTMs on cancer pathology and MTA efficacy are not well-investigated. Table 1.5 summarises known aberrations in tubulin PTMs in some cancers. For example, an increase in HDAC6 (and hence, decrease in α -tubulin K40 acetylation) correlated with better prognosis in breast cancer and an increase in sensitivity to anti-cancer endocrine treatment.²⁸⁵ Irregularities of the tyrosination-detyrosination cycle have been reported in multiple cancers due to suppression or dysregulation of TTL and were all generally associated with higher malignancy grades, poor prognosis and poor clinical outcomes.²⁸⁶ In agreement, a recent study found that VASH-1 expression positively and significantly correlates with bladder cancer stage, pathological grade and metastasis.²⁸⁷ Together, these data suggest that an increase in α -tubulin detyrosination may negatively impact on patient outcomes. Increases in tubulin polyE are associated with paclitaxel-resistant breast cancer cell lines.²⁸⁸

Table 1.5 Known aberrations of tubulin PTMs in cancer.

Tubulin PTM	Alteration	Cancer	Outcome	REFs
α -K40(Ac)	HDAC6 up-regulation	Breast cancer	Correlates with improved prognosis	285
Tyrosination/ Detyrosination	TTL down-regulation	Several non-epithelial tumours	Decrease in tyrosination augments tumour progression	286
	TTL down-regulation	Breast cancer cell line	Increased detyrosination and polyE on α -tubulin	289
	TTL down-regulation	Prostate cancer	Correlates with aggressiveness and metastasis	290, 291
	Differential TTL expression	Neuroblastoma	Correlates with worse prognosis and clinical outcome	292
Glutamylation	Overall increase in polyE	Breast cancer cell line	Associated with taxane-resistance	288

While significant advances in deciphering the functions of tubulin code have been made over the last decade, the functions of many of its components remain unclear. Furthermore, based on current literature, there is evidence to suggest that the tubulin code can impact on MTA efficacy in a cancer type- and drug class-dependent related manner. For this reason, we investigated the tubulin code in glioblastoma stem cell models to aid in the assessment and development of CMPD1 as an MTA for the treatment of glioblastoma.

1. 5. Thesis aims

The research summarised in the preceding sections suggests that efficacious targeting of glioblastoma tumours requires brain permeable chemotherapy able to target tumour cells regardless of their genetic background. MTAs offer this non-targeted approach. In 2014, our laboratory discovered that the small-molecule inhibitor CMPD1, developed initially as an inhibitor of MAPK-activated protein kinase 2 (MK2), exerted its potent cytotoxic effects via the inhibition of microtubule dynamics, independently of MK2.²¹⁴ Owing to its small size and favourable molecular properties, CMPD1 was a prime candidate for the development of anti-cancer treatment for CNS malignancies. Since then, hit-to-lead optimisation of CMPD1 led to the development of BBB-permeable MTAs.²¹⁶ The most advanced analogue is in preclinical development with commercial partners, and hence, all data related to this drug candidate are commercial-in-confidence. This PhD dissertation studies the efficacy of CMPD1 and other MTAs in patient-derived glioblastoma cell lines, and the mechanisms through which these cells survive high concentrations of MTAs.

The overarching aim of this PhD candidature was to investigate the efficacy of CMPD1 in disease-relevant glioblastoma models in order to establish the therapeutic potential of a novel class of MTAs based on the CMPD1 pharmacophore. The principal aim was to investigate whether the tubulin code of glioblastoma stem cells impacts on MTA efficacy (**Chapter 3**). These studies, published in *ACS Pharmacology and Translational Science* (2019),¹ identified that a subpopulation of glioblastoma tolerant persists survive MTA treatment via non-mutational dormancy. Given that non-mutational dormancy and drug tolerance are driven largely by epigenetic chromatin remodelling, the subsequent studies aimed to investigate global histone modification marks in MTA-tolerant cells using mass spectrometry (**Chapter 4**) and identify druggable epigenetic targets to eradicate MTA-tolerant glioblastoma cells (**Chapter 5**). In parallel, as KDM4 enzymes were highly upregulated in DTPs, and due to the lack of potent KDM4 inhibitors, a high throughput KDM4 inhibitor screening assay was developed using AlphaScreen technology (**Chapter 6**).

Additionally, the work completed during this PhD candidature contributed to the finding that MTAs induce unique cell morphological 'shrinkages,' a characteristic that can guide the identification of microtubules as drug targets or off-targets (published in *Pharmacological Research*, 2018).²⁹³ A colchicine-binding assay was developed to confirm that CMPD1 and its analogue bind to the colchicine-binding domain of tubulin while analogues caged with photolabile protecting groups do not (published in *ACS*

Medicinal Chemistry Letters, 2017).²¹⁵ Lastly, having established a high throughput biochemical DYRK1A kinase inhibition assay during my Honours project (2014),^{294, 295} I screened newly synthesised novel heterocyclic biphenolic analogues (published in *Bioorganic & Medicinal Chemistry*, 2018)²⁹⁶ and flexible azaindole analogues (published in *Australian Journal of Chemistry*, 2018)²⁹⁷ for DYRK1A inhibition. Published manuscripts containing this work are presented in **Chapter 7**.

Chapter 2

Materials and Methods

CHAPTER 2. MATERIALS AND METHODS

2. 1. Experimental models and materials

2. 1. 1. Glioblastoma cell line models

Standard glioblastoma cell lines.

A172, U251 and U87 glioblastoma cell lines were obtained from the European Collection of Cell Cultures (EACC, Salisbury, UK) through Cell Bank Australia in 2014. Cells were cultured in DMEM supplemented with Foetal Bovine Serum (FBS, 10 % v/v) and Antibiotic-Antimycotic solution (both Life Technologies, CA, USA) at 37 °C and 5 % CO₂. All cell cultures were routinely tested for mycoplasma infection, and the cumulative length of culturing did not exceed 20 passages.

Glioblastoma stem cell (GSC) lines.

GSC lines were derived from glioblastoma patient specimens. Characterisation of these cell lines includes RNA sequencing, mutational profiling, subtype assignment and proteomic data which are available online at <https://www.qimrberghofer.edu.au/our-research/commercialisation/q-cell/>. Table 2.1 outlines the genotypes of these cell lines. GSC lines were cultured in KnockOut DMEM/F-12 basal medium supplemented with StemPro NSC SFM supplement, GlutaMAX-1CTS (2 nM), EGF (20 ng/mL), FGF- β (10 ng/mL) and Antibiotic-Antimycotic solution (all Life Technologies) as adherent cells on flasks coated with MatriGel Matrix (Corning Life Sciences, MA, USA). The protocols were approved by the Human Ethics Committee of The University of Sydney (HREC2013/131) and the Human Ethics Committee of the Royal Brisbane & Women's Hospital (RBWH 2004/161). All cell cultures were routinely tested for mycoplasma infection, and the cumulative length of culturing did not exceed 15 passages.

Table 2.1 Pathway alterations of GSC lines.

Single nucleotide variants, intragenic deletions and gene copy number changes in genes in pathways frequently affected by genomic changes in glioblastoma detected in the primary glioblastoma cell lines. SNVs shown in bold are homozygous, otherwise heterozygous. Blanks indicate wild type genes. Adapted from Q-cell (<https://www.qimrberghofer.edu.au/our-research/commercialisation/q-cell/>).

Pathway	Gene	Classical				Mesenchymal				Proneural			
		WK1	PB1	HW1	SB2b	RN1	FPW1	RK1	MN1	JK2	SJH1	MMK1	BAH1
RTK	EGFR			A289V	A289V H304Y								vIII
	MET				C800F	T992I			E168D		H289R V589M R721Q		
	EPHA2												
PI3K	PIK3CA	H1047Y			Y1021H								
	PIK3R1												
	PIK3C2G		X1446S		A2T				P129T				
	PIK3C2A												T1415A
MAPK	PTEN		R130*	<i>Spl jct</i>			R130Q					F56V	V133I
	NF1						<i>Spl jct</i>				<i>Spl jct</i>		
P53	MYC												
	TP53									R110L	G105C		
RB1	MDM2				W329C								
	CDKN2A												
Chromatin modifiers	CDKN2B												
	IDH1				V178I							Y183C	
	ATRX							D808G					
	SETD2	E670K			T451A			R472H					
	ACVR1												
	H3F3A												
	HIST1H3B												
HIST1H3C													
MGMT promoter methylation		No	No	Yes	Yes	No	No	Yes	No	No	No	No	Yes
Patient Gender (M/F)		M	M	F	M	M	M	F	F	M	M	F	F

Homozygous deletion Heterozygous deletion Amplification Gain

2. 1. 2. Reagents and chemicals

Table 2.2 Key resources.

REAGENT or RESOURCE	SOURCE	IDENTIFIER
Experimental Models: Glioblastoma Cell Lines		
A172	ECACC	88062428
U87	ECACC	89081402
U251	ECACC	09063001
BAH1	QMRI Berghofer	QIMR-B001
FPW1	QMRI Berghofer	QIMR-B002
HW1	QMRI Berghofer	QIMR-B003
JK2	QMRI Berghofer	QIMR-B004
MMK1	QMRI Berghofer	QIMR-B005
MN1	QMRI Berghofer	QIMR-B006
PB1	QMRI Berghofer	QIMR-B007
RK11	QMRI Berghofer	QIMR-B008
RN1	QMRI Berghofer	QIMR-B009
SB2b	QMRI Berghofer	QIMR-B010
SJH1	QMRI Berghofer	QIMR-B011
WK1	QMRI Berghofer	QIMR-B012
Antibodies		
Total α -tubulin	Cell Signaling Technology	Cat# 2144, RRID: AB_2210548
Total β -tubulin	Abcam	Cat# ab6046, RRID: AB_2210370
Total γ -tubulin	Cell Signaling Technology	Cat# 5886, RRID: AB_10836184
β I-tubulin	Abcam	Cat# ab179511
β II-tubulin	Abcam	Cat# ab179512
β III-tubulin	Abcam	Cat# ab18207, RRID: AB_444319
β IV-tubulin	Abcam	Cat# ab11315, RRID: AB_297919
Tyrosinated α -tubulin	MerckMillipore	Cat# ABT171
Detyrosinated α -tubulin	MerckMillipore	Cat# AB3201; RRID: AB_177350
Δ 2 α -tubulin	MerckMillipore	Cat# AB3202; RRID: AB_177351
Acetyl K40 α -tubulin	Abcam	Cat# ab179484
Phospho-S172 β III-tubulin	Abcam	Cat# ab76286; RRID: AB_1523210
Polyglutamate α/β -tubulin	Adipogen	Cat# AG-20B-0020; RRID: AB_2490210
Nestin	R&D Systems	Cat# MAB1259; AB_2251304
SOX2	R&D Systems	Cat# AF2018; RRID: AB_355110
Hsp90	R&D Systems	Cat# MAB3286; RRID: AB_2121072
β -actin	Abcam	Cat# ab8227; RRID: AB_2305186
GAPDH	Cell Signaling Technology	Cat# 97166; RRID: AB_2756824
H3K4(Me3)	Abcam	Cat# ab12209; RRID: AB_442957
H3K9(Me1)	Abcam	Cat# ab9045; RRID: AB_306963
H3K9(Me2)	Abcam	Cat# ab1220; RRID: AB_449854
H3K9(Me3)	Abcam	Cat# ab8898; RRID: AB_306848
H3K27(Me1)	Cell Signaling Technology	Cat# 84932; RRID: AB_2800043
H3K27(Me2)	Abcam	Cat# 24684; RRID: AB_448222
H3K27(Me3)	Cell Signaling Technology	Cat# 9733; RRID: AB_2616029
H3K36(Me1)	Abcam	Cat# ab9048; RRID: AB_306964
H3K36(Me2)	Abcam	Cat# ab9049; RRID: AB_1280939
H3K36(Me3)	Abcam	Cat# ab9050; RRID: AB_306966
Total Histone H3	Cell Signaling Technology	Cat# 4499; RRID: AB_10544537
Cleaved H3 (Thr22)	Cell Signaling Technology	Cat# 12576; RRID: AB_2797961
Histone 3.1/3.2	Abcam	Cat# ab176840, RRID: AB_2715502

Histone 3.3	MerckMillipore	Cat# ABE154, RRID: AB_2811170
KDM4A	Novus Biologicals	Cat# NBP1-49602, RRID: AB_10011703
KDM4D	Novus Biologicals	Cat# NBP1-03357, RRID: AB_1521485
KDM4E	MerckMillipore	Cat# ABE1081
CTSL1	R&D Systems	Cat# AF952; RRID: AB_355737
Rabbit IgG, HRP-linked	Cell Signaling Technology	Cat# 7074; RRID: AB_2099233
Mouse IgG, HRP-linked	Cell Signaling Technology	Cat# 7076; RRID: AB_330924
Mouse IgG, Alexa Fluor488	Life Technologies	Cat# A10680; RRID: AB_2534062
Rabbit IgG, AlexaFluor594	Life Technologies	Cat# A11012; RRID: AB_141359
FITC-conjugated CD243 (MDR1)	ThermoFisher Scientific	Cat# 11-2439-41, RRID: AB_11220073
PE-eFluor610-conjugated p-Erk1/2	ThermoFisher Scientific	Cat# 61-9109-41, RRID: AB_2574675
APC-conjugated p-p38 MAPK	ThermoFisher Scientific	Cat# 17-9078-42; RRID: AB_2573290
Anti-Rabbit Detection Module for Jess, Wes, Peggy Sue or Sally Sue	ProteinSimple	Cat# DM-001
Anti-Mouse Detection Module for Jess, Wes, Peggy Sue or Sally Sue	ProteinSimple	Cat# DM-002
Chemicals, Peptides, and Recombinant Proteins		
CMPD1	Santa Cruz	Cat# Sc-203138, CAS: 41179-33-3
Colchicine	Tocris	Cat# 1364, CAS: 64-86-8
Nocodazole	Tocris	Cat# 1228, CAS: 31430-18-9
Tivantinib	Selleckchem	Cat# S2753, CAS: 905854-02-6
Paclitaxel	Tocris	Cat# 1097, CAS: 33069-62-4
Vinblastine	Tocris	Cat# 1256, CAS:143-67-9
Ixabepilone	AdooQ Bioscience	Cat# A11449; CAS: 219989-84-1
Verapamil	Sigma-Aldrich	Cat# V4629; CAS: 152-11-4
MK571	Sigma-Aldrich	Cat# M7571; CAS: 115103-85-0
CP-100356	Sigma-Aldrich	Cat# PZ0171; CAS: 142715-48-8
Elacridar	Tocris	Cat# 4646; CAS: 143851-98-3
Zosuquidar	Tocris	Cat# 5456; CAS: 167465-36-3
SCG Probe Set (inhibitors of epigenetic readers, writers and erasers)	Cayman Chemicals	Cat# 17748
CPI-169	Cayman Chemicals	Cat# 18299; CAS: 1450655-76-1
CPI-1205	AdooQ Bioscience	Cat# A16357; CAS: 1621862-70-1
EPZ6438 (Tazemetostat)	Cayman Chemicals	Cat# 16174; CAS: 1403254-99-8
GSK126	Cayman Chemicals	Cat# 15415; CAS: 1346574-57-9
CTSL1 inhibitor I	MerckMillipore	Cat# 219421; CAS: 108005-94-3
QC6352	MedChemExpress	Cat# HY-104048; CAS: 1851373-36-8
IOX1	Sigma-Aldrich	Cat# SML0067; CAS: 5852-78-8
Antibiotic/antimycotic 100X	Life Technologies	Cat# 15240112
Foetal bovine serum	InterPath	Cat# SFBS-f
Bovine serum albumin	Sigma-Aldrich	Cat# A7030, CAS: 9048-6-8
Nuclear-ID Red DNA stain	Enzo Lifesciences	Cat# ENZ-52406
Prolong Gold Antifade Mountant with DAPI	Life Technologies	Cat# P36935
Dako Fluorescence Mounting Medium	Agilent	Cat# S3023
Fixation buffer	BioLegend	Cat# 420801
Vybrant DyeCycle Violet	ThermoFisher Scientific	Cat# V35003
H3K9Me2-biotin peptide	AnaSpec	Cat# AS-64359
H3K9Me3-biotin peptide	AnaSpec	Cat# AS-64360
Ammonium Iron (III) Sulphate	Sigma-Aldrich	Cat# 221260; CAS: 7783-83-7
L-Ascorbic Acid	Sigma-Aldrich	Cat# A5960; CAS: 50-81-7
2-oxoglutarate (2-OG)	Sigma-Aldrich	Cat# 75892; CAS: 305-72-6
Streptavidin-HRP	GeneTex	Cat# GTX30949
Critical Commercial Assays		
Pierce BCA protein assay kit	ThermoFisher Scientific	Cat# 23225
SimplyBlue SafeStain (Coomassie G-250 solution)	ThermoFisher Scientific	Cat# LC6060

Amido Black Staining Solution	Sigma-Aldrich	Cat# A8181
Immobilin Western HRP Substrate Luminol Peroxidase	MerckMillipore	Cat# WBKLS0500
CellTiter-Blue	Promega	Cat# G808B
LIVE/DEAD™ Fixable Near-IR Dead Cell Stain kit	ThermoFisher Scientific	Cat# L10119
RNeasy mini kit	Qiagen	Cat# 74104
Applied Biosystems High-Capacity cDNA Reverse Transcription kit	Life Technologies	Cat# 4368814
KAPA SYBR FAST Universal 2X qPCR Master Mix	Kapa Biosystems	Cat# KK4602
12-230 kDa Wes Separation Module	ProteinSimple	Cat# SM-W004
Tubulin Polymerisation Assay Kit	Cytoskeleton	Cat# BK006P
Subcellular Fractionation Kit for Cultured Cells	ThermoFisher Scientific	Cat# 78840
Histone Extraction Kit	Abcam	Cat# ab113476
AlphaScreen General IgG Detection Kit	PerkinElmer	Cat# 6760617
Oligonucleotides (All validated QuantiTect Primer Assays)		
Hs_NR2F1_1_SG	Qiagen	Cat# QT00089355
Hs_BHLHE41_1_SG (DEC2)	Integrated DNA Technologies	Fwd: 5'-GGTTAGCGGAGCAATGCGCA-3' Rev: 5'-AACCGGCATTGGGGAACCGTC-3'
Hs_CDKN1A_1_SG (p21 ^{Cip1})	Qiagen	Cat# QT00005803
Hs_CDKN1B_2_SG (p27 ^{Kip1})	Integrated DNA Technologies	Fwd: 5'-CTGATGCTGTTGCTCGGTTA-3' Rev: 5'-TGCAGACTCTGGGACATCTG-3'
Hs_KDM1A_1_SG	Qiagen	Cat# QT00099442
Hs_KDM1B_1_SG	Qiagen	Cat# QT01153572
Hs_KDM2A_1_SG	Qiagen	Cat# QT00020888
Hs_KDM2B_1_SG	Qiagen	Cat# QT00087640
Hs_KDM3A_1_SG	Qiagen	Cat# QT00088879
Hs_KDM3B_1_SG	Qiagen	Cat# QT00085617
Hs_JMJD1C_1_SG (KDM3C)	Qiagen	Cat# QT00066976
Hs_KDM4A_1_SG	Qiagen	Cat# QT00028399
Hs_KDM4B_1_SG	Qiagen	Cat# QT00060949
Hs_KDM4C_1_SG	Qiagen	Cat# QT00027440
Hs_KDM4D_1_SG	Qiagen	Cat# QT00232190
Hs_KDM4D_2_SG	Qiagen	Cat# QT01680609
Hs_KDM4E_1_SG	Qiagen	Cat# QT00244671
Hs_KDM4E_2_SG	Qiagen	Cat# QT01841994
Hs_KDM4E_3_SG	Qiagen	Cat# QT01862308
Hs_KDM5A_1_SG	Qiagen	Cat# QT00013265
Hs_KDM5B_1_SG	Qiagen	Cat# QT00060648
Hs_KDM5C_1_SG	Qiagen	Cat# QT00041503
Hs_KDM5D_1_SG	Qiagen	Cat# QT00014070
Hs_KDM6A_1_SG	Qiagen	Cat# QT00094654
Hs_KDM6B_1_SG	Qiagen	Cat# QT00098742
Hs_KDM7A_1_SG	Qiagen	Cat# QT00038654
Hs_PHF8_1_SG (KDM7B)	Qiagen	Cat# QT00023485
Hs_PHF2_1_SG (KDM7C)	Qiagen	Cat# QT00044555
Hs_KDM8_1_SG	Qiagen	Cat# QT00026999
Hs_SUV39H1_1_SG (KMT1A)	Qiagen	Cat# QT00091042
Hs_SUV39H2_1_SG (KMT1B)	Qiagen	Cat# QT00094311
Hs_EHMT2_1_SG (KMT1C)	Qiagen	Cat# QT00088627
Hs_EHMT1_1_SG (KMT1D)	Qiagen	Cat# QT00084602
Hs_SETDB1_1_SG (KMT1E)	Qiagen	Cat# QT00086142
Hs_SETDB2_1_SG (KMT1F)	Qiagen	Cat# QT00067494
Hs_KMT2A_2_SG	Qiagen	Cat# QT00247464
Hs_KMT2B_1_SG	Qiagen	Cat# QT00015778
Hs_KMT2C_1_SG	Qiagen	Cat# QT00029316

Hs_KMT2D_2_SG	Qiagen	Cat# QT01762096
Hs_KMT2E_1_SG	Qiagen	Cat# QT00053900
Hs_KIAA0339_1_SG (KMT2F)	Qiagen	Cat# QT00042427
Hs_KIAA1076_1_SG (KMT2G)	Qiagen	Cat# QT01016799
Hs_ASH1L_1_SG (KMT2H)	Qiagen	Cat# QT00083335
Hs_HYPB_1_SG (KMT3A)	Qiagen	Cat# QT00087416
Hs_NSD1_1_SG (KMT3B)	Qiagen	Cat# QT00035476
Hs_SMYD2_1_SG (KMT3C)	Qiagen	Cat# QT00011886
Hs_SMYD1_1_SG (KMT3D)	Qiagen	Cat# QT00080031
Hs_SMYD3_1_SG (KMT3E)	Qiagen	Cat# QT00089950
Hs_WHSC1_1_SG (KMT3F)	Qiagen	Cat# QT00018998
Hs_WHSC1L_1_SG (KMT3G)	Qiagen	Cat# QT00008162
Hs_DOTL1_1_SG (KMT4)	Qiagen	Cat# QT00074032
Hs_EZH2_1_SG (KMT6A)	Qiagen	Cat# QT00054614
Hs_EZH1_1_SG (KMT6B)	Qiagen	Cat# QT00030275
Hs_SET7_1_SG (KMT7)	Qiagen	Cat# QT00079282
Hs_PRDM2_1_SG (KMT8A)	Qiagen	Cat# QT00055300
Hs_PRDM9_1_SG (KMT8B)	Qiagen	Cat# QT01023631
Hs_PRDM6_1_SG (KMT8C)	Qiagen	Cat# QT01173774
Hs_PRDM8_2_SG (KMT8D)	Qiagen	Cat# QT01665062
Hs_MSD1_1_SG (KMT8E)	Qiagen	Cat# QT00211169
Hs_PRDM16_1_SG (KMT8F)	Qiagen	Cat# QT00016975
Hs_EEF1A_1_SG	Qiagen	Cat# QT00999894
Hs_RRNA18S_1_SG	Qiagen	Cat# QT00199367
Hs_ACTB_1_SG	Qiagen	Cat# QT00095431
Hs_GAPDH_1_SG	Qiagen	Cat# QT00079247
Key Software and Algorithms		
Prism v8.0	GraphPad	https://www.graphpad.com/scientific-software/prism/
ImageLab v6.0.1	Bio-Rad	http://www.bio-rad.com/en-au/product/image-lab-software?ID=KRE6P5E8Z
IncuCyte IC S3 v2018A	Essen Bioscience	https://www.essenbioscience.com/en/products/software/incucyte-s3-software-v2018a/
"Cell calculator ++" doubling time calculator	Doubling-time.com	http://www.doubling-time.com/compute_more.php (Roth, V. 2006)
GRcalculator	REFs ^{298, 299}	http://www.grcalculator.org/grtutorial/Home.html
FlowJo v10.3	FlowJo	https://www.flowjo.com/solutions/flowjo/downloads
Compass for Simple Westerns	ProteinSimple	https://www.proteinsimple.com/compass/downloads/
Fiji (ImageJ)	ImageJ	https://imagej.net/Fiji/Downloads
Skyline	MacCoss Lab Software	https://skyline.ms/
CalcuSyn v.2.0	BioSoft	http://www.biosoft.com/w/calculusyn.htm
PyMOL	Schrödinger	https://pymol.org

2. 2. Immunoblots

2. 2. 1. Tubulin code analysis

For tubulin code analysis, whole-cell lysates were prepared by adding 1 mL RIPA buffer to a T175 flask of unsynchronised cells at 80-90% confluency. Protein concentrations were determined with Pierce BCA assay kit (ThermoFisher Scientific), following manufacturer's instructions. Samples were prepared with Bolt LDS loading buffer and Bolt sample reducing agent (Life Technologies) and heated at 95 °C for 5 min. For all tubulin immunoblots in **Figure 3.1**, 5 µg of total protein were resolved (2 h, 95 V) on 4-12% Bolt Bis-Tris gels and transferred onto PVDF membranes using iBlot 2, P3 (20 V) for 7 min (all Life Technologies).

30 µg of total protein was loaded for SOX2 and 1 µg of total protein was loaded for α - and β -tubulin immunoblots in **Figure 3.5e**, while other conditions remained unchanged. Membranes were blocked with 5% BSA in TBST, incubated with primary antibody in 5% BSA in TBST overnight at 4 °C, and with secondary antibody for 1 h at room temperature. All primary antibodies were used at concentrations recommended by the manufacturers. Membranes were washed in TBST 3 times (10 min) both before and after the addition of secondary antibody. All secondary antibody preparations were in 5% skim milk in TBST, with the exception for anti-tyrosinated α -tubulin and anti-phospho- β III tubulin, which were prepared in 5% BSA, as the casein in the skim milk can interfere with the antigen-recognising regions of those antibodies. Detection was performed with Immobilon Western HRP Substrate Luminol-Peroxidase kit (MerckMillipore) and the ChemiDoc MP Imaging System (Bio-Rad). Densitometry quantification was done in ImageLab software (Bio-Rad).

2. 2. 2. Histone code analysis

Histones were extracted from sample using the Histone extraction kit (Abcam) as per manufacturer's instructions. Protein concentrations were determined with Pierce BCA assay kit (ThermoFisher Scientific), following manufacturer's instructions. For all histone immunoblots in **Figure 4.17-Figure 4.19**, 1 µg of histone extracts were resolved (30 min, 200 V) on 12% Bolt Bis-Tris gels and transferred onto nitrocellulose membranes using iBlot 2, P4 (15 V) for 7 min (all Life Technologies). Nitrocellulose membranes were used as their

smaller pore size is better suited for the transfer of histone proteins (~11-17 kDa).³⁰⁰ Other conditions remained unchanged.

Whole-cell lysates from treatment-naïve parental and DTP cells were used to analyse changes in histone modifying-enzymes (**Figure 5.7**, **Figure 5.18**). Protein concentrations were determined with Pierce BCA assay kit (ThermoFisher Scientific), following manufacturer's instructions. 30 µg of protein were resolved (30 min, 200 V) on 4-12% Bolt Bis-Tris gels and transferred onto PVDF membranes using iBlot 2, P3 (20 V) for 7 min (all Life Technologies). Membranes were probed with KDM4D, KDM4E, CTSL1 or GAPDH1 antibodies. Other conditions remained unchanged.

2. 3. Capillary immunoassay

Total cell lysates (WK1, RN1, JK2 and RK11) at 1 µg/µL (α-tubulin) and 0.25 µg/µL (β-tubulin) were analysed using the automated capillary electrophoresis, Wes (ProteinSimple) as per manufacturer's instructions. Wes Separation Capillary Cartridges for 12-230 kDa (ProteinSimple) were used. The same primary antibodies as used in immunoblotting were used for the capillary immunoassay at 1:50 dilution (α-tubulin) and 1:1,000 dilution (β-tubulin). Signals were detected with Anti-Rabbit Detection Module for Jess, Wes, Peggy Sue or Sally Sue (ProteinSimple) and were quantified using Compass software (ProteinSimple).

2. 4. Cell-based assays

2. 4. 1. CellTitre-Blue viability assay

All cell lines were plated in 96-well plates at a density of 2,000 cells/well, except PB1 cells, which were seeded at 8,000 cells/well. Drug-tolerant persister (DTP) cells were seeded at 8,000 cell/well. Cells were treated with DMSO or test compounds at an 8-point dilution row for 5 days. CellTitre-Blue (Promega) was added (1:10) to each well and incubated at 37 °C for 2-4 h. Fluorescence was measured with a Tecan M200 PRO+ microplate reader (Tecan) at (Ex/Em 530/590). Data were normalised to DMSO-treated controls (set as 1). Relative IC₅₀, E_{max}, h, AUC and per-division GR₅₀, GR_{max}, h_{GR}, and GR_{AOC} metrics were calculated from viability data and proliferation rates using the *GRcalculator* online tool.^{298, 299} Graphs were recreated from the *GRcalculator* online tool using Prism v8.0 (GraphPad). For combination studies, the Chou-Talalay theorem³⁰¹ was used to calculate combination indices in the CalcuSyn software (BioSoft).

2. 4. 2. Proliferation rate assay

The proliferation rate of glioblastoma cells was determined using IncuCyte Live-Cell Imaging platform (Essen Bioscience). Cells were seeded at 500, 1000, 2000 and 4000 cells/well. Proliferation was monitored by analysing the occupied area (% confluence) of cell images over 7 days using the IncuCyte IC S3 2018A software (Essen Bioscience). Population doubling times were computed with several time points, from different initial cell densities, on doubling-time.com using the “cell calculator++” tool (Roth V., 2006).

2. 4. 3. DTP generation and expansion

WK1, FPW1 and RKI1 cells (1.5×10^4 cells/cm²) were plated and treated the next day with colchicine (500 nM), CMPD1 (25 μ M) or tivantinib (25 μ M) for 14 days. These concentrations were chosen as they were 25 \times the average observed GR₅₀ concentrations in viability assays. Fresh media containing drug was added every 3 days. At Day 14, drug-tolerant persisters were allowed to recover in drug-free media. Cells were monitored every 3 days until they regained their morphology and expansion started when cells resembled their parental cell line. Images were taken using Zeiss Axio Vert.A1 microscope using the ZEN 2 – blue edition software (Zeiss).

2. 4. 4. Nuclear-ID DNA Red staining

WK1, RN1, JK2, FPW1 and RKI1 (1×10^5) were seeded on Matrigel-coated black imaging 12-well plates (Eppendorf) and treated with MTA (500 nM colchicine or 25 μ M CMPD1) \pm efflux pump inhibitors or epigenetic probes for 14 days. Fresh media containing drugs was added every 3 days. Untreated (Day 0) and treated (Day 14) cells were stained with Nuclear-ID red stain (Enzo Lifesciences) at 1:1,000 dilution in StemPro media. Cells were incubated with the stain for 30 min prior to washing with Phosphate Buffered Saline (PBS) three times and covered with Fluorescence Mounting Medium (Dako), diluted 1:10 in PBS. Images were taken using Zeiss Axio Scope.A1 and ZEN 2 – blue edition software (Zeiss). Fiji was used to quantify stained cells.

2. 4. 5. Immunofluorescence imaging

WK1 and RKI1 cells (8×10^3) were seeded onto glass coverslips coated with MatriGel for 24 hours, then treated with colchicine (5 - 500 nM) for 5 days. For nestin, α/β -tubulin

analysis, WK1, RN1, JK2 and RK11 cells (1×10^5). Cells were fixed with ice-cold paraformaldehyde (4%) solution for 20 min at RT and blocked in 5% bovine serum albumin in PBS for 20 min. Cells were incubated with anti-nestin (1:25, R&D Systems), anti- α -tubulin (1:10, Cell Signaling Technology) and anti- β -tubulin (1:200, Abcam). Secondary antibodies were Alexa488-conjugated anti-mouse IgG (against nestin) and Alexa594-conjugated anti-rabbit IgG (against β -tubulin) (Life Technologies). Cell nuclei were counterstained using Prolong Gold Mounting Media with DAPI (Life Technologies). Images were acquired under 40X objectives on a Zeiss Axio Scope.A1 microscope using ZEN 2 – blue edition software (Zeiss). Images were processed using Fiji.

2. 4. 6. Clonogenic outgrowth assays

RK11 or FPW1 cells were seeded in 6-well plates (4000 cells/well) and treated with vehicle (DMSO) or inhibitors (single agents or in combination) for 14 days. Cells were allowed to recover in drug-free media for an additional 14 days. On Day 28, the colonies were washed three times with PBS, then incubated with a fix/stain solution of methanol (50%) and toluidine blue (1%) for 2 h at 4 °C. Colonies were counted using the ImageJ software and normalized to untreated controls (set as 100%).

2. 5. Quantitative Polymerised Chain Reaction

Reverse-Transcriptase Quantitative Polymerised Chain Reaction (RT-qPCR) was carried out according to standard protocols. RK11 cells were treated with colchicine (500 nM) or CMPD1 (25 μ M) for 14 days. Fresh media containing drug was added every 3 days. Cells were lysed at Day 0 (untreated) and Day 14. RNeasy mini kit (Qiagen) was used to isolate RNA from cell lysates as per manufacturer's instructions. cDNA was generated using Applied Biosystems High-Capacity cDNA Reverse Transcription kit (Life Technologies) as per manufacturer's instructions. qRT-PCR was performed using primers listed in **Table 2.2** (Quantitect validated primers, Qiagen) with KAPA SYBR FAST Universal 2 \times qPCR Master Mix (Kapa Biosystems). RT-PCR was run on LightCycler 480 (Roche). The cycling condition were as follows: 10 min at 95 °C followed by 45 cycles, each consisting of 10 s at 95 °C and 30 s at 60 °C. Samples were run in triplicate. Threshold cycles (C_T) were calculated using the LightCycler® 480 software. Relative quantification using the comparative C_T method was used to analyse to the data output. The *ACTB1*, *GAPDH*, *EEF1A* and 18S rRNA primers were used as loading controls. Values were expressed as fold change over corresponding values for the control by the $2^{-\Delta\Delta C_T}$ method.

2. 6. Sequential Window Acquisition of All Theoretical Fragment Ion

Spectra Mass Spectrometry (SWATH-MS)

2. 6. 1. Sample preparation

All solvents, acids and bases used were HPLC-grade (Sigma-Aldrich). All reactions were carried out in Protein-LoBind Eppendorf tubes. A summary of the workflow is illustrated in **Figure 2.1**.

Cell fractionation

The Sub-Cellular Fractionation Kit (ThermoFisher Scientific) was used to obtain chromatin-bound fractions from snap-frozen FPW1 and RK11 cell pellets as per manufacturer's instructions. The samples were then supplemented with 50 mM sodium bicarbonate, 1X Protease Inhibitor Cocktail (Roche), 1 mM PMSF, 1 mM sodium orthovanadate and 10 mM sodium butyrate (All Sigma-Aldrich). Protein concentration was measured using Pierce BCA Protein Assay (ThermoFisher Scientific).

Protein precipitation

Proteins were precipitated using standard ice-cold methanol: chloroform (HPLC grade, Sigma-Aldrich) precipitation technique. Samples were then air-dried and resubstituted to ~ 2.5 mg/mL in 50 mM sodium bicarbonate. The pH was adjusted to 8.0 using ammonium hydroxide and formic acid solutions (HPLC grade, Sigma-Aldrich). Samples were sonicated using a SonoPlus Mini20 (Bandelin) for 3 times (15 s) at 90% amplitude.

Protein derivatisation and digestion

Histones were propionylated before and after digestion with trypsin (as per the method described in *REF*³⁰²). Briefly, 1-part propionylation reagent (1:3 propionic anhydride: acetonitrile) (HPLC grade, Sigma-Aldrich) was added to 4-part of samples, and the pH was adjusted to 8.0 using ammonium hydroxide solution (1 M). Samples were incubated at room temperature for 15 min then vacuum-dried at ambient temperature. Samples were then reduced with 10 mM DL-dithiothreitol (DTT) for 30 min at 37 °C, then alkylated with 100 mM 2-iodoacetamide at room temperature in the dark. The pH was adjusted to 8.0 by dropping a few ammonium bicarbonate crystals into the solution as needed. 2 µg of trypsin (Sigma-Aldrich) were added per 100 µg of protein, and samples were incubated overnight at 37 °C. The trypsinisation reaction was stopped by freezing

samples at -80°C . Samples were freeze-dried and then reconstituted in 100 mM ammonium bicarbonate. Finally, this was followed by another round of propionylation as described above.

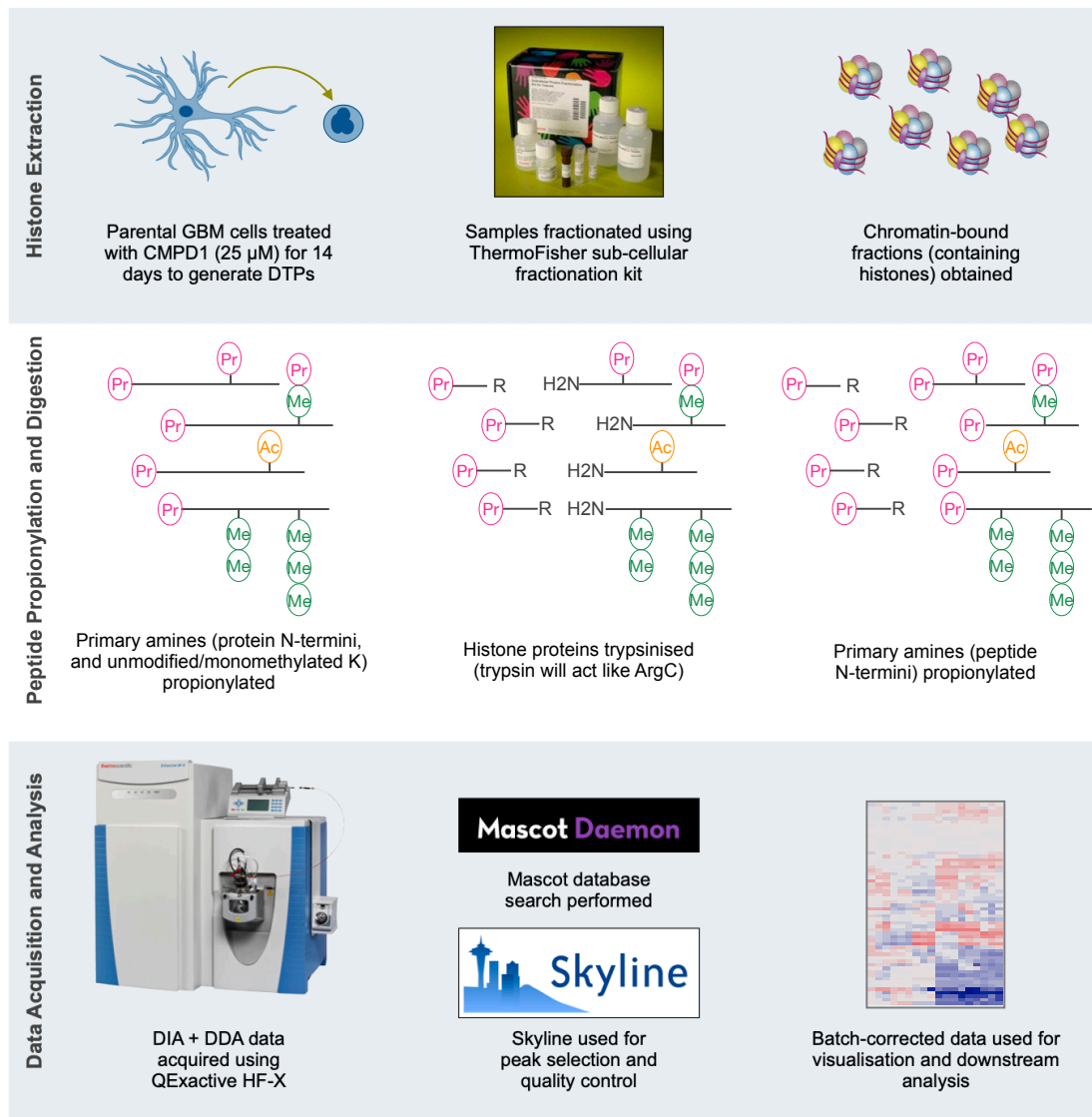


Figure 2.1 Histone SWATH mass spectrometry workflow.

FPW1 or RK11 were harvested at Day 0 (Untreated) or Day 14 following treatment with CMPD1 (25 μM). Cells were then fractionated to the chromatin-bound fraction was collected. Histones are then subjected to propionyl labelling and digested by trypsin, which will be able to C-terminally cleave arginine residues but not modified or labelled lysine residues. Newly generated N-termini are subjected to further propionylation. Each sample was injected 4 times: the first injection is acquired using the DDA method for library generation, while DIA injection was performed in triplicates. Peptides were identified using Mascot search engine while spectral libraries generation and peak selection were performed in Skyline. All histone peptides were verified manually using MS1 spectra.

Sample desalting

Samples were acidified with 1% trifluoroacetic acid (TFA). Samples were then desalted using Oasis HLB Sep-Pak columns (Waters) equilibrated with methanol and acetonitrile. The columns were then washed 3 times with 0.1% TFA prior to addition to the samples.

Samples were transferred into the columns and washed 3 times with 5% acetonitrile and 0.1% TFA before the addition of the elution buffer (50% acetonitrile and 0.1% TFA). Samples were then vacuum dried at ambient temperature overnight.

2. 6. 2. Nano-liquid chromatography and electrospray ionisation tandem mass spectrometry

For LC/MS-MS, 1 µg of propionylated histones in loading buffer (3% acetonitrile, 0.1% TFA) was injected onto a 30 cm × 75 µm inner diameter column packed in-house with 1.9 µm C18AQ particles (Dr Maisch GmbH, HPLC) using a Dionex Ultimate 3000 nanoflow UHPLC. Peptides were separated using a linear gradient of 5–35% buffer B over 120 min at 300 nL/min at 55 °C (buffer A consisted of 0.1% (v/v) formic acid; while buffer B was 80% (v/v) acetonitrile and 0.1% (v/v) formic acid). All MS analyses were performed using a Q-Exactive HFX mass spectrometer. For Data-Dependent Acquisition (DDA): after each full-scan MS1 (R = 120,000 at 200 m/z, 300–1600 m/z; 3×10^6 AGC; 110 ms max injection time), up to 10 most abundant precursor ions were selected for MS/MS (R = 45,000 at 200 m/z; 2×10^5 AGC; 86 ms max injection time; 30 normalised collision energy; peptide match preferred; exclude isotopes; 1.3 m/z isolation window; minimum charge state of +2; dynamic exclusion of 15 s). This resulted in a duty cycle of ~ 1.3 s. For DIA: after each full-scan MS1 (R = 60,000 at 200 m/z (300–1600 m/z; 3×10^6 AGC; 100 ms max injection time), 54×10 m/z isolations windows (loop count = 27) in the 390–930 m/z range were sequentially isolated and subjected to MS/MS (R = 15,000 at 200 m/z, 5×10^5 AGC; 22 ms max injection time; 30 normalised collision energy). 10 m/z isolation window placements were optimised in Skyline³⁰³ to result in an inclusion list starting at 395.4296 m/z with increments of 10.00455 m/z. This resulted in a duty cycle of ~ 2.2 s.

2. 6. 3. Database search and spectral library generation

Database searches were performed Mascot v2.4. Spectra were searched against the human SwissProt database (May 2019; 559,634 entries) using a precursor-ion and product-ion mass tolerance of ± 10 ppm and ± 0.02 Da, respectively. The enzyme was specified as ArgC with 1 missed cleavage. Variable modifications were set as follows: acetyl(K), propionyl(K), monomethyl + propionyl(K), dimethyl(K) and trimethyl(K), propionyl(N-term), oxidation(M), carbamidomethyl(C).

All DIA data were processed using Skyline (v20.1).³⁰³ Reference spectral libraries were built in Skyline with .dat files using the BiblioSpec algorithm.³⁰⁴ A False Discovery Rate (FDR) of 5% was set and a reverse decoy database was generated using Skyline.

2. 6. 4. Histone PTM quantification using DDA and DIA

Precursor and product ion extracted ion chromatograms were generated using extraction windows that were two-fold the full-width at half maximum for both MS1 and MS2 filtering. Ion-match tolerance was set to 0.055 m/z. For MS1 filtering, the first three isotopic peaks with charges +2 to +4 were included while for MS2, b- and y-type fragments ions with charges +1 to +3 were considered.

To ensure correct peak identification and assignment, the dot product between peptide precursor ion isotope distribution intensities and theoretical intensities (idotp) had to be ≥ 0.90 . In addition, retention times of identified peptides based on Mascot searches, and relative retention times based on the hydrophobicity of PTMs were also considered.³⁰² Finally, manual inspection of key fragment ions was also performed. Ultimately, MS1 spectra (M , $M + 1$, and $M + 2$) were used for quantitation.

A peptide family is defined as a group of peptides spanning the same residues within the histone H3 proteins. As these peptides have the same sequence but contain different post-translational modifications, they are termed 'peptidoforms.' For instance, H3 residues 9-17 (KSTGGKAPR), which contains lysine K9 and K14, is a peptide family containing 10 peptidoforms: H3 K9K14, K9(Me1)K14, K9(Me2)K14, K9(Me3)K14, K9(Ac)K14, K9K14(Ac), K9(Me1)K14(Ac), K9(Me2)K14(Ac), K9(Me3)K14(Ac), and K9(Ac)K14(Ac). The peak area of each individual peptide was divided by the sum of peak areas of all peptides within the same peptide family. In cases of isobaric and co-eluting peptides that represented the same set of precursor peaks, namely H3 K27(Me2)K36(Me3) and K27(Me3)K36(Me2), the average of the two peaks identified was used, and both peptides were quantified as a unit.

2. 6. 5. Data normalisation and statistical analysis

Processed MS1 quantifications were first Log transformed (base 2) and then quantile-normalised across samples. Data from the two cell types (*i.e.* FPW1 and RK11) were subsequently analysed independently. For data from each cell type, Combat R package³⁰⁵ was used to remove experimental batch effects.³⁰⁵ Batch corrected data

were used for downstream analyses including hierarchical clustering, heatmap visualisation and bar graphs.

2. 7. KDM4 AlphaScreen assay development

2. 7. 1. Peptide validation by dot blots

1 μ L of varying concentrations of H3K9(Me3)-biotin peptide (Anaspec) were blotted on activated PVDF membranes and incubated with primary antibodies in 5% BSA in TBST overnight. To test antibody specificity, membranes were blocked with 5% BSA in TBST, incubated with primary antibodies for H3K9(Me1), H3K9(Me2) and H3K9(Me3) (both Abcam) in 5% BSA in TBST overnight at 4 °C, and with secondary antibody for 1 h at room temperature. To test for biotin-conjugation, membranes were incubated with streptavidin-HRP (GeneTex) for 1 h at room temperature, according to manufacturer's instructions. Membranes were then washed in TBST 3 times (10 min) both before and after the addition of secondary antibody or after incubation with streptavidin-HRP. Detection was performed with Immobilon Western HRP Substrate Luminol-Peroxidase kit (MerckMillipore) and the ChemiDoc MP Imaging System (Bio-Rad).

2. 7. 2. Peptide and enzyme assessment by RapidFire mass spectrometry

KDM4A activity was assessed by RapidFire-MS using H3K9(Me3)-biotin (AnaSpec) as a substrate. All steps were performed in assay buffer constituting of MES (50 mM, pH 7.0), sodium chloride (50 mM) and TCEP (1 mM). 0.5 mL of assay buffer containing 1.25 \times KDM4A enzymes (188 nM) was transferred into wells of a 96-deep-well polypropylene block, and the enzyme reaction was initiated by the addition of 100 μ L of 6 \times substrate in assay buffer containing the H3K9(Me3)-biotin peptide (60 μ M) and the cofactors Fe²⁺ (60 μ M), L-ascorbic acid (600 μ M) and 2-OG (60 μ M). The deep-well block was transferred to a RapidFire RF360 high-throughput sampling robot connected to a 6530 Accurate-Mass Quadrupole Time-of-Flight mass spectrometer (Agilent) operated in positive ion mode. Samples were aspirated under vacuum for 400 ms and applied to a C4 solid-phase extraction cartridge. The solid-phase extraction was washed to remove non-volatile buffer salts with water containing 0.1% (vol/vol) formic acid applied at a flow rate of 1.5 ml/min for 6.0 s, and peptides were eluted onto the mass spectrometer with 85% acetonitrile, 25% water containing 0.1% formic acid at a flow rate of 1.25 ml/min for 6.0 s. The cartridge was re-equilibrated with water for 500 ms. A cycle of aspiration, aqueous wash, organic elution and re-equilibration takes approximately 15

s; for the establishment of enzyme progress curves, a sample was aspirated every 3.5 min for 75 min. Ion chromatogram data were extracted for the +6 charge state for the trimethyl substrate and the dimethyl product, and peak-area data for extracted ion chromatograms were integrated using RapidFire Integrator software (Agilent). The fractional conversion of dimethyl substrate to monomethyl product was calculated as a percentage of change in peptide peak areas using the equation:

$$\text{Demethylation (\%)} = \frac{\text{H3K9(Me2)}}{\text{H3K9(Me2)} + \text{H3K9(Me3)}} \times 100$$

Demethylation was plotted over time for each of the enzymes tested, and Kinetic curves were fitted using Prism (v8.0, GraphPad).

2. 7. 3. Optimised AlphaScreen assay

Streptavidin-conjugated donor and Protein A-conjugated acceptor AlphaBeads (20 µg/mL each) were pre-incubated with H3K9(Me2) antibody (Abcam) in assay buffer (50 mM HEPES (pH 7.5), 0.02% BSA and 0.01% Tween-20) for 1 h in the dark prior to starting the demethylation reaction. AlphaScreen assays were carried out in shallow 384-well AlphaPlates (PerkinElmer) in a total volume of 20 µL.

For inhibition studies, compounds were incubated with KDM4A (3 nM) for 15 min at room temperature prior to the addition of the peptide master-mix. Enzyme solutions were prepared at 2×. For screening the compound library, DMSO stock solutions were diluted in assay buffer (final concentrations 1 and 20 µM). For IC₅₀ curves, 10-point serial dilution rows were prepared at a log₃-scale (0.003-100 µM). QC6352, IOX1 and 2,4-PDCA are known inhibitors of KDM4A and were used to validate the assay.

The peptide master-mix, containing H3K9(Me3)-biotin (30 nM) (AnaSpec), Iron (III) Sulphate (1 µM), 2-OG (10 µM) and L-ascorbic acid (100 µM) (all Sigma-Aldrich) in assay buffer, was added to each well to initiate the demethylation of the H3K9(Me3) peptide to H3K9(Me2); The reaction was incubated for 20 min at room temperature. Both enzyme and test-compound solutions were prepared at 4×, while the peptide master-mix was prepared at 2×, for a 10 µL reaction volume.

The reaction was stopped with the addition of the stop solution made of sodium chloride (200 nM) and EDTA (7.5 mM, pH 8.0) in assay buffer, followed by the addition of the pre-incubated AlphaScreen beads. Both the stop solution and the AlphaScreen

beads were prepared at 4×, for a final volume of 20 μL. The plate was sealed with adhesive plate foils (ThermoFisher Scientific) and incubated for 1-2 h in the dark. Readings were taken using Tecan INFINITE M1000, using the AlphaScreen format. Inhibition (%) was calculated relative to blank wells (containing peptide master-mix only) and no-inhibition wells (containing only DMSO vehicle). IC₅₀ curves were generated using a four-parameter logistics fit on Prism (GraphPad).

2. 8. Statistical analysis

2. 8. 1. Correlations between the tubulin code and MTA metrics

All statistical analyses were performed using Prism v8.0 (GraphPad). For immunoblotting analysis in **Chapter 3**, two-way ANOVA, in which mean value for each cell line was compared to the mean value in the A172 cell line, was performed. Correlation analysis between tubulin isoforms and post-translational modifications (**Figures 1**), proliferation rates (**Figure 2**) and MTA efficacy metrics (**Suppl. Tables 1-4**) was performed using Spearman's correlation method (Prism v8.0, GraphPad). Spearman's correlation was performed as not all datasets followed a normal distribution (**Figure 3**). Two-tailed p-values are listed for these correlations.

2. 8. 2. Statistical tests of comparison

The data and statistical analysis comply with the recommendations on experimental design and analysis in pharmacology. All immunoblots and immunofluorescence images are representatives of at least three independent experiments. All cellular and biochemical assays were repeated at least three times unless otherwise indicated, and each experiment was run in duplicate or triplicate. All results are expressed as mean ± SEM, unless otherwise indicated. An unpaired *t*-test was performed for comparison of two data sets, and one- or two-way ANOVA followed by Tuckey's post hoc test was used for the comparison of multiple data sets unless otherwise indicated. In all cases, $p < 0.05$ was the threshold significant.

Chapter 3

Lower tubulin expression in glioblastoma stem cells attenuates efficacy of microtubule-targeting agents

CHAPTER 3. LOWER TUBULIN EXPRESSION IN GLIOBLASTOMA STEM CELLS ATTENUATES EFFICACY OF MICROTUBULE-TARGETING AGENTS

3. 1. Preface

This work was published in:

- **Abbassi R. H.;** Recasens, A.; Indurthi, D. C.; Johns, T. G.; Stringer, B. W.; Day, B. W.; Munoz, L. *ACS Pharmacol Transl Sci* **2019**, *2*, 402-413.
<https://pubs.acs.org/doi/10.1021/acsptsci.9b00045>

Further permission related to the material excerpted should be directed to the ACS publishing group.

ACS Pharmacology & Translational Science

NOVEMBER/DECEMBER 2019 VOLUME 2 NUMBER 6 PUBLS.ACS.ORG/PTSCI

 ACS Publications
Most Trusted. Most Cited. Most Read.

www.acs.org

Abbassi et al. (2019) was featured in ACS Editors' Choice and sponsored for immediate, free open-access release by ACS due to its potential for broad public interest. The article was featured on the cover of the issue and constitutes **Chapter 3** of this thesis.

Z-stack image of β -tubulin expression in glioblastoma stem cells (RK11). Colours are assigned based on the depth of β -tubulin in the cell.

Image credit: Dr. Jonathan David Teo, Charles Perkins Centre, University of Sydney.

Lower Tubulin Expression in Glioblastoma Stem Cells Attenuates Efficacy of Microtubule-Targeting Agents

Ramzi H. Abbassi,[†] Ariadna Recasens,[†] Dinesh C. Indurthi,[†] Terrance G. Johns,[‡] Brett W. Stringer,[§] Bryan W. Day,[§] and Lenka Munoz^{*,†,‡,§}

[†]Faculty of Medicine and Health, Charles Perkins Centre, The University of Sydney, John Hopkins Drive, Sydney, New South Wales 2006, Australia

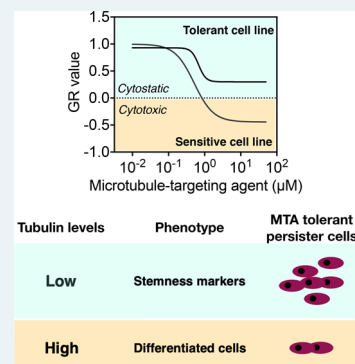
[‡]Oncogenic Signalling Laboratory and Brain Cancer Discovery Collaborative, Telethon Kids Institute, Perth Children's Hospital, 15 Hospital Avenue, Nedlands, Western Australia 6009, Australia

[§]QIMR Berghofer Medical Research Institute, 300 Herston Road, Herston, Queensland 4006, Australia

Supporting Information

ABSTRACT: Sensitivity to microtubule-targeting agents (MTAs) varies among cancers and predicting the response of individual cancer patients to MTAs remains challenging. As microtubules possess vast molecular heterogeneity generated by tubulin isotypes and their post-translational modifications, we questioned whether this heterogeneity can impact MTA sensitivity. We investigated microtubule heterogeneity in 15 glioblastoma cell lines and measured sensitivity of orthogonal MTAs using a per-division growth rate inhibition method that corrects for the confounding effects of variable cell proliferation rates. We found that the tubulin profile is unique for each glioblastoma cell line and that the total α - and β -tubulin levels impact on MTA sensitivity. The baseline levels of α - and β -tubulin were up to 20% lower in cells that were not effectively killed by MTAs. We report that lower α/β -tubulin expression is associated with lack of cell differentiation and increased expression of stemness markers. The dedifferentiated stem-like cells with low α/β -tubulin levels survive MTAs treatment via reversible nonmutational dormancy. Our findings provide novel insights into the relationships between microtubules and MTAs and lay a foundation for better understanding of the sensitivity of cancer cells to MTAs.

KEYWORDS: glioblastoma, microtubule-targeting agents, tubulin code, drug sensitivity, drug-tolerant persister cells



INTRODUCTION

Microtubules are cytoskeletal polymers composed of α/β -tubulin heterodimers and are involved in mitosis, cell motility, intracellular transport, and maintenance of cell shape. Because of their multiple cellular functions, microtubules are the direct target of microtubule-targeting agents (MTAs) that are clinically used to kill cancer cells.¹ Although microtubules are highly conserved in their 3D structures, there is a significant diversity at the molecular level.² Microtubule diversity stems from genes encoding for eight α - and nine β -tubulin isotypes, and from their post-translational modifications.³ These modifications range from the well-known phosphorylation to tubulin-specific modifications such as detyrosination and associated removal of penultimate glutamate yielding $\Delta 2$ α -tubulin. Together, tubulin isotypes and their post-translational modifications form the *tubulin code*, which fine-tunes specific functions of microtubules.²

Tubulin heterogeneity has been associated with tumor resistance to MTAs.⁴ For example, the overexpression of βIII -, βIV -, and βV -tubulins caused acquired resistance to taxanes and vinca alkaloids.⁵ Post-translational modifications have been also proposed to affect the efficacy of MTAs;^{1,4} however, this remains unsubstantiated by experimental data. In addition to

the acquired resistance, drug-tolerant states contribute to the reduction of cancer drug efficacy. Initial exposure of cells to cancer drugs does not kill all cells, giving rise to a subpopulation of surviving cells that has been named drug-tolerant persister cells. Drug-tolerant persister cells usually use epigenetic reprogramming to survive the treatment and when drugs are removed, they regrow into a new population that is as equally drug-sensitive as the parental population.^{6–9} Two studies to date have shown that exposure of cancer cells to taxanes generates drug-tolerant persister cells,^{10,11} suggesting that the drug tolerance plays a role in MTA efficacy.

Glioblastoma is the most aggressive primary brain tumor with a median patient survival of 15 months. Given the extensive intratumoral molecular heterogeneity of glioblastomas¹² and the lack of molecularly targeted drugs that can permeate the blood–brain barrier,¹³ glioblastoma remains a major unmet medical need. Although MTAs showed promising efficacy against glioblastoma cells, clinically approved MTAs are ineffective for the treatment of these tumors as their large molecular weight (>800 g/mol) and polarity renders them

Received: July 3, 2019

Published: July 30, 2019

unable to cross the blood–brain barrier. Hence, there has been increasing research interest toward the development of effective MTA delivery methods^{14–16} or identification of small-molecule MTAs able to cross the blood–brain barrier.^{17–20}

To advance the development of MTAs as pharmacological agents against glioblastoma, we characterized microtubules in three standard (U87, U251, A172) and 12 glioblastoma stem cell (GSC) lines.²¹ In parallel, we determined efficacy of clinical MTAs (paclitaxel, vinblastine, ixabepilone) and colchicine-site binders (colchicine, nocodazole, tivantinib, and CMPD1).^{19,22,23} Colchicine-site binders are generally smaller compared to taxanes, epothilones and *vinca* alkaloids and as the molecular weight is a critical parameter for blood–brain barrier permeability,²⁴ this subclass of MTAs is more relevant to the development of glioblastoma therapeutics. We calculated conventional drug sensitivity metrics IC_{50} , Hill coefficient h (marker of cell-to-cell variability), E_{max} (maximum efficacy), and area under the curve (AUC) which combines IC_{50} with E_{max} .²⁵ However, because the drug sensitivity is often confounded by unequal division rates across cell lines, we also performed growth rate (GR) inhibition analysis which yielded per-division drug potency (GR_{50}), efficacy (GR_{max}), Hill coefficient (h_{GR}), and area-over the curve (GR_{AOC}).^{26–28} Finally, we investigated if some components of the *tubulin code* mediate MTA sensitivity.

RESULTS

Tubulin Isoforms and Post-translational Modifications. As the tubulin expression is predominantly regulated post-transcriptionally such that protein levels poorly reflect the transcript levels,^{29,30} we investigated microtubule modifications by immunoblotting lysates from unsynchronized cells at three different passages. The absolute values of immunoblot signals were not normalized to the house-keeping proteins GAPDH, Hsp90, or β -actin as their levels varied greatly between cell lines (Figure 1). Equal loading was monitored with Coomassie staining (Figure S1) and immunoblot signals were normalized to the corresponding signals in A172 (Figure S2) and RN1 (Figure S3) cells. Both normalizations revealed comparable variability in the expression of tubulin isoforms and their modifications. The coefficients of variation (CV) show 20%, 25%, and 69% variability in the total expression of α -, β -, and γ -tubulin, respectively. The variability of the individual β -tubulin isoforms levels ranged from 26% (β I- and β III-) to 54% (β II-tubulin, Figure 1a).

When assessing the post-translational modifications, we found 12%, 89%, and 133% variability across the levels of tyrosinated, detyrosinated, and $\Delta 2$ α -tubulin, respectively (Figure 1b). The acetylation of α -tubulin, with the exception of WK1 and JK2 lines, was high in the GSC lines when compared to the standard cell lines (CV = 49%). There was a 53% variability in the phosphorylation of β III-tubulin and 58–72% variability in the polyglutamylation of α - and β -tubulin (Figure 1b). In summary, tubulin isoforms and their post-translational modifications varied greatly (up to 133% variability) across 15 glioblastoma cell lines.

MTAs Sensitivity. Multiparametric analysis of the dose–response curves fitted to the relative cell count (Figure 2a and Figure S4) yielded values for IC_{50} , E_{max} , AUC, and Hill coefficient h (Tables S3–S6). Live-cell imaging revealed that standard A172, U87, and U251 cells had overall shorter doubling times (35–55 h, Figure 3b). The doubling time of

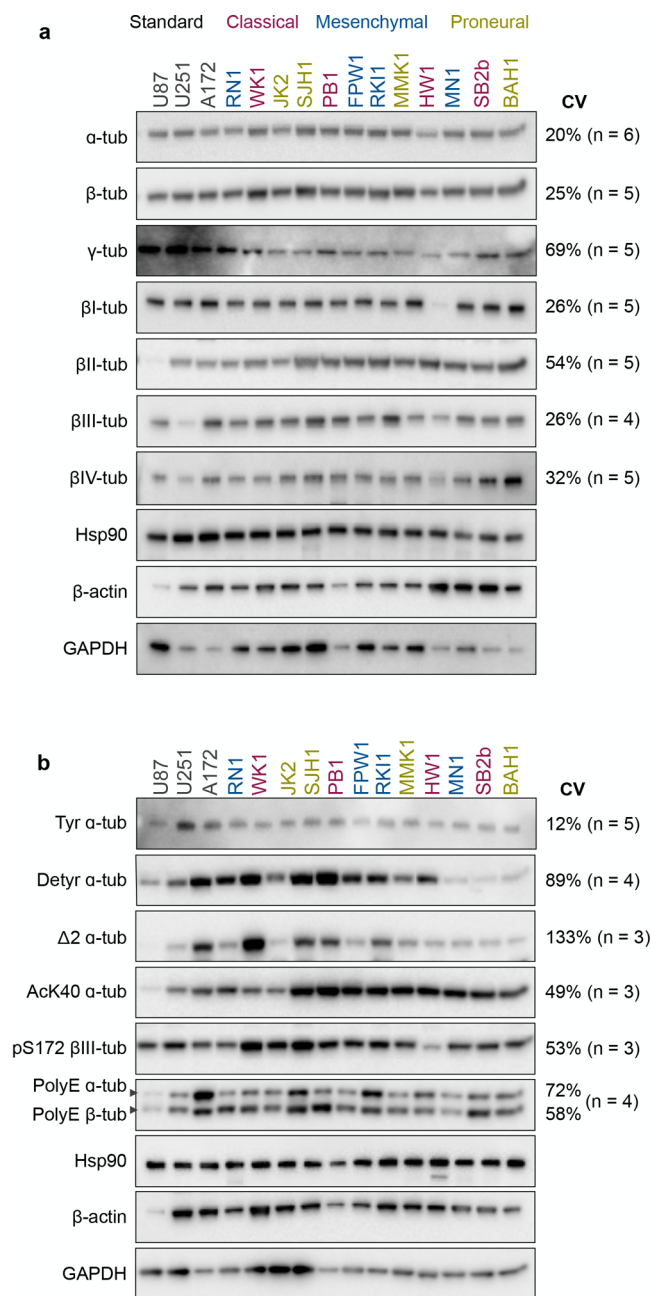


Figure 1. Tubulin isoforms and post-translational modifications in glioblastoma cells. Western blot (5 μ g of total protein) analysis of tubulin isoforms (a) and their post-translational modifications (b) in glioblastoma cell lines. Colors of the cell lines indicated the glioblastoma subtype: classical, mesenchymal, and proneural. Representative immunoblots and coefficient of variation (CV) of at least three independent experiments are shown. Quantification and normalization are presented in Figures S2 and S3.

GSC lines ranged from 49 h (proneural MMK1) to 140 h (proneural SJH1), with no clear trend for cell lines representing the same glioblastoma subtype. We then used the *GRcalculator* tool and the population doubling times to generate GR curves (Figure 2c and Figure S4) and calculated GR metrics (Tables S3–S6) for colchicine (Figure 2d), nocodazole (Figure 2e), tivantinib (Figure 2f) and CMPD1 (Figure 2g). We used GR metrics to analyze glioblastoma cell sensitivity to MTAs, as they incorporate cell proliferation rates

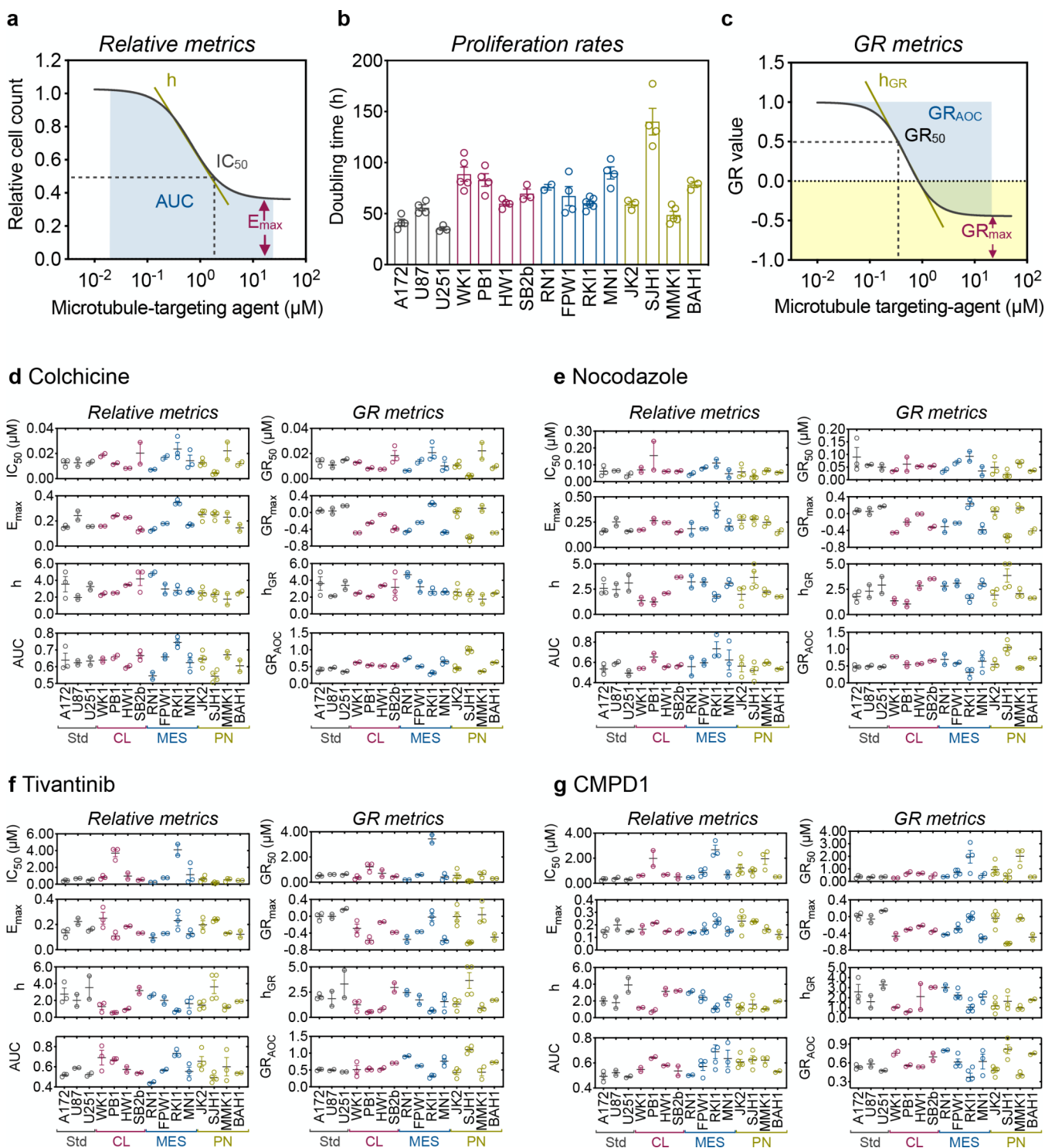


Figure 2. MTA sensitivity in glioblastoma cells. (a) Schematic of relative drug sensitivity metrics calculated from a dose–response curve fitted to a relative cell count. (b) Proliferation rates of glioblastoma cell lines were determined with the InCuCyte platform and CellCounter ++ online tool. (c) Schematic of grow inhibition (GR) metrics from a dose–response curve fitted to GR values. Relative and GR metrics for colchicine (d), nocodazole (e), tivantinib (f) and CMPD1 (g) were calculated from dose responses determined with CellTiter-Blue viability assay after 5 days of drug treatment and proliferation rates using the GRcalculator tool. Data are mean \pm SEM ($n = 3$). All values are listed in Tables S3–S6.

and are therefore considered more accurate descriptors of drug efficacy.²⁶

Within the MTAs binding to the colchicine site on microtubules, colchicine was the most potent MTA ($GR_{50} \sim 10$ nM, Figure 3d) with fully cytostatic effect in the classical HW1, proneural JK2, and MMK1 cell lines (GR_{max} close to 0).

Positive GR_{max} in the mesenchymal RK11 line indicates a partially cytostatic effect. In the remaining cell lines, GR_{max} centered around -0.4 , which corresponds to partial cytotoxicity. However, the GR_{max} values for colchicine did not reach the value of -1 , which corresponds to the killing of all cells. This incomplete cell killing efficacy implicates that each

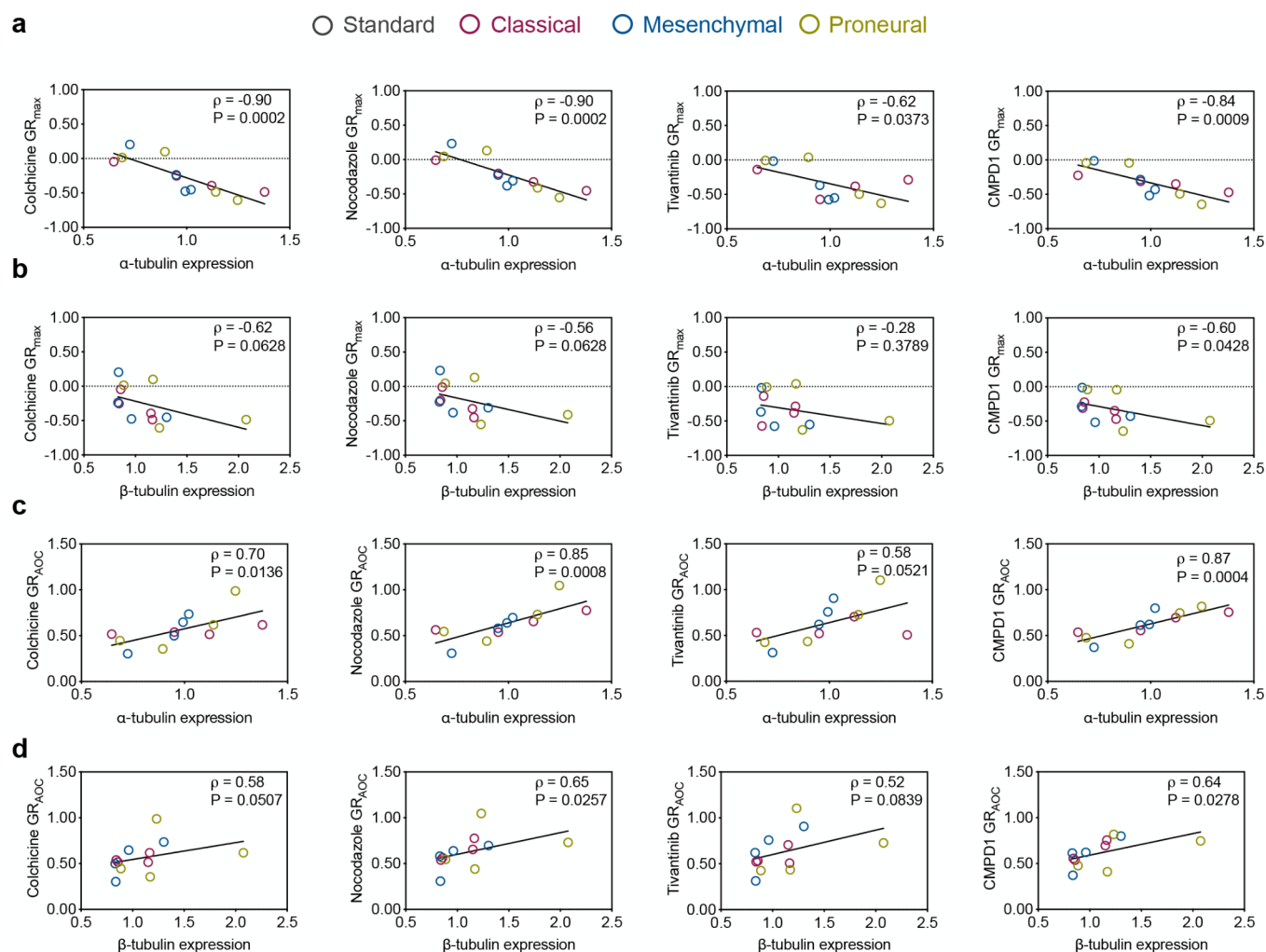


Figure 3. Spearman's correlations between tubulin expression and MTA efficacy. (a,b) Pairwise distribution and correlation of GR_{max} and the expression of α -tubulin and β -tubulin glioblastoma stem cell lines. (c,d) Pairwise distribution and correlation of GR_{AOC} and the expression of α -tubulin and β -tubulin glioblastoma stem cell lines.

glioblastoma cell line contains a subpopulation of cells able to survive colchicine treatment. This is supported by the shallow slope (low h_{GR} values) of the dose–response curves (Figure 3d), an indicator of high cell-to-cell variability. GR_{AOC} values were also low ($GR_{AOC} < 1$) for the majority of cell lines, further confirming weak colchicine efficacy. Cell lines HW1, RK11, JK2, and MMK1 were identified as the least sensitive to colchicine (GR_{max} close to 0 or positive; low GR_{AOC}) and presenting high cell-to-cell variability (low h_{GR}). Although proneural SJH1 cell line reached the lowest negative GR_{max} value ($GR_{max} = -0.75$), we do not consider this cell line as the most sensitive one. The population doubling time for SJH1 cells was 140 h, corresponding to a 0.8 division over the course of a 120 h viability assay, and GR values obtained from slow growing cell lines were considered to be ambiguous.³¹ Similar drug sensitivity metrics were obtained for nocodazole (Figure 3e), tivantinib (Figure 3f) and CMPD1 (Figure 3g).

In summary, the per-division metrics unanimously identified HW1, RK11, JK2, and MMK1 as the least MTA sensitive (GR_{max} close to 0 or positive, low GR_{AOC} , low h_{GR}). The most sensitive cells to MTAs were WK1 and MN1 with the lowest negative GR_{max} and the highest positive GR_{AOC} values. Intriguingly, glioblastoma sensitivity to MTAs is not subtype specific and within each subtype there were cell lines with high

(mesenchymal MN1) and low (mesenchymal RK11) sensitivity. Another important observation was that despite a 20-fold difference in potency, colchicine ($GR_{50} = 13$ nM) and CMPD1 ($GR_{50} = 273$ nM) displayed the same efficacy in the most sensitive WK1 cells ($GR_{max} = -0.48$ and -0.47 , respectively).

Correlations of the MTAs Sensitivity with the Tubulin Code. Given the observed tubulin heterogeneity (Figure 1) and MTAs sensitivity (Figure 2) in the GSC lines, we questioned whether the tubulin code has an effect on MTAs efficacy. We calculated Spearman's correlation coefficients between the tubulin code metrics normalized to A172 and MTAs parameters for each agent (Tables S7–S10). Data obtained with standard A172, U87, and U251 cell lines were excluded, as these cells were grown under different conditions (serum-grown vs serum-free media for GSC) and were found to possess nearly identical tubulin code profiles and MTA sensitivities.

While there were numerous correlations between the tubulin features and the relative (IC_{50} , E_{max} , h , AUC) metrics for individual MTAs, these correlations were not consistent across the four MTAs (Tables S7–S10). Importantly, consistent negative ($\rho < -0.6$; $P < 0.05$) correlations were found between the total levels of α -tubulin and the GR_{max} values of all four

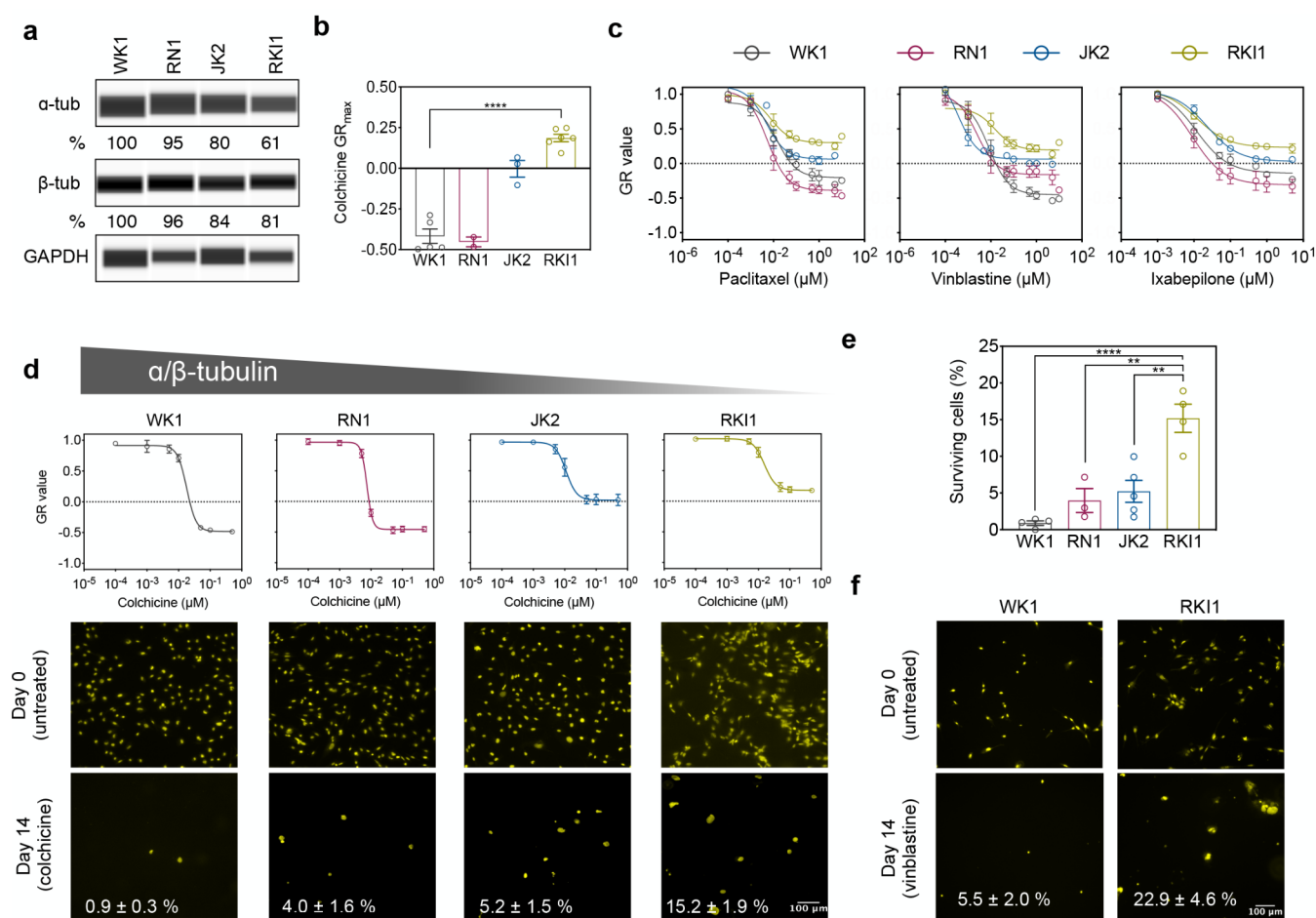


Figure 4. Cells with lower levels of α/β -tubulin generate more drug-tolerant cells. (a) Capillary-based immunoassays of total α - and β -tubulin. Representative images and mean value of three independent experiments are shown. (b) GR_{max} values for colchicine in four glioblastoma cell lines. ($n = 3-5$, one-way ANOVA). (c) RKI1 cells were treated with paclitaxel, vinblastine, and ixabepilone for 5 days and CellTiter-Blue viability assay was performed. GR values and dose–response curves were generated with the *GRcalculator* tool. Each curve is a mean of three independent cell viability assays, where each data point was done in triplicate. (d,e) GR curves for colchicine were extracted from Figure S4. Cells were treated with colchicine (500 nM) and stained with Nuclear-ID Red on day 0 and day 14. Representative images (d) and quantification (e) of five independent experiments are shown (mean \pm SEM). (f) Cells were treated with vinblastine (25 nM) and stained with Nuclear-ID Red on day 0 and day 14. Representative images and quantification (mean \pm SEM) of three independent experiments are shown.

drugs (Figure 3a). Negative correlations were also found between GR_{max} values of colchicine, nocodazole, CMPD1, and expression of β -tubulin ($\rho < -0.5$, $P < 0.06$). Furthermore, positive correlations were found between the GR_{AOC} and total α -tubulin (Figure 3c) as well as β -tubulin (Figure 3d). Except for tivantinib ($P < 0.08$), the remaining GR_{AOC} correlations were statistically significant ($\rho > 0.58$, $P < 0.05$). Since data obtained with BAH1 cells were identified as outliers, we reanalyzed data sets excluding BAH1 data and confirmed correlations between the MTA efficacy metrics and expression of α - and β -tubulin (Figure S5). Together, these correlations suggest that the lower expression of α/β -tubulin is linked to weak MTA efficacy (i.e., higher GR_{max} and lower GR_{AOC}).

Total Tubulin Levels Impact MTAs Efficacy. To validate the quantity of α/β -tubulins as determinants of cellular response to MTAs, we performed additional experiments with WK1, RN1 (higher α/β -tubulin expression), JK2, and RKI1 cells (lower α/β -tubulin expression). Quantitative capillary-based immunoassay analysis confirmed decreasing order of α - and β -tubulin expression in WK1 > RN1 > JK2 > RKI1 cells (Figure 4a). Colchicine treatment was cytotoxic to WK1 and RN1 but cytostatic to JK2 and RKI1 (Figure 4b).

The GR dose–response curves for paclitaxel, vinblastine, and ixabepilone exhibited the same efficacy trend (Figure 4c). These clinical MTAs were cytotoxic to WK1 and RN1 (higher α/β -tubulin expression) but cytostatic to JK2 and RKI1 cells (lower α/β -tubulin expression). To further confirm that overall tubulin levels may be linked to the efficacy of MTAs, we performed an orthogonal assay that quantifies surviving drug-tolerant cells.^{8,10} On the basis of the colchicine GR curves (Figure 4d), we hypothesized that surviving subpopulations will be larger in JK2 and RKI1 cells. As expected, significantly more colchicine-tolerant persistor cells were detected in RKI1 cells when compared to WK1 and RN1 (Figure 4d,e). Similarly, the percentage of drug-tolerant cells was larger in the vinblastine-treated RKI1 cells when compared to vinblastine-treated WK1 cells (Figure 4f).

Fractional killing has been previously attributed to insufficient target engagement in surviving cells.²⁵ However, immunofluorescence of WK1 and RKI1 cells treated with colchicine revealed dose-dependent disruption of the microtubules in all cells, suggesting target engagement in the entire cell populations (Figure 5a). To ensure that cell survival was not due to the overexpression of drug efflux proteins, we

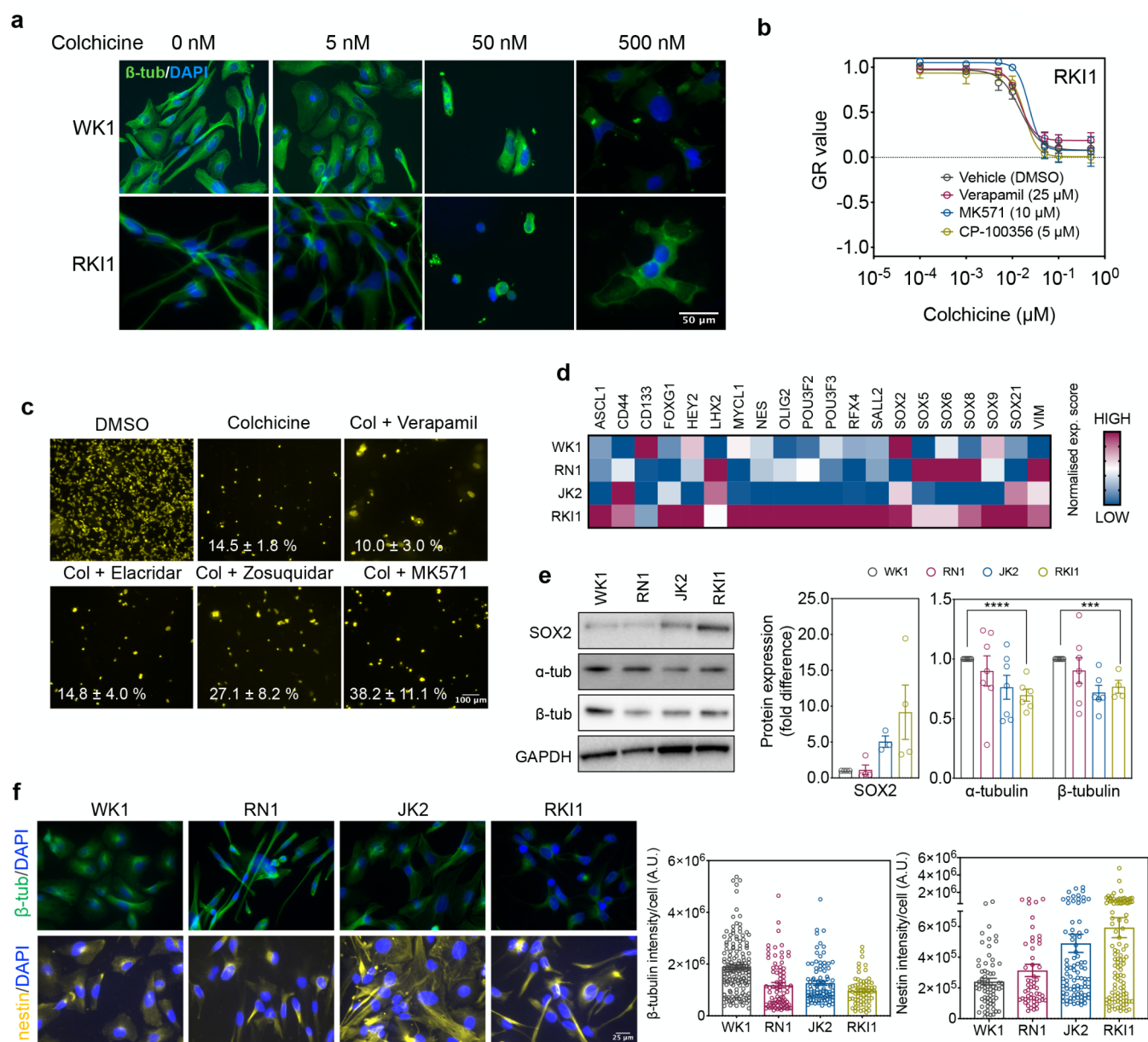


Figure 5. Target engagement and expression of stem-cell markers. (a) WK1 and RKI1 cells were treated with colchicine for 5 days and stained with Alexa488-labeled anti- β -tubulin antibody (green) and DAPI (blue). Representative images of two independent experiments are shown. (b) RKI1 cells were treated with colchicine \pm efflux inhibitors for 5 days and CellTiter-Blue viability assay was performed. GR values and dose–response curves were generated with the *GRcalculator* tool. (c) RKI1 cells were treated with 500 nM colchicine (Col) \pm verapamil (25 μ M), elacridar (1 μ M), zosuquidar (1 μ M), and MK571 (10 μ M) for 14 days and stained with Nuclear-ID Red. Representative images and quantification (mean \pm SEM) of 3–6 independent experiments are shown. (d) Heat map representation of the RNA-seq expression (red, high; blue, low) pattern of the transcription factors specific for glioblastoma stem cells in WK1, RN1, JK2, and RKI1 cells. (e) Western blot analysis of SOX2 (30 μ g of total protein), α - and β -tubulin (1 μ g total protein). Representative immunoblots and quantification presented as fold change relative to WK1 (set as 1) are shown. Data are mean \pm SEM ($n = 4$ –7; unpaired *t* test WK1 vs RKI1, **** $P < 0.001$, **** $P < 0.0001$). (f) Cells were fixed and stained with AlexaFluor594-labeled anti- β -tubulin (green), AlexaFluor488-labeled anti-nestin (yellow) antibodies and DAPI (blue). Representative images and quantification of three independent experiments are shown.

performed control experiments with inhibitors of drug efflux pumps. The GR curves for colchicine (Figure 5b), CPD1, and paclitaxel (Figure S6a,b) were identical between naïve RKI1 cells and RKI1 cells cotreated with efflux inhibitors verapamil, MK571, and CP-100356. Furthermore, the size of the RKI1 subpopulation surviving a 14-day treatment with colchicine did not decrease when cells were cotreated with verapamil (MDR1/BCRP inhibitor³²), elacridar, and zosuqui-

dar (MDR1 inhibitors³³) or MK571 (MRP1 inhibitor³⁴) (Figure 5c). Finally, flow cytometry analysis revealed no changes in MDR1 levels between colchicine-naïve (day 0) and colchicine-surviving cells (day 14) (Figure S6). Together, these data suggest that cell lines with lower α/β -tubulin expression are less sensitive to MTAs and generate larger populations of drug-tolerant cells. This phenomenon appears

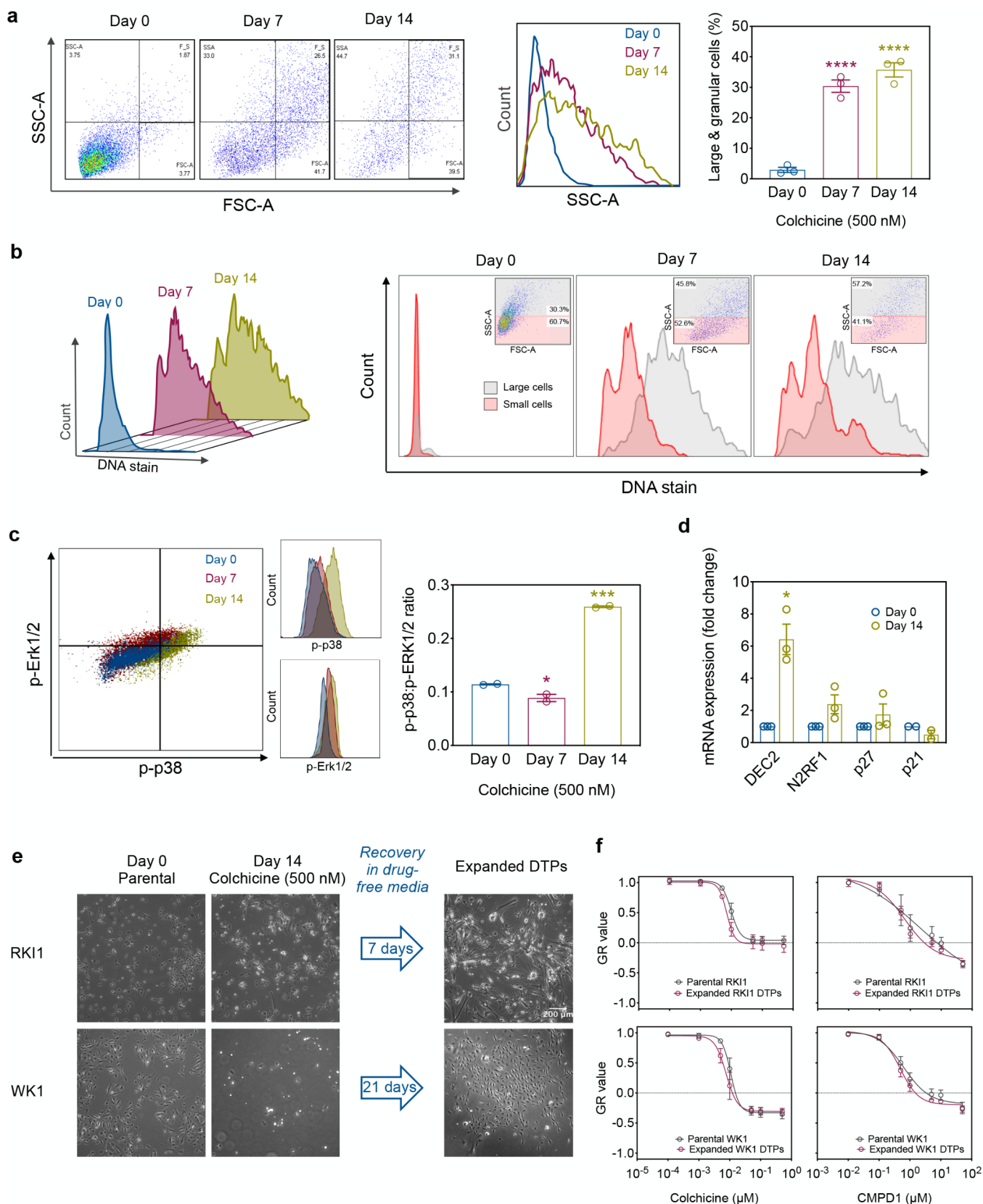


Figure 6. Prolonged colchicine treatment induces dormancy. (a) RK11 cells were treated with colchicine (500 nM), stained, and analyzed by flow cytometry for size (FSC-A) and granularity (SSC-A). Geometric mean of FSC-A (size) and SSC-A (granularity) was graphed using Prism v7.0 (GraphPad). Data are mean \pm SEM ($n = 3$). (b) RK11 cells were treated with colchicine (500 nM), stained for DNA with Vybrant DyeCycle Violet Stain and analyzed by flow cytometry. Representative FACS plots of three independent experiments are shown. (c) RK11 cells were treated with colchicine (500 nM), stained with PE-eFluor610 conjugated p-ERK1/2 and APC conjugated p-p38 antibodies. The geometric mean of p-p38:p-ERK1/2 was graphed using Prism v7.0 (GraphPad). Data are mean \pm SEM ($n = 3$). (d) Lysates of untreated (day 0) and colchicine (500 nM)

Figure 6. continued

treated (day 14) RKI1 cells were analyzed by RT-PCR. mRNA levels were normalized to GAPDH mRNA. Data are mean \pm SEM ($n = 3$). (e) RKI1 and WK1 cells (day 0) were treated with colchicine (500 nM) for 14 days (day 14). Cells were allowed to recover until they regained their normal morphology (expanded DTPs). (f) RKI1 and (g) WK1 parental and expanded DTPs were treated with colchicine and CMPD1. GR curves were generated from dose responses determined with CellTiter-Blue viability assay after 5 days of drug treatment using the GRcalculator tool. Each curve is a mean of three independent cell viability assays, where each data point was done in triplicate.

to be independent of drug efflux proteins and insufficient target engagement.

MTA Tolerant Cells Overexpress Stemness Markers and Convert to Dormant Cells. We observed that MTA tolerant RKI1 cells were proliferating faster than MTA-sensitive WK1 cells (Figure 2b). As fast proliferation is a functional criterion of glioblastoma stem cells,³⁵ we hypothesized that the degree of stemness might be related to MTA sensitivity. Data from RNA sequencing analysis revealed that 13 out of 20 transcription factors specific for glioblastoma stem cells^{35–37} are upregulated in RKI1 cells (low MTA sensitivity) when compared to WK1 (high MTA sensitivity) cells (Figure 5d). At the protein level, SOX2 expression increases as the expression of α/β -tubulin decreases (Figure 5e). Having also confirmed lower β -tubulin expression in the JK2 and RKI1 cells by immunofluorescence, we further show that the expression of nestin is higher in the MTA-tolerant JK2 and RKI1 cells compared to the MTA-sensitive WK1 and RN1 (Figure 5f). Thus, MTA tolerant cell lines express higher levels of stemness markers and lower baseline levels of α/β -tubulin.

To further understand how glioblastoma cells survive MTA treatment, we performed flow cytometry analysis of colchicine-surviving RKI1 cells and found that drug-tolerant cells expressed features of dormant cells:^{38–40} large granular morphology (Figure 6a) and polyploidy (Figure 6b), high p38:p-ERK1/2 ratio (Figure 6c) and upregulation of the key dormancy markers DEC2, NR2F1, and p27 (Figure 6d). On the contrary, the levels of mRNA coding for p21, which is a marker of senescence (irreversible cell cycle arrest), decreased (Figure 6d). As dormancy is reversible, colchicine-surviving RKI1 and WK1 cells were allowed to recover in the absence of the drug and then expanded. The fraction of drug-tolerant cells was smaller in the WK1 cell line compared to that in the RKI1, and WK1 surviving cells required longer recovery time. However, both RKI1 and WK1 drug-tolerant subpopulations eventually regained proliferation (Figure 6e). The MTA dose-response curves for the parental (drug-naive) and expanded drug-tolerant persister cells were indistinguishable (Figure 6f,g), implicating that drug-sensitive cells arise from drug-tolerant cells. Thus, the incomplete killing of glioblastoma stem cells by MTAs is not caused by a stable subpopulation of drug-resistant cells but rather by a fraction of cells that is able to resonate between proliferative (i.e., drug-sensitive) and dormant (i.e., drug-tolerant) states. These drug-tolerant fractions are larger and more aggressive in cell lines expressing lower baseline levels of α - and β -tubulin.

DISCUSSION

The analysis of the tubulin heterogeneity and MTA efficacy presented in this paper provides novel insights into the relationships between microtubules and MTAs. Furthermore, our data showing that the tubulin expression and post-translational modifications within a tissue-specific cancer type are unique for each cell line expand the concept of cancer heterogeneity. Genetic and epigenetic profiling have revealed

the existence of various molecular subtypes within a tissue-specific tumor, but these subclassifications have been largely limited to alteration in signaling pathways and not to the house-keeping proteins such as tubulin.

Prior literature has reported variability in the expression of β -tubulin isoforms.³⁰ However, other components of the tubulin code, such as α - and γ -tubulin and the post-translational modifications were not known. We observed a considerable variability (19–133%) in the levels of α -, β -, and γ -tubulin and their post-translational modifications. Thus, in addition to cell signaling abnormalities found in glioblastoma (Table S1), such as EGFR amplification and PTEN deletion,¹² microtubule modifications appear unique for each tumor. The cell line-specific tubulin code is likely a connection to different phenotypes of these cell lines, and we anticipate that deeper understanding of these differences will improve our effort to effectively target glioblastoma cells. Importantly, we also show that the tubulin characteristics found in the standard glioblastoma cell lines routinely used in research are not representative of those found in the clinically relevant glioblastoma stem cell lines. As such, future studies into the roles of the tubulin code in glioblastoma should not be based on data obtained from the standard serum-grown cell lines.

MTAs sensitivity was variable across glioblastoma cell lines, ranging from partially cytotoxic to partially cytostatic responses. We found that the glioblastoma cell sensitivity to MTAs is independent of tubulin isoforms and the post-translational modifications investigated in this project. Surprisingly, the baseline levels of α - and β -tubulin correlated with the sensitivity to MTAs. The most sensitive cells contained the highest levels of α - and β -tubulin. This finding is in agreement with the concept that high expression of the targeted protein is usually a good predictor of responsiveness to drugs targeting that protein.⁴¹ However, while this hypothesis has been validated with receptor ligands and molecularly targeted cancer drugs, MTAs were not expected to fit into this concept, as microtubules are abundantly expressed in every cell. Our data showing that MTAs sensitivity declines with the decreasing levels of α - and β -tubulins points toward similarities in the mechanism of action of molecularly targeted drugs and MTAs. Moreover, our work confirms that drug efficacy parameters on a per-division basis have higher information content than conventional metrics.^{25,26,42} While the conventional dose-response curves fitted to relative cell count were overlapping, the growth rate corrected curves revealed significant differences in the maximum efficacy (Figure S4). Furthermore, when correlating MTA sensitivity with tubulin features, the per-division GR_{max} and GR_{AOC} but not the conventional E_{max} and AUC metrics enabled us to identify the relationship between the α/β -tubulin levels and sensitivity to MTAs.

The most prevalent model of MTAs efficacy is based on the extensive clinical and *in vitro* data indicating that β -tubulin isoforms overexpression is involved in resistance to taxanes and *vinca* alkaloids (reviewed in ref 30). Our somewhat contrasting

data show that the high baseline levels of α/β -tubulin are determinants of good MTAs sensitivity in glioblastoma models. Nevertheless, it is important to highlight the difference in the experimental approaches. The majority of MTAs efficacy studies analyzed the expression of tubulin isotypes in drug-resistant cancer cells grown in media containing MTAs, thus describing mechanisms of the acquired resistance. Here, we have taken a different approach and analyzed how basal tubulin levels affect the first exposure of cells to MTAs. Furthermore, we identified that low α/β -tubulin levels mark MTAs tolerance but not resistance. Although not strictly defined, the difference between drug tolerance and resistance lies in the ability of a cell to proliferate in the presence of the drug.⁴³ Unlike resistant cells which survive and proliferate in the presence of a drug, tolerant cells are able to survive but do not proliferate while exposed to the drug. As we show in the follow-up experiments, MTA treatment led to survival of drug-tolerant persister cells which resumed proliferation only upon the MTA removal.

Finally, we show that decreased α/β -tubulin expression is associated with lack of cell differentiation. The higher is the dedifferentiation state, the lower is the α/β -tubulin expression. Intriguingly, dedifferentiated cells survive the first exposure to MTA chemotherapy by activating a dormant state. Similar observations have been reported with molecularly targeted kinase inhibitor dasatinib.⁸ Whether the MTA-induced dormancy in glioblastoma cells is a primary step preceding acquired drug resistance remains to be investigated.

Small molecule MTAs able to penetrate the blood–brain barrier are in the preclinical and clinical development. In cancer treatments, the personalized medicine approach to genetically diverse tumors is now well-established with molecularly targeted drugs. We show in this study that chemotherapy with MTAs might face the same challenge, as tubulin profile and sensitivity to MTAs vary greatly across glioblastoma cell lines. We discovered that low α/β -tubulin expression limits the efficacy of MTAs, arguing the *one-drug-fits-all* concept for MTAs.

METHODS

Cell Lines. Standard A172 (cat. no. 88062428), U251 (cat. no. 09063001) and U87 (cat. no. 89081402) glioblastoma cell lines were obtained from the European Collection of Authenticated Cell Cultures (ECACC, Salisbury, UK) through Cell Bank Australia in 2014. Cells were cultured in DMEM supplemented with 10% FBS (InterPath) and antibiotic–antimycotic solution (Life Technologies) at 37 °C and 5% CO₂. Glioblastoma stem cell lines were derived from glioblastoma specimens. The protocols were approved by the Human Ethics Committee of the Royal Brisbane & Women's Hospital (RBWH 2004/161). The RNA sequencing, mutational profile (Table S1), and subtype assignment for these cells have been published.²¹ GSC lines were cultured in KnockOut DMEM/F-12 basal medium supplemented with StemPro NSC SFM supplement, 2 mM GlutaMAX-ICTS, 20 ng/mL EGF, 10 ng/mL FGF- β , and antibiotic–antimycotic solution (all Life Technologies) as adherent cells on flasks coated with MatriGel Matrix (Corning Life Sciences). All cell cultures were routinely tested for mycoplasma infection, and the cumulative length of culturing did not exceed 15 passages.

Western Blotting. Cell lysates were prepared by adding 1 mL RIPA buffer to a T175 flask of unsynchronized cells at 80–90% confluency. Protein concentrations were determined with Pierce BCA assay kit (ThermoFisher Scientific), following

manufacturer's instructions. Lysates were resolved (2 h, 95 V) on 4–12% SDS-PAGE gels and transferred onto PVDF membranes using iBlot 2, P3 for 7 min (all Life Technologies). Membranes were blocked with 5% BSA in TBST, incubated with primary antibodies (Table S2) in 5% BSA in TBST overnight at 4 °C and with secondary antibody for 1 h at room temperature. All secondary antibody preparations were in 5% skim milk in TBST, with the exception of antityrosinated α tubulin and antiphospho β III-tubulin, which were prepared in 5% BSA. Detection was performed with Immobilon Western HRP Substrate Luminol-Peroxidase reagent (MerckMillipore) and the ChemiDoc MP Imaging System (Bio-Rad). Densitometry quantification was done with ImageLab software (BioRad).

Cell Viability. Cells (2×10^3 cells/well) were plated in 96-well plates, with the exception of PB1 cells (8×10^3 cells/well). Cells were treated with DMSO (vehicle), colchicine (Tocris, cat. no. 1364), nocodazole (Tocris, cat. no. 1228), tivantinib (Selleckchem, cat. no. S2753), CMPD1 (Santa Cruz, cat. no. sc-203138), paclitaxel (Tocris, cat. no. 1097), vinblastine (Tocris, cat. no. 1256) and ixabepilone (AdooQ Bioscience, cat. no. A11449), at log 3 8-point dilution row for 5 days, with or without cotreatment with efflux pump inhibitors verapamil (Sigma-Aldrich, cat. no. V4629), MKS71 (Sigma-Aldrich, cat. no. M7571) or CP-100356 (Sigma-Aldrich, cat. no. PZ0171). CellTiter-Blue dye (Promega) was added at 37 °C for 2–4 h, and fluorescence was measured with a Tecan M200 PRO+ microplate reader (Tecan) at 585 nm. Data were normalized to DMSO-treated controls (set as 1). Relative and per-division metrics were calculated from the viability data and proliferation rates using the *GRcalculator* online tool.^{26,42} Graphs were recreated from the *GRcalculator* online tool using Prism 7.0 (GraphPad).

Proliferation Rate. Cells were seeded at 500, 1×10^3 , 2×10^3 , and 4×10^3 cells/well in the 96-well plates. Proliferation was monitored by analyzing the occupied area (% confluence) of cell images over 7 days using the InCuCyte IC S3 2018A software (Essen Bioscience). Population doubling times were computed with several time points, from different initial cell densities using the “cell calculator++” tool (doubling-time.com; Roth V., 2006).

DTP Generation and Expansion. WK1 and RKI1 cells (1×10^6) were treated with 500 nM colchicine for 14 days. Fresh media with drug was added every 3 days. At day 14, drug-tolerant persisters were allowed to recover in drug-free media. Cells were monitored every 3 days until they regained their morphology and expansion started when cells resembled their parental cell lines. Images were taken using Zeiss Axio Vert.A1 microscope and ZEN 2–blue edition software (Zeiss). Expanded DTPs were seeded at 2×10^3 cells/well density for the viability assays in Figure 7.

Flow Cytometry. RKI1 cells (1.2×10^6) were treated with colchicine (500 nM) and samples were collected at day 0 (untreated), day 7, and day 14. Floating and adherent cells were washed with ice-cold PBS. For cell viability, samples were stained using LIVE/DEAD Fixable Near-IR Dead Cell Stain Kit (ThermoFisher Scientific) for 30 min at 4 °C in the dark as per manufacturer's instructions. Samples were centrifuged at 300g for 5 min at 4 °C, washed with ice-cold PBS with 2% FBS (blocking buffer), and incubated in FITC conjugated human-CD243 (*MDR-1*) antibody/ 10^6 cells (ThermoFisher Scientific, 1:10 in blocking buffer) in 50 μ L reaction volume on ice for 45 min. Samples were centrifuged, washed twice with the blocking

buffer, and incubated in fixation buffer (BioLegend) for 10 min at room temperature (RT) as per manufacturer's instructions, followed by permeabilization by adding 350 μL of ice-cold 100% methanol with vortexing. For dormancy analysis, samples were washed twice with blocking buffer before being incubated with p-ERK1/2 (PE-eFluor610 conjugate, ThermoFisher Scientific) and p-p38 (APC conjugate, ThermoFisher Scientific) antibodies/ 10^6 cells in 1:10 dilution with blocking buffer in 50 μL reaction vol for 45 min on ice. For DNA analysis, samples were washed twice with blocking buffer and stained with Vybrant DyeCycle Violet Stain (ThermoFisher Scientific) at 37 $^\circ\text{C}$ for 30 min as per manufacturer's instructions. Samples were analyzed on LSRFortessa X-20 running FACSDiVa v6 software (BD Biosciences). Live and dead cells were discriminated by a live cell gating, and expression levels of CD243, p-ERK1/2, p-p38, and DNA analyses were performed on the live cell gate; all data were analyzed using FlowJo v10.3. Unstained and single stained samples were used as compensation controls.

Nuclear-ID Red Staining. WK1, RN1, JK2, and RK11 (1×10^5) were treated with 500 nM colchicine $\pm 25 \mu\text{M}$ verapamil, 1 μM elacridar (Tocris, cat no. 4646), 1 μM zosuquidar (Tocris, cat no. 5456) or 10 μM MK571 (Sigma-Aldrich, cat no. M7571) for 14 days. Fresh media containing drugs was added every 3 days. Untreated (day 0) and treated (day 14) cells were stained with Nuclear-ID red stain (Enzo Lifesciences) at 1:1,000 dilution in StemPro media. Cells were incubated with the stain for 30 min prior to mounting onto microscope slides using Dako Fluorescence Mounting Medium (Agilent). Images were taken using Zeiss Axio Scope.A1 and ZEN 2–blue edition software (Zeiss) and processed using Fiji.

Capillary Immunoassay. Total cell lysates at 1 $\mu\text{g}/\mu\text{L}$ (α -tubulin) and 0.25 $\mu\text{g}/\mu\text{L}$ (β -tubulin) were analyzed using an automated capillary electrophoresis system Wes (ProteinSimple), as per manufacturer's instructions. Wes Separation Capillary Cartridges for 12–230 kDa (ProteinSimple) were used. The primary antibodies used in Western blotting were also used for the capillary immunoassay at 1:50 dilution (α -tubulin, GAPDH) or 1:1,000 dilution (β -tubulin). Signals were detected with Anti-Rabbit and Anti-Mouse Detection Modules for Jess, Wes, Peggy Sue, or Sally Sue and analyzed using Compass software (all ProteinSimple).

qRT-PCR. qRT-PCR was carried out according to standard protocols. RK11 cells (1.2×10^6) were treated with colchicine (500 nM) for 14 days. Fresh media containing colchicine was added every 3 days. Cells were lysed at day 0 (untreated) and day 14. RNeasy mini kit (Qiagen) was used to isolate RNA from cell lysates as per manufacturer's instructions. cDNA was generated using Applied Biosystems High-Capacity cDNA Reverse Transcription kit (Life Technologies) as per manufacturer's instructions. qRT-PCR was performed using DEC2, p27 (both Integrated DNA Technologies), N2RF1 (Qiagen, cat no. QT00089355), p21 (Qiagen, cat no. QT00005803), and GAPDH primers (Qiagen, cat no. QT00079247) with KAPA SYBR FAST Universal 2X qPCR Master Mix (Kapa Biosystems). RT-PCR was run on LightCycler 480 (Roche). The cycling conditions were as follows: 10 min at 95 $^\circ\text{C}$ followed by 40 cycles, each consisting of 10 s at 95 $^\circ\text{C}$ and 30 s at 60 $^\circ\text{C}$. Samples were run in triplicate. Threshold cycles (C_t) were calculated using the LightCycler 480 software. Relative quantification using the comparative C_t method was used to analyze the data output.

Values were expressed as fold change over corresponding values for the control by the $2^{-\Delta\Delta C_t}$ method.

Immunofluorescence. For β -tubulin immunofluorescence in DTPs, cells (8×10^3) were treated with colchicine (5–500 nM) for 5 days. For nestin and β -tubulin immunofluorescence, untreated cells (1×10^5) were fixed with ice-cold 4% PFA for 20 min at RT and blocked in 5% BSA/PBS for 20 min. Cells were incubated with anti-nestin (1:25, R&D Systems) and anti- β -tubulin antibody (1:200, Abcam). Secondary antibodies were Alexa488-conjugated antimouse IgG (against nestin) and Alexa594-conjugated antirabbit IgG (against β -tubulin) (Life Technologies). Cell nuclei were counterstained using Prolong Gold mounting media with DAPI (Life Technologies). Images were acquired under 40 \times objectives on a Zeiss Axio Scope.A1 microscope using ZEN 2–blue edition software (Zeiss). Images were processed using Fiji software.

Data and Statistical Analysis. The data and statistical analysis comply with the recommendations on experimental design and analysis in pharmacology. All immunoblots and immunofluorescence images are representatives of at least three independent experiments. All cellular assays were repeated at least three times, and each was run in duplicate or triplicate. All results are expressed as mean \pm SEM. All statistical analyses were performed using Prism v7.0 (Graph-Pad). Correlation analysis between tubulin isotypes/post-translational modifications and MTA efficacy was performed using Spearman's correlation method as not all data sets followed a normal distribution. Two-tailed P values are listed for these correlations. An independent *t* test was performed for comparison of two data sets, and 1-way ANOVA followed by Tukey's post hoc test was used when there were multiple groups to compare. In all cases, $P < 0.05$ was considered significant.

■ ASSOCIATED CONTENT

📄 Supporting Information

The Supporting Information is available free of charge on the ACS Publications website at DOI: 10.1021/acsptsci.9b00045.

Genotypes of glioblastoma stem cell lines; details of primary antibodies; MTAs sensitivity metric values; Spearman's correlation coefficients between MTAs sensitivity metrics with tubulin code; representative image of Coomassie stained gels; expression of tubulin isotypes and post-translational modifications normalized to A172 and RN1 signals; dose–response curves for MTAs in glioblastoma cell lines; Spearman's correlations between tubulin expression and MTAs efficacy excluding BAH1 data; data obtained with inhibitors of efflux pumps (PDF)

■ AUTHOR INFORMATION

Corresponding Author

*E-mail: lenka.munoz@sydney.edu.au. Tel.: +61 2 9351 2315. Fax: +61 2 8627 1606.

ORCID

Lenka Munoz: 0000-0002-7625-5646

Author Contributions

R.H.A. and L.M. designed the study. R.H.A., A.R. and D.I.V. performed experiments and data analysis under L.M. supervision. T.G.J., B.W.S. and B.W.D. generated, characterized, and provided GSC lines.

Notes

The authors declare no competing financial interest.

ACKNOWLEDGMENTS

This work was supported by funding from The University of Sydney, Brain Foundation Australia, Cancer Institute New South Wales and the National Health & Medical Research Council of Australia. R.H.A. is supported by The University of Sydney RTP scholarship, and L.M. has been supported by Cancer Institute NSW Career Development Fellowship (15/CDF/107).

REFERENCES

- (1) Steinmetz, M. O., and Prota, A. E. (2018) Microtubule-targeting agents: Strategies to hijack the cytoskeleton. *Trends Cell Biol.* 28, 776–792.
- (2) Roll-Mecak, A. (2019) How cells exploit tubulin diversity to build functional cellular microtubule mosaics. *Curr. Opin. Cell Biol.* 56, 102–108.
- (3) Gadadhar, S., Bodakuntla, S., Natarajan, K., and Janke, C. (2017) The tubulin code at a glance. *J. Cell Sci.* 130, 1347.
- (4) Kavallaris, M. (2010) Microtubules and resistance to tubulin-binding agents. *Nat. Rev. Cancer* 10, 194–204.
- (5) Parker, A. L., Teo, W. S., McCarroll, J. A., and Kavallaris, M. (2017) An emerging role for tubulin isotypes in modulating cancer biology and chemotherapy resistance. *Int. J. Mol. Sci.* 18, 1434.
- (6) Hangauer, M. J., et al. (2017) Drug-tolerant persister cancer cells are vulnerable to GPX4 inhibition. *Nature* 551, 247–250.
- (7) Sharma, S. V., et al. (2010) A chromatin-mediated reversible drug-tolerant state in cancer cell subpopulations. *Cell* 141, 69–80.
- (8) Liao, B. B., et al. (2017) Adaptive chromatin remodeling drives glioblastoma stem cell plasticity and drug tolerance. *Cell Stem Cell* 20, 233–246.
- (9) Roesch, A., et al. (2013) Overcoming intrinsic multidrug resistance in melanoma by blocking the mitochondrial respiratory chain of slow-cycling JARID1B(high) cells. *Cancer Cell* 23, 811–825.
- (10) Dalvi, M. P., et al. (2017) Taxane-platin-resistant lung cancers co-develop hypersensitivity to JumoniC Demethylase inhibitors. *Cell Rep.* 19, 1669–1684.
- (11) Goldman, A., et al. (2015) Temporally sequenced anticancer drugs overcome adaptive resistance by targeting a vulnerable chemotherapy-induced phenotypic transition. *Nat. Commun.* 6, 6139.
- (12) Brennan, C. W., et al. (2013) The somatic genomic landscape of glioblastoma. *Cell* 155, 462–477.
- (13) Tanaka, S., Louis, D. N., Curry, W. T., Batchelor, T. T., and Dietrich, J. (2013) Diagnostic and therapeutic avenues for glioblastoma: no longer a dead end? *Nat. Rev. Clin. Oncol.* 10, 14–26.
- (14) Liu, Y., et al. (2014) Paclitaxel loaded liposomes decorated with a multifunctional tandem peptide for glioma targeting. *Biomaterials* 35, 4835–4847.
- (15) Kang, T., et al. (2014) iNGR-modified PEG-PLGA nanoparticles that recognize tumor vasculature and penetrate gliomas. *Biomaterials* 35, 4319–4332.
- (16) Zhang, B., et al. (2015) UPA-sensitive ACP-PP-conjugated nanoparticles for multi-targeting therapy of brain glioma. *Biomaterials* 36, 98–109.
- (17) Senese, S., et al. (2014) Chemical dissection of the cell cycle: probes for cell biology and anti-cancer drug development. *Cell Death Dis.* 5, No. e1462.
- (18) Prabhu, S., Harris, F., Lea, R., and Snape, T. J. (2014) Small-molecule clinical trial candidates for the treatment of glioma. *Drug Discovery Today* 19, 1298–1308.
- (19) Gurgis, F., Akerfeldt, M., Heng, B., Wong, C., Adams, S., Guillemain, G., Johns, T., Chircop, M., and Munoz, L. (2015) Cytotoxic activity of the MK2 inhibitor CMPD1 in glioblastoma cells is independent of MK2. *Cell Death Discovery* 1, 15028.
- (20) Phoa, A. F., et al. (2015) Pharmacology of novel small-molecule tubulin inhibitors in glioblastoma cells with enhanced EGFR signalling. *Biochem. Pharmacol.* 98, 587–601.
- (21) Stringer, B. W., et al. (2019) A reference collection of patient-derived cell line and xenograft models of proneural, classical and mesenchymal glioblastoma. *Sci. Rep.* 9, 4902.
- (22) Katayama, R., et al. (2013) Cytotoxic activity of tivantinib (ARQ 197) is not due solely to c-MET inhibition. *Cancer Res.* 73, 3087–3096.
- (23) Wang, Y., et al. (2016) Structures of a diverse set of colchicine binding site inhibitors in complex with tubulin provide a rationale for drug discovery. *FEBS J.* 283, 102–111.
- (24) Rankovic, Z. (2017) CNS Physicochemical property space shaped by a diverse set of molecules with experimentally determined exposure in the mouse brain. *J. Med. Chem.* 60, 5943–5954.
- (25) Fallahi-Sichani, M., Honarnejad, S., Heiser, L. M., Gray, J. W., and Sorger, P. K. (2013) Metrics other than potency reveal systematic variation in responses to cancer drugs. *Nat. Chem. Biol.* 9, 708.
- (26) Hafner, M., Niepel, M., Chung, M., and Sorger, P. K. (2016) Growth rate inhibition metrics correct for confounders in measuring sensitivity to cancer drugs. *Nat. Methods* 13, 521.
- (27) Hafner, M., Niepel, M., Subramanian, K., and Sorger, P. K. (2017) Designing drug-response experiments and quantifying their results. *Curr. Protocols Chem. Biol.* 9, 96–116.
- (28) Niepel, M., Hafner, M., Chung, M., and Sorger, P. K. (2017) Measuring Cancer Drug Sensitivity and Resistance in Cultured Cells. *Curr. Protocols Chem. Biol.* 9, 55–74.
- (29) Vilmar, A., Garcia-Foncillas, J., Huariz, M., Santoni-Rugiu, E., and Sorensen, J. B. (2012) RT-PCR versus immunohistochemistry for correlation and quantification of ERCC1, BRCA1, TUBB3 and RRM1 in NSCLC. *Lung Cancer* 75, 306–312.
- (30) Parker, A. L., Teo, W. S., McCarroll, J. A., and Kavallaris, M. (2017) An emerging role for tubulin isotypes in modulating cancer biology and chemotherapy resistance. *Int. J. Mol. Sci.* 18, 1434.
- (31) Hafner, M., et al. (2017) Quantification of sensitivity and resistance of breast cancer cell lines to anti-cancer drugs using GR metrics. *Sci. Data* 4, 170166.
- (32) Mittapalli, R. K., et al. (2016) ABCG2 and ABCB1 Limit the Efficacy of Dasatinib in a PDGF-B-Driven Brainstem Glioma Model. *Mol. Cancer Ther.* 15, 819.
- (33) Seaman, S., et al. (2017) Eradication of tumors through simultaneous ablation of CD276/B7-H3-positive tumor cells and tumor vasculature. *Cancer Cell* 31, 501–515.
- (34) Zang, X., et al. (2018) A Promising Microtubule Inhibitor Deoxydopodophyllotoxin Exhibits Better Efficacy to Multidrug-Resistant Breast Cancer than Paclitaxel via Avoiding Efflux Transport. *Drug Metab. Dispos.* 46, 542.
- (35) Lathia, J. D., Mack, S. C., Mulkearns-Hubert, E. E., Valentim, C. L. L., and Rich, J. N. (2015) Cancer stem cells in glioblastoma. *Genes Dev.* 29, 1203–1217.
- (36) Suva, M. L., Rheinbay, E., Gillespie, S. M., Patel, A. P., Wakimoto, H., Rabkin, S. D., Riggi, N., Chi, A. S., Cahill, D. P., Nahed, B. V., Curry, W. T., Martuza, R. L., Rivera, M. N., Rossetti, N., Kasif, S., Beik, S., Kadri, S., Tirosch, I., Wortman, I., Shalek, A. K., Rozenblatt-Rosen, O., Regev, A., Louis, D. N., and Bernstein, B. E. (2014) Reconstructing and Reprogramming the Tumor-Propagating Potential of Glioblastoma Stem-like Cells. *Cell* 157, 580–594.
- (37) Pollard, S. M., et al. (2009) Glioma Stem Cell Lines Expanded in Adherent Culture Have Tumor-Specific Phenotypes and Are Suitable for Chemical and Genetic Screens. *Cell Stem Cell* 4, 568–580.
- (38) Mirzayans, R., Andrais, B., and Murray, D. (2018) Roles of Polyploid/Multinucleated Giant Cancer Cells in Metastasis and Disease Relapse Following Anticancer Treatment. *Cancers* 10, E118 DOI: 10.3390/cancers10040118.
- (39) Sosa, M. S., Avivar-Valderas, A., Bragado, P., Wen, H.-C., and Aguirre-Ghisso, J. A. (2011) ERK1/2 and p38 α / β Signaling in Tumor Cell Quiescence: Opportunities to Control Dormant Residual Disease. *Clin. Cancer Res.* 17, 5850.

(40) Fluegen, G., et al. (2017) Phenotypic heterogeneity of disseminated tumour cells is preset by primary tumour hypoxic microenvironments. *Nat. Cell Biol.* 19, 120.

(41) Niepel, M., et al. (2013) Profiles of Basal and Stimulated Receptor Signaling Networks Predict Drug Response in Breast Cancer Lines. *Sci. Signaling* 6, No. ra84.

(42) Hafner, M., Niepel, M., and Sorger, P. K. (2017) Alternative drug sensitivity metrics improve preclinical cancer pharmacogenomics. *Nat. Biotechnol.* 35, 500–502.

(43) Recasens, A., and Munoz, L. (2019) Targeting Cancer Cell Dormancy. *Trends Pharmacol. Sci.* 40, 128–141.

Lower tubulin expression in glioblastoma stem cells attenuates efficacy of microtubule-targeting agents

Ramzi H. Abbassi¹, Ariadna Recasens¹, Dinesh C. Indurthi¹, Terrance G. Johns², Brett W. Stringer³,
Bryan W. Day³, Lenka Munoz^{1*}

¹ Faculty of Medicine and Health, Charles Perkins Centre, The University of Sydney, NSW 2006, Australia

² Oncogenic Signalling Laboratory and Brain Cancer Discovery Collaborative, Telethon Kids Institute, Perth Children's Hospital, 15 Hospital Avenue, Nedlands, WA 6009, Australia

³ QIMR Berghofer Medical Research Institute, 300 Herston Road, Herston, QLD 4006, Australia

Supplementary Information

Table S1. Genotypes of glioblastoma stem cell lines.

Table S2. Details of primary antibodies.

Table S3. Colchicine sensitivity metric values.

Table S4. Nocodazole sensitivity metric values.

Table S5. Tivantinib sensitivity metric values.

Table S6. CMPD1 sensitivity metric values.

Table S7. Spearman's correlation coefficients between colchicine sensitivity metrics (Table S3) with tubulin code (Figure S2).

Table S8. Spearman's correlation coefficients between nocodazole sensitivity metrics (Table S4) with tubulin code (Figure S2).

Table S9. Spearman's correlation coefficients between tivantinib sensitivity metrics (Table S5) with tubulin code (Figure S2).

Table S10. Spearman's correlation coefficients between CMPD1 sensitivity metrics (Table S6) with tubulin code (Figure S2).

Figure S1. Representative image of Coomassie stained gel to demonstrate equal protein load across 15 cell lines.

Figure S2. Expression of tubulin isotypes and post-translational modifications normalised to A172 signals.

Figure S3. Expression of tubulin isotypes and post-translational modifications normalised to RN1 signals.

Figure S4. Dose-response curves for MTAs in glioblastoma cell lines.

Figure S5. Spearman's correlations between tubulin expression and MTAs efficacy excluding BAH1 data.

Figure S6. Inhibitors of efflux pumps do not alter the efficacy of MTAs.

Table S1. Genotypes of glioblastoma stem cell lines.

Pathway	Gene	Classical				Mesenchymal				Proneural			
		WK1	PB1	HW1	SB2b	RN1	FPW1	RKI1	MN1	JK2	SJH1	MMK1	BAH1
RTK	<i>EGFR</i>			A289V	A289V H304Y								vIII
	<i>MET</i>				C800F	T992I			E168D		H289R		
	<i>EPHA2</i>										V589M R721Q		
PI3K	<i>PIK3CA</i>	H1047Y			Y1021H								
	<i>PIK3R1</i>												
	<i>PIK3C2G</i>		X1446S		A2T				P129T				
	<i>PIK3C2A</i>												T1415A
	<i>PTEN</i>		R130*	<i>Spl jct</i>			R130Q					F56V	V133I
MAPK	<i>NF1</i>						<i>Spl jct</i>				<i>Spl jct</i>		
	<i>MYC</i>												
P53	<i>TP53</i>									R110L	G105C		
	<i>MDM2</i>				W329C								
RB1	<i>CDKN2A</i>												
	<i>CDKN2B</i>												
Chromatin modifiers	<i>IDIH1</i>				V178I							Y183C	
	<i>ATRX</i>							D808G					
	<i>SEDT2</i>	E670K			T451A			R472H					
Patient Gender (M/F)		M	M	F	M	M	M	F	F	M	M	F	F

Homozygous deletion
 Heterozygous deletion
 Amplification
 Gain

Table S2. Details of primary antibodies.

Antibody	Supplier	Identifier
Total α -tubulin	Cell Signaling Technology	Cat# 2144, RRID: AB_2210548
Total β -tubulin	Abcam	Cat# ab6046, RRID: AB_2210370
Total γ -tubulin	Cell Signaling Technology	Cat# 5886, RRID: AB_10836184
β I-tubulin	Abcam	Cat# ab179511
β II-tubulin	Abcam	Cat# ab179512
β III-tubulin	Abcam	Cat# ab18207, RRID: AB_444319
β IV-tubulin	Abcam	Cat# ab11315, RRID: AB_297919
Tyrosinated α -tubulin	MerckMillipore	Cat# ABT171
Detyrosinated α -tubulin	MerckMillipore	Cat# AB3201; RRID: AB_177350
Δ 2 α -tubulin	MerckMillipore	Cat# AB3202; RRID: AB_177351
Acetyl K40 α -tubulin	Abcam	Cat# ab179484;
Phospho S172 β III-tubulin	Abcam	Cat# ab76286; RRID: AB_1523210
Polyglutaminated $\alpha\beta$ -tubulin	Adipogen	Cat# AG-20B-0020; RRID: AB_2490210
SOX2	R&D Systems	Cat# AF2018; RRID: AB_355110
GAPDH	Cell Signaling Technology	Cat# 97166
Nestin	R&D Systems	Cat# MAB1259; AB_2251304
Rabbit IgG, HRP-linked	Cell Signaling Technology	Cat# 7074; RRID: AB_2099233
Mouse IgG, HRP-linked	Cell Signaling Technology	Cat# 7076; RRID: AB_330924
Mouse IgG, Alexa Fluor 488	Life Technologies	Cat# A10680; RRID: AB_2534062
Rabbit IgG, AlexaFluor594	Life Technologies	Cat# A11012; RRID: AB_141359
FITC-conjugated CD243 (MDR1)	ThermoFisher Scientific	Cat# 11-2439-41, RRID: AB_11220073
PE-eFluor610-conjugated p-Erk1/2	ThermoFisher Scientific	Cat# 61-109-41
APC-conjugated p-p38 MAPK	ThermoFisher Scientific	Cat# 17-9078-42; RRID: AB_2573290
Anti-Rabbit Detection Module for Jess, Wes, Peggy Sue or Sally Sue	ProteinSimple	Cat# DM-001

Table S3. Colchicine sensitivity metric values.

Cell line	Colchicine IC ₅₀ (μM)	Colchicine E _{max}	Colchicine h	Colchicine AUC	Colchicine GR ₅₀ (μM)	Colchicine GR _{max}	Colchicine h _{GR}	Colchicine GR _{AOC}
A172	0.013 ± 0.002	0.151 ± 0.008	3.547 ± 0.917	0.639 ± 0.041	0.013 ± 0.002	0.042 ± 0.018	3.613 ± 0.808	0.389 ± 0.036
U87	0.013 ± 0.003	0.243 ± 0.036	1.960 ± 0.250	0.624 ± 0.014	0.011 ± 0.002	0.034 ± 0.072	2.125 ± 0.045	0.454 ± 0.024
U251	0.013 ± 0.001	0.156 ± 0.001	3.260 ± 0.400	0.633 ± 0.024	0.015 ± 0.001	0.159 ± 0.002	3.400 ± 0.500	0.346 ± 0.017
WK1	0.019 ± 0.001	0.159 ± 0.001	2.350 ± 0.160	0.640 ± 0.013	0.013 ± 0.001	-0.486 ± 0.001	2.465 ± 0.105	0.619 ± 0.019
PB1	0.012 ± 0.001	0.241 ± 0.009	2.500 ± 0.030	0.659 ± 0.011	0.008 ± 0.001	-0.253 ± 0.019	2.070 ± 0.080	0.539 ± 0.017
HW1	0.008 ± 0.001	0.226 ± 0.002	3.465 ± 0.075	0.599 ± 0.009	0.007 ± 0.001	-0.046 ± 0.005	3.375 ± 0.075	0.517 ± 0.011
SB2b	0.020 ± 0.009	0.128 ± 0.009	4.193 ± 0.807	0.666 ± 0.016	0.018 ± 0.004	-0.394 ± 0.024	3.160 ± 0.954	0.514 ± 0.023
RN1	0.007 ± 0.001	0.129 ± 0.011	4.805 ± 0.195	0.546 ± 0.021	0.006 ± 0.001	-0.453 ± 0.030	4.675 ± 0.225	0.736 ± 0.036
FPW1	0.017 ± 0.001	0.179 ± 0.001	2.980 ± 0.590	0.659 ± 0.013	0.014 ± 0.002	-0.237 ± 0.002	3.220 ± 0.630	0.499 ± 0.015
RKI1	0.024 ± 0.005	0.347 ± 0.011	2.797 ± 0.310	0.746 ± 0.019	0.021 ± 0.004	0.204 ± 0.018	2.667 ± 0.222	0.304 ± 0.022
MN1	0.014 ± 0.004	0.167 ± 0.005	2.650 ± 0.123	0.624 ± 0.029	0.010 ± 0.003	-0.475 ± 0.011	2.610 ± 0.110	0.647 ± 0.048
JK2	0.013 ± 0.001	0.253 ± 0.020	2.493 ± 0.282	0.646 ± 0.022	0.011 ± 0.001	0.014 ± 0.040	2.593 ± 0.364	0.446 ± 0.030
SJH1	0.004 ± 0.001	0.249 ± 0.016	2.300 ± 0.233	0.543 ± 0.017	0.002 ± 0.001	-0.606 ± 0.029	2.293 ± 0.229	0.989 ± 0.037
MMK1	0.022 ± 0.007	0.231 ± 0.037	1.755 ± 0.675	0.672 ± 0.020	0.022 ± 0.007	0.099 ± 0.070	1.750 ± 0.550	0.356 ± 0.018
BAH1	0.012 ± 0.001	0.146 ± 0.028	2.550 ± 0.170	0.606 ± 0.035	0.009 ± 0.001	-0.486 ± 0.001	2.460 ± 0.140	0.619 ± 0.019

Table S4. Nocodazole sensitivity metric values.

Cell line	Nocodazole IC₅₀ (μM)	Nocodazole E_{max}	Nocodazole h	Nocodazole AUC	Nocodazole GR₅₀ (μM)	Nocodazole GR_{max}	Nocodazole h_{GR}	Nocodazole GR_{AOC}
A172	0.062 ± 0.018	0.161 ± 0.009	2.580 ± 0.455	0.534 ± 0.030	0.090 ± 0.038	0.063 ± 0.021	1.780 ± 0.312	0.471 ± 0.041
U87	0.065 ± 0.001	0.251 ± 0.038	2.465 ± 0.575	0.594 ± 0.015	0.059 ± 0.002	0.050 ± 0.074	2.310 ± 0.630	0.491 ± 0.033
U251	0.040 ± 0.012	0.161 ± 0.006	3.105 ± 0.805	0.494 ± 0.025	0.049 ± 0.011	0.168 ± 0.013	2.915 ± 0.835	0.474 ± 0.018
WK1	0.070 ± 0.015	0.173 ± 0.003	1.360 ± 0.330	0.541 ± 0.001	0.036 ± 0.004	-0.453 ± 0.007	1.355 ± 0.245	0.776 ± 0.001
PB1	0.155 ± 0.085	0.265 ± 0.024	1.245 ± 0.266	0.653 ± 0.037	0.062 ± 0.028	-0.203 ± 0.051	1.036 ± 0.274	0.538 ± 0.061
HW1	0.061 ± 0.002	0.245 ± 0.001	2.090 ± 0.030	0.557 ± 0.010	0.053 ± 0.002	-0.009 ± 0.001	2.855 ± 0.295	0.563 ± 0.010
SB2b	0.062 ± 0.004	0.154 ± 0.010	3.685 ± 0.015	0.567 ± 0.013	0.054 ± 0.004	-0.324 ± 0.025	3.530 ± 0.010	0.655 ± 0.012
RN1	0.045 ± 0.009	0.185 ± 0.063	3.225 ± 0.605	0.558 ± 0.091	0.036 ± 0.007	-0.310 ± 0.137	2.805 ± 0.295	0.697 ± 0.154
FPW1	0.081 ± 0.007	0.185 ± 0.001	3.190 ± 0.270	0.597 ± 0.025	0.070 ± 0.007	-0.225 ± 0.002	3.085 ± 0.255	0.581 ± 0.032
RKI1	0.111 ± 0.022	0.365 ± 0.035	1.773 ± 0.185	0.734 ± 0.070	0.093 ± 0.019	0.232 ± 0.057	1.610 ± 0.211	0.308 ± 0.084
MN1	0.047 ± 0.024	0.210 ± 0.028	3.070 ± 0.206	0.625 ± 0.099	0.034 ± 0.018	-0.380 ± 0.061	3.023 ± 0.209	0.639 ± 0.175
JK2	0.058 ± 0.024	0.270 ± 0.035	1.991 ± 0.595	0.563 ± 0.058	0.049 ± 0.021	0.046 ± 0.069	1.923 ± 0.452	0.545 ± 0.079
SJH1	0.034 ± 0.009	0.278 ± 0.017	3.665 ± 0.580	0.519 ± 0.040	0.021 ± 0.007	-0.553 ± 0.032	3.855 ± 0.662	1.047 ± 0.086
MMK1	0.064 ± 0.006	0.247 ± 0.025	2.197 ± 0.171	0.595 ± 0.008	0.066 ± 0.006	0.131 ± 0.046	2.063 ± 0.259	0.441 ± 0.006
BAH1	0.055 ± 0.004	0.155 ± 0.020	1.750 ± 0.020	0.536 ± 0.006	0.036 ± 0.003	-0.411 ± 0.049	1.625 ± 0.015	0.731 ± 0.004

Table S5. Tivantinib sensitivity metric values.

Cell line	Tivantinib IC₅₀ (μM)	Tivantinib E_{max}	Tivantinib h	Tivantinib AUC	Tivantinib GR₅₀ (μM)	Tivantinib GR_{max}	Tivantinib h_{GR}	Tivantinib GR_{AOC}
A172	0.438 ± 0.045	0.135 ± 0.020	2.757 ± 0.736	0.517 ± 0.008	0.508 ± 0.058	-0.004 ± 0.055	2.040 ± 0.158	0.509 ± 0.016
U87	0.690 ± 0.028	0.225 ± 0.026	2.010 ± 0.720	0.588 ± 0.003	0.614 ± 0.001	-0.003 ± 0.053	1.850 ± 0.740	0.497 ± 0.021
U251	0.488 ± 0.105	0.159 ± 0.012	3.535 ± 1.385	0.523 ± 0.017	0.611 ± 0.067	0.163 ± 0.024	3.305 ± 1.365	0.442 ± 0.003
WK1	0.811 ± 0.129	0.250 ± 0.047	1.268 ± 0.339	0.691 ± 0.073	0.361 ± 0.083	-0.287 ± 0.099	1.231 ± 0.334	0.507 ± 0.127
PB1	3.710 ± 0.430	0.108 ± 0.016	0.546 ± 0.020	0.668 ± 0.012	1.220 ± 0.210	-0.572 ± 0.043	0.531 ± 0.034	0.521 ± 0.018
HW1	0.973 ± 0.368	0.185 ± 0.004	0.946 ± 0.135	0.574 ± 0.028	0.712 ± 0.272	-0.139 ± 0.009	0.805 ± 0.158	0.532 ± 0.038
SB2b	0.523 ± 0.059	0.132 ± 0.002	3.180 ± 0.390	0.538 ± 0.005	0.440 ± 0.064	-0.383 ± 0.005	2.965 ± 0.455	0.705 ± 0.003
RN1	0.242 ± 0.001	0.095 ± 0.024	2.575 ± 0.185	0.443 ± 0.010	0.194 ± 0.004	-0.526 ± 0.074	2.445 ± 0.225	0.889 ± 0.018
FPW1	0.760 ± 0.003	0.129 ± 0.001	2.000 ± 0.440	0.566 ± 0.010	0.578 ± 0.037	-0.368 ± 0.002	1.735 ± 0.455	0.621 ± 0.012
RKI1	4.105 ± 0.665	0.231 ± 0.043	0.758 ± 0.085	0.732 ± 0.021	3.435 ± 0.325	-0.018 ± 0.089	0.644 ± 0.083	0.313 ± 0.029
MN1	1.137 ± 0.720	0.126 ± 0.016	1.615 ± 0.529	0.554 ± 0.043	0.412 ± 0.147	-0.576 ± 0.039	1.556 ± 0.519	0.758 ± 0.080
JK2	0.621 ± 0.164	0.198 ± 0.032	1.446 ± 0.239	0.654 ± 0.048	0.539 ± 0.192	-0.008 ± 0.109	1.307 ± 0.257	0.425 ± 0.064
SJH1	0.172 ± 0.038	0.236 ± 0.005	3.623 ± 0.795	0.492 ± 0.022	0.093 ± 0.011	-0.629 ± 0.010	3.645 ± 0.782	1.104 ± 0.047
MMK1	0.533 ± 0.121	0.131 ± 0.005	1.186 ± 0.169	0.601 ± 0.091	0.614 ± 0.144	0.039 ± 0.162	0.916 ± 0.187	0.434 ± 0.110
BAH1	0.446 ± 0.004	0.122 ± 0.027	1.895 ± 0.025	0.537 ± 0.004	0.293 ± 0.003	-0.496 ± 0.072	1.705 ± 0.025	0.727 ± 0.009

Table S6. CMPD1 sensitivity metric values.

Cell line	CMPD1 IC₅₀ (μM)	CMPD1 E_{max}	CMPD1 h	CMPD1 AUC	CMPD1 GR₅₀ (μM)	CMPD1 GR_{max}	CMPD1 h_{GR}	CMPD1 GR_{AOC}
A172	0.321 ± 0.054	0.143 ± 0.017	1.985 ± 0.325	0.493 ± 0.024	0.369 ± 0.066	0.019 ± 0.044	2.587 ± 0.734	0.534 ± 0.022
U87	0.386 ± 0.095	0.200 ± 0.036	1.795 ± 0.685	0.522 ± 0.021	0.328 ± 0.061	-0.059 ± 0.087	1.606 ± 0.615	0.584 ± 0.050
U251	0.301 ± 0.050	0.148 ± 0.007	3.910 ± 0.870	0.489 ± 0.007	0.357 ± 0.030	0.140 ± 0.016	3.270 ± 0.340	0.476 ± 0.009
WK1	0.613 ± 0.031	0.166 ± 0.030	1.180 ± 0.040	0.548 ± 0.017	0.273 ± 0.005	-0.472 ± 0.070	1.037 ± 0.103	0.755 ± 0.030
PB1	1.985 ± 0.635	0.215 ± 0.007	0.784 ± 0.181	0.643 ± 0.008	0.661 ± 0.113	-0.311 ± 0.015	0.603 ± 0.108	0.556 ± 0.014
HW1	0.685 ± 0.030	0.149 ± 0.008	3.140 ± 0.380	0.581 ± 0.004	0.629 ± 0.036	-0.225 ± 0.020	2.111 ± 1.299	0.537 ± 0.002
SB2b	0.514 ± 0.173	0.145 ± 0.012	3.205 ± 0.035	0.537 ± 0.039	0.434 ± 0.147	-0.349 ± 0.029	3.040 ± 0.020	0.696 ± 0.061
RN1	0.466 ± 0.016	0.138 ± 0.005	3.065 ± 0.175	0.502 ± 0.003	0.380 ± 0.020	-0.430 ± 0.013	3.015 ± 0.275	0.799 ± 0.007
FPW1	0.867 ± 0.148	0.160 ± 0.016	2.440 ± 0.245	0.573 ± 0.032	0.704 ± 0.114	-0.286 ± 0.039	2.263 ± 0.241	0.614 ± 0.049
RKI1	2.673 ± 0.366	0.230 ± 0.015	1.111 ± 0.162	0.689 ± 0.055	1.965 ± 0.510	-0.013 ± 0.031	1.061 ± 0.224	0.372 ± 0.065
MN1	0.693 ± 0.205	0.150 ± 0.015	2.137 ± 0.316	0.635 ± 0.066	0.476 ± 0.151	-0.517 ± 0.035	2.073 ± 0.290	0.622 ± 0.118
JK2	1.229 ± 0.301	0.230 ± 0.035	1.169 ± 0.180	0.608 ± 0.021	0.940 ± 0.225	-0.041 ± 0.078	1.189 ± 0.272	0.477 ± 0.029
SJH1	0.953 ± 0.129	0.227 ± 0.004	1.607 ± 0.535	0.626 ± 0.032	0.435 ± 0.156	-0.646 ± 0.007	1.641 ± 0.538	0.818 ± 0.071
MMK1	1.960 ± 0.455	0.163 ± 0.012	1.028 ± 0.074	0.621 ± 0.019	2.010 ± 0.415	-0.044 ± 0.029	0.974 ± 0.128	0.411 ± 0.024
BAH1	0.518 ± 0.006	0.123 ± 0.025	1.965 ± 0.055	0.531 ± 0.006	0.352 ± 0.008	-0.492 ± 0.068	1.790 ± 0.080	0.747 ± 0.014

Table S7. Spearman's correlation coefficients between colchicine sensitivity metrics (Table S3) with tubulin code (Figure S2).

(*P < 0.05; **P < 0.01; ***P < 0.005; ****P < 0.001)

	Colchicine IC ₅₀	Colchicine E _{max}	Colchicine h	Colchicine AUC	Colchicine GR ₅₀	Colchicine GR _{max}	Colchicine hGR	Colchicine GRAOC
Tyr-α	-0.161	-0.510	0.266	-0.228	-0.161	-0.340	0.245	0.193
Detyr-α	-0.007	0.350	-0.280	0.039	-0.091	-0.112	-0.196	0.168
Δ2-α	0.154	0.217	-0.182	0.161	0.049	-0.200	-0.273	0.025
AcK40-α	-0.238	-0.070	-0.014	-0.154	-0.259	-0.133	-0.280	0.175
PolyE-α	-0.287	0.517	0.084	-0.210	-0.357	0.140	0.112	0.014
Total α	-0.168	-0.545	-0.168	-0.368	-0.245	-0.897****	-0.245	0.701*
βI	0.042	-0.615	-0.196	-0.133	0.070	-0.487	-0.294	0.326
βII	-0.147	-0.014	0.028	-0.221	-0.259	-0.382	-0.077	0.263
βIII	-0.343	0.294	-0.217	-0.298	-0.427	-0.368	-0.287	0.284
βIV	-0.720*	-0.350	0.126	-0.823**	-0.699*	-0.620*	0.154	0.641*
pS172 βIII	-0.231	0.245	-0.497	-0.207	-0.259	-0.319	-0.392	0.333
PolyE β	0.168	0.189	0.147	0.308	0.112	0.151	0.161	-0.207
Total β	-0.322	-0.476	-0.217	-0.525	-0.329	-0.616*	-0.259	0.581*
Total γ	-0.224	-0.224	-0.126	-0.221	-0.252	-0.469	-0.133	0.392

Table S8. Spearman's correlation coefficients between nocodazole sensitivity metrics (Table S4) with tubulin code (Figure S2).

(*P < 0.05; **P < 0.01; ***P < 0.005; ****P < 0.001)

	Nocodazole IC₅₀	Nocodazole E_{max}	Nocodazole h	Nocodazole AUC	Nocodazole GR₅₀	Nocodazole GR_{max}	Nocodazole h_{GR}	Nocodazole GR_{AOC}
Tyr-α	-0.042	-0.599*	-0.259	-0.434	-0.196	-0.329	-0.322	0.455
Detyr-α	0.406	0.375	-0.357	0.217	0.098	-0.084	-0.385	-0.007
Δ2-α	0.378	0.172	-0.238	-0.042	0.091	-0.224	-0.182	0.133
AcK40-α	-0.063	-0.053	-0.161	-0.021	-0.126	-0.077	0.021	-0.063
PolyE-α	-0.196	0.585*	-0.063	0.000	-0.154	0.175	0.056	-0.182
Total α	-0.315	-0.501	0.133	-0.503	-0.615*	-0.902***	0.098	0.853***
βI	-0.287	-0.588*	0.168	-0.427	-0.301	-0.476	0.035	0.517
βII	0.049	-0.032	-0.301	-0.350	-0.175	-0.357	-0.224	0.350
βIII	-0.063	0.273	-0.392	-0.385	-0.322	-0.315	-0.294	0.294
βIV	-0.839***	-0.280	0.294	-0.804**	-0.762**	-0.580	0.357	0.713*
pS172 βIII	-0.042	0.301	-0.266	-0.259	-0.259	-0.252	-0.406	0.287
PolyE β	0.720*	0.067	-0.406	0.378	0.392	0.105	-0.329	-0.203
Total β	-0.692*	-0.357	0.203	-0.706*	-0.671*	-0.559	0.105	0.650*
Total γ	-0.119	-0.161	0.007	-0.448	-0.287	-0.441	-0.182	0.531

Table S9. Spearman's correlation coefficients between tivantinib sensitivity metrics (Table S5) with tubulin code (Figure S2).

(*P < 0.05; **P < 0.01; ***P < 0.005; ****P < 0.001)

	Tivantinib IC₅₀	Tivantinib E_{max}	Tivantinib h	Tivantinib AUC	Tivantinib GR₅₀	Tivantinib GR_{max}	Tivantinib hGR	Tivantinib GRAOC
Tyr-α	-0.287	-0.126	0.224	-0.126	-0.378	-0.007	0.224	0.063
Detyr-α	0.406	0.217	-0.329	0.441	0.119	-0.196	-0.329	-0.154
Δ2-α	0.203	0.483	-0.154	0.294	0.126	-0.168	-0.154	-0.098
AcK40-α	0.105	-0.378	-0.217	-0.203	0.154	-0.308	-0.217	0.273
PolyE-α	0.294	0.350	-0.238	0.126	0.224	-0.077	-0.238	-0.063
Total α	-0.490	0.028	0.566*	-0.427	-0.776**	-0.615*	0.566	0.580
βI	-0.685*	-0.287	0.476	-0.483	-0.622*	-0.154	0.476	0.378
βII	0.000	0.245	-0.042	-0.007	-0.126	-0.259	-0.042	0.140
βIII	-0.021	0.343	-0.077	0.070	-0.147	-0.294	-0.077	0.056
βIV	-0.720*	-0.098	0.643	-0.748**	-0.769**	-0.420	0.643	0.664*
pS172 βIII	-0.203	0.231	0.014	0.140	-0.357	-0.161	0.014	-0.042
PolyE β	0.685*	0.245	-0.434	0.629*	0.497	0.035	-0.434	-0.392
Total β	-0.783**	-0.133	0.503	-0.622*	-0.797**	-0.280	0.503	0.524
Total γ	-0.462	0.189	0.322	-0.126	-0.510*	-0.231	0.322	0.154

Table S10. Spearman's correlation coefficients between CMPD1 sensitivity metrics (Table S6) with tubulin code (Figure S2).

(*P < 0.05; **P < 0.01; ***P < 0.005; ****P < 0.001)

	CMPD1 IC₅₀	CMPD1 E_{max}	CMPD1 h	CMPD1 AUC	CMPD1 GR₅₀	CMPD1 GR_{max}	CMPD1 h_{GR}	CMPD1 GR_{AOC}
Tyr-α	-0.601*	-0.336	0.252	-0.755**	-0.636*	-0.154	0.238	0.420
Detyr-α	0.406	0.503	-0.490	0.434	0.021	-0.077	-0.517	0.098
Δ2-α	0.245	0.280	-0.238	0.315	-0.161	-0.133	-0.322	0.119
AcK40-α	0.028	-0.413	0.035	0.182	-0.035	-0.245	-0.056	-0.063
PolyE-α	0.287	0.336	0.000	0.503	0.168	0.126	-0.035	-0.231
Total α	-0.510	-0.280	0.140	-0.392	-0.818**	-0.846***	0.084	0.874***
βI	-0.497	-0.510	0.063	-0.608*	-0.490	-0.476	0.070	0.538
βII	-0.098	-0.098	0.000	-0.028	-0.448	-0.294	-0.091	0.308
βIII	0.126	0.252	-0.238	0.175	-0.322	-0.252	-0.294	0.252
βIV	-0.622*	-0.406	0.490	-0.566	-0.615*	-0.559*	0.476	0.657*
pS172 βIII	0.168	0.483	-0.538	0.063	-0.210	-0.203	-0.517*	0.371
PolyE β	0.252	0.371	-0.119	0.273	0.056	0.238	-0.189	-0.182
Total β	-0.552	-0.448	0.133	-0.531	-0.608*	-0.601*	0.098	0.643*
Total γ	-0.308	0.098	-0.077	-0.371	-0.559	-0.315	-0.091	0.608*

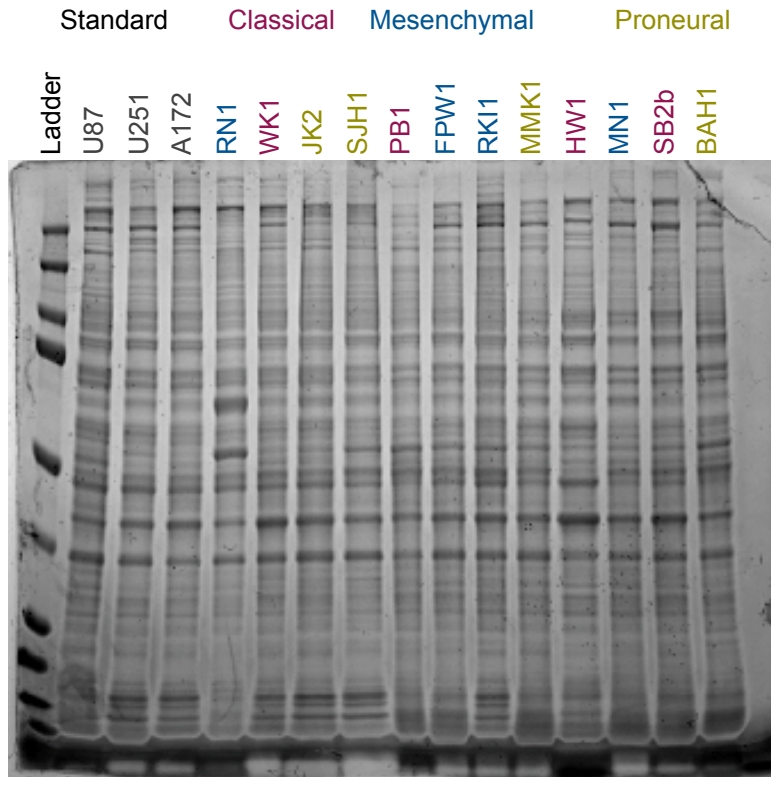


Figure S1. Representative image of Coomassie stained gel to demonstrate equal protein load across 15 cell lines.

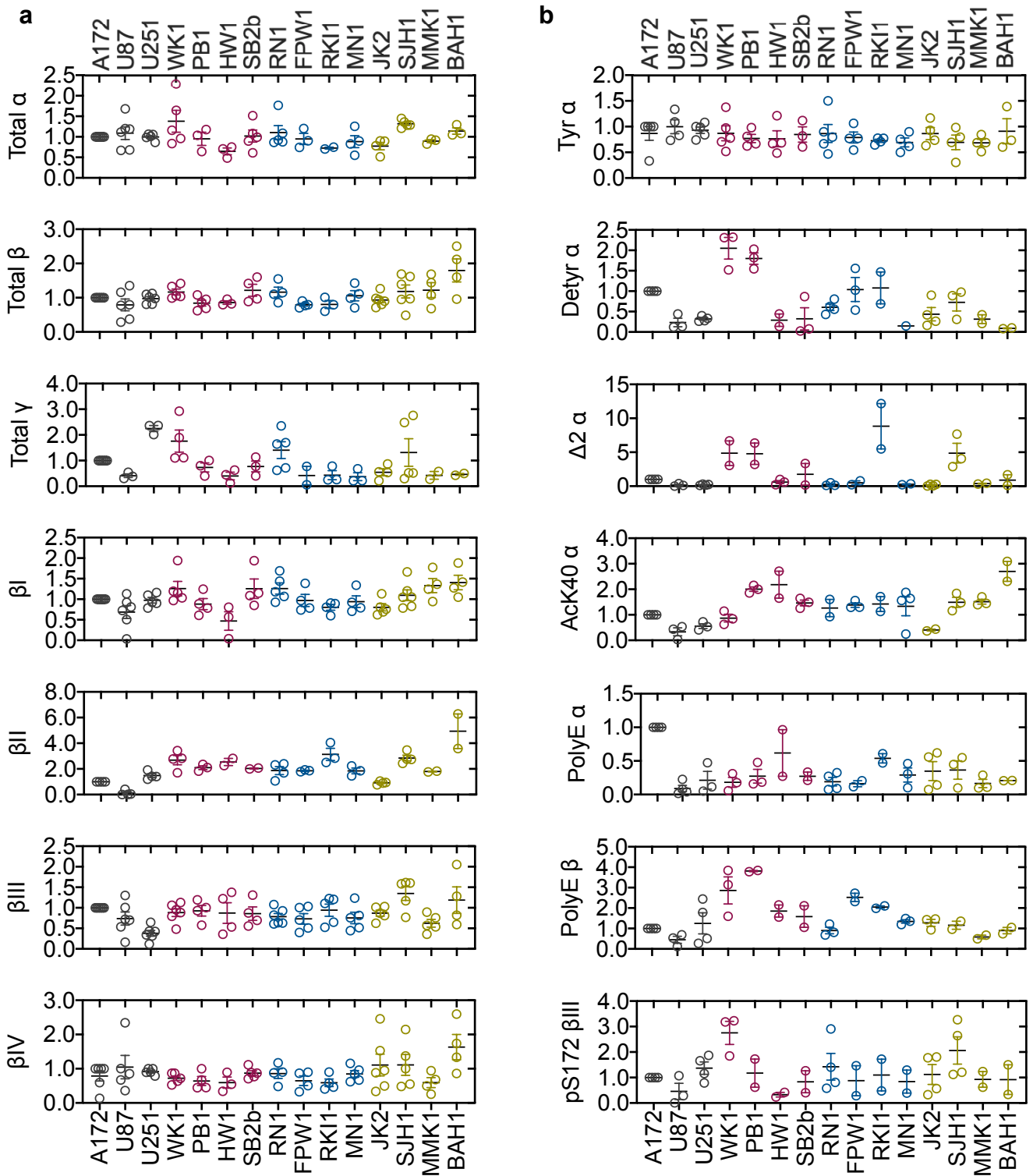


Figure S2. Expression of tubulin isotypes and post-translational modifications normalised to A172 signals. Cell lysates (5 μ g total protein) were analysed by Western blotting using specific antibodies. Representative immunoblots are shown in Figure 1. Quantifications of tubulin isotypes (a) and post-translational modifications (b) are presented as fold change relative to A172 (set as 1). Data are mean \pm SEM (n = 4-6).

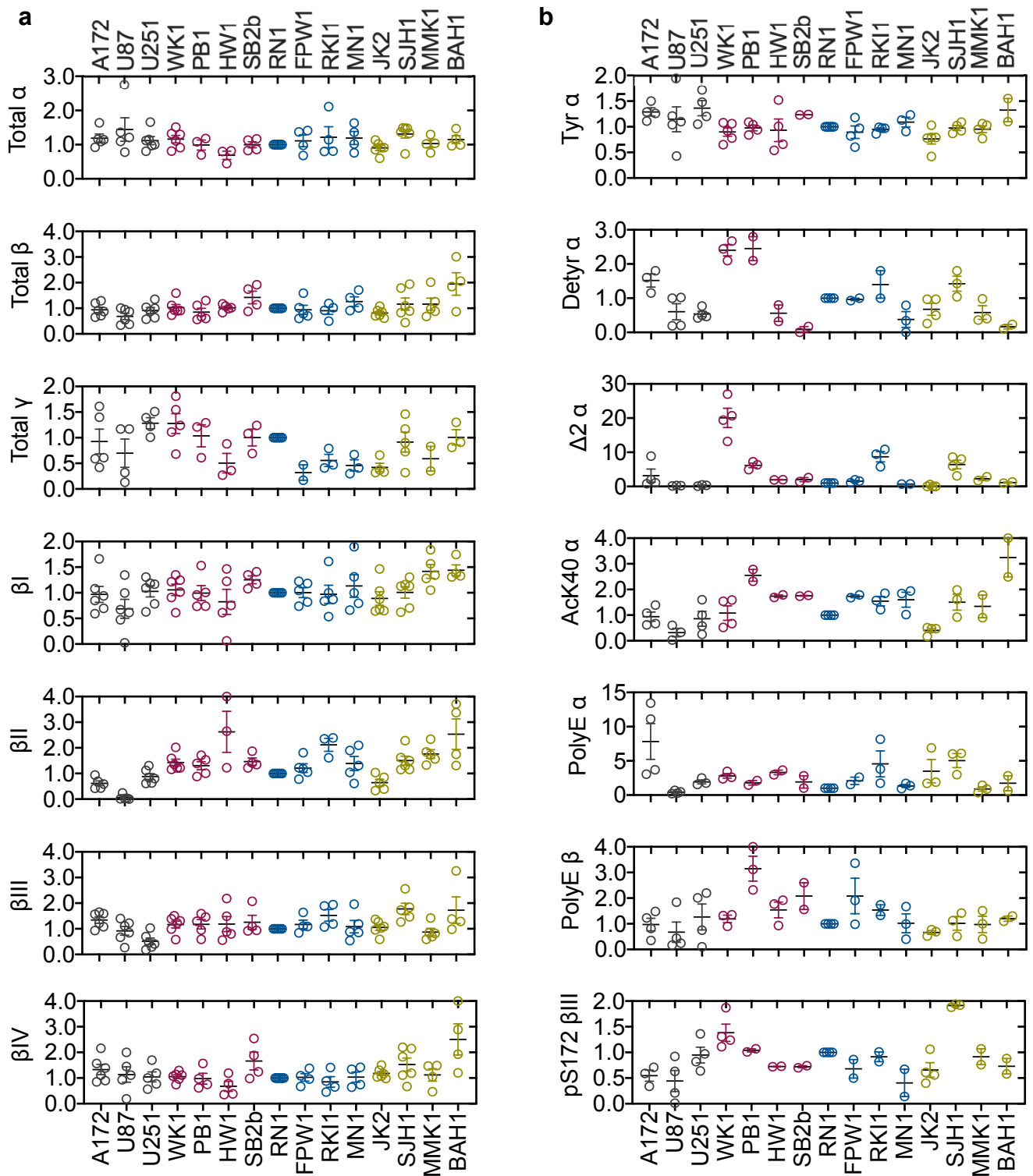


Figure S3. Expression of tubulin isotypes and post-translational modifications normalised to RN1 signals. Cell lysates (5 μ g total protein) were analysed by Western blotting using specific antibodies. Representative immunoblots are shown in Figure 1. Quantifications of tubulin isotypes (**a**) and post-translational modifications (**b**) are presented as fold change relative to RN1 (set as 1). Data are mean \pm SEM (n = 4-6).

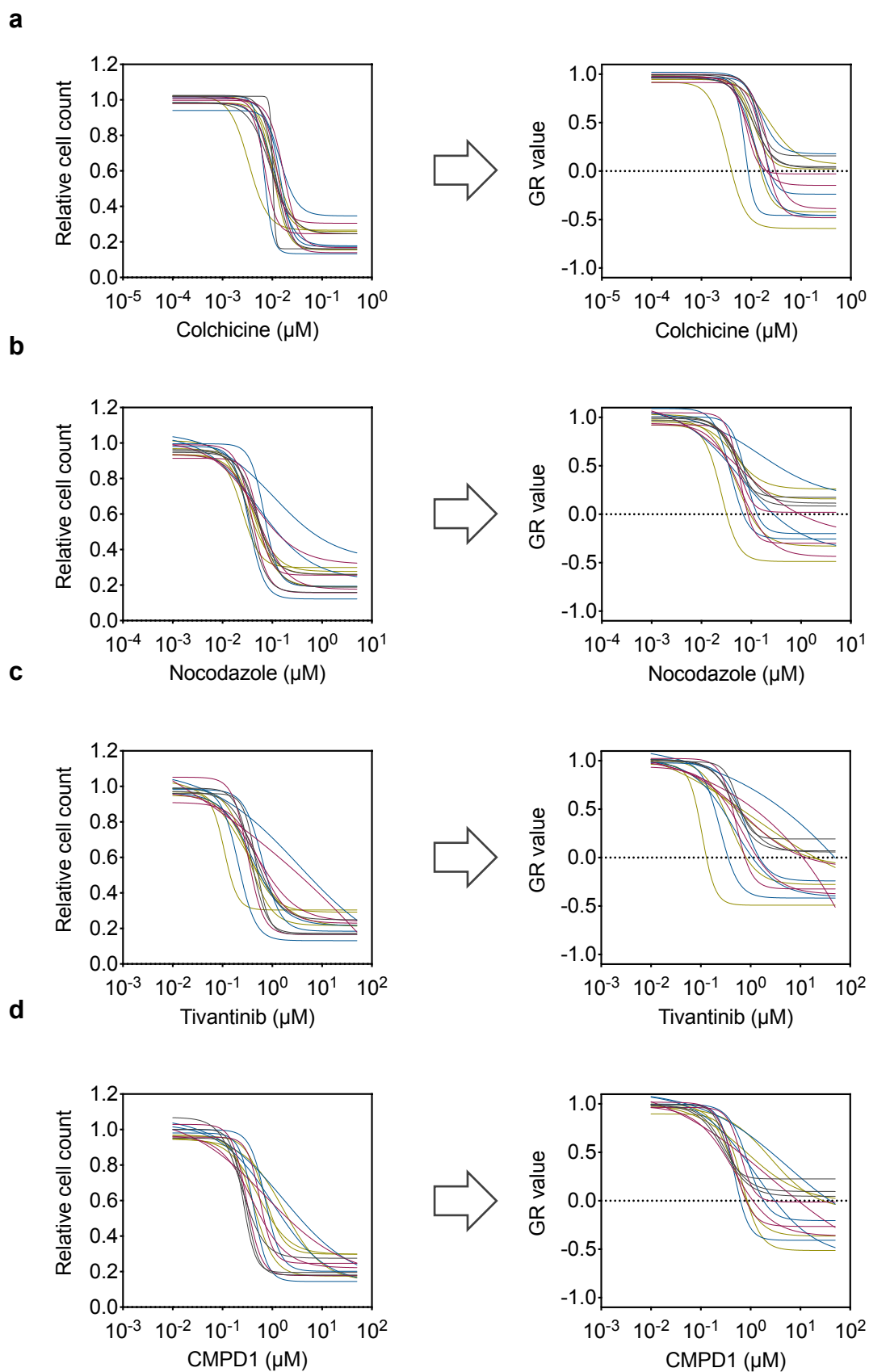


Figure S4. Dose-response curves for MTAs in glioblastoma cell lines. Relative and GR dose-response curves for (a) colchicine, (b) nocodazole, (c) tivantinib and (d) CMPD1 were generated from dose responses determined with CellTiter-Blue viability assay after 5 days of drug treatment and doubling time using the GRcalculator tool. Each curve represents the mean of three independent cell viability assays, where each data point was done in triplicate.

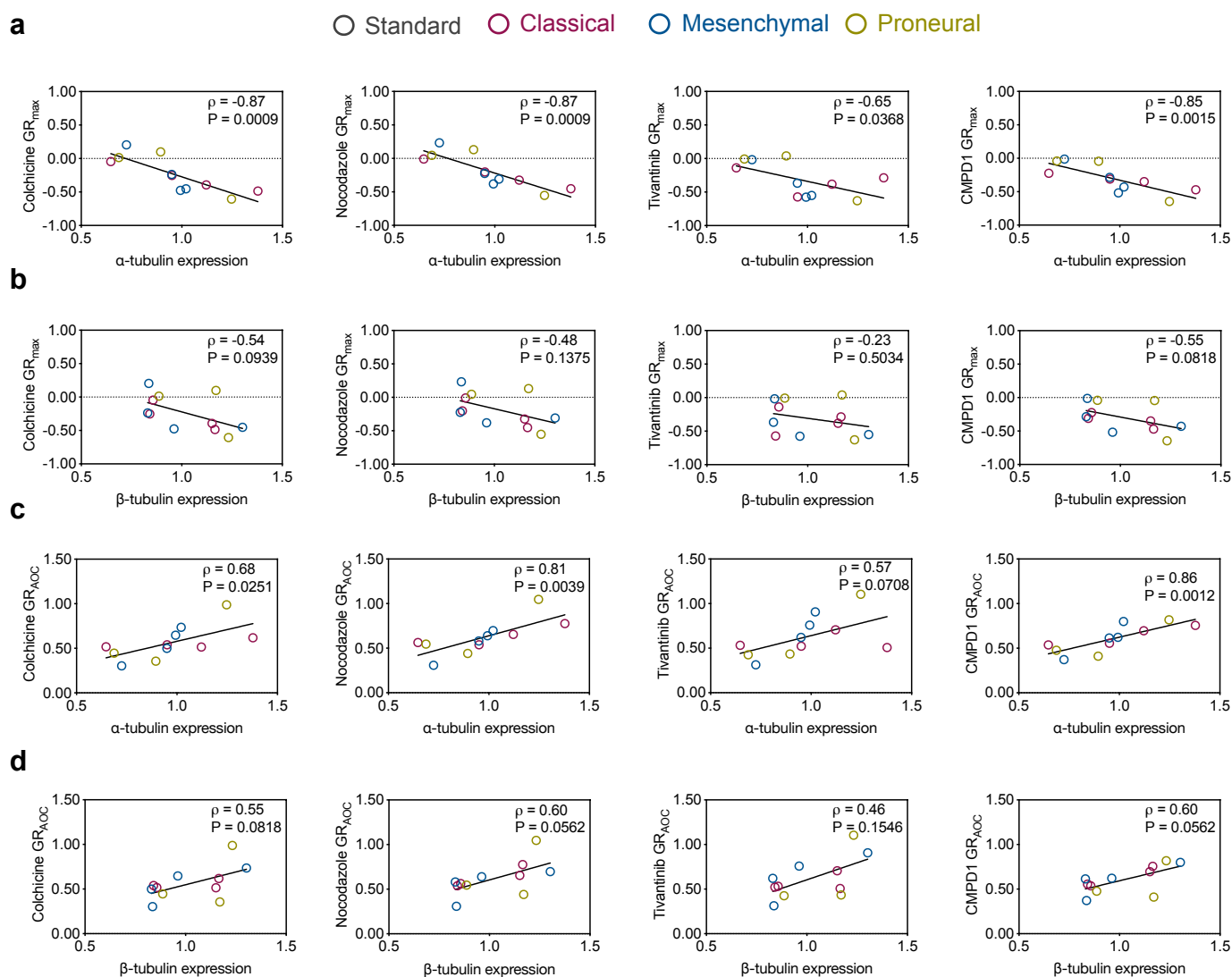


Figure S5. Spearman's correlations between tubulin expression and MTAs efficacy excluding BAH1 data. Pairwise distribution and correlation of GR_{max} and the expression of (a) α -tubulin and (b) β -tubulin in glioblastoma stem cell lines. Pairwise distribution and correlation of GR_{AOC} and the expression of (c) α -tubulin and (d) β -tubulin in glioblastoma stem cell lines.

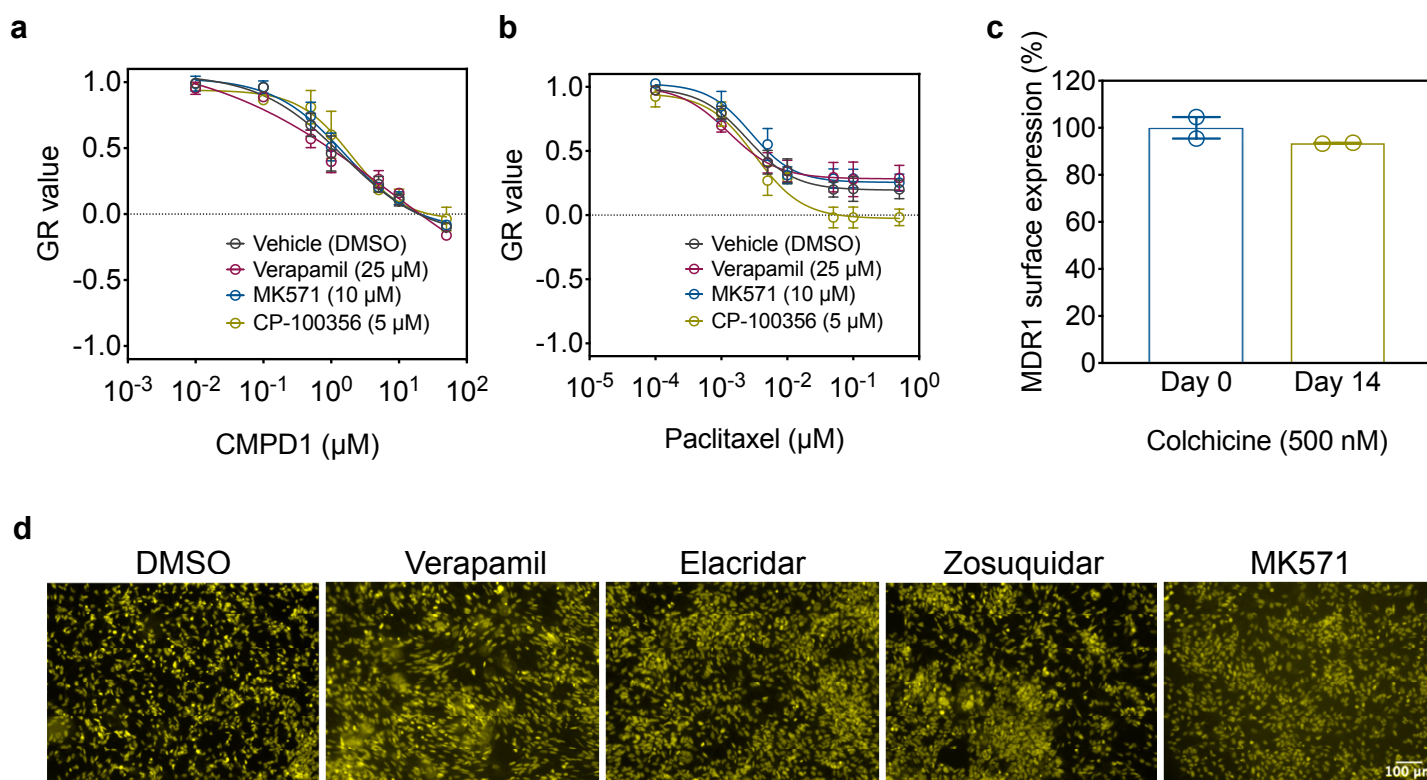


Figure S6. Inhibitors of efflux pumps do not alter the efficacy of MTAs in RKI1 cells.

GR dose-response curves for **(a)** CMPD1 or **(b)** paclitaxel in the presence or absence of efflux pump inhibitor verapamil, MK571 or CP-100356 were generated from dose-response curves of RKI1 cells obtained in a 5 day CellTiter-Blue viability assay and RKI1 doubling time. Each curve is a mean of three independent cell viability assays, where each data point was performed in triplicate. **(c)** RKI1 cells were treated with colchicine (500 nM, 14 days) then stained with FITC-conjugated CD243 (MDR-1) antibody and analysed by flow cytometry. Geometric mean of CD243 surface expression was graphed using Prism v7.0 (GraphPad). Data are mean \pm SEM from 3 independent experiments.

Chapter 4

Quantification of CMPD1-induced changes to histone modifications using SWATH Mass Spectrometry

CHAPTER 4. QUANTIFICATION OF CMPD1-INDUCED CHANGES TO HISTONE MODIFICATIONS USING SWATH-MS

4. 1. Introduction

We have determined that glioblastoma cells expressing higher levels of total tubulin are more prone to cell death following MTA treatment.¹ This observation is in agreement with pharmacological principles specifying that a higher concentration of the drug target (*i.e.*, tubulin and microtubules) increases target binding and occupancy and, therefore, amplifies the cellular response (*i.e.*, cell death).³⁰⁶ However, while cells with higher levels of total tubulin were more sensitive to MTAs, even the most MTA-sensitive cell lines contained drug-tolerant persisters (DTPs). Furthermore, the DTPs that emerged after prolonged treatment with colchicine recovered during drug holidays. The recovered cells exhibited the same sensitivity to the colchicine as the treatment-naïve parental population.¹ Similarly, three studies report the existence of DTPs after taxane treatment, and these DTPs were able to recover during drug holidays.^{154, 155} Most drug tolerance mechanisms reported in cancer cell models are facilitated through changes in chromatin.¹⁴³ Thus, this chapter focuses on the epigenetic chromatin remodelling in DTPs.

4. 1. 1. Chromatin remodelling in drug-tolerant persisters

Within eukaryotic cells, DNA is tightly wrapped around octameric histone core complexes, forming assemblies reminiscent of ‘beads-on-a-string’. Each histone complex contains an octameric core of four heterodimers: two H2A–H2B and two H3–H4 dimers. 147 base-pairs of DNA wrap around this histone core complex, and together, they form a single nucleosome – the functional unit of chromatin. Nucleosomes are compacted into chromatin, which, in turn, is supercoiled and condensed into chromosomes (**Figure 4.1a**).³⁰⁷

There are two cytologically visible ground states of chromatin: transcriptionally repressive and densely packed heterochromatin and transcriptionally permissive and accessible euchromatin. Throughout development, ageing and disease, phenotypic cellular states are dynamically regulated by changes to chromatin structure. Chromatin-remodelling mechanisms make DNA more accessible for replication, repair or gene transcription. Numerous studies showed that dysregulation of these epigenetic mechanisms contributes to cancer formation, progression and treatment evasion.³⁰⁷

Epigenetic mechanisms controlling gene expression include DNA methylation, histone variant deposition and histone post-translational modifications. DNA methylation

occurs at transposon or gene initiator regions and is generally repressive. DNA is methylated by DNA methyltransferases (DNMTs) while its demethylation is largely regulated by ten-eleven translocation (TET) proteins. Methylation of DNA physically impedes the binding of transcriptional proteins and allows the binding of the methyl-CpG-binding domain (MBD) proteins to DNA. In turn, MBDs recruit other repressive chromatin-remodelling enzymes such as histone deacetylases (HDACs), ultimately causing the formation of heterochromatin.³⁰⁸ Tumours often exhibit hypermethylated DNA at promoter regions of tumour suppressor genes and hypomethylated DNA at promoter regions of oncogenes.³⁰⁹

The deposition of histone variants into nucleosomes and presence of histone-modifying enzymes also contribute to chromatin remodelling. Analogous to the tubulin code, a 'histone code' exists due to the existence of these histone variants and combinatorial histone PTMs that occur on histone cores and N-terminal tails. Consequentially, the histone code generates patterns of molecular signals that impact on nucleosome stability, and hence, chromatin state.³¹⁰ Several studies associate aberrations in histone variant or PTM expressions with oncogenesis and disease progression in many cancer types (discussed in **Chapter 4** and **Chapter 5**).

Histone variants

While each nucleosome is made of the four histone subunits, histones H2A and H3 have multiple variants that can be deposited throughout the cell cycle to perform different functions (**Figure 4.1b**). All histones share a histone fold domain (HFD) that enables them to bind and form nucleosomes. The canonical histone complex is composed of the histone variants H2A, H2B, H3.1 (or H3.2) and H4 and these subunits are deposited over the entire genome in a replication-dependent manner.^{311, 312} Non-canonical histone variants include H2A.X, H2A.Z, macroH2A, H2ABBD, H3.3 and CenH3.³¹² These variants are deposited or exchanged by various chaperon complexes in response to different stimuli and in a replication-independent manner.

Non-canonical histone H3.3 differs from the canonical H3.1/3.2 in only four to five amino acid residues and is found in telomeric, pericentromeric and euchromatic regions of chromosomes, predominantly near actively transcribed genes.³¹³ The H3.3 variant is differentially deposited into telomeres and pericentric heterochromatin by the death-associated protein (DAXX)/ATRAX complex chaperon³¹⁴ and into chromatin by the HIRA/UBN1/CABIN1/ASF1 α (HUCA) chaperon complex.³¹⁵ Histone H3.3 maintains the genome integrity by supporting heterochromatic structures in chromosomes during

development and epigenetic reprogramming. CenH3 is a unique H3 variant found exclusively in centromeric regions and is essential for kinetochore assembly during cell division. CenH3 is deposited by HJURP chaperon.³¹⁶ Histone H2A variants are shown in **Figure 4.1b**.

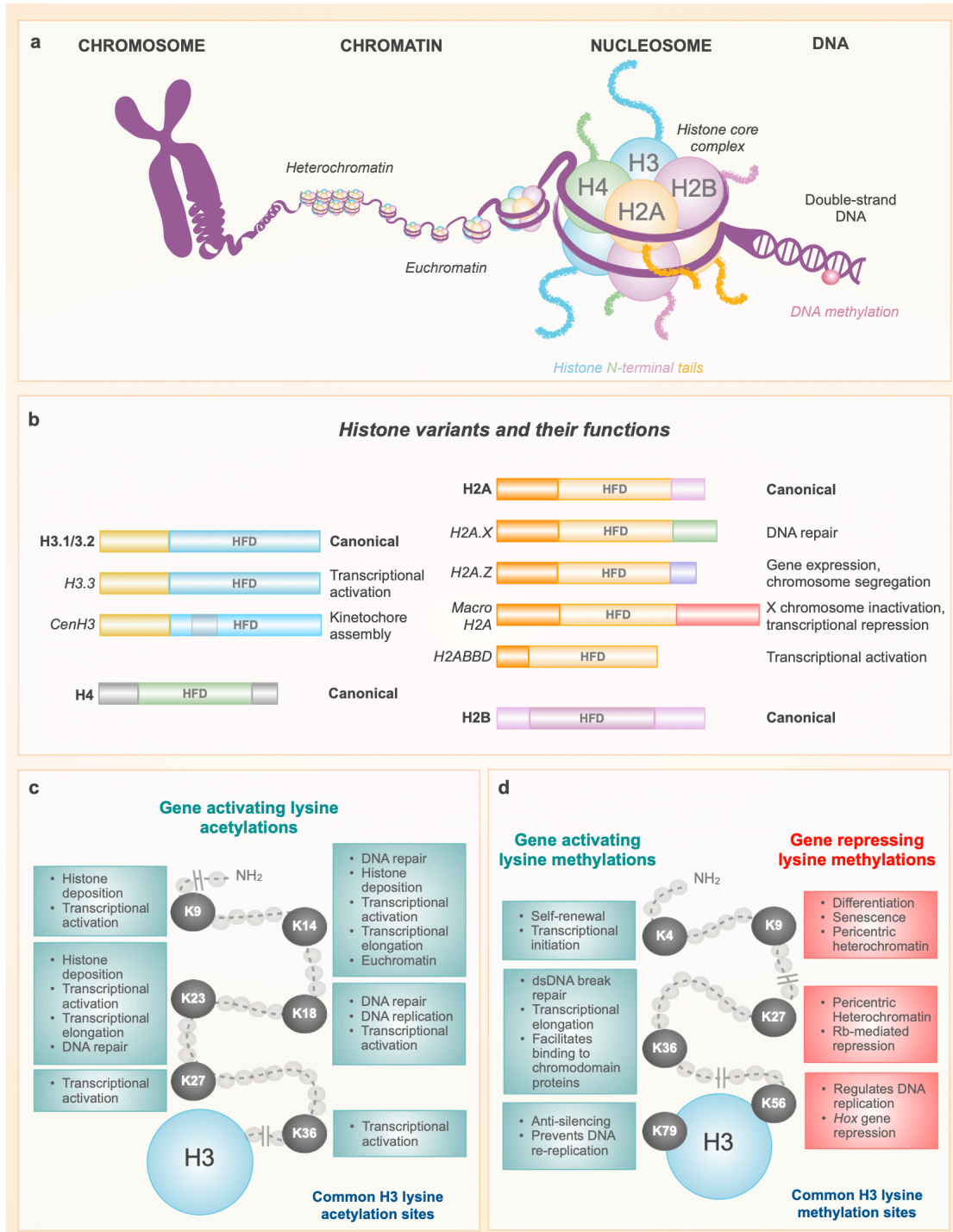


Figure 4.1 The role of the histone code in regulating gene expression.

(a) Chromosomes are formed by supercoiling of chromatin. Accessible chromatin for DNA transcription, replication and repair is known as heterochromatin while inaccessible chromatin is known as euchromatin. The functional unit of chromatin is known as the nucleosome, an assembly of 147 base pairs of DNA and an octameric histone core. The histone core complex consists of H3, H4, H2A and H2B subunits, each of which can be modified to strengthen or weaken their interaction with DNA. (b) Canonical (**bold**) and non-

canonical (*italic*) histone core variants. (c) Acetylation of histone H3 on lysine (K) residues is generally gene-activating, while (d) methylation can be either activating or repressing. *HFD*: Histone Fold Domain.

Histone post-translational modifications

Post-translational modifications occur on all histone subunits and variants. The most dynamically modified histone subunit is H3. The major histone H3 modifications are lysine acetylation and lysine mono-, di-, and trimethylation. Lysine acetylation is associated with gene activation, as the addition of the negative acetyl group (CH_3COO^-) on histone tails neutralises the positive charge of histone lysine residues. This net reduction in positive charges weakens the interactions between histones and the negatively charged DNA, making genes more accessible. Histone H3 lysine acetylation is known to occur on lysine residues K9, K14, K18, K23, K27 and K36 (**Figure 4.1c**).³¹⁷

Unlike acetylation, methylation of lysine residues does not change the charge of histone tails and can be gene-activating or -repressing depending on the lysine site being modified. Lysine methylations alter the binding of effector proteins known as histone code readers. Histone H3 can be methylated on lysine residues K4, K9, K27, K36, K56 and K79 (**Figure 4.1d**).³¹⁷ Other modifications such as serine/threonine phosphorylation, lysine SUMOylation and arginine mono- and (α)symmetric dimethylation can also occur, but these are less characterised.³¹⁷ Intricate control over histone PTMs is regulated by histone-modifying enzymes, which are further investigated in **Chapter 5**.

Histone H3 post-translational modifications in drug-tolerant persisters

Several studies investigating mechanisms of survival in drug-tolerant persisters demonstrate changes in histone H3 modifications. In lung cancer cells, tolerance to the EGFR-targeted inhibitor erlotinib is associated with a decrease in gene-activating H3K4 methylation,^{144, 318, 319} an increase in gene-repressing H3K9 and H3K27 methylations and a global decrease in H3 lysine acetylation across the entire DTP population.³¹⁹ Similarly, lung cancer cells surviving several cycles of docetaxel-cisplatin doublet chemotherapy globally exhibited a decrease in H3K4 methylation and an increase in H3K27 methylation at transcription start sites of downregulated genes.¹⁵⁴ However, these same DTPs displayed an increase in H3K4 methylation and a decrease in H3K27 methylation at upregulated genes. Specifically, histone H3.3, which is deposited at active transcription sites, exhibited a decrease in methylation, and hence, inhibition, at lysine K27.¹⁵⁴ In glioblastoma, cells tolerant to dasatinib exhibited a decrease in H3K27 methylation and an increase in H3K27 acetylation at stemness, quiescence and survival

genes.¹⁰⁶ These findings are consistent with the notion that DTPs convert to an overall transcriptionally repressed, dormant state, but upregulate genes that promote stemness, dormancy and survival.¹⁴³ As a result of changes in histone modifications in DTPs, inhibition of histone-modifying enzymes or other effector proteins reduced DTP viability in several cancer models (see **Table 5.1**). As most changes in DTPs are mediated via histone H3, we focused our study on changes within this subunit of the nucleosome.

To identify targetable histone-modifying enzymes in glioblastoma tolerance to MTAs, we first aimed to profile changes in histone H3 methylation and acetylation. When studying the tubulin code, our analysis was limited by the availability of commercial antibodies. Therefore, to study the histone code we opted to use a comprehensive and unbiased mass spectrometry-based approach, known as Sequential Window Acquisition of all Theoretical Mass Spectra (SWATH-MS). Several research teams verified the reproducibility and robustness of SWATH-MS for large-scale protein quantification by performing the same experiment independently.³²⁰ SWATH-MS has also been previously used to quantify histone post-translational modifications of histone H3 and H4 in breast cancer cells treated with the HDAC inhibitor suberoylanilide hydroxamic acid (SAHA).³²¹ However, SWATH-MS has not been previously used to study changes to histone modifications during drug tolerance.

4. 1. 2. Sequential window acquisition of all theoretical mass spectra assays

Common antibody-based methods used to study changes in histone PTMs include immunoblotting, immunofluorescence and chromatin immunoprecipitation (ChIP). However, these methods have significant drawbacks due to epitope occlusion, innate differences in binding efficacy and the cross-reactivity of antibodies.³²²⁻³²⁵ As a result, antibody-based assays are intrinsically semi-quantitative. Antibodies also fail to detect combinatorial modifications, which are abundant in histones. By comparison, “liquid chromatography coupled to tandem mass spectrometry (LC-MS/MS) offers a comprehensive and unbiased method for the identification and quantification of histone PTMs, including combinatorial modifications.”³²¹ Moreover, MS-based methods can be quantitative and are much more reproducible (**Table 4.1**).³²⁶

In conventional bottom-up proteomic mass-spectrometry techniques, also known as ‘shotgun proteomics’, protein extracts are digested with proteolytic enzymes like trypsin and the digested peptides are analysed LC-MS/MS. Peptides are identified by comparing their mass-to-charge (m/z) ratios with those predicted from protein sequence databases (e.g., SwissProt). Additionally, confidence in peptide identity can be increased

by isolating and fragmenting the peptide, and comparing the m/z of the fragments (tandem MS: MS/MS) to those of annotated peptide spectral libraries.³²⁶ Therefore, protein identification and quantification can be derived from the quantity of identified peptides. Shotgun proteomics is a form of Data-Dependent Acquisition (DDA), where a survey scan (MS1) is performed and a fixed number of ions over a m/z range are selected based on observed intensity and analysed by MS/MS. DDA dataset analysis is relatively straightforward but is dependent on *a priori* knowledge of gene products and its protein sequence coverage is limited by the peptides identified. DDA is unable to differentiate between co-eluting isobaric peptides (peptides that have the same retention time and m/z), which frequently co-exist within histone protein extracts. Furthermore, DDA is not suitable for studying changes in histone PTMs as datasets often do not contain information on peptides or proteins present at lower concentrations.³²⁷

Due to limitations of DDA, other bottom-up targeted methods like Selected Reaction Monitoring (SRM) or Parallel Reaction Monitoring (PRM) were developed. In contrast to DDA, SRM/PRM scan for preselected ions at the MS1 levels. If present, the peptide is isolated and fragmented and MS2 spectra for preselected peptides are recorded. Scanning for MS1-MS2 ion pairs in such a targeted fashion results in extreme accuracy, specificity and reproducibility.³²⁷ PRM was employed to study changes in histone PTMs in lung cancer cells tolerant to erlotinib.³¹⁹ While such targeted approaches have overcome many limitations of shotgun proteomics, SRM/PRM fail to deconvolute co-eluting and isobaric peptides for quantification.³²⁶ Moreover, although SRM/PRM are excellent for verifying hypotheses regarding changes in specific site modifications, such methods are incapable of identifying changes in sites that were not preselected.

An emerging strategy for studying complex protein samples, such as histone extracts, is SWATH-MS. SWATH-MS employs a Data-Independent Acquisition (DIA) of proteolytically digested peptides. In DIA mode, a quadrupole mass filter is coupled to an Orbitrap mass analyser. The Orbitrap analyser scans precursor ion (MS1) spectra of peptides co-eluting at a given retention time over a given m/z range (e.g., 300 – 1600 m/z) (**Figure 4.2a**). The ionised peptides in the sample that fall within a predefined m/z range (e.g., 390 – 930 m/z) are then incrementally isolated and fragmented at specified isolation windows (e.g., a 10 m/z window). Following fragmentation within each isolation window, isolated fragment (MS2) spectra are systemically and consecutively scanned by the Orbitrap analyser across the entire predefined m/z range. In the example shown in **Figure 4.2b**, 54 scans are performed over a 390-930 m/z range with a 10 m/z isolation windows. After repeated cycles of MS1 and MS2 scans, an extensive data set of continuous scans of all detectable precursor and fragment ions is generated.³²⁶

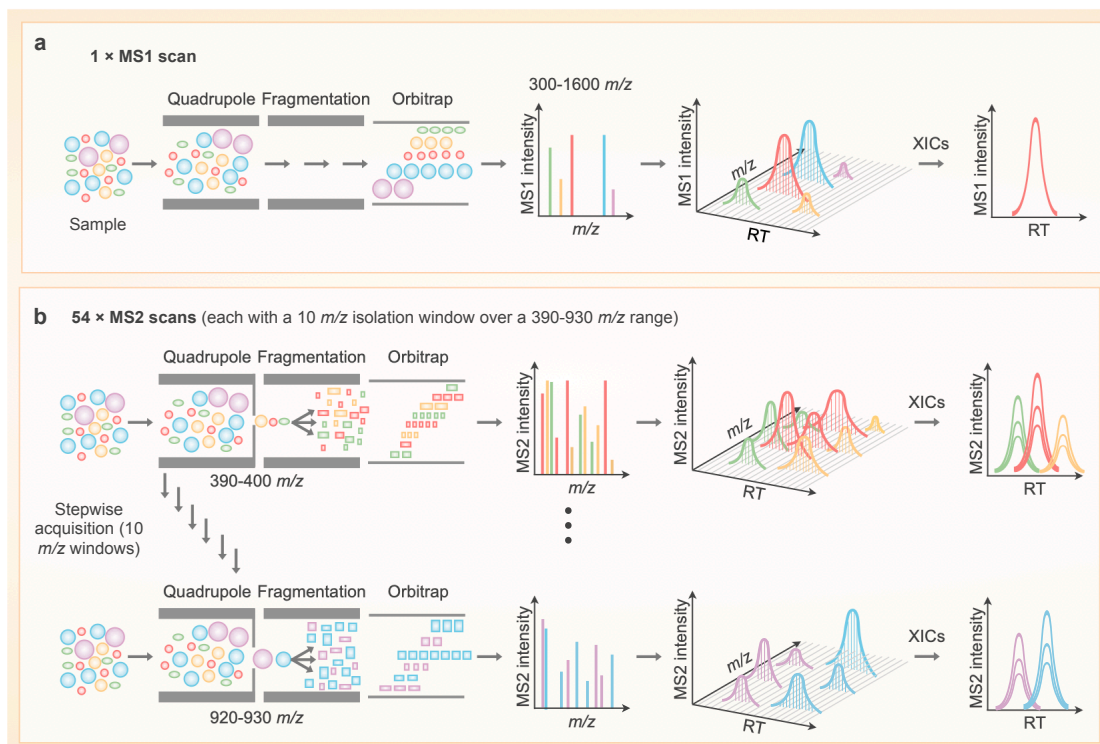


Figure 4.2 Principle of SWATH-MS assays for large-scale proteomics.

In SWATH-MS, a quadrupole mass filter and an Orbitrap mass analyser are employed. **(a)** A single precursor ion (MS1) scan is recorded, followed by **(b)** a series of fragment ion (MS2) spectra in consecutive precursor isolation windows (e.g., 10 m/z) over a defined mass range (e.g., 390–930 m/z).

The principle behind SWATH-MS is the use of prior knowledge of chromatographic and mass spectrometric behaviours of peptides to selectively identify and extract chromatograms from unbiased and comprehensive DIA datasets. Accurate identification of peptides relies on peptide-centric analysis, wherein peptide query parameters (PQPs) have to be monitored. PQPs include (i) peptide or fragment sequence, (ii) the dominant (M , $M + 1$, $M + 2$) precursors m/z , (iii) 4-10 of the most intense fragment (b^+ and y^+) ion m/z values from fragmented peptides, (iv) expected fragmentation patterns and (v) expected retention times. PQPs are obtained from spectral libraries (obtained from methods such as DDA). As such, DDA scans are usually run alongside DIA scans for spectral library generation. The Skyline software integrates all steps of spectral library generation and was, therefore, used in this study. To assess the goodness-of-fit of the peak areas of MS1 spectra to the expected isotope distribution (M , $M + 1$ and $M + 2$) of each peptide, Skyline calculates the dot product (idotp). Similarly, peak areas of MS2 spectra (b^+ and y^+ ions) are compared with those of corresponding intensities in the spectral library using 'dotp'. A dot product value closer to '1.00' implies a better fit, with '1.00' being a perfect score.³⁰³

Table 4.1 Comparison of antibody- and label-free MS-based techniques.

DDA: Data-Dependent Acquisition; DIA: Data-Independent Acquisition; SRM: Selected Reaction Monitoring; PRM: Parallel Reaction Monitoring
 (+++: best performance; ++: medium performance; +: suboptimal performance.)

	Antibody-based methods	Shotgun-MS (DDA)	Targeted-MS (SRM/PRM)	SWATH-MS (DIA)
Ease of data acquisition	++ Easy, limited by commercial availability of antibodies	+++ Easiest, default setup on most mass spectrometers	+ Hard, requires generation and optimisation of synthetic peptide libraries for data acquisition	++ Easy, requires definition of mass range to cover precursor isolation window and number of MS2 scans per cycle
Ease of data analysis	+++ Easiest, although techniques are generally semi-quantitative	+++ Easiest, several software available	++ Easy, several software available	+ Hard, requires PQPs, stringent data quality control, sophisticated algorithms and software, and statistical analysis of large sets of data
Peptide detection and/or multiplexing	+ Requires sophisticated and expensive platforms	+++ 1,000's of peptides quantifiable per MS injection	++ 100's of peptides quantifiable per MS injection	+++ 1,000's of peptides quantifiable per MS injections
Reproducibility	+ Low due to cross-reactivity, epitope occlusion and batch-to-batch variations of polyclonal antibodies	+ Low due to biased sampling of DDA against low abundance peptides	+++ High due to targeted data acquisition	+++ High due to peptide-centric scoring
Retrospective analysis of extracted ion chromatograms	N/A	++ Possible only at MS1 level	+ Not possible	+++ Possible at MS1 and MS2 levels

The main advantages of SWATH-MS are its superior run-to-run reproducibility and ability to deconvolute co-eluting isobaric peptides, provided they possess unique fragment ions. SWATH-MS is ideal for hypothesis generation due to its wide-range and untargeted datasets. Furthermore, as both MS1 and MS2 information are collected, retrospective analysis of acquired data is achievable.^{320, 326}

Given the advantages of the unbiased and global approach of SWATH-MS, we employed this methodology to identify changes in histone H3 methylations and acetylation in glioblastoma cells tolerant to microtubule-targeting agents. We studied glioblastoma cells tolerant to CMPD1 and focused on the histone H3 subunit. These experiments were performed in FPW1 and RK11 glioblastoma stem cell line, as these

exhibited the highest tolerance (e.g. highest GR_{max} values) to CMPD1 and tivantinib treatment,¹ and are, thus, likely to generate the largest number of persisters.

4. 2. Results

4. 2. 1. Glioblastoma cells are tolerant to CMPD1 and tivantinib

To confirm that both CMPD1 and tivantinib exhibit fractional efficacy in FPW1 and RK11 cells and derive drug-tolerant persisters, viability and survival assays were performed. To quantify the fraction of drug-tolerant cells in parental populations, RK11 and FPW1 cells were treated with high concentrations of CMPD1 or tivantinib (25 μ M, ~25-fold higher the GR_{50}) for 14 days. Cells were stained with Nuclear-Red ID DNA stain and imaged at Day 0 and Day 14 of treatment.

In the FPW1 cell line, 39 ± 1.0 % and 33 ± 3.0 % of cells survived CMPD1 and tivantinib treatments, respectively. In the RK11 cell line, 39.5 ± 5.5 % and 29 ± 6.0 % of cells survived CMPD1 and tivantinib treatments, respectively (**Figure 4.3a**). Notably, DTPs derived from both cells and using both drugs exhibited larger and polypoidal nuclei compared to their untreated counterparts, consistent with our findings from RK11 cells treated with colchicine (**Chapter 3**).

As treatment-induced dormancy is thought to be reversible,¹⁴³ CMPD1- and tivantinib-tolerant FPW1 and RK11 cells were allowed to recover in drug-free media and were monitored with light microscopy (**Figure 4.3b**). DTPs derived from both cell lines and using both CMPD1 and tivantinib were generally able to recover in drug-free media and resume proliferation after two weeks (Day 28). However, RK11 cells treated with CMPD1 needed an additional 5 days in drug-free media (Day 33) to resume proliferation (**Figure 4.3c**).

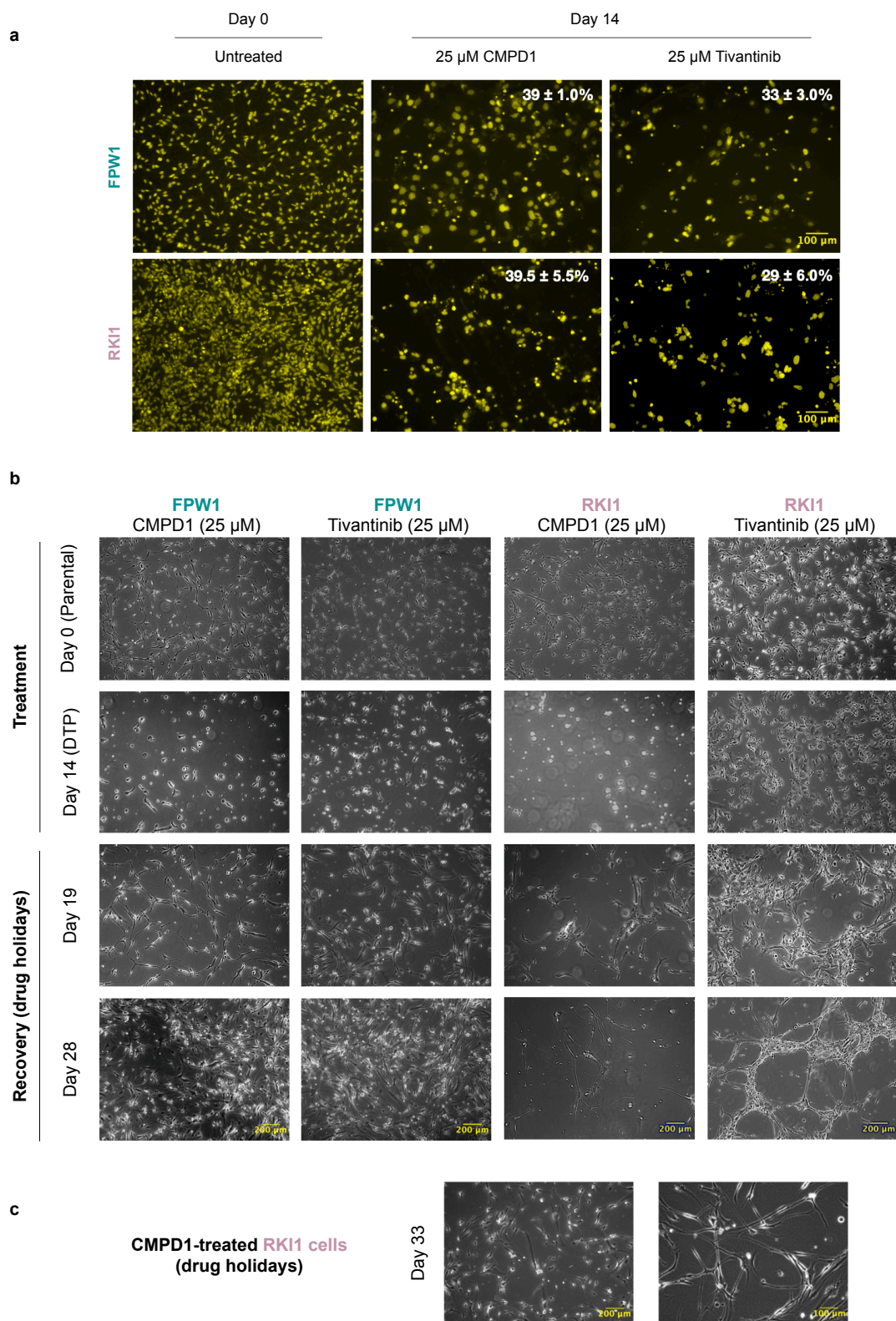


Figure 4.3 RK11 and FPW1 cells are tolerant to CMPD1 and tivantinib.

(a) RK11 and FPW1 cells were treated with CMPD1 or tivantinib (25 μ M) and stained with Nuclear-ID Red on Day 0 and Day 14. Representative images and the means of two independent experiments are shown. (b) CMPD1- and tivantinib-tolerant FPW1 and RK11 cells recover and resume proliferation in 'drug holidays.' Representative images of two independent experiments are shown. (c) RK11 cells tolerant to CMPD1 require a longer time in drug-free media to recover when compared to other drug-cell line combinations.

Next, we compared the sensitivity of parental and recovered DTP cells to CMPD1 and tivantinib. Parental (drug-naïve) and recovered DTP cells (drug holidays) were exposed to the CMPD1 or tivantinib for 5 days. Cell viability was assessed using the CellTitre-Blue assay kit. Concentration-response curves and the change in cell viability between Day 0 and Day 5 were used to generate GR curves and determine GR metrics using the *GRcalculator* tool, as per methods previously described.^{298, 299, 328} In FPW1 cells (**Figure 4.4a**), CMPD1 exhibited similar potencies in parental cells ($GR_{50} = 0.7 \pm 0.11 \mu\text{M}$) and recovered CMPD1-tolerant cells ($GR_{50} = 1.1 \pm 0.61 \mu\text{M}$). Similarly, the differences in efficacy between parental ($GR_{\text{max}} = -0.3 \pm 0.04$) and recovered DTP ($GR_{\text{max}} = -0.4 \pm 0.10$) cells were not significant. In parental FPW1 cells, tivantinib had a potency ($GR_{50} = 0.6 \pm 0.04 \mu\text{M}$) and efficacy ($GR_{\text{max}} = -0.37 \pm 0.002$) similar to that observed in recovered tivantinib-tolerant cells potency ($GR_{50} = 1.1 \pm 0.65 \mu\text{M}$, $GR_{\text{max}} = -0.2 \pm 0.07$).

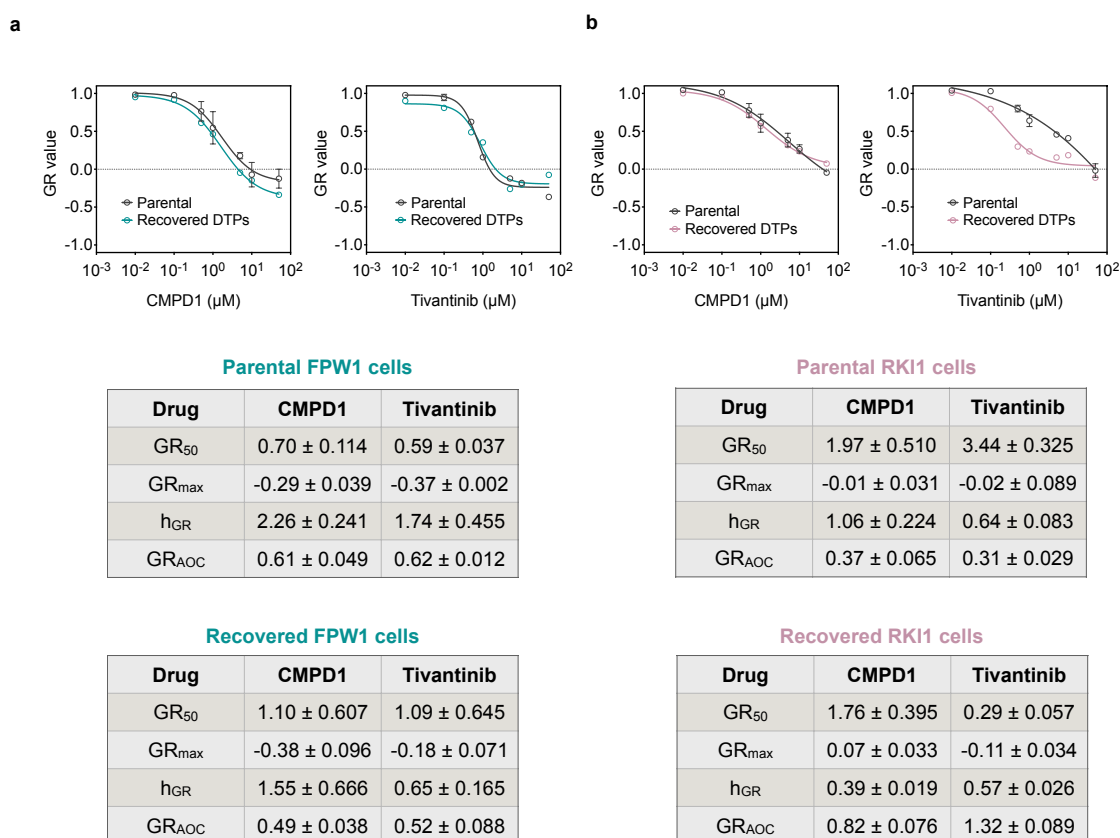


Figure 4.4 RKI1 and FPW1 cells are tolerant to CMPD1 and tivantinib.

Recovered DTPs were obtained by allowing cells exposed to a 14-day treatment of CMPD1- or tivantinib ($25 \mu\text{M}$) to recover in drug-free media. Recovered cells were re-exposed to MTA treatment for 5-days. Concentration-response curves for CMPD1 and tivantinib were measured using CellTitre-Blue viability assay in FPW1 and RKI1 cells. (**a**) GR concentration-response curves and (**b**) GR metrics for parental and

recovered DTPs are shown. Each condition was performed in technical triplicates. Data represent mean \pm SEM ($n = 3-4$).

In the RK11 cell line (**Figure 4.4b**), CMPD1 had the same potencies and efficacies in parental ($GR_{50} = 1.9 \pm 0.51 \mu\text{M}$, $GR_{max} = 0.0 \pm 0.03$) and recovered DTPs ($GR_{50} = 1.8 \pm 0.40 \mu\text{M}$, $GR_{max} = 0.1 \pm 0.03$). On the other hand, tivantinib was less potent and efficacious on parental cells ($GR_{50} = 3.4 \pm 0.32 \mu\text{M}$, $GR_{max} = -0.02 \pm 0.089$), compared to recovered DTP cells ($GR_{50} = 0.2 \pm 0.06 \mu\text{M}$, $GR_{max} = -0.11 \pm 0.03$).

The GR viability curves were indistinguishable between treatment-naïve (parental) cells and recovered DTPs in every case, with the exception of RK11 DTPs recovered from tivantinib treatment. Unexpectedly, these cells were more sensitive to tivantinib than treatment-naïve parental cells (**Figure 4.4b**).

In summary, CMPD1 and tivantinib were unable to induce complete cytotoxicity (*i.e.*, $GR_{max} = -1$) and were predominantly cytostatic in short-term viability assays. This fractional killing generates a large number of DTPs that survive long-term exposures to high concentrations of MTAs. Indeed, the surviving DTPs recovered during drug holidays and exhibited the same sensitivity to MTAs as treatment naïve parental cells, suggesting reversible epigenetic mechanisms of survival. Therefore, to quantify changes in histone H3 methylation and acetylation in DTPs, we employed the SWATH-MS method for analysing chromatin extracts from parental and CMPD1-tolerant cells.

4. 2. 2. Histone extraction from cells

Histone extraction from cells is required for SWATH-MS. To first assess the fractionation efficiency of the Subcellular Fractionation Kit (ThermoFisher), the cytoplasmic, soluble nuclear and chromatin-bound nuclear fractions derived from parental FPW1 cells were analysed by immunoblotting. The Histone Extraction Kit (Abcam) was used on cells from the same parental FPW1 sample to compare histone purity. The histone extracts (Abcam kit) and chromatin-bound nuclear fractions exhibited similar and high quantities of purified histone H3 proteins. Minimal levels of histone H3 were found in the cytoplasmic and soluble-nuclear fractions. Moreover, GAPDH, a cytoplasmic protein, was predominantly present in cytoplasmic fractions (**Figure 4.5**). These immunoblots demonstrate the purity of subcellular fractions obtained with both kits. The Subcellular Fractionation Kit was then used to obtain chromatin-bound nuclear fractions from treatment-naïve parental and CMPD1-tolerant DTP cells (**Figure 4.6**).

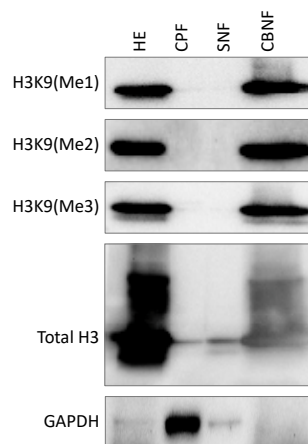


Figure 4.5 Immunoblots confirming subcellular fractionation.

Histones extracts (HE) were obtained from FPW1 cells using the Histone Extraction Kit (Abcam). In parallel, the Subcellular Fractionation Kit (ThermoFisher) was used on FPW1 cells to obtain Cytoplasmic Fractions (CPF), Soluble Nuclear Fractions (SNF) and Chromatin-Bound Nuclear Fractions (CBNF). Each fraction (20 µg) was analysed by immunoblotting and membranes were probed with H3K9(Me1), H3K9(Me2), H3K9(Me3), Total H3 or GAPDH antibodies.

4. 2. 3. Mass spectrometry data acquisition and analysis

Following subcellular fractionation of parental and CMPD1-tolerant FPW1 and RK11 cells from three independent experiments, single injections of chromatin-bound nuclear fractions (1 µg) from each sample were used to create the DDA spectral library. Triplicate DIA scans on each chromatin-bound fraction were then performed. A total of 12 DDA datasets and 36 DIA datasets were collected. Histone peptides in the DDA datasets were identified via database searches using Mascot (Matrix Science). The DDA search results were then imported and annotated in Skyline, resulting in a targeted library containing 66 histone peptides with 106 precursor ions and 1,629 product ions derived from histone H3.1/3.2 and H3.3 proteins. DIA runs were then imported in Skyline and peak areas for each of the 66 peptides (identified from DDA spectral libraries) were quantified in each DIA run. A total of 2,376 peptide peak areas were quantified (Figure 4.6).

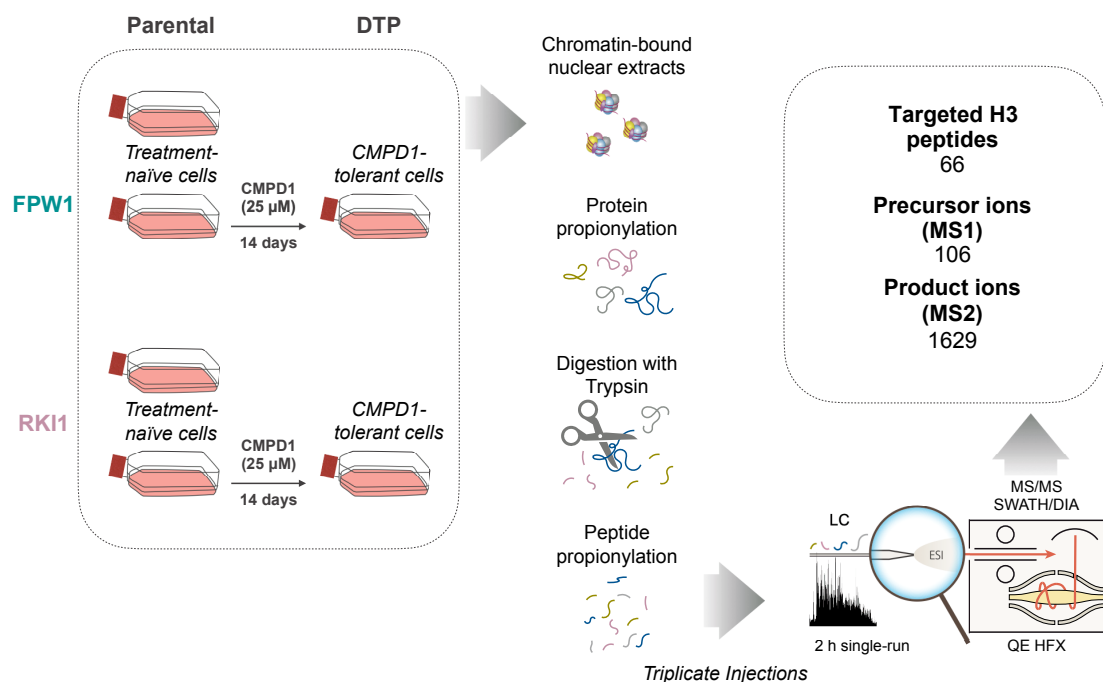


Figure 4.6 Experimental workflow for quantifying changes in histone PTMs in glioblastoma cells.

FPW1 and RK11 cells were treated with CMPD1 (25 μM) for 14 days to generate DTPs. Chromatin-bound nuclear fractions were obtained from treatment-naïve (parental) and CMPD1-tolerant persister (DTP) cells and analysed by SWATH-MS. A targeted search for histone H3.1/3.2 and H3.3 proteins yielded 66 peptidoforms which were tracked and quantified. ESI: Electron-Spray Ionisation.

Conventionally, peptides are denoted by modifications on residues being studied.^{319, 321} For example, the histone H3 peptide spanning residues 9 to 17, H3(9-17) KSTGGKAPR, contains lysine residues K9 and K14. The unmodified form of the peptide is denoted by K9K14, whereas the K9 mono-methylated and K14 acetylated form of the peptide is denoted by K9(Me1)K14(Ac). This convention is adopted for the analysis of the results. The 66 modified histone H3 peptides detected were grouped into nine 'peptide families' based on their peptide sequences:

H3	(3-8)	<u>TK4</u>QTAR
H3	(9-17)	<u>K9</u>STGG<u>K14</u>APR
H3	(18-26)	<u>K18</u>QLAT<u>K23</u>AAR
H3.1/3.2	(27-40)	<u>K27</u>SAPATGGV<u>K36</u>KPHR
H3.3	(27-40)	<u>K27</u>SAPSTGGV<u>K36</u>KPHR
H3	(54-63)	YQ<u>K56</u>STELLIR
H3	(64-69)	<u>K64</u>LPFQR
H3	(73-83)	EIAQDF<u>K79</u>TDLR
H3	(117-128)	VTIMP<u>K112</u>DIQLAR

The peak area of each peptidoform (a modified version of the same peptide) was expressed as a percentage of its peptide family within each sample. While the

absolute intensities of a given peptide varied across technical and biological replicates (e.g., **Figure 4.7b**), we compared the abundance of each peptidofrom relative to its peptide family (%) across samples. This controls for sample loading variations. Nonetheless, the coefficient of variance of peak areas of a given peptide between triplicate injections did not exceed 20%, demonstrating the high quality of our data. Only unmodified versions of peptides *H3(54-63)*, *H3(64-69)* and *H3(117-128)* were detected in all samples, *i.e.*, they constituted 100% of their peptide family. Therefore, these three peptides were excluded from subsequent analysis. Quality control (*idotp* > 0.9, *dotp* > 0.9) of spectral library matching was performed for every peptide in each sample.

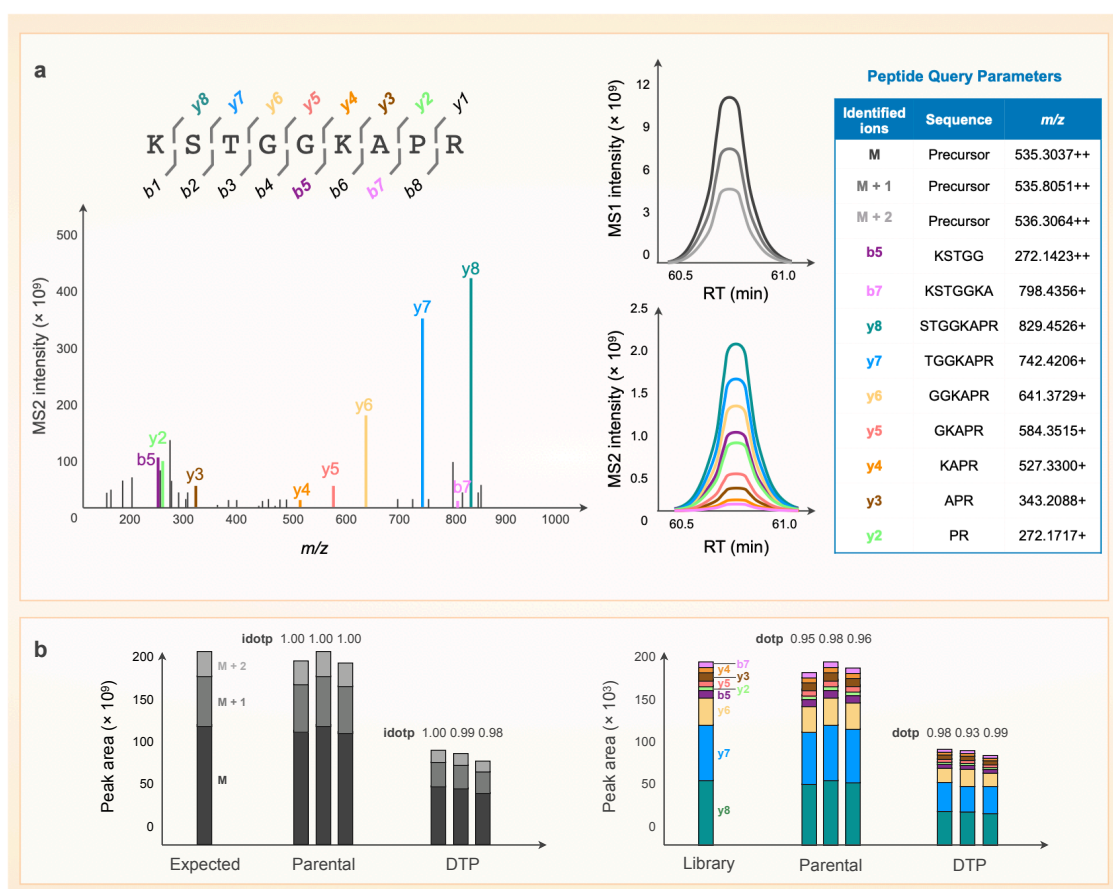


Figure 4.7 SWATH-MS data quality control.

(a) Peptide query parameters for the unmodified histone peptide KSTGGKAPR, containing lysine K9 and K14. Peptide fragmentation generates a series of b+ and y+ ions that guide the identification of the peptide. (b) Skyline integrates spectral libraries and uses peak area dot products to assess goodness-of-fit of observed versus expected values; *idotp* assesses MS1 spectra against expected isotopic distribution while *dotp* assess MS2 spectra against corresponding intensities from generated spectral libraries.

Peptide query parameters are used in SWATH-MS assays to confidently identify each peptide. For example, the PQQs for unmodified peptide K9K14 in a biological repeat of parental and persister FPW1 cells is shown (**Figure 4.7a**). Three precursor (MS1)

and nine fragment (MS2) ions were identified. Peak area similarity scores (idotp and dotp) of technical replicates between treated and untreated samples were all greater than 0.9 (Figure 4.7b). Similarity scores were manually checked for each of the 2,376 peptide peak areas in the dataset. Peptides with idotp or dotp scores lower than 0.9 were excluded from the analysis.^{320, 326} Quality control (idotp > 0.9) of spectral library matching was performed for every peptide in each sample.

4. 2. 4. H3 variant and post-translational changes in CMPD1-tolerant cells

As histone H3 variants share high sequence homology, most of the peptides identified within samples were pooled from histone variants H3.1, H3.2 and H3.3. Exceptions were the peptides spanning residues 27-40, which were unique to either H3.1/3.2 or H3.3. Therefore, H3.1/3.2 and H3.3 variant levels were compared by assessing levels of the unique H3.1/3.2(27-40) and H3.3(27-40) peptides within each sample.

To quantify total levels of H3.1/3.2 and H3.3 between parentals and DTPs, the sum of the raw peak areas of the H3.1/3.2(27-40) peptide family was divided by the sum of the raw peak areas of the H3.3(27-40) peptide family within each sample. In both the FPW1 and RKI1 cell lines, the H3.1/3.2 to H3.3 ratio decreased to 0.6-fold in DTPs relative to parentals (both $p \leq 0.001$) (Figure 4.8), suggesting an increase in histone H3.3 deposition in DTPs.

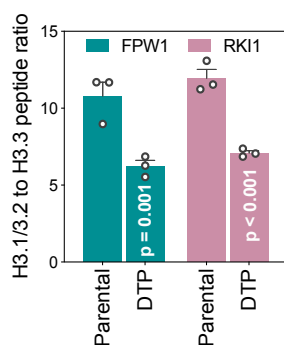


Figure 4.8 Ratio of the H3.1/3.2 K27K36 to the H3.3 K27K36 peptide families.

The sum of peak areas of the H3.1/3.2 peptide family was divided by the sum of peak areas of the H3.3 peptide family within each sample (prior to data normalisation). Data are mean \pm SEM from three independent experiments performed in triplicates. A paired *t*-test was performed between parental and DTP cells in each cell line.

MS1 peak area quantifications of peptidofoms identified in Skyline with high confidence were first log-transformed (base 2) and then quantile-normalised across samples. Combat R package was used to remove experimental batch effects.³⁰⁵ Peptide-centric heatmaps for FPW1 (Figure 4.9) and RKI1 (Figure 4.10) were then constructed. These

heatmaps illustrate the Log₂ fold-change in the normalised abundance of each peptide relative to treatment-naïve parental cells.

Overall, CMPD1 induced site-specific changes in methylation and acetylation on histone H3 peptides. Heatmaps of both cell lines show that DTPs exhibit variable changes in histone H3 methylation and global decreases in histone H3 acetylation (Figure 4.9 and Figure 4.10).

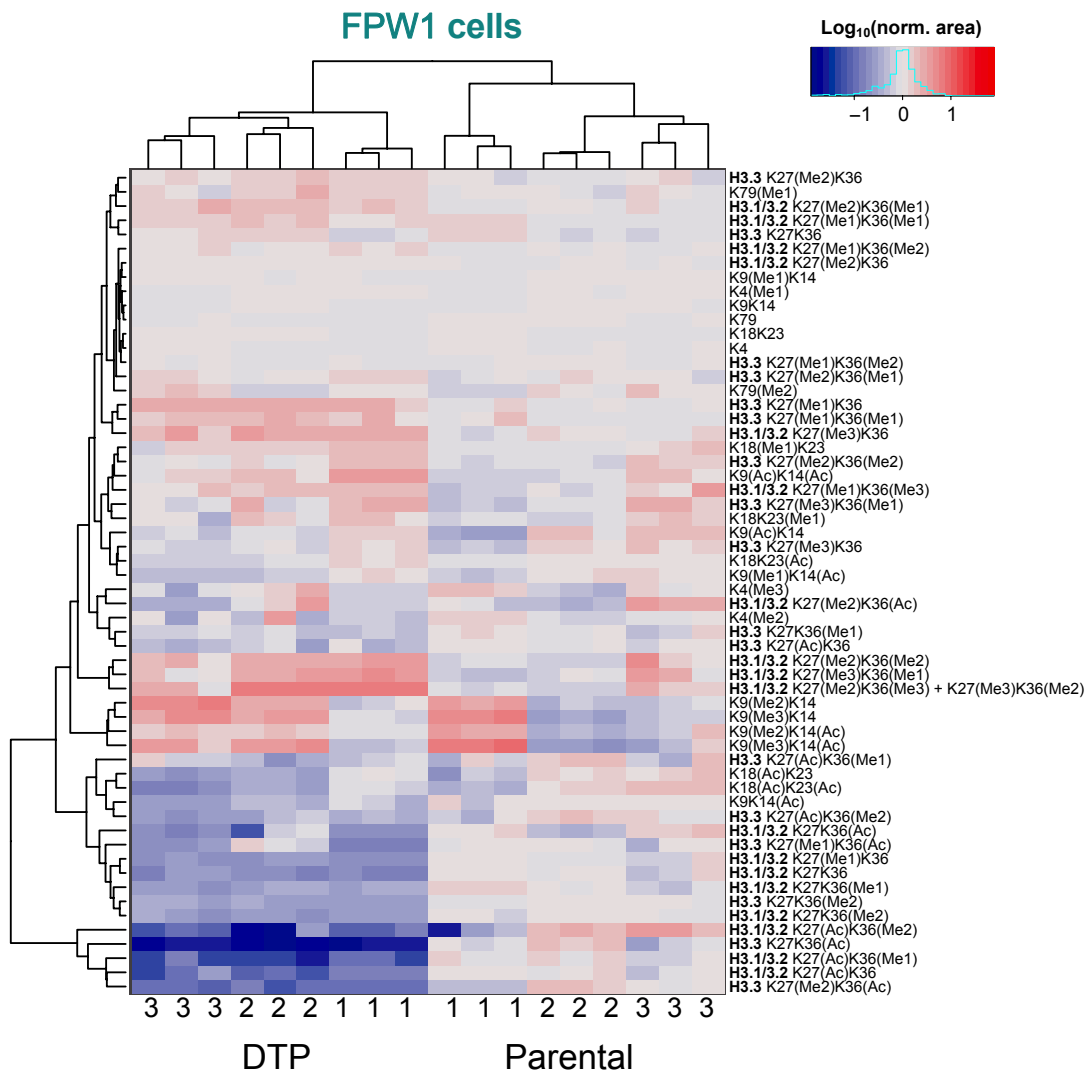


Figure 4.9 Changes in histone H3 modifications in CMPD1-tolerant FPW1 persisters.

Parental and DTP cells analysed using SWATH-MS. Peak areas exported from Skyline and peptide intensities expressed as percentages of their peptide families. Heatmap displaying log₂-transformed peak areas for 66 unmodified, methylated and acetylated H3 peptides. Peptides are pooled from histone H3.1, H3.2 and H3.3 variants, with the exception of peptides spanning residues 27-40 that are unique to either H3.1/3.2 or H3.3. Variant-specific peptides are indicated. Data represent parental-DTP pairs from three biological repeats (1, 2 or 3) performed in triplicates.

To obtain a more detailed understanding of changes in site-specific histone H3 modifications in drug-tolerant persisters, normalised values were extracted from the heatmap matrices and stratified by peptide family. Average fold-changes from three

independent biological repeats of parentals and DTPs were plotted on an anti-Log₂ scale. A Welch's *t*-test was performed to determine significant changes in normalised peptide abundance between treatment-naïve parental and DTP cells.

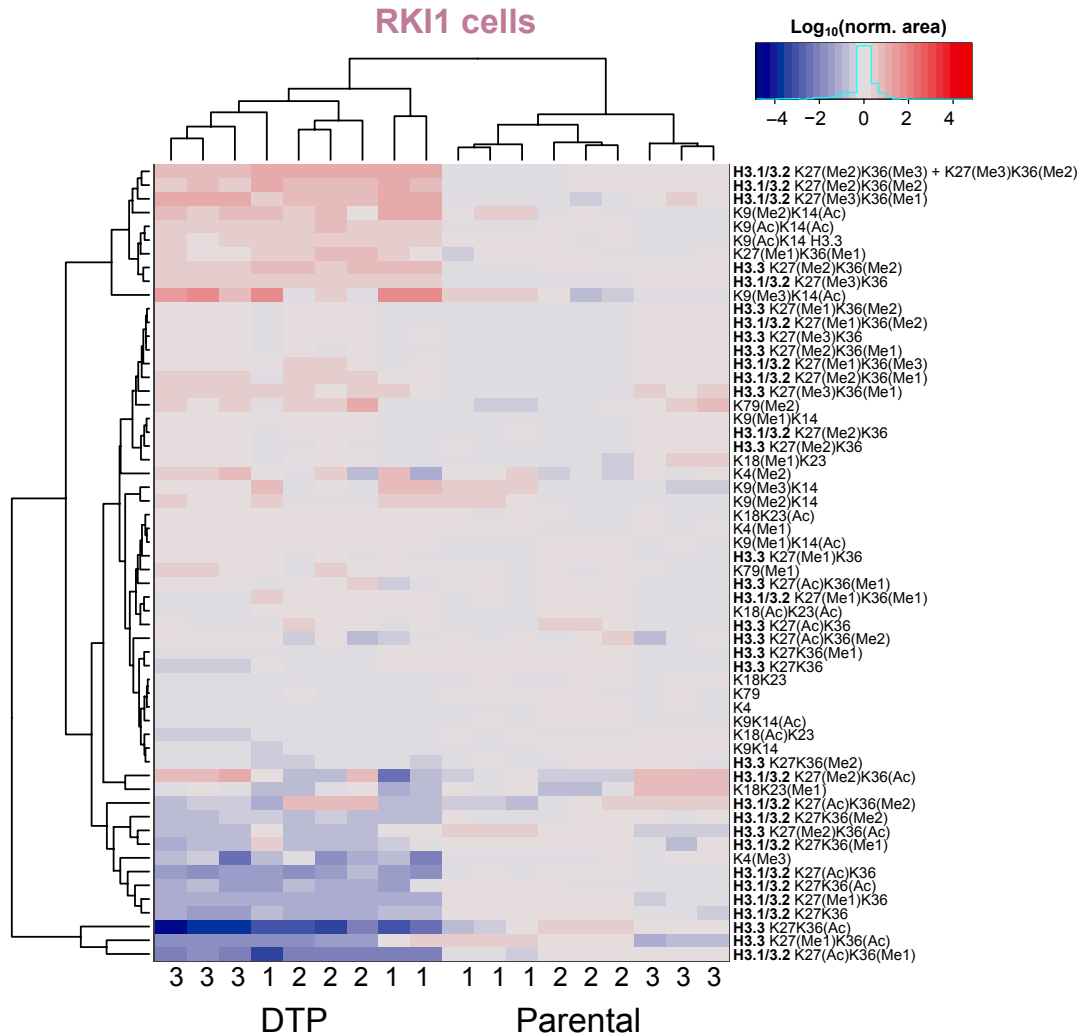


Figure 4.10 Changes in histone H3 modifications in CMPD1-tolerant RK11 persisters.

Parental and DTP cells analysed using SWATH-MS. Peak areas exported from Skyline and peptide intensities expressed as percentages of their peptide families. Heatmap displaying log₂-transformed peak areas for 66 unmodified, methylated and acetylated H3 peptides. Peptides are pooled from histone H3.1, H3.2 and H3.3 variants, with the exception of peptides spanning residues 27-40 that are unique to either H3.1/3.2 or H3.3. Variant-specific peptides are indicated. Data represent parental-DTP pairs from three biological repeats (1, 2 or 3) performed in triplicates.

The H3(3-8) TKQTAR family consisted of 4 peptidofoms containing lysine K4:

- | | |
|---------|---------|
| K4 | K4(Me2) |
| K4(Me1) | K4(Me3) |

CMPD1-tolerant FPW1 cells did not exhibit significant changes in H3K4 mono-, di- or tri-methylation (**Figure 4.11a**). CMPD1-tolerant RK11 cells exhibited a decrease to 0.9-fold in the abundance of the unmodified peptidofrom K4 ($p < 0.05$), a 1.1-fold increase in K4(Me1) ($p < 0.01$), a 1.5-fold increase in K4(Me2) ($p < 0.05$) and a 0.5-fold decrease in K4(Me3) relative to parentals ($p < 0.001$) (**Figure 4.11b**).

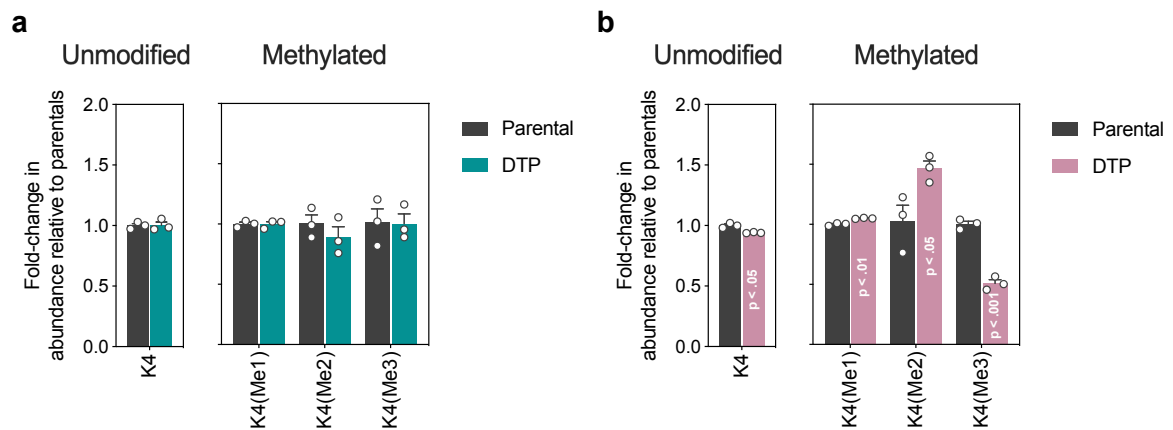


Figure 4.11 Changes in histone H3K4 modifications in DTPs.

Fold-change (anti-Log₂) in peptide abundance within the *H3(3-8) TKQTAR* peptide family in **(a)** FPW1 and **(b)** RK11 cells upon treatment with CMPD1 (25 μ M) for 14 days. Data are mean \pm SEM from three independent experiments. Welch's *t*-test was performed between DTP and parentals.

The *H3(9-17) TKQTAR* family consisted of 10 peptidofoms containing lysine K9 and K14:

K9K14	K9(Ac)K14	K9(Me2)K14(Ac)
K9(Me1)K14	K9K14(Ac)	K9(Me3)K14(Ac)
K9(Me2)K14	K9(Ac)K14(Ac)	
K9(Me3)K14	K9(Me1)K14(Ac)	

In FPW1 samples, the abundance of peptidofoms within this family did not significantly change in DTP cells when compared to parental cells (**Figure 4.12a**). On the other hand, RK11 persisters showed a 1.5-fold increase in the diacetylated peptide K9(Ac)K14(Ac) abundance ($p < 0.05$). On average, while not deemed statistically significant, RK11 persisters exhibited a 2.0-fold increase in K9(Me2)K14(Ac) and a 2.5-fold increase in K9(Me3)K14(Ac) compared to parentals (**Figure 4.12b**).

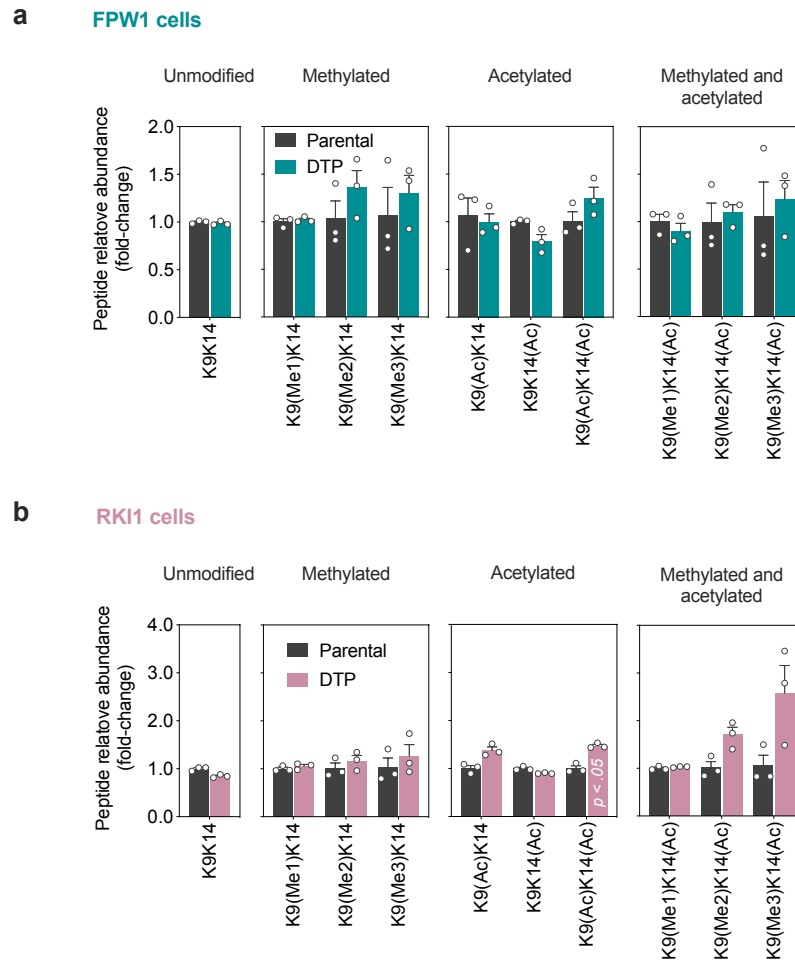


Figure 4.12 Changes in histone H3K9K14 modifications in DTPs.

Fold-change (anti-Log₂) in peptide abundance within the H3(9-17) TKQTAR peptide family in (a) FPW1 and (b) RK11 cells upon treatment with CMPD1 (25 μM) for 14 days. Data are mean ± SEM from three independent experiments. Welch's *t*-test was performed between DTP and parentals.

The H3(18-26) KQLATKAAR family consisted of 6 peptidofoms containing lysine K18 and K23:

K18K23	K18K23(Me1)	K18K23(Ac)
K18(Me1)K23	K18(Ac)K23	K18(Ac)K23(Ac)

Mono-methylation on K18 and K23 in human cells has only been reported in a few studies.^{329, 330} In our hands, K18(Me1)K23 and K18K23(Me1) were detected with high confidence at MS1 and MS2 levels, albeit at relatively low intensities. Nonetheless, no significant changes in the abundance of these peptides were detected in FPW1 (Figure 4.13a) or RK11 (Figure 4.13b) persister cells relative to their parental counterparts.

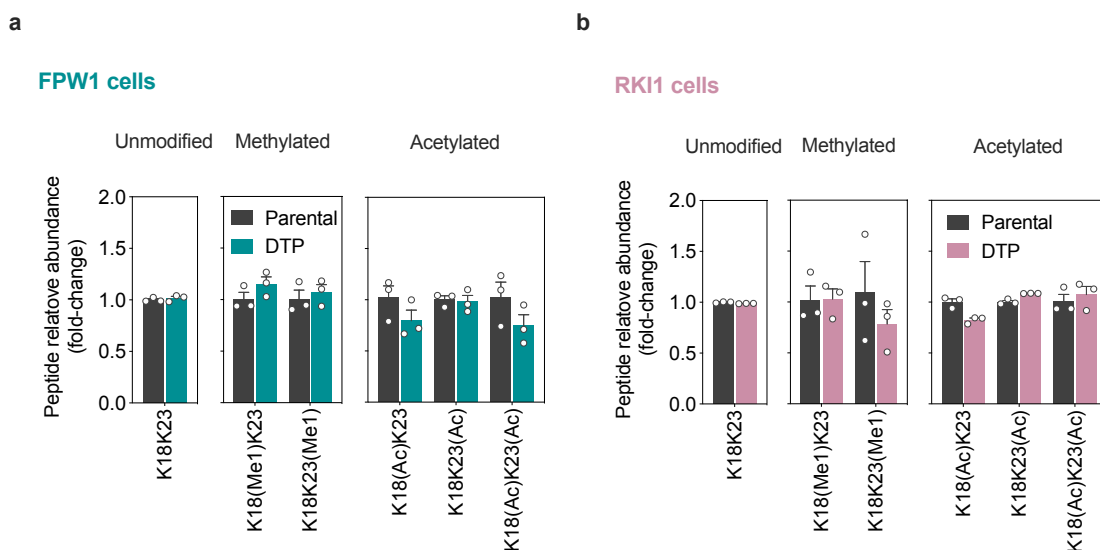


Figure 4.13 Changes in histone H3K18K23 modifications in DTPs.

Fold-change (anti-Log₂) in peptide abundance within the *H3(18-26) KQLATKAAR* peptide family in (a) FPW1 and (b) RK11 cells upon treatment with CMPD1 (25 μ M) for 14 days. Data are mean \pm SEM from three independent experiments. Welch's *t*-test was performed between DTP and parentals.

The *H3.1/3.2(27-40) KSAPATGGVKKPHR* peptide family *H3.1/3.2(27-40) KSAPATGGVKKPHR* peptide family consisted of 18 peptidofoms containing lysine K27 and K36:

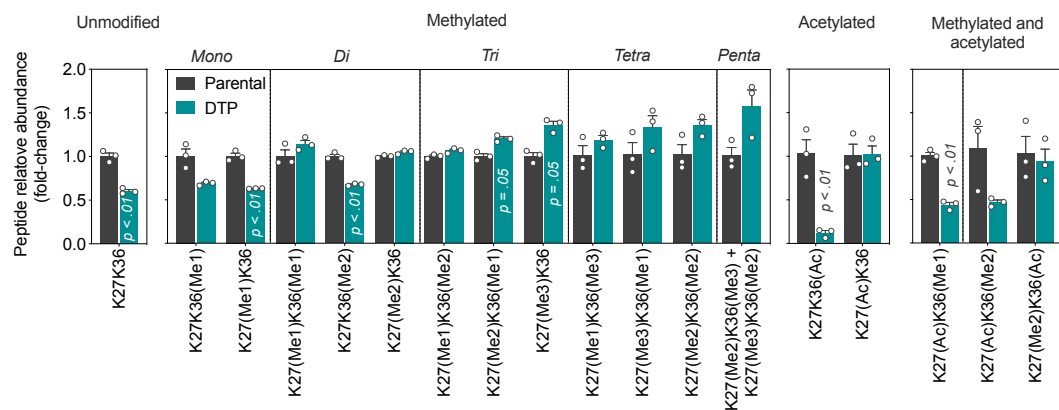
K27K36	K27(Me1)K36(Me2)	K27(Me2)K36(Me2)
K27K36(Me1)	K27(Me2)K36(Me1)	K27K36(Ac)
K27(Me1)K36	K27(Me3)K36	K27(Ac)K36
K27(Me1)K36(Me1)	K27(Me3)K36(Me1)	K27(Ac)K36(Me1)
K27K36(Me2)	K27(Me1)K36(Me3)	K27(Ac)K36(Me2)
K27(Me2)K36	K27(Me3)K36(Me2)+ K27(Me2)K36(Me3)	K27(Me2)K36(Ac)

Peptides of this family are unique to the canonical histone H3.1/3.2. The penta-methylated peptides K27(Me2)K36(Me3) and K27(Me3)K36(Me2) were co-eluting and isobaric (same retention time and *m/z*). However, these could not be parsed based on MS2 spectra because, while they do possess unique *y*⁺ or *b*⁺ ions that distinguish them from one another, they also co-elute with K27(Me2)K36(Me2) and K27(Me3)K36(Me3). Therefore, the peak identified constitutes the sum of both peptides and hence, they were analysed as one unit.

This peptide family exhibited the most significant changes in DTPs relative to parentals in both cell lines. In FPW1 cells (Figure 4.14a), the unmodified peptide K27K36 and mono-methylated peptide K27(Me1)K36 decreased to 0.6-fold (both *p* < 0.01) in DTPs relative to parentals. The levels of mono-methylated peptide K27K36(Me1) also

decreased to 0.6-fold but the difference did not reach significance. K27K36(Me2) levels decreases to 0.7-fold ($p < 0.01$). Furthermore, DTPs showed an increased abundance of tri-, tetra- and penta-methylated peptides relative to parentals, although the differences were not significant. By contrast, the abundance of three out of five acetylated peptides decreased in DTPs. K27K36(Ac) levels decreased to 0.2-fold ($p < 0.01$), while K27(Ac)K36 did not change relative to parental cells; the abundance of K27(Ac)K36(Me1) ($p < 0.01$) and K27(Ac)K36(Me2) decreased to 0.4-fold relative to parental cells.

a FPW1 cells



b RK11 cells

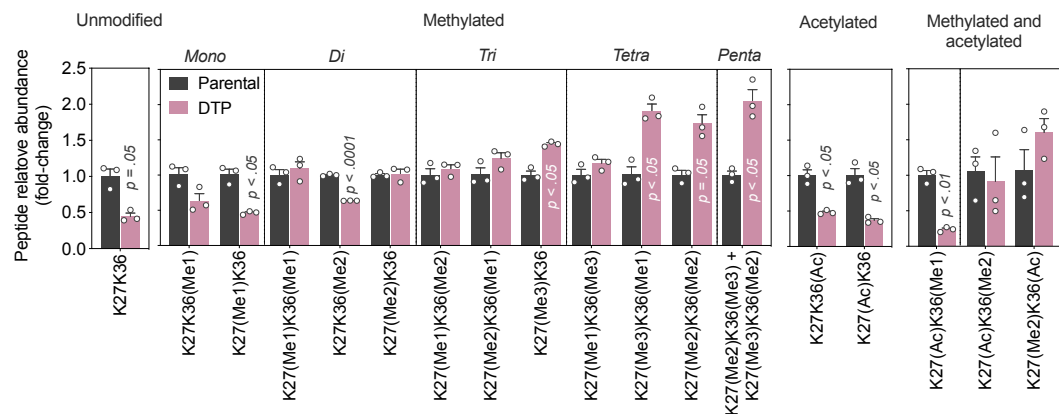


Figure 4.14 Changes in histone H3.1/3.2K27K36 modifications in DTPs.

Fold-change (anti-Log₂) in peptide abundance within the H3.1/3.2(27-40) KSAPATGGVKKPHR peptide family in (a) FPW1 and (b) RK11 cells upon treatment with CMPD1 (25 μ M) for 14 days. Data are mean \pm SEM from three independent experiments. Welch's *t*-test was performed between DTP and parentals.

Similar trends were observed in RK11 persister cells (Figure 4.14b). The abundance of the unmodified K27K36 ($p = 0.05$), K27(Me1)K36 ($p < 0.05$), K27K36(Me2) ($p < 0.001$) all decreased to 0.5- to 0.6-fold in DTPs relative to parentals. By contrast, abundances of tri-, tetra- and penta-methylated peptides increased in DTPs, with tri-methylated K27(Me3)K36, tetra-methylated K27(Me3)K36(Me1) and penta-methylated

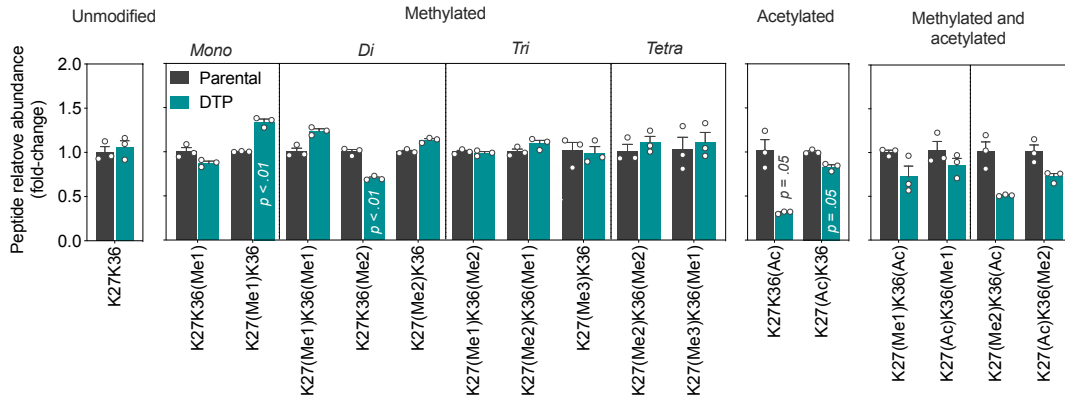
K27(Me2)K36(Me3) + K27(Me3)K36(Me2) (all $p < 0.05$) increasing between 1.2- to 1.7-fold. The abundance of K27K36(Ac), K27(Ac)K36 (both $p < 0.05$) and K27(Ac)K36(Me1) ($p < 0.01$) decreased to 0.3- to 0.5-fold in DTPs when compared to parentals. Together, these data indicate that H3K27 and K36 tri-methylation increase, whereas H3K27 and K36 acetylation decreases in CMPD1-tolerant cells.

The H3.3(27-40) KSAPSTGGVKKPHR peptide family, which contains lysine residues K27 and K36, consisted of 17 peptides containing lysine K27 and K36:

K27K36	K27(Me1)K36(Me2)	K27(Ac)K36
K27K36(Me1)	K27(Me2)K36(Me1)	K27(Ac)K36(Me1)
K27(Me1)K36	K27(Me3)K36	K27(Me1)K36(Ac)
K27(Me1)K36(Me1)	K27(Me3)K36(Me1)	K27(Ac)K36(Me2)
K27K36(Me2)	K27(Me2)K36(Me2)	K27(Me2)K36(Ac)
K27(Me2)K36	K27K36(Ac)	

The changes in modifications of H3.3 peptides in DTPs were not as significant as those for H3.1/3.2 peptides. In FPW1 cells, K27(Me1)K36 abundance increased to 1.4 fold ($p < 0.01$) while K27K36(Me2) abundance decreased to 0.6 fold ($p < 0.01$) in DTPs relative to parentals. Changes in other methylated peptides were negligible (**Figure 4.15a**). On the other hand, the abundance of all acetylated H3.3 peptides decreased in DTPs relative to parentals, but the changes did not reach significance. Similar trends were observed in RK11 cells, although none of the changes reached statistical significance. The abundances of the di-methylated peptide K27(Me1)K36(Me1) and the tetra-methylated peptides K27(Me2)K36(Me2) and K27(Me3)K36(Me1) increased to 1.5-fold in DTPs when compared to parentals. The abundances of five out of six acetylated peptides decreased in DTPs compared to parental, with K27K36(Me2) exhibiting the largest decrease to 0.2-fold (**Figure 4.15b**). Interestingly, not all the same modifications were detected in the H3.1/3.2 and H3.3 peptide families, with the tetra-methylated peptide K27(Me1)K36(Me3) and the penta-methylated peptides K27(Me2)K36(Me3) + K27(Me3)K36(Me2) only being detected in H3.1/3.2 and K27(Me1)K36(Ac) only in H3.3.

a FPW1 cells



b RK11 cells

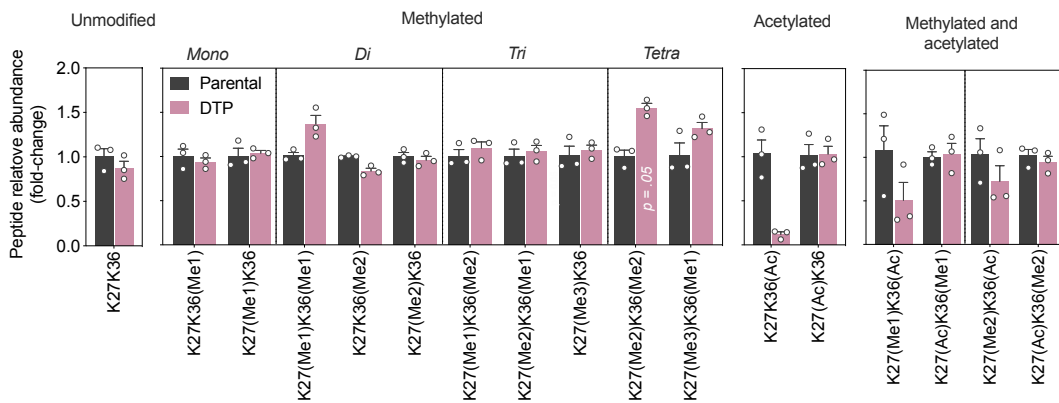


Figure 4.15 Changes in histone H3.3K27K36 modifications in DTPs.

Fold-change (anti-Log₂) in peptide abundance within the H3.3(27-40) KSAPSTGGVKKPHR peptide family in (a) FPW1 and (b) RK11 cells upon treatment with CMPD1 (25 μM) for 14 days. Data are mean ± SEM from three independent experiments. Welch's *t*-test was performed between DTP and parentals.

The H3(73-83) EIAQDFKTDLR peptide family contained three peptides containing K79:

K79

K79(Me1)

K79(Me2)

CMPD1-tolerant cells in the FPW1 (Figure 4.16a) and RK11 (Figure 4.16b) cell lines did not exhibit any significant changes in lysine K79 methylation when compared to treatment-naïve parental cells.

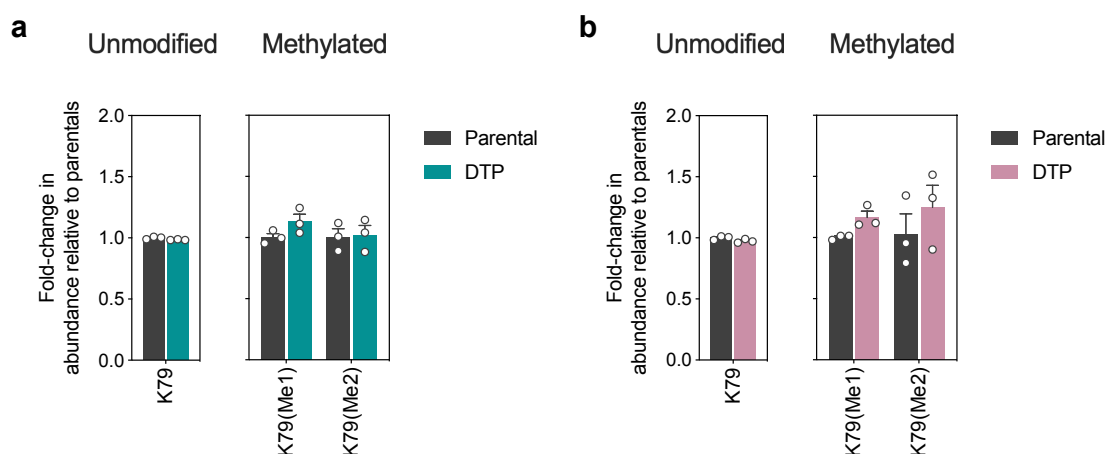


Figure 4.16 Changes in histone H3K79 modifications in DTPs.

Fold-change (anti-Log₂) in peptide abundance within the *H3(73-83) EIAQDFKTDLR* peptide family in (a) FPW1 and (b) RK11 cells upon treatment with CMPD1 (25 μM) for 14 days. Data are mean ± SEM from three independent experiments. Welch's *t*-test was performed between DTP and parentals.

In summary, the changes in deposition and post-translational modifications of histone H3 variants in CMPD1-tolerant cells relative to treatment-naïve parental cells imply an overall repressive state. Our data indicated that histone H3.3 deposition, a mark of epigenetic reprogramming, increases in drug-tolerant cells. There were site-specific changes unique to each cell line. For example, a decrease in the gene-activating K4(Me3) in CMPD1-tolerant RK11 cells, but not FPW1 cells, was observed. At histone H3.1/3.2, drug-tolerant subpopulations exhibited a decrease in the gene-activating K27(Ac) and K36(Ac) and an increase in gene-repressing K27(Me3). Unexpectedly, an increase in the gene-activating H3K36(Me3) was also observed. In particular, the abundance of peptides that expressed methylation of both K27 and K36 increased in drug-tolerant persisters. As for histone H3.3, gene-activating acetylation of K36 decreased considerably in drug-tolerant cells relative to parentals (Table 4.2).

Table 4.2 Summary of SWATH-MS results.

(Me1: mono-methylation; Me2: di-methylation; Me3: tri-methylation; Ac: Acetylation.)

	FPW1 drug-tolerant persisters	RK11 drug-tolerant persisters
H3.1/3.2 to H3.3 ratio	Decreased	Decreased
K4	No change	Decreased in Me3
K9K14	No change	Increased Me2/Me3 at K9 Increased Ac at K14
K18K23	No change	No change
H3.1/3.2 K27K36	Increased Me2/Me3 at K27 and K36 Decreased Ac at K27 and K36	Increased Me2/Me3 at K27 and K36 Decreased Ac at K27 and K36
H3.3 K27K36	Decreased Ac at K36	Decreased Ac at K36
K79	No change	No change

4. 2. 5. Confirmation of MS data by immunoblotting

To support the results obtained with SWATH-MS (Table 4.2), histones were extracted from treatment-naïve parental and CMPD1-tolerant FPW1 and RK11 cells using the Histone Extraction Kit (Abcam). Histone extracts were analysed by immunoblotting using antibodies against histone variants and specific histone methylation sites that were analysed by MS (Figure 4.17).

Expression levels of histone H3 variants (H3.1/3.2 and H3.3), as well as total histone H3 levels, were assessed in parental and CMPD1-derived DTPs. In FPW1 persister cells, canonical histone H3.1/3.2 levels increased by 1.6-fold compared to parentals. Histone H3.3 also increased by 2-fold in FPW1 persisters ($p < 0.01$). Consistent with the increase in H3 variants in FPW1 cells, DTPs exhibited a 2-fold increase in total histone H3 expression (all variants) compared to parentals (Figure 4.17a). On the other hand, CMPD1-tolerant RK11 cells only exhibited a 1.3-fold increase in H3.3 and a decrease to 0.8-fold in H3.1/3.2 compared to parentals. Total H3 levels did not change significantly in RK11 persisters. However, total histone H3 blots consistently showed a secondary band in DTP samples, skewing the total levels of total histone H3 between each parental-DTP pair. As such, H3 variants (and subsequently modifications) were not normalised to total H3. Instead, amido black B membrane staining was performed to monitor the protein loading.³³¹ Immunoblot DTP signals were normalised to the corresponding parental signals and expressed as fold-change on a Log₂ scale (Figure 4.17b).

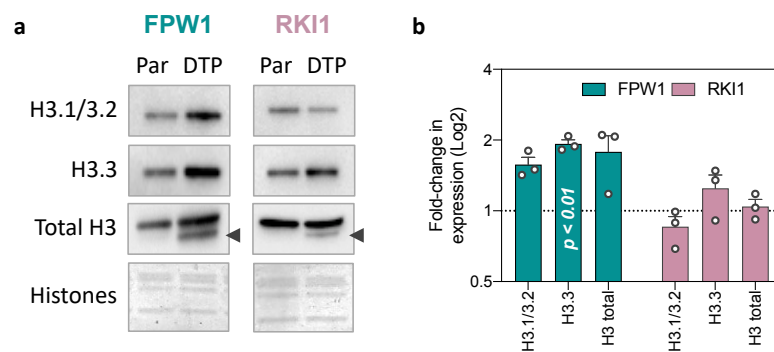


Figure 4.17 Immunoblot analysis of H3 variants in parental and CMPD1-tolerant persisters.

(a) Representative images of immunoblots comparing total H3 and H3 variant expression between paired parental (Par) and DTP samples (1 μ g of histone extract). Equal loading was monitored using amido black B membrane stain. Cleaved histone H3 bands are indicated by arrows. (b) Fold-change in protein expression (Log₂) in FPW1 and RK11 CMPD1-tolerant persisters relative to their parentals. Data are mean \pm SEM ($n = 3$). A paired t -test was performed to test for significance in protein expression between DTPs and parentals.

To confirm the changes in K9, K27 and K36 methylations in DTPs observed in SWATH-MS, mono-, di- and tri-methylations of these sites were assessed by immunoblotting. Immunoblots revealed that DTPs of both cell lines did not exhibit significant changes in H3K9 methylation (Figure 4.18a, b). Furthermore, in accordance with MS results, H3K27(Me3) increased by 3-fold in FPW1 persisters ($p \leq 0.001$) and by 2-fold in RKI1 persisters ($p < 0.05$) compared to their parental populations (Figure 4.18c, d). While methylation at K36 increased (1.6- to 3.2-fold) in DTPs from both cell lines, the results did not reach statistical significance (Figure 4.18e, f).

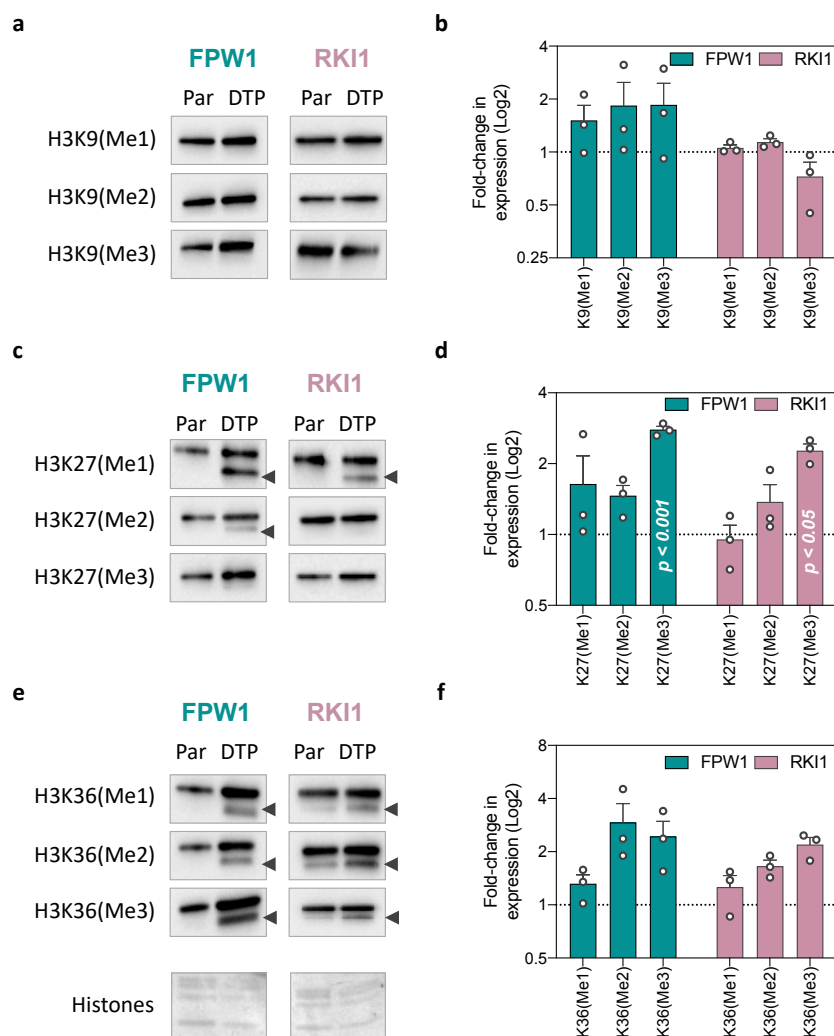


Figure 4.18 Immunoblot analysis of H3 methylation in parental and CMPD1-tolerant persisters.

Representative images and quantifications of immunoblots comparing total (a, b) H3K9, (c, d) H3K27 and (e, f) H3K36 methylation marks between paired parental (Par) and DTP samples (1 μ g of histone extract). Equal loading was monitored using amido black B membrane stain. Fold-change in PTM expression (Log₂) in FPW1 (green) and RKI1 (pink) CMPD1-tolerant persisters (DTPs) relative to their parental cells. Cleaved histone H3 bands are indicated by arrows. Data are mean \pm SEM ($n = 3$). A paired t -test was performed to test for significance in PTM expression between DTPs and parentals.

As indicated in **Figure 4.17** and **Figure 4.18**, we observed a secondary band in some histone H3 blots in DTP groups. This band was found in all total histone H3, H3K27(Me1), H3K36(Me1), H3K36(Me2) and H3K36(Me3) blots. The band was not observed in any H3K9 blots, however. The secondary histone H3 band has been previously identified as the cleaved histone H3 product at threonine residue T22.³³¹ To confirm that the secondary H3 band observed is the cleaved product of H3, expression levels of the H3 T22 cleaved product were assessed in parental and DTP cells using commercial antibodies (**Figure 4.19a**). As expected, the cleaved form of H3 exhibited an increase in DTPs, with almost a 3.7-fold increase in FPW1 cells and a 1.8-fold increase in RKI1 cells, on average.

Cleavage is a form of permanent removal of the gene-activating H3K4 methylation marks.³³¹ Hence, we assessed levels of H3K4(Me3), which exhibited a non-significant 2-fold increase in FPW1 persisters, which is inconsistent with the SWATH analysis. By contrast, in agreement with the SWATH data, H3K4(Me3) decreased in RKI1 persisters to 0.5-fold. However, the results did not reach significance. H3K4(Me3) blots lacked the secondary 'cleaved' H3 band, as expected (**Figure 4.19b**).

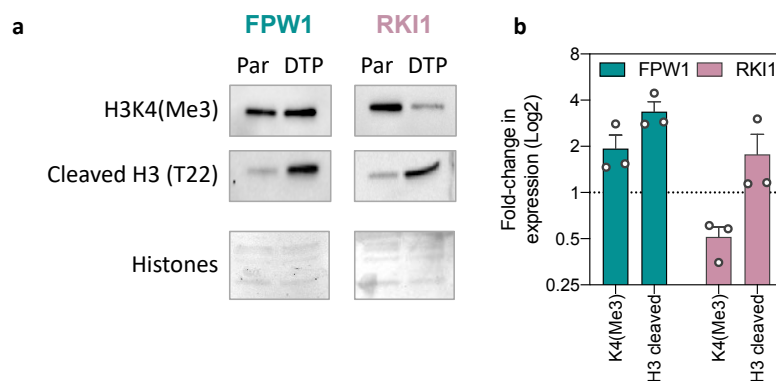


Figure 4.19 Immunoblot analysis of H3 cleavage in parental and CMPD1-tolerant persisters. (a) Representative images of immunoblots comparing H3K4(Me3) and cleaved H3 (T22) marks between paired parental (Par) and DTP samples (1 μ g of histone extract). Equal loading was monitored using amido black B membrane stain. (b) Fold-change in PTM expression (Log2) in FPW1 (green) and RKI1 (pink) CMPD1-tolerant persisters (DTPs) relative to their parental cells. Data are mean \pm SEM (n = 3). A paired *t*-test was performed to test for significance in protein or PTM expression between DTPs and parentals.

In summary, the immunoblotting data supported the mass spectrometry analysis. Methylation at histone H3 lysine residues K27 and K36, histone H3.3 deposition and histone H3 cleavage all increased in DTP relative to parental cells. In RKI1 persisters, methylation at K4 also decreased.

4. 3. Discussion

In the current study, we adapted a SWATH-MS workflow³²¹ that allows for a comprehensive and reproducible analysis of histone PTMs. We demonstrate for the first time that SWATH-MS is a suitable method for studying changes in histone modifications in drug-tolerant cells relative to their untreated counterparts. In our hands, SWATH-MS was superior to immunoblotting in terms of quantitation and the amount of information acquired. Software such as Spectronaut (Biognosys) contain automated algorithms that can analyse DIA datasets but have been reported to fail to identify some modified peptides or resolve co-eluting isobaric peptides using unique fragment b⁺ and y⁺ ions if any.³²¹ Therefore, we performed thorough manual peak identification using Skyline.

Most of the changes we observed to histone H3 variants and modifications in CMPD1-tolerant cells are consistent with the previously published changes in DTP models. The most significant increases in histone modifications in DTPs occurred on the canonical histone H3.1/3.2 variant peptides containing lysine residues K27 and K36, with both sites exhibiting an increase in di- and tri-methylation and a decrease in acetylation. Our findings are consistent with observations from targeted PRM-MS studies on erlotinib-tolerant lung cancer cells.³¹⁹ Other researchers performed RNA-seq analysis on parental and taxane-platin tolerant lung cancer cells to identify upregulated and downregulated genes in drug tolerance. RNA-seq was followed with ChIP-seq analysis at differentially expressed genes, revealing an increase in K27 methylation at downregulated genes (globally across the DTP cell population) and a decrease in K27 methylation at upregulated genes in DTPs.¹⁵⁴

SRM-MS assays performed on histones isolated from lung cancer cells, found a decrease in gene-repressing K27 methylation at H3.3 in cells tolerant to taxane-platin co-treatment compared to parental cells.¹⁵⁴ Our data is inconsistent with this finding as we observed no changes in H3.3 K27 and K36 methylations, but rather a decrease in K36 acetylation at this H3 variant in DTPs. Plausibly, the discrepancies in the H3.3 modifications observed are a result of the differences in cellular genotypes and phenotypes, and the treatment used to derive DTPs.

Nonetheless, we show for the first time that the levels of histone H3.3 increase in DTPs. The increase H3.3 deposition in CMPD1-tolerant persister cells is indicative of transcriptional reprogramming.^{331, 332} ChIP-seq analysis targeted at quiescence NOTCH-pathway genes in glioblastoma cells tolerant to dasatinib showed that H3K27 methylation increased and H3K27 acetylation decreased at NOTCH intracellular binding

domain (N1ICD)-bound elements, thereby increasing expression of quiescence proteins.¹⁰⁶ While it may seem paradoxical that methylation on gene-repressing (K27) and gene-activating (K36) sites are occurring at the same time, several studies have previously reported a bivalency of gene-activating and gene-repressing histone methylations. This bivalency results in chromatin being in a 'poised' state, where genes are expressed at low levels but are poised for rapid activation.³³³

As histone H3.3 deposition is associated with aggressive transcriptional programming that enables treatment evasion, metastasis and differentiation,^{332, 334} it is postulated that observed increase in H3.3 in DTPs is associated with the activation of survival genes in select chromatic regions. RNA sequencing (RNA-seq) analysis on parental and DTP cells is required to identify upregulated and downregulated genes. This can be followed with ChIP-seq to associate the genes with changes in histone PTMs.

While this study demonstrated that immunoblotting techniques for studying histone PTMs generally lack the ability to detect obscure combinatorial modifications, immunoblots revealed the proteolytic cleavage of histone H3 in DTPs. The histone H3 proteolytic cleavage is involved in oncogene-induced and replicative senescence. Moreover, the protease cathepsin L1 (CTSL1) preferentially cleaves the H3.3 variant over other H3 variants.³³¹ Ectopic expression of the cleaved product of H3.3 was sufficient to induce cell cycle senescence by facilitating transcriptional silencing of Rb/E2F target genes. Cleavage is a form of permanent removal of the H3K4 methylation marks, as it occurs at threonine residue T22.³³¹ This is consistent with the increase of H3.3 and the resultant increase of H3 cleavage observed in DTPs, particularly in FPW1 cells. Cleavage was much more marked in FPW1 persisters compared to RK11 persisters. Although cell senescence is generally thought to be irreversible, compared to reversible drug-induced cell dormancy,¹⁴³ this H3 cleavage mechanism may be employed in both cellular states.

We found that RK11 persister cells exhibited a significant decrease in the gene-activating H3K4 tri-methylation, which is consistent with previous studies.^{144, 318, 319} While FPW1 persister cells did not exhibit a change in H3K4 methylation, we suspect that the large increase in total histone H3 levels could have masked the decrease in abundance of this modification. Although not yet substantiated with experimental data in cancer, an increase in the overall expression levels of histone H3 is associated with an increase in genomic instability and an increase in the lifespan in yeast cells. The authors of these studies hypothesise that this genomic instability is similar to that seen in cancers.^{335, 336} In addition, pluripotent embryonic stem cells increase their histone content upon

differentiating into neuronal progenitors.³³⁷ Hence, the increase in histone content in FPW1 cells may contribute to their switch to a less proliferative and drug-tolerant state.

The data presented in this chapter suggest that the epigenetic mechanisms that enable cancer cells to tolerate highly cytotoxic treatments are cell- and drug-specific. For example, CMPD1 did not induce the same changes in FPW1 and RK11 persisters, even though they are both glioblastoma cell lines of the mesenchymal subtype. We note that RK11 possess point mutations in the chromatin-remodelling protein ATRX (D808G) and the histone lysine methyltransferase KMT3A (R472H), also known as SETD2, an enzyme that tri-methylates H3K36 (Table 2.1). Whether these mutations affect protein function is unknown. However, an inactive, mutated ATRX may explain the lower H3.3 deposition in nucleosomes of RK11 persisters. Inactivating mutations in KMT3A would not agree with our findings of increased K36 methylation. Therefore, this mutation either has no effect on, or causes a gain-of-function of, KMT3A. Further studies are needed to confirm these observations.

Taken together, these data indicate that drug-tolerant cells exhibit global increases in methylations and decreases in acetylation. These changes indicate a genetically repressive chromatin state. However, the deposition of histone H3.3 is expected to be found at upregulated genes that enable DTP survival, as we see an enrichment of this H3 variant in DTPs.

Several studies reported pharmacological approaches to target DTPs, including the inhibition of epigenetic enzymes. In particular, inhibition of proteins that add modifications (writers), recognise modifications (readers) and remove modifications (erasers) on histones. As histone H3 methylation levels increased in cells tolerant to microtubule-targeting agents, we questioned whether inhibition of enzymes is responsible for the changes in the histone code would eradicate these cells or prevent their regrowth. Hence, we next investigated the levels of histone methylation writers (KMTs) and erasers (KDMs) and the histone cleaving enzyme CTSL1 in parentals and DTPs.

Chapter 5

Pharmacological assessment of
histone-modifying enzymes as targets
in CMPD1-tolerant persisters

CHAPTER 5. PHARMACOLOGICAL ASSESSMENT OF HISTONE-MODIFYING ENZYMES AS TARGETS IN CMPD1-TOLERANT PERSISTERS

5. 1. Introduction

Having demonstrated that CMPD1-tolerant persisters exhibited global decreases in H3K4(Me3), H3K27(Ac) and H3K36(Ac) and increases in H3K27(Me3) and H3K36(Me3) (Figure 4.9 and Figure 4.10), we questioned if histone-modifying enzymes govern drug tolerance and whether their inhibition can eradicate CMPD1-tolerant cells.

Our results indicate an altered activity of the enzymes that add chemical groups to histones (writers) or enzymes that reverse post-translational modifications (erasers) between the treatment-naïve parental cells and DTP cells. In terms of histone lysine methylation, the writers are histone lysine methyltransferases (KMTs), and the erasers are histone lysine demethylases (KDMs). In terms of lysine acetylation, the writers are histone lysine acetyltransferases (KATs), and the erasers are histone deacetylases (HDACs). Indeed, several studies demonstrated the role of KMTs, KDMs and HDACs in drug tolerance and showed that their inhibition reduces the number of surviving DTPs. Therefore, subsequent sections discuss the role of histone writers and erasers in drug tolerance, with a focus on histone H3 methylation.³³⁸

5. 1. 1. Histone H3 lysine methyltransferases and demethylases

The KMT family of proteins is divided into 8 subfamilies (KMT1-8), with each subfamily possessing between 2 and 7 isoforms (Figure 5.1). KMT1-3 and KMT5-8 contain the Su(var)3-9, Enhancer of Zeste and Trithorax (SET) methyltransferase domain. The SET domain, comprising of ~110 amino acids, requires the methyl donor cofactor S-adenosyl-methionine (SAM) for its methyltransferase activity, with some SET-domain KMTs being functional only when complexed with other proteins.³³⁹ KMT4, on the other hand, contains a seven-beta-strand (7 β S) methyltransferase domain; 7 β S also requires SAM as a methyl donor for its methyltransferase activity. While KMTs possess the catalytic site, they often require multi-subunit complexes to optimise their activity and selectivity for histone residues.³³⁸

The KMT1 subfamily is comprised of six isoforms (KMT1A-F). The KMT1A-E isoforms specifically methylate H3K9 and H3K9(Me1), yielding mono- and di-methylated lysine K9, respectively. On the other hand, KMT1F methylates H3K9(Me2), yielding

trimethylated H3K9.³⁴⁰ In addition, KMT1C methylates unmodified and mono-methylated H3K56 residues during the G1 phase of the cell cycle.³⁴¹ As this subfamily demethylates the H3 lysine residues K9, K27 and K56, KMT1 enzymes are generally gene activating.

The KMT2 subfamily contains 8 isoforms (KMT2A-H). All members of this subfamily, with the exception of the inactive KMT2E isoform, methylate H3K4, thereby activating genes.³⁴² Interestingly, each isoform forms complexes with three core subunits: WD-repeat protein 5, retinoblastoma binding protein 5 and ASH2L, but further associate with other proteins that direct them spatiotemporally. KMT2A or KMT2B participate in mono-, di- and, to a much lower extent, tri-methylation of H3K4. By contrast, KMT2C or KMT2D mono-methylate H3K4 at distal regulatory enhancers, while KMT2F and KMT2G mainly tri-methylate H3K4 at transcription start sites.³⁴² While KMT2E lacks methyltransferase activity, it recognises H3K4 and maintains stemness by inhibiting H3.3 deposition and preventing differentiation.³³⁴ KMT2H possess similar activity to KMT2A/B, albeit its association with chromatin is independent of the multi-subunit complex; in addition, it also displays activity on H3K36(Me1) and H3K36(Me2) substrates.^{343, 344} Thus, since members of the KMT2 subfamily demethylate lysine residues K4 and K36, their activity is usually gene repressive.

The KMT3 is comprised of seven isoforms (KMT3A-G). KMT3A (also known as SETD2) is a crucial regulator of DNA mismatch repair by methylating H3K36(Me2). KMT3A is the only isoform that tri-methylates H3K36. KMT3B, KMT3C, KMT3F and KMT3G all methylate unmodified H3K36 and H3K36(Me1), yielding mono- and di-methylated residues. However, KMT3D mono-, di- and tri-methylates H3K4, whereas KMT3E only di- and tri-methylates H3K4.³⁴⁵

The KMT4 subfamily consists of a unique isoform and is responsible for mono-, di- and tri-methylation of H3K79, which plays a crucial role in transcriptional and cell cycle regulations.³⁴⁶ Unlike other KMTs, which act on histone H3, the KMT5 subfamily (KMT5A-C) methylate histone H4 on lysine residue K20.³⁴⁷

The KMT6 subfamily contains two members: KMT6A (also known as EZH2) and KMT6B (also known as EZH1). Both isoforms can mono-, di- and tri-methylate H3K27, thereby inducing gene repression. KMT6A and KMT6B are not functionally redundant, as each plays a separate role in cell cycle progression by associating with Polycomb repressive 2 (PRC2) complexes, which are pivotal regulators of repressive gene states.³⁴⁸ The core of PRC2 consists of a zinc finger subunit (Suz12) and the embryonic ectoderm

development (EED) protein in addition to KMT6A/B; nonetheless, these core subunits can form secondary complexes that have distinct functions.³⁴⁹

The KMT7 subfamily contains one isoform that specifically monomethylates H3K4.³⁵⁰ The KMT8 subfamily comprises of 6 isoforms (KMT8A-F), which all act on H3K9. KMT8A and KMT8B mono-, di- and tri-methylate H3K9, while KMT8D, KMT8F and KMT8F putatively mono-methylate H3K9.³⁵¹ KMT8C putatively methylate H4K20, although further validation of this data is needed.³⁵²

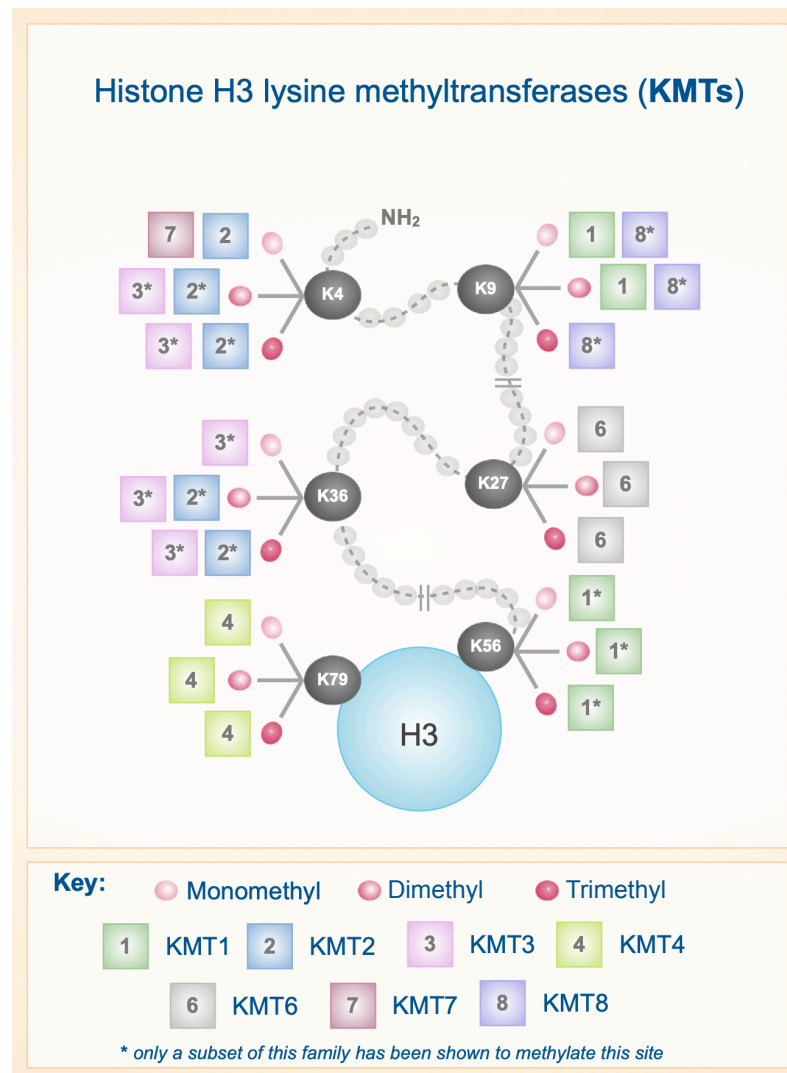


Figure 5.1 histone H3 lysine methyltransferases and their sites of action.
Histone lysine methyltransferase (KMT) protein subfamilies methylate histone H3.

The KDM family of proteins is divided into 8 subfamilies (KDM1-8), with most subfamilies possessing multiple isoforms (**Figure 5.2**).² Members of the KDM1 subfamily contain the flavin adenine dinucleotide (FAD)-dependent amine oxidase domain. This domain converts the ϵ -amine of the methylated lysine to an unstable imine that readily hydrolyses to formaldehyde. Imine formation requires a lone electron pair in the nitrogen

of methyl lysine, and hence, KDM1 cannot demethylate trimethylated lysine residues as they contain quaternary amines, which lack lone electron pairs.³⁵³ The KDM2-8 subfamilies contain the catalytic Jumonji C domain (JmjC). JmjC demethylase activity is dependent on Fe(II) ions, 2-oxoglutarate (2-OG) and oxygen and involves the hydroxylation of the methyl group to formaldehyde, resulting in demethylation. KDMs exhibit differential activity on different histone H3 lysine residues.²

Like KMTs, KDMs act selectively on specific histone lysine residues. The KDM1 subfamily consists of two isoforms, KDM1A/B. Both isoforms demethylate H3K4(Me1) and H3K4(Me2) substrates. Interestingly, when KDM1A forms complexes with androgen receptors, it switches its demethylase selectivity to H3K9(Me1) and H3K9(Me2) substrates.³⁵⁴ As H3K4 methylation is gene activating and H3K9 methylation is gene repressing, the KDM1 subfamily has varying effects on gene expression and is involved in regulating cell differentiation and self-renewal.²

The KDM2 subfamily (KDM2A/B) acts by demethylating the gene activating marks, H3K36(Me1) and H3K36(Me2).³⁵⁵ KDM2B is also reported to demethylate H3K4(Me3) and represses transcription of ribosomal RNA genes.³⁵⁶ KDM2B also demethylates H3K79(Me2) and H3K79(Me3) and induces transcriptional repression via sirtuin-1-mediated chromatin silencing.³⁵⁷ Methylations of histone H3 lysine residues K4, K36 and K79, are gene activating (**Figure 4.1d**), and so, the KDM2 subfamily has an overall gene repressing effect.

KDM3A and its two isoforms, KDM3B and KDM3C, all selectively demethylate H3K9(Me1) and H3K9(Me2).³⁵⁸ As H3K9 methylation is a prominent marker of heterochromatin and inactive genes (**Figure 4.1d**), the KDM3 subfamily is generally gene-activating. KDM3A has also been reported to induce gene transcription, independently of its histone demethylase activity, by interacting with the ATP-dependent SWI/SNF chromatin remodelling complex.³⁵⁹

The KDM4 subfamily is comprised of five isoforms (KDM4A-E). In addition to the JmjC domain, KDM4A, KDM4B and KDM4C also contain the plant homeodomain (PHD) and Tudor domains.³⁶⁰ By contrast, KDM4D and KDM4E are structurally divergent and lack the PHD and Tudor domains. While all five isoforms demethylate H3K9(Me2) and H3K9(Me3), only KDM4A-C also demethylate H3K36(Me2) and H3K36(Me3).^{2, 360} Paradoxically, while the KDM4 subfamily is involved with directing differentiation during development, they are also required for maintaining pluripotent stem cell states.³⁶⁰ In addition, KDM4A-C associate with other non-histone proteins, such as KMT1C, SWI/SNF

chromatin-remodelling complex, phospho-Rb, or HDAC1-3, to regulate gene expression independently of catalytic activity.³⁶¹⁻³⁶⁴

The KDM5 subfamily (KDM5A-D) selectively demethylates H3K4(Me2) and H3K4(Me3). All four isoforms share high sequence homology and contain the ARID domain in DNA-binding region and JmjC, JmjN and PHD domains in the histone-binding regions. Despite the high homology, KDM5 isoforms differ in their functions and binding to other non-histone proteins to regulate gene expression.³⁶⁵

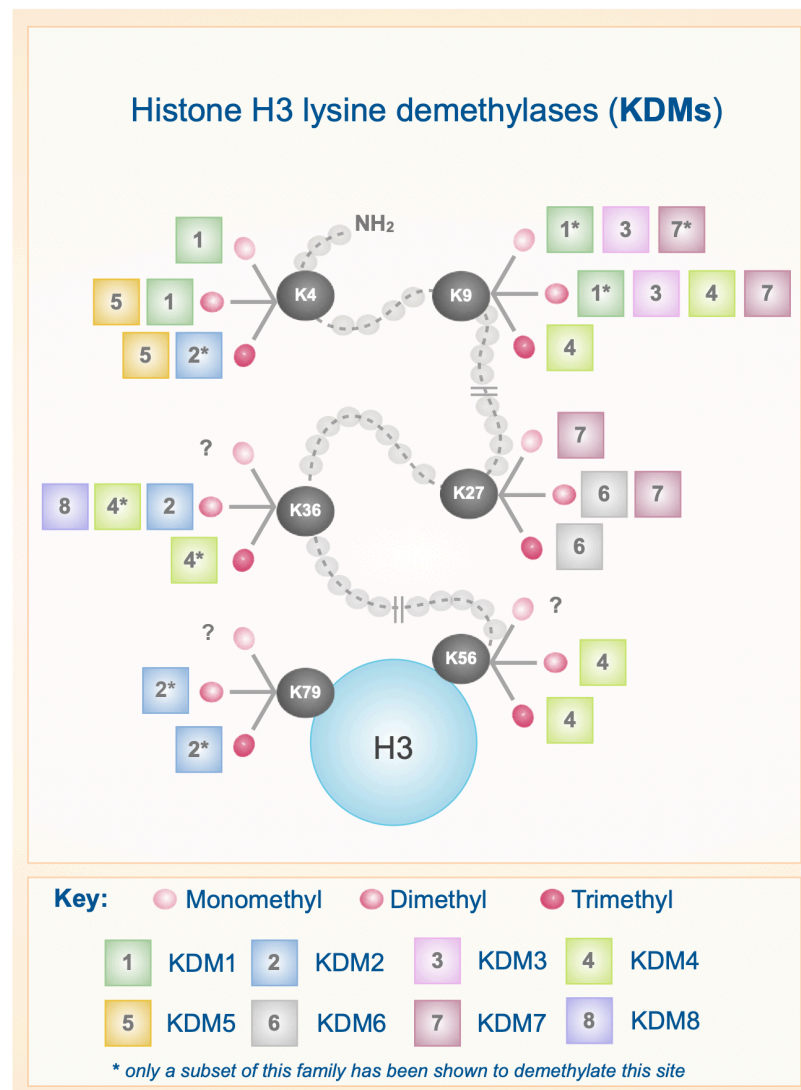


Figure 5.2 histone H3 lysine demethylases and their sites of actions.

Histone lysine demethylase (KDM) subfamilies, with distinct lysine demethylation sites on histone H3.

Similarly, the KDM6 subfamily (KDM6A-C) selectively demethylates H3K27(Me2) and H3K27(Me3), thereby leading to gene activation. KDM6A associates with KMT2C and KMT2D, which methylate H3K4, and is involved in regulating cell differentiation. Therefore, decreases in H3K27 methylation are often associated with increases in H3K4 methylation.³⁶⁶

The KDM7 subfamily (KDM7A-C) are all associated with transcriptional silencing during brain development and act specifically on mono- and di-methylated H3K9 and H3K27 residues.³⁶⁷ KDM8 is an endopeptidase that is recently reported to have putative H3K36(Me2) demethylase activity; however, further validation is needed to confirm its demethylase activity *in vivo*.²

5. 1. 2. Protein targets in drug-tolerant persister cells

In support of the role of epigenetics in cancer cell survival and relevance to our model of DTPs, the histone lysine demethylases KDM3,^{106, 154} KDM5,^{106, 144, 153, 318, 368} KDM6^{106, 154} and KDM7¹⁵⁴ are upregulated in several DTP models and associated with changes in histone H3 methylations (Table 5.1).

In melanoma, the increase in KDM5 in DTPs induced the demethylation of H3K4(Me3), resulting in slower cell-cycle progression and self-renewal (Figure 4.1d).^{153, 368} In dasatinib-tolerant glioblastoma cells, KMT6A expression decreased, and KDM6 expression increased, both of which increase H3K27 demethylation. The decrease in H3K27(Me3) results in a redistribution of repressive chromatin and a slow-cycling stem-like subpopulation of cells that express higher levels of NOTCH-signalling genes. Cells treated with the KDM5/6 inhibitor GSK-J4 and KDM6 CRISPR-knockout cells did not exhibit loss of methylation at H3K27 and were less effective at forming DTPs, suggesting a dependence on KDM6 for DTP survival.¹⁰⁶ In lung cancer, cells tolerant to paclitaxel in combination with carboplatin exhibited a global decrease in histone H3K27 methylation. However, H3K27 methylation was increased at transcription start sites of down-regulated pro-apoptotic genes, while H3K4 methylation was decreased.¹⁵⁴ Similarly, in paclitaxel-tolerant lung cancer cells, KMT6A was upregulated, leading to an increase in H3K27(Me3). Treatment with the KMT6 inhibitor UNC1999 resulted in a reduction in the number of paclitaxel-tolerant cells.³⁶⁹ Other studies report changes in histone deacetylases (HDACs) in drug tolerance, particularly leading to increases in H3K27(Ac).^{106, 144, 319} Additionally, carboplatin monotherapy in ovarian cancer cells caused DNA hypermethylation and inhibition of the DNA methyltransferase (DNMT) was sufficient to prevent tumour outgrowth *in vitro* and *in vivo*.³⁷⁰

Other studies reported the upregulation of metabolic enzymes that modulate oxidative phosphorylation and protect cells from reactive oxygen species or pro-survival kinases in DTPs. Therefore, therapeutic approaches to eliminate DTPs may include the inhibition of epigenetic enzymes that regulate gene expression, protective oxidative

enzymes or upregulated pro-survival kinases.¹⁴³ However, since we demonstrated changes in post-translational histone marks, we have focused on the epigenetic targeting of glioblastoma cells.

Table 5.1 Reported mechanisms of DTP survival in several cancers.

DTP: Drug-Tolerant Persisters; KMT: Histone lysine methyltransferase; KDM: Histone lysine demethylase; HDAC: histone deacetylase; DNMT: DNA methyltransferase; BRD4: bromodomain 4; ALDH: aldehyde dehydrogenase.

Drug	Cancer cell line	Epigenetic mechanism employed by DTPs	Phenotypic switch exhibited by DTPs	Intervention to suppress or eliminate DTPs	REF
Dasatinib	Glioblastoma	Increased KDM3, KDM5, KDM6 Decreased KMT6A Decreased H3K27 methylation Increased H3K27 acetylation	Slow-cycling stem cells expressing NOTCH quiescence signalling pathway proteins	KDM5/6 inhibition	106
Erlotinib	Lung	Increased KDM5 Decreased H3K4 methylation Decreased H3K14 acetylation	Increased stem cell marker CD133 Dependence on IGF-1R for survival	HDAC inhibition IGF-1R inhibition	144
	Lung	Increased KDM5 mRNA Decreased H3K4 methylation	Not investigated	KDM5 inhibition	318
	Lung	Increased KMT1C, KMT1E, KMT6B Decreased H3K4 methylation Increased H3K9, H3K27 methylation Decreased global H3K acetylation	Increased ALDH Activation of interferon response/antiviral defence genes (LINE-1)	HDAC inhibition	319
AZ628	Melanoma	Increased KDM5 mRNA Increased H3K4 methylation	Not investigated	KDM5 inhibition	318
	Colon	Not investigated	Activation of interferon response and antiviral defence genes	HDAC inhibition	319
Trametinib	Breast	Increased BRD4 Increased KDM5B Increased KMT6A	Compensatory MAPK and PI3K pathway kinase upregulation Increased differentiation-state heterogeneity	BRD4 and PI3K co-inhibition	371
Paclitaxel	Breast	Increased KMT6 Increased H3K27 methylation at transposable elements	Activation of interferon response/antiviral defence genes (LINE-1)	KMT6 inhibition	369
Paclitaxel-carboplatin	Lung	Increased KDM3B, KDM5B Decreased global H3K27 methylation	Decreased expression of apoptotic genes	KDM5/6 inhibition	154
Carboplatin	Ovarian	DNA hypermethylation	Enrichment for cells expressing ALDH ^{HI} and stemness genes	DNMT inhibition	370
Cisplatin	Colorectal	Not investigated	Increased stem cell marker CD133 and CD44 Dependence on IGF-1R for survival	HDAC inhibition	144
	Lung	Not investigated	Increased stem cell marker CD133 and CD44 Dependence on IGF-1R for survival	HDAC inhibition IGF-1R inhibition	144
	Melanoma	Increased KDM5B	Increased oxidative phosphorylation proteins	Mitochondrial ATP-synthase inhibition	153

HDAC inhibitors are comprehensively characterised in glioblastoma cell models and are known to increase the expression of the tumour suppressor p21, resulting in cell cycle arrest.³⁷² Preclinical trials showed that the pan-HDAC inhibitor SAHA, also known

as vorinostat, significantly increase glioblastoma stem cell apoptosis in combination with bortezomib.³⁷³ However, Phase II trials showed a lack of efficacy of this combination in primary glioblastoma patients.³⁷⁴ As HDAC inhibitors have been repeatedly trialled in clinical, we focussed on changes in histone methylation writers (KMTs) and erasers (KDMs) as these proteins have the potential to be novel druggable targets.

5. 2. Results

5. 2. 1. Gene expression of histone lysine modifiers in drug-tolerant persisters

To assess whether KMT transcript levels change in DTPs, we performed qPCR analysis on treatment-naïve parental cells and CMPD1-derived DTP cells. Transcript levels of 31 genes encoding the KMT family were normalised to four housekeeping genes (*GAPDH*, *ACTB1*, *rRNA S18* and *EEF1A*) to monitor for consistent changes in expression. Fold-change of transcript levels from parental cells (set as 1) to DTP was calculated and expressed on a log₂ scale. Paired *t*-tests were performed between transcript levels in parental and DTP cells for each primer.

In FPW1 persister cells (Figure 5.3), normalisation to *EEF1A* yielded conflicting results with the other housekeeping genes. The apparent decrease of most KMT transcript levels when normalised to *EEF1A* suggests that tolerance to CMPD1 increases *EEF1A* expression in FPW1 cells. Therefore, *EEF1A* normalisation was not further considered. When normalised to other three housekeeping genes, 22 KMT genes showed no change in expression, and 9 KMT genes were overexpressed in DTPs relative to parentals. *KMT3E*, *KMT7*, *KMT8B*, *KMT8C* and *KMT8E* transcript levels exhibited 4- to 5-fold increases, while *KMT2A*, *KMT6A*, *KMT8D* and *KMT8F* transcript levels exhibited 2- to 3-fold increases in DTPs compared to parentals.

In RK11 cells (Figure 5.4), normalisation to all housekeeping genes yielded consistent results. 17 genes showed no change expression in DTPs relative to parentals. 11 genes were overexpressed, with *KMT3E*, *KMT7*, *KMT8B*, *KMT8C*, *KMT8D* and *KMT8E* transcript levels increasing by 3- to 5-fold, while *KMT1F*, *KMT2A*, *KMT6A*, *KMT8A*, and *KMT8F* transcript levels increased by 2- to 5-fold in DTPs compared to parentals. By contrast, *KMT1A* and *KMT6B* decreased by 2-fold while *KMT3D* transcript levels decreased by 4-fold in DTPs relative to parentals.

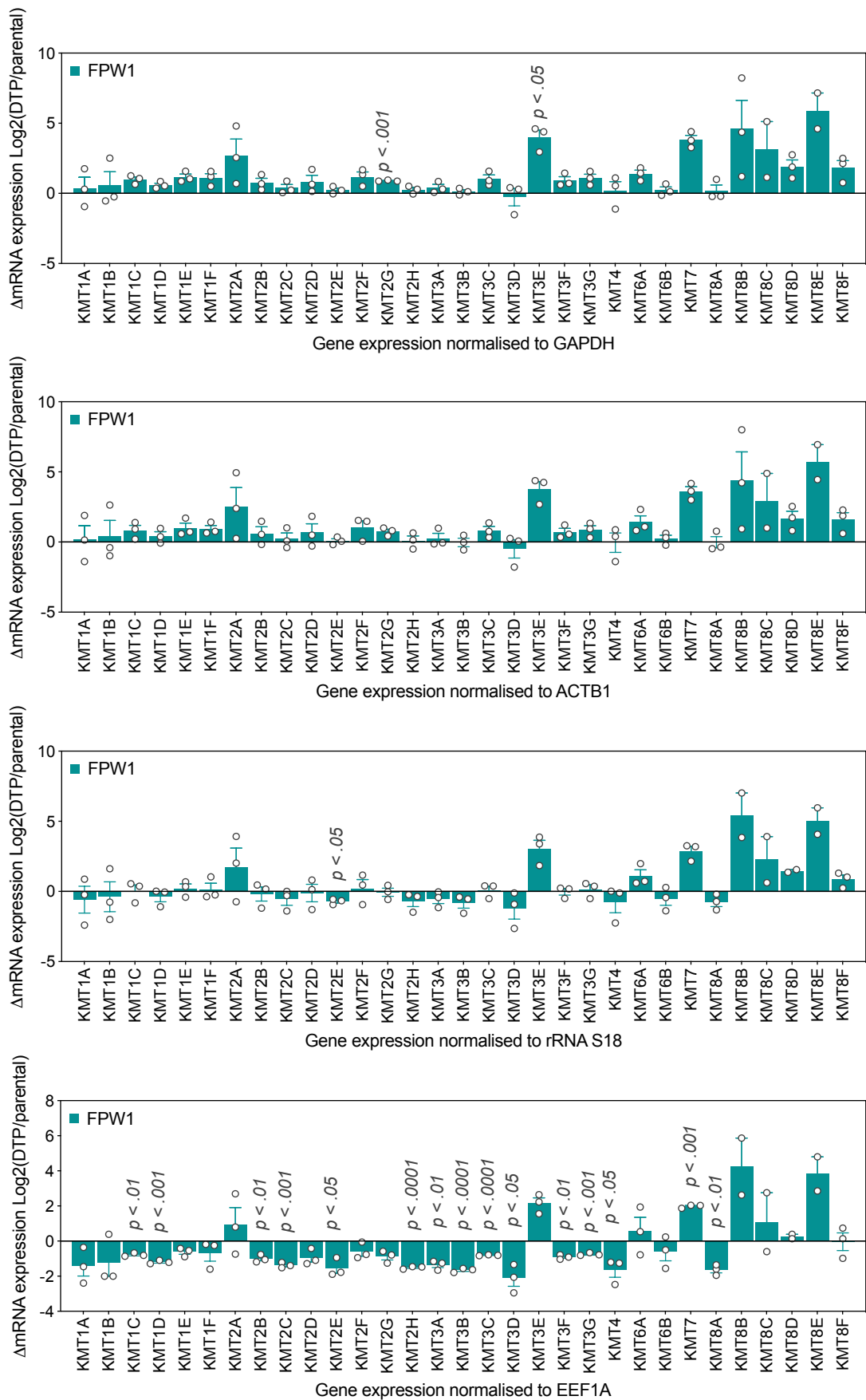


Figure 5.3 Transcript levels of histone lysine methyltransferases in CMPD1-tolerant FPW1 cells. KMT gene expression levels in parental and CMPD1-tolerant FPW1 cells (DTP) normalised to GAPDH, ACTB1, rRNA S18 or EEF1A. Expression levels in DTPs are expressed as fold-change (Log_2) relative to parental. Data are mean \pm SEM (n= 2-3).

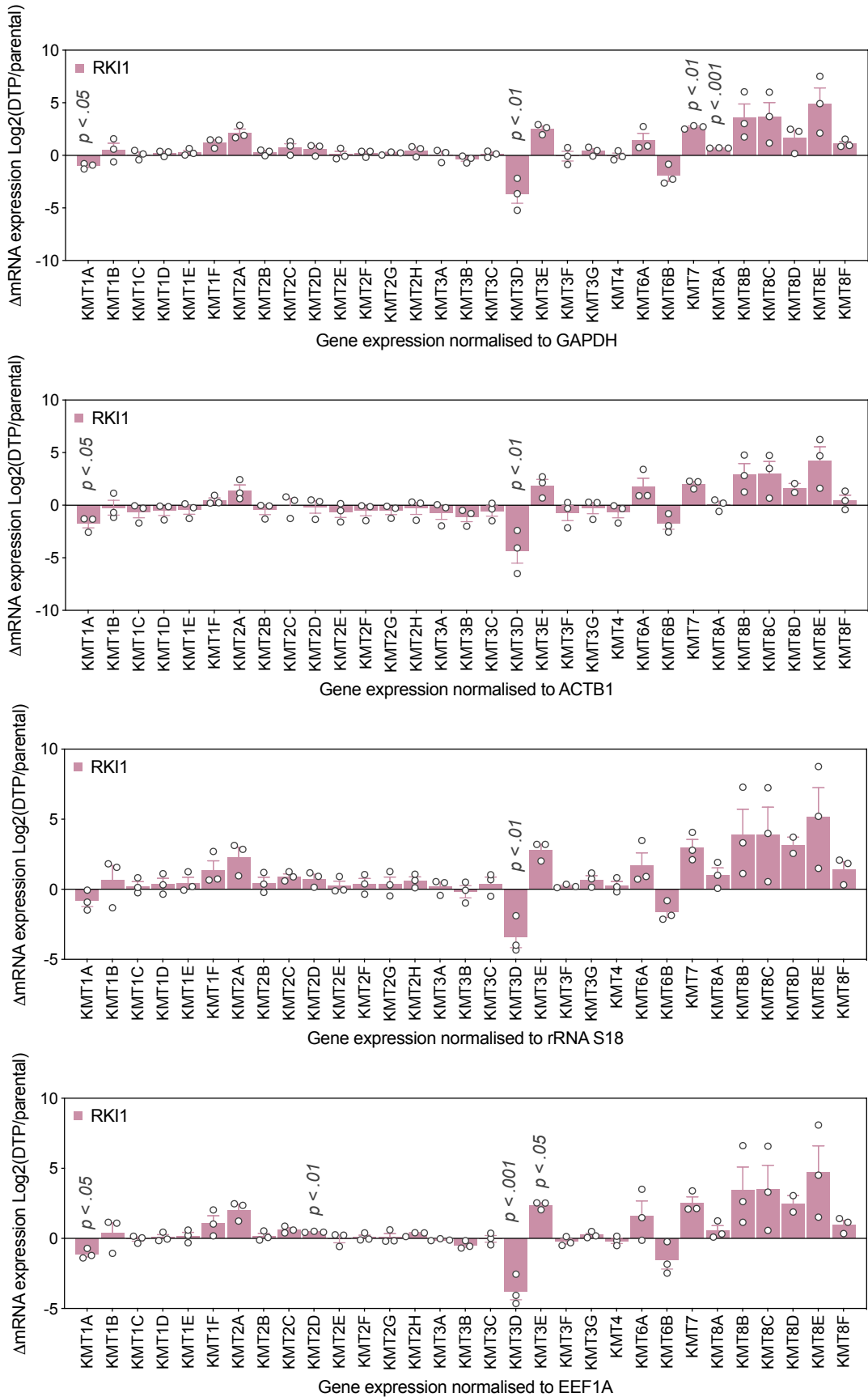


Figure 5.4 Transcript levels of histone lysine methyltransferases in CMPD1-tolerant RKI1 cells.

KMT gene expression levels in parental and CMPD1-tolerant RKI1 cells (DTP) normalised to GAPDH, ACTB1, rRNA S18 or EEF1A. Expression levels in DTPs are expressed as fold-change (Log_2) relative to parental. Data are mean \pm SEM (n= 2-3).

Next, transcript levels of 22 genes encoding the KDM family were analysed and normalised to the four housekeeping genes (*GAPDH*, *ACTB1*, *rRNA S18* and *EEF1A*). In FPW1 persister cells (**Figure 5.5**), *KDM4D* and *KDM4E* transcript levels increased by 5- and 10-fold, respectively, while transcript levels of the remaining 20 KDMs remained unchanged relative to parental cells. In RKI1 cells (**Figure 5.6**), *KDM4D* and *KDM4E* transcript levels increased by 5- and 10-fold relative to parentals, respectively. Moreover, *KDM3C* and *KDM4D* transcript levels increased by 6- to 8-fold, albeit with considerable variability.

As *KDM4E* exhibited the largest increases in DTPs derived from both cell lines, we validated expression levels of *KDM4D* and *KDM4E* transcripts in FPW1 and RKI1 parental and persister cells using orthogonal primers (**Figure 5.7a**). The orthogonal *KDM4D* primer showed no difference in expression between parentals and DTPs, while two orthogonal *KDM4E* primers confirmed the significant increase in *KDM4E* levels in DTPs compared to parentals. Furthermore, we performed immunoblot analysis on whole-cell lysates obtained from parental and CMPD1-tolerant FPW1 cells (**Figure 5.7b**). On a protein level, the expression of *KDM4D* decreased to 0.4-fold ($p < 0.001$), while the expression of *KDM4E* increased to 2.3-fold in DTPs relative to parental cells (**Figure 5.7c**).

In summary, expression levels of KMTs and KDMs vary considerably in CMPD1-tolerant cells compared to treatment-naïve cells. Overall, we observed more increases in *KMT* transcripts relative to *KDM* transcripts, which may explain the overall increase in histone H3 methylation in DTPs as per SWATH-MS (**Figure 4.9**, **Figure 4.10**). Furthermore, orthogonal *KDM4D* primers demonstrated either an increase or no change in expression levels, whereas immunoblots revealed that *KDM4D* protein decreases DTPs relative to parentals. On the other hand, three orthogonal *KDM4E* primers yielded consistent increases in DTPs relative to parentals, and the results agreed with the immunoblot analysis of *KDM4E* levels.

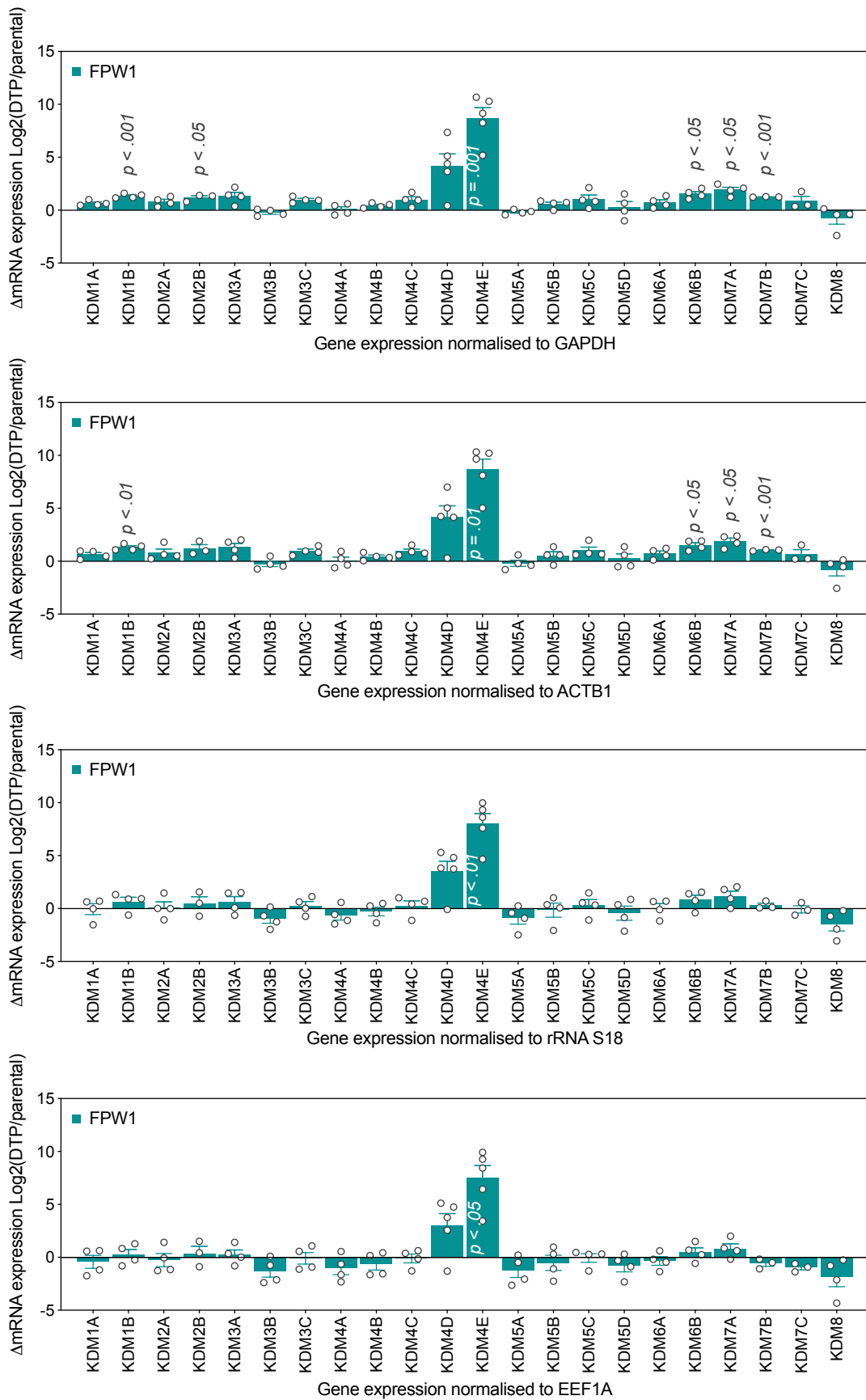


Figure 5.5 Transcript levels of histone lysine demethylases in CMPD1-tolerant FPW1 cells.

KDM gene expression levels in parental and CMPD1-tolerant FPW1 cells (DTP) normalised to GAPDH, ACTB1, rRNA S18 or EEF1A. Expression levels in DTPs are expressed as fold-change (Log_2) relative to parental. Data are mean \pm SEM (n= 3-5).

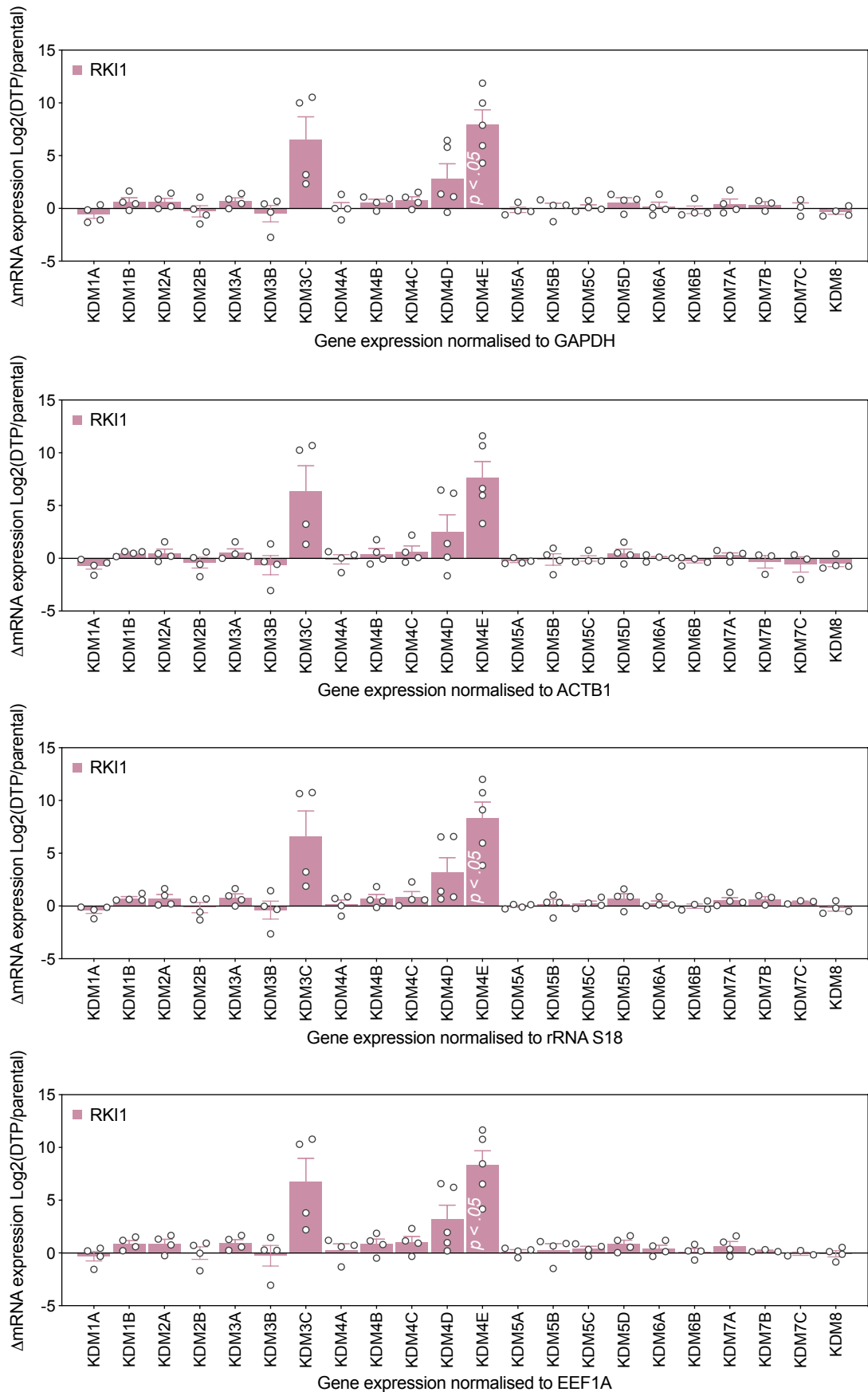


Figure 5.6 Transcript levels of histone lysine demethylases in CMPD1-tolerant RKI1 cells.

KDM gene expression levels in parental and CMPD1-tolerant RKI1 cells (DTP) normalized to GAPDH, ACTB1, rRNA S18 or EEF1A. Expression levels in DTPs are expressed as fold-change (Log₂) relative to parental. Data are mean \pm SEM (n= 3-5).

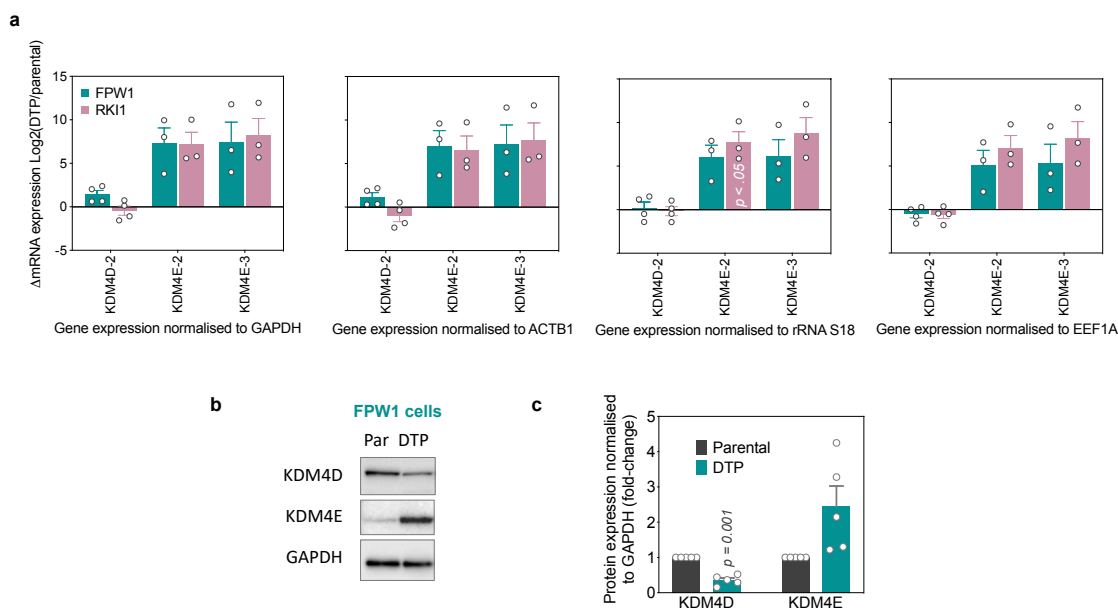


Figure 5.7 Confirmation of KDM4D and KDM4E transcript changes in drug-tolerant cells.

(a) KDM gene expression levels in parental and CMPD1-tolerant cells (DTP) normalised to GAPDH, ACTB1, rRNA S18 or EEF1A. Expression levels in DTPs are expressed as fold-change (Log₂) relative to parental. Data are mean \pm SEM (n= 3-4). (b) Representative immunoblots and (c) quantification of KDM4D and KDM4E in FPW1 parental and DTP cells. Data are mean \pm SEM (n= 5).

5. 2. 2. Screening epigenetic probes against parental and persister cells

To further investigate the role of epigenetic enzymes, we screened a library of epigenetic probes[†] obtained from the Structural Genomics Consortium (SGC, University of Oxford) and selective KDM5 and KDM6 inhibitors from our collaborator Prof. Paul Brennan (University of Oxford), against parental and DTP cells. DTP cells were derived from 14-day treatment with CMPD1 or tivantinib (Figure 5.8a). The library contained inhibitors targeting a variety of epigenetic enzymes including KMTs, KDMs, peptidyl arginine deiminase (PAD4) and protein arginine methyltransferases (PRMTs), chromodomain (histone methyl reader) proteins, histone lysine acetyltransferase (KAT) and bromodomain (histone acetyl readers) proteins. Cells were treated at IC₉₀ concentrations for 5 days to achieve significant target engagement as recommended by the SGC. Cell viability was measured using CellTitre Blue and expressed as a percentage (%) of untreated controls (Figure 5.8b).

Out of the 38 inhibitors tested, two KMT and three KDM inhibitors reduced the viability of parental or persister cells in both cell lines. In the FPW1 cell line, both CMPD1- and tivantinib-tolerant persister cells were sensitive to UNC1999, a dual KMT6A/KMT6B

[†] An epigenetic probe is a well-characterised inhibitor of a specific epigenetic enzyme and can be used to study the biological role of that enzyme at certain concentrations.

inhibitor, displaying 52.4% and 54.4% cell viability relative to untreated controls, respectively. By contrast, parental FPW1 cells were not as sensitive to UNC1999, with 80% cell viability relative to untreated controls. In the RK11 cell line, CMPD1-tolerant persisters were moderately sensitive to GSK343, a selective KMT6A inhibitor (62.1% viability), whereas tivantinib-tolerant persisters were less sensitive (71.8% viability). Parental cells were not affected (102.2% viability). RK11 cells were more sensitive to UNC1999 treatment than FPW1 cells. UNC1999 reduced the viability of both CMPD1- and tivantinib-tolerant persister cells to 42%, while also reducing the viability of parental cells to 73.2% compared to untreated controls.

QC6352, a KDM4 inhibitor, significantly reduced the viability of parental FPW1 cells to 19% but had a weak effect on FPW1 cells tolerant to CMPD1 (75.6% viability) and tivantinib (88.6% viability). Similarly, QC6352 reduced the viability of parental RK11 cells to 37.8% but had a weak effect on RK11 cells tolerant to CMPD1 (76.1% viability) and tivantinib (69% viability). The selective KDM6 inhibitor, KDOBA-67 α , decreased the viability of parental, CMPD1-tolerant and tivantinib-tolerant persister FPW1 cells to 32.5%, 42.5% and 47.1%, respectively, relative to untreated controls. Similarly, KDOBA-67 α diminished the viability of parental, CMPD1-tolerant and tivantinib-tolerant persister RK11 cells to 32.5%, 42.5% and 47.1%, respectively, relative to untreated controls. The dual KDM5/6 inhibitor, GSK-J4, reduced the viability of parental, CMPD1-tolerant and tivantinib-tolerant FPW1 cells to 44.5%, 37.6% and 61.8%, respectively. Similarly, GSK-J4 diminished the viability of parental, CMPD1-tolerant and tivantinib-tolerant RK11 cells to 41.5%, 37.2% and 67.0%, respectively.

In addition, the KAT2A/B inhibitor, L-Moses, and the BRD4 bromodomain inhibitor, JQ1, reduced the viability of parental FPW1 cells to 51.3% and 47.8%, respectively, but had little to no effect on DTP cell viability relative to controls. The PAD4 inhibitor, GSK484, decreased the viability of RK11 parental cells to 54% relative to untreated controls. In summary, parental glioblastoma cell lines were sensitive to the KDM4, KDM5 and KDM6 inhibitors, while DTPs were sensitive to KMT6, KDM5 and KDM6 inhibitors.

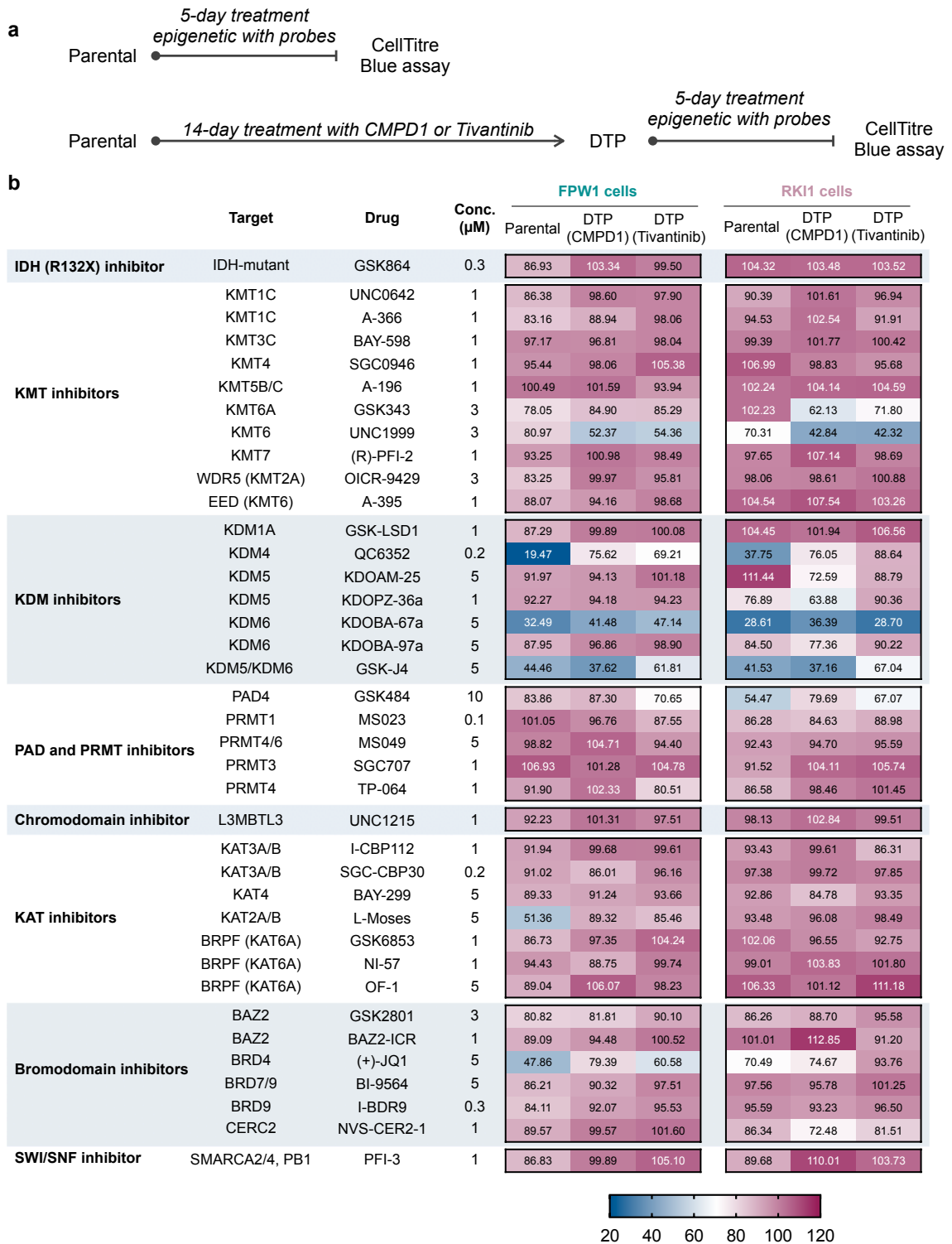


Figure 5.8 Effect of epigenetic probes on the viability of parental and drug-tolerant cells.

(a) Drug-tolerant cells were derived from treatment with CMPD1 or tivantinib (25 μM) for 14 days. Treatment-naïve parental cells, CMPD1-tolerant cells and tivantinib-tolerant cells, from both the FPW1 and RKI1 cell lines, were treated with epigenetic probes for 5 days and cell viability was measured at Day 5 using CellTitre Blue. (b) Heatmap displaying mean values of FPW1 and RKI1 cell viability relative to untreated controls (%) (n = 3). The SEM between biological repeats did not exceed 20% of the mean.

To establish the efficacy metrics of the KMT and KDM inhibitors that reduced viability of parental or DTP glioblastoma cells (Figure 5.8), 5-day concentration-response viability assays were performed on parental cells and CMPD1-tolerant cells, as per the GR method. GR viability curves and metrics for UNC1999 (KMT6 inhibitor), QC6352 (KDM4 inhibitor), GSK-J4 (KDM5/6 inhibitor) and KDOBA-67a (KDM6 inhibitor) are shown for FPW1 (Figure 5.9) and RK11 (Figure 5.10) cell lines. Unpaired *t*-tests were performed between corresponding GR metrics of each inhibitor in parental versus DTP cells.

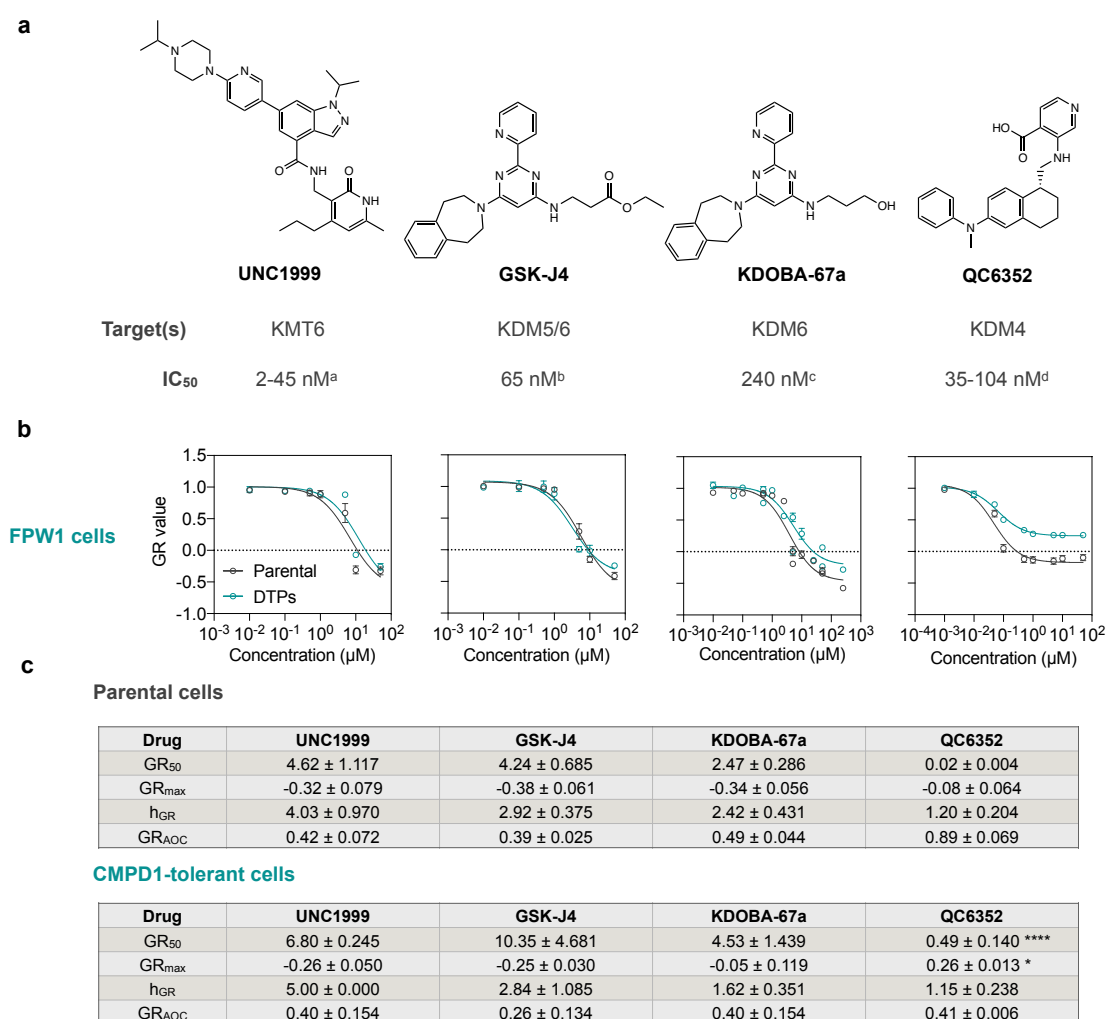


Figure 5.9 Assessment of FPW1 cell sensitivity to KMT and KDM inhibitors.

(a) Chemical structures, protein targets and *in vitro* IC₅₀ of UNC1999, GSK-J4, KDOBA-67a and GSK-J4 (REFs a³⁷⁵, b³⁷⁶, c³⁷⁷ and d³⁷⁸⁻³⁸⁰). (b) Parental and CMPD1-tolerant (DTP) FPW1 cells were treated with epigenetic probes for 5 days. Concentration-response curves for CMPD1 and tivantinib were measured using CellTitre-Blue viability assays. (c) GR metrics for parental and DTPs were calculated using the online GRcalculator tool. Data represent mean ± SEM (n = 3-5). Unpaired *t*-tests of corresponding GR metrics between parental and DTP cells were performed (* p < 0.05, **** p < 0.0001).

In the FPW1 cell line, parental and DTP cells were equally sensitive to UNC1999, GSK-J4 and KDOBA-67a and no significant differences were detected between corresponding GR metrics in parentals and DTPs (all p > 0.05) (Figure 5.9b). For the KDM4

inhibitor QC6352, both the GR_{50} (25-fold, $p < 0.0001$) and GR_{max} (0.26 vs. -0.08, $p < 0.05$) were significantly higher in DTPs compared with parental cells (**Figure 5.9c**).

Similar results were observed in RK11 cells (**Figure 5.10b**). The KMT6 inhibitor UNC1999 exhibited the same GR_{50} in parental and DTP cells; however, its maximal efficacy value (GR_{max}) was significantly lower in DTPs compared to parentals (-0.58 vs. -0.23, $p < 0.01$) indicating that drug-tolerant cells are more sensitive to KMT6 inhibition. GSK-J4 and KDOBA-67a had similar effects on parentals and DTPs with no significant differences in their GR metrics (all $p > 0.05$). For QC6352, both GR_{50} (more than 500-fold, $p < 0.00001$) and GR_{max} (0.61 vs. 0.28, $p < 0.01$) were significantly higher in DTPs compared with parental cells.

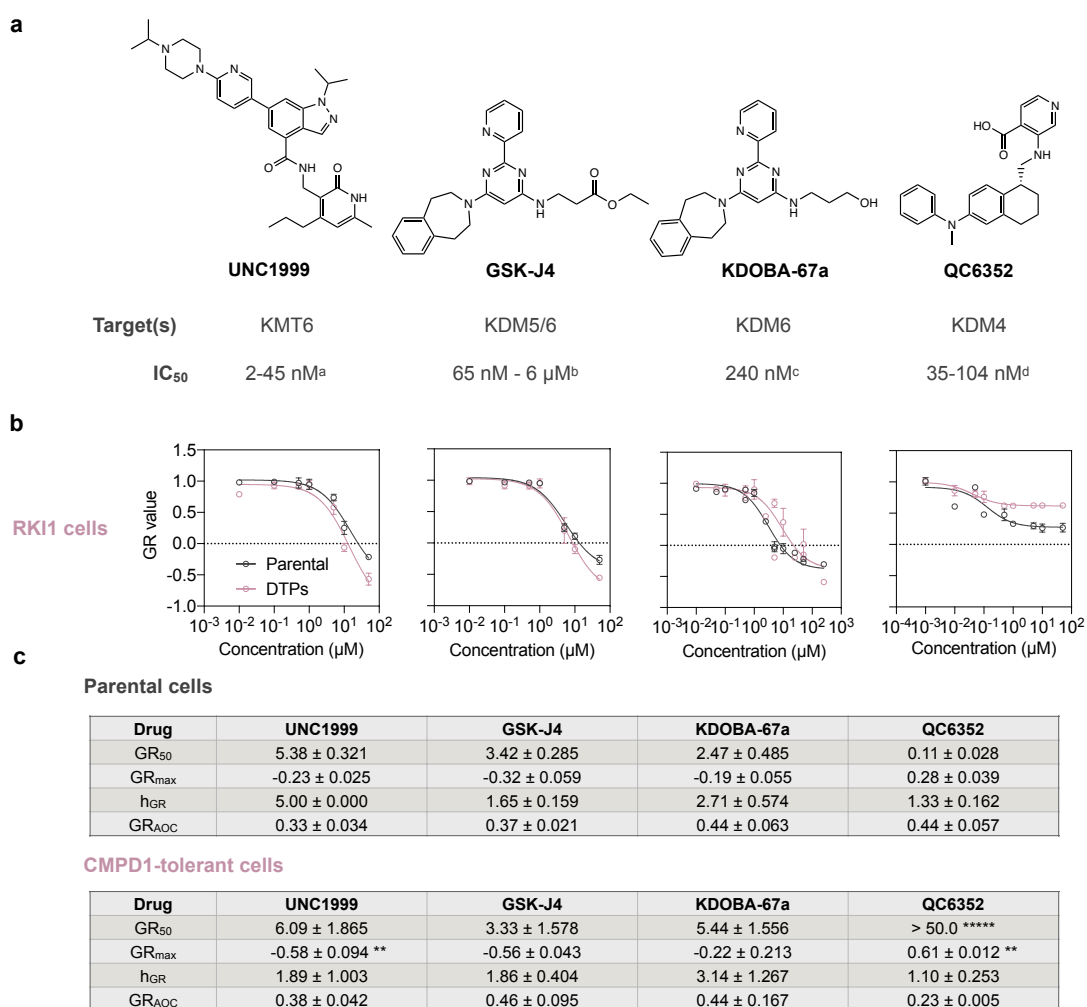


Figure 5.10 Assessment of RK11 cell sensitivity to KMT and KDM inhibitors.

(a) Chemical structures, protein targets and *in vitro* IC_{50} of UNC1999, GSK-J4, KDOBA-67a and GSK-J4 (REFs a³⁷⁵, b³⁷⁶, c³⁷⁷ and d³⁷⁸⁻³⁸⁰). (b) Parental and CMPD1-tolerant (DTP) FPW1 cells were treated with epigenetic probes for 5 days. Concentration-response curves for CMPD1 and tivantinib were measured using CellTiter-Blue viability assays. (c) GR metrics for parental and DTPs were calculated using the online GRcalculator tool. Data represent mean ± SEM (n = 3-5). Unpaired *t*-tests of corresponding GR metrics between parental and DTP cells were performed (** $p < 0.01$, ***** $p < 0.00001$).

Since the KMT6 inhibitor UNC1999 significantly reduced cell viability of CMPD1-tolerant persisters, particularly in the RK11 cell line, we performed further viability assays testing other KMT6 inhibitors GSK126, CPI-169, CPI-1205 and tazemetostat in FPW1 (**Figure 5.11**) and RK11 (**Figure 5.12**) cell lines. While all tested KMT6 inhibitors share a pyridonemethyl-amide motif, they possess unique structural features. UNC1999 contains an indazole core and GSK126 possesses a benzopyrrole core; however, both compounds contain the pyridine-2-yl-piperazine tail (**Figure 5.11**). CPI-169 and CPI-1205 also contain a benzopyrrole core but have different motifs on the nitrogen atom of benzopyrrole and lack the pyridine-2-yl-piperazine tail. Additionally, these two inhibitors have the pyridonemethyl-amide group positioned on pyrrole moiety of the benzopyrrole core in comparison to UNC1999 and GSK126. Lastly, tazemetostat contains an entirely different scaffold based on the pyridonemethyl-amide motif.³⁴⁸

In the FPW1 cell line, GSK126 had a GR_{50} of 15.5 μM in parental cells and 6.56 μM in DTP cells ($p < 0.05$). CPI-169, CPI-1205 and tazemetostat were equally potent and efficacious in parental and DTP cells (**Figure 5.11b**). Notably, both CPI-169 and CPI-1205, which lack the pyridine-2-yl-piperazine tail, were less efficacious on both parental and DTP cells, compared to UNC1999 and GSK126. Tazemetostat, which further lacks the benzopyrrole core, had no effect on parental or DTP cell viability relative to untreated controls ($GR_{50} > 50 \mu\text{M}$) (**Figure 5.11c**).

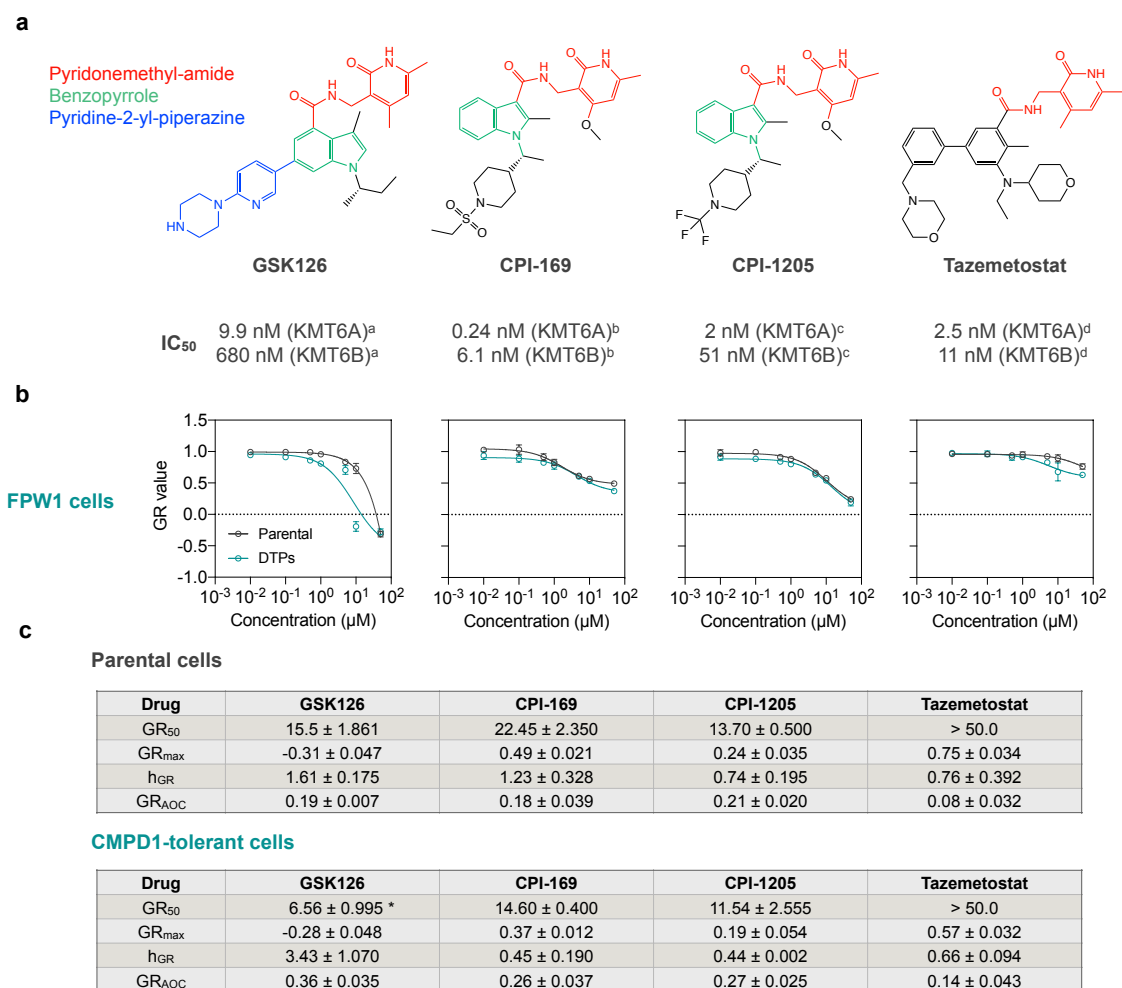


Figure 5.11 Assessment of FPW1 cell sensitivity to orthogonal KMT6 inhibitors.

(a) Chemical structures, protein targets and *in vitro* IC₅₀ of GSK126, CPI-169, CPI-1205 and tazemetostat (REFs a³⁸¹, b³⁸², c³⁸³ and d³⁸⁴). (b) Parental and CMPD1-tolerant (DTP) FPW1 cells were treated with epigenetic probes for 5 days. Concentration-response curves for CMPD1 and tivantinib were measured using CellTitre-Blue viability assays. (c) GR metrics for parental and DTPs were calculated using the online GRcalculator tool. Data represent mean ± SEM (n = 3). Unpaired *t*-tests of corresponding GR metrics between parental and DTP cells were performed (* p < 0.05).

In the RK11 cell line, CMPD1-tolerant cells were somewhat more sensitive to KMT inhibition than parental cells (Figure 5.12b). GSK126 was more potent (GR₅₀ 5.5 vs. 7.4 µM, p = 0.1) and significantly more efficacious (GR_{max} -0.57 vs. -0.21, p < 0.05) in DTP cells compared to parentals. CPI-169 was more potent (GR₅₀ 9.8 vs. > 50 µM, p < 0.001) and efficacious (GR_{max} 0.37 vs. 0.49, p = 0.07) in DTPs than parental cells. Similarly, CPI-1205 was more potent (GR₅₀ 10.3 vs. 23.7 µM, p = 0.1) and efficacious (GR_{max} 0.31 vs. 0.67, p = 0.05) in DTPs than parental cells. Tazemetostat potency and efficacy did not differ between parental and DTP cells (p > 0.05) (Figure 5.12c).

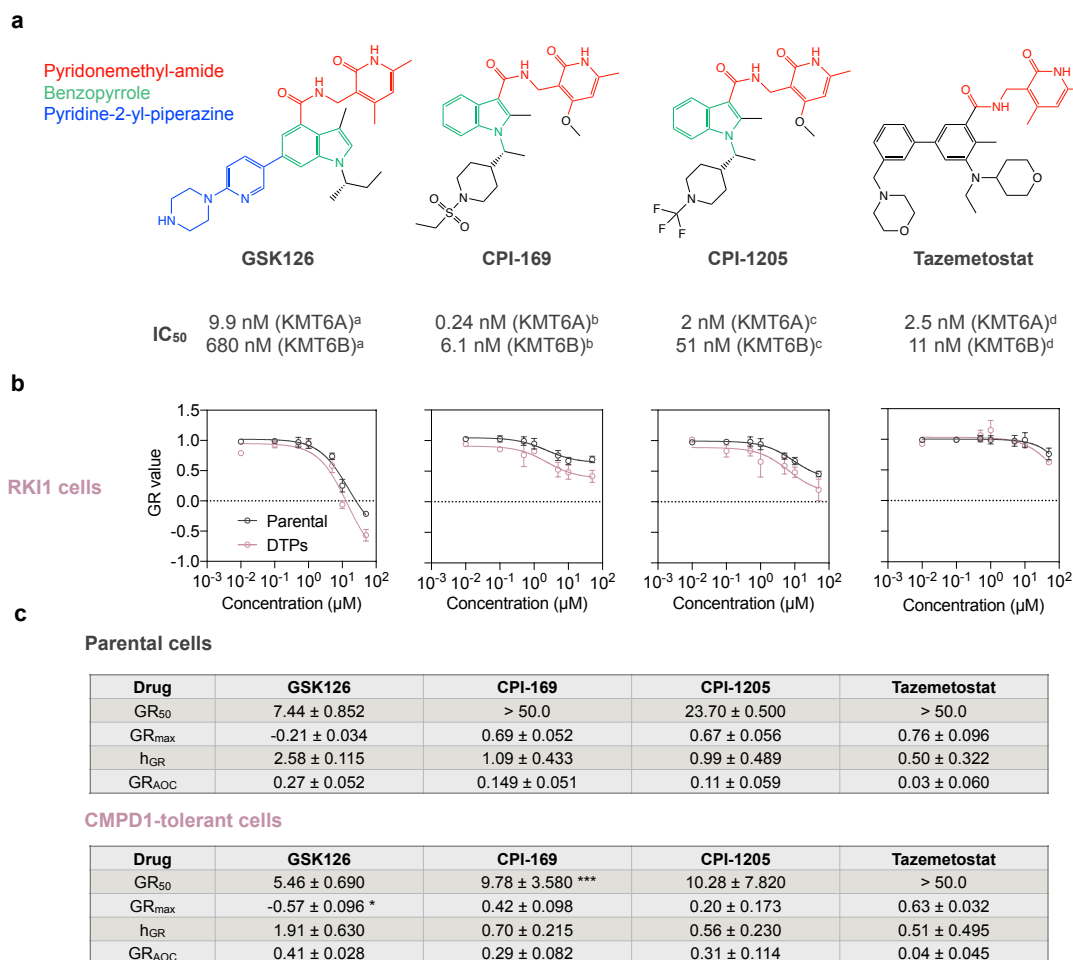


Figure 5.12 Assessment of RKI1 cell sensitivity to orthogonal KMT6 inhibitors.

(a) Chemical structures, protein targets and *in vitro* IC₅₀ of GSK126, CPI-169, CPI-1205 and tazemetostat (REFs a³⁸¹, b³⁸², c³⁸³ and d³⁸⁴). (b) Parental and CMPD1-tolerant (DTP) FPW1 cells were treated with epigenetic probes for 5 days. Concentration-response curves for CMPD1 and tivantinib were measured using CellTitre-Blue viability assays. (c) GR metrics for parental and DTPs were calculated using the online GRcalculator tool. Data represent mean ± SEM (n = 3). Unpaired *t*-tests of corresponding GR metrics between parental and DTP cells were performed (* p < 0.05, *** p < 0.001).

In summary, these data suggest that DTP cells are somewhat more sensitive to KMT6 inhibition than the parental cells. However, the effectiveness of the two structurally related inhibitors, UNC1999 and GSK126, relative to the other KMT6 inhibitors, suggest potential off-targets. On the other hand, KDM4 inhibition resulted in potent cytostatic effects on parental cells but had no effect on DTP cells. KDM6 inhibition was effective in both parental and DTP glioblastoma cells. Nonetheless, all epigenetic probes tested failed to achieve complete killing (GR_{max} = -1) of the entire cell population. Therefore, we questioned whether these drugs could eradicate DTPs in combination with CMPD1.

5. 2. 3. Combination studies of CMPD1 and epigenetic probes

To assess drug-drug interactions between CMPD1 and KMT6, KDM6 or KDM4 inhibitors, the anti-proliferative effects of drug combinations were assessed in 5-day viability assays employing FPW1 and RKI1 cells. Serial dilutions of CMPD1 were combined with serial dilutions of the KMT6 inhibitor UNC1999, KDM5/6 inhibitor GSK-J4, KDM6 inhibitor KDOBA-67a and KDM4 inhibitor QC6352, following the Chou-Talalay method.³⁰¹ Combination Index (CI) was calculated using the CompuSyn software (BioSoft) at 50% (CI₅₀), 25% (CI₇₅) and 10% (CI₉₀) cell viability relative to the control. CI values between 0 and 1 indicate synergism, equal to 1 indicate an additive effect, and greater than 1 indicate antagonism in the inhibitor combination.³⁰¹

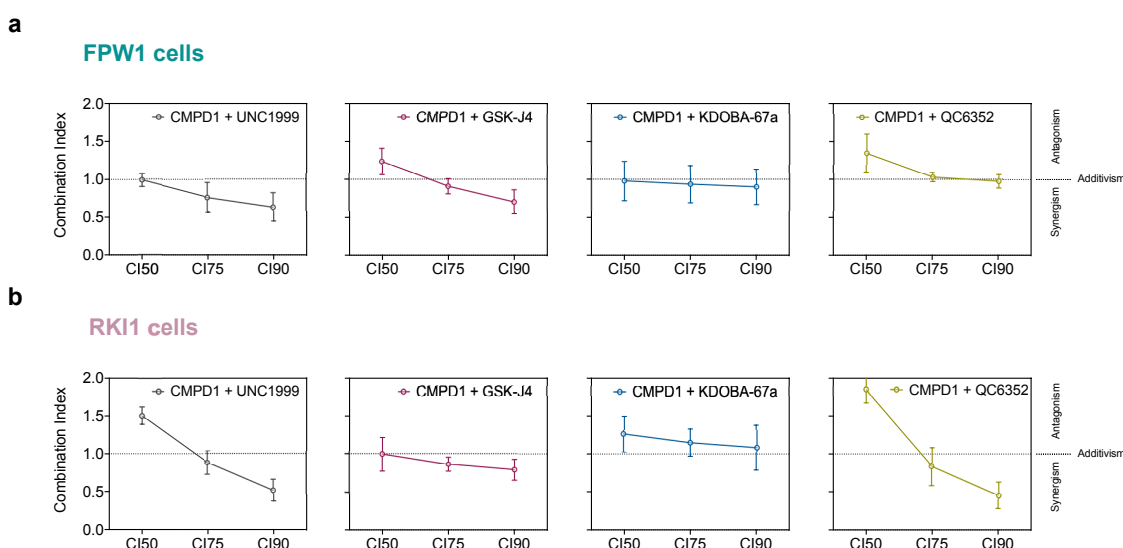


Figure 5.13 Chou-Talalay analysis of CMPD1 and epigenetic probes in combinations.

CMPD1 combination with UNC1999, GSK-J4, KDOBA-67a or QC6352 in (a) FPW1 and (b) RKI1 cells. Combination indices (Cis) were calculated at 50%, 75% and 90% dose inhibitory values from replicate CellTitre-Blue viability assays. Data are mean \pm SEM (n = 3-5).

In FPW1 cells (Figure 5.13a), the effect of UNC1999 on cell viability was additive (CI = 1) with CMPD1 at CI₅₀ and weakly synergistic (CI = 0.5–0.8) at CI₇₅ and CI₉₀. GSK-J4 showed weak antagonism (CI = 1.3), additivity (CI = 1) and weak synergism (CI = 0.6) with CMPD1 at CI₅₀, CI₇₅, and CI₉₀, respectively. KDOBA-67a had additive effects (CI = 1) with CMPD1 at all concentrations. QC6352 was antagonistic with CMPD1 at CI₅₀ (CI = 1.4) and additive at CI₇₅ and CI₉₀ (CI = 1).

In RKI1 cells (Figure 5.13b), UNC1999 was antagonistic at CI₅₀ (CI = 1.5), and synergistic (CI = 0.5–0.9) at CI₇₅ and CI₉₀ in combination with CMPD1. GSK-J4 was additive to weakly synergistic (CI = 0.8–1) in combination with CMPD1 at all

concentrations, while KDOBA-67a was weakly antagonistic (CI = 1.1–1.2) at all concentrations. QC6352 exhibited strong antagonism (CI = 1.8) at CI₅₀ in combination with CMPD1 while displaying additive (CI = 1) and synergistic (CI = 0.5) effects CI₇₅ and CI₉₀, respectively. In summary, CMPD1 in combination with the KMT6 inhibitor UNC1999 or KDM4 inhibitor QC6352 had synergistic effects, while the combination with the KDM5/6 inhibitor GSK-J4 and KDM6 inhibitor KDOB-67a had an overall additive effect in 5-day viability assays.

As the onset of epigenetic changes is generally slow,³⁸⁵ we also performed long-term viability assays. Cells were treated with epigenetic probes for 14 days and stained with Nuclear-ID Red DNA stain. As the epigenetic probes are not cytotoxic to treatment-naïve parental cells at the recommended concentrations, cells were seeded at low density to prevent over-confluence. Fold-changes in cell numbers were calculated relative to the initial cell number on Day 0 (set as 1).

Treatment of FPW1 cells (**Figure 5.14a**) with the KMT6 inhibitors UNC1999 and GSK-343, or KDM6 inhibitor KDOBA-67a did not significantly change the number of cells at Day 14 relative to vehicle (DMSO), implicating that these inhibitors do not attenuate glioblastoma cell proliferation as single agents. By contrast, the KDM5/6 inhibitor GSK-J4 reduced the number of cells at the end of the treatment. At Day 14, cells treated with DMSO exhibited a 12-fold increase in number relative to Day 0, while cells treated with GSK-J4 had a 6-fold increase ($p < 0.05$). Treatment with the KDM4 inhibitor QC6352 had a strong cytostatic effect, with a strongly significant difference in the number of cells Day 14 compared to vehicle (1.4-fold vs. 12-fold, $p < 0.01$), in both cell lines (**Figure 5.14b**).

Similar trends were observed in RK11 cells (**Figure 5.14a**). Treatment with UNC1999, GSK-343, GSK-J4 or KDOBA-67a, had no effect on the number of cells at Day 14 relative to vehicle (DMSO). On the other hand, treatment with QC6352 had a strong cytostatic effect, with a significant difference in the number of cells at Day 14 compared to vehicle (1.5-fold vs. 15-fold), in both cell lines (**Figure 5.14b**).

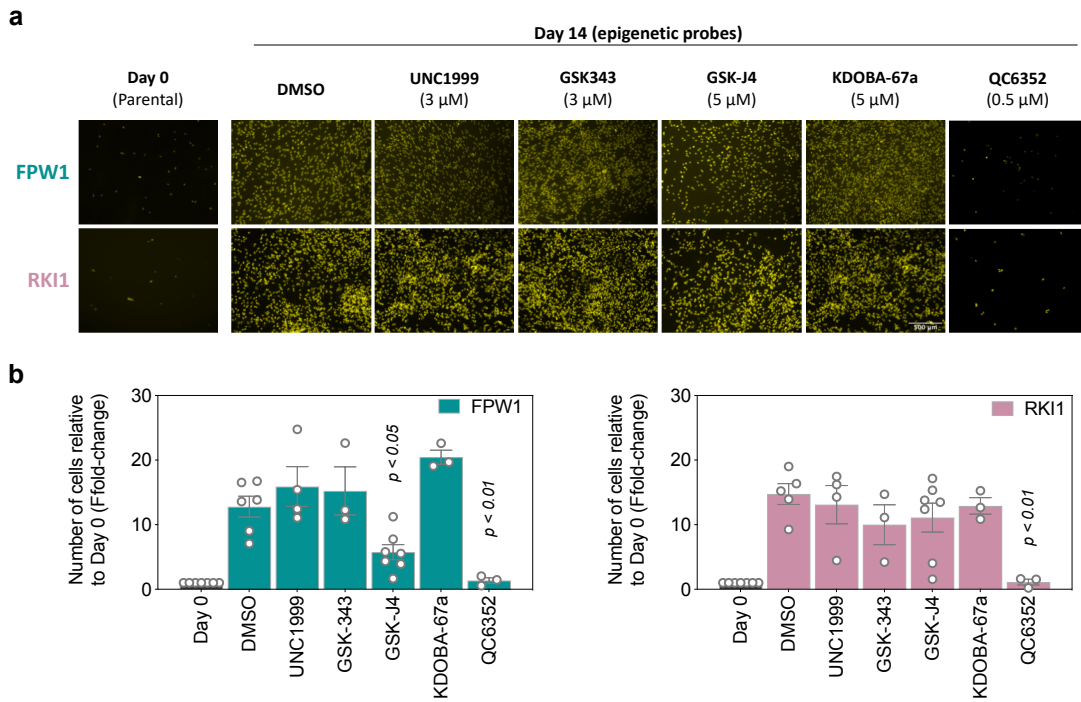


Figure 5.14 Long-term effect of KMT and KDM inhibition on glioblastoma cell proliferation.

FPW1 and RKI1 cells were treated with vehicle (DMSO), UNC1999, GSK343, QC6352, GSK-J4 or KDOBA-67a for 14 days. Cells were stained with Nuclear-ID red on Day 0 and Day 14. **(a)** Representative images and **(b)** quantification of cells on Day 0 (set as 1) and Day 14. Data are mean \pm SEM ($n = 3-7$). One-way ANOVA was performed between untreated (DMSO) and treated cells at Day 14 was performed.

To assess the effect of KMT6, KDM4 and KDM6 inhibition on the number of surviving CMPD1-tolerant persisters, FPW1 and RKI1 cells were treated with CMPD1 for 14 days in the presence or absence of UNC1999, GSK343, QC6352, GSK-J4 or KDOBA-67a (**Figure 5.15a**). Cells were seeded at a higher density, and the number of surviving cells was quantified at Day 14 relative to cells at Day 0 (set as 1). In both cell lines, the number of CMPD1-tolerant cells was reduced to 0.25- to 0.3-fold relative to Day 0, which represents $\sim 30\%$ of surviving cells and is consistent with data reported in **Chapter 4**). Cells treated with CMPD1 in combination with the epigenetic probes exhibited a reduction to 0.25-to 0.45-fold in cell number relative to Day 0, with no statistically significant differences between any of the treatment groups (**Figure 5.15b**).

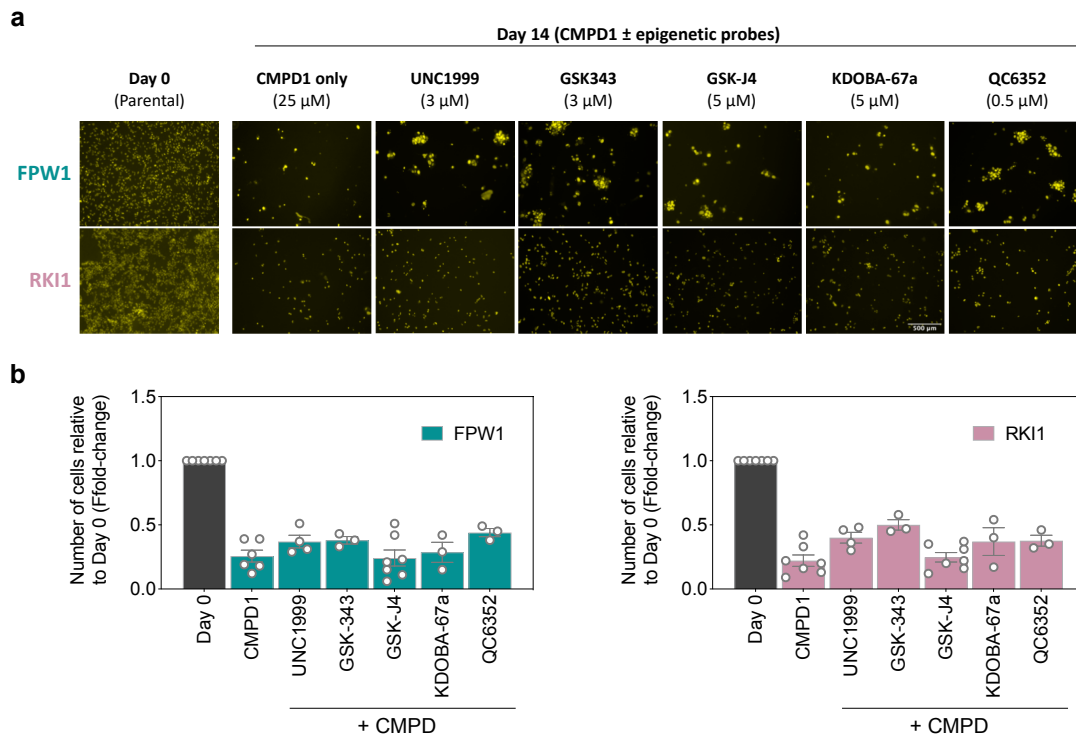


Figure 5.15 Long-term effect of KMT and KDM inhibition on DTP survival.

FPW1 and RK11 cells were treated with CMPD1 in combination with UNC1999, GSK343, QC6352, GSK-J4 or KDOBA-67a for 14 days. Cells were stained with Nuclear-ID red on Day 0 and Day 14. **(a)** Representative images and **(b)** quantification of cells on Day 0 (set as 1) and Day 14. Data are mean ± SEM (n = 3-7).

Finally, we performed clonogenic outgrowth assays to test the effect of co-treatment with CMPD1 and KMT/KDM-inhibitors on the recovery of drug-tolerant cells. FPW1 and RK11 cells were treated with the KMT6 inhibitors UNC1999 and GSK126, the KDM5/6 inhibitor GSK-J4 or the KDM4 inhibitor QC6352 in the presence or absence of CMPD1 at clinically plausible concentrations (300 and 500 nM) for 14 days. Cells were then allowed to recover in drug-free media for an additional 14 days. Recovered colonies were stained at Day 28.

In the FPW1 cell line (**Figure 5.16a**), treatment with 300 and 500 nM of CMPD1 resulted in a reduction in the number of colonies to 70% and 60%, respectively, relative to untreated controls (set as 100%). Co-treatment with the KMT6 inhibitors UNC1999 and GSK126 weakly potentiated the inhibition of colony formation by CMPD1 at 500 nM, as the relative number of colonies reduced to 30% and 20%, respectively. GSK-J4 reduced the number of colonies to 20% relative to controls and was effective with and without co-treatment with CMPD1. The KDM4 inhibitor QC6352 resulted in the total inhibition of colony formation with and without co-treatment with CMPD1 (**Figure 5.16b**).

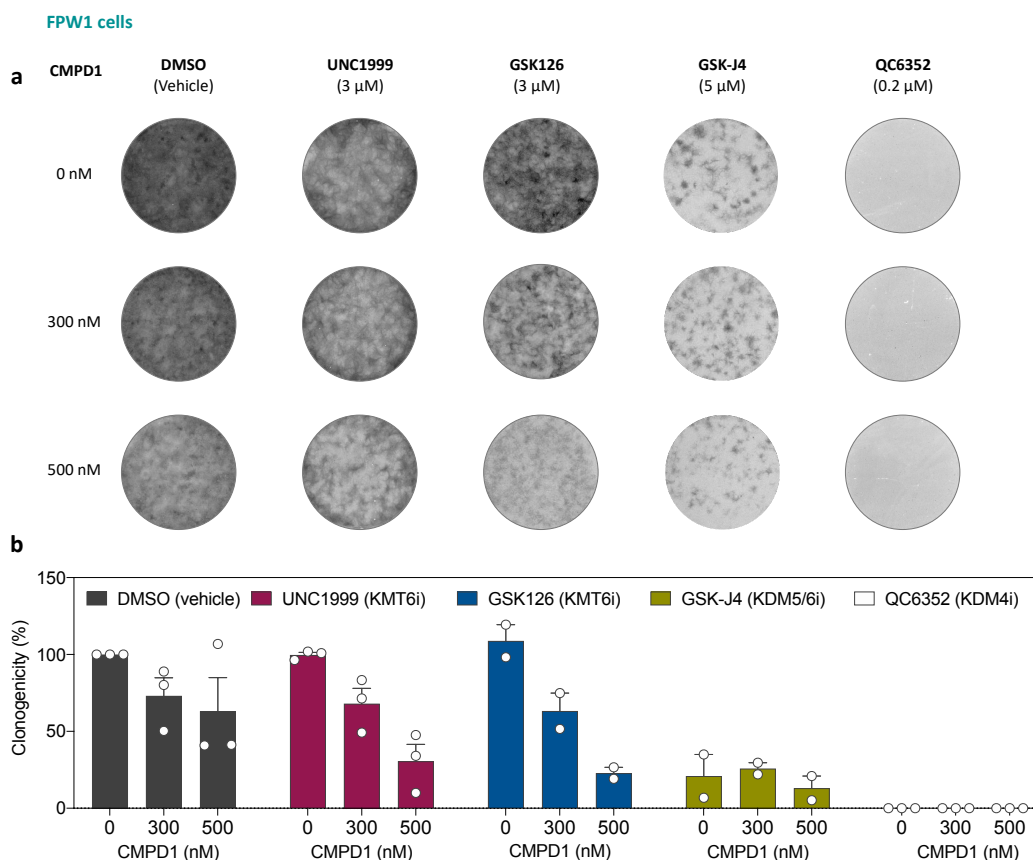


Figure 5.16 Effect of KMT and KDM inhibition on CMPD1-tolerant FPW1 cell recovery.

FPW1 cells were treated with CMPD1 in combination with UNC1999, GSK343, GSK-J4, KDOBA-67a or QC6352 for 14 days. Cells recovered in drug-free media for an additional 14 days and colonies were stained. (a) Representative images and (b) quantification of colonies. Data are mean \pm SEM (n = 2-3).

In the RK11 cell line (Figure 5.17a), treatment with 300 and 500 nM of CMPD1 resulted in a reduction in the number of colonies to 80% and 40%, respectively, relative to untreated controls (set as 100%). Co-treatment with the KMT6 inhibitors UNC1999 and GSK126 did not increase the killing-efficacy of CMPD1 in these cells. However, the data was variable and, therefore, inconclusive. GSK-J4 reduced the number of colonies to 20% relative to controls and prevented colony formation at 300 and 500 nM of CMPD1. The KDM4 inhibitor QC6352 resulted in complete inhibition of colony formation with and without co-treatment with CMPD1 (Figure 5.17b).

In conclusion, the tested epigenetic probes failed to eliminate DTPs or prevent their formation. However, our data suggest that treatment with GSK-J4, and to a greater extent, QC6352, is able to prevent DTP recovery.

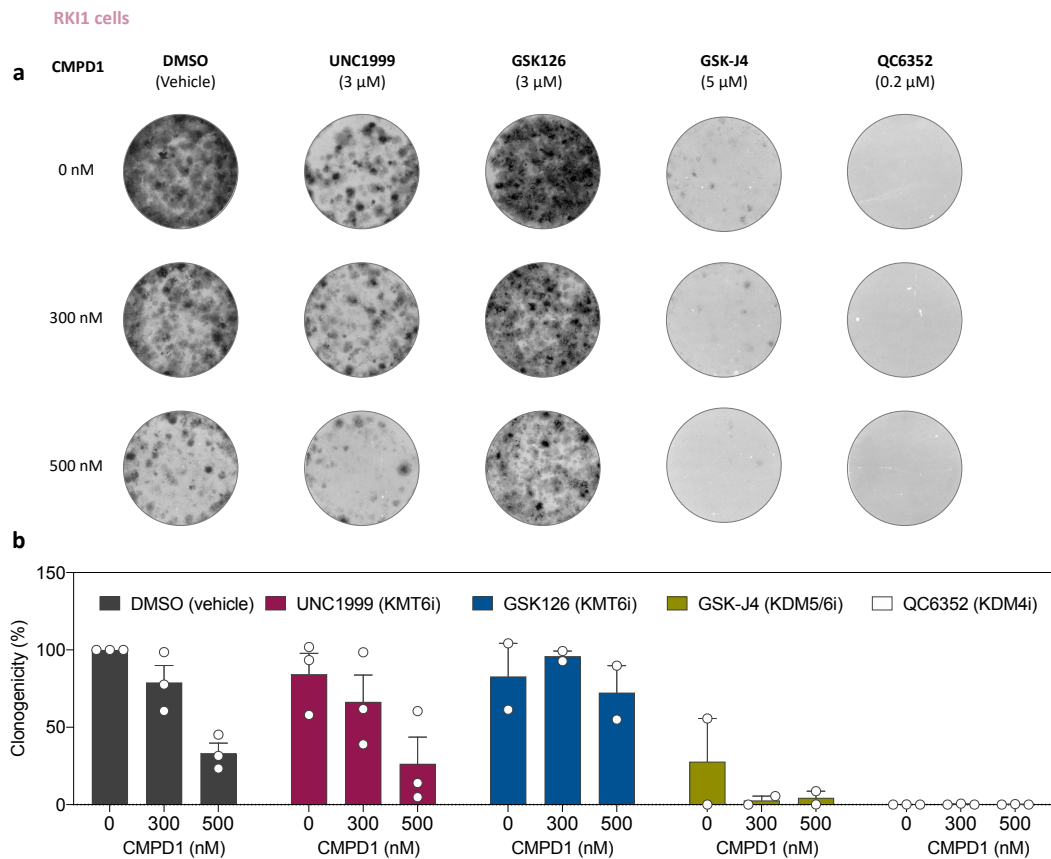


Figure 5.17 Effect of KMT and KDM inhibition on CMPD1-tolerant RK11 cell recovery.

FPW1 cells were treated with CMPD1 in combination with UNC1999, GSK343, GSK-J4, KDOBA-67a or QC6352 for 14 days. Cells recovered in drug-free media for an additional 14 days and colonies were stained. (a) Representative images and (b) quantification of colonies. Data are mean \pm SEM (n = 2-3).

5. 2. 4. Cathepsin L1 in drug tolerance

In our immunoblot analysis of histone modifications, we observed a marked increase in histone H3 cleavage in DTP cells relative to parental cells (Figure 4.19). Following this observation, we investigated the role of the histone cleaving enzyme cathepsin L1 (CTSL1) in tolerance of glioblastoma cells to CMPD1.

To assess whether CTSL1 levels change in DTPs, we analysed CTSL1 expression in parental and CMPD1-tolerant FPW1 and RK11 cells (Figure 5.18a), using Hsp90 as a loading control. Cathepsin L1 is activated by autolysis and has two preliminary forms, pro-cathepsin and intermediate cathepsin, which vary in molecular mass and thus, can be identified on immunoblots.³⁸⁶ Both cell lines expressed low levels of pro-cathepsin L1 (top band) and intermediate forms (middle band) and high levels of mature active form (bottom band) of CTSL1. The levels of CTSL1 increased to 1.25-fold, although the results were variable and did not reach statistical significance (Figure 5.18b).

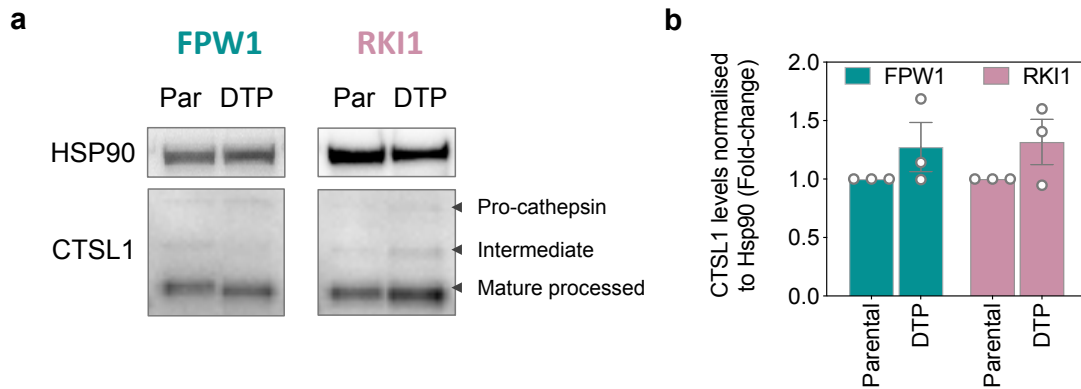


Figure 5.18 Levels of CTSL1 expression in parental and CMPD1-tolerant cells.

Immunoblot analysis of CTSL1 (30 μ g of total protein) in parental (Par) and CMPD1-tolerant (DTP) whole-cell lysates. Hsp90 was used as a loading control. **(a)** Representative immunoblots and **(b)** quantification presented as fold change relative to parental (set as 1) are shown. Data are mean \pm SEM ($n = 3$).

While CTSL1 levels did not change significantly in DTPs, its activity may still be altered by regulating enzymes. Therefore, to identify the effect of the CTSL1 inhibition, FPW1 cells treated with vehicle (DMSO) or CTSL1 inhibitor (CTSL-i) were stained with Nuclear-ID Red DNA stain at Day 0 and Day 14. CTSL-i did not change the number of cells at the end of the treatment when compared with vehicle (DMSO) (**Figure 5.19a**), with both treatment groups increasing in number by approximately 35-fold (**Figure 5.19b**). Next, to identify the effect of CTSL1 inhibition on DTP cell survival, FPW1 and RKI1 cells were treated with CMPD1 for 14 days in the presence or absence of CTSL-i (1, 3 and 5 μ M) (**Figure 5.19c**). This combination did not change the number of surviving DTP cells relative to CMPD1 alone, with all treatment groups reducing the number of cells to 0.25- to 0.3-fold relative to Day 0 ($\sim 30\%$ surviving cells) (**Figure 5.19d**). Together, these results suggest that CTSL1 does not contribute to the maintenance of drug-tolerant states.

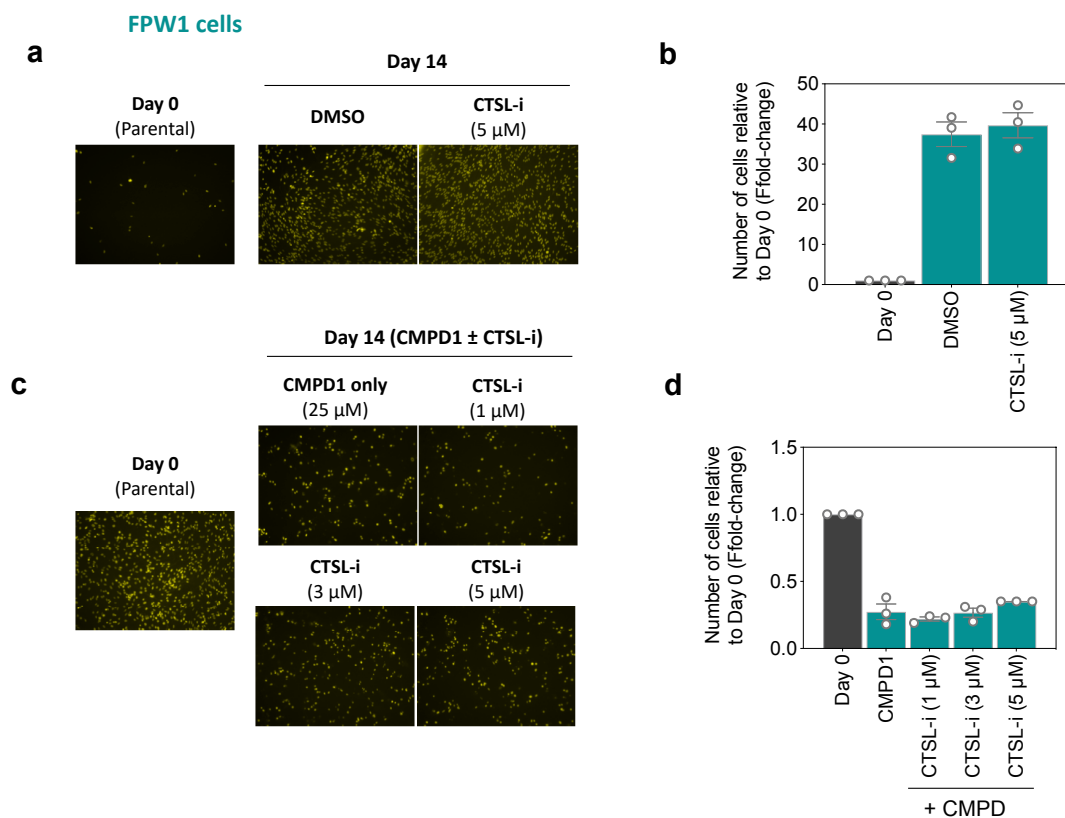


Figure 5.19 Effect of CTSL inhibition on DTP survival.

FPW1 and RK11 cells were treated with CMPD1 in combination with CTSL-i for 14 days. Cells were stained with Nuclear-ID red on Day 0 and Day 14. (a) Representative images and (b) quantification of cells on Day 0 (set as 1) and Day 14. Data are mean \pm SEM ($n = 3$).

5. 3. Discussion

The research presented in this chapter assessed the potential of histone lysine methyltransferases and demethylases as novel druggable targets in glioblastoma, particularly to prevent tumour regrowth. We found that CMPD1-tolerant persisters display differential expression of KMT and KDM genes, providing evidence for the role of epigenetic enzymes in drug tolerance. Notably, DTPs exhibited more increases in KMT transcript levels when compared to KDM transcript levels, consistent with the global increases in methylation observed in SWATH-MS analysis (Chapter 4).

However, we did not identify direct correlations between the changes in KMT and KDM transcript levels and the corresponding H3 lysine residues upon which the protein products act. Further validation of KMT and KDM expressions is needed on the transcript and protein levels to confirm any changes in DTPs. Notably, KMT and KDM enzyme activity is influenced by cellular metabolism and the availability of cofactors such as SAM and 2-OG, which are involved in the Krebs, folate and methionine cycles and other fundamental metabolic pathways.³⁸⁷ As several studies have demonstrated that DTPs

switch to oxidative metabolism,^{145, 152, 153} it is plausible that KMT6 and KDM activity is changing as a result, leading to the changes in histone modifications observed in DTPs (Table 4.2).³⁸⁸

Although changes in KMT6 transcript levels were negligible, DTP cells demonstrated increased sensitivity to some KMT6 inhibitors when compared to treatment-naïve cells. The KMT6 inhibitor UNC1999 attenuated cell proliferation at 10 μ M and was cytotoxic to cells at 50 μ M. However, these concentrations are significantly higher than the recommended target engagement concentration of 3 μ M (Figure 5.9, Figure 5.10). Similarly, the structurally related UNC1999 analogue, GSK126, induced a similar response in glioblastoma cells to UNC1999, with DTPs being more sensitive to GSK126 than parental cells (Figure 5.11, Figure 5.12). The orthogonal KMT6 inhibitors CPI-169, CPI-1205 and tazemetostat had little to no effect on the viability of parental and CPMD1-tolerant cells.

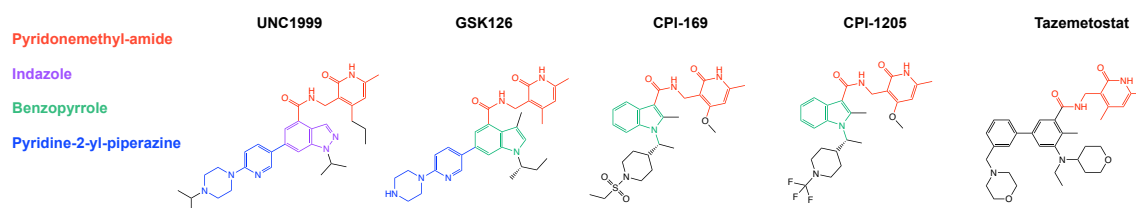


Figure 5.20 Structural comparison of KMT6 inhibitors.

The inconsistent sensitivity of glioblastoma cells to KMT6 inhibitors suggests that the efficacy of UNC1999 and GSK126 is not related to KMT6 inhibition. This is further supported by analysis of the pharmacophores of tested KMT6 inhibitors (Figure 5.20). UNC1999, GSK126, CPI-169, CPI-1205 and tazemetostat all share the pyridonemethyl-amide motif, which binds to KMT6A/B by competing with the cofactor SAM for its binding site on the SET domain.³⁸⁹ However, only UNC1999 and GSK126 contain the pyridine-2-yl-piperazine tail; they also share bioisosteric indazole and benzopyrrole cores. By contrast, CPI-169 and CPI-1205, in which the benzopyrrole core is retained, but the pyridine-2-yl-piperazine is replaced with piperidine moieties lose some of the inhibitory activity on cell proliferation. Tazemetostat, which further lacks the benzopyrrole core, has no effect on the viability of parental or DTP cells (Figure 5.11, Figure 5.12). Furthermore, inhibition of EED, which is essential for KMT6/PCR2 activity, by the probe A-395, had no effect the viability of parental or MTA-tolerant cells (Figure 5.8).

Thus, at the recommended target engagement concentrations, the KMT6 inhibitors did not reduce the number of emerging DTPs (Figure 5.15) and did not attenuate the self-renewal capacity of recovering glioblastoma cells (Figure 5.16, Figure 5.17). Together, these data suggest that UNC1999 and GSK126 may be acting on DTPs via KMT6-independent mechanisms and the pyridine-2-yl-piperazine moiety is crucial for this off-target activity. Further investigation and identification of mechanisms by which UNC1999 and GSK126 target drug-tolerant glioblastoma cells may provide a novel therapeutic avenue for killing residual DTP cells.

We further discovered that both treatment-naïve and drug-tolerant cells were also sensitive to the inhibition of the H3K27 demethylases, particularly to the KDM6 inhibitor KDOBA-67a and the KDM5/6 inhibitor GSK-J4. Importantly, the anti-proliferative activities of these inhibitors were observed at recommended target engagement concentrations. Treatments with selective KDM5 inhibitors KDOAM-25 and KDOPZ-36a were not effective at reducing cell viability of parental or MTA-tolerant cells (Figure 5.8). The response of glioblastoma cells to these inhibitors indicates a dependence on KDM6, but not KDM5. Similarly, dasatinib-tolerant glioblastoma cells were sensitive to KDM5/6 inhibition by GSK-J4, further supporting DTP dependence on KDM6.¹⁰⁶ Interestingly, prolonged treatment with GSK-J4, but not KDOBA-67a inhibited FPW1 cell proliferation (Figure 5.14). However, both GSK-J4 and KDOBA67-a failed to reduce the number of DTPs in combination with CMPD1 (Figure 5.15). Therefore, KDM6 inhibition may slow down DTP recovery, these cells appear to be dependent on other molecular pathways that circumvent KDM6 inhibition, as they are still able to recover partially.

We also confirmed the increase in *KDM4E* transcripts and *KDM4E* protein expression (Figure 5.7). It is not clear if the increase in *KDM4E* expression is involved in DTP survival, as up until recently, *KDM4E* was believed to be a pseudogene.² Further studies are warranted to investigate whether *KDM4E* has a role in drug tolerance. Nonetheless, both treatment-naïve and drug-tolerant cells were sensitive to *KDM4* inhibition. In short-term viability assays, QC6352 had a strong cytostatic effect on parental cells and a partial cytostatic effect on DTPs (Figure 5.9, Figure 5.10). Given that persister cells are slow-cycling,^{106, 144, 152} the cytostatic effect of QC6352 on cell proliferation may be apparent in treatments longer than 5 days. In long-term assays, the *KDM4* inhibitor, QC6352, potently inhibited proliferation of glioblastoma cells as a single agent (Figure 5.14) but did not decrease the number of viable DTPs derived from CMPD1 treatment (Figure 5.15). QC6352 also inhibited the self-renewal capacity of treatment naïve cells and CMPD1-tolerant cells, even after 14 days in drug-free media

(Figure 5.16, Figure 5.17). While other cell-permeable and selective KDM4 inhibitors and CRISPR-knockout experiments are still needed to establish the role of KDM4 during both cell proliferation and drug tolerance, our findings support that QC6352 may be a novel therapeutic lead for the treatment of glioblastoma. Having demonstrated a potent effect of QC6352 in glioblastoma cells, we next aimed to establish a high throughput assay to develop novel KDM4 inhibitors (**Chapter 6**).

Lastly, to investigate whether histone cleavage is essential in drug tolerance, we assessed CTSL1 expression (Figure 5.18) and cellular efficacy of the CTSL1 inhibitor CTSL-i (Figure 5.19). We demonstrate that CTSL1 is present in its active form in glioblastoma cells; however, its inhibition does not reduce the number of surviving DTPs. These data suggest that the increase of histone H3 cleavage observed in DTPs may be a result of increased histone deposition, coupled with the active form of the CTSL1 present in parental FPW1 and RK11 cells, and hence, their emergent DTPs. However, histone H3 cleavage does not appear to be crucial for the survival of DTPs.

In conclusion, we show that glioblastoma cells exhibit epigenetic changes and are somewhat sensitive to epigenetic inhibition. Nonetheless, no treatment or treatment combination succeeded at killing DTPs, demonstrating the resilience of these cells and their potential ability to drive tumour recurrence. Further *in vivo* studies are required to understand the role of DTPs in cancer. Our findings provide evidence that UNC1999, GSK126 and GSK-J4 prevented recovery of DTP cells and thus, these inhibitors are suitable leads for targeting DTPs. Nevertheless, the exact mechanism of action of these compounds remains to be established. Furthermore, we identified that KDM4 inhibition may provide a novel therapeutic approach to targeting glioblastoma.

Chapter 6

Development of KDM4 Activity Assay
Using AlphaScreen Technology

CHAPTER 6. DEVELOPMENT OF KDM4 ACTIVITY ASSAY USING ALPHASCREEN TECHNOLOGY

6. 1. Introduction

While KDM4 inhibitor QC6352 had a potent effect on inhibiting proliferation in both parental and persister cells, there is a lack of orthogonal KDM4 inhibitors to validate these findings. In order to aid the development of novel KDM4 inhibitors, we established a biochemical assay to measure inhibition of KDM4 by test compounds. This assay uses AlphaScreen technology due to its high throughput, sensitivity and time efficiency.³⁹⁰ Subsequent sections will focus on known KDM4 inhibitors and the principle behind AlphaScreen assays.

6. 1. 1. KDM4 enzymes and inhibitors

The KDM4 subfamily of proteins, which contain JmjC demethylase domains, is involved in a wide range of biological functions, including cell cycle regulation transcriptional regulation, senescence and heterochromatin formation. Although the functions of KDM4 enzymes are yet to be fully elucidated, a growing body of evidence supports their roles in cancer.^{2, 391} Aberrant expression of KDM4 enzymes leads to genomic instability and tumorigenesis.³⁹²

Like other JmjC domain KDMs, the KDM4 enzyme subfamily is dependent on Fe(II) and α -ketoglutarate (2-OG) (**Figure 6.2**). In the KDM4 catalytic site, the Fe(II) ion is chelated by residues H188, E190, H276 and three water molecules. 2-OG displaces two water molecules and forms hydrogen bonds (H-bonds) with the Fe(II) ion via its C1 carboxylate oxygen and its C2 ketone oxygen. The C5 carboxylate moiety of 2-OG also forms H-bonds with Y132, N198 and K206 in the KDM4 binding site. A negative oxygen ion attacks the positively charged Fe(II) ion, displacing the remaining water molecule. The now negatively charged Fe(III)–O₂ complex, in turn, attacks the C2 position of 2-OG, resulting in 2-OG decarboxylation to succinate and the release of carbon dioxide. Nearby methylated lysine residues form a H-bond with the carboxylate group in the Fe(IV)=O₂ complex. The C–H bond in the aminomethyl group of lysine residues is then broken, forming a carbon free radical. The hydroxyl group in the Fe(IV)=O₂ complex is transferred from the Fe(III) ion to the carbon free radical. Next, succinate is displaced from the metal complex by water or 2-OG and the reaction is repeated. At last, the aminomethyl group is readily hydroxylated, releasing formaldehyde (**Figure 6.2**).^{391, 393, 394}

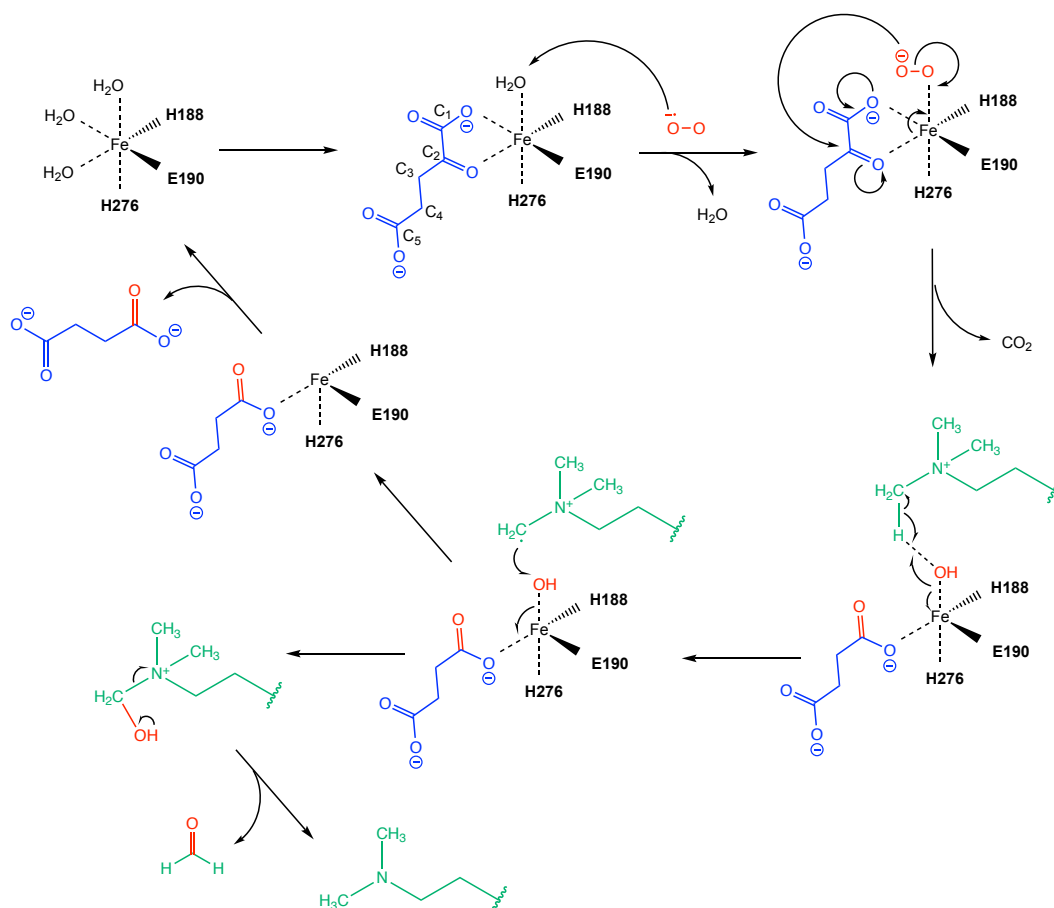


Figure 6.1 Demethylation reaction by KDM4 enzymes.

2-OG (blue) binds to Fe(II) ion chelated by H188, E190 and H276 on KDM4. A negatively charged oxygen molecule (red) attack 2-OG at C5, releasing carbon dioxide and yielding succinate. Methylated residues (green) in the vicinity form H-bonds with the carboxylate moiety in the iron complex, forming a carbon free radical. The hydroxyl group from the iron complex is then transferred to the aminomethyl group of the lysine residue, readily hydrolysing the methyl group and releasing formaldehyde. The product of this reaction is a demethylated lysine residue.

The catalytic site of KDMs is highly conserved, and so, developing selective inhibitors for KDM subfamilies, let alone isoforms within each subfamily, is challenging.³⁹⁵ Furthermore, due to the hydrophobicity of the binding pocket in JmjC domain proteins, KDM inhibitors are faced with a significant challenge for small-molecule drug discovery. Several lead compounds containing carboxylic acid motifs demonstrated potency *in vitro* but failed to show cellular efficacy.³⁸⁰ The main class of KDM4 inhibitors are 2-OG competitive agents that mimic the interactions of 2-OG with the Fe(II) and key residues in the binding pocket (Figure 6.2a). Other classes include metal cofactor disruptors and histone-substrate competitive peptide inhibitors.^{360, 395}

Pyridine-2,4-dicarboxylic acid (2,4-PDCA) is a broad spectrum 2-OG oxygenase (including JmjC demethylase) inhibitor developed as a scaffold for further

drug development. 2,4-PDCA is a 2-OG competitive inhibitor as it coordinates with the Fe(II) ion in a bidentate fashion, via its pyridinyl N-atom and 2-carboxylate moieties when binding to KDM4A. As expected, co-crystal structures reveal that the Fe(II) metal also chelates KDM4A residues H188, E190 and H276. A water molecule completes the six-coordinate metal complex (**Figure 6.2b**). Furthermore, the pyridine ring of 2,4-PDCA forms hydrophobic interactions with Y177, F185 and W208.³⁹⁶

The 8-hydroxyquinoline derivative, IOX1, is another small-molecule inhibitor that mimics the interactions with the Fe(II) ion and carboxylate interactions involved in 2-OG binding. In the KDM4 2-OG-binding site, the hexadentate Fe(II) complex is chelated by the pyridinyl N-atom and phenolic hydroxyl moieties of IOX1. The 5-carboxylate moiety forms ionic and H-bonds with K206 and Y132 (**Figure 6.2c**). In addition, IOX1 exhibits π -stacking between the quinoline ring motif and residue F185.³⁹⁷ Although IOX1 has shown inhibitory activity against KDM3, KDM5 and KDM6 enzymes, it has paved the way to developing more selective and cell-permeable inhibitors. ML324 is a cell-permeable KDM4 inhibitor (**Figure 6.2a**); however, its selectivity to KDM4 over other JmjC KDMs has not yet been established. Structure-activity relationship (SAR) studies revealed that while the carboxyl group at the C5 position in IOX1 increases potency, it reduced cell permeability. In contrast, ML324, which contains a para-substituted benzamide linker with an amine tail increases cell-permeability without compromising potency or stability.³⁹⁸ Another analogue, the *n*-octyl-IOX1 ester (**Figure 6.2a**), has increased cell permeability compared to IOX1, but inhibits KDM2, KDM3, KDM4 and KDM6 with comparable potencies to KDM4. Thus, it has been proposed that increasing the length of the alkyl chain is likely to increase the binding affinity to the hydrophobic region leading to the active site.³⁷⁹ However, it must be noted increasing lipophilicity generally increases non-selective interactions and decreases ligand efficiency.³⁹⁹ Therefore, increasing hydrophobicity of the compound is not an ideal way of increasing binding.

The most recent cell-permeable and selective KDM4 inhibitor QC6352 was based on 2,4-PDCA. QC6352 is 7 to 40 times more selective to KDM4 over KDM2, KDM3, KDM5, KDM6 and KDM7 enzymes. Co-crystal structures of QC6352 and KDM4C show that the carboxyl motif forms H-bonds with residues Y132 and K206, while the pyridinyl N-atom ligates Fe(II) ion (**Figure 6.2d**). Moreover, π -stacking occurs between the pyridine motif and F185.³⁸⁰

Given the lack of orthogonal and cell permeable KDM4 inhibitors, we used AlphaScreen technology to establish a KDM4 inhibition assay. This assay was then used to screen a library of compounds synthesised by the team of Prof. Adam McCluskey

(University of Newcastle) in order to identify new lead molecules for the development of KDM4 inhibitors. These compounds were selected from an existing library based on *in silico* docking studies.

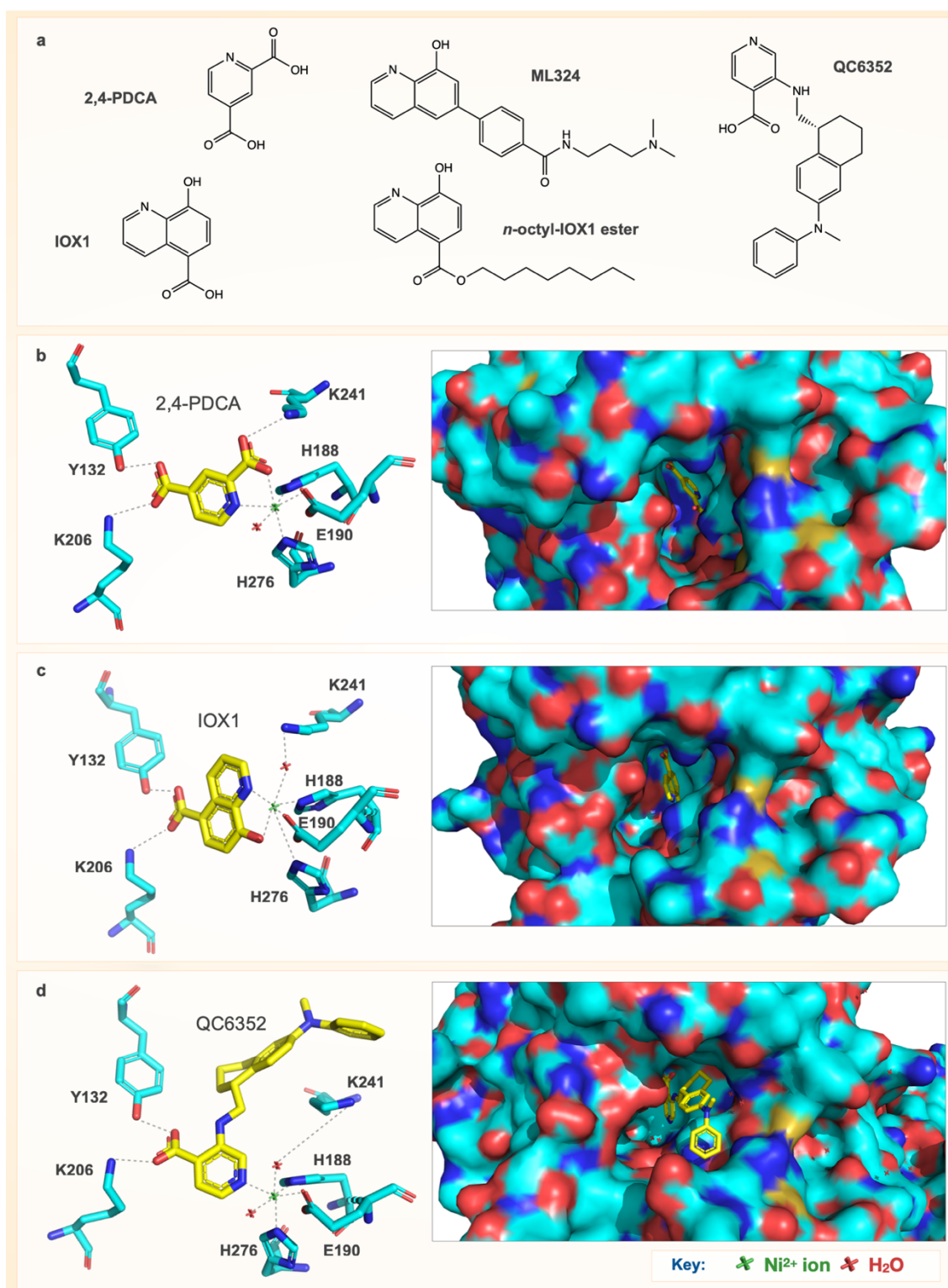


Figure 6.2 Binding sites of KDM4 inhibitors.

Co-crystal structures of (a) 2,4-PDCA bound to KDM4A (PDB: 2VD7), (b) IOX1 bound to KDM4A (PDB: 3NJY) and (c) QC6352 bound to KDM4C (PDB: 5VGI). Non-covalent bonds are displayed as dashed lines. Note that Ni(II) is used as a surrogate ion for Fe(II) in co-crystal structures. Molecular models created using PyMOL (Schrödinger).

6. 1. 2. The principle of AlphaScreen technology

AlphaScreen (Amplified Luminescence Proximity Homogenous Assay Screen) is one of the most versatile throughput technologies used in drug discovery. AlphaScreen assays rely on the non-enzymatic shuffling of singlet oxygen species from Donor beads to nearby Acceptor beads upon photoexcitation at 680 nm. The acceptor beads, in turn, emit a detectable chemiluminescence signal at 520-620 nm.⁴⁰⁰

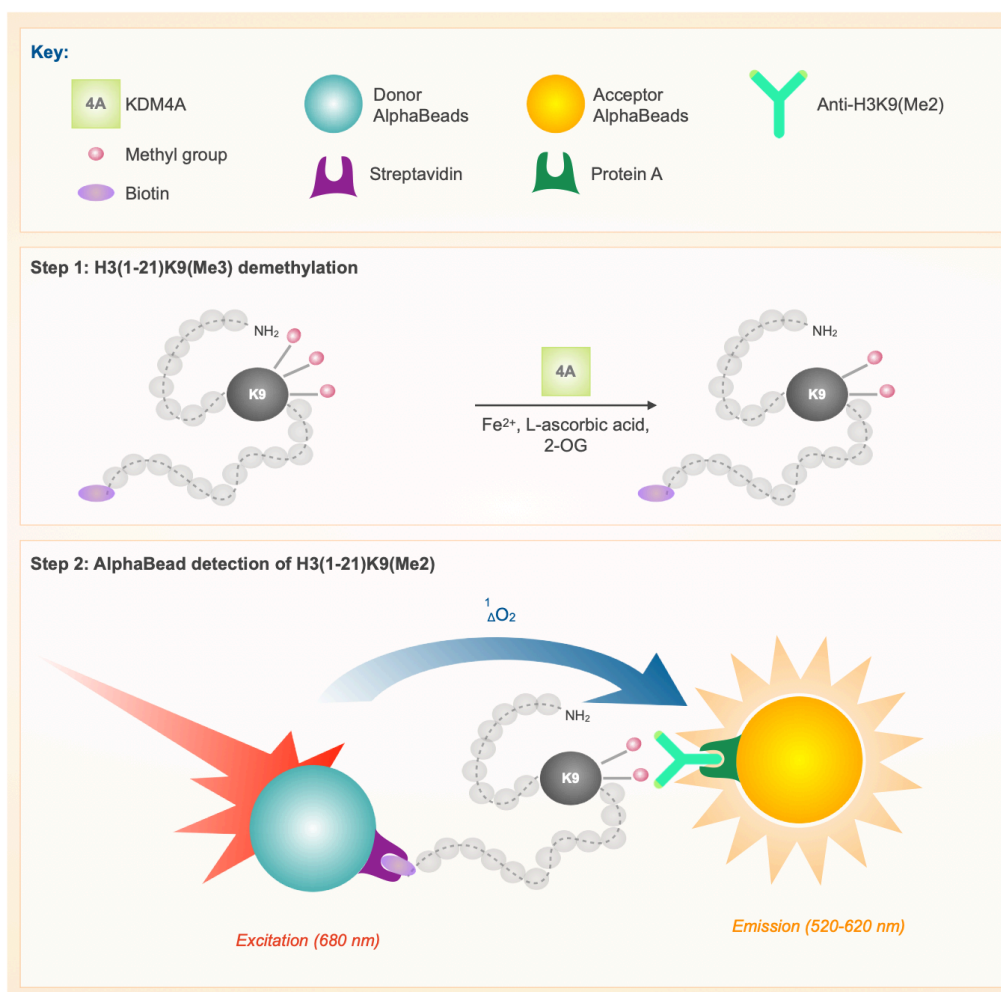


Figure 6.3 Measuring KDM4A demethylase activity using AlphaScreen technology.

H3K9(Me3)-biotin is demethylated by KDM4A in the presence of Fe²⁺, L-ascorbic acid and 2-OG. The H3K9(Me2)-biotin product binds to donor beads. Anti-H3K9(Me2) recognises the H3K9(Me2)-biotin product and, in turn, is sequestered by protein A on acceptor beads. Once the peptide brings the beads in proximity and upon excitation at 680 nm, a singlet oxygen species is transferred from the donor to the acceptor beads, emitting a chemiluminescence signal at 520-620 nm.

Acceptor and donor beads are brought together in close proximity by the presence and co-recognition of an analyte of interest.⁴⁰⁰ In the present assay, we aimed to measure the basal activity of a recombinant KDM4A enzyme in demethylating a synthetic histone H3 peptide that spans residues 1-21 and is tri-methylated at K9. The

rate of conversion of H3K9(Me3) to H3K9(Me2) by KDM4A was assessed, and hence, our analyte of interest is H3K9(Me2). The donor beads are conjugated with streptavidin, and the acceptor beads with protein A, to facilitate co-recognition of the analyte. The H3K9(Me3) synthetic peptide is biotinylated, and hence, biotin motif binds to streptavidin on donor beads. Protein A on acceptor binds to any IgG antibodies, and so, an H3K9(Me2) antibody used in AlphaScreen assays by other teams⁴⁰⁰ was employed.

In the presence of the cofactors Fe(II), L-ascorbic acid and 2-OG, KDM4A converts H3K9(Me3)-biotin to H3K9(Me2)-biotin. The antibody recognises the analyte and brings beads in proximity, generating a chemiluminescence signal (**Figure 6.3**). In the presence of an active inhibitor, the amount of H3K9(Me2) relative to the control is reduced, allowing the assessment of KDM4A inhibition potencies of tested compounds.³⁷⁹

6. 2. Results

6. 2. 1. Peptide and antibody validation

As AlphaScreen beads, biotinylated-peptides and IgG antibodies differ from batch-to-batch,⁴⁰¹ every AlphaScreen assay necessitate optimisation. Hence, a series of experiments were carried out to validate different components of a KDM4A AlphaScreen assay adapted from a previously published study.⁴⁰²

LC-MS analysis of H3K9(Me3)-biotin peptide. The expected (2764.2 g/mol) corresponded to the observed (2764.6 g/mol) molecular masses, as shown in the deconvoluted spectra of observed peaks (**Figure 6.4a**). To assess peptide integrity and antibody selectivity, dot blot analysis of H3K9(Me3)-biotin was performed at eight-point serial dilutions (1 μ L drops, 0-1000 nM). Membranes were probed with antibodies against H3K9(Me1), H3K9(Me2) and H3K9(Me3). As expected, H3K9(Me1) antibody failed to detect any signal even at the highest concentration. The H3K9(Me2) antibody showed concentration-dependent cross-reactivity against the H3K9(Me3) peptide. However, the selectivity of the H3K9(Me3) antibody to the H3K9(Me3) peptide was superior compared to that of the H3K9(Me2) antibody at every concentration (**Figure 6.4b**).

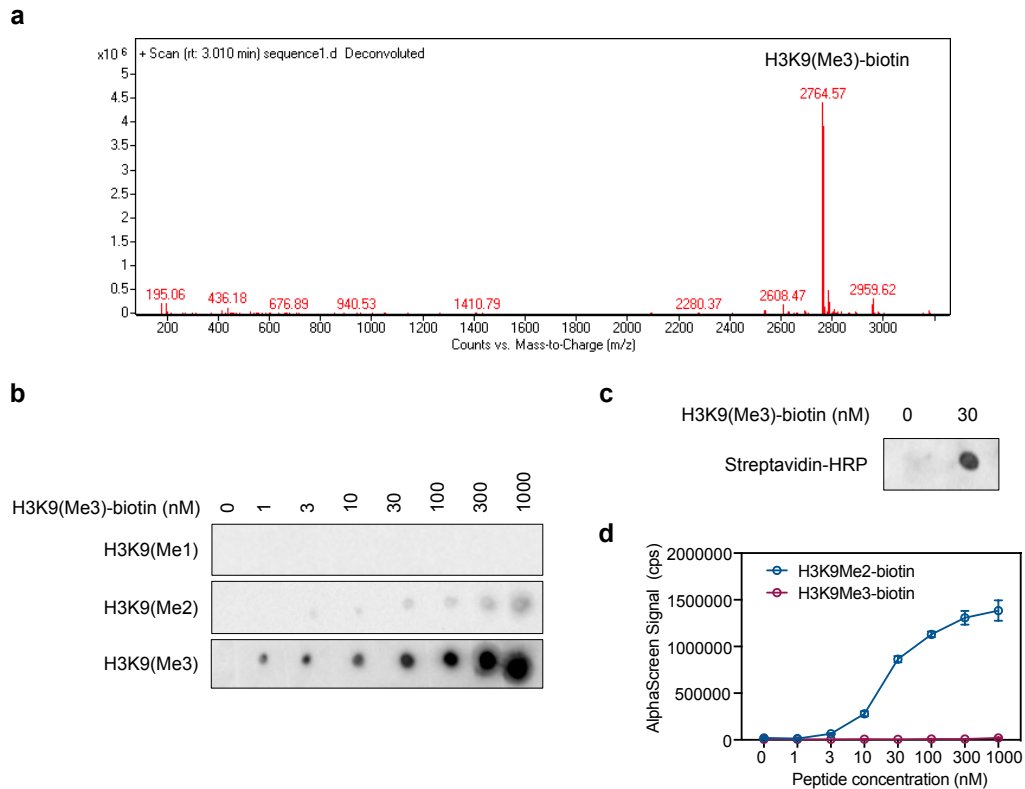


Figure 6.4 Validating H3K(1-21) K9(Me3)-biotin peptide and antibody specificity.

(a) Mass spectrum of H3K9(Me3)-biotin peptide confirms expected molecular mass (2764 g/mol). (b) Dot blots of 1 μ L droplets of increasing concentrations (0-1000 nM) of H3K9(Me3)-biotin peptide. Membranes probed with antibodies against mono-, di- and trimethylated H3K9 to confirm peptide selectivity. (c) Dot blots of H3K9(Me3)-biotin peptide (30 nM) blotted with streptavidin-HRP to confirm peptide biotinylation. Representative images of two independent experiments are shown. (d) AlphaScreen beads were incubated with H3K9(Me2) antibody (0.03 g/mL) and increasing concentrations (0-1000 nM) of either the H3K9(Me2)-biotin or H3K9(Me3)-biotin peptides. Data are mean \pm SEM of raw values (n=2).

Next, to assess biotinylation of the peptide, we blotted 1 μ L drops of 0 or 30 nM of the H3K9(Me3)-biotin peptide on PVDF membranes. This concentration was chosen as it is the same concentration of the peptide used in the AlphaScreen assay. The membranes were probed with streptavidin-HRP. As streptavidin binds to biotin, the biotinylated peptide gave a measurable signal compared to the control (0 nM) (Figure 6.4c). Lastly, to demonstrate the specificity of the H3K9(Me2) antibody, synthetic H3K9(Me2)-biotin and H3K9(Me)-biotin peptides were titrated with AlphaScreen beads and H3K9(Me2) antibody. At concentrations as high as 1000 nM, the H3K9(Me2)-biotin peptide consistently generated greater counts per minute (cpm) than H3K9(Me3)-biotin (Figure 6.4d). In summary, we confirmed that the H3K9(Me3) peptide (used as a KDM4 substrate) is of correct molecular mass, is selectively recognised by the H3K9(Me3) antibody and is biotinylated. We also confirmed that the H3K9(Me2)-biotin peptide (catalytic product

of KDM4) is, in the context of AlphaScreen assay conditions, selectively recognised by H3K9(Me2) antibody.

6. 2. 2. KDM4 enzyme validation

A plasmid construct encoding KDM4A residues 1-359, provided by Prof. Paul Brennan (University of Oxford, UK) was used to produce recombinant KDM4A enzyme at the Sydney Analytical core facility. Briefly, the plasmid was amplified by PCR and transformed into *E. coli* BL21 (DE3). KDM4A enzyme was extracted from cells and purified by nickel-affinity and size-exclusion chromatography. A KDM4 fraction was further purified using anion-exchange columns (detailed protocol in **Appendix**).

The expected molecular mass of the recombinant KDM4 is 44 kDa. To confirm the molecular mass of KDM4A, we performed RapidFire mass spectrometry on two fractions separated by the anion-exchange purification step (KDM4A-Pur1 and KDM4A-Pur2). We also obtained a sample of KDM4A enzyme (KDM4A-Oxford) derived from the same plasmid construct and purified by our collaborators Prof. Christopher Schofield and Dr. Anthony Tumber (University of Oxford, UK). All three KDM4 samples were compared to a commercially available recombinant KDM4A enzyme designed for AlphaScreen assays by BPS Bioscience (KDM4-BPS). The KDM4-BPS enzyme was produced from a plasmid construct encoding residues 1-350, and its expected molecular mass is 42 kDa. Equal amounts of all KDM4 samples were analysed by RapidFire mass spectrometry. The observed molecular masses of the KMD4A-Pur1, KDM4A-Pur2 and KDM4-Oxford matched their expected molecular mass (44 kDa) as evident from the deconvoluted spectra (**Figure 6.5a**). However, while the KDM4-BPS enzyme had a prominent peak at the expected molecular mass (42 kDa), it also had an impurity at 44 kDa (**Figure 6.5b**).

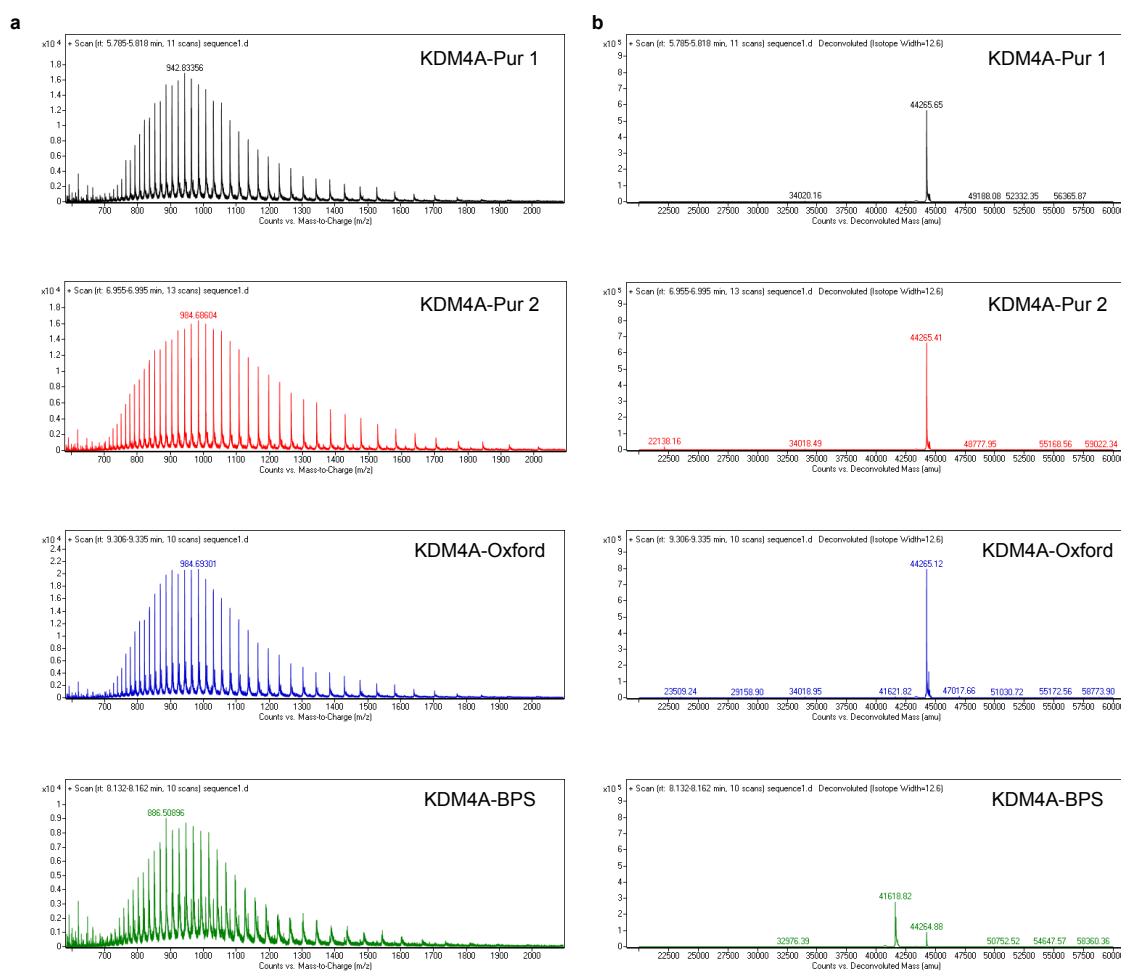


Figure 6.5 Assessing the integrity of KDM4A preparations.

Recombinant KDM4A enzymes (188 nM) were analysed by RapidFire-MS. (a) Raw data and (b) deconvoluted spectra acquired from the four recombinant KDM4A enzyme preparations.

Next, we used RapidFire mass spectrometry to evaluate the demethylase activity of recombinant KDM4 enzymes using the H3K9(Me3) peptide. Mass spectra for the substrate H3K9(Me3)-biotin and the product H3K9(Me2)-biotin were monitored in real-time at every 3.5 min. The percentage of the demethylated product at any given time point was calculated by dividing the peak area of the product peptide by the sum of the peak areas of both the substrate and product peptides. Demethylation (%) was plotted as a function of time and KDM4A enzyme kinetics were assessed (Figure 6.6). KDM4A-Pur2 and KDM4-Oxford were the most active KDM4 preparations, both demethylating 45-50% of the substrate H3K9(Me3) within 60 min. KDM4A-Pur1 was less active, reaching a 40% conversion rate in 60 min. KDM4A-BPS was the least active, showing minimal demethylase activity. In addition to containing an impurity, the lack of activity indicates that the integrity of the enzyme had been compromised (< 20% demethylation in 60 min).

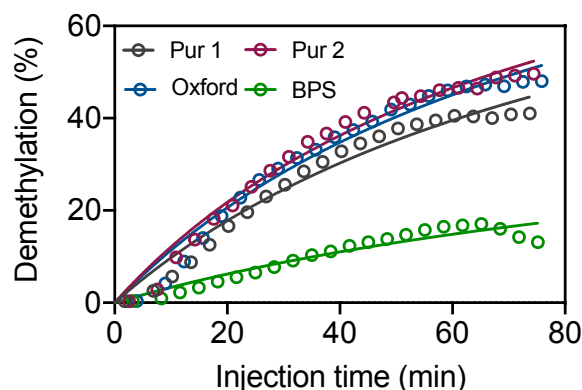


Figure 6.6 Assessing the activity of KDM4A enzymes by RapidFire mass spectrometry.

Four recombinant KDM4A (188 nM) activity was assessed by RapidFire-MS. Reaction was initiated by the addition of the substrate H3K9(Me3)-biotin (60 μ M) and the cofactors Fe²⁺ (60 μ M), L-ascorbic acid (600 μ M) and 2-OG (60 μ M) for 75 min. Extracted ion chromatograms for the trimethyl substrate and the dimethyl product were integrated using the RapidFire Integrator software (Agilent). The amount of demethylation (%) at each time-point was calculated as the peak of the dimethyl product divided by the sum of peak areas of the product and substrate. Data represent one experiment performed in triplicates.

6. 2. 3. AlphaScreen assay validation

Having verified the structural and functional integrities of substrate H3K9(Me3) and the KDM4 enzymes, we performed the KDM4A demethylation assay followed by AlphaScreen detection. We used varying concentrations (0.01-0.03 μ g/mL) of H3K9(Me2) antibody to determine the best signal-to-noise ratio (Figure 6.7). The highest signal-to-noise ratio was observed when H3K9(Me2) antibody was employed at 0.07 μ g/mL concentration. This H3K9(Me2) antibody concentration was used for all subsequent AlphaScreen assays.

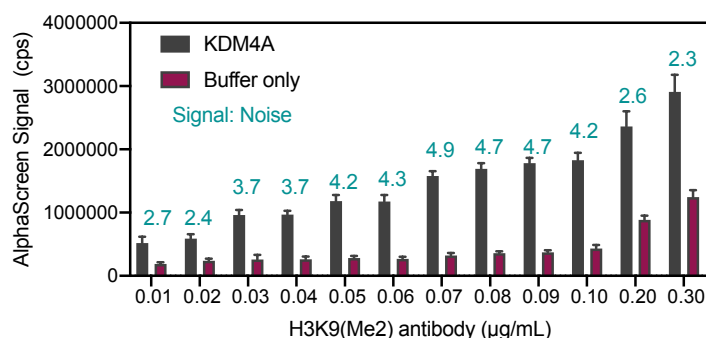


Figure 6.7 Determining the optimal H3K9(Me2) antibody concentration.

AlphaScreen beads were pre-incubated with H3K9(Me2) antibody (0.01-0.20 μ g/mL). Recombinant KDM4A (3 nM) was incubated with H3K9(Me3)-biotin peptide (30 nM) and the cofactors 2-OG (10 μ M), Fe²⁺ (1 μ M) and L-ascorbic acid (100 μ M) for 20 min. Signals were detected after incubation with AlphaScreen beads and H3K9(Me2) antibody. Data represent mean \pm SEM (n=3).

To validate the KDM4 inhibition assay, we determined IC_{50} values for pan-KDM inhibitors 2,4-PDCA and IOX1 and KDM4 inhibitor QC6352; and compared our values to published IC_{50} values, which were also obtained using KDM4 AlphaScreen assay with similar substrate-to-enzyme ratios and cofactor concentrations. We obtained IC_{50} values of 297 nM and 280 nM for 2,4-PDCA and IOX1, respectively (Figure 6.8a). These values are comparable to previously published values (Table 6.1). However, in our hands, QC6352 was almost ten times less potent in inhibiting KDM4 (IC_{50} 9.7 μ M, Figure 6.8a) when compared to previously published values (IC_{50} = 35-104 nM, Table 6.1).³⁷⁸⁻³⁸⁰

Given that these published values were determined in a KDM4 inhibition assay using 0.02% BSA as blocking agent,³⁸⁰ whereas we used 0.1% BSA (in line with methodology in REF⁴⁰²), we tested the potency of the inhibitors in KDM4A inhibition assays using 0.2% BSA in the final buffer. Reducing the BSA concentration slightly decreased the IC_{50} values of 2,4-PDCA to 113 nM and IOX1 to 78 nM, implicating that BSA concentration has little impact on the potency of these two KDM4 inhibitors. Nevertheless, decreasing the BSA concentration considerably reduced the IC_{50} of QC6352 from 9.7 μ M (0.1% BSA, Figure 6.8a) to 0.3 μ M (0.02% Figure 6.8b). Given the impact of BSA on the potency of some KDM4 inhibitors, subsequent assays were carried out at 0.2% BSA.

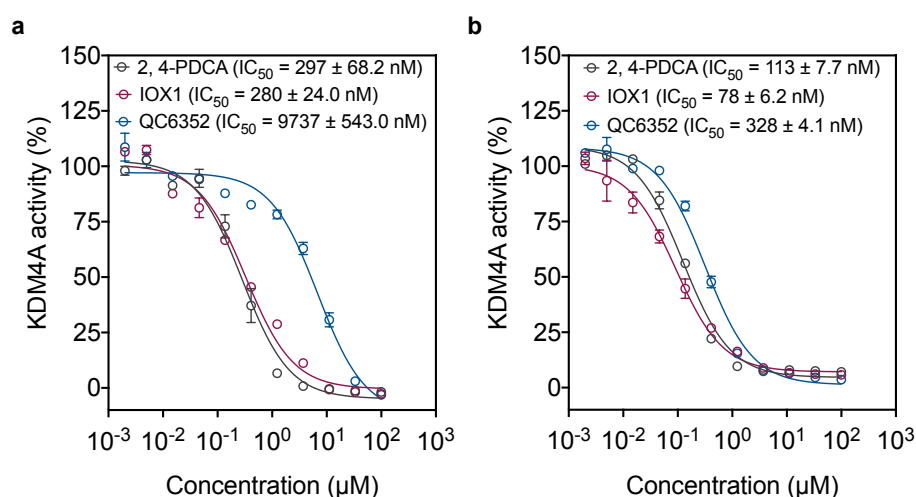


Figure 6.8 Effect of BSA on KDM4A inhibition by QC6352.

2,4-PDCA, IOX1 and QC6352 were tested for KDM4A inhibition in AlphaScreen assay buffer containing (a) 0.1% (w/v) and (b) 0.02% (w/v) BSA. Compounds (10-point serial dilutions) were pre-incubated with recombinant KDM4A (3 nM) for 15 min. The demethylation reaction was initiated by the addition of the H3K9(Me3)-biotin peptide (30 nM) and the cofactors 2-OG (10 μ M), Fe²⁺ (1 μ M) and L-ascorbic acid (100 μ M) and incubated for 20 min. Signals were detected after incubation with AlphaScreen beads and H3K9(Me2) antibody (0.07 μ g/mL). Data are mean \pm SEM (n = 3-6).

In summary, we have validated the KDM4 AlphaScreen assay and have obtained IC₅₀ values for three KDM4 inhibitors comparable with previously published data (Figure 6.8b, Table 6.1).

Table 6.1 IC₅₀ values of KDM4 inhibitors using AlphaScreen assays.

Inhibitor	KDM4A IC ₅₀	Published KDM4 IC ₅₀
2,4-PDCA	297 ± 68.2 nM	200-900 nM ³⁹⁰
IOX1	280 ± 24.0 nM	200-600 nM ^{363, 365}
QC6352	328 ± 4.1 nM	35-104 nM ³⁷⁸⁻³⁸⁰

6. 2. 4. Screening for hit molecules to develop KDM4 inhibitors

A library of 46 analogues (provided by Dr. Jennifer Baker and Professor Adam McCluskey, University of Newcastle) was screened for KDM4A inhibition. These analogues contained benzothiazinone (1-10), methyl-benzothiazinone (11-19), benzoxazinone (20-29), dimethylaminopropyl-benzoxazinone (30-35), quinazolinone (36-44), imidazoquinazolinone (45) or benzoxazinone-dione (46) heterocyclic cores (Figure 6.9). All compounds were screened at 1 and 20 μM, and their potency to inhibit KDM4 was compared to uninhibited KDM4 activity (set as 100%).

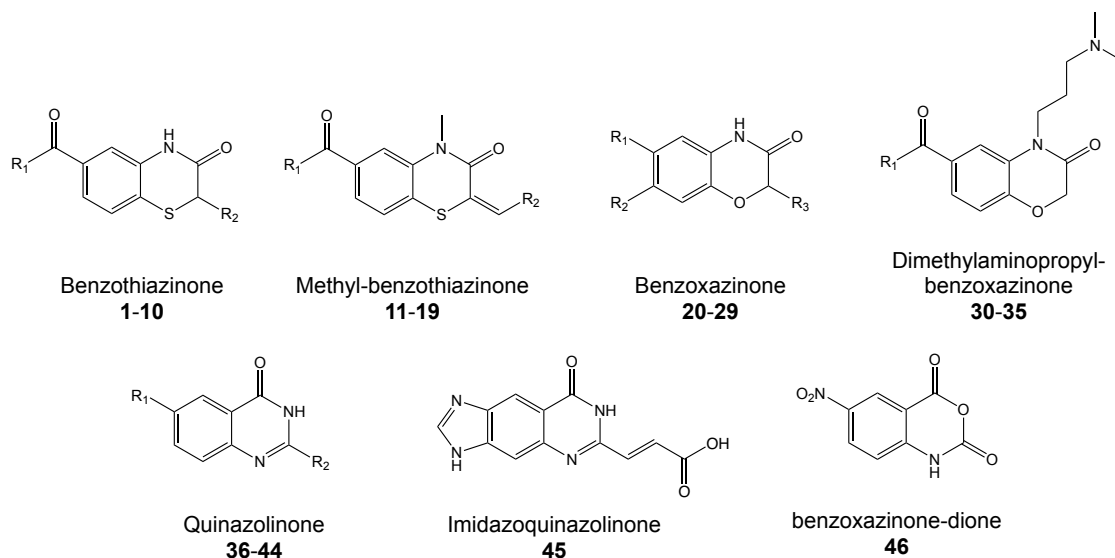


Figure 6.9 Heterocyclic core structures of compounds screened for KDM4 inhibition.

In the series of benzothiazinone analogues **1-10** (Table 6.2), only compound **4** inhibited KDM4A, with residual KDM4 activity at 20 μM being 22.5%. Other benzothiazinone analogues failed to inhibit KDM4 activity. Unlike other analogues, compound **4** contains a propyl-dimethylamino side chain, suggesting this motif is an important part of the pharmacophore.

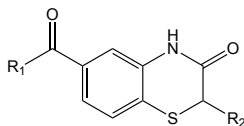
None of the methyl-benzothiazinone analogues **11-19** (Table 6.3) inhibited KDM4A by more than 30 % at 20 μM . Compounds **5** and **11** only differ due to the latter containing a methyl group on the benzothiazinone core; however, the residual KDM4A activity at 20 μM is 68% and 99%, respectively. Therefore, a single methyl group on the heterocyclic ring structure reduces inhibition. On the other hand, benzoxazinones **20-29** (Table 6.4) showed a slightly improved inhibition of KDM4A. Compound **29**, containing an ethyl acetamide at the R₁ side chain and a 3-dimethylaniline at the R₂ side chain, reduced KDM4 activity to 55.5% when used at 20 μM .

The dimethylaminopropyl-benzoxazinone analogues **30-35** (Table 6.5) contained the most potent inhibitors against KDM4A. Notably, these analogues contain the propyl-dimethylamino side chain found in compound **4** within the benzothiazinone series. Replacement of the carboxylic acid group in the R₁ side chain in compound **30** with an amide functionalised with a cinnamyl group in compound **31** did not increase inhibition of KDM4A. Importantly, methylation of the terminal phenyl yielded compound **32** that reduced KDM4A activity to 65.4% when used at 1 μM and to 1.7% when used at 20 μM . Addition of a methoxy moiety in compound **33** caused minor loss of potency in inhibiting KDM4A. Substitution of the terminal phenyl with an indole group in analogue **34**, and the bromo-indole analogue **35**, used at 20 μM , reduced KDM4A activity to 2% and 6.3%, respectively. Both analogues inhibited KDM4 by approximately 50% when used at 1 μM .

None of the quinazolinone **36-44**, imidazoquinazolinone **45** and benzoxazine-dione **46** analogues inhibited KDM4A by more than 50% at 20 μM , indicating that these core structures are not suitable for KDM4 inhibition (Table 6.6, Table 6.7).

Table 6.2 Inhibition of KDM4A activity by benzothiazinone analogues 1-10.

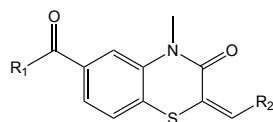
Compounds (1 or 20 μM) were pre-incubated with recombinant KDM4A enzyme (3 nM) for 15 min. The reaction was initiated by the addition of H3K9(Me3)-biotin peptide (30 nM) and cofactors 2-OG (10 μM), Fe^{2+} (1 μM) and L-ascorbic acid (100 μM) for 20 min. Signals were detected after incubation with AlphaScreen beads and H3K9(Me2) antibody (0.07 $\mu\text{g}/\text{mL}$) for 1 h. Data are mean \pm SEM (n=2).



Compound	R ₁	R ₂	KDM4A activity (%) at 1 μM	KDM4A activity (%) at 20 μM
1			74.5 \pm 3.85	75.0 \pm 2.73
2			81.8 \pm 3.95	90.8 \pm 9.56
3			88.6 \pm 4.09	110.2 \pm 5.47
4			101.7 \pm 7.44	22.5 \pm 5.33
5			76.4 \pm 1.89	68.3 \pm 6.86
6			87.7 \pm 5.87	113.5 \pm 5.28
7			91.0 \pm 5.29	108.2 \pm 2.61
8			109.83 \pm 2.40	68.6 \pm 2.52
9			97.0 \pm 4.03	99.8 \pm 3.08
10			95.7 \pm 7.26	89.3 \pm 4.72

Table 6.3 Inhibition of KDM4A activity by methyl-benzothiazinone analogues 11-19.

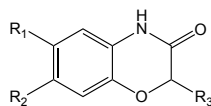
Compounds (1 or 20 μM) were pre-incubated with recombinant KDM4A enzyme (3 nM) for 15 min. The reaction was initiated by the addition of H3K9(Me3)-biotin peptide (30 nM) and cofactors 2-OG (10 μM), Fe^{2+} (1 μM) and L-ascorbic acid (100 μM) for 20 min. Signals were detected after incubation with AlphaScreen beads and H3K9(Me2) antibody (0.07 $\mu\text{g}/\text{mL}$) for 1 h. Data are mean \pm SEM (n=2).



Compound	R ₁	R ₂	KDM4A activity (%) at 1 μM	KDM4A activity (%) at 20 μM
11			78.8 \pm 8.24	117.7 \pm 15.17
12			79.0 \pm 7.44	99.2 \pm 7.73
13			81.4 \pm 9.50	126.0 \pm 17.09
14			101.0 \pm 6.08	104.7 \pm 6.75
15			98.5 \pm 4.90	79.3 \pm 1.36
16			101.3 \pm 2.49	141.0 \pm 6.30
17			83.0 \pm 4.31	77.0 \pm 6.67
18			78.0 \pm 5.23	68.3 \pm 2.70
19			78.3 \pm 7.38	87.8 \pm 3.09

Table 6.4 Inhibition of KDM4A activity by benzoxazinone analogues 20-29.

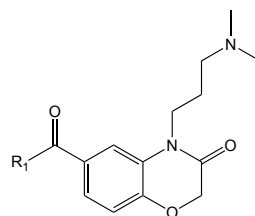
Compounds (1 or 20 μM) were pre-incubated with recombinant KDM4A enzyme (3 nM) for 15 min. The reaction was initiated by the addition of H3K9(Me3)-biotin peptide (30 nM) and cofactors 2-OG (10 μM), Fe^{2+} (1 μM) and L-ascorbic acid (100 μM) for 20 min. Signals were detected after incubation with AlphaScreen beads and H3K9(Me2) antibody (0.07 $\mu\text{g}/\text{mL}$) for 1 h. Data are mean \pm SEM (n=2).



Compound	R ₁	R ₂	R ₃	KDM4A activity (%) at 1 μM	KDM4A activity (%) at 20 μM
20				79.0 \pm 6.92	73.3 \pm 4.91
21				81.0 \pm 3.46	79.5 \pm 2.67
22				113.8 \pm 9.18	106.8 \pm 5.20
23				75.6 \pm 1.17	68.3 \pm 1.45
24				84.3 \pm 6.71	77.0 \pm 7.28
25				83.2 \pm 5.10	79.5 \pm 5.67
26				83.0 \pm 14.57	81.0 \pm 9.26
27				85.3 \pm 3.25	80.8 \pm 7.75
28				81.0 \pm 3.49	62.8 \pm 11.21
29				72.0 \pm 4.57	55.5 \pm 5.65

Table 6.5 Inhibition of KDM4A activity by dimethylaminopropyl-benzoxazinone analogues 30-35.

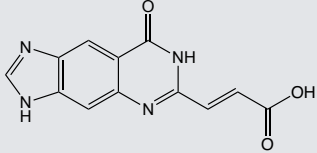
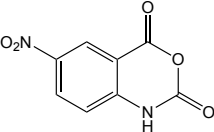
Compounds (1 or 20 μM) were pre-incubated with recombinant KDM4A enzyme (3 nM) for 15 min. The reaction was initiated by the addition of H3K9(Me3)-biotin peptide (30 nM) and cofactors 2-OG (10 μM), Fe^{2+} (1 μM) and L-ascorbic acid (100 μM) for 20 min. Signals were detected after incubation with AlphaScreen beads and H3K9(Me2) antibody (0.07 $\mu\text{g}/\text{mL}$) for 1 h. Data are mean \pm SEM (n=2).



Compound	R ₁	KDM4A activity (%) at 1 μM	KDM4A activity (%) at 20 μM
30		87.5 \pm 3.42	74.5 \pm 11.16
31		99.3 \pm 3.43	88.7 \pm 6.75
32		65.4 \pm 5.24	1.7 \pm 0.76
33		84.7 \pm 3.38	15.5 \pm 2.59
34		53.2 \pm 3.26	2.0 \pm 0.37
35		48.7 \pm 4.42	6.3 \pm 0.61

Table 6.7 Inhibition of KDM4A activity by analogues 45-46.

Compounds (1 or 20 μM) were pre-incubated with recombinant KDM4A enzyme (3 nM) for 15 min. The reaction was initiated by the addition of H3K9(Me3)-biotin peptide (30 nM) and cofactors 2-OG (10 μM), Fe^{2+} (1 μM) and L-ascorbic acid (100 μM) for 20 min. Signals were detected after incubation with AlphaScreen beads and H3K9(Me2) antibody (0.07 $\mu\text{g}/\text{mL}$) for 1 h. Data are mean \pm SEM (n=2).

Compound	Structure	KDM4A activity (%) at 1 μM	KDM4A activity (%) at 20 μM
45		72.0 \pm 2.68	49.5 \pm 4.35
46		100.6 \pm 4.83	97.5 \pm 3.70

In summary, methyl-benzothiazinone **11-19**, quinazolinone **36-44**, imidazoquinazolinone **45** and benzoxazine-dione **46** analogues failed to inhibit KDM4 by more than 50% when used at 20 μM concentration, indicating that these core structures are not suitable for development of KDM4 inhibitors. Conversely, compounds **4**, **32**, **33**, **34** and **35** inhibited KDM4 by more than 50% when used at 20 μM , with several showing inhibition at 1 μM concentration.

6. 2. 5. Establishing KDM4 potency of hit compounds

To cross-validate the identified hits with greater than 50% KDM4A activity inhibition at 20 μM and determine their IC_{50} , we measured KDM4A activity following treatment with compounds **4**, **32**, **33**, **34** and **35** at ten-point serial dilutions (Figure 6.10). QC6352 was used as a positive control with each independent repeat. In terms of potency, **35** has the lowest IC_{50} (1.7 μM), followed by **32** (9.2 μM), while the **4**, **33** and **34** which all had high micromolar range potencies (18-25 μM).

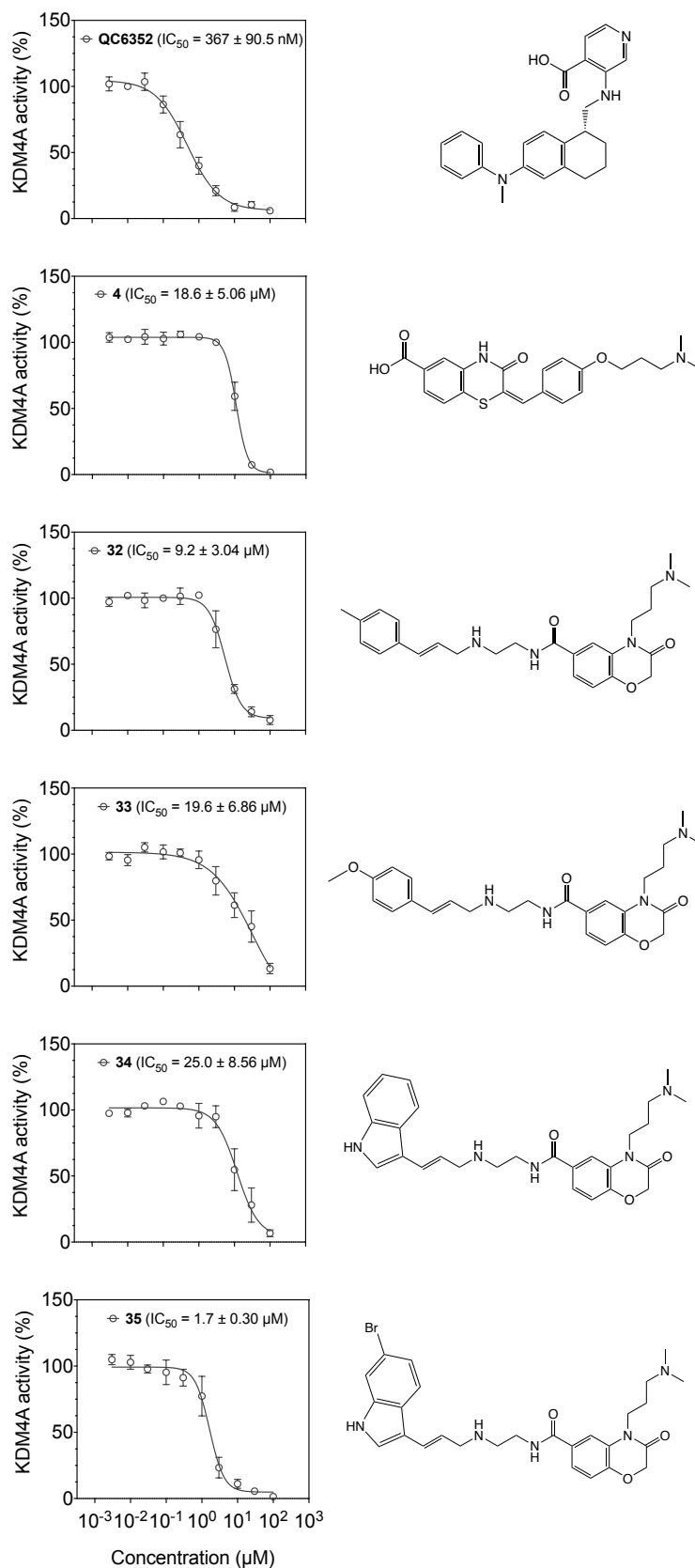


Figure 6.10 IC_{50} values of identified KDM4A inhibitor hits.

Compounds (tested at 10-point serial dilutions) were pre-incubated with recombinant KDM4A enzyme (3 nM) for 15 min. The demethylation reaction was initiated by the addition of the H3K9(Me3)-biotin peptide (30 nM) and the cofactors 2-OG (10 μM), Fe^{2+} (1 μM) and L-ascorbic acid (100 μM) and incubated for 20 min. Signals were detected after incubation with AlphaScreen beads and H3K9(Me2) antibody (0.07 $\mu\text{g}/\text{mL}$). Data are mean \pm SEM (n=3-6).

6. 3. Discussion

We successfully established the KDM4A AlphaScreen activity assay and identified two novel hits in the screened library. The compounds screened provide further insight into the binding pockets of KDM4A and a steppingstone for fragment docking and linking to develop better inhibitors. The same strategy was employed during the development of QC6352: analysis of two fragments models, 5-carboxypyridine and 5-amino-salicylate, was used to develop a fusional novel potent KDM4 inhibitor.³⁸⁰

In general, KDM4A inhibition by benzoxazinones **30-35** was greater than that of benzothiazinones **1-10**, indicating that an O-atom, rather than an N-atom, in the heterocyclic core is more suited for the pharmacophore. A common factor between the five hits, of benzothiazinone **4** and benzoxazinones **32-35**, is the presence of the propyl-dimethylamino group, indicating that this motif contributes to stronger inhibition. The propyl-dimethylamino group is likely to be protonated at physiological pH, increasing the number of H-bonds with KDM4A.

Molecular docking analysis (performed by Dr. Jennifer Baker) of hits **4** and **32-35** to KDM4A provided insight into the binding of these analogues (Figure 6.11). All five compounds lose key H-bonds with Y132 and K206, which are observed in the binding of 2,4-PDCA, IOX1 and QC6352 to KDM4 enzymes. Benzothiazinone **4** ligates Fe(II) via the carboxylic motif. On the other hand, benzoxazinones **32-35** ligate Fe(II) via the dimethyl-propylamine group. An additional H-bond is observed between the bromine atom and K241 in **35**, which explains why this hit molecule was the most potent against KDM4A. X-ray co-crystal structures and further SAR studies are required to confirm the binding site.

While compound **4** inhibited KDM4 activity, it will not be considered for further development. The compound contains several problematic functional groups which are reactive and may interfere with AlphaScreen technology. For instance, the sulphur atom is likely to oxidise at physiological conditions. Furthermore, the α - β unsaturated amide moiety is reactive and could lead to Michael adduct with reactive amino-acid residues.

Importantly, a counter screen is required to validate the hits are not pan-assay interference compounds (PAINS) and/or false positives.⁴⁰³ The dose-dependent inhibition we observed with these compounds somewhat confirm the on-target effect; however, further confirmation is still needed.

In summary, the benzoxazinone analogues are suitable candidates for future hit-to-lead optimisation. The KDM4A AlphaScreen assay will be used to test newly synthesised analogues. The challenge lies within balancing the lipophilicity for cell membrane and blood-brain barrier permeability and the hydrophilicity for increasing H-bonds between inhibitor and ligand.^{380, 391} Nonetheless, strategic positioning of a limited number of heteroatoms has led to the development of many potent inhibitors, and therefore, molecule docking coupled with SAR studies will aid in the design of KDM4 inhibitors.

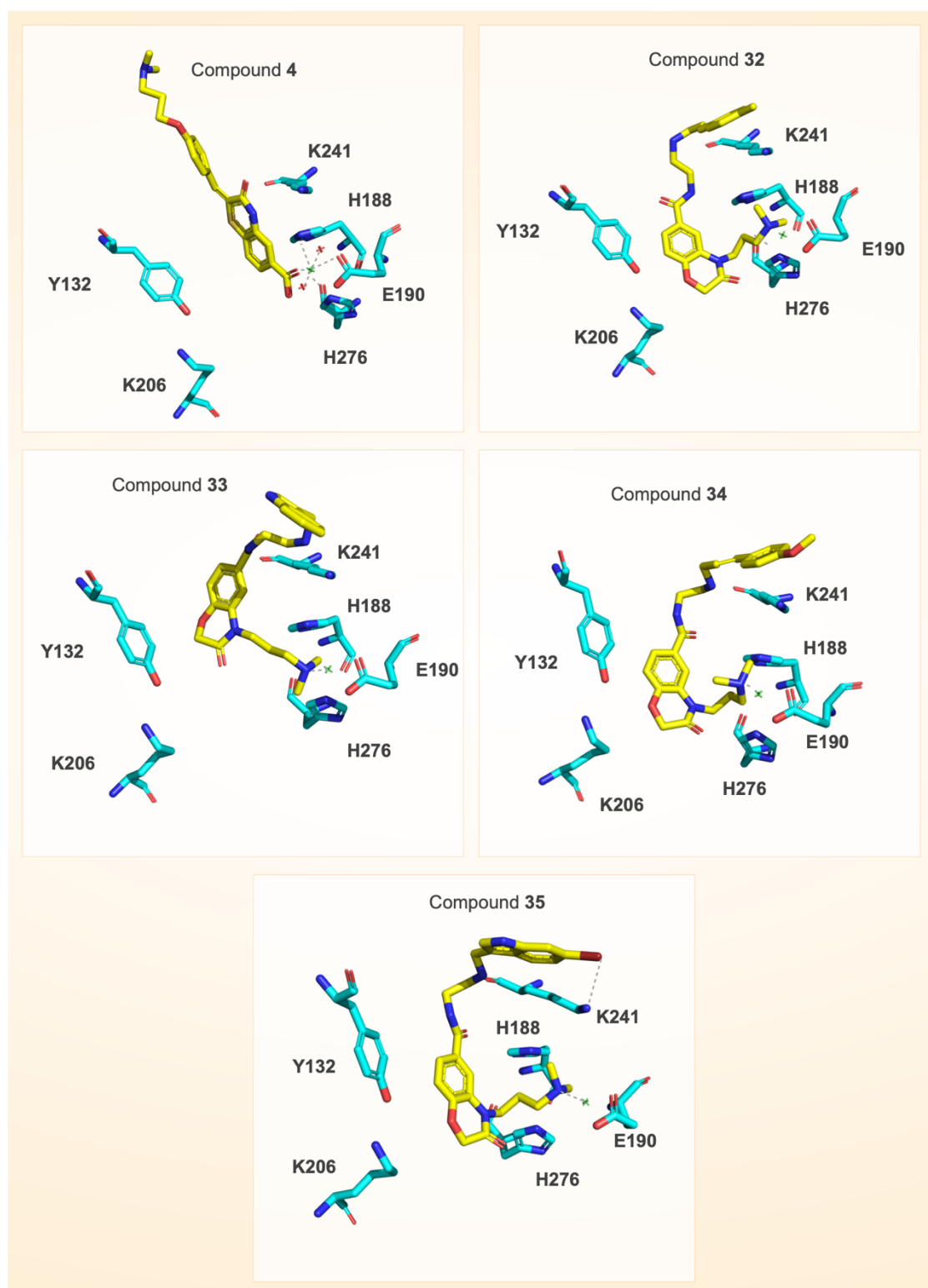


Figure 6.11 Hypothetical molecular docking of benzothiazinone and benzoxazinone.

Molecular docking analysis of hit compounds performed by Dr. Jennifer Baker. Non-covalent bonds are displayed as dashed lines. Molecular models created using PyMOL (Schrödinger).

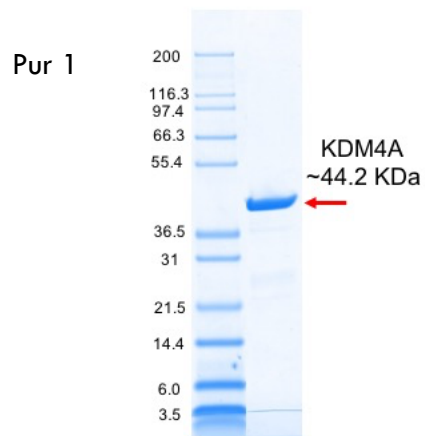
APPENDIX. KDM4A Protein Expression and Purification

A construct encoding KDM4A (JMJD2A) residues 1-359 was amplified by PCR from expressed sequence tag (EST) clone and cloned into pNIC289-Bsa4. The expression plasmid was transformed into phage-resistant derivative of *E. coli* BL21 (DE3) carrying the pRARE2 plasmid. 12 L of TB media containing kanamycin (50 µg/mL) and chloramphenicol (34 µg/mL) were inoculated with overnight culture (5 mL/L) and grown at 37 °C in baffled flasks. Expression was induced with Isopropyl-β-D-thiogalactoside (0.2 mM) at $A_{600} = 0.8$ and allowed to continue for 18 h at 18 °C. Bacterial cells were then collected by centrifugation and frozen at -80 °C. Frozen cell pellets were thawed and resuspended in lysis buffer which consisted of HEPES (50 mM, pH 7.5), NaCl (500 mM), imidazole (20 mM), TCEP (0.5 mM), PMSF (0.5 mM) and benzonase (15 units/mL). Cells were disrupted by high-pressure homogenisation followed by sonication and cell debris was removed by centrifugation.

Purification 1 (Pur 1): Recombinant KDM4A was purified by nickel-affinity (1 mL HisTrap FF crude) and size-exclusion chromatography (120 mL HiLoad 16/60 Superdex 200) on an AKTExpress system. The supernatant was loaded onto nickel-affinity column (0.8 mL/min), washed with 10 column volumes of lysis buffer, 50 column volumes lysis buffer with imidazole (40 mM), and then eluted with lysis buffer containing imidazole (250 mM). The A280 peak was automatically collected and loaded on the gel filtration column (1 mL/min) in HEPES (10 mM, pH 7.5), NaCl (500 mM), glycerol (5% v/v) and TCEP (0.5 mM). EDTA (1 mM) was added to pooled fractions overnight. Finally, the protein was exchanged in HEPES (10 mM, pH 7.5), NaCl (500 mM), glycerol (5% v/v) and TCEP (0.5 mM), concentrated to 25 mg/mL, flash frozen in liquid nitrogen and stored at -80 °C.

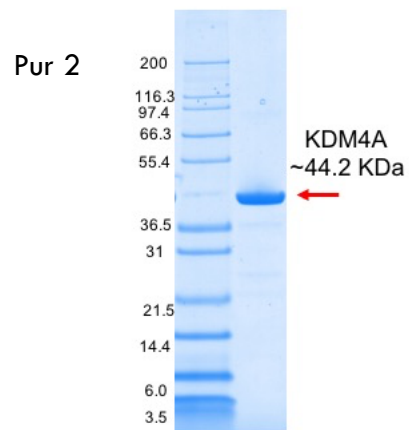
Purification 2 (Pur 2): Following gel filtration and dialysis, a fraction of the protein was further purified using an anion exchange column (5 mL HiTrap Q HP) developed with a gradient from 50-500 mM NaCl in Tris-HCl (50 mM, pH 8.5). All columns were supplied by GE Healthcare. Finally, the protein was exchanged in HEPES (10 mM, pH 7.5), NaCl (500 mM), glycerol (5% v/v) and TCEP (0.5 M), concentrated to 13 mg/mL, flash frozen in liquid nitrogen and stored at -80 °C.

Post Size exclusion chromatography



Sample frozen post 2-step purification

Post Ion exchange chromatography purification



Sample frozen post 3-step purification

Figure 6.12 Coomassie Blue staining of SDS-PAGE gels of prepared protein samples.

The experiments above and this report were done by:

Dr Chandrika Deshpande

Staff Scientist, Protein Production and Characterisation
Drug Discovery / Sydney Analytical / Core Research Facilities
THE UNIVERSITY OF SYDNEY
chandrika.deshpande@sydney.edu.au

Chapter 7

Additional publications

CHAPTER 7. ADDITIONAL PUBLICATIONS

7. 1. Preface

The work arising from this dissertation contributed to the following publications. The author has performed the experiments and analysed the data presented in the figures and tables shown in parentheses (in their entirety) for each manuscript:

- Hoque, M.; **Abbassi, R. H.**; Froio, D; Man, J.; Johns, T. G.; Stringer, B. W.; Day, B. W.; Pajic, M.; Kassiou, M.; Munoz, L., Changes in cell morphology guide identification of tubulin as the off-target for protein kinase inhibitors. *Pharmacol Res* **2018**, 134, 166-178. (**Figure 2**). <https://doi.org/10.1016/j.phrs.2018.06.023>
- Döbber, A.; Phoa, A. F.; **Abbassi, R. H.**; Stringer, B. W.; Day, B. W., Johns, T. G.; Abadleh, M.; Peifer, C.; Munoz, L. Development and biological evaluation of a photoactivatable small molecule microtubule-targeting agent. *ACS Med Chem Lett* **2017**, 8, 395-400. (**Figure 4**) <https://doi.org/10.1021/acsmchemlett.6b00483>
- Zhou, Q; Reekie, T. A.; **Abbassi, R. H.**; Indurthi, D. C.; Font, J. S.; Ryan, R. M.; Munoz, L.; Kassiou, M., Synthesis and in vitro evaluation of diverse heterocyclic diphenolic compounds as inhibitors of DYRK1A. *Bioorg Med Chem* **2018**, 26 (22), 5852-5869. (**Table 1**) <https://doi.org/10.1016/j.bmc.2018.10.034>
- Zhou, Q; Reekie, T. A.; **Abbassi, R. H.**; Indurthi, D. C.; Font, J. S.; Ryan, R. M.; Rendina, L. M.; Munoz, L.; Kassiou, M., Flexible analogues of azaindole DYRK1A inhibitors elicit cytotoxicity in glioblastoma cells. *Aust J Chem* **2018**, 71 (10), 781-799. (**Table 1**) <https://doi.org/10.1071/CH18251>

In addition, the author generated the figures presented in the following review:

- Sterling, J.; Menezes, S. V.; **Abbassi, R. H.**, Munoz, L. Histone lysine demethylases and their functions in cancer. *Int J Cancer* **2021**, 148, 2375-2388. (**Figures 1 and 2**) <https://doi.org/10.1002/ijc.33375>

Further permission related to the material excerpted should be directed to the respective publishing groups.



Changes in cell morphology guide identification of tubulin as the off-target for protein kinase inhibitors

Monira Hoque^a, Ramzi H. Abbassi^a, Danielle Froio^b, Jennifer Man^b, Terrance G. Johns^c, Brett W. Stringer^d, Bryan W. Day^d, Marina Pajic^{b,e}, Michael Kassiou^f, Lenka Munoz^{a,*}

^a The University of Sydney, Faculty of Medicine and Health, Charles Perkins Centre, NSW 2006, Australia

^b The Kinghorn Cancer Centre, The Garvan Institute of Medical Research, Sydney, NSW 2010, Australia

^c Oncogenic Signalling Laboratory and Brain Cancer Discovery Collaborative, Telethon Kids Institute, 100 Roberts Road, Subiaco, WA 6008, Australia

^d QIMR Berghofer Medical Research Institute, 300 Herston Road, Herston, QLD 4006, Australia

^e St Vincent's Clinical School, Faculty of Medicine, University of New South Wales, NSW 2010, Australia

^f The University of Sydney, School of Chemistry, NSW 2006, Australia

ARTICLE INFO

Keywords:

Kinase inhibitors
Microtubule-targeting agents
Off-targets
Cell morphology
Glioblastoma

ABSTRACT

In the field of kinase inhibitors for applications in cancer research, tubulin is emerging as a targeted cellular protein that can significantly contribute to their activities. However, investigation of kinase inhibitors beyond the kinome is an area often neglected. Herein, we describe the results of pharmacological studies using drugs targeting kinases, tubulin or both. A key finding is that if cells are treated with a kinase inhibitor unintentionally targeting tubulin, their characteristic shape will diminish within a short timeframe. These changes in cell morphology are not seen when cells are treated with *bona fide* kinase inhibitors that do not directly target tubulin. Thus, early changes in cell morphology upon treatments are a strong indication that the inhibitor is directly targeting tubulin. Recognizing tubulin as a target of kinase inhibitors will build confidence in the future mechanistic studies using kinase inhibitors.

1. Introduction

Determining the mechanism of action by which kinase inhibitors affect cells is crucial for their development as molecular probes for pharmacological research and as effective drugs for therapy. The importance of target validation has been substantially emphasized, as the inconsistencies in the mechanistic studies often contribute to the low data reproducibility and to the high attrition rates in clinical trials [1–4].

A great proportion of cancer research uses kinase inhibitors with the aim to kill malignant cells. Advanced technology platforms have been developed to profile kinase inhibitors across the kinome and kinases targeted by a given inhibitor are usually covered in the literature. The mechanism of cell-killing efficacy of the kinase inhibitor is then attributed to the inhibition of the published kinase(s). However, as recently demonstrated, inhibition of the intended kinase(s) is not always the mechanism of action underlying cytotoxicity [5–13]. Various non-kinase proteins have emerged as targets responsible for cytotoxic

activity of kinase inhibitors, with microtubules being one of the most prominent non-kinase targets.

Microtubules are hollow tubes composed of α/β -tubulin heterodimers and the main component of the cytoskeleton. Polymerization of α/β -tubulin heterodimers is required to form microtubules, and this process must occur faster in mitosis than in other cell cycle phases, as mitotic microtubules are crucial for the correct segregation of chromosomes [14]. This phenomenon explains why compounds that bind to tubulin and interfere with tubulin polymerization are effective in killing rapidly proliferating cancer cells [15]. The large class of tubulin-targeting agents contains structurally diverse molecules. Intriguingly, some kinase inhibitors directly bind to tubulin, and their effects on tubulin polymerization, rather than on kinase activity, underlies their cytotoxic efficacy.

For example, tivantinib was developed as a type II kinase inhibitor of the MET proto-oncogene-encoded kinase of the hepatocyte growth factor receptor class to treat cancers characterized by sustained MET activation, mutation or gene amplification [16]. However, follow-up

Abbreviations: ALK, anaplastic lymphoma kinase; ATP, adenosine triphosphate; BCR-ABL, Breakpoint cluster region–Abelson; DMEM, Dulbecco Modified Eagle Medium; EGFR, epidermal growth factor receptor; FUCCI, Fluorescence Ubiquitination Cell Cycle Indicator; HER, human epidermal growth factor receptor; MET, receptor tyrosine kinase Met; MERTK, Mer tyrosine kinase; PLK4, Polo-like kinase 4

* Corresponding author at: School of Medical Sciences and Charles Perkins Centre, The University of Sydney, NSW 2006, Australia.

E-mail address: lenka.munoz@sydney.edu.au (L. Munoz).

<https://doi.org/10.1016/j.yphrs.2018.06.023>

Received 22 March 2018; Received in revised form 13 June 2018; Accepted 22 June 2018

Available online 23 June 2018

1043-6618/ © 2018 Elsevier Ltd. All rights reserved.

mechanistic studies have shown that the cytotoxic activity of tivantinib is independent of MET inhibition and results instead from the direct binding to tubulin and inhibiting tubulin polymerization [6,7].

The list of kinase inhibitors directly targeting tubulin is increasing [4,13] and these discoveries highlight the importance of expanding the pharmacology of kinase inhibitors beyond the kinome. Kinase inhibitors targeting tubulin cannot be recognized in the commonly used kinome-wide screens and overall toxicity screens. Identification of off-targets, particularly those that contribute to the desired cellular efficacy, requires detailed, orthogonal and multidisciplinary drug-target validation approach [1,3,4,13]. These extensive studies are usually performed for a limited number of kinase inhibitors. Yet, recognizing tubulin as a target of a given kinase inhibitor would impact on the future use of this compound, and would correctly guide medicinal chemists in the chemical optimization and pharmacologists in their mechanistic studies. As such, there is a clear need for a feasible methodology that would enable an early identification of tubulin as a non-kinase target for kinase inhibitors.

Given that microtubules are crucial not only for mitosis, but are also critical determinants of the cell shape and morphology, we hypothesized that a kinase inhibitor that unintentionally targets tubulin would cause changes in cell morphology not otherwise seen. We reveal herein the results of a cell morphology analysis using cancer drugs that target kinases, tubulin or both. We show that these drugs have different effects on cell morphology, depending on the cellular proteins they target. As a cellular model, we employed A172 glioblastoma cells because of their high differentiation status and star-shaped morphology. The prominent shape of A172 cells allows us to clearly demonstrate changes in the cell morphology upon drug treatment. We also demonstrate that changes in cell morphology are apparent in melanoma, pancreatic and breast cancer cells as well as in glioblastoma stem cell lines, which contain cells of different sizes and shapes. Thus, our methodology is applicable to diverse cancer cell lines and can be routinely employed in any laboratory using kinase inhibitors.

2. Materials and methods

2.1. Drugs

Tivantinib (Selleckchem TX, USA; #S2753), (R)-crizotinib (Selleckchem #S1068), vinblastine (Tocris Bioscience, UK; #1256), ponatinib (Selleckchem #S1490), centrinone (Tocris Bioscience #5687), paclitaxel (Tocris Bioscience #1097), alisertib (Selleckchem #S1133), dacomitinib (Selleckchem #S2727), UNC2025 (Selleckchem #S7576), CMPD1 (Santa Cruz Biotechnology, TX, USA; #SC-203138), colchicine (Tocris Bioscience #1364), ixabepilone (AdooQ Bioscience, CA, USA; #A11449), tofacitinib (Selleckchem #S2789), vemurafenib (Selleckchem #S1267), idelalisib (Selleckchem #S2226), trametinib (Selleckchem #S2673) and palbociclib (Selleckchem #S1116) were used as received.

2.2. Cell culture

A172 glioblastoma, breast cancer MDA-MB-231 and melanoma SK-MEL-28 cell lines were obtained from the European Collection of Cell Cultures (EACC, Salisbury, UK) through Cell Bank Australia. A172 and SK-MEL-28 cells were cultured in DMEM medium, MDA-MB-231 in RPMI1640 medium, both supplemented with GLUTAmax, 10% FBS and Antibiotic-Antimycotic (all Life Technologies, CA, USA) at 37 °C and 5% CO₂. To derive A172-FUCCI cell line, A172 cells were transduced with the CSII-EF-MCS vectors expressing the Fluorescent Ubiquitination-based Cell Cycle Indicator (FUCCI) mKO2-hCdt1(30/120) or mAG-hGem(1/110), and the packaging and envelope plasmids pCMV-R 8.2, pMDG and pRSV-Rev, respectively. After selection using zeocin, cells were subcloned and sorted for green and red fluorescence subsequently to produce a cell line stably expressing the FUCCI system (A172-

FUCCI). A172-FUCCI cells were cultured in DMEM medium supplemented with 10% FBS and Antibiotic-Antimycotic (both Life Technologies) at 37 °C and 5% CO₂. Glioblastoma stem cell lines RN1, WK1 and MMK1 were derived from glioblastoma specimens. Full characterization of these cell lines, RNA sequencing, mutational profile and subtype assignment is available online (<http://www.qimrberghofer.edu.au/our-research/commercialisation/q-cell/>). RN1, WK1 and MMK1 cell lines were cultured in KnockOut DMEM/F-12 basal medium supplemented with StemPro NSC SFM supplement, 2 mM GlutaMAX-ICTS, 20 ng/mL EGF, 10 ng/mL FGF-β and Antibiotic-Antimycotic solution (all Life Technologies) as adherent cells on flasks coated with MatriGel Matrix (Corning Life Sciences, MA, USA) at 37 °C and 5% CO₂. The Kinghorn Cancer Centre (TKCC) pancreatic adenocarcinoma 05 (TKCC-05) cell line has been whole genome sequenced [17], confirmed by STR profiling as unique (cellbankaustralia.com) and cultured in DMEM/F-12 (Thermo Fisher Scientific, AU) supplemented with 15 mM HEPES (Thermo Fisher Scientific, AU), 10 ng/mL EGF, 0.1 IU/mL insulin (Novo Nordisk, DK), 40 ng/mL hydrocortisone (Sigma Aldrich US), 0.12% glucose and 7.5% FBS as previously described [18]. The protocols were approved by the Human Ethics Committee of The University of Sydney (HREC 2013/131), the Human Ethics Committee of the Royal Brisbane & Women's Hospital (RBWH 2004/161) and Sydney Local Health District Human Research Ethics Committee X11-0220. All cell cultures were routinely tested for mycoplasma infection and the cumulative length of culturing did not exceed 20 passages.

2.3. Tubulin polymerization assay

Fluorescence-based tubulin polymerization assay was conducted in a final volume of 55 μL using the Tubulin Polymerization Assay kit (Cytoskeleton, CO, USA) as per manufacturer's instructions. Briefly, porcine brain tubulin was incubated with test compounds at 37 °C and fluorescence was measured using with Tecan M200 PRO + microplate reader (Tecan, Switzerland) at 355 nm excitation and 460 nm emission.

2.4. Cell viability assay

A172, MMK1, RN1, WK1, MDA-MB-231, SK-MEL-28 (2×10^3 cells/well) and TKCC-05 (0.8×10^3 cells/well) cells were seeded onto a 96-well plate and treated on the following day with vehicle or test drugs (0.001–50 μM) for 72–96 h. 10 μL of CellTiter-Blue reagent (Promega, WI, USA) was added to each well and incubated at 37 °C for 1–4 h. Fluorescence was measured with Tecan M200 PRO + microplate reader (Tecan, Switzerland) at 585 nm. Data were normalized to controls (set as 100% viability) and EC₅₀ values calculated by non-linear regression analysis using Prism 6.0 (GraphPad, La Jolla, CA, USA).

2.5. Cell morphology analysis

A172, SK-MEL-28 (2×10^3 cells/well), MDA-MB-231 (10×10^3 cells/well), MMK1, RN1, WK1, TKCC-05 (4×10^3 cells/well) cell lines were seeded onto a 96-well plate and treated the following day with vehicle or test drugs. Plates were placed into IncuCyte S3 Live-cell Analysis System (Essen Bioscience, Sartorius, Ann Arbor, USA). Images were taken at 30 min, then at regular 2-hour intervals using the 10× objective.

2.6. Cell cycle analysis

A172-FUCCI cells (2×10^3 cells/well) were seeded onto a 96-well plate and treated the following day with vehicle or test drugs. Plates were placed into IncuCyte S3 Live-cell analysis system (Essen Bioscience, Sartorius, Ann Arbor, USA) for 24 h. Images were taken at 30 min, then at regular 2-hour intervals using the 10× objective in green (acquisition time 300 ms) and red channels (acquisition time 400 ms). The number of cells in G0-G1 phases (red), G1/S transition

(yellow or overlap) and S-G2-M phases (green) were quantified using InCuCyte S3 Basic Analysis software (Essen Bioscience). The ratio of G0-G1, G1/S and S-G2-M cells in Fig. 4b was calculated as a percentage of total cells counted for each treatment condition. Morphological changes were observed in phase images at various time points.

2.7. Annexin V staining

A172 cells (1.5×10^5) were plated into 6-well plates and treated with test drugs (4–48 h). Floating and attached cells were collected, centrifuged ($200 \times g$), washed with cold PBS and stained using the LIVE/DEAD Near IR Dead Cell Stain Kit (Life Technologies) according to manufacturer's instructions. Cells were washed with 2% FBS in PBS, centrifuged ($200 \times g$) and resuspended in 4% PFA fixation buffer for 10 min at room temperature. Fixed cells were stained using the Annexin V-FITC Early Apoptosis Detection Kit (Cell Signaling Technology, Massachusetts, USA) for 2 h on ice. Cells were pipetted through a cell strainer to achieve single cell suspension and analysed by flow cytometry (BD LSRFortessa™, BD Biosciences, USA) using FlowJo Software (BD Biosciences).

2.8. Immunofluorescence imaging

A172 cells (3×10^4 cells) were seeded onto glass coverslips and treated the following day with vehicle or test drugs for 30 min and 4 h. Cells were fixed with 4% paraformaldehyde for 20 min at RT, washed with PBS, then blocked in 1% bovine serum albumin/0.3% Triton X in PBS for 30 min. Cells were incubated with β -tubulin antibody (Abcam #11308) and Alexa488-conjugated anti-mouse IgG (Life Technologies #A-11029). Cell nuclei were counterstained using Prolong Gold mounting media with DAPI (4',6'-diamidino-2-phenylindole, Life Technologies). Images were acquired under $100\times$ (oil) objective on a Zeiss upright fluorescence Axio Scope.A1 microscope and analyzed using Zeiss Zen microscope software (Carl Zeiss Microscopy, USA).

3. Results

3.1. Test drugs

For initial testing, we have selected 5 well-known and commercially available cancer drugs (Fig. 1). Tivantinib was developed as a non-ATP competitive inhibitor binding to the inactive conformation of MET kinase ($K_i = 355$ nM) [16,19]. Tivantinib also binds to tubulin in the colchicine binding site and inhibits tubulin polymerization [20,21]. We

compared tivantinib to (*R*)-crizotinib, an orthogonal MET/ALK inhibitor (MET: $K_d = 0.2$ nM; ALK: $K_d = 4.4$ nM) [22]. Previous studies excluded tubulin as a target of (*R*)-crizotinib [7], which we also confirmed in this study (Fig. 2a). Vinblastine (Fig. 1) is the proto-typical and one of the most used tubulin inhibitors. Vinblastine binds to tubulin in the vinca binding site and inhibits tubulin polymerization. Both tivantinib and vinblastine disrupt formation of the mitotic spindle, which is necessary for the separation of duplicated chromosomes during mitosis. Through this mechanism vinblastine and tivantinib induce mitotic arrest, a hallmark of all tubulin inhibitors [23].

As controls, we have included centrinone and ponatinib (Fig. 1). Centrinone inhibits Polo-like kinase 4 (PLK4, $IC_{50} = 0.16$ nM) [24], a serine-threonine kinase that controls the formation of centrosomes, the major microtubule-organizing centers. In mitosis, centrosomes generate a radial organization of microtubules necessary for the separation of duplicated chromosomes between daughter cells. Thus, in regard to its mechanism of action, centrinone shares similarities with vinblastine. Both vinblastine and centrinone disrupt the function of microtubules in mitosis, however vinblastine acts through direct interaction with tubulin, whereas centrinone acts indirectly via PLK4 inhibition. Ponatinib is a type II multi-targeted kinase inhibitor developed against BCR-ABL kinase and its mutants (BCR-ABL: $IC_{50} = 8.6$ nM; BCR-ABL T315I: $IC_{50} = 40$ nM) [25]. In addition to BCR-ABL kinases, ponatinib inhibits numerous other kinases; however, to our best knowledge ponatinib does not target tubulin and microtubules either directly or indirectly. To confirm or dispute tubulin as a direct target for these test drugs, we performed an in vitro tubulin polymerization assay. Purified tubulin was incubated with paclitaxel (positive control drug increasing tubulin polymerization) and test drugs tivantinib, (*R*)-crizotinib, vinblastine, centrinone and ponatinib (Fig. 2a). Compared to control, paclitaxel enhanced tubulin polymerization, whereas vinblastine and tivantinib inhibited tubulin polymerization. (*R*)-crizotinib, centrinone and ponatinib did not affect the rate of tubulin polymerization (Fig. 2a), confirming that these kinase inhibitors do not directly target tubulin.

To ensure that the test drugs were used in cellular experiments at concentrations at which they exhibit an effect on cells, we determined their cellular efficacy (EC_{50}) in CellTiter-Blue viability assay using A172 glioblastoma cells (Fig. 2b). Viability of A172 cells was most potently attenuated by vinblastine ($EC_{50} = 2$ nM). Tivantinib and ponatinib reduced viability of A172 cells with low sub-micromolar efficacy ($EC_{50} = 0.3$ and 0.1 μ M, respectively); whereas (*R*)-crizotinib was effective at higher concentrations ($EC_{50} = 0.9$ μ M). The weakest efficacy was determined for centrinone ($EC_{50} = 2.8$ μ M).

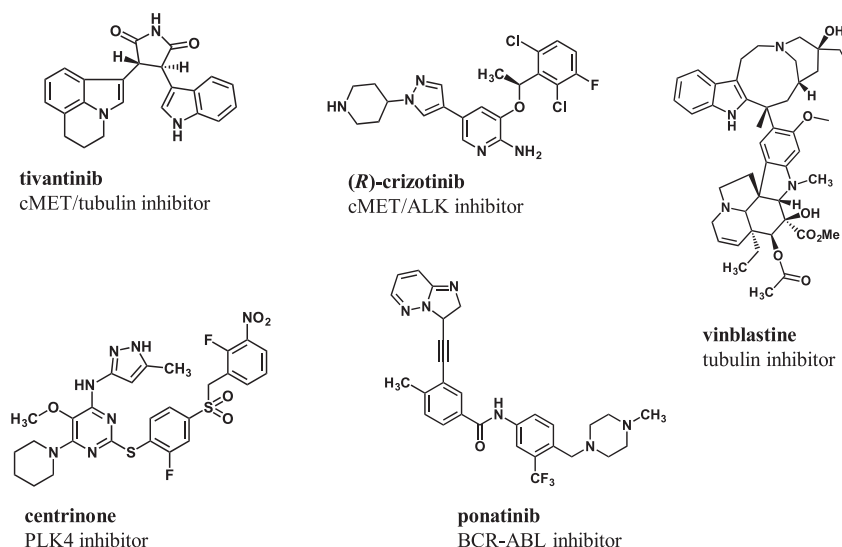


Fig. 1. Structures of test drugs.

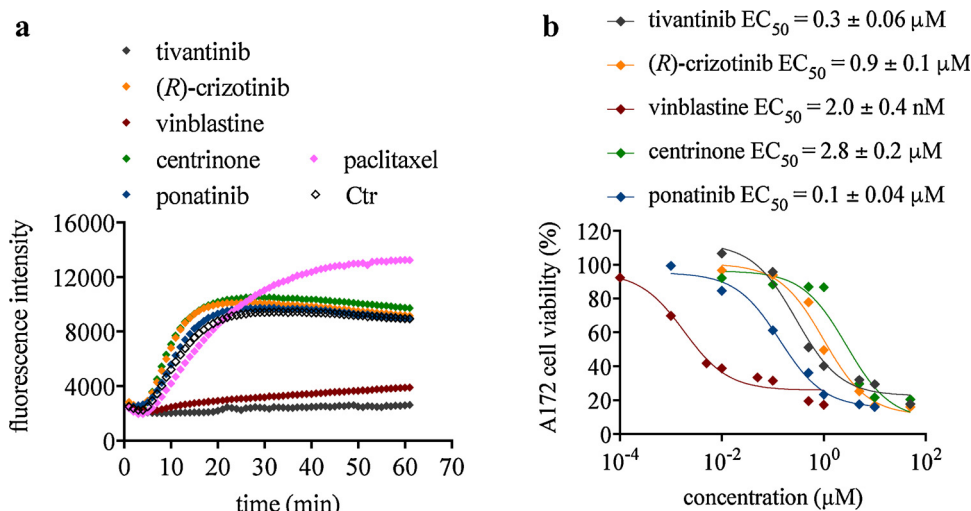


Fig. 2. Activity of test drugs in tubulin polymerization (a) and cell viability (b) assays. (a) Porcine brain tubulin was incubated with DMSO (Ctr), paclitaxel (3 μM), vinblastine (3 μM), tivantinib (50 μM), (R)-crizotinib (50 μM), centrinone (50 μM) and ponatinib (50 μM). Assembly of microtubules was monitored by an increase in fluorescence. Data represent mean from two independent experiments. (b) Cellular efficacy (EC_{50}) in A172 glioblastoma cells was determined with CellTiter-Blue viability assay after 72 h of drug treatment. EC_{50} values are mean \pm SEM from three independent experiments performed in triplicate.

3.2. Cell morphology analysis

To investigate cell morphology changes upon drug treatments, asynchronous A172 glioblastoma cells were treated with drugs at approximately 5-fold higher concentrations than EC_{50} values determined in the cell viability assay (Fig. 2b). To monitor morphology of cells, we used the image-based IncuCyte platform (Essen Bioscience) that enables continuous monitoring of live cells. In our previous studies using tubulin inhibitors [5,26,27] we observed early changes in cell morphology. Therefore, images were taken at 30 min and then every 2 h using a $10\times$ objective (Fig. 3). Treatment of A172 cells with tubulin-targeting drugs tivantinib (1.25 μM) and vinblastine (10 nM) induced changes in cell morphology within 30 min. Cells lost their star-like or elongated shapes, became rounded and smaller (Fig. 3, black arrows). This ‘shrinkage’ effect was not seen when cells were treated with kinase inhibitors (R)-crizotinib (5 μM), centrinone (15 μM) and ponatinib (0.5 μM) for up to 8 h.

3.3. Analysis of cell cycle and apoptosis

Rounding and retraction from neighboring cells is a feature of cells undergoing mitosis, and mitotic cells possess characteristic sphere-like shapes (Fig. 3, orange arrows). Thus, rounding of cells could be mistaken as cells entering mitosis during the cell cycle. To analyse the cell cycle progression upon drug treatments, we infected A172 cells with Fluorescence Ubiquitination Cell Cycle Indicator (FUCCI) lentiviruses expressing mKO2-hCdt1 (red) and mAG-hGeminin (green) [28]. As the protein levels of Cdt1 and Geminin change during the cell cycle, the color of the cell changes from red (G0-G1 phases, mKO2 positive cells) through yellow (G1/S transition) to green (S-G2-M phases, mAG positive cells; Fig. 4a). The mKO2/mAG negative cells (colorless cells) are cells straight post-division. IncuCyte-based imaging of A172-FUCCI cells treated with test drugs revealed that the distribution of cells within the cell cycle phases remained comparable with untreated cells and there was no significant increase in the percentage of S-G2-M cells within 8 h of treatment (Fig. 4b). The changes in the cell cycle distribution were significant only after 24 h of drug treatments. Tubulin

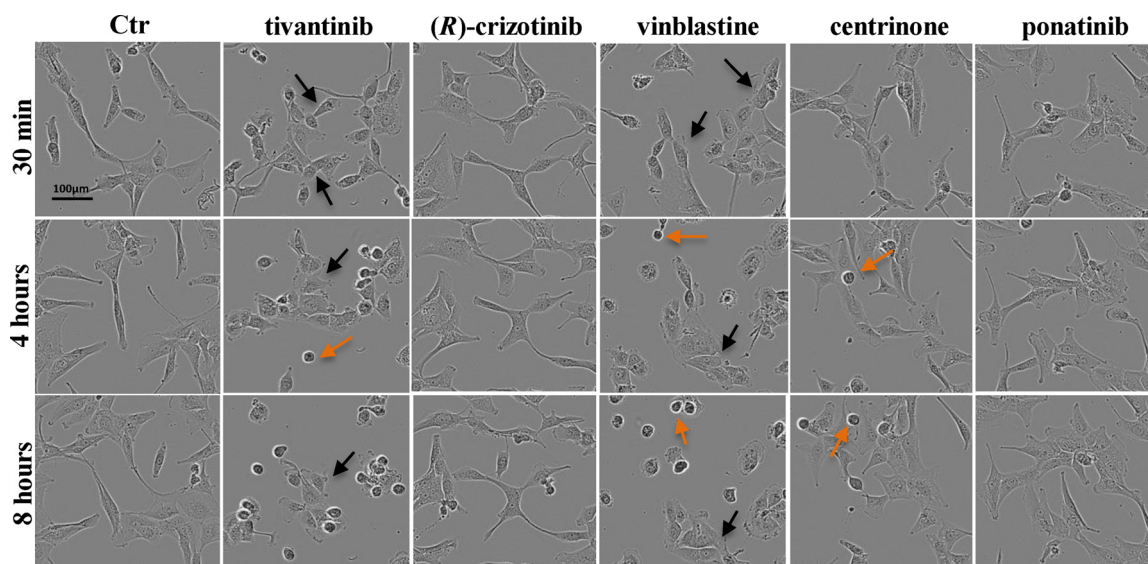


Fig. 3. Morphology of A172 glioblastoma cells during exposure to test drugs. Asynchronous A172 glioblastoma cells were treated with tivantinib (1.25 μM), (R)-crizotinib (5 μM), vinblastine (10 nM), centrinone (15 μM) and ponatinib (0.5 μM). Images were captured at indicated time points with a $10\times$ objective using the IncuCyte™ platform from Essen Biosciences. A172 cells treated with tivantinib and vinblastine lost the star-like and elongated shapes; they became rounded and smaller (black arrows). This effect was not seen when cells were treated with *bona fide* kinase inhibitors (R)-crizotinib, centrinone and ponatinib. Orange arrows indicate mitotic cells. (For interpretation of the references to colour in this figure legend, the reader is referred to the web version of this article.)

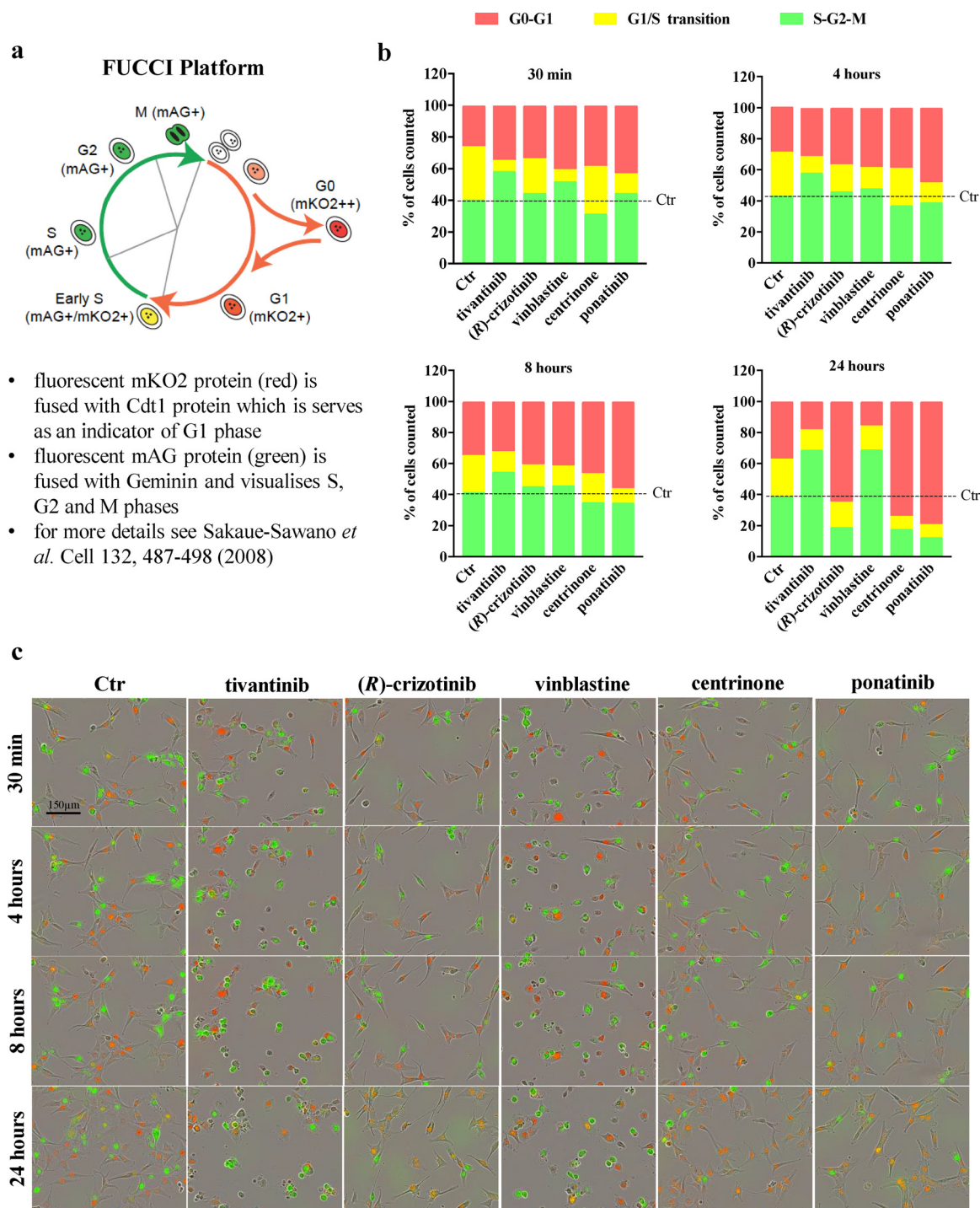


Fig. 4. Cell cycle analysis. (a) Schematic diagram of the FUCCI platform. (b) A172-FUCCI cells were treated with tivantinib (1.25 μ M), (R)-crizotinib (5 μ M), vinblastine (10 nM), centrinone (15 μ M) and ponatinib (0.5 μ M). Live cell imaging (IncuCyte, Essen Bioscience) was used to distinguish three different populations. Quantification (b) and representative images (c) of two independent experiments performed with six replicates are shown. (For interpretation of the references to colour in the text, the reader is referred to the web version of this article.)

inhibitors tivantinib and vinblastine increased the percentage of green S-G2 and mitotic (M) cells; whereas (R)-crizotinib, centrinone and ponatinib increased the percentage of cells arrested in the G0-G1 phases (red cells). These data are in agreement with the published mechanisms of action for these drugs [6,24,29,30].

Furthermore, images collected during the cell cycle analysis phenocopy the images in Fig. 3. Upon treatment with tubulin inhibitors tivantinib and vinblastine, all cells regardless of the cell cycle stage lost their characteristic shapes (Fig. 4c). The morphology and cell cycle

distribution of A172-FUCCI cells treated with (R)-crizotinib, centrinone and ponatinib did not change up to 8 h. At 24 h, these kinase inhibitors significantly increased the percentage of cells in the G0-G1 phases (more red cells); however, all cells retained their morphology.

Cell shrinkage is also the first prominent morphological feature of cells undergoing apoptosis and tubulin inhibitors induce apoptosis through the mitochondrial apoptotic pathway [15]. In order to determine whether onset of apoptosis underlies the cell shrinkage observed in cells treated with tivantinib and vinblastine, we quantified

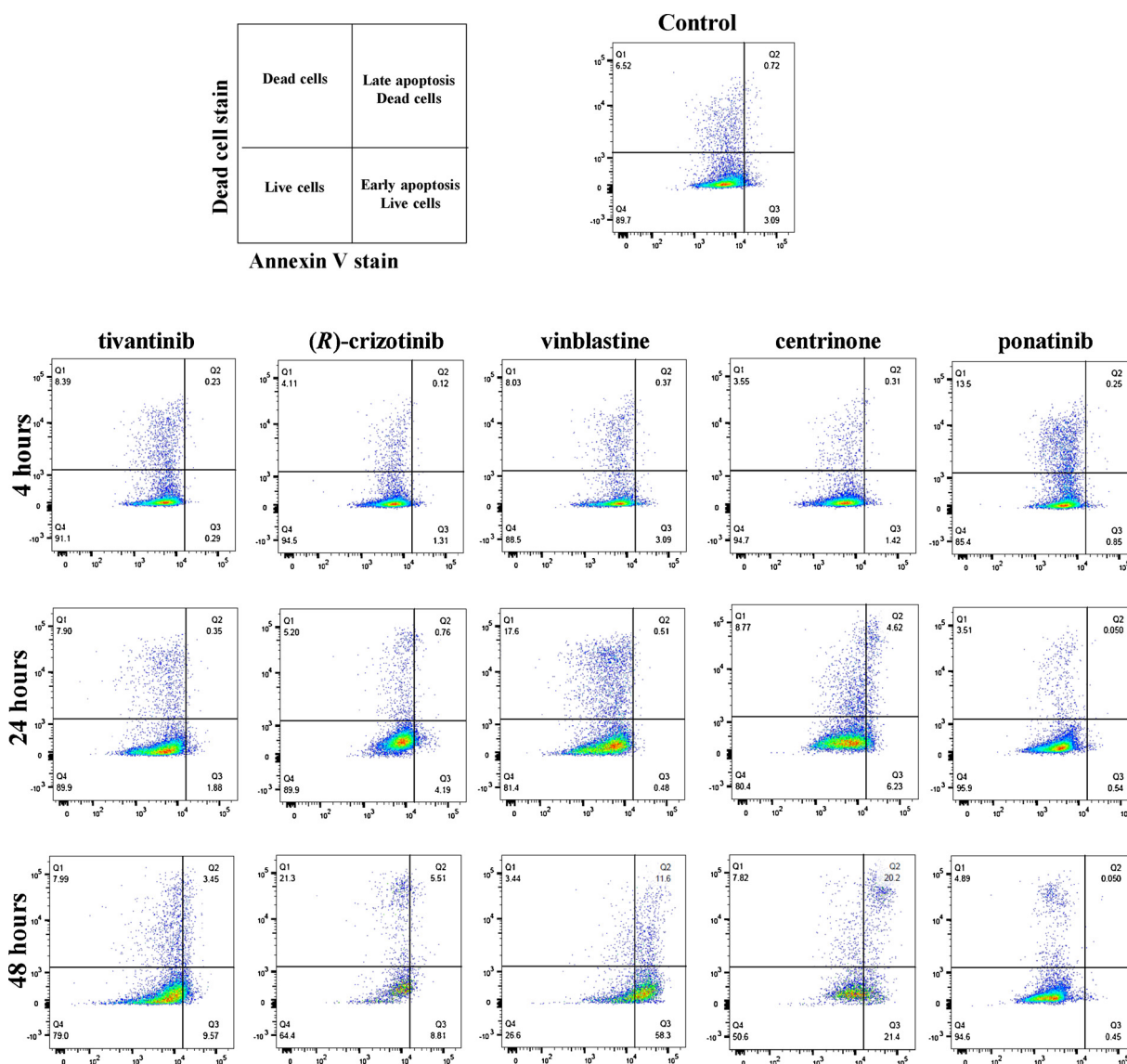


Fig. 5. Analysis of apoptosis upon drug treatment. A172 cells were treated with tivantinib (1.25 μM), (*R*)-crizotinib (5 μM), vinblastine (10 nM), centrinone (15 μM) and ponatinib (0.5 μM). Cell were stained with LIVE/DEAD™ Fixable Near-IR Stain and Annexin V-FITC, then analysed with flow cytometry. Representative images of two independent experiments are shown.

apoptosis in drug-treated A172 cells by Annexin V staining (Fig. 5). Treatment of A172 cells with all five tested drugs did not increase the basal level of Annexin V-positive cells (3.8% for Ctr vs 0.5–3.5% for test drugs, Fig. 5, Q3) within first 4 h of treatment. At 24 h post-treatment, only centrinone increased the quantity of apoptotic cells to 10%. At 48 h post-treatment, the percentage of apoptotic cells increased to > 10% when cells were treated with tivantinib and (*R*)-crizotinib; and to > 40% when cells were treated with vinblastine and centrinone (Fig. 5, Q2 + Q3). Surprisingly, ponatinib did not induce apoptosis up to 48 h, suggesting that this kinase inhibitor might have cytostatic effect or it activates alternative cell death pathways. Together these data suggest that the shrinking and rounding of cells observed within first 4 h of treatment with the tubulin inhibitors vinblastine and tivantinib is neither due to mitosis nor only onset of apoptosis.

3.4. Immunofluorescence imaging of the tubulin network

As the shrinking of cells upon short-term (4 h) treatment with tubulin inhibitors is not caused by mitotic arrest (Fig. 4) or onset of apoptosis (Fig. 5), we hypothesized that the changes in cell morphology

are most likely due to the direct effect on the microtubule network. To this end, we performed immunofluorescence imaging of β -tubulin in A172 glioblastoma cells treated with test drugs (Fig. 6). Microtubule network in untreated control cells is interconnected and appears filamentous (Fig. 6a). By contrast, the microtubule network was highly fragmented and disconnected in cells treated with the tubulin inhibitors vinblastine and tivantinib, with cells losing their characteristic shape within 30 min (Fig. 6a). Kinase inhibitors (*R*)-crizotinib, centrinone and ponatinib did not display any effect on the tubulin network or the cell shape up to 4 h (Fig. 6b).

3.5. Drugs directly targeting tubulin rapidly change morphology of cells

Data presented in Figs. 3–6 suggest that tivantinib and vinblastine, both directly targeting tubulin, induce prominent cell morphology changes within few hours after the administration of the drug to cells. To confirm whether early changes in cell morphology are indicative of direct tubulin targeting, we evaluated morphology changes of A172 cell treated with additional 12 drugs (Fig. 7) targeting kinases, tubulin or both. Alisertib is an inhibitor of Aurora A kinase ($\text{IC}_{50} = 1.2 \text{ nM}$), which

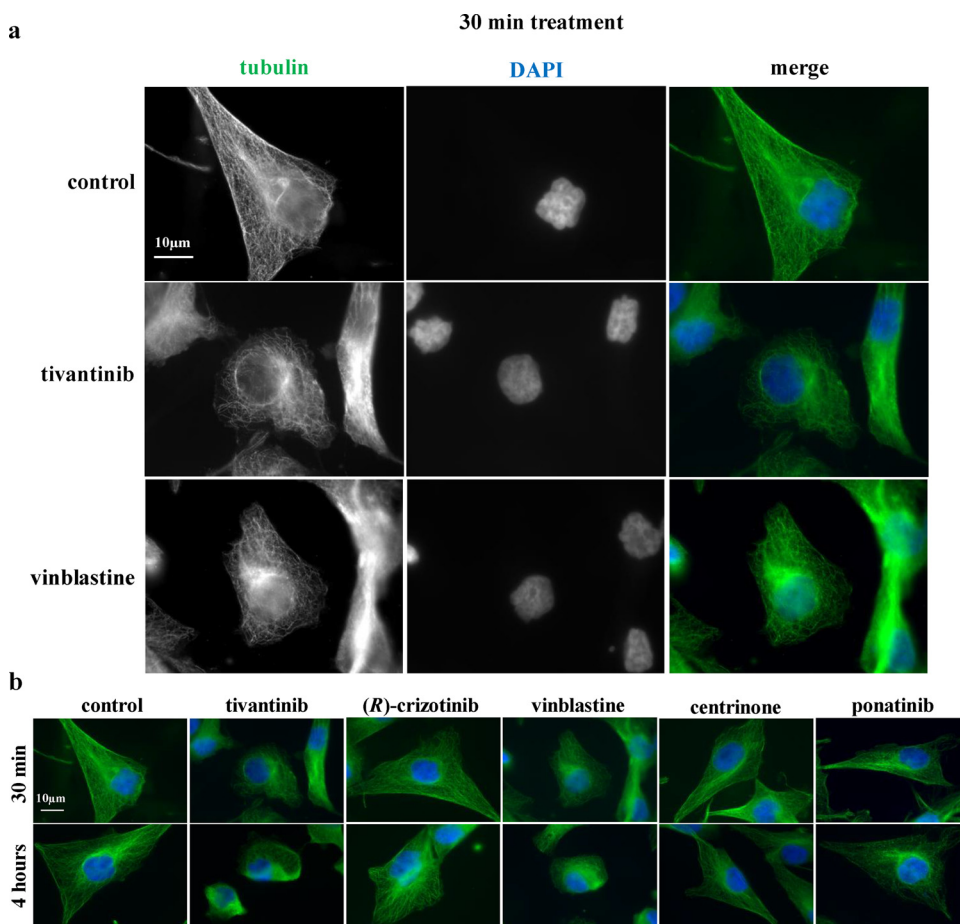


Fig. 6. A172 glioblastoma cells were treated with tivantinib (1.25 μ M), (*R*)-crizotinib (5 μ M), vinblastine (10 nM), centrinone (15 μ M) and ponatinib (0.5 μ M) for 30 min and 4 h. Cells were fixed and stained with Alexa488-labelled anti- β -tubulin antibody (green) and DAPI (blue). Images were acquired under 100 \times objectives on a Zeiss upright fluorescence Axio Scope.A1 microscope. Representative images of two independent experiments are shown. (For interpretation of the references to colour in this figure legend, the reader is referred to the web version of this article.)

plays important roles in mitosis [31]. Dacomitinib is an irreversible inhibitor of EGFR (IC_{50} = 6 nM), HER2 (IC_{50} = 45 nM) and HER4 (IC_{50} = 73 nM) receptor tyrosine kinases [32]. UNC2025 is an inhibitor of TAM family of receptor tyrosine kinases: Tyro3 (IC_{50} = 17 nM), AXL (IC_{50} = 14 nM) and MERTK (IC_{50} = 0.74 nM) [33]. Tofacitinib is a kinase inhibitor with IC_{50} of 1 nM, 20 nM and 112 nM against JAK3, JAK2, and JAK1, respectively [34]. Trametinib inhibits MEK1 and MEK2 (IC_{50} = 0.92 and 1.8 nM, respectively) with no inhibition of the c-Raf, B-Raf and ERK1/2 kinases [35]. Idelalisib is a PI3K δ inhibitor with IC_{50} = 2.5 nM [36]. Vemurafenib inhibits mutated B-Raf^{V600E} (IC_{50} = 31 nM) with 10-fold higher selectivity over wild-type B-Raf [37]. Palbociclib is a selective inhibitor of CDK4 and CDK6 with IC_{50} of 11 nM and 16 nM, respectively [38]. CMPD1 was developed as an allosteric p38 MAPK inhibitor selectively blocking MK2 kinase activation (IC_{50} = 330 nM) [39], however follow-up studies showed that CMPD1 inhibits tubulin polymerisation and its cytotoxic activity is independent of inhibition of the p38-MK2 pathway [5]. Colchicine, paclitaxel and ixabepilone are well-established tubulin inhibitors binding to colchicine and taxol binding sites on tubulin dimers [15]. We first determined their cellular efficacy (Fig. 7a) in CellTiter-Blue viability assay using A172 glioblastoma cells and then treated asynchronous A172 cells with each drug at 2–20 \times EC_{50} concentration. Morphology changes were monitored up to 24 h with IncuCyte platform, taking 10 \times images every 2 h. Similar to data obtained with tivantinib and vinblastine (Fig. 3), drugs directly targeting tubulin, i.e. CMPD1, colchicine, paclitaxel and ixabepilone induced changes in cell morphology within 4 h (Fig. 7b). Cells lost their characteristic star-like shapes, they rounded

up and appeared smaller. This shrinkage effect was not seen when cells were treated with kinase inhibitors alisertib, UNC2025, tofacitinib, trametinib, idelalisib and vemurafenib for up to 24 h. Dacomitinib and

palbociclib changed cell morphology after 24 h, however there were no changes at 4 h (Fig. 7c).

3.6. Morphology of glioblastoma stem cells

Serum-cultured A172 cells are highly differentiated and all cells present star-like or elongated shapes. Thus, the morphology changes upon treatment with tubulin inhibitors were prominent and could be observed at 10 \times magnification (Figs. 3, 4c and Figure 7b). To investigate whether changes in cell morphology are apparent also in cells with less defined shapes, we analyzed glioblastoma stem cell lines treated with tivantinib, vinblastine and (*R*)-crizotinib. The WK1, RN1 and MMK1 stem cell lines represent classical, mesenchymal and proneural glioblastoma subtypes, respectively (phenotype and genotype details are available online, see Methods). These cells are continuously grown in serum-free stem cell culture medium, which maintains the stemness, heterogeneity and genotype of the original tumours [40–42]. Compared to serum-cultured and differentiated A172 glioblastoma cells, these stem cells are smaller, less differentiated and present variety of shapes and sizes (Fig. 8). Dose-response curves and EC_{50} values for tivantinib, vinblastine and (*R*)-crizotinib determined in a cell viability assay (5 days treatment) are provided in Fig. 8a–c. We then treated WK1, RN1 and MMK1 cells with each drug at concentration at least 2-fold higher than the determined EC_{50} values (Fig. 8). When cells were treated with tubulin inhibitors tivantinib and vinblastine, cells lost their characteristic shape and shrivelled to rounded-up cells within 4 h (Fig. 8, black arrows). These changes were not observed in cells treated with (*R*)-crizotinib, a kinase inhibitor that does not inhibit tubulin polymerization (Fig. 8).

Finally, we extended our work to melanoma, breast and pancreatic cancer cell lines (Fig. 9). Similar to images obtained with A172 (Fig. 3)

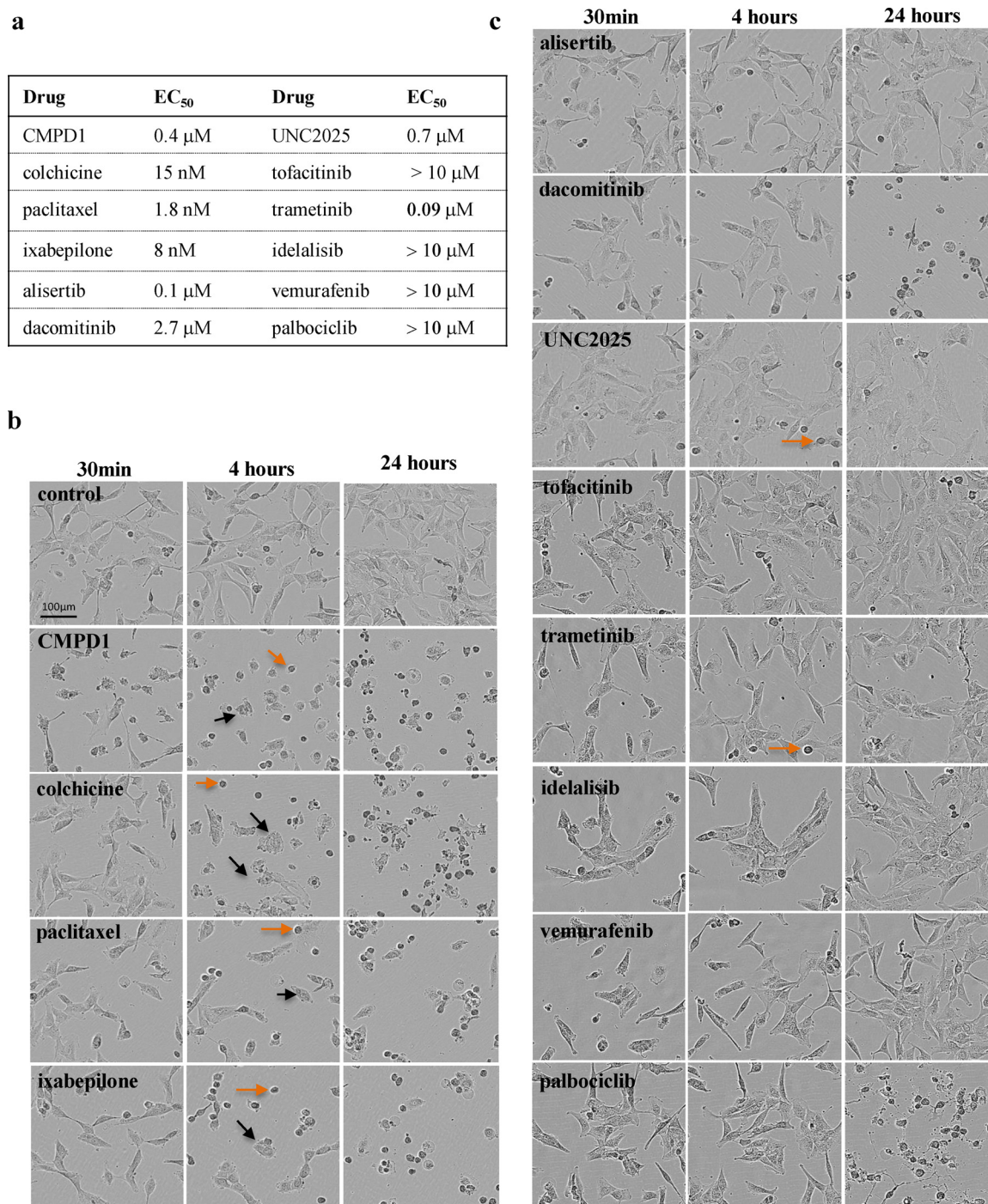


Fig. 7. Morphology changes. (a) Cellular efficacy (EC₅₀) in A172 glioblastoma cells was determined with CellTiter-Blue viability assay after 72 h drug treatment. EC₅₀ values are mean from three independent experiments performed in triplicate. (b) A172 cells were treated with CMPD1 (2 μM), colchicine (70 nM), paclitaxel (15 nM) and ixabepilone (50 nM). (c) A172 cells were treated with alisertib (2 μM), dacomitinib (14 μM), UNC2025 (5 μM), tofacitinib (10 μM), trametinib (10 μM), idelalisib (10 μM), vemurafenib (10 μM) and palbociclib (10 μM). Images were taken with a 10× objective (IncuCyte). When treated with CMPD1, colchicine, paclitaxel and ixabepilone (panels in b), cells shrivelled within 4 h (black arrows). This effect was not seen when cells were treated with kinase inhibitors (panels in c). Orange arrows indicate mitotic cells.

and glioblastoma stem cells (Fig. 8), melanoma SK-MEL-28 (Fig. 9a), breast cancer MDA-MB-231 (Fig. 9b) and pancreatic adenocarcinoma TKCC-05 (Fig. 9c) cells changed their morphology and shrivelled up within 4 h when treated with tivantinib and vinblastine. (R)-crizotinib did not change SK-MEL-28 and MDA-MB-231 cell morphologies up to 24 h (Fig. 9a and b). Unexpectedly, pancreatic TKCC-05 cells shrivelled up within 30 min of the treatment with (R)-crizotinib (Fig. 9c), however they recovered their morphology within 4 h, suggesting that these

reversible changes in cell morphology were most likely due to the mechanical stress, rather than irreversible modification of the tubulin network, as seen with tivantinib and vinblastine (Fig. 9b).

4. Discussion and conclusions

In this study, we analyzed morphology changes in 7 different cancer cell lines treated with 17 cancer drugs. Four drugs (vinblastine,

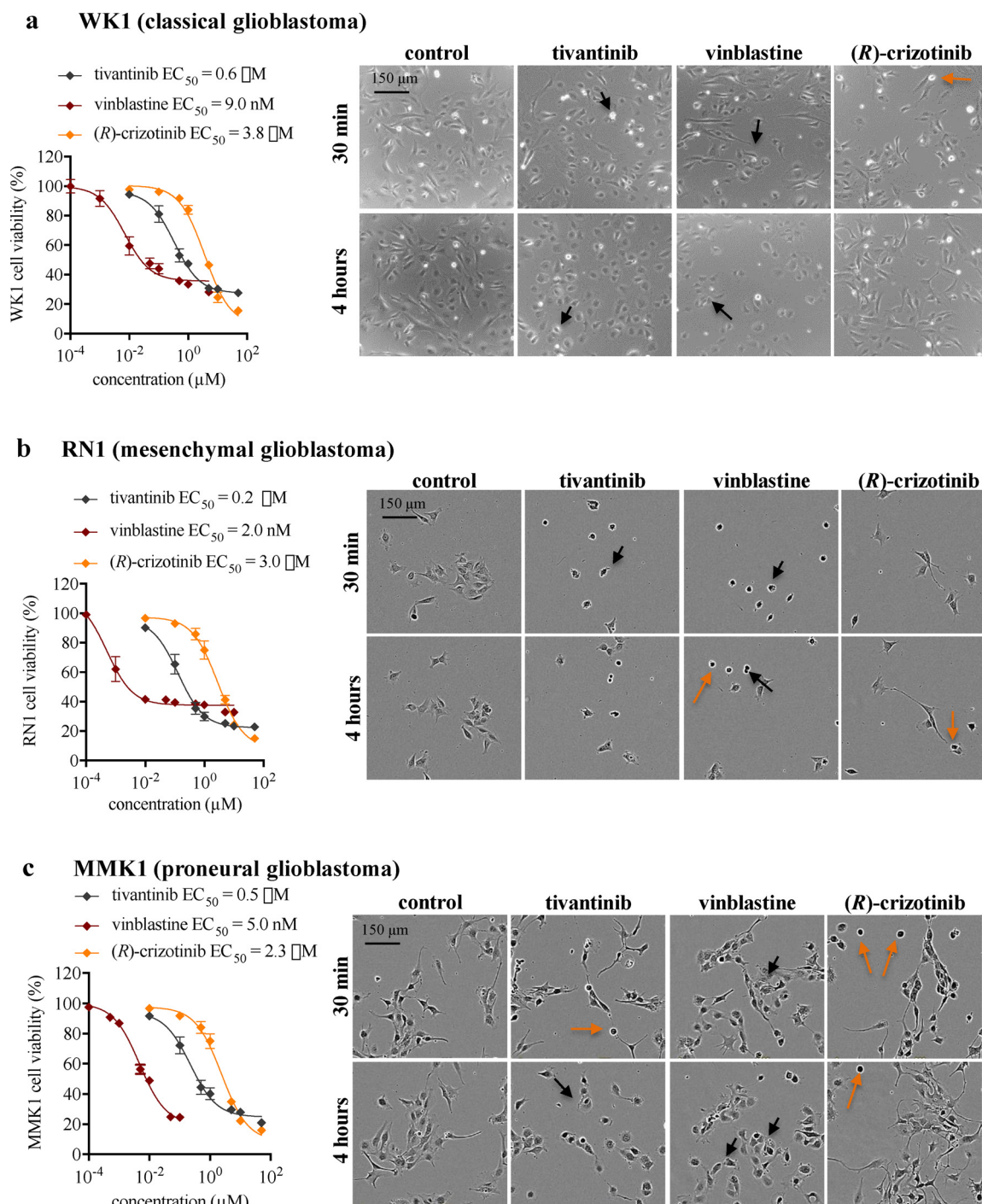


Fig. 8. Morphology changes in glioblastoma stem cell lines. Cellular efficacies (EC_{50}) in WK1 (a), RN1 (b) and MMK1 (c) glioblastoma stem cell lines were determined with CellTiter-Blue viability assay after 5 days of drug treatment. EC_{50} values are mean from three independent experiments performed in triplicate. Each cell line was treated with tivantinib ($3 \mu\text{M}$), vinblastine (50 nM) and (R)-crizotinib ($5 \mu\text{M}$). Images were taken with a $10\times$ objective (IncuCyte). When treated with tivantinib and vinblastine, cells shriveled within 4 h of treatment (black arrows). This effect was not seen when cells were treated with a *bona fide* kinase inhibitor (R)-crizotinib. Orange arrows indicate mitotic cells.

colchicine, paclitaxel, ixabepilone) directly target tubulin, two agents are kinase inhibitors directly binding to tubulin (tivantinib, CMPD1) and eleven drugs are structurally different kinase inhibitors without tubulin-targeting activity (Table 1). In order to cover a wide range of kinase inhibitors, targets of tested inhibitors include receptor tyrosine kinases (e.g. EGFR), intracellular tyrosine kinases (e.g. JAK), intracellular serine-threonine kinases (e.g. B-Raf), dual specificity kinases (e.g. MEK) and mitotic kinases (e.g. PLK4, Aurora). Furthermore, as kinase inhibitors vary in their binding modes, we have selected type I

(e.g. vemurafenib), type II (e.g. ponatinib) and type III (e.g. trametinib) inhibitors (Table 1). Our key finding is that only drugs directly binding to tubulin cause changes in cell morphology within hours of treatment (Table 1). Importantly, cells' characteristic shape diminished within a short timeframe in which there were no changes in the cell cycle distribution (i.e. no increase in mitotic cells) and in which we could not detect any apoptotic cells. The changes in cell morphology were not seen when cells were treated with *bona fide* kinase inhibitors that do not directly target tubulin. Importantly, cells treated with centrinone, a

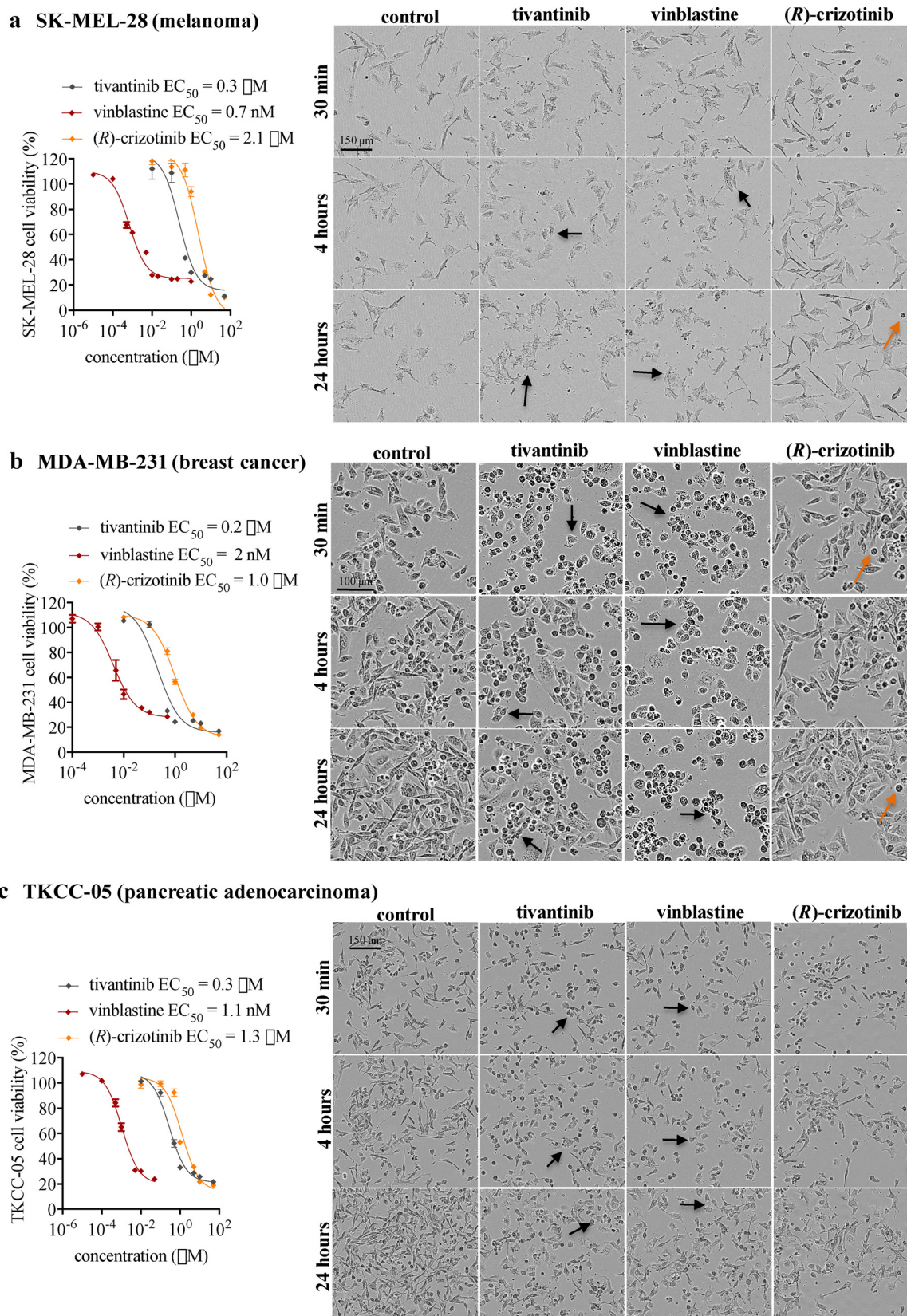


Fig. 9. Morphology changes in melanoma, breast and pancreatic cancer cell lines. (a) Cellular efficacies (EC_{50}) in SK-MEL-28 (a), MDA-MB-231 (b) and TKCC-05 (c) cell lines were determined with CellTiter-Blue viability assay. EC_{50} values are mean from three independent experiments performed in triplicate. (a) SK-MEL-28 cells were treated with tivantinib (1.5 μM), vinblastine (3.5 nM) and (R)-crizotinib (4 μM). (b) MDA-MB-231 cells were treated with tivantinib (1 μM), vinblastine (10 nM) and (R)-crizotinib (2 μM). (c) a) TKCC-05 cells were treated with tivantinib (1.5 μM), vinblastine (5.5 nM) and (R)-crizotinib (2.5 μM). Images were taken with a 10 \times objective (IncuCyte). When treated with tivantinib and vinblastine, cells shrivelled within 4 h of treatment (black arrows). This effect was not seen when cells were treated with a *bona fide* kinase inhibitor (R)-crizotinib. Orange arrows indicate mitotic cells.

Table 1

Summary of morphology changes induced by tested drugs. For kinase inhibitors, the nominal kinase target and known binding modes [53] are listed.

Drug	Nominal kinase	Type of the nominal kinase Binding mode of the inhibitor	Effect on microtubules MTA classification	Effect on A172 cell morphology
Vinblastine	–	–	Inhibits microtubule polymerisation Microtubule-destabilising agent	Cell shrinkage within 4 h
Colchicine	–	–	Inhibits microtubule polymerisation Microtubule-destabilising agent	Cell shrinkage within 4 h
Paclitaxel	–	–	Enhances microtubule polymerisation Microtubule-stabilising agent	Cell shrinkage within 4 h
Ixabepilone	–	–	Enhances microtubule polymerisation Microtubule-stabilising agent	Cell shrinkage within 4 h
CMPD1	p38 MAPK	Serine-threonine kinase Type III inhibitor	Inhibits microtubule polymerisation Microtubules destabilising agent	Cell shrinkage within 4 h
Tivantinib	MET	Receptor tyrosine kinase Type II inhibitor	Inhibits microtubule polymerisation Microtubules destabilising agent	Cell shrinkage within 4 h
(R)-Crizotinib	MET	Receptor tyrosine kinase Type I inhibitor	–	No changes at 24 h
Centrinone	PLK4	Intracellular serine-threonine kinase	Indirectly via PLK4 inhibits microtubule-organizing centres	No changes at 24 h
Ponatinib	BCR-ABL	Intracellular tyrosine kinase Type II inhibitor	–	No changes at 24 h
Alisertib	Aurora A	Intracellular serine-threonine kinase	–	No changes at 24 h
Dacomitinib	EGFR	Receptor tyrosine kinase Type I inhibitor, irreversible	–	No changes at 4 h Cell shrinkage at 24 h
UNC2025	MERTK, Flt3 (equal potency)	Receptor tyrosine kinases Type I inhibitor	–	No changes at 24 h
Tofacitinib	JAK3	Intracellular tyrosine kinases Type I inhibitor	–	No changes at 24 h
Trametinib	MEK	Intracellular dual specificity kinase Type III inhibitor	–	No changes at 24 h
Idelalisib	PI3K δ	Lipid kinase ATP competitive	–	No changes at 24 h
Vemurafenib	B-Raf	Intracellular serine-threonine kinase Type I inhibitor	–	No changes at 24 h
Palbociclib	CDK4/6	Intracellular serine-threonine kinase Type I inhibitor	–	No changes at 4 h Cell shrinkage at 24 h

kinase inhibitor that disrupts the function of tubulin and microtubules indirectly via inhibiting PLK4 kinase, maintained their characteristic morphology up to 24 h of the treatment. Furthermore, alisertib which inhibits mitotic kinase Aurora A (thereby inducing mitotic arrest, which is also a hallmark of tubulin targeting drugs) did not change cell morphology up to 24 h. Thus, early – in our models within 4 h – changes in cell morphology imply that a test drug directly disrupts the microtubule network. We propose that early changes in cell morphology upon drug treatments are a strong indication that the test drug is directly targeting tubulin. Such observations should be followed up with a biochemical tubulin polymerization assay to validate tubulin as a target of a given kinase inhibitor.

We demonstrate that the cell morphology changes are observable in serum-grown homogenous cell lines with defined cell body shapes (e.g. A172 glioblastoma) as well as in glioblastoma stem cell lines, in which cell body shapes and sizes are variable. Furthermore, changes to cell morphology are not specifically unique to glioblastoma models, as we observed equivalent morphology changes in melanoma, breast and pancreatic cancer cells. We also show that these rapid changes in cell morphology are due to the drug's direct effect on tubulin polymerization and disruption of the microtubule network within the cytoskeleton. Most importantly, changes in cell morphology upon drug treatments are observable using the 10 \times magnification of a standard microscope, thus can be performed in any laboratory using kinase inhibitors.

Our study offers a feasible approach to identify tubulin as a potential non-kinase target, however it does not offer a pathway to the absolute delineation of the mechanism of action of a given kinase inhibitor. The cytotoxic efficacy of a kinase inhibitor that also targets tubulin might be a sum of inhibiting both targets, which would be best described as a dual kinase-tubulin inhibitor. In some cases, when the targeted kinase is not crucial for a given cancer cell proliferation/survival, the cytotoxic activity of an inhibitor targeting both kinases and tubulin, is most likely linked to tubulin targeting. To comprehensively

delineate a mechanism of action of a drug requires follow-up drug-target validation and detailed pharmacological investigations [4,13]. Our study offers a fast approach to identify tubulin as a potential off-target.

Why is this important? An immense number of kinase inhibitors is being used to understand the deregulated signalling pathways in cancer cells. Unintentional targeting of tubulin will most likely increase the cellular efficacy of a given kinase inhibitor and provide misguided interpretations. For example, mechanistic studies using a kinase inhibitor that also targets tubulin will result in incorrect links between the targeted signalling pathway and the disease. Needless to say, data obtained with a dual kinase-tubulin inhibitor will not be reproducible by others using orthogonal kinase inhibitor that does not inhibit tubulin. In the drug development campaigns, whether a newly developed inhibitor is a molecularly targeted agent against a kinase or a chemotherapeutic agent targeting tubulin will have implications for lead optimization. The primary focus of kinase inhibitor campaigns is on the inhibitor's potency and kinome selectivity. The main challenge in the field of tubulin inhibitors is to develop agents against which cancer cells will not acquire resistance. Finally, a correct mechanism of action of a new cancer drug will define the selection of preclinical disease models and guide the design of clinical trials.

The main advantage of our methodology is its simplicity and feasibility. Identification of a new cellular target for a given efficacious drug can be approached via CRISPR-mediated chemical-genetic screens [13] or direct chemoproteomic pull-down followed by a proteomic screen to identify all proteins that bind to the inhibitor [43,44]. Alternatively, new drug targets can be identified indirectly using through computational interference using COMPARE platform, Connectivity Map [45,46] or Cancer Therapeutics Response Portal [47–49]. While these direct and indirect platforms are helpful in characterising the cellular mechanism of action of a small molecule, they entail extensive experiments and expertise. The cell morphology observation approach

presented in this article does not require any additional experiments and can be completed within the standard cell viability assay.

The majority of kinase inhibitors that have been identified to directly target tubulin (e.g. tivantinib, CMPD1, rigosertib) [13,20,27] bind to the colchicine binding site of tubulin. The large group of colchicine-site binders provided information of how these agents interact with the colchicine domain, which led to the development of several pharmacophore models [21,50–52]. Whether the structures of kinase inhibitors targeting tubulin align with these pharmacophore models has not been investigated so far. However, the docking of tivantinib into the colchicine binding site [21] revealed that the tivantinib binding mode is different from the previous docking models. Thus, the pharmacophore models developed on the colchicine-site binders might not be directly applicable to kinase inhibitors.

In summary, we describe features of cell morphology changes that can be readily used to identify kinase inhibitors unintentionally targeting tubulin. Recognizing tubulin as a direct target of a new kinase inhibitor will build confidence in the future development of *bona fide* kinase inhibitors and lay solid mechanistic foundations upon which the scientific community can build. We acknowledge that 17 cancer drugs are a limited sample size of the large arsenal of cancer drugs available to scientists, and based on our study we cannot make definitive conclusions about the whole class of kinase inhibitors. Similarly, few cancer models used in this study do not represent all types of cancers, and some cancer cells might respond differently to drugs targeting tubulin. However, we believe that the presented study will help to raise awareness about non-kinase targets of kinase inhibitors and highlight the importance of observing cell morphology upon cancer drug treatment. Further studies will investigate if changes in cell morphology could guide identification of tubulin as an off-target not only for kinase inhibitors but also for other cancer drug classes, such as epigenetic drugs, proteasome inhibitors, PARP inhibitors or apoptosis inducers exemplified by venetoclax. Such studies would validate the predictive power of cell morphology in pharmacological research.

Conflict of interest declaration

All authors declare no conflict of interest.

Acknowledgements

This work was supported by the National Health & Medical Research Council of Australia (APP1106145). TGJ, BWS and BWD are members of the Brain Cancer Discovery Collaborative, which is supported by the Cure Brain Cancer Foundation. MP is supported by Cancer Institute NSW Career Development Fellowship (17/CDF/002), The Philip Hemstrich Fellowship in Pancreatic Cancer and Avner Pancreatic Cancer Foundation. LM is supported by Cancer Institute NSW Career Development Fellowship (15/CDF/107) and Brain Foundation Australia.

References

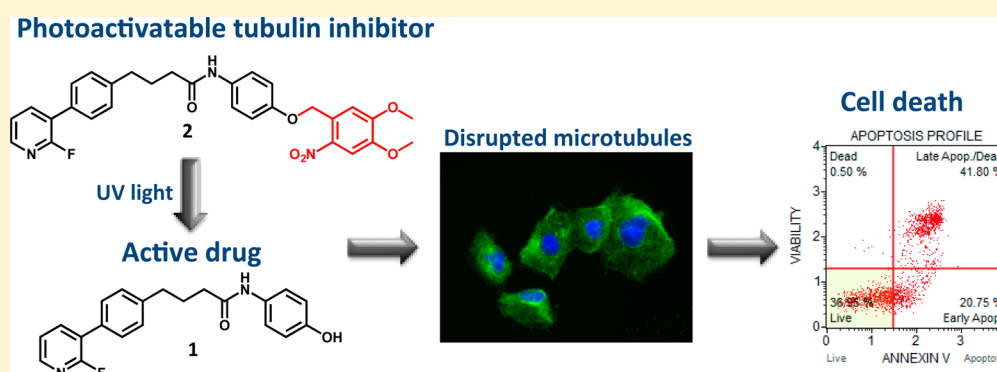
- J. Blagg, P. Workman, Chemical biology approaches to target validation in cancer, *Curr. Opin. Pharmacol.* 17 (2014) 87–100.
- C.H. Arrowsmith, et al., The promise and peril of chemical probes, *Nat. Chem. Biol.* 11 (2015) 536–541.
- J. Blagg, P. Workman, Choose and use your chemical probe wisely to explore cancer biology, *Cancer Cell* 32 (2017) 9–25.
- L. Munoz, Non-kinase targets of protein kinase inhibitors, *Nat. Rev. Drug Discov.* 16 (2017) 424–440.
- F. Gurgis, et al., Cytotoxic activity of the MK2 inhibitor CMPD1 in glioblastoma cells is independent of MK2, *Cell Death Discov.* 1 (2015) 15028.
- C. Basilico, et al., Tivantinib (ARQ197) displays cytotoxic activity that is independent of its ability to bind MET, *Clin. Cancer Res.* 19 (2013) 2381–2392.
- R. Katayama, et al., Cytotoxic activity of tivantinib (ARQ 197) is not due solely to c-MET inhibition, *Cancer Res.* 73 (2013) 3087–3096.
- J.K. Cheong, et al., IC261 induces cell cycle arrest and apoptosis of human cancer cells via CK1 δ/ϵ and Wnt/ β -catenin independent inhibition of mitotic spindle formation, *Oncogene* 30 (2011) 2558–2569.
- P. Ross-Macdonald, et al., Identification of a nonkinase target mediating cytotoxicity of novel kinase inhibitors, *Mol. Cancer Ther.* 7 (2008) 3490–3498.
- P. Ciceri, et al., Dual kinase-bromodomain inhibitors for rationally designed poly-pharmacology, *Nat. Chem. Biol.* 10 (2014) 305–312.
- A. Dittmann, et al., The commonly used PI3-kinase probe LY294002 is an inhibitor of BET bromodomains, *ACS Chem. Biol.* 9 (2014) 495–502.
- B.R. Lanning, et al., A road map to evaluate the proteome-wide selectivity of covalent kinase inhibitors, *Nat. Chem. Biol.* 10 (2014) 760–767.
- M. Jost, et al., Combined CRISPRi/a-based chemical genetic screens reveal that rigosertib is a microtubule-destabilizing agent, *Mol. Cell* 68 (2017) 210–223.
- J. Mccarroll, A. Parker, M. Kavallaris, Microtubules and their role in cellular stress in cancer, *Front. Oncol.* 4 (2014) 153.
- C. Dumontet, M.A. Jordan, Microtubule-binding agents: a dynamic field of cancer therapeutics, *Nat. Rev. Drug Discov.* 9 (2010) 790–803.
- N. Munshi, et al., ARQ 197, a novel and selective inhibitor of the human c-Met receptor tyrosine kinase with antitumor activity, *Mol. Cancer Ther.* 9 (2010) 1544–1553.
- N. Waddell, et al., Whole genomes redefine the mutational landscape of pancreatic cancer, *Nature* 518 (2015) 495.
- A. Chou, et al., Tailored first-line and second-line CDK4-targeting treatment combinations in mouse models of pancreatic cancer, *Gut* (2017), <http://dx.doi.org/10.1136/gutjnl-2017-315144Y> PMID: 29080858.
- S. Eathiraj, et al., Discovery of a novel mode of protein kinase inhibition characterized by the mechanism of inhibition of human mesenchymal-epithelial transition factor (c-Met) protein autophosphorylation by ARQ 197, *J. Biol. Chem.* 286 (2011) 20666–20676.
- A. Aoyama, et al., Tivantinib (ARQ 197) exhibits antitumor activity by directly interacting with tubulin and overcomes ABC transporter-mediated drug resistance, *Mol. Cancer Ther.* 13 (2014) 2978–2990.
- Y. Wang, et al., Structures of a diverse set of colchicine binding site inhibitors in complex with tubulin provide a rationale for drug discovery, *FEBS J.* 283 (2016) 102–111.
- F. Cappuzzo, et al., Management of crizotinib therapy for ALK-rearranged non-small cell lung carcinoma: an expert consensus, *Lung Cancer* 87 (2015) 89–95.
- C. Dominguez-Brauer, et al., Targeting mitosis in cancer: emerging strategies, *Mol. Cell* 60 (2015) 524–536.
- Y.L. Wong, et al., Reversible centriole depletion with an inhibitor of Polo-like kinase 4, *Science* 348 (2015) 1155.
- W.-S. Huang, et al., Discovery of 3-[2-(imidazo[1,2-b]pyridazin-3-yl)ethynyl]-4-methyl-N-{4-[(4-methylpiperazin-1-yl)methyl]-3-(trifluoromethyl)phenyl}benzamide (AP24534), a potent, orally active pan-inhibitor of Breakpoint Cluster Region-Abelson (BCR-ABL) kinase including the T315I gatekeeper mutant, *J. Med. Chem.* 53 (2010) 4701–4719.
- A.F. Phoa, et al., Pharmacology of novel small-molecule tubulin inhibitors in glioblastoma cells with enhanced EGFR signalling, *Biochem. Pharmacol.* 98 (2015) 587–601.
- A. Döbber, et al., Development and biological evaluation of a photoactivatable small molecule microtubule-targeting agent, *ACS Med. Chem. Lett.* 8 (2017) 395–400.
- A. Sakaue-Sawano, et al., Visualizing spatiotemporal dynamics of multicellular cell-cycle progression, *Cell* 132 (2008) 487–498.
- M. Kavallaris, Microtubules and resistance to tubulin-binding agents, *Nat. Rev. Cancer* 10 (2010) 194–204.
- D.-H. Kim, Y. Kwak, N.D. Kim, T. Sim, Antitumor effects and molecular mechanisms of ponatinib on endometrial cancer cells harboring activating FGFR2 mutations, *Cancer Biol. Ther.* 17 (2016) 65–78.
- M.G. Manfredi, et al., Characterization of alisertib (MLN8237), an investigational small-molecule inhibitor of Aurora A kinase using novel *in vivo* pharmacodynamic assays, *Clin. Cancer Res.* 17 (2011) 7614.
- J.A. Engelman, et al., PF00299804, an irreversible pan-ERBB inhibitor, is effective in lung cancer models with EGFR and ERBB2 mutations that are resistant to gefitinib, *Cancer Res.* 67 (2007) 11924.
- W. Zhang, et al., UNC2025, a potent and orally bioavailable MER/FLT3 dual inhibitor, *J. Med. Chem.* 57 (2014) 7031–7041.
- M.E. Flanagan, et al., Discovery of CP-690,550: a potent and selective Janus kinase (JAK) inhibitor for the treatment of autoimmune diseases and organ transplant rejection, *J. Med. Chem.* 53 (2010) 8468–8484.
- T. Yamaguchi, R. Kakefuda, N. Tajima, Y. Sowa, T. Sakai, Antitumor activities of JTP-74057 (GSK1120212), a novel MEK1/2 inhibitor, on colorectal cancer cell lines *in vitro* and *in vivo*, *Int. J. Oncol.* 39 (2011) 23–31.
- B.J. Lannutti, et al., CAL-101, a p110 δ selective phosphatidylinositol-3-kinase inhibitor for the treatment of B-cell malignancies, inhibits PI3K signaling and cellular viability, *Blood* 117 (2011) 591.
- G. Bollag, et al., Clinical efficacy of a RAF inhibitor needs broad target blockade in BRAF-mutant melanoma, *Nature* 467 (2010) 596.
- D.W. Fry, et al., Specific inhibition of cyclin-dependent kinase 4/6 by PD 0332991 and associated antitumor activity in human tumor xenografts, *Mol. Cancer Ther.* 3 (2004) 1427.
- W. Davidson, et al., Discovery and characterization of a substrate selective p38 α inhibitor, *Biochemistry* 43 (2004) 11658–11671.
- B.W. Day, et al., Glioma surgical aspirate: a viable source of tumor tissue for experimental research, *Cancers* 5 (2013) 357–371.
- B.W. Day, et al., EphA3 maintains tumorigenicity and is a therapeutic target in glioblastoma multiforme, *Cancer Cell* 23 (2013) 238–248.
- S.M. Pollard, et al., Glioma stem cell lines expanded in adherent culture have

- tumor-specific phenotypes and are suitable for chemical and genetic screens, *Cell Stem Cell* 4 (2009) 568–580.
- [43] K. Wang, et al., Chemistry-based functional proteomics for drug target deconvolution, *Expert Rev. Proteom.* 9 (2012) 293–310.
- [44] M. Schenone, V. Dancik, B.K. Wagner, P.A. Clemons, Target identification and mechanism of action in chemical biology and drug discovery, *Nat. Chem. Biol.* 9 (2013) 232–240.
- [45] J. Lamb, et al., The connectivity map: using gene-expression signatures to connect small molecules, genes, and disease, *Science* 313 (2006) 1929–1935.
- [46] J. Lamb, The connectivity map: a new tool for biomedical research, *Nat. Rev. Cancer* 7 (2007) 54–60.
- [47] A. Basu, et al., An interactive resource to identify cancer genetic and lineage dependencies targeted by small molecules, *Cell* 154 (2013) 1151–1161.
- [48] B. Seashore-Ludlow, et al., Harnessing connectivity in a large-scale small-molecule sensitivity dataset, *Cancer Discov.* 5 (2015) 1210–1223.
- [49] M.G. Rees, et al., Correlating chemical sensitivity and basal gene expression reveals mechanism of action, *Nat. Chem. Biol.* 12 (2016) 109–116.
- [50] T.L. Nguyen, et al., A common pharmacophore for a diverse set of colchicine site inhibitors using a structure-based approach, *J. Med. Chem.* 48 (2005) 6107–6116.
- [51] Y. Lu, J. Chen, M. Xiao, W. Li, D.D. Miller, An overview of tubulin inhibitors that interact with the colchicine binding site, *Pharm. Res.* 29 (2012) 2943–2971.
- [52] W. Li, H. Sun, S. Xu, Z. Zhu, J. Xu, Tubulin inhibitors targeting the colchicine binding site: a perspective of privileged structures, *Future Med. Chem.* 9 (2017) 1765–1794.
- [53] Z. Zhao, et al., Exploration of type II binding mode: a privileged approach for kinase inhibitor focused drug discovery? *ACS Chem. Biol.* 9 (2014) 1230–1241.

Development and Biological Evaluation of a Photoactivatable Small Molecule Microtubule-Targeting Agent

Alexander Döbber,^{†,‡} Athena F. Phoa,[†] Ramzi H. Abbassi,[†] Brett W. Stringer,[§] Bryan W. Day,[§] Terrance G. Johns,^{||,⊥} Mohammed Abadleh,^{‡,#} Christian Peifer,^{*,‡,§} and Lenka Munoz^{*,†,§}[†]School of Medical Sciences and Charles Perkins Centre, The University of Sydney, Sydney, NSW 2006, Australia[‡]Institute of Pharmacy, Christian-Albrechts-University of Kiel, Gutenbergstraße 76, 24118 Kiel, Germany[§]QIMR Berghofer Medical Research Institute, 300 Herston Road, Herston, QLD 4006, Australia^{||}Oncogenic Signalling Laboratory and Brain Cancer Discovery Collaborative, Centre for Cancer Research, Hudson Institute of Medical Research, 27-31 Wright Street, Clayton, VIC 3168, Australia[⊥]Monash University, Wellington Road, Clayton, VIC 3800, Australia

Supporting Information



ABSTRACT: Photoremovable protecting groups added to bioactive molecules provide spatial and temporal control of the biological effects. We present synthesis and characterization of the first photoactivatable small-molecule tubulin inhibitor. By blocking the pharmacophoric OH group on compound 1 with photoremovable 4,5-dimethoxy-2-nitrobenzyl moiety we developed the photocaged prodrug 2 that had no effect in biological assays. Short UV light exposure of the derivative 2 or UV-irradiation of cells treated with 2 resulted in fast and potent inhibition of tubulin polymerization, attenuation of cell viability, and apoptotic cell death, implicating release of the parent active compound. This study validates for the first time the photoactivatable prodrug concept in the field of small molecule tubulin inhibitors. The caged derivative 2 represents a novel tool in antitubulin approaches.

KEYWORDS: Photoactivatable caged prodrug, tubulin inhibitor, glioblastoma

Delivering bioactive molecules to cells with temporal and spatial precision is useful for elucidating complex biological processes. One method for regulating the action of bioactive molecules employs photolabile-protecting groups (PPGs).¹ The PPG is a chromophore covalently attached to the pharmacophoric moiety of the bioactive molecule, thus blocking its biological activity, a concept known as “caging”. The covalent bond between the bioactive molecule and the PPG is cleaved by irradiation with ultraviolet (UV) light, leading to the release of the parent bioactive molecule (“uncaging”). A number of PPGs have been developed for this purpose, including *p*-nitrobenzyl, 4,5-dimethoxy-2-nitrobenzyl (DMNB), and 6-bromo-7-hydroxycoumarine-4-ylmethyl,² and the caging concept has been successfully applied to phototrigger calcium, neurotransmitters, nucleic acids, and antibiotics.^{3,4} For example, photocaged rapamycin has been

used to induce controlled activity of the small GTPase Rac in the cellular context,⁵ and photocaged anisomycin has been employed to locally inhibit protein synthesis.⁶ Photocaged puromycin was effectively applied for spatiotemporal monitoring of mRNA translation.⁷ We have recently developed a number of caged kinase inhibitors that serve as valuable molecular probes to delineate signaling pathways.^{8–10} Furthermore, photocaging has been applied for delivery of molecules across membranes and for the control of side effects.^{11,12}

Microtubule-targeting agents (MTAs) disrupt polymerization of α - and β -tubulin to form microtubules. Microtubules are

Received: November 29, 2016

Accepted: March 15, 2017

Published: March 15, 2017

crucial for cell division in mitosis, and this explains why compounds that bind to tubulin and interfere with tubulin polymerization are highly effective in killing rapidly proliferating cancer cells. Importantly, tubulin has a crucial role also in nonmitotic cells, which underlies the overall success of MTAs in cancer therapy.^{13–15}

MTAs are structurally diverse and very often structurally complex molecules as the vast majority of these agents are natural products isolated from bacteria, plants, and marine sponges.¹⁶ With the long history of clinical efficacy, MTAs remain to date the most classical yet reliable chemotherapeutics. Microtubules targeting Vinca alkaloids (vinblastine, vincristine) and taxanes (paclitaxel, cabazitaxel) are frontline treatments for breast, ovarian, and hormone-refractory prostate cancers. However, the acquired resistance developed over the time of treatment has plagued the success of these drugs.

Mechanisms of MTA resistance are manifold, including overexpression of efflux proteins, point mutations at the paclitaxel-binding site, or polymorphism resulting in the overexpression of various β -tubulin isoforms.¹³ Another major limitation in the use of MTAs is the high rate of neuropathy induced by these compounds. This effect manifests itself as a painful peripheral axonal pain for which there is currently no effective symptomatic treatment.¹⁷ Myeloid toxicity and neutropenia is also frequently observed with MTAs, with subtle differences between compounds within the same family.

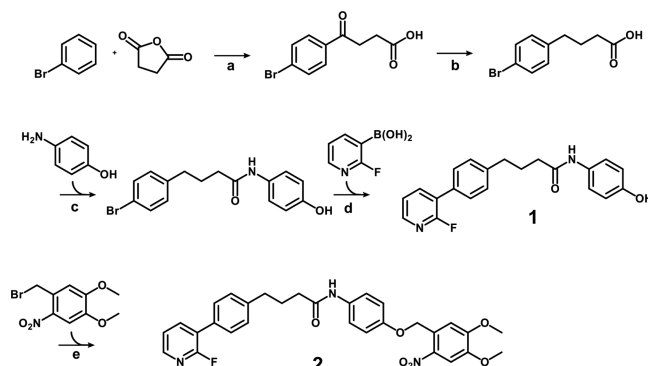
Clinically approved MTAs are ineffective for treatment of brain tumors as their large molecular weight (>800 g/mol) renders them unable to cross the blood–brain barrier. Hence, there has been increasing research interest toward the development of effective MTA delivery methods^{18–20} or identification of small-molecule tubulin inhibitors able to cross the blood–brain barrier.^{21,22} We discovered that a small-molecule known as CMPD1 and initially developed to inhibit p38 MAPK-MK2 signaling pathway,²³ primarily inhibits tubulin polymerization.²⁴ CMPD1 showed potent antimetabolic and apoptotic activity in a panel of cancer cells. This cytotoxic activity and the small molecular weight (349 g/mol) made CMPD1 an attractive lead for the development of potential chemotherapeutic agents for brain tumors. Recently, we reported synthesis of CMPD1 analogues with improved molecular properties and demonstrated their anticancer efficacy in patient-derived glioblastoma cells.²⁵

Herein, we present a novel concept in the class of small-molecule tubulin inhibitors. In order to reduce side effects associated with tubulin inhibitors, we developed a caged tubulin inhibitor by addition of a photoactivatable protecting group and describe its pharmacology in glioblastoma cells. We have chosen glioblastoma cell-based models as this heterogeneous brain cancer represents a major unmet medical need. Although glioblastoma was one of the first cancers to be profiled through The Cancer Genome Atlas project, making it genomically a well-characterized cancer,²⁶ the results of glioblastoma trials using inhibitors of oncogenic drivers have been disappointing so far.²⁷ Importantly, glioblastoma cells are sensitive to MTAs,^{22,25} suggesting that MTAs able to cross the blood–brain barrier could be effective in glioblastoma therapy. The photoactivatable approach presented in this work opens a new avenue to reduce side effects of MTAs as the active drug may be locally released at the tumor site.

To synthesize the photoactivatable tubulin inhibitor, the tubulin inhibitor **1** was converted into a photocaged derivative

2 (Scheme 1). We have chosen the 4,5-dimethoxy-2-nitrobenzyl (DMNB) as the PPG because of its excellent

Scheme 1. Synthesis of the Photoactivatable Tubulin Inhibitor **2**^a



^aReagents and conditions: (a) AlCl_3 , HCl, N_2 , 96 h; (b) Zn/Hg, HCl, toluene, 24 h; (c) PYBOP, DIPEA, DMF; (d) Pd(PPh_3)₄, Na_2CO_3 , EtOH/ H_2O , MW 130°C, 20 min; (e) K_2CO_3 , DMF, RT.

quantitative cleavage by UV irradiation.^{1,9,10} DMNB was attached to the phenol moiety of compound **1**, as the SAR study demonstrated that the removal of the OH group resulted in significant loss of cellular efficacy.²⁵ DMNB-caged derivative **2** was obtained in 60% yield in the final synthetic step using DMNB-bromide as a reagent, followed by reversed-phase chromatography purification. UV spectra of compounds **1** and **2** (Figure S1) revealed that inhibitor **1** shows no absorption at 365 nm, whereas the photoprodrug **2** possesses an absorption maximum around 350 nm. As the high absorption of photocaged molecules at the irradiation wavelength is crucial to trigger the PPG cleavage, we identified 365 nm as suitable irradiation wavelength.

In the photocaging concept it is essential that the parent molecule is sufficiently stable under the conditions used for uncaging by UV irradiation. Otherwise, the irradiation would degrade the released active drug immediately after the PPG cleavage. Initially, in an analytical setup to examine the UV stability of the tubulin inhibitor **1**, we used a light-emitting diode (LED) reactor and a wavelength of 365 nm (5400 mW, Figure S2, lamp A) to irradiate compound **1** (1 mM). HPLC and LC–MS analysis of samples collected over the period of 20 min confirmed that inhibitor **1** was stable under these conditions (Figure S3).

To determine the kinetics of the photorelease, caged analogue **2** was UV irradiated at 365 nm (2700 mW, Figure S2, lamp A), and samples were collected at indicated time points for quantitative HPLC analysis (Figure 1). After 1 min of irradiation, approximately 80% of the bioactive inhibitor **1** was released from the photoprodrug **2**. The reaction progress curve excellently fitted ($R^2 = 1$) to the exponential one-phase decay kinetics with a time constant (τ) of 0.605 min. The maximum measured concentration of parent inhibitor **1** was reached after 2 min of irradiation. This data confirm that DMNB-caged compound **2** possesses suitable uncaging kinetics.

To assess the inactivity of caged prodrug **2**, as well as reactivation and recovery of the cytotoxic effects, we performed a series of cell viability assays using U251 and patient-derived RN1 glioblastoma cells. The U251 cell line was established

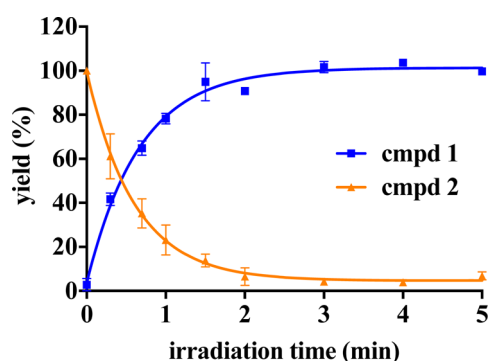


Figure 1. Photolytic characterization of the caged derivative 2. A solution of compound 2 (1 mM) was irradiated at 365 nm, and samples collected at indicated time points were analyzed by HPLC. Compound 2 was photolyzed to produce compound 1 in one-phase decay kinetics ($\tau = 0.605$ min, $R^2 = 1$). Data represent mean \pm SEM from two independent experiments performed in duplicate.

prior to genome analysis of glioblastoma tumors and is not assigned to any glioblastoma subtype. The patient-derived RN1 cell line was established in our laboratories^{28,29} and represents the most common (>60%) classical subtype of glioblastomas. RN1 cells were grown as stem cells under defined conditions in order to maintain the phenotype and genotype of the primary resected tumor.³⁰

First, we investigated the effects of UV light on cell viability in order to determine tolerable levels of UV exposure. We exposed U251 and RN1 cells to UV light up to 5 min (lamp B, 1800 mW, Figure S2) and after 24 h of incubation performed viability assay using Cell TiterBlue reagent. We found that U251 and RN1 cells tolerated a continuous UV light exposure of 1 min and 30s, respectively (Figure S4).

To assess the cytotoxic effects, cells were treated with uncaged inhibitor 1 and caged derivative 2 for 72 h, and cell viability assays were performed to evaluate the number of viable cells. The parent compound 1 decreased the viability of U251 and RN1 cells with EC_{50} values of 1.3 and 0.3 μ M, respectively (Figure 2), which is in good agreement with previously published data.^{24,25} UV irradiation of cells treated with compound 1 did not affect the efficacy of the uncaged derivative (Figure 2). In contrast to the bioactive compound 1 and as expected by our PPG design, caged derivative 2 had no significant cytotoxicity up to high micromolar concentrations ($EC_{50} = 72$ and 37.4 μ M for U251 and RN1, respectively), providing evidence that addition of the PPG to compound 1 resulted in the loss of cytotoxic activity. UV irradiation (30 s of RN1 and 1 min of U251 cells) restored the activity of compound 2 and efficacy in both cell lines was equivalent to the efficacy of the uncaged compound ($EC_{50} = 2.1$ and 1.2 μ M for U251 and RN1, respectively), suggesting that a recovery of the cytotoxic activity is achieved with a short period of UV irradiation.

To confirm that addition of the bulky PPG was detrimental to the cytotoxicity of compound 1, compound 3 containing a benzyl moiety on the phenolic OH group was synthesized and its cytotoxicity tested using U251 glioblastoma cells (Figure 3). Compound 3 affected U251 cell viability only at concentrations higher than 40 μ M. We also synthesized 4,5-dimethoxy-2-nitrobenzyl (*tert*-butoxycarbonyl)alaninate 4 to investigate if the DMNB moiety released via irradiation of the caged derivative 2 could be cytotoxic to the cells. Importantly, compound 4 when UV irradiated to release DMNB did not

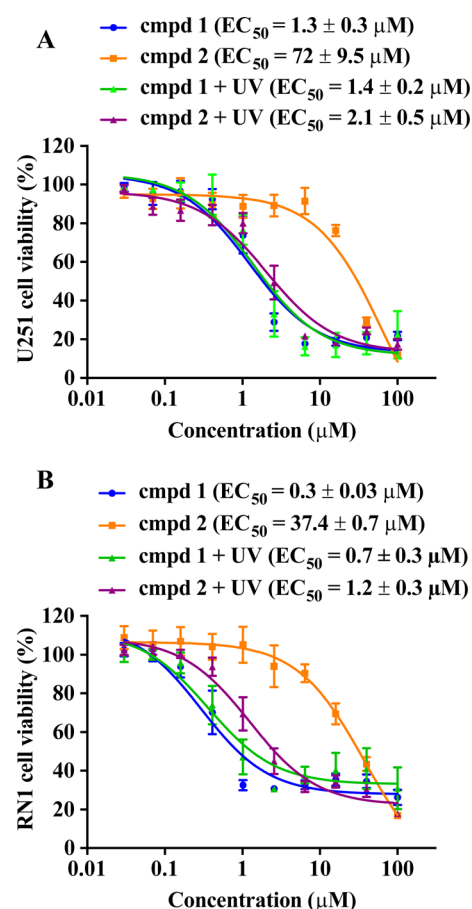


Figure 2. Evaluation of the uncaging protocol in a cell viability assay. (A) U251 and (B) patient-derived RN1 glioblastoma cells were grown as adherent cultures, treated with uncaged inhibitor 1 and caged derivative 2. U251 cells were UV irradiated (365 nm, 1800 mW) for 1 min, RN1 cells were irradiated for 30 s. Cellular efficacy (EC_{50}) values were determined using Cell TiterBlue viability assay after 72 h of drug treatment. Data represent mean \pm SEM from three independent experiments performed in triplicate.

change the viability of U251 cells up to 100 μ M concentration (Figure 3). Together, these data indicate that (i) the unsubstituted phenolic group is crucial for the biological activity of 1 and that (ii) cytotoxicity after UV irradiation results from uncaging the inhibitor 1 and not from the released DMNB.

To further validate that the caging with DMNB caused loss of biological activities determined for compound 1 in cells, we conducted an *in vitro* tubulin polymerization and tubulin binding assays using uncaged and caged analogues 1 and 2, respectively (Figure 4). Purified β -tubulin was incubated with clinical MTAs paclitaxel and vinblastine, as well as with compounds 1 and 2. Compared to control, paclitaxel enhanced tubulin polymerization, whereas vinblastine and compound 1 inhibited tubulin polymerization (Figure 4A), which is in agreement with their established mechanism of action.²⁴ In contrast, caged derivative 2 did not exhibit any effect on the kinetics of tubulin polymerization. However, if the same assay was performed with derivative 2 exposed to UV irradiation, the inhibition of tubulin polymerization was indistinguishable from that obtained with the uncaged compound 1. Thus, the uncaging of 2 by UV irradiation produced a bioactive molecule

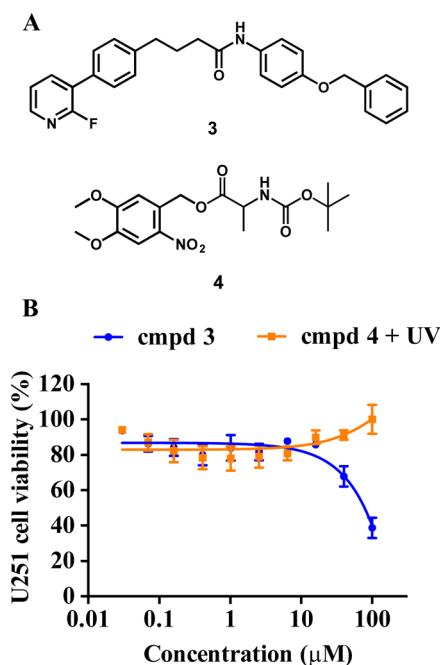


Figure 3. Efficacy of negative control compounds 3 and 4 in the cell viability assay. (A) Chemical structures of compounds 3 and 4. (B) Cellular efficacy of compound 3 and UV-irradiated (365 nm, 1800 mW, 1 min) compound 4 in U251 glioblastoma cells was determined using Cell TiterBlue viability assay after 72 h of drug treatment. Data represent mean \pm SEM from three independent experiments performed in triplicate.

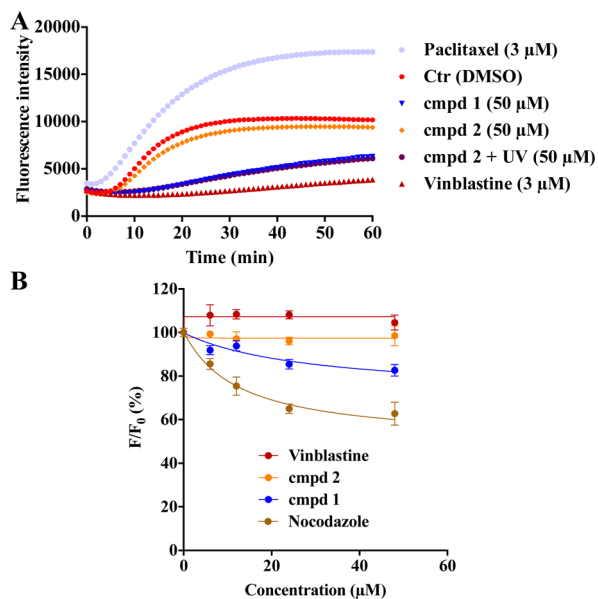


Figure 4. Tubulin polymerization and colchicine binding assay. (A) Porcine brain tubulin was incubated with paclitaxel, vinblastine, and compounds 1 and 2 \pm UV irradiation (365 nm, 1800 mW, 5 min). Assembly of microtubules was monitored by an increase in fluorescence. Data represent the mean from three independent experiments; each data point was performed in triplicate. (B) Colchicine binding assay. Porcine tubulin was incubated with colchicine and tested compounds. Fluorescence intensity (F) was normalized to the fluorescence of the colchicine–tubulin complex (F_0). Data represent mean \pm SEM from four independent experiments.

inhibiting tubulin polymerization with the same efficacy as the unmodified tubulin inhibitor 1 (Figure 4A).

Small molecules inhibiting tubulin polymerization predominantly bind into the colchicine binding site on tubulin.³¹ To investigate the binding site of compound 1, we performed fluorescence-based colchicine binding assay.^{32,33} Competition of the inhibitor and colchicine for the binding site will decrease the intrinsic fluorescence of colchicine–tubulin complex by reducing the amount of colchicine bound. With this assay, we confirmed that compound 1, but not the caged derivative 2, decreased the intrinsic colchicine fluorescence in a dose-dependent manner (Figure 4B). Nocodazole, tubulin inhibitor binding to the colchicine site (positive control) also efficiently decreased the fluorescence, whereas vinblastine (negative control) had no effect on the fluorescence. The observation that compound 1 caused a weaker decrease in the fluorescence compared to nocodazole suggests that compound 1 is likely to bind in the vicinity or allosterically to colchicine.

We next examined in greater detail how addition of the PPG to compound 1 alters the microtubule network in cells. For this, U251 glioblastoma cells were treated with 1 and 2, and the effect on the microtubules was investigated via immunofluorescence staining of β -tubulin. Treatment of U251 cells with compound 1 (5 μM) led to a disassembly of microtubules and pronounced changes in cell morphology (Figure 5). However,

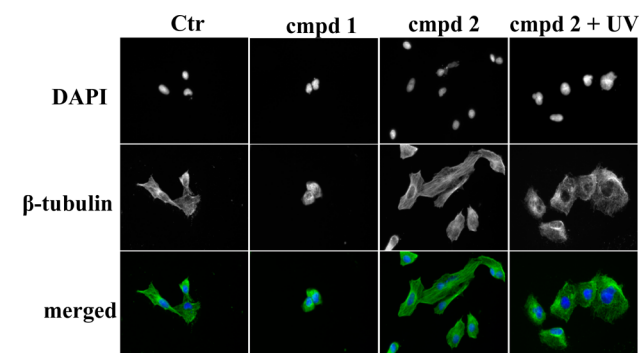


Figure 5. Immunofluorescence imaging of treated cells. U251 cells treated with compounds 1 and 2 and UV-irradiated (365 nm, 1800 mW, 5 min) compound 2. All treatments were done with 5 μM concentration for 24 h. Cells were fixed and stained with Alexa488-labeled anti- β -tubulin antibody (green) or DAPI (blue). Representative images of two independent experiments are shown.

treatment with compound 2 had no effect on cell morphology and the tubulin network; the images of cells treated with 2 resembled the images of untreated control cells. Importantly, if cells were treated with UV irradiated (365 nm, 1800 mW, 5 min) compound 2, cells rounded up and lost their star-shaped structure. Furthermore, tubulin filaments lost their organization, suggesting that UV irradiation of compound 2 released a compound that acts as tubulin inhibitor and disrupts the highly organized tubulin network in cells.

Microtubule targeting agents not only characteristically disrupt the tubulin network and cell morphology as demonstrated in Figure 5, they also induce apoptosis through the intrinsic (mitochondrial) apoptotic pathway.³⁴ In order to determine whether this mechanism contributes to the cellular efficacy of the caged derivative 2 after UV irradiation, we quantified apoptosis in drug-treated RN1 cells by Annexin V staining (Figure 6). UV irradiation (365 nm, 1800 mW, 30 s) of the patient-derived RN1 cells did not increase the basal level of

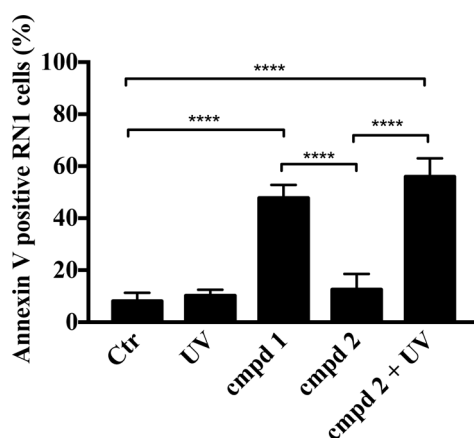


Figure 6. Tubulin inhibitor **1** and caged derivative **2** combined with UV irradiation induce apoptosis in RN1 glioblastoma cells. Cells were treated with **1** and **2** ($5 \mu\text{M} \pm$ UV irradiation) for 48 h. Control cells received an equivalent amount of DMSO or UV irradiation (365 nm, 1800 mW, 30 s). Cells were stained with Annexin V and analyzed using the MUSE Cell Analyzer. Data represent mean \pm SEM from three independent experiments (**** $P < 0.0001$, one-way ANOVA followed by Tukey's multiple comparison test).

Annexin V-positive cells (8.1% and 10.1% for Ctr and UV treated cells, respectively; Figure 6). Treatment of RN1 cells with the parent bioactive compound **1** ($5 \mu\text{M}$, 48 h) increased the amount of apoptotic cells to 47.8%. In agreement with previous data, compound **2** was ineffective in inducing apoptosis (12.6% of Annexin V-positive cells). However, the quantity (55.9%) of apoptotic RN1 cells when treated with compound **2** combined with UV irradiation (365 nm, 1800 mW, 30 s) was comparable to the quantity of apoptotic cells after treatment with compound **1** (47.8%), further confirming that the uncaging with UV light released an active compound.

In summary, we have described the synthesis of the novel photocaged tubulin inhibitor **2**, as well as its photolytic and pharmacological characterization. By using DMNB as photolabile protecting group to cage a small molecule tubulin inhibitor, we demonstrate spatial and temporal photoinducible toxicity to glioblastoma cells, inhibition of tubulin polymerization, and induction of apoptotic cell death. Collectively, these data show for the first time that caging concept combined with UV irradiation can be used to control the activity of small molecule tubulin inhibitors. This concept offers a novel tool for pharmacological studies and potentially a novel therapeutic approach to reduce the side effects of microtubule-targeting agents.

■ ASSOCIATED CONTENT

Supporting Information

The Supporting Information is available free of charge on the ACS Publications website at DOI: 10.1021/acsmchemlett.6b00483.

Experimental details, compounds characterization, and Figures S1–S5 (PDF)

■ AUTHOR INFORMATION

Corresponding Authors

*E-mail: lenka.munoz@sydney.edu.au.

*E-mail: cpeifer@pharmazie.uni-kiel.de.

ORCID

Christian Peifer: 0000-0003-1532-7826

Lenka Munoz: 0000-0002-7625-5646

Present Address

#College of Pharmacy, Taibah University, Almadinah Almonawwarrah 41477, Saudi Arabia.

Author Contributions

A.D. and M.A. synthesized and characterized compounds presented in this study. A.D. and A.F.P. designed, performed, and analyzed all biological assays, except for the colchicine binding assay, which was designed, performed, and analyzed by R.H.A. B.W.S., B.W.D., and T.J.G. derived and characterized RN1 patient-derived glioblastoma cells. L.M. and P.F. designed the study concept and supervised the study. All authors have given approval to the final version of the manuscript.

Funding

L.M. is a Cancer Institute NSW Career Development Fellow (grant reference 15/CDF/1-07). This study was partially funded by the National Foundation for Medical Research and Innovation (NFMRI) and Sydney Medical School Foundation grants to L.M.; and DFG (German Research Society) grant PE 1605/2-1 to C.P. A.F.P. is supported by The University of Sydney Australian Postgraduate Award scholarship. M.A. was funded by the German Academic Exchange Service (DAAD) and A.D. via the DAAD/PROMOS scholarship funds from the Federal German Ministry for Education and Research. T.G.J. was supported by the NH&MRC (Project Grant #1028552) and Cure Brain Cancer Foundation. T.G.J., B.W.S., and B.W.D. are members of the Brain Cancer Discovery Collaborative, which is supported by the Cure Brain Cancer Foundation. This work was partly supported by the Victorian Government's Operational and Infrastructure Support Program (to T.G.J.).

Notes

The authors declare no competing financial interest.

■ ABBREVIATIONS

DMNB, 4,5-dimethoxy-2-nitrobenzyl; MAPK, mitogen-activated protein kinase; MK2, MAPK-activated protein kinase 2; MTA, microtubule-targeting agent; PPG, photolabile-protecting group

■ REFERENCES

- (1) Klán, P.; Šolomek, T.; Bochet, C. G.; Blanc, A.; Givens, R.; Rubina, M.; Popik, V.; Kostikov, A.; Wirz, J. Photoremovable protecting groups in chemistry and biology: Reaction mechanisms and efficacy. *Chem. Rev.* **2013**, *113* (1), 119–191.
- (2) Givens, R. S.; Rubina, M.; Wirz, J. Applications of p-hydroxyphenacyl (pHP) and coumarin-4-ylmethyl photoremovable protecting groups. *Photochem. Photobiol. Sci.* **2012**, *11* (3), 472–488.
- (3) Mayer, G.; Heckel, A. Biologically active molecules with a "Light Switch". *Angew. Chem., Int. Ed.* **2006**, *45* (30), 4900–4921.
- (4) Cui, J.; Gropeanu, R. A.; Stevens, D. R.; Rettig, J.; Campo, A. d. New photolabile BAPTA-based Ca^{2+} cages with improved photo-release. *J. Am. Chem. Soc.* **2012**, *134* (18), 7733–7740.
- (5) Umeda, N.; Ueno, T.; Pohlmeier, C.; Nagano, T.; Inoue, T. A photocleavable rapamycin conjugate for spatiotemporal control of small GTPase activity. *J. Am. Chem. Soc.* **2011**, *133* (1), 12–14.
- (6) Goard, M.; Aakalu, G.; Fedoryak, O. D.; Quinonez, C.; St. Julien, J.; Poteet, S. J.; Schuman, E. M.; Dore, T. M. Light-mediated inhibition of protein synthesis. *Chem. Biol.* **2005**, *12* (6), 685–693.
- (7) Buhr, F.; Kohl-Landgraf, J.; tom Dieck, S.; Hanus, C.; Chatterjee, D.; Hegelein, A.; Schuman, E. M.; Wachtveitl, J.; Schwalbe, H. Design of photocaged puromycin for nascent polypeptide release and

spatiotemporal monitoring of translation. *Angew. Chem., Int. Ed.* **2015**, *54* (12), 3717–3721.

(8) Gropeanu, R. A.; Baumann, H.; Ritz, S.; Mailänder, V.; Surrey, T.; del Campo, A. Phototriggerable 2',7-caged paclitaxel. *PLoS One* **2012**, *7* (9), e43657.

(9) Horbert, R.; Pinchuk, B.; Davies, P.; Alessi, D.; Peifer, C. Photoactivatable prodrugs of antimelanoma agent vemurafenib. *ACS Chem. Biol.* **2015**, *10* (9), 2099–2107.

(10) Zindler, M.; Pinchuk, B.; Renn, C.; Horbert, R.; Döbber, A.; Peifer, C. Design, synthesis, and characterization of a photoactivatable caged prodrug of imatinib. *ChemMedChem* **2015**, *10* (8), 1335–1338.

(11) Fan, N.-C.; Cheng, F.-Y.; Ho, J.-A. A.; Yeh, C.-S. Photo-controlled targeted drug delivery: Photocaged biologically active folic acid as a light-responsive tumor-targeting molecule. *Angew. Chem., Int. Ed.* **2012**, *51* (35), 8806–8810.

(12) Dcona, M. M.; Mitra, D.; Goehe, R. W.; Gewirtz, D. A.; Lebman, D. A.; Hartman, M. C. T. Photocaged permeability: a new strategy for controlled drug release. *Chem. Commun.* **2012**, *48* (39), 4755–4757.

(13) Kavallaris, M. Microtubules and resistance to tubulin-binding agents. *Nat. Rev. Cancer* **2010**, *10* (3), 194–204.

(14) Mccarroll, J.; Parker, A.; Kavallaris, M. Microtubules and their role in cellular stress in cancer. *Front. Oncol.* **2014**, *4*, 153.

(15) Komlodi-Pasztor, E.; Sackett, D.; Wilkerson, J.; Fojo, T. Mitosis is not a key target of microtubule agents in patient tumors. *Nat. Rev. Clin. Oncol.* **2011**, *8* (4), 244–250.

(16) Dumontet, C.; Jordan, M. A. Microtubule-binding agents: a dynamic field of cancer therapeutics. *Nat. Rev. Drug Discovery* **2010**, *9* (10), 790–803.

(17) Kudlowitz, D.; Muggia, F. Defining risks of taxane neuropathy: Insights from randomized clinical trials. *Clin. Cancer Res.* **2013**, *19* (17), 4570–4577.

(18) Liu, Y.; Ran, R.; Chen, J.; Kuang, Q.; Tang, J.; Mei, L.; Zhang, Q.; Gao, H.; Zhang, Z.; He, Q. Paclitaxel loaded liposomes decorated with a multifunctional tandem peptide for glioma targeting. *Biomaterials* **2014**, *35* (17), 4835–4847.

(19) Kang, T.; Gao, X.; Hu, Q.; Jiang, D.; Feng, X.; Zhang, X.; Song, Q.; Yao, L.; Huang, M.; Jiang, X.; Pang, Z.; Chen, H.; Chen, J. iNGR-modified PEG-PLGA nanoparticles that recognize tumor vasculature and penetrate gliomas. *Biomaterials* **2014**, *35* (14), 4319–4332.

(20) Zhang, B.; Zhang, Y.; Liao, Z.; Jiang, T.; Zhao, J.; Tuo, Y.; She, X.; Shen, S.; Chen, J.; Zhang, Q.; Jiang, X.; Hu, Y.; Pang, Z. UPA-sensitive ACP-PP-conjugated nanoparticles for multi-targeting therapy of brain glioma. *Biomaterials* **2015**, *36*, 98–109.

(21) Senese, S.; Lo, Y. C.; Huang, D.; Zangle, T. A.; Gholkar, A. A.; Robert, L.; Homet, B.; Ribas, A.; Summers, M. K.; Teitell, M. A.; Damoiseaux, R.; Torres, J. Z. Chemical dissection of the cell cycle: probes for cell biology and anti-cancer drug development. *Cell Death Dis.* **2014**, *5* (10), e1462.

(22) Prabhu, S.; Harris, F.; Lea, R.; Snape, T. J. Small-molecule clinical trial candidates for the treatment of glioma. *Drug Discovery Today* **2014**, *19* (9), 1298–1308.

(23) Davidson, W.; Frego, L.; Peet, G. W.; Kroe, R. R.; Labadia, M. E.; Lukas, S. M.; Snow, R. J.; Jakes, S.; Grygon, C. A.; Pargellis, C.; Werneburg, B. G. Discovery and characterization of a substrate selective p38 α inhibitor. *Biochemistry* **2004**, *43* (37), 11658–11671.

(24) Gurgis, F.; Åkerfeldt, M. C.; Heng, B.; Wong, C.; Adams, S.; Guillemain, G. J.; Johns, T. G.; Chircop, M.; Munoz, L. Cytotoxic activity of the MK2 inhibitor CMPD1 in glioblastoma cells is independent of MK2. *Cell Death Discovery* **2015**, *1*, 15028.

(25) Phoa, A. F.; Browne, S.; Gurgis, F. M. S.; Åkerfeldt, M. C.; Döbber, A.; Renn, C.; Peifer, C.; Stringer, B. W.; Day, B. W.; Wong, C.; Chircop, M.; Johns, T. G.; Kassiou, M.; Munoz, L. Pharmacology of novel small-molecule tubulin inhibitors in glioblastoma cells with enhanced EGFR signalling. *Biochem. Pharmacol.* **2015**, *98* (4), 587–601.

(26) The Cancer Genome Atlas (TCGA) network. Comprehensive genomic characterization defines human glioblastoma genes and core pathways. *Nature* **2008**, *455* (7216), 1061–1068.

(27) Reardon, D. A.; Wen, P. Y.; Mellingshoff, I. K. Targeted molecular therapies against epidermal growth factor receptor: Past experiences and challenges. *Neuro-Oncology* **2014**, *16* (suppl 8), viii7–viii13.

(28) Day, B.; Stringer, B.; Wilson, J.; Jeffree, R.; Jamieson, P.; Ensby, K.; Bruce, Z.; Inglis, P.; Allan, S.; Winter, C.; Tolleson, G.; Campbell, S.; Lucas, P.; Findlay, W.; Kadrian, D.; Johnson, D.; Robertson, T.; Johns, T.; Bartlett, P.; Osborne, G.; Boyd, A. Glioma Surgical Aspirate: A Viable Source of Tumor Tissue for Experimental Research. *Cancers* **2013**, *5* (2), 357–371.

(29) Day, B. W.; Stringer, B. W.; Al-Ejeh, F.; Ting, M. J.; Wilson, J.; Ensby, K. S.; Jamieson, P. R.; Bruce, Z. C.; Lim, Y. C.; Offenhäuser, C.; Charmsaz, S.; Cooper, L. T.; Ellacott, J. K.; Harding, A.; Leveque, L.; Inglis, P.; Allan, S.; Walker, D. G.; Lackmann, M.; Osborne, G.; Khanna, K. K.; Reynolds, B. A.; Lickliter, J. D.; Boyd, A. W. EphA3 maintains tumorigenicity and is a therapeutic target in glioblastoma multiforme. *Cancer Cell* **2013**, *23* (2), 238–248.

(30) Pollard, S. M.; Yoshikawa, K.; Clarke, I. D.; Danovi, D.; Stricker, S.; Russell, R.; Bayani, J.; Head, R.; Lee, M.; Bernstein, M.; Squire, J. A.; Smith, A.; Dirks, P. Glioma stem cell lines expanded in adherent culture have tumor-specific phenotypes and are suitable for chemical and genetic screens. *Cell Stem Cell* **2009**, *4* (6), S68–S80.

(31) Lu, Y.; Chen, J.; Xiao, M.; Li, W.; Miller, D. D. An Overview of tubulin inhibitors that interact with the colchicine binding site. *Pharm. Res.* **2012**, *29*, 2943–2971.

(32) Zheng, Y.-B.; Gong, J.-H.; Liu, X.-J.; Wu, S.-Y.; Li, Y.; Xu, X.-D.; Shang, B.-Y.; Zhou, J.-M.; Zhu, Z.-L.; Si, S.-Y.; Zhen, Y.-S. A novel nitrobenzoate microtubule inhibitor that overcomes multidrug resistance exhibits antitumor activity. *Sci. Rep.* **2016**, *6*, 31472.

(33) Ibbeson, B. M.; Laraia, L.; Alza, E.; O'Connor, C. J.; Tan, Y. S.; Davies, H. M. L.; McKenzie, G.; Venkiteman, A. R.; Spring, D. R. Diversity-oriented synthesis as a tool for identifying new modulators of mitosis. *Nat. Commun.* **2014**, *5*, 3155.

(34) Gan, P. P.; McCarroll, J. A.; Po'uha, S. T.; Kamath, K.; Jordan, M. A.; Kavallaris, M. Microtubule dynamics, mitotic arrest, and apoptosis: Drug-induced differential effects of β III-tubulin. *Mol. Cancer Ther.* **2010**, *9* (5), 1339–1348.



Synthesis and *in vitro* evaluation of diverse heterocyclic diphenolic compounds as inhibitors of DYRK1A



Qingqing Zhou^a, Tristan A. Reekie^a, Ramzi H. Abbassi^b, Dinesh Indurthi Venkata^b, Josep S. Font^c, Renae M. Ryan^c, Lenka Munoz^b, Michael Kassiou^{a,*}

^a School of Chemistry, The University of Sydney, New South Wales 2006, Australia

^b School of Medical Sciences, Discipline of Pathology and Charles Perkins Centre, The University of Sydney, New South Wales 2006, Australia

^c School of Medical Sciences, Discipline of Pharmacology, The University of Sydney, New South Wales 2006, Australia

ABSTRACT

Dual-specificity tyrosine phosphorylation-related kinase 1A (DYRK1A) is a dual-specificity protein kinase that catalyses phosphorylation and autophosphorylation. Higher DYRK1A expression correlates with cancer, in particular glioblastoma present within the brain. We report here the synthesis and biological evaluation of new heterocyclic diphenolic derivatives designed as novel DYRK1A inhibitors. The generation of these heterocycles such as benzimidazole, imidazole, naphthyridine, pyrazole-pyridines, bipyridine, and triazolopyrazines was made based on the structural modification of the lead DANDY and tested for their ability to inhibit DYRK1A. None of these derivatives showed significant DYRK1A inhibition but provide valuable knowledge around the importance of the 7-azaindole moiety. These data will be of use for developing further structure-activity relationship studies to improve the selective inhibition of DYRK1A.

1. Introduction

Protein kinases catalyse protein phosphorylation and are therefore linked to the occurrence of multiple diseases including neurodegenerative disorders and cancer.^{1,2} Inhibitors targeting protein kinases are regarded as potential new therapeutic agents for researchers.^{3,4} DYRK1A (dual-specificity tyrosine phosphorylation-related kinase 1A) is a dual-specificity protein kinase that catalyses not only autophosphorylation on its own tyrosine residue, but the phosphorylation of serine and threonine residues of its substrates.⁵ The DYRK1A gene is the only DYRK member (others including DYRK1B, DYRK2, DYRK3 and DYRK4) located on 21q22.2 of human chromosome 21,⁶ which encodes more than 300 annotated genes, one third of which are overexpressed in Down syndrome (DS).⁷ Recent studies indicated that the DYRK1A expression level is correlated with cancer. For example, an upregulation of over 30% of DYRK1A levels has been found in glioblastoma cells, a cancer that represents approximately 15% of brain tumours.⁸ It has been suggested that DYRK1A inhibition by DYRK1A inhibitors leads to cancer cell apoptosis.⁹ The development of novel DYRK1A inhibitors has consequently attracted considerable interest as new chemotherapeutic agents.

There are several compounds with inhibitory activity for DYRK1A. Some have been isolated from natural sources, with examples including harmine,¹⁰ variolins,¹¹ meriolins¹² and staurosporine.^{13,14} All of these natural leads possess an indolocarbazole ring system. Purely synthetic

inhibitors also exist, though they possess very similar structural features namely with the heterocyclic cores, which include imidazopyridine,¹⁵ imidazopyridazine,¹⁶ pyridoquinazoline,¹⁷ thiazoloquinazoline,¹⁸ pyrrolopyrimidines.^{9,19} Recently discovered lead compounds DANDY (1) represent one chemotype of the most potent DYRK1A inhibitors.¹⁹ That study showed that variable hydroxy substitution gave potent compounds, including mono substitution (**1a**, IC₅₀ = 23.1 nM) and dihydroxylation (**1b**, IC₅₀ = 3.0 nM) among others. In our previous studies,⁹ we were able to improve potency without increasing phenyl substitution and thus generate a molecule that was more likely to cross the blood-brain barrier. Our previous studies also suggested that the N–C–N moiety of DANDY plays an important role in maintaining DYRK1A inhibition.^{9,20} It is still unclear if other heterocyclic cores with a similar arrangement are tolerated, or potentially provide a more potent scaffold. Herein, we present the synthesis of a new and diverse group of heterocyclic compounds. They correspond to the 7-azaindole DANDY by maintaining the characteristic diphenol moieties and dinitrogen functionality (shown in pink in Fig. 1). Different spatial arrangements of two nitrogen atoms were studied by designing heterocycles such as benzimidazole-2-amine **2**, 2-acetamide **3**, imidazole **4**, naphthyridine **5**, pyrazole-pyridines **6** and **7**, bipyridine **8**, and triazolopyrazines **9** and **10**. Additionally, the 7-membered analogue **11** with an intrinsic diphenol has also been investigated. We decided to maintain single hydroxy substitution on the phenyl groups to improve drug-like properties and reduce toxicity associated with oxidation to the

* Corresponding author.

E-mail address: michael.kassiou@sydney.edu.au (M. Kassiou).

<https://doi.org/10.1016/j.bmc.2018.10.034>

Received 17 August 2018; Received in revised form 19 October 2018; Accepted 27 October 2018

Available online 28 October 2018

0968-0896/ © 2018 Elsevier Ltd. All rights reserved.

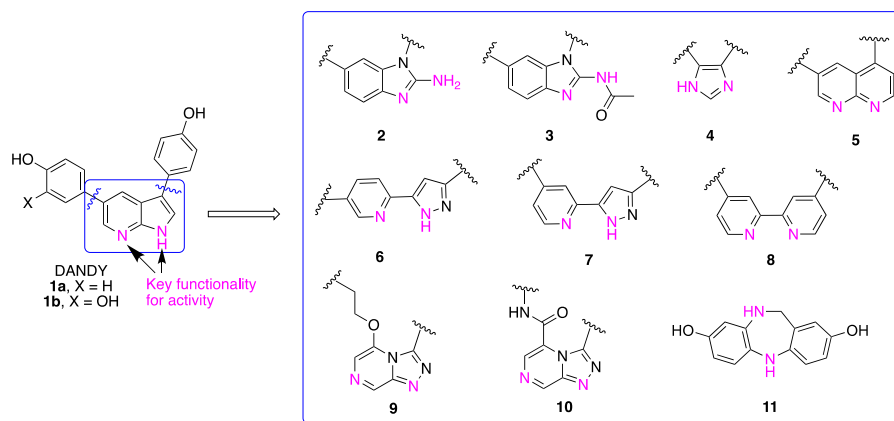


Fig. 1. Generalised heterocyclic cores based on 7-azaindole core of DANDY.

quinone. With these novel analogues in hand, we then explored their inhibitory activity against DYRK1A.

2. Results and discussion

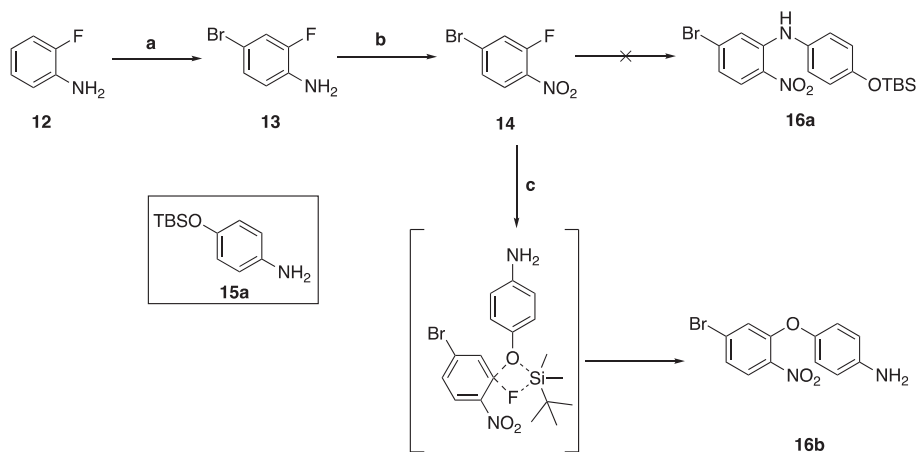
We synthesised benzimidazole-2-amine **2** and benzimidazole-2-acetamide **3** starting from commercially available 2-fluoroaniline (**12**) (Scheme 1). The selectively brominated intermediate **13** was achieved by treatment with *N*-bromosuccinimide (NBS) in chloroform in 90% yield. The aniline **13** was then oxidised to nitro compound **14** in the presence of hydrogen peroxide in trifluoroacetic acid (TFA) at 75 °C for 2 h. It was planned that the subsequent nucleophilic substitution could be achieved by treatment with *tert*-butyldimethylsilyl ether (OTBS)-aniline **15a** under basic conditions. Unexpectedly, the desired product **16a** was not obtained, and the by-product **16b** was produced instead. We proposed that the silicon atom in the TBS protecting group favoured bond formation with the fluorine atom of **14**, resulting in the formation of a four-membered transition state (Scheme 1), and eventually producing ether **16b**.

To avoid the formation of **16b**, the compound **14** was treated with 4-aminophenol and potassium carbonate in anhydrous dimethylformamide at 90 °C (Scheme 2), and the desired amine **16c** was successfully obtained in moderate yield. Nitro reduction to **17** by iron powder in acetic acid was realised at room temperature in excellent yield. Cyclisation to intermediate **18** was achieved in the presence of cyanogen bromide to proceed in 78% yield at room temperature.²¹ The

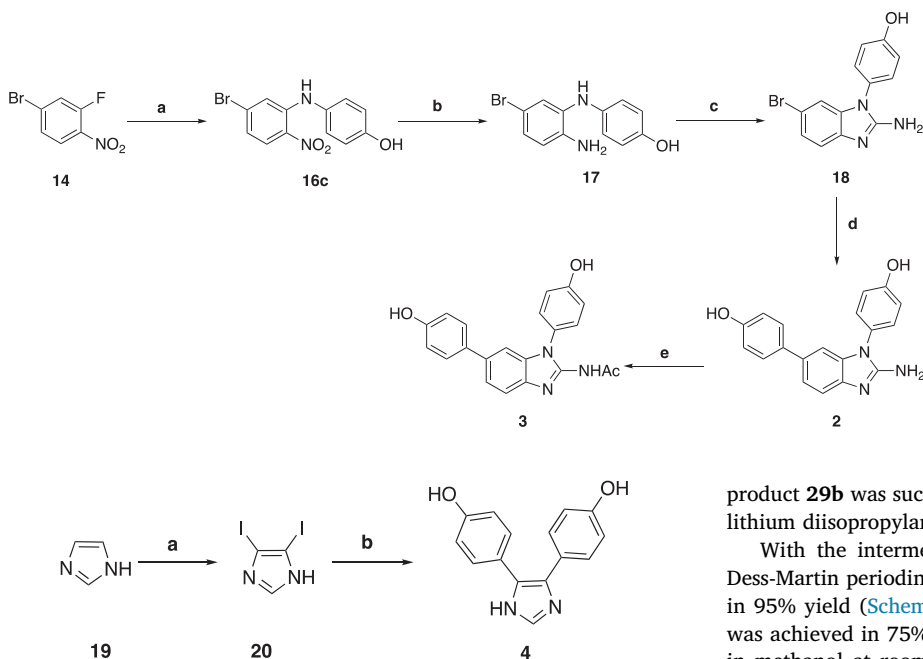
2-aminobenzimidazole analogue **2** was achieved using a standard Suzuki coupling reaction, followed by acetylation to afford the 2-acetamide benzimidazole analogue **3** in moderate 65% yield (Scheme 2).

Imidazole-based analogue **4** could be easily obtained from imidazole **19** first by treatment with iodine in the presence of potassium iodide and aqueous sodium hydroxide at room temperature. The regioselective diiodinated intermediate **20** was acquired in excellent yield (Scheme 3).²² The diarylation of **20** was achieved through a double-Suzuki coupling reaction. The conditions described previously by using potassium carbonate as a base were initially trialled, but failed to afford the desired product **4**. We assumed that the strong basicity of imidazole combined with the addition of potassium carbonate increased the pH to a point that was detrimental to the reaction.²³ The use of milder base dipotassium phosphate and the addition of phase transfer catalyst tetra-*n*-butylammonium bromide (TBAB) afforded analogue **4** in 35% yield.

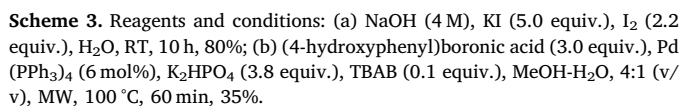
Analogue **5** was achieved through known synthetic routes.²⁴ The regioselective bromination of 2-aminonicotinate **21** gave the 3-bromopyridine **22** in 90% yield,²⁵ and subsequent esterification under classical conditions furnished **23** in excellent yield (Scheme 4). The cyclisation of **23** was achieved by treatment with *N,N*-dimethylformamide dimethyl acetal (DMF-DMA) in a sealed tube at high temperatures to afford the imine intermediate, followed by the treatment with *n*-BuLi and MeCN at –78 °C and subsequent addition of acetic acid to give **24** in 35% yield in a one pot reaction sequence. Decyanation of **24** was performed by treatment with concentrated hydrochloric acid at 150 °C in a sealed tube to give compound **25** in 33% yield after neutralisation.



Scheme 1. Reagents and conditions: (a) NBS (1.0 equiv.), CHCl₃, RT, 2 h, 90%; (b) aq-H₂O₂ (30%, 5.0 equiv.), TFA, 75 °C, 2 h, 75%; (c) **15a** (1.1 equiv.), K₂CO₃ (1.5 equiv.), DMF, 90 °C, 3 h, 80%.



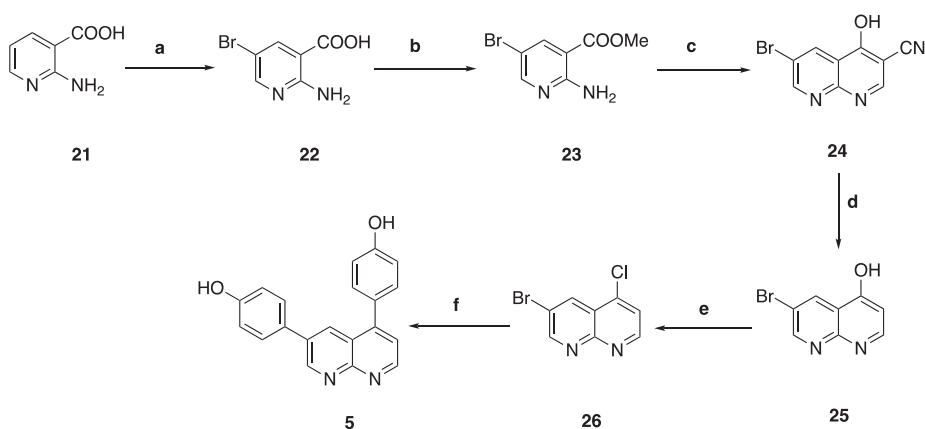
Scheme 2. Reagents and conditions: (a) 4-aminophenol (1.1 equiv.), K_2CO_3 (1.5 equiv.), anhydrous DMF, 90 °C, 3 h, 65%; (b) Fe (5.0 equiv.), AcOH, RT, 2 h, 95%; (c) BrCN (5 M in CH_3CN , 1.2 equiv.), MeCN- H_2O , 3:1 (v/v), RT, 16 h, 78%; (d) (4-hydroxyphenyl)boronic acid (1.5 equiv.), $Pd(PPh_3)_4$ (2 mol%), aq. K_2CO_3 (2 M, 3.0 equiv.), 1,4-dioxane, 110 °C, 4 h, 30%; (e) Ac_2O (1.1 equiv.), AcOH, 110 °C, 3 h, 65%.



Scheme 3. Reagents and conditions: (a) NaOH (4 M), KI (5.0 equiv.), I_2 (2.2 equiv.), H_2O , RT, 10 h, 80%; (b) (4-hydroxyphenyl)boronic acid (3.0 equiv.), Pd(PPh_3)₄ (6 mol%), K_2HPO_4 (3.8 equiv.), TBAB (0.1 equiv.), MeOH- H_2O , 4:1 (v/v), MW, 100 °C, 60 min, 35%.

Given that triflates act as pseudohalides in coupling reactions,²⁶ we initially attempted the triflation of the hydroxy group on compound **25** (not shown here). However, the triflate intermediate appeared unstable in this heterocyclic system as observed by TLC monitoring. Instead, chlorination was achieved by treatment with phosphoryl chloride at 105 °C in a sealed tube to give chloro-substituted intermediate **26**. Subsequent Suzuki coupling was achieved using the more reactive [1,1'-bis(diphenylphosphino)ferrocene]palladium(II) dichloride catalyst and microwave irradiation at 130 °C. Thus, analogue **5** could be obtained in good overall yield.

For the synthesis of **6**, we initially elected to use benzaldehyde **28a** as the reactant by treatment with **27a** in the presence of lithium diisopropylamide at -78 °C to proceed intermediate **29a**. Unfortunately, the reaction was sluggish and yielded a complex mixture of products after stirring for another 12 h at room temperature (Scheme 5). We assumed that the HOMO of the nucleophile **27a** and the LUMO of the electrophile **28a** might not match with each other due to the electronic effects from the aromatic systems. Therefore, we decided to swap the functional groups of ketone **27a** and aldehyde **28a** to aldehyde **27b** and ketone **28b**, respectively (Scheme 5). As predicted, the desired aldol

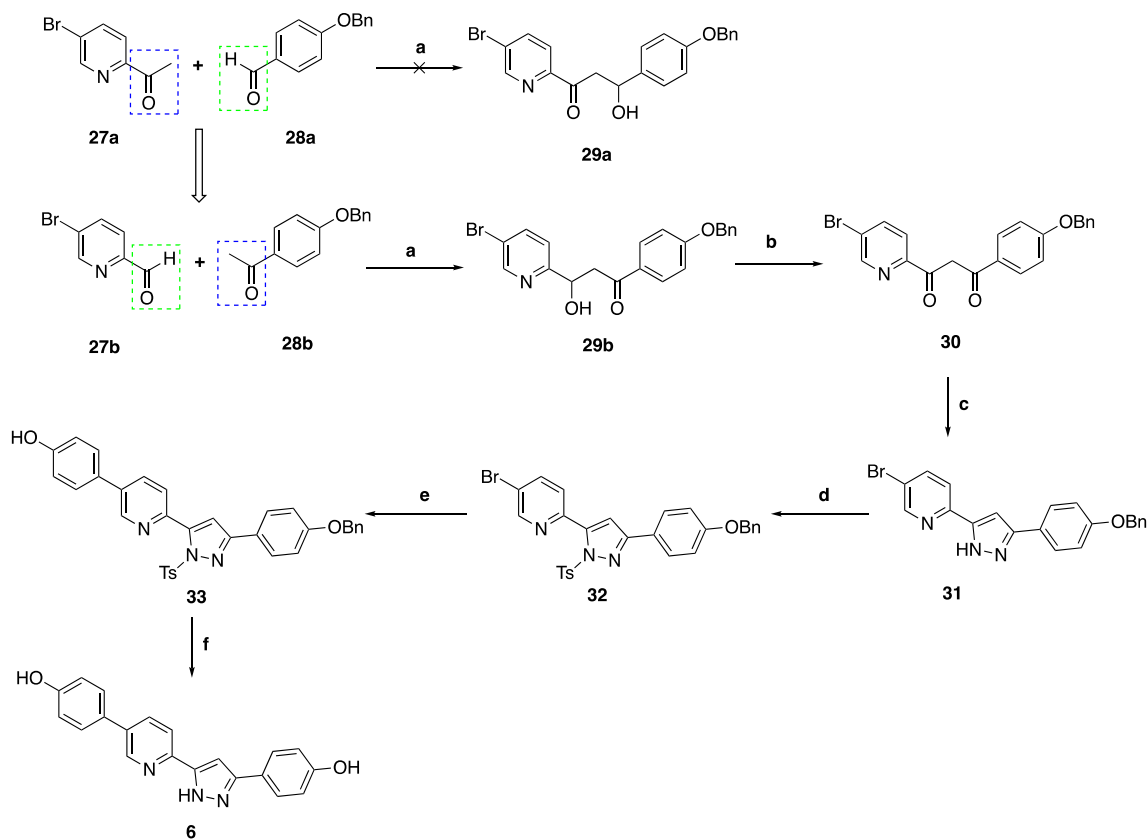


Scheme 4. Reagents and conditions: (a) Br_2 (1.3 equiv.), AcOH, RT, 20 h, 90%; (b) H_2SO_4 (8.0 equiv.), MeOH, 80 °C, 18 h, 94%. (c) (1) DMF-DMA (10.0 equiv.), 110 °C, 3 h; (2) $n-BuLi$ (2.2 equiv.), MeCN (2.2 equiv.), THF, -78 °C 1 h; (3) AcOH (3.0 equiv.), -40 °C, 2 h, then RT, 20 h, 35% over three steps; (d) aq. HCl (32%), 150 °C, 3 h, 33%; (e) $POCl_3$, 105 °C, 3 h, 93%; (f) (4-hydroxyphenyl)boronic acid (2.5 equiv.), $PdCl_2(dppf)$ (20 mol%), aq. K_2CO_3 (2 M, 6.0 equiv.), 1,4-dioxane, MW, 130 °C, 3 h, 85%. $dppf$ = 1,1'-ferrocenediyl-bis(diphenylphosphine).

product **29b** was successfully achieved in 78% yield by treatment with lithium diisopropylamide in a similar protocol as described above.

With the intermediate **29b** available, subsequent oxidation with Dess-Martin periodinane (DMP) was employed to furnish 1,3-dione **30** in 95% yield (Scheme 5). The formation of pyrazole intermediate **31** was achieved in 75% yield by treatment with hydrazine monohydrate in methanol at room temperature.²⁷ No reaction occurred when this substrate was treated with (4-hydroxyphenyl)boronic acid under standard Suzuki coupling conditions. A proposed explanation for this lies in the formation of a complex between the palladium catalyst and pyridine-*N* and pyrazole moieties (a typical bidentate coordination site), thus reducing the catalytic reactivity of the palladium catalyst in the reaction. Therefore, the pyrazole-*N* was protected with the tosyl group and the resulting **32** was treated with (4-hydroxyphenyl)boronic acid under the Suzuki coupling conditions, which finally afforded aryl-substituted compound **33** in 85% yield. Removal of the tosyl and benzyl protecting groups could be easily achieved in two sequential steps, and analogue **6** was eventually furnished in reasonable yield.

The pyrazole-pyridine based analogue **7**, with the phenol substitution at the C-4 position was also investigated (Scheme 6). In a similar manner to that of analogue **6**, compound **7** could be derived from the cyclisation of a 1,3-dione, which could be originally achieved from the aldol condensation between aldehyde and ketone with the optimised conditions described above. 2-Amino-4-bromopyridine (**34**) was then chosen as the starting material which was first coupled with boronic acid **35** to afford 4-aryl intermediate **36**. Iodination at the C-2 position of **36** could be furnished by a Sandmeyer reaction using diodomethane as the solvent and halogen source with catalytic hydrogen iodide to give the desired compound **37** in 25% yield.²⁸ The 2-aldehyde containing compound **38** was furnished by the lithium-halogen exchange and quenching with dimethylformamide in a moderate 50% yield. The subsequent aldol condensation with **28b** gave the aldol product **39** in



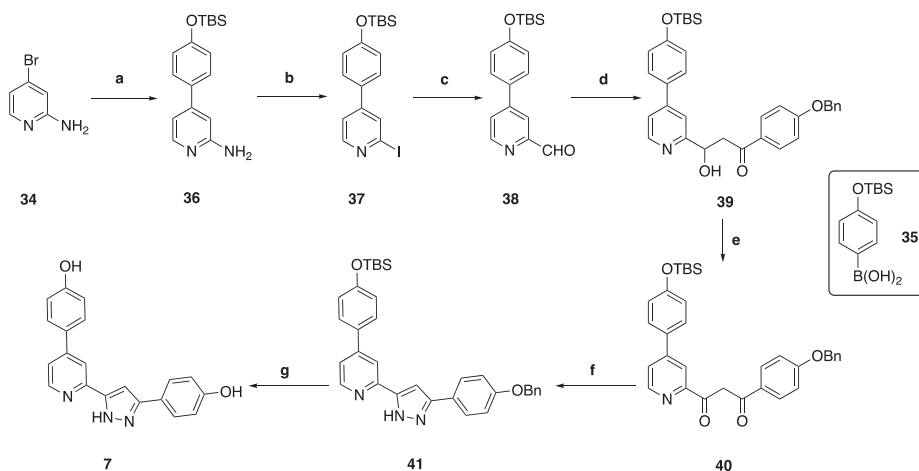
Scheme 5. Reagents and conditions: aldehyde (1.0 equiv.), ketone (1.05 equiv.), LDA (1.1 equiv.), THF, -78°C to RT, 1 h, 78%; (b) DMP (1.5 equiv.), CH_2Cl_2 , RT, 30 min, 95%; (c) $\text{N}_2\text{H}_4\cdot\text{H}_2\text{O}$ (2.0 equiv.), MeOH, RT, 48 h, 75%; (d) TsCl (1.1 equiv.), NaH (60% in mineral oil, 2.0 equiv.), CH_2Cl_2 , 0°C -RT, 30 min, 95%; (e) (4-hydroxyphenyl)boronic acid (1.5 equiv.), $\text{Pd}(\text{PPh}_3)_4$ (2 mol%), aq. K_2CO_3 (2 M, 3.0 equiv.), 1,4-dioxane, 100°C , 4 h, 85%; (f) 1) KOH (5.0 equiv.), MeOH, 75°C , 1 h; 2) Pd/C (10 wt%), H_2 , MeOH, RT, 5 h, 45% over two steps.

60% yield. Oxidation by DMP and subsequent pyrazole formation yielded intermediate **41** and the two sequential deprotection steps eventually afforded analogue **7**.

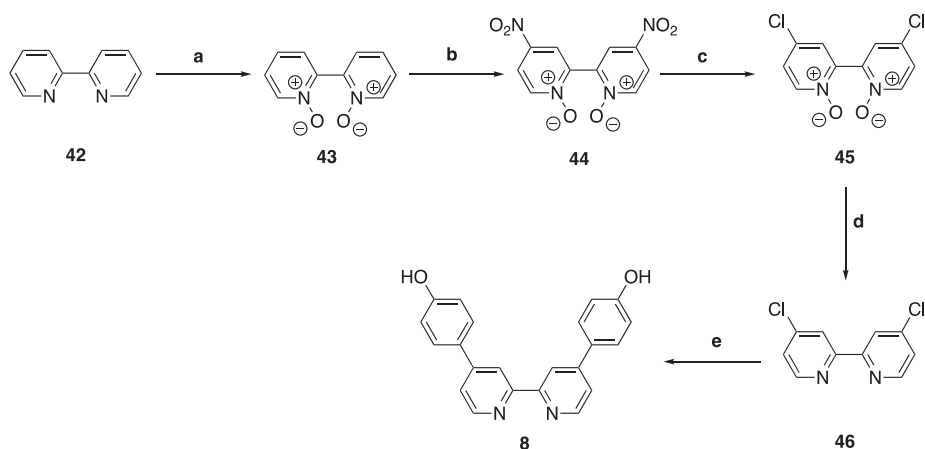
Analogue **8** is a known compound reported by Constable and co-workers.²⁹ Using 2,2'-bipyridine **42** as the starting material, it was first treated with hydrogen peroxide in acetic acid to achieve *N*-oxide **43** in high yield. The dinitro-substitution at the *para*-positions of **43** was achieved by treatment with a mixture of sulfuric acid and nitric acid at 100°C (Scheme 7). The low yield of 20% after 20 h of heating presumably resulted from the use of the normal nitric acid instead of fuming nitric acid as previously reported.³⁰ The following chloro-substitution could be achieved by treatment with acetyl chloride in acetic

acid at 100°C to afford **45** in good yield.³⁰ Reduction of *N*-oxide **45** was performed in the presence of phosphorus trichloride to give **46** in excellent yield, which was further coupled with (4-hydroxyphenyl)boronic acid to furnish the desired compound **8** in moderate overall yield.³⁰

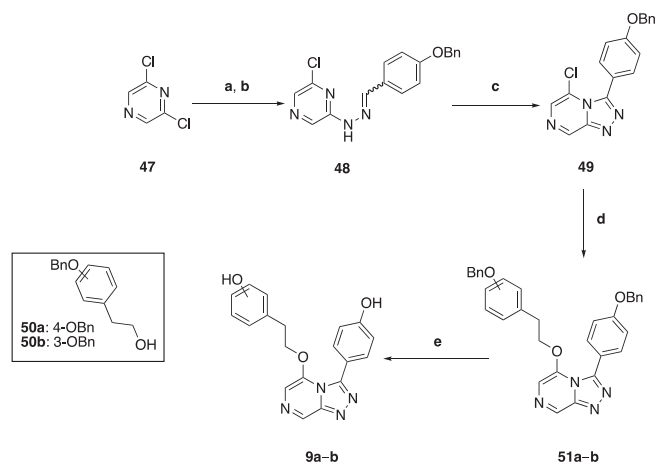
The next core under investigation was triazolopyrazine. Considering the spatial arrangements of diphenol substitutions on lead compound **1**, we designed triazolopyrazine analogues with linkers between the phenols and triazolopyrazine core to give the optimal structural arrangements. Therefore, analogues **9a** and **10a** were proposed, in addition to meta-hydroxy-substituted **9b** and **10b**, in order to investigate more diversified analogues (see as Schemes 8 and 9, respectively).



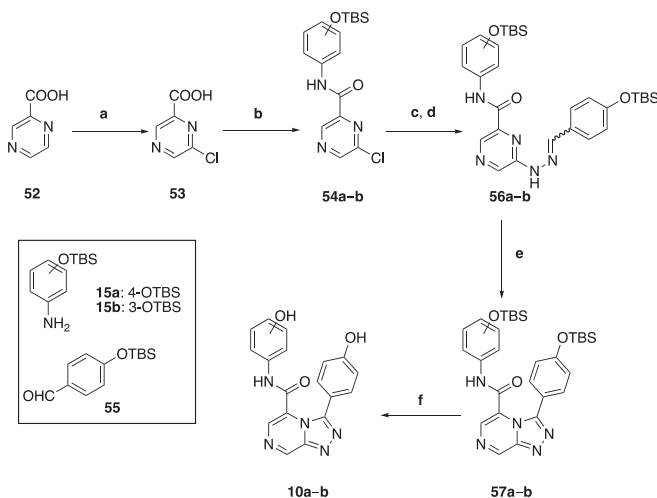
Scheme 6. Reagents and conditions: (a) **35** (1.5 equiv.), $\text{Pd}(\text{PPh}_3)_4$ (2 mol%), aq. K_2CO_3 (2 M, 3.0 equiv.), 1,4-dioxane, 100°C , 4 h, 87%; (b) isopentyl nitrite (20.0 equiv.), aq. HI (57%, 2 mol%), CH_2I_2 , RT, 24 h, 25%; (c) *n*-BuLi (1.1 equiv.), DMF (1.5 equiv.), toluene, -78°C , 1 h, 50%; (d) **28b** (1.05 equiv.), LDA (1.1 equiv.), THF, -78°C to RT, 1 h, 60%; (e) DMP (1.5 equiv.), CH_2Cl_2 , RT, 30 min, 75%; (f) $\text{N}_2\text{H}_4\cdot\text{H}_2\text{O}$ (2.0 equiv.), MeOH, RT, 48 h, 70%; (g) 1) Pd/C (10 wt%), H_2 , MeOH, RT, 5 h; 2) TBAF (2.0 equiv.), THF, RT, 30 min, 55% over two steps.



Scheme 7. Reagents and conditions: (a) aq-H₂O₂ (30%, 5.0 equiv.), AcOH, RT to 70 °C, 15 h; (b) H₂SO₄ (21.0 equiv.), HNO₃ (8.4 equiv.), 100 °C, 20 h, 20%; (c) acetyl chloride (5.0 equiv.), AcOH, 100 °C, 12 h, 85%. (d) PCl₃ (20.0 equiv.), 65 °C, 20 h, 95%; (e) (4-hydroxyphenyl)boronic acid (2.5 equiv.), PdCl₂(dppf) (5 mol%), aq. K₂CO₃ (2 M, 5.0 equiv.), 1,4-dioxane, 110 °C, 4 h, 40%.



Scheme 8. Reagents and conditions: (a) N₂H₄·H₂O (1.1 equiv.), ethanol, 80 °C, 8 h; (b) 4-(benzyloxy)benzaldehyde **28a** (1.1 equiv.), ethanol, 80 °C, 10 h, 70% over two steps. (c) PhI(OAc)₂ (1.0 equiv.), CH₂Cl₂, RT, 12 h, 85%; (d) **50a** or **50b** (1.1 equiv.), KOH (3.0 equiv.), 18-crown-6 (0.07 equiv.), toluene, 40 °C, 4 h, 69–73%; (e) Pd/C (10 wt%), H₂, MeOH, RT, 2 h, 67–70%.



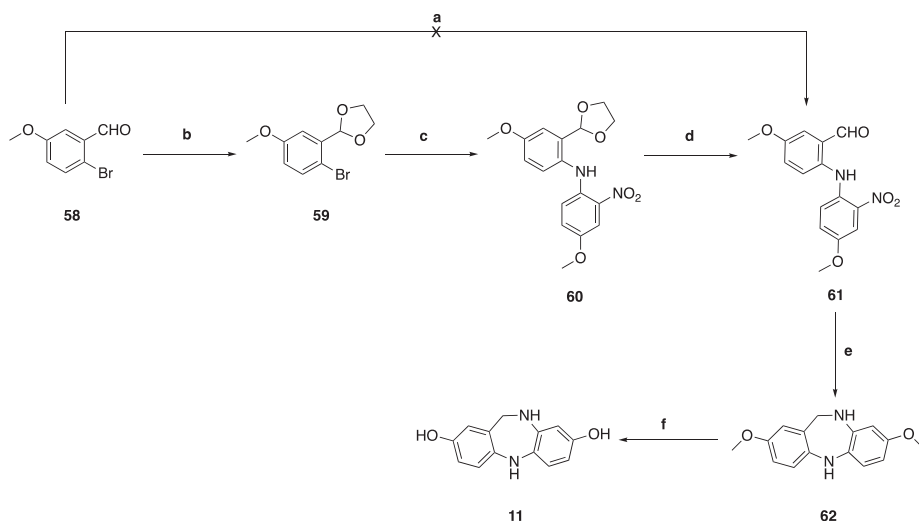
Scheme 9. Reagents and conditions: (a) (1) Na₂WO₄·2H₂O (0.025 equiv.), aq-H₂O₂ (30%, 1.1 equiv.), H₂SO₄ (1 M), pH = 2, RT to 80 °C, 2 h; (2) POCl₃, 120 °C, 2 h, 70% over two steps; (b) (1) oxalyl chloride (1.5 equiv.), DMF (0.1 equiv.), CH₂Cl₂, 0 °C to RT, 2 h; (2) **15a** or **15b** (1.0 equiv.), triethylamine (1.1 equiv.), CH₂Cl₂, RT, 2 h, 80–85% over two steps; (c) N₂H₄·H₂O (1.1 equiv.), ethanol, 80 °C, 8 h; (d) **55** (1.1 equiv.), ethanol, 80 °C, 10 h, 78–85% over two steps. (e) PhI(OAc)₂ (1.0 equiv.), CH₂Cl₂, RT, 12 h, 80–87%; (f) TBAF (2.0 equiv.), THF, RT, 30 min, 95–97%.

The synthesis of triazolopyrazine analogues **9a–b** could be achieved from the commercially available 2,6-dichloropyrazine **47** shown in [Scheme 8](#). The formation of hydrazone **48** was achieved in two sequential steps. Firstly, treatment of **47** with hydrazine monohydrate in ethanol gave the hydrazone intermediate, which was then reacted with 4-(benzyloxy)benzaldehyde **28a** to give hydrazone **48** in 70% yield over two steps.³¹ The oxidative heterocyclisation of hydrazone **48** to triazolopyrazine intermediate **49** was easily achieved using (diacetoxyiodo)benzene in dichloromethane at room temperature in excellent yield.³² The following nucleophilic substitution reactions with alcohols **50a–b**, using 18-crown-6 and potassium hydroxide, could be achieved to give ethers **51a–b** in moderate yields (69–73%). Hydrogenolysis of **51a–b** then gave the desired compounds **9a–b** in reasonable yields ([Scheme 8](#)).

The synthesis of triazolopyrazine analogues **10a–b** could be achieved in a similar manner as that described above ([Scheme 9](#)). Pyrazine-2-carboxylic acid **52** was first oxidised to give *N*-oxide intermediate as reported previously.³³ The subsequent chlorination³⁴ was achieved by treatment with phosphoryl chloride at high temperature to give the chloro-intermediate **53** in 70% yield over two steps. Amide formation was performed via the acetyl chloride intermediate, followed by the treatment with *para*- or *meta*-OTBS aniline **15a–b** and triethylamine in anhydrous dichloromethane to give the amides **54a–b** in good yields (80–85%). The following reactions were performed in a similar manner to those described in [Scheme 8](#), hydrazones **56a–b** were obtained in 78–85% yields over two steps and further converted to the cyclised compounds **57a–b** in good yields. The deprotection of the TBS groups gave the desired compounds **10a–b** in excellent yields.³⁵

The synthesis of 7-membered analogue **11** could be achieved from commercially available starting material **58**. Nucleophilic substitution with 4-methoxy-2-nitroaniline was unsuccessful under basic conditions at high temperatures ([Scheme 10](#)). However, a Buchwald-Hartwig cross coupling reaction could be utilised by first protecting the aldehyde **58** as the dioxolane **59**, then coupling with 4-methoxy-2-nitroaniline to obtain the desired secondary amine **60**. The following acetal deprotection was easily carried out by treatment with trifluoroacetic acid in chloroform to give the desired intermediate **61** in 90% yield. Compound **62** could be obtained from **61** in one pot via a cascade process. Initial reduction of the nitro moiety to the aniline was followed by intramolecular condensation with the aldehyde. Subsequent imine reduction in the presence of hydrogen gave **62**.^{36,37} Finally, the 7-membered analogue **11** was successfully obtained after demethylation under classical conditions in reasonable yield.

With the completed synthesis of these derivatives, their potency for DYRK1A inhibition was determined in a kinase inhibition assay using recombinant DYRK1A, Woodtide as a substrate and an ATP concentration of 100 μM. The lead compound **1a** at 1 μM was confirmed to have almost complete inhibitory potency against DYRK1A.⁹ Next, we



Scheme 10. Reagents and conditions: (a) NaH (60% in mineral oil, 1.5 equiv.), 4-methoxy-2-nitroaniline (1.0 equiv.), THF, 0 to 70 °C, 24 h; (b) TsOH (0.01 equiv.), ethane-1,2-diol (5.0 equiv.), toluene, 125 °C, 24 h, 95%; (c) 4-methoxy-2-nitroaniline (1.0 equiv.), Pd(OAc)₂ (10 mol%), Cs₂CO₃ (1.5 equiv.), toluene, 120 °C, 3 h, 89%; (d) TFA (6.0 equiv.), CHCl₃, RT, 30 min, 90%; (e) Pd/C (10 wt%), H₂, MeOH, RT, 4 h, 75%; (f) BBr₃ (6.0 equiv.), CH₂Cl₂, RT, 10 h, 50%; TsOH = *p*-toluenesulfonic acid.

tested the analogues described above at two concentrations (1 μM vs 10 μM) (Table 1).

An analysis of the results gave some important insights into the structure-activity relationship about these molecules. Interestingly, naphthyridine **5**, the most structurally related compound to the lead compound **1a** with the NH moiety replaced with N, showed the best

DYRK1A inhibitory potency among these new derivatives (reducing activity to 67% and 30% at 1 μM and 10 μM, respectively), though much lower potency than that of compound **1a**, highlighting the importance of the NH moiety in maintaining DYRK1A inhibition. Furthermore, pyrazole-pyridine-based analogue **6** or **11** failed to show any inhibitory potency against DYRK1A at both 1 μM and 10 μM.

Table 1
DYRK1A inhibition assay at different concentrations (1 μM vs 10 μM).

Compound	Structures	DYRK1A remaining activity at 1 μM (%)	DYRK1A remaining activity at 10 μM (%)	Compound	Structures	DYRK1A remaining activity at 1 μM (%)	DYRK1A remaining activity at 10 μM (%)
1a		3.3 ± 0.3	3.3 ± 0.3	8		90 ± 15.3	83 ± 9.5
2		74 ± 5.5	43 ± 21.5	9a		94 ± 11.2	99 ± 5.5
3		106 ± 10.3	107 ± 14.7	9b		94 ± 10.5	91 ± 9.0
4		100 ± 13.0	79 ± 11.0	10a		99 ± 12.1	99 ± 10.7
5		67 ± 15.8	30 ± 9.5	10b		104 ± 8.4	102 ± 8.7
6		110 ± 4.1	98 ± 10.6	11		104 ± 16.7	113 ± 14.7
7		64 ± 5.1	9 ± 1.2				

Compound **11** with its fused ring structure showed no inhibition of DYRK1A, which may indicate that aromaticity between the two nitrogen atoms is essential, as is the phenol group on each side chain. Analogue **7**, with a closer distance between the two phenol substituents in comparison to **6**, exhibited reduced DYRK1A activity at both 1 μM (64%) and 10 μM (9%). This may suggest that the two phenols at a specific distance between each other may play an important role in maintaining DYRK1A inhibition. However, this is not replicated with *para*-hydroxy analogues **9a** and **10a** and *meta*-hydroxy analogues **9b** and **10b**, all of which were mostly ineffectual against DYRK1A with activity staying above 90%. The slight change between **9a** and **9b** (99% and 91% at 10 μM , respectively) suggests that the hydroxyl group plays an important role in DYRK1A inhibition, as even subtle modification from *para* to *meta* substitution changes inhibitory activity.

3. Conclusions

We have presented a series of synthetic methods in this paper that have generated 12 novel compounds containing a variety of heterocyclic cores. All these novel compounds were assessed in a DYRK1A inhibition assay. However, none of these derivatives showed significant DYRK1A inhibition. Regardless, biological studies have provided us with the valuable knowledge that the 7-azaindole heterocyclic core shows more potent activity against DYRK1A than other heterocycles, even when maintaining the diphenolic characteristics. Analogue **5** is the most potentially bioactive molecule among these new series of compounds though, comparing analogue **5** to lead compound **1a** has hinted that the NH moiety is important, probably to act as a hydrogen bond donor in the binding modes. By comparing analogues **6** with **7**, we have shown that the distance between the two phenols has strong effects on the DYRK1A inhibition. These data will be of use for designing further structure-activity relationship studies to further improve the selective inhibition of DYRK1A.

4. Experimental

4.1. General chemical synthesis details

Unless noted otherwise, commercially obtained reagents were used as purchased without further purification. Solvents for flash chromatography were distilled prior to use, or used as purchased for HPLC grade, with the eluent mixture reported as the volume/volume ratio (v/v). Unless otherwise stated, reactions were performed under an atmosphere of nitrogen. Flash chromatography was performed using Merck Kieselgel 60 (230–400 mesh) silica gel. Analytical thin-layer chromatography (TLC) was performed using Merck aluminum-backed silica gel 60 F254 (0.2 mm) plates (Merck, Darmstadt, Germany), which were visualized using shortwave (254 nm) ultraviolet fluorescence. Melting points were measured with open capillaries using a Stanford Research Systems (SRS) MPA160 melting point apparatus with a with a rate of 5 $^{\circ}\text{C}/\text{min}$ and are uncorrected. Infrared absorption spectra were reported as vibrational frequency (cm^{-1}). Nuclear magnetic resonance spectra were recorded at 300 K on Bruker Advance DRX200, DRX300, DRX400 or DRX500 spectrophotometers. The data are reported as chemical shift (δ ppm) relative to the residual protonated solvent resonance (CDCl_3 : δ 7.26, d_6 -DMSO: δ 2.50, d_3 -MeOD: δ 3.31, D_2O : δ 4.79 and d_6 -acetone: δ 2.05), the carbon of the solvent resonance (CDCl_3 : δ 77.16, d_6 -DMSO: δ 39.52, d_3 -MeOD: δ 49.00 and d_6 -acetone: δ 29.84/206.26),³⁸ relative integral, multiplicity (s = singlet, br.s = broad singlet, d = doublet, dd = doublet of doublets, t = triplet, m = multiplet, etc.) and coupling constants (J Hz). Low-resolution mass spectra (LRMS) was obtained from a ThermoQuest Finnigan LCQ Deca ion trap mass spectrometer with electro-spray ionisation in either positive (+ESI) or negative (-ESI) mode. Data is expressed as observed mass (m/z), assignment (M = molecular ion), and relative intensity (%). High-resolution mass spectra (HRMS) was performed on a Bruker Apex Qe

7 T Fourier Transform Ion Cyclotron Resonance (FTICR) mass spectrometer equipped with an Apollo II ESI dual source. Samples were run with syringe infusion at 150 $\mu\text{L}/\text{hr}$ on a Cole Palmer syringe pump into electrospray ionization (ESI). Atmospheric pressure chemical ionization (APCI) was performed by utilising MeOH. High performance liquid chromatography (HPLC) analysis of organic purity was conducted on a Waters Alliance 2695 instrument using a SunFire™ C18 column (5 μm , 2.1×150 mm) and detected using a Waters 2996 photodiode array (PDA) detector set at 254 nm. Separation was achieved using water (solvent A) and acetonitrile (solvent B) at flow rate of 0.2 mL/min and a gradient of 0% B to 100% (HPLC Method A) or 0% B to 40% (HPLC Method B) over 30 min. HPLC data is reported as percentage purity and retention time (RT) in minutes.

4-Bromo-2-fluoroaniline (13). This compound was prepared following a literature procedure.³⁹ To a suspension of 2-fluoroaniline (**12**) (2.22 g, 20 mmol) in CHCl_3 (50 mL) was added NBS (3.56 g, 20 mmol), and the resulting mixture was stirred at RT for 2 h. After completion monitored by TLC, the mixture was quenched with sat. $\text{Na}_2\text{S}_2\text{O}_3$ (aq.) and extracted with CH_2Cl_2 (3×20 mL). The combined organic layers were dried over MgSO_4 and concentrated *in vacuo*. The crude product was purified by flash chromatography (hexane/ethyl acetate 10:1) to give the product **13** as an orange oil (3.42 g, 90%); R_f (hexane/ethyl acetate 6:1): 0.35; $^1\text{H NMR}$ (300 MHz, CDCl_3): δ 7.14 (1H, dd, $J = 2.1, 10.5$ Hz), 7.05 (1H, d, $J = 8.4$ Hz), 6.65 (1H, t, $J = 9.0$ Hz), 3.72 (2H, br.s); $^{13}\text{C NMR}$ (75 MHz, CDCl_3): δ 151.5 (d, $J_{\text{CF}} = 241.5$ Hz), 133.9 (d, $J_{\text{CF}} = 12.8$ Hz), 127.5 (d, $J_{\text{CF}} = 3.0$ Hz), 118.8 (d, $J_{\text{CF}} = 21.8$ Hz), 117.9 (d, $J_{\text{CF}} = 3.8$ Hz), 109.0 (d, $J_{\text{CF}} = 9.0$ Hz). The spectroscopic data matched that reported in the literature.³⁹

4-Bromo-2-fluoro-1-nitrobenzene (14). This compound was prepared following a literature procedure.³⁹ To a solution of **13** (1.26 g, 6.6 mmol) in TFA (13 mL) was added aq- H_2O_2 (30%, 3.4 mL, 33 mmol) dropwise over 30 min, and the resulting mixture was stirred at 75 $^{\circ}\text{C}$ for 1 h. After completion monitored by TLC, the mixture was poured into ice (20 mL), the pale yellow precipitate was obtained and filtered, washed by cold water and dried under reduced pressure to get the desired compound **14** without further purification (1.09 g, 75%). R_f (hexane/ethyl acetate 10:1): 0.45; $^1\text{H NMR}$ (400 MHz, CDCl_3): δ 7.97 (1H, t, $J = 8.0$ Hz), 7.50 (1H, dd, $J = 2.0, 10.0$ Hz), 7.47–7.44 (1H, m); $^{13}\text{C NMR}$ (100 MHz, CDCl_3): δ 155.4 (d, $J_{\text{CF}} = 268$ Hz), 136.4, 129.4 (d, $J_{\text{CF}} = 9.0$ Hz), 128.1 (d, $J_{\text{CF}} = 4.0$ Hz), 127.1 (d, $J_{\text{CF}} = 2.0$ Hz), 122.1 (d, $J_{\text{CF}} = 24.0$ Hz). The spectroscopic data matched that reported in the literature.³⁹

5. General procedure A for the TBS protection

The compounds could be prepared according to the literature.⁴⁰ To a solution of hydroxy substrate (1.0 equiv.) in anhydrous DMF (0.05 M) was added imidazole (2.5 or 5.0 equiv.) at 0 $^{\circ}\text{C}$, followed by the addition of TBSCl (1.5 or 3.5 equiv.). The reaction mixture was allowed to warm to RT for 12 h. After completion monitored by TLC, the mixture was extracted with ethyl acetate (3×30 mL) and H_2O (50 mL), the organic layers were dried over MgSO_4 and concentrated *in vacuo*.

4-((tert-Butyldimethylsilyloxy)aniline (15a). This compound was prepared according to general procedure A by treating 4-aminophenol (2.18 g, 0.02 mol), imidazole (3.2 g, 0.05 mol) and TBSCl (4.53 g, 0.03 mol). The residue was purified by flash chromatography (hexane/ethyl acetate 10:1 \rightarrow 5:1) to give the product **15a** as pale yellow oil (4.0 g, 87%). R_f (hexane/ethyl acetate 2:1): 0.45; $^1\text{H NMR}$ (300 MHz, d_6 -DMSO): δ 6.53 (2H, d, $J = 8.7$ Hz), 8.46 (2H, d, $J = 8.7$ Hz), 4.59 (2H, s), 0.93 (9H, s), 0.11 (6H, s); $^{13}\text{C NMR}$ (75 MHz, d_6 -DMSO): δ 145.5, 142.8, 119.9, 114.9, 25.6, 17.8, -4.6. The spectroscopic data matched that reported in the literature.⁴¹

3-((tert-Butyldimethylsilyloxy)aniline (15b). This compound was prepared according to general procedure A by treating 3-aminophenol (1.09 g, 0.01 mol), imidazole (1.60 g, 0.025 mol) and TBSCl (2.27 g, 0.015 mol). The crude product was purified by flash chromatography

(hexane/ethyl acetate 10:1 → 5:1) to give the product **15b** as pale yellow oil (2.07 g, 93%). R_f (hexane/ethyl acetate 2:1): 0.45; $^1\text{H NMR}$ (500 MHz, CDCl_3): δ 6.99 (1H, t, $J = 8.0$ Hz), 6.31–6.26 (2H, m), 6.21–6.20 (1H, m), 3.46 (2H, br.s), 0.99 (9H, s), 0.20 (6H, s); $^{13}\text{C NMR}$ (125 MHz, CDCl_3): δ 156.9, 147.8, 130.1, 110.7, 108.7, 107.3, 25.9, 18.3, –4.2. The spectroscopic data matched that reported in the literature.⁴²

4-(5-Bromo-2-nitrophenoxy)aniline (16b). To a solution of **14** (220 mg, 1 mmol) in DMF (10 mL) was added K_2CO_3 (207 mg, 1.5 mmol), followed by the addition of 4-((*tert*-butyldimethylsilyloxy)aniline **15a** (245 mg, 1.1 mmol). The resulting mixture was heated to 90 °C and stirred for 3 h. After completion monitored by TLC, the mixture was extracted with ethyl acetate (3 × 10 mL) and H_2O . The combined organic layers were dried over MgSO_4 and concentrated *in vacuo*. The crude product was purified by flash chromatography (hexane/ethyl acetate 5:1 → 2:1) to give the product **16b** as a pale yellow semisolid (247 mg, 80%); R_f (hexane/ethyl acetate 4:1): 0.25; $^1\text{H NMR}$ (400 MHz, d_6 -DMSO): δ 7.96 (1H, d, $J = 8.8$ Hz), 7.42 (1H, dd, $J = 2.0$, 8.8 Hz), 6.96 (1H, d, $J = 2.0$ Hz), 6.88 (2H, dd, $J = 2.0$, 10.8 Hz), 6.65 (2H, dd, $J = 2.0$, 10.8 Hz), 5.26 (2H, br. s); $^{13}\text{C NMR}$ (100 MHz, d_6 -DMSO): δ 152.6, 146.7, 143.6, 138.8, 127.4, 127.2, 125.1, 121.1, 120.3, 115.0; **HRMS** (ESI+) Calc. for $\text{C}_{12}\text{H}_9\text{N}_2\text{O}_3\text{Br}$ [M + Na]⁺ 330.9689/332.9668, found 330.9691/332.9670. **IR** (neat, cm^{-1}): $\tilde{\nu}$ 3475, 3385, 3098, 3085, 1615, 1505, 1466, 1231, 824, 528.

4-((5-Bromo-2-nitrophenyl)amino)phenol (16c). To a solution of **14** (220 mg, 1 mmol) in anhydrous DMF (10 mL) was added K_2CO_3 (207 mg, 1.5 mmol), followed by the addition of 4-aminophenol (120 mg, 1.1 mmol). The resulting mixture was heated to 90 °C and stirred for 3 h. After completion monitored by TLC, the mixture was extracted with ethyl acetate (3 × 10 mL) and H_2O . The combined organic layer was dried over MgSO_4 and concentrated *in vacuo*. The crude product was purified by flash chromatography (hexane/ethyl acetate 10:1 → 4:1) to give the product **16c** as a pale orange solid (201 mg, 65%); **m.p.** 151–152 °C; R_f (hexane/ethyl acetate 4:1): 0.30; $^1\text{H NMR}$ (300 MHz, d_6 -DMSO): δ 9.65 (1H, br.s), 9.40 (1H, br.s), 8.02 (1H, d, $J = 9.0$ Hz), 7.14 (2H, d, $J = 8.1$ Hz), 6.92–6.84 (4H, m); $^{13}\text{C NMR}$ (75 MHz, d_6 -DMSO): δ 156.1, 145.0, 131.0, 130.2, 129.0, 128.2, 127.7, 119.4, 117.7, 116.3; **HRMS** (ESI+) Calc. for $\text{C}_{12}\text{H}_9\text{N}_2\text{O}_3\text{Br}$ [M + Na]⁺ 330.9689/332.9668, found 330.9692/332.9672. **IR** (neat, cm^{-1}): $\tilde{\nu}$ 3349, 3089, 1602, 1556, 1475, 1241, 1198, 747, 531.

4-((2-Amino-5-bromophenyl)amino)phenol (17). To a solution of **16c** (308 mg, 1 mmol) in acetic acid (15 mL) was added iron powder (280 mg, 5 mmol), and the resulting mixture was stirred at RT for 12 h. After completion monitored by TLC, the volatile was removed under reduced pressure and the residue was washed with sat. NaHCO_3 (aq.) and extracted with ethyl acetate (3 × 15 mL). The combined organic layers were dried over MgSO_4 and concentrated *in vacuo*. The crude product was purified by flash chromatography ($\text{CH}_2\text{Cl}_2/\text{MeOH}$ 100:1) to give the product **17** as a brown solid (265 mg, 95%); **m.p.** 145–147 °C; R_f (hexane/ethyl acetate 1:1): 0.25; $^1\text{H NMR}$ (400 MHz, d_6 -DMSO): δ 6.91 (1H, dd, $J = 2.4$, 8.4 Hz), 6.75 (2H, dd, $J = 2.4$, 6.8 Hz), 6.68 (1H, d, $J = 8.4$ Hz), 6.59 (2H, dd, $J = 2.4$, 6.8 Hz), 6.55 (1H, d, $J = 2.4$ Hz), 5.08 (2H, br.s), 4.97 (1H, br.s); $^{13}\text{C NMR}$ (100 MHz, d_6 -DMSO): δ 146.1, 145.7, 145.3, 138.4, 125.1, 120.2, 118.4, 116.2, 114.8, 105.5; **HRMS** (ESI+) Calc. for $\text{C}_{12}\text{H}_{11}\text{BrN}_2\text{O}$ [M + H]⁺ 279.0128/281.0107, found 279.0125/281.0104. **IR** (neat, cm^{-1}): $\tilde{\nu}$ 3500, 3400, 2896, 1610, 1598, 1510, 1220, 756, 520.

4-(2-Amino-6-bromo-1H-benzo[d]imidazol-1-yl)phenol (18). This compound was prepared following a literature procedure.²¹ To a solution of **17** (200 mg, 0.72 mmol) in the mixture solvent of MeCN- H_2O (4:1 (v/v), 10 mL) was added cyanogen bromide (158 μL , 0.79 mmol, 5 M in MeCN) at 0 °C. and the resulting mixture was allowed to warm to RT for 16 h. After completion monitored by TLC, the mixture was treated with sat. NaHCO_3 (aq.) (10 mL) and extracted with ethyl acetate (3 × 15 mL). The combined organic layers were dried over MgSO_4 and concentrated *in vacuo*. The residue was purified by flash

chromatography ($\text{CH}_2\text{Cl}_2/\text{MeOH}$ 100:1 → 20:1) to give the product **18** as a pale pink solid (171 mg, 78%); **m.p.** 273–274 °C; R_f ($\text{CH}_2\text{Cl}_2/\text{MeOH}$ 15:1): 0.20; $^1\text{H NMR}$ (400 MHz, d_6 -DMSO): δ 9.98 (1H, s), 7.24 (2H, dd, $J = 2.0$, 6.4 Hz), 7.14 (1H, dd, $J = 0.4$, 8.4 Hz), 7.11 (1H, dd, $J = 1.6$, 8.4 Hz), 6.96 (2H, dd, $J = 2.0$, 6.4 Hz), 6.81 (1H, dd, $J = 0.4$, 1.6 Hz), 6.35 (2H, s); $^{13}\text{C NMR}$ (100 MHz, d_6 -DMSO): δ 157.8, 155.3, 141.6, 136.8, 128.5, 125.0, 123.8, 116.8, 116.4, 110.4, 110.3; **HRMS** (ESI+) Calc. for $\text{C}_{13}\text{H}_{10}\text{BrN}_3\text{O}$ [M + H]⁺ 304.0080/304.0059, found 304.0083/306.0062. **IR** (neat, cm^{-1}): $\tilde{\nu}$ 3330, 3205, 1647, 1514, 1449, 1272, 1247, 1122, 800, 727, 586, 432.

6. General procedure B for Suzuki coupling reaction

To a solution of aryl-halide (1.0 equiv.) in 1,4-dioxane (0.02 M) was added arylboronic acid (1.2 equiv.), aq. K_2CO_3 (2 M, 2.0 equiv.), and Pd (PPh_3)₄ (2 mol%), and the reaction was heated to 100–110 °C for 4 h under argon. After completion monitored by TLC, the reaction mixture was cooled to RT, solvent was removed under reduce pressure, and then partitioned between H_2O and ethyl acetate. The aqueous layer was extracted with ethyl acetate, and the combined organic layers were dried over MgSO_4 and concentrated *in vacuo*.

6.1. 4,4'-(2-Amino-1H-benzo[d]imidazole-1,6-diyl)diphenol (2)

This compound was prepared according to general procedure B by treating **18** (61 mg, 0.2 mmol) with (4-hydroxyphenyl)boronic acid (33 mg, 0.24 mmol) at 110 °C. The residue was purified by flash column chromatography ($\text{CH}_2\text{Cl}_2/\text{MeOH} = 50:1 \rightarrow 10:1$) to afford the product **2** as a pale yellow solid (10 mg, 30%). **m.p.** 249–250 °C; R_f ($\text{CH}_2\text{Cl}_2/\text{MeOH}$ 10:1): 0.35; $^1\text{H NMR}$ (400 MHz, d_6 -DMSO): δ 9.85 (1H, br.s), 9.36 (1H, s), 7.42 (2H, dd, $J = 2.0$, 6.4 Hz), 7.35 (1H, d, $J = 1.6$ Hz), 7.26 (2H, dd, $J = 2.0$, 6.8 Hz), 7.06 (1H, dd, $J = 1.6$, 8.0 Hz), 6.97 (2H, dd, $J = 2.0$, 6.8 Hz), 6.82 (2H, dd, $J = 2.0$, 6.4 Hz), 6.79 (1H, d, $J = 8.0$ Hz), 6.14 (2H, br.s); $^{13}\text{C NMR}$ (100 MHz, d_6 -DMSO): δ 157.3, 156.2, 154.9, 143.4, 134.5, 133.8, 132.6, 128.1, 127.5, 125.8, 117.1, 116.5, 115.5, 112.6, 107.6; **HRMS** (ESI+) Calc. for $\text{C}_{19}\text{H}_{15}\text{N}_3\text{O}_2$ [M + H]⁺ 318.1237, found 318.1241. **IR** (neat, cm^{-1}): $\tilde{\nu}$ 3337, 3135, 2954, 2921, 2852, 1633, 1608, 1540, 1513, 1459, 1218, 1170, 1101, 835, 801, 513. **HPLC**: 96.0% (HPLC Method A), RT: 16.8 min.

6.2. N-(1,6-bis(4-hydroxyphenyl)-1H-benzo[d]imidazol-2-yl)acetamide (3)

To a solution of **2** (30 mg, 0.10 mmol) in acetic acid (1 mL) was added acetic anhydride (10 μL , 0.11 mmol) at RT. And the resulting mixture was stirred at 110 °C for 3 h. After completion monitored by TLC, the solvent was removed under reduced pressure and the residue was neutralised with sat. NaHCO_3 (aq.) and extracted with ethyl acetate (3 × 15 mL). The combined organic layers were dried over MgSO_4 and concentrated *in vacuo*. The crude product was purified by flash chromatography ($\text{CH}_2\text{Cl}_2/\text{MeOH} = 50:1 \rightarrow 10:1$) to afford the product **3** as a pale yellow solid (25 mg, 38%). **m.p.** 207–209 °C; R_f ($\text{CH}_2\text{Cl}_2/\text{MeOH}$ 10:1): 0.25; $^1\text{H NMR}$ (400 MHz, d_6 -DMSO): δ 10.28 (1H, br.s), 9.86 (1H, s), 9.45 (1H, s), 7.77 (1H, s), 7.50 (2H, d, $J = 8.4$ Hz), 7.43 (1H, d, $J = 8.0$ Hz), 7.24 (2H, d, $J = 8.0$ Hz), 7.16 (1H, d, $J = 8.4$ Hz), 6.93 (2H, d, $J = 8.4$ Hz), 6.85 (2H, d, $J = 8.4$ Hz), 1.95 (3H, s); $^{13}\text{C NMR}$ (100 MHz, d_6 -DMSO): δ 170.3, 157.9, 157.1, 141.7, 141.6, 135.6, 134.6, 132.2, 128.3, 128.0, 126.5, 122.0, 116.5, 116.4, 116.2, 110.7, 23.0; **HRMS** (ESI+) Calc. for $\text{C}_{21}\text{H}_{17}\text{N}_3\text{O}_3$ [M + H]⁺ 360.1343, found 360.1346. **IR** (neat, cm^{-1}): $\tilde{\nu}$ 3274, 2953, 2921, 2852, 1587, 1550, 1513, 1366, 1203, 834, 808, 560. **HPLC**: 96.6% (HPLC Method A), RT: 16.6 min.

6.3. 4,5-Diiodo-1H-imidazole (20)

This compound was prepared following a literature procedure.²² To

a solution of imidazole **19** (1.11 g, 16 mmol) in NaOH (4 M, 60 mL) was added a solution of KI (13.3 g, 80 mmol) and I₂ (8.88 g, 35 mmol) in H₂O (50 mL) dropwise. The resulting mixture stirred at RT for 10 h. After completion monitored by TLC, the mixture was reduced to pH = 8 with acetic acid, and the resulting white precipitate was filtered and washed with cold water. The remaining solid was air dried to afford the product **20** as a white creamy solid (4.1 g, 80%). **m.p.** 188–190 °C; *R_f* (hexane/ethyl acetate 1:1): 0.15; ¹H NMR (300 MHz, *d*₆-DMSO): δ 7.77 (1H, s); ¹³C NMR (75 MHz, *d*₆-DMSO): δ 141.8, 86.9. The spectroscopic data matched that reported in the literature.⁴³

6.4. 4,4'-(1H-Imidazole-4,5-diyl)diphenol (**4**)

This compound was prepared following a literature procedure.²³ The mixture of 4,5-diiodo-1H-imidazole **20** (0.11 g, 0.34 mmol), (4-hydroxyphenyl)boronic acid (141 mg, 1.02 mmol), TBAB (11 mg, 0.034 mmol), K₂HPO₄ (226 mg, 1.30 mmol) and Pd(PPh₃)₄ (25 mg, 6 mol%) were transferred to a microwave reactor tube equipped with a magnetic stirring bar, followed by the addition of a mixture solvent of MeOH/H₂O (5 mL, 4:1), and the resulting mixture was degassed and back-filled with nitrogen and then stirred at 100 °C (100 W) with microwave irradiation for 60 min. After completion monitored by TLC, the reaction mixture was dissolved in aq. HCl (10%, 10 mL) and stirred vigorously. The mixture was washed with ethyl acetate (2 × 10 mL), the combined aqueous layers were neutralised with sat. NaHCO₃ (aq.) and extracted with ethyl acetate (3 × 10 mL). The combined organic layers were washed with H₂O, dried over MgSO₄ and concentrated *in vacuo*. The crude product was purified by flash chromatography (CH₂Cl₂: MeOH = 50:1 → 10:1) to afford the product **4** as a white solid (30 mg, 35%). *R_f* (CH₂Cl₂/MeOH 10:1): 0.25; ¹H NMR (400 MHz, *d*₆-DMSO): δ 9.44 (2H, br.s), 7.67 (1H, s), 7.25 (4H, d, *J* = 8.4 Hz), 6.72 (4H, d, *J* = 8.4 Hz); ¹³C NMR (100 MHz, *d*₆-DMSO): δ 156.3, 134.4, 128.6, 125.6, 124.3, 115.2. **HRMS** (ESI+) Calc. for C₁₅H₁₂N₂O₂ [M+Na]⁺ 275.0791, found 275.0794. **HPLC**: 97.7% (HPLC Method A), RT: 13.3 min. The spectroscopic data matched that reported in the literature.⁴⁴

6.5. 2-Amino-5-bromonicotinic acid (**22**)

This compound was prepared following a literature procedure.²⁵ To a suspension of 2-aminonicotinic acid **21** (3.75 g, 27 mmol) in glacial acetic acid (15 mL) was added a solution of bromine (1.8 mL, 35 mmol) in glacial acetic acid (3 mL) and the mixture was stirred at RT for 20 h. After completion monitored by TLC, the resulting precipitate was filtered and washed with glacial acetic acid 3 times. The remaining solid was air dried and then recrystallised from boiling methanol to afford the product **22** as white crystalline needles (5.2 g, 90%). ¹H NMR (400 MHz, *d*₆-DMSO): δ 8.36 (1H, d, *J* = 2.6 Hz), 8.25 (1H, d, *J* = 2.6 Hz), 7.95–7.79 (2H, br.s); ¹³C NMR (100 MHz, *d*₆-DMSO): δ 166.6, 156.5, 149.9, 143.8, 109.3, 103.7. The spectroscopic data matched that reported in the literature.²⁵

6.6. Methyl 2-amino-5-bromonicotinate (**23**)

To a solution of 2-amino-5-bromonicotinic acid **22** (1.0 g, 4.6 mmol) in MeOH (10 mL) was added sulphuric acid (2.0 mL, 36.8 mmol) dropwise and the mixture was stirred at 80 °C for 18 h. After completion monitored by TLC, the solvent was removed under reduced pressure. The residue was neutralised with sat. NaHCO₃ (aq.) and extracted with ethyl acetate (3 × 20 mL). The combined organic layers were dried over MgSO₄ and concentrated *in vacuo* to afford the product **23** as a white powder (1.0 g, 94%) without further purification. **m.p.** 148–149 °C; *R_f* (CH₂Cl₂/MeOH 20:1): 0.55; ¹H NMR (400 MHz, *d*₆-DMSO): δ 8.24 (1H, d, *J* = 2.4 Hz), 8.21 (1H, d, *J* = 2.4 Hz), 6.68–6.19 (2H, br.s), 3.89 (3H, s); ¹³C NMR (100 MHz, *d*₆-DMSO): δ 166.6, 158.0, 154.4, 142.0, 107.5, 106.1, 52.4. **HRMS** (ESI+) Calc. for C₇H₇N₂O₂Br

[M+H]⁺ 230.9764/232.9743, found 230.9765/232.9745. **IR** (neat, cm⁻¹): ν̄ 3425, 3131, 2918, 1704, 1620, 1223, 796, 526.

6.7. 6-Bromo-4-hydroxy-1,8-naphthyridine-3-carbonitrile (**24**)

This compound was prepared following a literature procedure.²⁴ To a sealed tube was added a mixture of methyl 2-amino-5-bromonicotinate **23** (500 mg, 2.16 mmol) and *N,N*-dimethylformamide dimethyl acetal (3 mL, 21.6 mmol), and stirred at 110 °C for 3 h. The volatiles were concentrated under reduced pressure, and the crude intermediate was dissolved in anhydrous THF (30 mL), which would be used immediately in the following step.

To a solution of *n*-BuLi (2.5 M in hexane, 1.9 mL, 4.75 mmol) in anhydrous THF (10 mL) was added anhydrous acetonitrile (248 μL, 4.75 mmol) dropwise at -78 °C under nitrogen atmosphere. The resulting reaction mixture was stirred at -78 °C for 20 min. To the resulting white suspension was added dropwise the intermediate solution described above, and the reaction mixture was stirred at -78 °C for 30 min, then at -40 °C for 2 h. Acetic acid (370 μL, 6.48 mmol) was added and the resulting yellow suspension was warmed to RT and stirred for 10 h. After completion monitored by TLC, the mixture was diluted with H₂O (20 mL) and extracted with ethyl acetate (3 × 15 mL). The combined organic layers were washed with H₂O (2 × 15 mL) and brine, dried over MgSO₄ and concentrated *in vacuo*. The crude product was purified by flash chromatography (hexane/ethyl acetate = 5:1 → 1:1) to afford the product **24** as an orange solid (190 mg, 35%). ¹H NMR (400 MHz, *d*₆-DMSO): δ 13.43–13.41 (1H, br.s), 8.97 (1H, d, *J* = 2.4 Hz), 8.85 (1H, s), 8.61 (1H, d, *J* = 2.4 Hz); ¹³C NMR (100 MHz, *d*₆-DMSO): δ 174.0, 154.8, 148.6, 148.4, 136.5, 121.2, 116.5, 115.9, 95.3. The spectroscopic data matched that reported in the literature.²⁴

6.8. 6-Bromo-1,8-naphthyridin-4-ol (**25**)

This compound was prepared following a literature procedure.²⁴ To a sealed tube was added a mixture of 6-bromo-4-hydroxy-1,8-naphthyridine-3-carbonitrile **24** (100 mg, 0.40 mmol) in aq. HCl (32%, 2 mL) and stirred at 150 °C for 3 h. After cooling to room temperature, the reaction mixture was neutralised with ammonia solution, extracted with ethyl acetate (3 × 10 mL). The combined organic layers were washed with H₂O (2 × 10 mL), dried over MgSO₄ and concentrated *in vacuo*. The crude product was purified by flash chromatography (CH₂Cl₂: MeOH = 50:1 → 20:1) to afford the product **25** as a pale yellow solid (30 mg, 33%). ¹H NMR (300 MHz, *d*₆-DMSO): δ 12.4 (1H, br.s), 8.84 (1H, s), 8.53 (1H, s), 7.98 (1H, d, *J* = 7.5 Hz), 6.15 (1H, d, *J* = 7.5 Hz); ¹³C NMR (75 MHz, *d*₆-DMSO): δ 176.5, 153.6, 149.1, 140.9, 136.3, 121.3, 114.3, 110.0. The spectroscopic data matched that reported in the literature.²⁴

6.9. 3-Bromo-5-chloro-1,8-naphthyridine (**26**)

This compound was prepared following a literature procedure.²⁴ To a sealed tube was added a mixture of 6-bromo-1,8-naphthyridin-4-ol **25** (30 mg, 0.13 mmol) in POCl₃ (1 mL) and stirred at 105 °C for 3 h. After cooling to RT, the reaction mixture was poured into ice, and the resulting mixture was neutralised with sat. NaHCO₃ (aq.) and extracted with ethyl acetate (3 × 5 mL). The combined organic layers were washed with H₂O (2 × 5 mL), dried over MgSO₄ and concentrated *in vacuo*. The crude product was purified by flash chromatography (hexane/ethyl acetate = 5:1 → 3:1) to afford the product **26** as a white solid (29 mg, 93%). ¹H NMR (400 MHz, CDCl₃): δ 9.16 (1H, d, *J* = 2.4 Hz), 9.02 (1H, d, *J* = 4.8 Hz), 8.75 (1H, d, *J* = 2.4 Hz), 7.61 (1H, d, *J* = 4.8 Hz); ¹³C NMR (100 MHz, CDCl₃): δ 155.8, 155.0, 153.4, 142.1, 135.3, 123.0, 122.8, 119.5. The spectroscopic data matched that reported in the literature.²⁴

6.10. 4,4'-(1,8-Naphthyridine-3,5-diyl)diphenol (5)

A mixture of 3-bromo-5-chloro-1,8-naphthyridine **26** (15 mg, 0.06 mmol), (4-hydroxyphenyl)boronic acid (21 mg, 0.15 mmol) and aq. K_2CO_3 (2 M, 180 μ L, 0.36 mmol) in 1,4-dioxane (1 mL) was degassed, and then $PdCl_2(dppf)$ (9 mg, 0.012 mmol) was added. The resulting mixture was degassed and back-filled with nitrogen, and then stirred at 130 °C (100 W) in microwave under nitrogen atmosphere for 2 h. After completion monitored by TLC, the reaction mixture was concentrated under reduced pressure, and diluted with H_2O (5 mL), neutralised with sat. NH_4Cl (aq.) and extracted with ethyl acetate (3 \times 5 mL). The combined organic layers were washed with H_2O (5 mL), dried over $MgSO_4$ and concentrated *in vacuo*. The crude product was purified by flash chromatography (CH_2Cl_2 : MeOH = 50:1 \rightarrow 10:1) to afford the product **5** as a yellow solid (16 mg, 85%). **m.p.** 211–213 °C; R_f (CH_2Cl_2 /MeOH 15:1): 0.30; 1H NMR (400 MHz, d_6 -DMSO): δ 9.90 (1H, s), 9.78 (1H, s), 9.38 (1H, s), 9.04 (1H, br.s), 8.37 (1H, d, J = 2.4 Hz), 7.62 (2H, d, J = 8.4 Hz), 7.54 (1H, d, J = 4.4 Hz), 7.48 (2H, d, J = 8.4 Hz), 7.00 (2H, d, J = 8.4 Hz), 6.92 (2H, d, J = 8.4 Hz); ^{13}C NMR (100 MHz, d_6 -DMSO): δ 158.7, 158.5, 155.4, 152.8, 152.5, 149.6, 134.2, 131.5, 130.7, 129.0, 127.6, 127.3, 122.7, 121.1, 116.7, 116.3. **HRMS** (ESI+) Calc. for $C_{20}H_{14}N_2O_2$ [M+Na]⁺ 337.0947, found 337.0950. **IR** (neat, cm^{-1}): ν 3363, 2921, 1606, 1512, 1265, 831, 559, 527. **HPLC**: 98.5% (HPLC Method A), RT: 15.5 min.

7. General procedure C for condensation reactions

The compounds were prepared following a literature procedure.^{45,46} To a solution of halogenated pyridine substrate (1.0 equiv.) in anhydrous toluene (0.05 M) was added *n*-BuLi (1.1 equiv., 2.5 M in hexane) dropwise at -78 °C, and the resulting mixture was stirred for 30 min. *N,N*-dimethylacetamide or DMF (1.5 equiv.) was added dropwise and the mixture was stirred for another 30 min. After completion, the reaction was quenched with sat. NH_4Cl (aq.) and extracted with ethyl acetate (3 \times 15 mL). The organic layer was dried over $MgSO_4$ and concentrated *in vacuo*.

7.1. 1-(5-Bromopyridin-2-yl)ethan-1-one (27a)

This compound was prepared according to general procedure C by treating 2,5-dibromopyridine (237 mg, 1 mmol) with *N,N*-dimethylacetamide (44 μ L, 1.5 mmol). The crude product was purified by flash chromatography (hexane/ethyl acetate 10:1) to give the product **27a** as a white solid (160 mg, 80%); R_f (hexane/ethyl acetate 8:1): 0.45; 1H NMR (300 MHz, $CDCl_3$): δ 8.70 (1H, s), 7.95–7.88 (2H, m), 2.66 (3H, s); ^{13}C NMR (75 MHz, $CDCl_3$): δ 199.2, 151.9, 150.2, 139.6, 125.4, 123.0, 25.8. The spectroscopic data matched that reported in the literature.⁴⁵

7.2. 5-Bromopicolinaldehyde (27b)

This compound was prepared according to general procedure C by treating 2,5-dibromopyridine (237 mg, 1 mmol) with DMF (115 μ L, 1.5 mmol). The crude product was purified by flash chromatography (hexane/ethyl acetate 10:1) to give the product **27b** as an off-brown solid (149 mg, 80%); R_f (hexane/ethyl acetate 8:1): 0.45; 1H NMR (400 MHz, $CDCl_3$): δ 10.03 (1H, s), 8.85 (1H, dd, J = 0.8, 2.0 Hz), 8.02 (1H, ddd, J = 0.8, 2.0, 8.0 Hz), 7.85 (1H, dd, J = 0.8, 8.0 Hz); ^{13}C NMR (100 MHz, $CDCl_3$): δ 192.4, 151.7, 151.3, 140.0, 126.3, 122.8. The spectroscopic data matched that reported in the literature.⁴⁷

8. General procedure D for benzyl protection

The compounds were prepared following a literature procedure.⁴⁸ To a solution of hydroxyaryl substrate (1.0 equiv., 1 mmol) in DMF (0.05 M) was added K_2CO_3 (1.5 equiv., 1.5 mmol), followed by the dropwise addition of benzyl bromide (1.2 equiv., 1.2 mmol) at RT, and

the mixture was stirred at RT for 12 h. After completion monitored by TLC, the solvent was removed under reduced pressure, and the residue was washed with H_2O (30 mL) and extracted with ethyl acetate (3 \times 20 mL), the organic layers were dried over $MgSO_4$ and concentrated *in vacuo*.

8.1. 4-(Benzyloxy)benzaldehyde (28a)

The compounds were prepared according to general procedure D by treating 4-hydroxybenzaldehyde (1.22 g, 0.01 mol) with K_2CO_3 (2.07 g, 0.015 mol) and benzyl bromide (1.42 mL, 0.012 mol). The crude product was purified by flash chromatography (hexane/ethyl acetate 10:1 \rightarrow 5:1) to give the product **28a** as a white solid (1.97 g, 93%). R_f (hexane/ethyl acetate 4:1): 0.35; 1H NMR (300 MHz, $CDCl_3$): δ 9.89 (1H, s), 7.84 (2H, d, J = 7.8 Hz), 7.43–7.35 (5H, m), 7.08 (2H, d, J = 7.8 Hz), 5.15 (2H, s); ^{13}C NMR (75 MHz, $CDCl_3$): δ 190.9, 163.8, 136.0, 132.1, 130.2, 128.8, 128.4, 127.6, 115.3, 70.4. The spectroscopic data matched that reported in the literature.⁴⁹

8.2. 1-(4-(Benzyloxy)phenyl)ethan-1-one (28b)

This compound was prepared according to general procedure D by treating 1-(4-hydroxyphenyl)ethan-1-one (1.36 g, 0.01 mol) with K_2CO_3 (2.07 g, 0.015 mol) and benzyl bromide (1.42 mL, 0.012 mol). The crude product was purified by flash chromatography (hexane/ethyl acetate 10:1 \rightarrow 5:1) to give the product **28b** as a white solid (2.17 g, 96%); R_f (hexane/ethyl acetate 4:1): 0.50; 1H NMR (400 MHz, $CDCl_3$): δ 7.94 (2H, dd, J = 2.0, 6.8 Hz), 7.45–7.33 (5H, m), 7.01 (2H, dd, J = 2.0, 6.8 Hz), 5.12 (2H, s), 2.55 (3H, s); ^{13}C NMR (100 MHz, $CDCl_3$): δ 196.8, 162.7, 136.3, 130.7, 130.6, 128.7, 128.3, 127.5, 114.6, 70.2, 26.4. The spectroscopic data matched that reported in the literature.⁵⁰

9. General procedure E for aldol condensation

LDA formation: To a solution of *N,N*-diisopropylethylamine (1.3 equiv.) in anhydrous THF was added *n*-BuLi (1.2 equiv.) dropwise at -78 °C. After addition, the resulting mixture was stirred at -78 °C for 30 min before using.

To a solution of LDA (1.3 equiv.) in solvent (10 mL) was added ketone (1.1 equiv.) at -78 °C, and the resulting mixture was stirred for 30 min. To the mixture above was added a solution of aldehyde (1.0 equiv.) in the corresponding solvent (0.1 M) dropwise, after addition, the resulting mixture was slowly warmed up to 25 °C. After completion monitored by TLC, the reaction was quenched with sat. NH_4Cl (aq.) and extracted with ethyl acetate (3 \times 15 mL). The organic layer was dried over $MgSO_4$ and concentrated *in vacuo*. The crude product was purified by flash chromatography.

9.1. 1-(4-(Benzyloxy)phenyl)-3-(5-bromopyridin-2-yl)-3-hydroxypropan-1-one (29b)

This compound was prepared according to general procedure E by treating **27b** (186 mg, 1.0 mmol) with LDA (1.2 mmol) and **28b** (249 mg, 1.1 mmol). After completion monitored by TLC, the reaction was quenched with sat. NH_4Cl (aq.) and extracted with ethyl acetate (3 \times 15 mL). The organic layer was dried over $MgSO_4$ and concentrated *in vacuo*. The crude product was purified by flash chromatography (hexane/ethyl acetate 10:1 \rightarrow 3:1) to give the product **29b** as a white solid (322 mg, 78%); **m.p.** 133–134 °C; R_f (hexane/ethyl acetate 3:1): 0.25; 1H NMR (400 MHz, $CDCl_3$): δ 8.58 (1H, d, J = 2.4 Hz), 7.93 (2H, d, J = 9.0 Hz), 7.82 (1H, dd, J = 2.4, 8.4 Hz); 7.51 (1H, d, J = 8.0 Hz), 7.43–7.32 (5H, m), 6.99 (2H, d, J = 9.0 Hz), 5.31 (1H, p, J = 4.0 Hz), 5.12 (2H, s), 4.31 (1H, d, J = 4.8 Hz), 3.60 (1H, dd, J = 3.6, 17.6 Hz), 3.36 (1H, dd, J = 8.0, 17.6 Hz); ^{13}C NMR (100 MHz, $CDCl_3$): δ 198.6, 163.2, 160.7, 149.7, 139.4, 136.1, 130.7, 129.9, 128.8, 128.4, 127.5, 122.1, 119.2, 114.8, 70.3, 70.2, 45.0; **HRMS** (ESI+) Calc. for

$C_{21}H_{18}BrNO_3$ $[M+Na]^+$ 434.0362/436.0342, found 434.0365/436.0345. IR (neat, cm^{-1}): $\tilde{\nu}$ 3257, 2890, 1672, 1601, 1571, 1253, 1170, 1011, 828, 699, 543.

10. General procedure F for the oxidation of alcohols

To a solution of alcohol substrate (1.0 equiv.) in CH_2Cl_2 (0.05 M) was added Dess-Martin periodinane (DMP) (1.5 equiv.), and the mixture was stirred at RT for 30 min. After completion monitored by TLC, the mixture was quenched with sat. $NaHCO_3$ (aq.) (5 mL) and the resulting mixture was extracted with CH_2Cl_2 (3×10 mL), the organic layers were dried over $MgSO_4$ and concentrated *in vacuo*.

10.1. 1-(4-(Benzyloxy)phenyl)-3-(5-bromopyridin-2-yl)propane-1,3-dione (30)

This compound was prepared according to general procedure F by treating **29b** (206 mg, 0.5 mmol) with DMP (318 mg, 0.75 mmol). The crude product was purified by flash chromatography (hexane/ethyl acetate 10:1 \rightarrow 5:1) to give the product **30** as a yellow solid (195 mg, 95%). **m.p.** 162–163 °C; R_f (hexane/ethyl acetate 8:1): 0.50; 1H NMR (400 MHz, $CDCl_3$): δ 16.54 (1H, br.s), 8.73 (1H, d, $J = 2.0$ Hz), 8.04 (2H, d, $J = 8.8$ Hz), 8.01–7.96 (2H, m), 7.46–7.35 (6H, m), 7.05 (2H, d, $J = 8.8$ Hz), 5.15 (2H, s); ^{13}C NMR (100 MHz, $CDCl_3$): δ 186.9, 180.9, 162.8, 151.2, 150.5, 139.8, 136.3, 129.9, 128.8, 128.4, 128.3, 127.6, 124.0, 123.2, 115.0, 93.1, 70.3; **HRMS** (ESI+) Calc. for $C_{21}H_{16}BrNO_3$ $[M+Na]^+$ 432.0206/434.0185, found 432.0205/434.0185. IR (neat, cm^{-1}): $\tilde{\nu}$ 3031, 2944, 1588, 1510, 1492, 1451, 1242, 1170, 999, 826, 800, 624, 518.

11. General procedure G for the formation of pyrazoles

The compounds were prepared following a literature procedure.²⁷ To a solution of 1,3-dione (1.0 equiv.) in MeOH (0.05 M) was added $N_2H_4 \cdot H_2O$ (64%, 2.0 equiv.), and the resulting mixture was stirred at RT for 48 h under nitrogen. After completion monitored by TLC, the solvent was removed under reduced pressure, and the residue was treated with H_2O (10 mL) and extracted with ethyl acetate (3×10 mL). The combined organic layers were dried over $MgSO_4$ and concentrated *in vacuo*.

11.1. 2-(3-(4-(Benzyloxy)phenyl)-1H-pyrazol-5-yl)-5-bromopyridine (31)

This compound was prepared according to general procedure G by treating **30** (150 mg, 0.37 mmol) with $N_2H_4 \cdot H_2O$ (58 μ L, 0.74 mmol). The crude product was purified by flash chromatography (hexane/ethyl acetate 5:1 \rightarrow 2:1) to give the product **31** as a pale yellow solid (113 mg, 75%). **m.p.** 241–243 °C; R_f (hexane/ethyl acetate 1:1): 0.30; 1H NMR (400 MHz, d_6 -DMSO): δ 13.45 (1H, br.s), 8.72 (1H, s), 8.17–8.07 (1H, m), 7.97–7.87 (1H, m), 7.78–7.76 (2H, m), 7.48–7.32 (5H, m), 7.16–7.11 (3H, m), 5.16 (2H, s); ^{13}C NMR (100 MHz, d_6 -DMSO): δ 158.8, 151.5, 150.3, 144.1, 139.8, 137.4, 128.9, 128.3, 128.2, 127.1, 122.3, 121.4, 119.0, 115.8, 115.5, 100.5, 69.8; **HRMS** (ESI+) Calc. for $C_{21}H_{16}BrN_3O$ $[M+Na]^+$ 428.0369/430.0348, found 428.0367/430.0346. IR (neat, cm^{-1}): $\tilde{\nu}$ 3201, 3061, 2888, 1613, 1590, 1448, 1242, 798, 734, 518, 498.

11.2. 2-(3-(4-(Benzyloxy)phenyl)-1-tosyl-1H-pyrazol-5-yl)-5-bromopyridine (32)

To a solution of **31** (101 mg, 0.25 mmol) in CH_2Cl_2 (10 mL) was added NaH (60% in mineral oil, 20 mg, 0.50 mmol) slowly at 0 °C, after 10 min, tosyl chloride (TsCl) (52 mg, 0.27 mmol) was added, and the resulting mixture was allowed to warm to RT for 30 min. After completion monitored by TLC, the mixture was quenched with H_2O (5 mL) and extracted with CH_2Cl_2 (3×5 mL), the organic layers were dried

over $MgSO_4$ and concentrated *in vacuo*. The crude product was purified by flash chromatography (hexane/ethyl acetate 10:1 \rightarrow 5:1) to give the product **32** as a white solid (133 mg, 95%). **m.p.** 152–154 °C; R_f (hexane/ethyl acetate 6:1): 0.55; 1H NMR (300 MHz, $CDCl_3$): δ 8.64 (1H, d, $J = 2.1$ Hz), 8.06 (1H, d, $J = 8.4$ Hz), 7.88 (1H, dd, $J = 2.1, 8.4$ Hz), 7.57 (2H, d, $J = 8.4$ Hz), 7.49–7.36 (7H, m), 7.18 (2H, d, $J = 8.4$ Hz), 7.03 (2H, d, $J = 8.4$ Hz), 6.89 (1H, s), 5.14 (2H, s), 2.36 (3H, s); ^{13}C NMR (75 MHz, $CDCl_3$): δ 159.8, 154.4, 150.4, 149.5, 149.1, 145.5, 139.3, 136.6, 134.7, 131.5, 129.6, 128.7, 128.2, 128.0, 127.6, 122.2, 121.7, 120.9, 114.2, 110.1, 70.1, 21.7; **HRMS** (ESI+) Calc. for $C_{28}H_{22}BrN_3O_3S$ $[M+Na]^+$ 582.0457/584.0437, found 582.0455/584.0435. IR (neat, cm^{-1}): $\tilde{\nu}$ 3023, 2940, 1611, 1510, 1384, 1177, 1107, 1005, 816, 576, 545.

11.3. 4-(6-(3-(4-(Benzyloxy)phenyl)-1-tosyl-1H-pyrazol-5-yl)pyridin-3-yl)phenol (33)

This compound was prepared according to general procedure B by treating **32** (112 mg, 0.2 mmol) with (4-hydroxyphenyl)boronic acid (41 mg, 0.3 mmol) at 110 °C. The crude product was purified by flash chromatography (hexane/ethyl acetate 5:1 \rightarrow 2:1) to afford the product **33** as a white solid (97 mg, 85%). **m.p.** 192–193 °C; R_f (hexane/ethyl acetate 2:1): 0.25; 1H NMR (400 MHz, $CDCl_3$): δ 8.77 (1H, dd, $J = 0.8, 2.4$ Hz), 8.20 (1H, dd, $J = 0.8, 8.4$ Hz), 7.90 (1H, dd, $J = 2.4, 8.4$ Hz), 7.59 (2H, d, $J = 8.4$ Hz), 7.49–7.47 (4H, m), 7.44–7.34 (5H, m), 7.17 (2H, d, $J = 8.0$ Hz), 7.03 (2H, d, $J = 8.8$ Hz), 6.96–6.94 (3H, m), 5.88 (1H, br.s), 5.14 (2H, s), 2.35 (3H, s); ^{13}C NMR (100 MHz, $CDCl_3$): δ 159.9, 156.5, 155.3, 149.7, 148.7, 147.3, 145.5, 136.8, 136.5, 134.9, 134.7, 131.6, 129.9, 129.8, 128.8, 128.5, 128.3, 128.1, 127.7, 122.0, 121.3, 116.4, 114.3, 110.4, 70.3, 21.8; **HRMS** (ESI+) Calc. for $C_{34}H_{27}N_3O_4S$ $[M+Na]^+$ 596.1614, found 596.1613. IR (neat, cm^{-1}): $\tilde{\nu}$ 3061, 2926, 1608, 1378, 1242, 1174, 1112, 826, 809, 662, 591, 568, 543.

11.4. 4-(6-(3-(4-Hydroxyphenyl)-1H-pyrazol-5-yl)pyridin-3-yl)phenol (6)

To a solution of **33** (46 mg, 0.08 mmol) in MeOH was added KOH (22 mg, 0.4 mmol) at RT, and the resulting mixture was stirred at 75 °C for 1 h. After completion monitored by TLC, the solvent was removed and the residue was diluted with H_2O and extracted with ethyl acetate (3×5 mL). The combined organic layers were washed with brine (5 mL) and dried over $MgSO_4$ and concentrated *in vacuo* to get the crude compound without further purification. To the crude intermediate obtained above in MeOH (5 mL) was added Pd/C (4 mg, 10 wt%) under nitrogen, and the mixture was stirred at room temperature for 5 h under 1 atm of hydrogen. After completion monitored by TLC, the Pd-C was filtered through Celite®, and the filtrate was concentrated under reduced pressure. The crude product was purified by flash chromatography (CH_2Cl_2 /MeOH 50:1 \rightarrow 15:1) to give the product **6** as a pale yellow solid (12 mg, 45% over two steps). **m.p.** 249–252 °C; R_f (CH_2Cl_2 /MeOH 10:1): 0.25; 1H NMR (400 MHz, d_6 -DMSO): δ 13.30 (1H, br.s), 9.68 (1H, br.s), 8.84 (1H, s), 8.07–8.06 (1H, m), 7.97–7.96 (1H, m), 7.67 (2H, d, $J = 8.4$ Hz), 7.62 (2H, d, $J = 8.8$ Hz), 7.14 (1H, s), 6.91 (2H, d, $J = 8.8$ Hz), 6.85 (2H, d, $J = 8.4$ Hz); ^{13}C NMR (100 MHz, d_6 -DMSO): δ 158.2, 157.9, 147.0, 134.7, 134.6, 134.4 (two overlapping signals), 134.3, 128.3, 127.9, 127.0, 119.8, 116.5, 116.0, 100.1, 100.0; **HRMS** (ESI+) Calc. for $(C_{20}H_{15}N_3O_2)_2$ $[M+Na]^+$ 681.2221, found 681.2217. IR (neat, cm^{-1}): $\tilde{\nu}$ 3292, 2921, 2851, 1610, 1598, 1449, 1247, 824, 793, 506. **HPLC**: 98.0% (HPLC Method A), RT: 16.1 min.

11.5. 4-((tert-Butyldimethylsilyloxy)phenyl)boronic acid (35)

This compound was prepared according to general procedure A by treating (4-hydroxyphenyl)boronic acid (1.38 g, 0.01 mol) with imidazole (3.2 g, 0.05 mol) and TBSCl (5.29 g, 0.035 mol). The crude product was purified by flash chromatography (hexane/ethyl acetate 10:1 \rightarrow

3:1) to give the product **35** as a white solid (2.27 g, 90%). R_f (hexane/ethyl acetate 1:1): 0.30; $^1\text{H NMR}$ (300 MHz, CDCl_3): δ 8.11 (2H, d, $J = 8.4$ Hz), 6.96 (2H, d, $J = 8.4$ Hz), 1.02 (9H, s), 0.26 (6H, s); $^{13}\text{C NMR}$ (75 MHz, CDCl_3): δ 159.9, 137.6, 119.9, 111.0, 25.8, 18.4, –4.2. The spectroscopic data matched that reported in the literature.⁵¹

11.6. 4-(4-((tert-Butyldimethylsilyloxy)phenyl)pyridin-2-amine) (36)

This compound was prepared according to general procedure B by treating 4-bromopyridin-2-amine **34** (346 mg, 2 mmol) and boronic acid **35** (756 mg, 3 mmol) at 100 °C. The crude product was purified by flash chromatography (hexane/ethyl acetate 10:1 → 3:1) to afford the product **36** as a white solid (522 mg, 87%). **m.p.** 117–119 °C; R_f (hexane/ethyl acetate 2:1): 0.20; $^1\text{H NMR}$ (400 MHz, CDCl_3): δ 8.08 (1H, dd, $J = 0.8, 5.6$ Hz), 7.47 (2H, dd, $J = 2.0, 6.4$ Hz), 6.90 (2H, dd, $J = 2.0, 6.4$ Hz), 6.85 (1H, dd, $J = 1.6, 5.6$ Hz), 6.66 (1H, dd, $J = 0.8, 1.6$ Hz), 4.46 (2H, s), 1.00 (9H, s), 0.23 (6H, s); $^{13}\text{C NMR}$ (100 MHz, CDCl_3): δ 159.0, 156.7, 150.0, 148.6, 131.8, 128.1, 120.6, 112.6, 105.8, 25.8, 18.4, –4.2; **HRMS** (ESI+) Calc. for $\text{C}_{17}\text{H}_{24}\text{N}_2\text{OSi}$ [$\text{M} + \text{H}$]⁺ 301.1731, found 301.1728. **IR** (neat, cm^{-1}): $\tilde{\nu}$ 3467, 3297, 3139, 2956, 2928, 2854, 1633, 1596, 1518, 1471, 1253, 1239, 1180, 912, 901, 835, 821, 801, 784, 693, 666, 468.

11.7. 4-(4-((tert-Butyldimethylsilyloxy)phenyl)-2-iodopyridine) (37)

This compound was prepared following a literature procedure.²⁸ To a solution of **36** (255 mg, 0.85 mmol) in CH_2Cl_2 (5 mL) was added isomyl nitrite (1.75 mL, 17 mmol) at RT under nitrogen. After 30 min, aq. HI (57%, 2.5 μL , 0.017 mmol) was added, and the resulting mixture was stirred at RT for 24 h. After completion monitored by TLC, the mixture was poured into a mixture of $\text{NH}_4\text{OH}/\text{H}_2\text{O}$ (1:1 (v/v), 50 mL) and extracted with CHCl_3 (2 × 25 mL). The combined organic layers were dried over MgSO_4 and concentrated *in vacuo*. The crude product was purified by flash chromatography (hexane/ethyl acetate 100:1 → 40:1) to afford the product **37** as colorless oil (85 mg, 25%). R_f (hexane/ethyl acetate 10:1): 0.40; $^1\text{H NMR}$ (400 MHz, CDCl_3): δ 8.34 (1H, dd, $J = 0.4, 5.2$ Hz), 7.90 (1H, dd, $J = 0.8, 1.6$ Hz), 7.48 (2H, dd, $J = 2.0, 6.4$ Hz), 7.42 (1H, dd, $J = 1.6, 5.2$ Hz), 6.93 (2H, dd, $J = 2.0, 6.4$ Hz), 1.00 (9H, s), 0.23 (6H, s); $^{13}\text{C NMR}$ (100 MHz, CDCl_3): δ 157.5, 150.8, 150.0, 132.2, 129.4, 128.4, 121.0, 120.8, 119.0, 25.8, 18.4, –4.2; **HRMS** (ESI+) Calc. for $\text{C}_{17}\text{H}_{22}\text{N}_2\text{OSiI}$ [$\text{M} + \text{H}$]⁺ 412.0588, found 412.0586. **IR** (neat, cm^{-1}): $\tilde{\nu}$ 2954, 2929, 2857, 1604, 1579, 1513, 1470, 1263, 911, 828.

11.8. 4-(4-((tert-Butyldimethylsilyloxy)phenyl)picolinaldehyde) (38)

This compound was prepared according to general procedure C by treating **37** (85 mg, 0.2 mmol) with DMF (23 μL , 0.3 mmol). The crude product was purified by flash chromatography (hexane/ethyl acetate 10:1) to give the product **38** as pale yellow oil (31 mg, 50%). R_f (hexane/ethyl acetate 10:1): 0.45; $^1\text{H NMR}$ (300 MHz, CDCl_3): δ 10.13 (1H, s), 8.78 (1H, d, $J = 5.1$ Hz), 8.16 (1H, d, $J = 1.2$ Hz), 7.69 (1H, dd, $J = 1.8, 5.1$ Hz), 7.60 (2H, d, $J = 8.7$ Hz), 6.96 (2H, d, $J = 8.7$ Hz), 1.00 (9H, s), 0.24 (6H, s); $^{13}\text{C NMR}$ (75 MHz, CDCl_3): δ 193.8, 157.7, 153.5, 150.7, 149.4, 129.9, 128.4, 125.0, 121.1, 119.0, 25.8, 18.4, –4.2; **HRMS** (ESI+) Calc. for $\text{C}_{18}\text{H}_{23}\text{NO}_2\text{Si}$ [$\text{M} + \text{Na}$]⁺ 336.1390, found 336.1338. **IR** (neat, cm^{-1}): $\tilde{\nu}$ 3331, 2957, 2927, 2858, 1714, 1604, 1515, 1462, 1263, 1037, 912, 830, 781.

11.9. 1-(4-(Benzyloxy)phenyl)-3-(4-(4-((tert-butyl dimethylsilyloxy)phenyl)pyridin-2-yl)-3-hydroxypropan-1-one) (39)

This compound was prepared according to general procedure E by treating **38** (62 mg, 0.2 mmol) with **28b** (50 mg, 0.22 mmol) and LDA (0.24 mmol). After completion monitored by TLC, the reaction was quenched with sat. NH_4Cl (aq.) and extracted with ethyl acetate

(3 × 15 mL). The combined organic layers were dried over MgSO_4 and concentrated *in vacuo*. The crude product was purified by flash chromatography (hexane/ethyl acetate 8:1) to give the product **39** as pale yellow semi-solid (65 mg, 60%). R_f (hexane/ethyl acetate 10:1): 0.25; $^1\text{H NMR}$ (400 MHz, CDCl_3): δ 8.53 (1H, dd, $J = 0.4, 5.2$ Hz), 7.96 (2H, d, $J = 9.2$ Hz), 7.76–7.75 (1H, m), 7.56 (2H, d, $J = 8.8$ Hz), 7.43–7.32 (6H, m), 6.99 (2H, d, $J = 9.2$ Hz), 6.93 (2H, d, $J = 8.8$ Hz), 5.42 (1H, dd, $J = 3.6, 8.4$ Hz), 5.12 (2H, s), 4.41 (1H br.s), 3.63 (1H, dd, $J = 3.6, 17.2$ Hz), 3.41 (1H, dd, $J = 8.4, 17.2$ Hz), 1.01 (9H, s), 0.24 (6H, s); $^{13}\text{C NMR}$ (100 MHz, CDCl_3): δ 198.8, 163.1, 162.2, 157.1, 149.1, 149.0, 136.2, 131.1, 130.8, 130.2, 128.8, 128.6, 128.4, 127.6, 120.8, 120.0, 118.0, 114.8, 70.7, 70.3, 45.6, 25.8, 18.4, –4.2; **HRMS** (ESI+) Calc. for $\text{C}_{33}\text{H}_{37}\text{NO}_4\text{Si}$ [$\text{M} + \text{Na}$]⁺ 562.2384, found 562.2380. **IR** (neat, cm^{-1}): $\tilde{\nu}$ 3487, 2955, 2929, 2857, 1660, 1599, 1514, 1253, 1172, 912, 900, 850, 833, 779, 613.

11.10. 1-(4-(Benzyloxy)phenyl)-3-(4-(4-((tert-butyl dimethylsilyloxy)phenyl)pyridin-2-yl)propane-1,3-dione) (40)

This compound was prepared according to general procedure F by treating **39** (54 mg, 0.1 mmol) with DMP (64 mg, 0.15 mmol). The crude product was purified by flash chromatography (hexane/ethyl acetate 5:1 → 3:1) to give the product **40** as a yellow solid (40 mg, 75%). **m.p.** 134–135 °C; R_f ($\text{CH}_2\text{Cl}_2/\text{MeOH}$ 20:1): 0.55; $^1\text{H NMR}$ (400 MHz, CDCl_3): δ 16.67 (1H, br.s), 8.70 (1H, d, $J = 5.2$ Hz), 8.35 (1H, d, $J = 1.2$ Hz), 8.08 (2H, d, $J = 8.8$ Hz), 7.63 (2H, d, $J = 8.8$ Hz), 7.60 (1H, dd, $J = 2.0, 5.2$ Hz), 7.54 (1H, s), 7.46–7.33 (5H, m), 7.06 (2H, d, $J = 8.8$ Hz), 6.97 (2H, d, $J = 8.4$ Hz), 5.15 (2H, s), 1.01 (9H, s), 0.25 (6H, s); $^{13}\text{C NMR}$ (100 MHz, CDCl_3): δ 187.0, 182.0, 162.8, 157.4, 153.2, 149.7, 149.3, 136.4, 130.5, 129.9, 128.8, 128.5, 128.4 (two overlapping signals), 127.7, 123.4, 121.0, 119.6, 115.0, 93.3, 70.3, 25.8, 18.4, –4.2; **HRMS** (ESI+) Calc. for $\text{C}_{33}\text{H}_{35}\text{NO}_4\text{Si}$ [$\text{M} + \text{H}$]⁺ 538.2408, found 538.2414. **IR** (neat, cm^{-1}): $\tilde{\nu}$ 2953, 2928, 2857, 1604, 1510, 1453, 1248, 1173, 911, 832, 805, 733, 659.

11.11. 2-(3-(4-(Benzyloxy)phenyl)-1H-pyrazol-5-yl)-4-(4-((tert-butyl dimethylsilyloxy)phenyl)pyridine) (41)

This compound was prepared according to general procedure G by treating **40** (53.8 mg, 0.1 mmol) and $\text{N}_2\text{H}_4 \cdot \text{H}_2\text{O}$ (7.8 μL , 0.2 mmol). The crude product was purified by flash chromatography ($\text{CH}_2\text{Cl}_2/\text{MeOH}$ 50:1 → 20:1) to give the product **41** as a pale yellow semi-solid (37 mg, 70%). R_f ($\text{CH}_2\text{Cl}_2/\text{MeOH}$ 15:1): 0.25; $^1\text{H NMR}$ (400 MHz, $d_3\text{-MeOD}$): δ 8.59 (1H, s), 8.24 (1H, s), 7.78–7.74 (4H, m), 7.62 (1H, s), 7.49–7.31 (5H, m), 7.20 (1H, s), 7.11 (2H, d, $J = 8.8$ Hz), 7.03 (2H, d, $J = 8.8$ Hz), 5.16 (2H, s), 1.05 (9H, s), 0.28 (6H, s); $^{13}\text{C NMR}$ (100 MHz, $d_3\text{-MeOD}$): δ 160.5, 158.6, 150.7, 150.6, 144.6, 138.6, 132.0, 130.7, 129.5 (two overlapping signals), 129.4, 129.2, 128.9, 128.6, 128.1, 121.9, 118.6, 116.4, 102.8, 101.6, 71.1, 26.1, 19.1, –4.3; **HRMS** (ESI+) Calc. for $\text{C}_{33}\text{H}_{35}\text{N}_3\text{O}_2\text{Si}$ [$\text{M} + \text{H}$]⁺ 534.2571, found 534.2568. **IR** (neat, cm^{-1}): $\tilde{\nu}$ 2952, 2928, 2856, 1606, 1515, 1471, 1454, 1254, 1175, 913, 835.

11.12. 4-(2-(3-(4-Hydroxyphenyl)-1H-pyrazol-5-yl)pyridin-4-yl)phenol (7)

To a solution of **41** (53 mg, 0.1 mmol) in MeOH was added Pd/C (5 mg, 10 wt%) under nitrogen atmosphere, and the mixture was stirred at room temperature for 4 h under 1 atm of hydrogen. After completion monitored by TLC, the Pd-C was filtered through Celite®, and the filtrate was concentrated under reduced pressure to get the crude compound without further purification. To the crude intermediate obtained above in THF (3 mL) was added TBAF (0.2 mL, 0.2 mmol, 1 M in THF). The resulting mixture was stirred at RT for 30 min. After completion monitored by TLC, the solvent was removed under reduced pressure. The crude product was purified by flash chromatography ($\text{CH}_2\text{Cl}_2/\text{MeOH}$ 20:1 → 10:1) to give the product **7** as an off-white solid (18 mg,

55% over two steps). **m.p.** 159–161 °C; R_f (CH₂Cl₂/MeOH 10:1): 0.15; ¹H NMR (500 MHz, *d*₆-DMSO): δ 13.29 (1H, br.s), 9.88 (1H, br.s), 9.60 (1H, br.s), 8.57 (1H, d, *J* = 5.0 Hz), 8.16 (1H, d, *J* = 1.0 Hz), 7.74 (2H, d, *J* = 7.0 Hz), 7.67 (2H, d, *J* = 8.5 Hz), 7.56 (1H, d, *J* = 4.0 Hz), 7.23 (1H, s), 6.93 (2H, d, *J* = 8.5 Hz), 6.84 (2H, d, *J* = 8.5 Hz); ¹³C NMR (125 MHz, *d*₆-DMSO): δ 159.5, 157.9, 150.4, 148.5, 133.0, 128.8 (two overlapping signals), 127.3, 127.2, 124.8, 123.7, 122.7, 119.8, 116.6, 116.2, 100.6; **HRMS** (ESI+) Calc. for C₂₀H₁₅N₃O₂ [M+H]⁺ 330.1237, found 330.1242. **IR** (neat, cm⁻¹): ν̄ 2953, 2921, 2852, 1601, 1515, 1451, 1373, 1253, 1172, 823, 799, 776, 567. **HPLC**: 98.4% (HPLC Method A), RT: 15.9 min.

11.13. [2,2'-Bipyridine] 1,1'-dioxide (43)

This compound was prepared following a literature procedure.⁵² To a solution of 2,2'-bipyridine **42** (1.0 g, 6.4 mmol) in acetic acid (15 mL) was added hydrogen peroxide (3.3 mL, 32 mmol, 30% (w/w) in H₂O) dropwise at RT, and the resulting mixture was heated to 70 °C and stirred for 15 h. After completion, the cooled mixture was added acetone (20 mL) forming a white precipitate, filtered and dried. The crude white solid was recrystallised from H₂O to get the desired pure compound **43** (1.08 g, 90%). R_f (CH₂Cl₂/MeOH 15:1): 0.35; ¹H NMR (300 MHz, D₂O): δ 8.46 (2H, d, *J* = 6.3 Hz), 7.88–7.83 (2H, m), 7.77–7.30 (4H, m); ¹³C NMR (75 MHz, D₂O): δ 142.3, 140.4, 132.4, 129.5, 129.1. The spectroscopic data matched that reported in the literature.⁵³

11.14. 4,4'-Dinitro-[2,2'-bipyridine] 1,1'-dioxide (44)

This compound was prepared following a literature procedure.³⁰ To a suspension of **43** (1.0 g, 5.3 mmol) in sulphuric acid (6 mL, 111 mmol) was added nitric acid (2.5 mL, 44 mmol) dropwise at 0 °C, and the resulting mixture was heated to 100 °C and stirred for 20 h. After completion monitored by TLC, the mixture was cooled to RT and ice (20 mL) was added to get yellow precipitate, filtered and washed with cold water and dried to get the desired compound **44** without further purification (295 mg, 20%). R_f (CH₂Cl₂/MeOH 15:1): 0.40; ¹H NMR (400 MHz, CDCl₃): δ 8.69 (2H, d, *J* = 3.2 Hz), 8.59 (2H, d, *J* = 7.2 Hz), 8.38 (2H, dd, *J* = 3.2, 7.2 Hz); ¹³C NMR (100 MHz, CDCl₃): δ 142.1, 141.2, 140.5, 123.8, 122.0. The spectroscopic data matched that reported in the literature.⁵³

11.15. 4,4'-Dichloro-[2,2'-bipyridine] 1,1'-dioxide (45)

This compound was prepared following a literature procedure.³⁰ To a suspension of **44** (100 mg, 0.36 mmol) in acetic acid (2 mL) was added acetyl chloride (0.13 mL, 1.8 mmol) dropwise at RT under nitrogen atmosphere, the resulting mixture was stirred for 2 h, and then heated to 100 °C for 12 h. After completion monitored by TLC, the volatile was removed under reduced pressure and the residue was treated with sat. NaHCO₃ (aq.) (2 mL) and CH₂Cl₂ (5 mL), and the off-white precipitate was obtained, filtered and washed with CH₂Cl₂ and dried to get the desired compound **45** without further purification (79 mg, 85%). R_f (CH₂Cl₂/MeOH 10:1): 0.20; ¹H NMR (400 MHz, *d*₆-DMSO + TFA): δ 8.42 (2H, d, *J* = 6.8 Hz), 7.93 (2H, d, *J* = 3.2 Hz), 7.68 (2H, dd, *J* = 3.2, 6.8 Hz); ¹³C NMR (100 MHz, *d*₆-DMSO + TFA): δ 143.0, 141.4, 132.3, 129.6, 128.5. The spectroscopic data matched that reported in the literature.⁵³

11.16. 4,4'-Dichloro-2,2'-bipyridine (46)

This compound was prepared following a literature procedure.³⁰ To a suspension of **45** (50 mg, 0.19 mmol) in CHCl₃ (5 mL) was added PCl₃ (0.33 mL, 3.8 mmol) dropwise at RT under nitrogen atmosphere, and the resulting mixture was heated to 65 °C and stirred for 20 h. After completion monitored by TLC, the mixture was poured into ice (5 mL)

and solid NaOH was added to make pH = 8, and then extracted with CH₂Cl₂ (3 × 10 mL). The combined organic layers were dried over MgSO₄ and concentrated *in vacuo*. The crude product was purified by flash chromatography (hexane/ethyl acetate 8:1) to give the product **46** as a white solid (41 mg, 95%); R_f (hexane/ethyl acetate 4:1): 0.4; ¹H NMR (300 MHz, CDCl₃): δ 8.55 (2H, d, *J* = 5.4 Hz), 8.43 (2H, d, *J* = 2.1 Hz), 7.32 (2H, dd, *J* = 2.1, 5.4 Hz); ¹³C NMR (75 MHz, CDCl₃): δ 156.5, 150.2, 145.5, 124.5, 121.9. The spectroscopic data matched that reported in the literature.⁵³

11.17. 4,4'-([2,2'-Bipyridine]-4,4'-diyl)diphenol (8)

A mixture of **46** (40 mg, 0.18 mmol), (4-hydroxyphenyl)boronic acid (62 mg, 0.45 mmol) and aq. K₂CO₃ (2 M, 450 μL, 0.9 mmol) in 1,4-dioxane (5 mL) was degassed, and then [1,1'-bis(diphenylphosphino)ferrocene]dichloropalladium(II) (6.5 mg, 0.009 mmol) was added. The resulting mixture was degassed and back-filled with nitrogen, and then heated at reflux for 4 h. After completion monitored by TLC, the reaction mixture was concentrated under reduced pressure, and then diluted with H₂O (5 mL), neutralised with sat. NH₄Cl (aq.) and extracted with ethyl acetate (3 × 5 mL). The combined organic layers were washed with H₂O (5 mL) and dried over MgSO₄ and concentrated *in vacuo*. The crude product was purified by flash chromatography (CH₂Cl₂: MeOH = 50:1 → 10:1) to afford the product **8** as a white solid (25 mg, 40%). **m.p.** 328–330 °C; R_f (CH₂Cl₂/MeOH 15:1): 0.30; ¹H NMR (400 MHz, *d*₆-DMSO): δ 9.88 (2H, br.s), 8.70 (2H, d, *J* = 5.2 Hz), 8.64 (2H, d, *J* = 1.6 Hz), 7.74 (4H, d, *J* = 8.8 Hz), 7.71 (2H, dd, *J* = 1.6, 5.2 Hz), 6.94 (4H, d, *J* = 8.8 Hz); ¹³C NMR (100 MHz, *d*₆-DMSO): δ 158.8, 155.8, 149.8, 148.0, 128.1, 127.7, 120.7, 116.8, 116.1. **HRMS** (ESI+) Calc. for C₂₂H₁₆N₂O₂ [M+Na]⁺ 363.1104, found 363.1110. **IR** (neat, cm⁻¹): ν̄ 3084, 2922, 1586, 1514, 1234, 826, 567. **HPLC**: 96.1% (HPLC Method A), RT: 18.7 min.

12. General procedure H for the synthesis of hydrazones

The compounds were prepared following a literature procedure.³¹ To a solution of chloro-pyrazine substrate (1.0 equiv.) in ethanol (0.05 M) was added hydrazine monohydrate (1.1 equiv.). The resulting mixture was stirred at 80 °C for 8 h. After completion monitored by TLC, the reaction mixture was cooled to RT, and the precipitate obtained filtered, washed by ethanol and dried to get a pale yellow solid. To a solution of the crude intermediate (1.0 equiv.) in ethanol (0.05 M) was added aryl-aldehyde (1.1 equiv.), and the resulting mixture was stirred at 80 °C for 10 h. After completion monitored by TLC, the reaction mixture was cooled to RT, and the precipitate was obtained and filtered, washed by ethanol and dried to get the products.

12.1. 2-(2-(4-(Benzyloxy)benzylidene)hydrazinyl)-6-chloropyrazine (48)

This compound was prepared according to general procedure H by treating **47** (1.49 0.01 mol) with **28a** (2.33 g, 0.011 mol) to give the product **48** as an off-white solid (2.37 g, 70%). **m.p.** 213–214 °C; R_f (hexane/ethyl acetate 2:1): 0.30; ¹H NMR (300 MHz, *d*₆-DMSO): δ 11.40 (1H, br.s), 8.52 (1H, s), 8.01–7.99 (2H, m), 7.66 (2H, d, *J* = 8.1 Hz), 7.46–7.30 (5H, m), 7.06 (2H, d, *J* = 8.1 Hz), 5.14 (2H, s); ¹³C NMR (75 MHz, *d*₆-DMSO): δ 159.5, 152.4, 145.5, 142.7, 136.8, 131.9, 128.6, 128.4, 128.2, 127.9, 127.7, 127.3, 115.1, 69.3; **HRMS** (ESI+) Calc. for C₁₈H₁₅ClN₄O [M+Na]⁺ 361.0827, found 361.0832. **IR** (neat, cm⁻¹): ν̄ 3167, 3030, 2860, 1608, 1569, 1511, 1380, 1245, 822, 720, 508.

13. General procedure I for the oxidative heterocyclisation

The compounds were prepared following a literature procedure.³² To a solution of hydrazone (1.0 equiv.) in CH₂Cl₂ (0.05 M) was added PhI(OAc)₂ (1.0 equiv.). The resulting mixture was stirred at RT for 12 h.

After completion monitored by TLC, the solvent was removed under reduced pressure.

13.1. 3-(4-(Benzyloxy)phenyl)-5-chloro-[1,2,4]triazolo[4,3-a]pyrazine (49)

This compound was prepared according to general procedure I by treating **48** (2.37 g, 7 mmol) with PhI(OAc)₂ (2.25 g, 7 mmol). The crude product was purified by flash chromatography (hexane/ethyl acetate 1:1) to give the product **49** as a white solid (2.00 g, 85%). **m.p.** 216–217 °C; *R_f* (hexane/ethyl acetate 1:1): 0.30; ¹H NMR (400 MHz, *d*₆-DMSO): δ 9.46 (1H, s), 8.06 (1H, s), 7.65 (2H, ddd, *J* = 2.8, 4.8, 9.6 Hz), 7.52–7.50 (2H, m), 7.45–7.41 (2H, m), 7.39–7.34 (1H, m), 7.19 (2H, ddd, *J* = 2.8, 4.8, 9.6 Hz), 5.22 (2H, s); ¹³C NMR (100 MHz, *d*₆-DMSO): δ 160.3, 147.8, 147.4, 143.2, 137.1, 133.3, 129.5, 128.9, 128.4, 128.3, 122.2, 119.8, 114.4, 69.9; **HRMS** (ESI+) Calc. for C₁₈H₁₃ClN₄O [M+Na]⁺ 359.0670, found 359.0668. **IR** (neat, cm⁻¹): ν̄ 3087, 2879, 1607, 1453, 1233, 750, 554.

13.2. 2-(4-(Benzyloxy)phenyl)ethan-1-ol (50a)

Step 1: The formation of 4-(2-hydroxyethyl)phenol. This compound was prepared following a literature procedure.⁵⁴ To a solution of 2-(4-hydroxyphenyl)acetic acid (760 mg, 5 mmol) in ethanol (20 mL) was added sulfuric acid (27 μL, 0.5 mmol), and the resulting mixture was heated at reflux for 3 h. After completion monitored by TLC, the solvent was removed under reduced pressure, and the crude product was dissolved in anhydrous THF (20 mL), followed by the addition of LiAlH₄ (228 mg, 6 mmol) slowly at 0 °C, and the resulting mixture was allowed to warm to RT for 12 h. After completion monitored by TLC, the solution was cooled to 0 °C, and quenched by Na₂SO₄·10H₂O solid and filtered through Celite®. The solvent was removed under reduced pressure and the residue was diluted with H₂O (20 mL) and extracted with ethyl acetate (3 × 20 mL). The combined organic layers were dried over MgSO₄ and concentrated *in vacuo*. The crude product was purified by flash chromatography (hexane/ethyl acetate 5:1 → 2:1) to give the product as an off-white solid (600 mg, 87%). *R_f* (hexane/ethyl acetate 2:1): 0.30; ¹H NMR (400 MHz, CDCl₃): δ 7.10 (2H, dd, *J* = 2.0, 6.4 Hz), 6.78 (2H, dd, *J* = 2.0, 6.4 Hz), 4.83 (1H, br.s), 3.83 (2H, dd, *J* = 6.4, 15.0 Hz), 2.80 (2H, t, *J* = 6.4 Hz); ¹³C NMR (100 MHz, CDCl₃): δ 154.4, 130.6, 130.3, 115.6, 64.0, 38.4. The spectroscopic data matched that reported in the literature.⁵⁴

Step 2: The benzyl protection of 4-(2-hydroxyethyl)phenol was realised according to general procedure D by treating 4-(2-hydroxyethyl)phenol (600 mg, 4.3 mmol) with benzyl bromide (613 μL, 5.2 mmol). The crude product was purified by flash chromatography (hexane/ethyl acetate 10:1 → 5:1) to give the product **50a** as a white solid (882 mg, 90%). *R_f* (hexane/ethyl acetate 4:1): 0.30; ¹H NMR (500 MHz, CDCl₃): δ 7.44–7.42 (2H, m), 7.40–7.37 (2H, m), 7.33–7.31 (1H, m), 7.14 (2H, d, *J* = 8.6 Hz), 6.93 (2H, d, *J* = 8.6 Hz), 5.05 (2H, s), 3.82 (2H, t, *J* = 6.5 Hz), 2.81 (2H, t, *J* = 6.5 Hz), 1.43 (1H, br.s); ¹³C NMR (125 MHz, CDCl₃): δ 157.6, 137.2, 130.8, 130.1, 128.7, 128.0, 127.5, 115.1, 70.1, 63.9, 38.4. The spectroscopic data matched that reported in the literature.⁴⁸

13.3. 2-(3-(Benzyloxy)phenyl)ethan-1-ol (50b)

This compound was prepared according to general procedure D by treating 3-(2-hydroxyethyl)phenol (600 mg, 4.3 mmol) with benzyl bromide (613 μL, 5.2 mmol). The crude product was purified by flash chromatography (hexane/ethyl acetate 10:1 → 5:1) to give the product **50b** as a white solid (912 mg, 93%). *R_f* (hexane/ethyl acetate 4:1): 0.35; ¹H NMR (300 MHz, CDCl₃): δ 7.37–7.22 (5H, m), 7.18–7.13 (1H, m), 6.79–6.74 (3H, m), 4.98 (2H, s), 3.77 (2H, t, *J* = 6.6 Hz), 2.76 (2H, t, *J* = 6.6 Hz); ¹³C NMR (75 MHz, CDCl₃): δ 159.1, 140.3, 137.1, 129.7, 128.7, 128.1, 127.6, 121.8, 115.9, 112.8, 70.1, 63.7, 39.3. The

spectroscopic data matched that reported in the literature.⁵⁵

14. General procedure J for the synthesis of ethers

To a solution of **49** (1.0 equiv.) in toluene (0.05 M) was added KOH (3.0 equiv.) and 18-crown-6 (0.07 equiv.), followed by the addition of **50a–b** (1.1 equiv.). The resulting mixture was stirred at 40 °C for 4 h. After completion monitored by TLC, the reaction mixture was washed with H₂O and extracted with ethyl acetate (3 × 10 mL). The combined organic layers were dried over MgSO₄ and concentrated *in vacuo*.

14.1. 5-(4-(Benzyloxy)phenethoxy)-3-(4-(benzyloxy)phenyl)-[1,2,4]triazolo[4,3-a]pyrazine (51a)

This compound was prepared according to general procedure J by treating **49** (674 mg, 2 mmol) with **50a** (502 mg, 2.2 mmol). The crude product was purified by flash chromatography (hexane/ethyl acetate 1:1 → 1:1.5) to give the product **51a** as a white solid (772 mg, 73%). **m.p.** 156–158 °C; *R_f* (hexane/ethyl acetate 1:1): 0.15; ¹H NMR (300 MHz, CDCl₃): δ 8.94 (1H, s), 7.52 (2H, d, *J* = 7.8 Hz), 7.38–7.19 (10H, m), 6.97 (2H, d, *J* = 7.8 Hz), 6.72 (2H, d, *J* = 8.1 Hz), 6.65 (2H, d, *J* = 8.1 Hz), 5.07 (2H, s), 4.93 (2H, s), 4.27 (2H, t, *J* = 5.4 Hz), 2.77 (2H, t, *J* = 5.4 Hz); ¹³C NMR (75 MHz, CDCl₃): δ 160.2, 157.7, 136.9, 136.4, 136.2, 132.3, 129.7, 128.7, 128.6, 128.1, 128.0, 127.4, 120.2, 115.0, 114.2, 108.0, 106.1, 71.6, 70.1, 70.0, 33.8; **HRMS** (ESI+) Calc. for C₃₃H₂₈N₄O₃ [M+Na]⁺ 551.2054, found 551.2050. **IR** (neat, cm⁻¹): ν̄ 3033, 2951, 2857, 1608, 1505, 1247, 830 695.

14.2. 5-(3-(Benzyloxy)phenethoxy)-3-(4-(benzyloxy)phenyl)-[1,2,4]triazolo[4,3-a]pyrazine (51b)

This compound was prepared according to general procedure J by treating **49** (674 mg, 2 mmol) with **50b** (502 mg, 2.2 mmol). The crude product was purified by flash chromatography (hexane/ethyl acetate 1:1 → 1:1.5) to give the product **51b** as a white solid (730 mg, 69%). **m.p.** 104–106 °C; *R_f* (hexane/ethyl acetate 1:1): 0.15; ¹H NMR (300 MHz, CDCl₃): δ 8.93 (1H, s), 7.49 (2H, d, *J* = 8.1 Hz), 7.35–7.18 (10H, m), 7.05 (1H, t, *J* = 7.8 Hz), 6.92 (2H, d, *J* = 8.1 Hz), 6.75 (1H, d, *J* = 7.8 Hz), 6.46 (1H, s), 6.40 (1H, d, *J* = 7.2 Hz), 5.01 (2H, s), 4.91 (2H, s), 4.30 (2H, t, *J* = 6.0 Hz), 2.81 (2H, t, *J* = 6.0 Hz); ¹³C NMR (75 MHz, CDCl₃): δ 160.2, 159.1, 144.2, 138.1, 136.9, 136.6, 136.5, 132.3, 129.8, 128.8, 128.7, 128.2, 128.1, 127.6, 127.5, 121.4, 120.2, 115.8, 114.3, 112.9, 108.2, 71.2, 70.2, 70.1, 34.6; **HRMS** (ESI+) Calc. for C₃₃H₂₈N₄O₃ [M+Na]⁺ 551.2054, found 551.2052. **IR** (neat, cm⁻¹): ν̄ 3032, 2917, 2853, 1607, 1506, 1243, 694.

15. General procedure K for the benzyl hydrogenolysis

To a solution of benzyl protected substrates (1.0 equiv.) in MeOH (0.05 M) was added Pd/C (10 wt%) under nitrogen atmosphere, and the mixture was stirred at RT for 2 h under 1 atm of hydrogen. After completion monitored by TLC, the Pd-C was filtered through Celite®, and the solvent was removed under reduced pressure.

15.1. 4-(5-(4-Hydroxyphenethoxy)-[1,2,4]triazolo[4,3-a]pyrazin-3-yl)phenol (9a)

This compound was prepared according to general procedure K by treating **51a** (700 mg, 1.3 mmol). The crude product was purified by flash chromatography (CH₂Cl₂/MeOH 50:1 → 10:1) to give the product **9a** as a pale yellow solid (317 mg, 70%). **m.p.** 235–237 °C; *R_f* (CH₂Cl₂/MeOH 10:1): 0.25; ¹H NMR (400 MHz, *d*₆-DMSO): δ 9.90 (1H, br.s), 9.17 (1H, br.s), 8.98 (1H, s), 7.53 (2H, dd, *J* = 2.0, 6.4 Hz), 7.50 (1H, s), 6.90 (2H, dd, *J* = 2.0, 6.8 Hz), 6.71 (2H, dd, *J* = 2.0, 6.4 Hz), 6.56 (2H, dd, *J* = 2.0, 6.8 Hz), 4.38 (2H, t, *J* = 6.4 Hz), 2.77 (2H, t, *J* = 6.4 Hz); ¹³C NMR (100 MHz, *d*₆-DMSO): δ 158.8, 155.9, 147.2,

146.6, 143.9, 135.0, 132.3, 129.8, 127.3, 118.4, 115.0, 114.4, 108.5, 71.7, 33.1; **HRMS** (ESI+) Calc. for $C_{19}H_{16}N_4O_3$ $[M+Na]^+$ 371.1115, found 371.1112. **IR** (neat, cm^{-1}): $\tilde{\nu}$ 3098, 2919, 1608, 1489, 1237, 826. **HPLC**: 98.8% (HPLC Method A), RT: 16.6 min.

15.2. 3-(2-((3-(4-Hydroxyphenyl)-[1,2,4]triazolo[4,3-a]pyrazin-5-yl)oxy)ethyl)phenol (9b)

This compound was prepared according to **general procedure K** by treating **51b** (700 mg, 1.3 mmol). The crude product was purified by flash chromatography ($CH_2Cl_2/MeOH$ 50:1 \rightarrow 10:1) to give the product **9b** as a pale yellow solid (303 mg, 67%). **m.p.** 245–246 °C; R_f ($CH_2Cl_2/MeOH$ 10:1): 0.25; **1H NMR** (500 MHz, d_6 -DMSO): δ 9.89–9.84 (1H, br.s), 9.26 (1H, br.s), 8.99 (1H, s), 7.54 (1H, s), 7.50 (2H, d, $J = 9.0$ Hz), 6.98 (1H, t, $J = 8.0$ Hz), 6.86 (2H, d, $J = 9.0$ Hz), 6.58 (1H, d, $J = 8.0$ Hz), 6.54 (1H, s), 6.34 (1H, d, $J = 8.0$ Hz), 4.43 (2H, t, $J = 7.0$ Hz), 2.80 (2H, t, $J = 7.0$ Hz); **^{13}C NMR** (125 MHz, d_6 -DMSO): δ 159.4, 158.0, 147.9, 147.3, 144.5, 139.1, 135.7, 132.9, 129.8, 120.2, 118.9, 116.2, 115.0, 114.1, 109.3, 71.9, 34.5; **HRMS** (ESI+) Calc. for $C_{19}H_{16}N_4O_3$ $[M+H]^+$ 349.1295, found 349.1295. **IR** (neat, cm^{-1}): $\tilde{\nu}$ 3102, 2956, 1608, 1510, 1439, 1242, 566. **HPLC**: 96.1% (HPLC Method A), RT: 16.8 min.

15.3. 6-Chloropyrazine-2-carboxylic acid (53)

This compound was prepared following a literature procedure.³³ To a solution of $Na_2WO_4 \cdot 2H_2O$ (0.025 equiv., 0.24 mmol) in H_2O (0.05 M) was added $aq H_2O_2$ (30%, 1.1 equiv., 1 mL) at RT, followed by the addition of H_2SO_4 (1 M) to make pH = 2, then pyrazine-2-carboxylic acid **52** (1.0 equiv., 8 mmol) was added, and the resulting suspension was stirred at 80 °C for 2 h. After completion monitored by TLC, the mixture was settled at RT until the precipitate was obtained, filtered and washed by H_2O and dried under reduced pressure to get white solid compound 3-carboxypyrazine 1-oxide without further purification. A solution of 3-carboxypyrazine 1-oxide (1.0 equiv., 7 mmol) in $POCl_3$ (3 mL) in sealed tube was heated to 120 °C and stirred for 2 h. After completion monitored by TLC, the reaction mixture was cooled to RT and poured to ice water (20 mL), neutralised with sat. Na_2CO_3 (aq.) and extracted with ethyl acetate (3 \times 20 mL). The combined organic layers were dried over $MgSO_4$ and concentrated *in vacuo*. The crude product was recrystallised from ethanol, filtered and washed by hexane, dried to get the product **53** as a white solid (880 mg, 70%). **m.p.** 158–160 °C; R_f (hexane/ethyl acetate 1:1): 0.25; **1H NMR** (500 MHz, d_6 -DMSO): δ 9.13 (1H, s), 9.00 (1H, s); **^{13}C NMR** (125 MHz, d_6 -DMSO): δ 163.8, 148.0, 147.8, 143.7, 143.3. The spectroscopic data matched that reported in the literature.⁵⁶

16. General procedure L for amide coupling reactions

The compounds were prepared following a literature procedure.⁵⁷ To a solution of carboxylic acid (1.0 equiv.) in anhydrous CH_2Cl_2 (0.1 M) was added oxalyl chloride (1.5 equiv.) and DMF (0.1 equiv.) at 0 °C, and the resulting mixture was allowed to warm to RT for 2 h. Then the volatiles were concentrated under reduced pressure, and the residue was dissolved in anhydrous CH_2Cl_2 (0.1 M), followed by the addition of aniline (1.0 equiv.) and triethylamine (1.1 equiv.), and the resulting mixture was stirred at RT for another 2 h. After completion monitored by TLC, the reaction mixture was quenched with H_2O and extracted with CH_2Cl_2 (3 \times 20 mL), and washed with 1% HCl solution, and then sat. Na_2CO_3 (aq.). The combined organic layers were dried over $MgSO_4$ and concentrated *in vacuo*.

16.1. N-(4-((tert-Butyldimethylsilyl)oxy)phenyl)-6-chloropyrazine-2-carboxamide (54a)

This compound was prepared according to general procedure L by

treating **53** (316 mg, 2 mmol) with **15a** (446 mg, 2 mmol). The crude product was purified by flash chromatography (hexane/ethyl acetate 10:1) to give the product **54a** as an off-white solid (582 mg, 80%). **m.p.** 115–116 °C; R_f (hexane/ethyl acetate 4:1): 0.55; **1H NMR** (500 MHz, $CDCl_3$): δ 9.37 (1H, s), 9.30 (1H, br.s), 8.78 (1H, s), 7.59 (2H, ddd, $J = 3.0, 5.5, 10.0$ Hz), 6.86 (2H, ddd, $J = 3.0, 5.5, 10.0$ Hz), 0.98 (9H, s), 0.20 (6H, s); **^{13}C NMR** (125 MHz, $CDCl_3$): δ 159.2, 153.1, 147.5, 147.4, 144.3, 142.3, 130.7, 121.6, 120.6, 25.8, 18.3, -4.3; **HRMS** (ESI+) Calc. for $C_{17}H_{22}ClN_3O_2Si$ $[M+Na]^+$ 386.1062, found 386.1061. **IR** (neat, cm^{-1}): $\tilde{\nu}$ 3374, 2950, 2930, 2855, 1686, 1591, 1261, 845.

16.2. N-(3-((tert-Butyldimethylsilyl)oxy)phenyl)-6-chloropyrazine-2-carboxamide (54b)

This compound was prepared according to general procedure L by treating **53** (316 mg, 2 mmol) with **15b** (446 mg, 2 mmol). The crude product was purified by flash chromatography (hexane/ethyl acetate 10:1) to give the product **54b** as yellow oil (619 mg, 85%). R_f (hexane/ethyl acetate 4:1): 0.55; **1H NMR** (300 MHz, $CDCl_3$): δ 9.41 (1H, s), 9.35 (1H, br.s), 8.81 (1H, s), 7.44 (1H, s), 7.28–7.21 (2H, m), 6.70–6.68 (1H, m), 1.02 (9H, s), 0.26 (6H, s); **^{13}C NMR** (75 MHz, $CDCl_3$): δ 159.4, 156.5, 147.6, 147.5, 144.2, 142.3, 138.0, 129.9, 117.0, 113.0, 112.1, 25.8, 18.3, -4.3; **HRMS** (ESI+) Calc. for $C_{17}H_{22}ClN_3O_2Si$ $[M+Na]^+$ 386.1062, found 386.1060. **IR** (neat, cm^{-1}): $\tilde{\nu}$ 3374, 2954, 2929, 2857, 1686, 1598, 1534, 1166, 779.

16.3. 4-((tert-Butyldimethylsilyl)oxy)benzaldehyde (55)

This compound was prepared according to general procedure A by treating 4-hydroxybenzaldehyde (488 mg, 4 mmol), imidazole (640 mg, 10 mmol) and $TBSCl$ (906 mg, 6 mmol). The crude product was purified by flash chromatography (hexane/ethyl acetate 10:1) to give the product **55** as colourless oil (802 mg, 85%). R_f (hexane/ethyl acetate 2:1): 0.45; **1H NMR** (300 MHz, $CDCl_3$): δ 9.88 (1H, s), 7.79 (2H, d, $J = 7.8$ Hz), 6.94 (2H, d, $J = 7.8$ Hz), 0.99 (9H, s), 0.24 (6H, s); **^{13}C NMR** (75 MHz, $CDCl_3$): δ 191.0, 161.6, 132.0, 130.5, 120.6, 25.7, 18.4, -4.2. The spectroscopic data matched that reported in the literature.⁵⁸

16.4. 6-(2-(4-((tert-Butyldimethylsilyl)oxy)benzylidene)hydrazinyl)-N-(4-((tert-butylidimethylsilyl)oxy)phenyl)pyrazine-2-carboxamide (56a)

This compound was prepared according to general procedure H by treating **54a** (364 mg, 1 mmol) with **55** (236 mg, 1 mmol) to give the product **56a** as a pale yellow solid (491 mg, 85%). **m.p.** 230–232 °C; R_f (hexane/ethyl acetate 1:1): 0.60; **1H NMR** (400 MHz, $CDCl_3$): δ 9.32 (1H, s), 8.94 (1H, s), 8.92 (1H, s), 8.31 (1H, s), 7.80 (1H, s), 7.62–7.55 (4H, m), 6.90 (2H, dd, $J = 2.0, 6.8$ Hz), 6.85 (2H, dd, $J = 2.0, 6.8$ Hz), 1.00 (9H, s), 0.99 (9H, s), 0.23 (6H, s), 0.20 (6H, s); **^{13}C NMR** (100 MHz, $CDCl_3$): δ 160.9, 157.7, 152.8, 150.5, 142.4, 141.3, 134.9, 134.8, 131.2, 128.5, 127.2, 121.4, 120.7, 120.6, 25.8 (two overlapping signals), 18.4, 18.3, -4.2, -4.3; **HRMS** (ESI+) Calc. for $C_{30}H_{43}N_5O_3Si_2$ $[M+Na]^+$ 600.2797, found 600.2794. **IR** (neat, cm^{-1}): $\tilde{\nu}$ 3374, 2953, 2928, 2885, 2856, 1675, 1582, 1505, 1253, 911.

16.5. 6-(2-(4-((tert-Butyldimethylsilyl)oxy)benzylidene)hydrazinyl)-N-(3-((tert-butylidimethylsilyl)oxy)phenyl)pyrazine-2-carboxamide (56b)

This compound was prepared according to general procedure H by treating **54b** (364 mg, 1 mmol) with **55** (236 mg, 1 mmol) to give the product **56b** as an off-white solid (451 mg, 78%). **m.p.** 212–214 °C; R_f (hexane/ethyl acetate 1:1): 0.60; **1H NMR** (400 MHz, $CDCl_3$): δ 9.36 (1H, s), 8.95 (1H, s), 8.93 (1H, s), 8.27 (1H, s), 7.81 (1H, s), 7.60 (2H, d, $J = 8.8$ Hz), 7.41 (1H, s), 7.23–7.22 (2H, m), 6.90 (2H, d, $J = 8.8$ Hz), 6.67–6.64 (1H, m), 1.01 (9H, s), 1.00 (9H, s), 0.25 (6H, s), 0.24 (6H, s); **^{13}C NMR** (100 MHz, $CDCl_3$): δ 161.1, 157.7, 156.5, 150.5, 142.5, 138.6, 135.0, 132.4, 129.9, 128.5, 127.2, 120.7, 120.1, 116.6, 112.8,

111.9, 25.8 (two overlapping signals), 18.4 (two overlapping signals), –4.2 (two overlapping signals); **HRMS** (ESI+) Calc. for $C_{30}H_{43}N_5O_3Si_2$ $[M+Na]^+$ 600.2797, found 600.2794. **IR** (neat, cm^{-1}): $\tilde{\nu}$ 3373, 2956, 2928, 2856, 1687, 1598, 1531, 1258, 828.

16.6. *N*,3-bis(4-((*tert*-Butyldimethylsilyl)oxy)phenyl)-[1,2,4]triazolo[4,3-*a*]pyrazine-5-carboxamide (**57a**)

This compound was prepared according to general procedure I by treating **56a** (289 mg, 0.5 mmol) with $PhI(OAc)_2$ (161 mg, 0.5 mmol). The crude product was purified by flash chromatography (hexane/ethyl acetate 1:1) to give the product **57a** as a pale yellow solid (250 mg, 87%). **m.p.** 99–101 °C; R_f (hexane/ethyl acetate 1:1): 0.25; **1H NMR** (400 MHz, $CDCl_3$): δ 9.17 (1H, s), 9.08 (1H, s), 8.09 (1H, s), 7.43 (2H, d, $J = 8.4$ Hz), 7.18 (2H, d, $J = 8.8$ Hz), 6.80 (2H, d, $J = 8.4$ Hz), 6.70 (2H, d, $J = 8.8$ Hz), 0.97 (9H, s), 0.96 (9H, s), 0.17 (6H, s), 0.14 (6H, s); **^{13}C NMR** (100 MHz, $CDCl_3$): δ 158.2, 156.8, 153.4, 145.7, 145.6, 130.6, 130.3, 130.0, 127.9, 125.4, 121.7, 120.5, 120.4, 119.1, 25.8, 25.7, 18.3 (two overlapping signals), –4.3, –4.4; **HRMS** (ESI+) Calc. for $C_{30}H_{41}N_5O_3Si_2$ $[M+Na]^+$ 598.2640, found 598.2639. **IR** (neat, cm^{-1}): $\tilde{\nu}$ 2956, 2929, 2857, 1676, 1607, 1535, 1251, 912, 778.

16.7. *N*-(3-((*tert*-Butyldimethylsilyl)oxy)phenyl)-3-(4-((*tert*-butyldimethylsilyl)oxy)phenyl)-[1,2,4]triazolo[4,3-*a*]pyrazine-5-carboxamide (**57b**)

This compound was prepared according to general procedure I by treating **56b** (289 mg, 0.5 mmol) with $PhI(OAc)_2$ (161 mg, 0.5 mmol). The crude product was purified by flash chromatography (hexane/ethyl acetate 1:1) to give the product **57b** as a pale yellow solid (230 mg, 80%). **m.p.** 95–97 °C; R_f (hexane/ethyl acetate 1:1): 0.25; **1H NMR** (400 MHz, $CDCl_3$): δ 9.26 (1H, s), 9.10 (1H, s), 8.11 (1H, s), 7.42 (2H, d, $J = 8.4$ Hz), 7.07–7.03 (2H, m), 6.88 (1H, d, $J = 8.4$ Hz), 6.77 (2H, d, $J = 8.4$ Hz), 6.59 (1H, dd, $J = 2.4, 8.4$ Hz), 0.95 (9H, s), 0.94 (9H, s), 0.16 (6H, s), 0.10 (6H, s); **^{13}C NMR** (100 MHz, $CDCl_3$): δ 158.1, 156.8, 156.1, 148.4, 145.4, 145.3, 137.8, 130.7, 129.8, 129.6, 125.3, 120.3, 118.7, 117.1, 112.7, 111.8, 25.7, 25.6, 18.2, 18.1, –4.4, –4.5; **HRMS** (ESI+) Calc. for $C_{30}H_{41}N_5O_3Si_2$ $[M+Na]^+$ 598.2640, found 598.2639. **IR** (neat, cm^{-1}): $\tilde{\nu}$ 2955, 2929, 2857, 1683, 1607, 1254, 837, 778.

17. General procedure M for the deprotection of TBS ethers

The compounds were prepared following a literature procedure.³⁵ To a solution of TBS-protected substrate (1.0 equiv.) in THF (0.05 M) was added TBAF (1 M, 2.0 equiv.). The resulting mixture was stirred at RT for 30 min. After completion monitored by TLC, the solvent was removed *in vacuo*.

17.1. *N*-3-bis(4-Hydroxyphenyl)-[1,2,4]triazolo[4,3-*a*]pyrazine-5-carboxamide (**10a**)

The compound was prepared according to general procedure M by treating **57a** (200 mg, 0.35 mmol) with TBAF (0.7 mL, 0.70 mmol). The crude product was purified by flash chromatography ($CH_2Cl_2/MeOH$ 50:1 \rightarrow 20:1) to give the product **10a** as a pale yellow solid (118 mg, 97%). **m.p.** 289–291 °C; R_f ($CH_2Cl_2/MeOH$ 20:1): 0.20; **1H NMR** (400 MHz, d_6 -DMSO): δ 10.54 (1H, s), 9.80–9.79 (1H, br.s), 9.55 (1H, s), 9.36–9.30 (1H, br.s), 8.19 (1H, s), 7.40 (2H, dd, $J = 2.0, 6.8$ Hz), 7.11 (2H, dd, $J = 2.0, 6.8$ Hz), 6.72 (2H, dd, $J = 2.0, 6.8$ Hz), 6.66 (2H, dd, $J = 2.0, 6.8$ Hz); **^{13}C NMR** (100 MHz, d_6 -DMSO): δ 159.4, 157.2, 154.7, 148.4, 146.1, 146.0, 130.2, 129.5, 125.6, 122.2, 118.1, 115.6, 115.4, 115.2; **HRMS** (ESI+) Calc. for $C_{18}H_{13}N_5O_3$ $[M+H]^+$ 348.1091, found 348.1091. **IR** (neat, cm^{-1}): $\tilde{\nu}$ 3184, 2920, 1668, 1512, 1276, 818. **HPLC**: 95.5% (HPLC Method A), RT: 13.6 min.

17.2. *N*-(3-Hydroxyphenyl)-3-(4-hydroxyphenyl)-[1,2,4]triazolo[4,3-*a*]pyrazine-5-carboxamide (**10b**)

The compound was prepared according to general procedure M by treating **57b** (200 mg, 0.35 mmol) with TBAF (0.7 mL, 0.70 mmol). The crude product was purified by flash chromatography ($CH_2Cl_2/MeOH$ 50:1 \rightarrow 20:1) to give the product **10b** as a pale yellow solid (115 mg, 95%). **m.p.** 239–242 °C; R_f ($CH_2Cl_2/MeOH$ 20:1): 0.20; **1H NMR** (500 MHz, d_6 -DMSO): δ 10.68 (1H, br.s), 9.57 (1H, s), 8.22 (1H, s), 7.40 (2H, dd, $J = 2.0, 6.5$ Hz), 7.05 (1H, t, $J = 8.0$ Hz), 6.94 (1H, t, $J = 2.0$ Hz), 6.77–6.75 (1H, m), 6.71 (2H, dd, $J = 2.0, 6.5$ Hz), 6.50–6.48 (1H, m); **^{13}C NMR** (125 MHz, d_6 -DMSO): δ 159.6, 158.0, 157.8, 148.6, 146.4, 146.3, 139.2, 130.6, 130.2, 129.8, 125.5, 118.1, 115.7, 112.2, 111.2, 107.6; **HRMS** (ESI+) Calc. for $C_{18}H_{13}N_5O_3$ $[M+Na]^+$ 370.0911, found 370.0911. **IR** (neat, cm^{-1}): $\tilde{\nu}$ 3245, 2922, 2852, 1622, 1602, 1459, 1222, 739. **HPLC**: 95.6% (HPLC Method A), RT: 14.6 min.

17.3. 2-(2-Bromo-5-methoxyphenyl)-1,3-dioxolane (**59**)

This compound was prepared following a literature procedure.⁵⁹ To a solution of 2-bromo-5-methoxybenzaldehyde **58** (1.0 g, 4.6 mmol) in toluene (15 mL) was added ethylene glycol (1.26 mL, 23 mmol) and *p*-toluenesulfonic acid (9.5 mg, 0.05 mmol), and the resulting mixture was heated at reflux under a Dean-Stark water separator for 24 h. After completion monitored by TLC, the cooled mixture was diluted with ethyl acetate (10 mL) and washed with H_2O and brine. The organic layer was dried over $MgSO_4$ and concentrated *in vacuo*. The crude product was purified by flash chromatography (hexane/ethyl acetate 20:1) to give the product **59** as colourless oil (1.1 g, 95%); R_f (hexane/ethyl acetate 10:1): 0.35; **1H NMR** (400 MHz, $CDCl_3$): δ 7.50 (1H, d, $J = 8.8$ Hz), 7.10 (1H, d, $J = 2.4$ Hz), 6.87 (1H, dd, $J = 2.4, 8.8$ Hz), 6.04 (1H, s), 4.15–4.13 (2H, m), 4.06–4.04 (2H, m), 3.79 (3H, s); **^{13}C NMR** (100 MHz, $CDCl_3$): δ 160.6, 128.7, 128.6, 123.4, 118.0, 113.5, 102.6, 65.4, 55.6. The spectroscopic data matched that reported in the literature.⁵⁹

17.4. *N*-(2-(1,3-Dioxolan-2-yl)-4-methoxyphenyl)-4-methoxy-2-nitroaniline (**60**)

This compound was prepared following a literature procedure.⁶⁰ To a mixture of **59** (518 mg, 2 mmol), 4-methoxy-2-nitroaniline (336 mg, 2 mmol), $Pd(OAc)_2$ (45 mg, 0.2 mmol), Cs_2CO_3 (978 mg, 3 mmol) and (\pm)-BINAP (62.3 mg, 0.1 mmol) in toluene (15 mL) was purged with nitrogen, and the resulting mixture was stirred at 120 °C for 3 h. After completion monitored by TLC, the cooled mixture was washed with H_2O and brine. The organic layer was dried over $MgSO_4$ and concentrated *in vacuo*. The crude product was purified by flash chromatography (hexane/ethyl acetate 8:1) to give the product **60** as orange oil (616 mg, 89%); R_f (hexane/ethyl acetate 4:1): 0.4; **1H NMR** (500 MHz, $CDCl_3$): δ 9.76 (1H, s), 7.59 (1H, d, $J = 3.0$ Hz), 7.38 (1H, d, $J = 8.5$ Hz), 7.35 (1H, d, $J = 9.0$ Hz), 7.04 (1H, dd, $J = 3.0, 9.0$ Hz), 6.89 (1H, d, $J = 2.5$ Hz), 6.63 (1H, dd, $J = 2.5, 8.5$ Hz), 5.75 (1H, s), 4.14–4.11 (2H, m), 4.00–3.98 (2H, m), 3.78 (3H, s), 3.75 (3H, s); **^{13}C NMR** (125 MHz, $CDCl_3$): δ 161.1, 151.7, 140.1, 136.6, 134.2, 130.3, 125.7, 121.8, 119.0, 108.9, 108.5, 107.4, 103.3, 65.3, 56.0, 55.5. **HRMS** (ESI+) Calc. for $C_{17}H_{18}N_2O_6$ $[M+Na]^+$ 369.1057, found 369.1060. **IR** (neat, cm^{-1}): $\tilde{\nu}$ 3349, 2954, 2890, 1613, 1584, 1505, 1279, 1215, 1032, 794.

17.5. 5-Methoxy-2-((4-methoxy-2-nitrophenyl)amino)benzaldehyde (**61**)

This compound was prepared following a literature procedure.⁶¹ To a solution of **60** (346 mg, 1 mmol) in $CHCl_3$ (15 mL) was added TFA (459 μ L, 6 mmol) dropwise, and the resulting mixture was stirred at RT for 30 min. After completion monitored by TLC, the mixture was

quenched with H₂O and extracted with CH₂Cl₂ (3 × 10 mL) and brine. The combined organic layers were dried over MgSO₄ and concentrated *in vacuo*. The crude product was purified by flash chromatography (hexane/ethyl acetate 4:1) to give the product **61** as an orange solid (272 mg, 90%); **m.p.** 161–163 °C; *R_f* (hexane/ethyl acetate 4:1): 0.35; ¹H NMR (400 MHz, CDCl₃): δ 11.17 (1H, s), 9.83 (1H, s), 7.64 (1H, d, *J* = 9.2 Hz), 7.59 (1H, d, *J* = 3.2 Hz), 7.55 (1H, d, *J* = 8.8 Hz), 7.15 (1H, dd, *J* = 3.2, 9.2 Hz), 6.70 (1H, d, *J* = 2.0 Hz), 6.52 (1H, dd, *J* = 2.0, 8.8 Hz), 3.87 (3H, s), 3.80 (3H, s); ¹³C NMR (100 MHz, CDCl₃): δ 192.0, 165.4, 154.9, 147.0, 141.3, 139.0, 129.9, 124.6, 122.4, 116.7, 109.0, 106.3, 99.1, 56.1, 55.7. **HRMS** (ESI+) *Calc.* for C₁₅H₁₄N₂O₅ [M + Na]⁺ 325.0795, found 325.0799. **IR** (neat, cm⁻¹): ν̄ 3282, 2842, 1644, 1611, 1564, 1508, 1233, 1025, 613, 567.

17.6. 2,8-Dimethoxy-10,11-dihydro-5H-dibenzo[b,e][1,4]diazepine (**62**)

To a solution of **61** (302 mg, 1 mmol) in MeOH (0.05 M) was added Pd/C (10 wt%, 30 mg) under nitrogen atmosphere, and the mixture was stirred at RT for 2 h under 1 atm of hydrogen. After completion monitored by TLC, mixture was filtered through Celite®, and the solvent was removed under reduced pressure. The crude product was purified by flash chromatography (hexane/ethyl acetate 1:1) to get the desired compound **62** as a pale yellow solid (192 mg, 75%). **m.p.** 170–172 °C; *R_f* (hexane/ethyl acetate 2:1): 0.30; ¹H NMR (400 MHz, *d*₆-DMSO): δ 7.84 (1H, br.s), 6.82 (1H, d, *J* = 7.6 Hz), 6.72 (1H, d, *J* = 8.8 Hz), 6.41 (1H, s), 6.29 (1H, d, *J* = 2.4 Hz), 6.23 (1H, s), 6.13 (1H, s), 5.58 (1H, br.s), 4.00 (2H, s), 3.68 (3H, s), 3.62 (3H, s); ¹³C NMR (100 MHz, *d*₆-DMSO): δ 159.4, 152.9, 146.1, 141.0, 129.6, 127.5, 119.6, 119.2, 105.5, 104.5, 102.9, 102.0, 55.4, 55.2, 50.8; **HRMS** (ESI+) *Calc.* for C₁₅H₁₆N₂O₂ [M + Na]⁺ 279.1104, found 279.1109. **IR** (neat, cm⁻¹): ν̄ 3333, 3278, 2992, 2833, 1617, 1598, 1505, 1451, 1219, 1036, 825, 795, 519.

17.7. 10,11-Dihydro-5H-dibenzo[b,e][1,4]diazepine-2,8-diol (**11**)

To a solution of **62** (128 mg, 0.5 mmol) in anhydrous CH₂Cl₂ (10 mL) was added BBr₃ (3 mL, 3 mmol) under nitrogen. The reaction mixture was allowed to warm to room temperature for 10 h, then quenched at 0 °C with MeOH and concentrated *in vacuo*. The crude product was purified by flash chromatography (CH₂Cl₂/MeOH 100:1 → 20:1) to give the product **11** as a brown solid (57 mg, 50%). **m.p.** 256–258 °C; *R_f* (CH₂Cl₂/MeOH 10:1): 0.40; ¹H NMR (500 MHz, *d*₆-DMSO): δ 10.99–10.90 (1H, br.s), 9.42 (1H, br.s), 8.64 (1H, s), 7.10 (1H, d, *J* = 9.0 Hz), 7.03 (1H, d, *J* = 8.0 Hz), 6.85 (1H, s), 6.75 (1H, d, *J* = 8.0 Hz), 6.50 (1H, s), 6.22 (1H, d, *J* = 8.0 Hz), 4.38 (2H, s); ¹³C NMR (125 MHz, *d*₆-DMSO): δ 158.4, 150.0, 143.6, 131.6, 129.8, 124.0, 121.1, 117.0, 110.0, 109.4, 106.5, 103.5, 51.8; **HRMS** (ESI+) *Calc.* for C₁₃H₁₂N₂O₂ [M + Na]⁺ 251.0791, found 251.0792. **IR** (neat, cm⁻¹): ν̄ 3385, 3312, 3286, 1612, 1517, 1470, 1222, 835, 806, 524. **HPLC**: 97.6% (HPLC Method B), RT: 12.4 min.

18. Purification of His-DYRK1a

Human Dyrk1A Kinase domain (126-490aa) with an N-terminal Histidine tag was expressed in E. coli BL21 (DE3) cells. 1 mL of a 10 mL O/N culture containing 50 μg/ml kanamycin and 34 μg/mL chloramphenicol, was used to inoculate a 1 L of Luria-Bertani (LB) media supplemented with the same antibiotics. The culture was grown at 37 °C until an OD₆₀₀ of 0.5 was reached, the temperature was then reduced to 18 °C. Expression was induced with the addition of 1 mM IPTG (isopropyl β-D-thiogalactoside) and incubated O/N at 18 °C. The cells were harvested by centrifugation, 6000 rpm for 10 min, and resuspended in lysis buffer (50 mM HEPES pH 7.5, 500 mM NaCl, 5% glycerol, 5 mM imidazole and 0.5 mM TCEP). The cell pellet was lysed using an emulsiflex C5 high-pressure homogenizer (avestin) in the presence of protease inhibitors. The insoluble debris was removed by

centrifugation at 10000 rpm for 30 min. The supernatant was bound to Ni-NTA resin (Ni²⁺ + nitrilotriacetate, Qiagen) and washed with 30 column volumes (CV) of lysis buffer and 5 CV of wash buffer (50 mM HEPES pH 7.5, 500 mM NaCl, 5% glycerol, 25 mM imidazole and 0.5 mM TCEP). The purified protein was finally eluted from the resin with 5 CV of elution buffer (50 mM HEPES pH 7.5, 500 mM NaCl, 5% glycerol, 250 mM imidazole and 0.5 mM TCEP). The His-Tag was cleaved with the addition of TEV protease (1 mg/ml) and incubated at 4 °C O/N. The eluted proteins were further purified by gel-filtration chromatography using an S200 16/60 column (GE healthcare) in 25 mM HEPES pH 7.5, 500 mM NaCl, 5 mM DTT.

19. Kinase inhibition assay

Active DYRK1A was assayed in Tris buffer (50 mM Tris-HCl, pH 7.5) containing 0.1 mM EGTA, 15 mM DTT, MgAc/ATP cocktail (0.5 mM HEPES pH 7.4; 10 mM Mg(CH₃COO)₂; 0.1 mM ATP), [^γ-³²P]-ATP 100–300 cpm/pmol and test compounds diluted in deionised water. As substrate, Woodtite (50 μM, Genscript) was used in DYRK1A assay. The reaction was initiated with 1 ng/μL DYRK1A. The reaction mixture was incubated at 30 °C for 10 min. Reaction was stopped by pipetting 10 μL of the reaction mixture onto P81 paper (Reaction Biology) and washing with 0.75% w/v H₃PO₄ and acetone. P81 papers were transferred to sample bags containing Optiphase Supermix scintillation cocktail (Perkin Elmer) and radioactivity (cpm) was measured with MicroBeta Trilux 2 counter (Perkin Elmer). Compounds were tested in triplicate at 1 μM and 10 μM for their ability to inhibit DYRK1A activity.

Acknowledgements

This work was supported by the National Health & Medical Research Council of Australia (APP1106145).

References

- Martin L, Latypova X, Wilson CM, et al. Tau protein kinases: involvement in Alzheimer's disease. *Ageing Res Rev.* 2013;12(1):289–309.
- Weinmann H, Metternich R. Editorial: drug discovery process for kinase inhibitors. *ChemBioChem.* 2005;6(3):455–459.
- Wu P, Nielsen TE, Clausen MH. FDA-approved small-molecule kinase inhibitors. *Trends Pharmacol Sci.* 2015;36(7):422–439.
- Johnson LN, Lewis RJ. Structural basis for control by phosphorylation. *Chem Rev.* 2001;101(8):2209–2242.
- Lochhead PA, Sibbet G, Morrice N, Cleghon V. Activation-loop autophosphorylation is mediated by a novel transitional intermediate form of DYRKs. *Cell.* 2005;121(6):925–936.
- Becker W, Joost H-G. Structural and functional characteristics of dyrk, a novel subfamily of protein kinases with dual specificity. *Prog Nucleic Acid Res Mol Biol.* 1998;62:1–17.
- Ronan A, Fagan K, Christie L, Conroy J, Nowak NJ, Turner G. Familial 4.3 Mb duplication of 21q22 sheds new light on the Down syndrome critical region. *J Med Genet.* 2007;44(7):448–451.
- Pozo N, Zahonero C, Fernandez P, et al. Inhibition of DYRK1A destabilizes EGFR and reduces EGFR-dependent glioblastoma growth. *J Clin Invest.* 2013;123(6):2475–2487.
- Zhou Q, Phoa AF, Abbassi RH, et al. Structural optimization and pharmacological evaluation of inhibitors targeting dual-specificity tyrosine phosphorylation-regulated kinases (DYRK) and CDC-like kinases (CLK) in glioblastoma. *J Med Chem.* 2017;60(5):2052–2070.
- Göckler N, Jofre G, Papadopoulos C, Soppa U, Tejedor FJ, Becker W. Harmine specifically inhibits protein kinase DYRK1A and interferes with neurite formation. *FEBS J.* 2009;276(21):6324–6337.
- Walker SR, Carter EJ, Huff BC, Morris JC. Variolins and related alkaloids. *Chem Rev.* 2009;109(7):3080–3098.
- Bettayeb K, Tirado OM, Marionneau-Lambot S, et al. Meriolins, a new class of cell death-inducing kinase inhibitors with enhanced selectivity for cyclin-dependent kinases. *Cancer Res.* 2007;67(17):8325–8334.
- Butler MS. Natural products to drugs: natural product-derived compounds in clinical trials. *Nat Prod Rep.* 2008;25(3):475–516.
- Sanchez C, Salas AP, Brana AF, et al. Generation of potent and selective kinase inhibitors by combinatorial biosynthesis of glycosylated indolocarbazoles. *Chem Commun.* 2009;27:4118–4120.
- Lawson M, Rodrigo J, Baratte B, et al. Synthesis, biological evaluation and molecular modeling studies of imidazo[1,2-a]pyridines derivatives as protein kinase inhibitors. *Eur J Med Chem.* 2016;123:105–114.

16. Bendjeddou LZ, Loacé N, Villiers B, et al. Exploration of the imidazo[1,2-b]pyridazine scaffold as a protein kinase inhibitor. *Eur J Med Chem.* 2017;125:696–709.
17. Zeinyeh W, Esvan YJ, Nauton L, et al. Synthesis and preliminary in vitro kinase inhibition evaluation of new diversely substituted pyrido[3,4-g]quinazoline derivatives. *Bioorg Med Chem Lett.* 2016;26(17):4327–4329.
18. Coutadeur S, Benyamine H, Delalonde L, et al. A novel DYRK1A (Dual specificity tyrosine phosphorylation-regulated kinase 1A) inhibitor for the treatment of Alzheimer's disease: effect on Tau and amyloid pathologies in vitro. *J Neurochem.* 2015;133(3):440–451.
19. Gourdain S, Dairou J, Denhez C, et al. Development of DANDYs, New 3,5-Diaryl-7-azaindoles demonstrating Potent DYRK1A Kinase Inhibitory Activity. *J Med Chem.* 2013;56(23):9569–9585.
20. Zhou Q, Reekie TA, Abbassi RH, et al. Flexible analogues of azaindole DYRK1A inhibitors elicit cytotoxicity in glioblastoma cells. *Aust J Chem.* 2018;71:789–797.
21. Nageswar Rao D, Rasheed S, Vishwakarma RA, Das P. Copper-catalyzed sequential N-arylation of C-amino-NH-azoles. *Chem Commun.* 2014;50(85):12911–12914.
22. Ferreri M, Drageset A, Gambarotti C, Bjorsvik H-R. Continuous flow synthesis of the iodination agent 1,3-diiodo-5,5-dimethyl-imidazolidine-2,4-dione telescoped with semi-continuous product isolation. *React Chem Eng.* 2016;1(4):379–386.
23. Sandtorv AH, Bjørsvik H-R. A three-way switchable process for suzuki cross-coupling, hydrodehalogenation, or an assisted tandem hydrodehalogenation and suzuki cross-coupling sequence. *Adv Synth Catal.* 2013;355(16):3231–3243.
24. Han F, Lin S, Liu P, et al. Discovery of a novel series of thienopyrimidine as highly potent and selective PI3K inhibitors. *ACS Med Chem Lett.* 2015;6(4):434–438.
25. Lu Y, Hendra R, Oakley AJ, Keller PA. Efficient synthesis and antioxidant activity of coelenterazine analogues. *Tetrahedron Lett.* 2014;55(45):6212–6215.
26. Jacks TE, Belmont DT, Briggs CA, et al. Development of a scalable process for CI-1034, an endothelin antagonist. *Org Process Res Dev.* 2004;8(2):201–212.
27. Fullam E, Talbot J, Abuhammed A, et al. Design, synthesis and structure-activity relationships of 3,5-diaryl-1H-pyrazoles as inhibitors of arylamine N-acetyltransferase. *Bioorg Med Chem Lett.* 2013;23(9):2759–2764.
28. Carroll FI, Liang F, Navarro HA, et al. Synthesis nicotinic acetylcholine receptor binding, and antinociceptive properties of 2-exo-2-(2'-substituted 5'-pyridinyl)-7-azabicyclo[2.2.1]heptanes. Epibatidine Analogues. *J Med Chem.* 2001;44(13):2229–2237.
29. Ce C, Hc E, Markus N, Ingo P, Margareta Z. *Functionalised 2,2'-bipyridine ligands for the preparation of metallostars; X-ray structures of free ligands and preparation of copper(I) and silver(I) complexes.* Kidlington: ROYAUME-UNI: Elsevier; 2003.
30. Ladouceur S, Swanick KN, Gallagher-Duval S, Ding Z, Zysman-Colman E. Strongly blue luminescent cationic Iridium(III) complexes with an electron-rich ancillary ligand: evaluation of their optoelectronic and electrochemiluminescence properties. *Eur J Inorg Chem.* 2013;2013(30):5329–5343.
31. Nelson PJ, Potts KT. 1,2,4-Triazoles. VI.1 The Synthesis of Some s-Triazolo[4,3-a]pyrazines. *J Org Chem.* 1962;27(9):3243–3248.
32. Demmer CS, Jørgensen M, Kehler J, Bunch L, Rasmussen LK. Synthesis and selective functionalization of [1,2,4]triazolo-[4,3-a]pyrazines. *Synlett.* 2015;26(04):519–524.
33. Servusová B, Paterová P, Mandíková J, et al. Alkylamino derivatives of pyrazinamide: synthesis and antimycobacterial evaluation. *Bioorg Med Chem Lett.* 2014;24(2):450–453.
34. Palamidessi G, Vigevani A, Zarini F. On the reaction of phosphorus oxychloride with pyrazinecarboxamide 4-oxide. *J Heterocycl Chem.* 1974;11(4):607–610.
35. Jadhav VH, Lee SB, Jeong H-J, Lim ST, Sohn M-H, Kim DW. An efficient and chemoselective deprotection of tert-butyl dimethylsilyl (TBDMS) ethers using tailor-made ionic liquid. *Tetrahedron Lett.* 2012;53(16):2051–2053.
36. Reekie TA, Kavanagh ME, Longworth M, Kassiou M. Synthesis of biologically active seven-membered-ring heterocycles. *Synthesis.* 2013;45(23):3211–3227.
37. Reekie TA, McGregor IS, Kassiou M. Pyrazolo[1,4]diazepines as non-peptidic probes of the oxytocin and vasopressin receptors. *Tetrahedron Lett.* 2014;55(33):4568–4571.
38. Gottlieb HE, Kotlyar V, Nudelman A. NMR chemical shifts of common laboratory solvents as trace impurities. *J Org Chem.* 1997;62(21):7512–7515.
39. Schlosser M, Ginanneschi A, Leroux F. In search of simplicity and flexibility: a rational access to twelve fluorinated carboxylic acids. *Eur J Org Chem.* 2006;2006(13):2956–2969.
40. Montanari S, Scavini L, Bartolini M, et al. Fatty Acid Amide Hydrolase (FAAH), Acetylcholinesterase (AChE), and Butyrylcholinesterase (BuChE): networked targets for the development of carbamates as potential anti-Alzheimer's disease agents. *J Med Chem.* 2016;59(13):6387–6406.
41. Brennan MR, Kim D, Fout AR. A synthetic and mechanistic investigation into the cobalt(i) catalyzed amination of aryl halides. *Chem Sci.* 2014;5(12):4831–4839.
42. Chou C-H, Chen Y-Y, Rajagopal B, et al. Thermally induced denitrogenative annulation for the synthesis of dihydroquinolinimines and chroman-4-imines. *Chem Asian J.* 2016;11(5):757–765.
43. Garden SJ, Torres JC, de Souza Melo SC, Lima AS, Pinto AC, Lima ELS. Aromatic iodination in aqueous solution. A new lease of life for aqueous potassium dichloriodate. *Tetrahedron Lett.* 2001;42(11):2089–2092.
44. Gust R, Keilitz R, Schmidt K, von Rauch M. Synthesis, structural evaluation, and estrogen receptor interaction of 4, 5-Bis(4-hydroxyphenyl)imidazoles. *Arch Pharm.* 2002;335(10):463–471.
45. Abarca B, Ballesteros R, Ballesteros-Garrido R, Colobert F, Leroux FR. Triazolopyridines. Part 26: the preparation of novel [1,2,3]triazolo[1,5-a]pyridine sulfoxides. *Tetrahedron.* 2008;64(17):3794–3801.
46. Wang X, Rabbat P, O'Shea P, Tillyer R, Grabowski EJJ, Reider PJ. Selective monolithiation of 2,5-dibromopyridine with butyllithium. *Tetrahedron Lett.* 2000;41(22):4335–4338.
47. Riddell IA, Ronson TK, Clegg JK, Wood CS, Bilbeisi RA, Nitschke JR. Cation- and anion-exchanges induce multiple distinct rearrangements within metallocsupramolecular architectures. *J Am Chem Soc.* 2014;136(26):9491–9498.
48. Lebegue N, Gallet S, Flouquet N, et al. Novel benzopyridothiadiazepines as potential active antitumor agents. *J Med Chem.* 2005;48(23):7363–7373.
49. Kurosawa W, Kan T, Fukuyama T. Stereocontrolled Total Synthesis of (–)-Ephedrine A (Orantine). *J Am Chem Soc.* 2003;125(27):8112–8113.
50. Noji M, Ohno T, Fuji K, Futaba N, Tajima H, Ishii K. Secondary benzylation using benzyl alcohols catalyzed by lanthanoid, scandium, and hafnium triflate. *J Org Chem.* 2003;68(24):9340–9347.
51. Horst MAVd, Stalcup TP, Kaledhonkar S, et al. Locked chromophore analogs reveal that photoactive yellow protein regulates biofilm formation in the deep sea bacterium *Idiomarina loihiensis*. *J Am Chem Soc.* 2009;131(47):17443–17451.
52. Magenau AJD, Kwak Y, Schröder K, Matyjaszewski K. Highly active bipyridine-based ligands for atom transfer radical polymerization. *ACS Macro Lett.* 2012;1(4):508–512.
53. Ten Brink G-J, Arends IWCE, Hoogenraad M, Verspui G, Sheldon RA. Catalytic conversions in water. Part 22: Electronic Effects in the (Diimine)palladium(II)-Catalysed aerobic oxidation of alcohols. *Adv Synth Catal.* 2003;345(4):497–505.
54. Baraldi PG, Cacciari B, Romagnoli R, et al. 7-Substituted 5-Amino-2-(2-furyl)pyrazolo[4,3-e]-1,2,4-triazolo[1,5-c]pyrimidines as A2A adenosine receptor antagonists: a study on the importance of modifications at the side chain on the activity and solubility. *J Med Chem.* 2002;45(1):115–126.
55. Tewes B, Frehland B, Schepmann D, et al. Enantiomerically Pure 2-Methyltetrahydro-3-benzazepin-1-ols selectively blocking GluN2B subunit containing N-Methyl-d-aspartate receptors. *J Med Chem.* 2015;58(15):6293–6305.
56. Josef J, Martin D, Jiri K, Dalibor S, Ivan R. Novel regioselective preparation of 5-chloropyrazine-2-carbonitrile from pyrazine-2-carboxamide and coupling Study of substituted Phenylsulfanylpyrazine-2-carboxylic acid derivatives. *Curr Org Chem.* 2005;9(1):49–60.
57. Bispo Md.LF, Gonçalves RSB, Lima CHd.S, Cardoso LNd.F, Lourenço MCS, de Souza MVN. Synthesis and Antitubercular evaluation of N-Arylpyrazine and N, N'-Alkyl-diylpyrazine-2-carboxamide derivatives. *J Heterocycl Chem.* 2012;49(6):1317–1322.
58. Keilitz J, Newman SG, Lautens M. Enantioselective Rh-catalyzed domino transformations of alkynylcyclohexadienones with organoboron reagents. *Org Lett.* 2013;15(5):1148–1151.
59. Echeverria P-G, Féraud C, Phansavath P, Ratovelomanana-Vidal V. Synthesis, characterization and use of a new tethered Rh(III) complex in asymmetric transfer hydrogenation of ketones. *Catal Commun.* 2015;62:95–99.
60. Di Santo R, Costi R, Cuzzucoli Crucitti G, et al. Design, synthesis, and structure-activity relationship of N-arylnaphthylamine derivatives as amyloid aggregation inhibitors. *J Med Chem.* 2012;55(19):8538–8548.
61. Li W, Li J, Wu Y, Fuller N, Markus MA. Mechanistic pathways in CF3COOH-mediated deacetalization reactions. *J Org Chem.* 2010;75(4):1077–1086.

Flexible Analogues of Azaindole DYRK1A Inhibitors Elicit Cytotoxicity in Glioblastoma Cells*

Qingqing Zhou,^A Tristan A. Reekie,^A Ramzi H. Abbassi,^B Dinesh Indurthi Venkata,^B Josep S. Font,^C Renae M. Ryan,^C Louis M. Rendina,^A Lenka Munoz,^B and Michael Kassiou^{A,D}

^ASchool of Chemistry, The University of Sydney, Sydney, NSW 2006, Australia.

^BSchool of Medical Sciences, Discipline of Pathology and Charles Perkins Centre, The University of Sydney, Sydney, NSW 2006, Australia.

^CSchool of Medical Sciences, Discipline of Pharmacology, The University of Sydney, Sydney, NSW 2006, Australia.

^DCorresponding author. Email: michael.kassiou@sydney.edu.au

DYRK1A is a novel target for epidermal growth factor receptor (EGFR)-dependent glioblastoma and it represents a promising strategy for cancer therapy. DYRK1A inhibition has been found to promote EGFR degradation in glioblastoma cells by triggering endocytosis and lysosomal degradation, thus reducing the self-renewal ability of tumorigenic cells. Using a deconstruction approach of a DYRK1A lead molecule DANDY (**1a**), a set of novel ring-opened compounds was prepared. Despite showing no activity towards DYRK1A, a reduction in the viability of glioblastoma cells was observed with some of the compounds. This suggests other mechanistic pathways are leading to the apoptosis of glioblastoma cells.

Manuscript received: 28 May 2018.

Manuscript accepted: 26 June 2018.

Published online:

Introduction

Glioblastoma, the most aggressive subtype of high-grade glioma (HGG), has been studied for decades.^[1] Patients with glioblastomas have a median survival time of ~15 months, with an extremely high chance of recurrence after initial therapy.^[2] The treatment currently used includes surgical resection, followed by chemo- and/or radiotherapeutic regimens (Fig. 1). For example, the use of 1,3-bis(2-chloroethyl)-1-nitrosourea (carmustine) is very common as an adjuvant concomitant with radiotherapy, which affords significant higher survival rates in comparison with radiotherapy alone.^[3] The alkylating agent temozolomide (TMZ) in addition to radiotherapy has notably prolonged survival rates among patients,^[4] and the co-administration of TMZ with sulfasalazine (SAS) was also demonstrated to reduce cell viability significantly in both primary glioblastomas and established A172 cells.^[5] Among these agents, the monoclonal antibody-derived avastin has been approved as a single drug to treat patients with recurrent HGG in their second-line treatment.^[1a] Pozo and coworkers recently reported a promising therapeutic intervention by targeting dual-specificity tyrosine phosphorylation-regulated kinase 1A (DYRK1A) for epidermal growth factor receptor (EGFR)-dependent glioblastomas.^[6] DYRK1A is upregulated in glioblastoma cells.^[6] The increased phosphorylation of sprouty2 mediated by DYRK1A blocks EGFR degradation as a result of overexpression of EGFR at the cell surface, and the enhanced

EGFR signalling eventually leads to tumour survival. In contrast, DYRK1A inhibition has been found to promote EGFR degradation in glioblastoma cells by triggering endocytosis and lysosomal degradation, thus reducing the self-renewal ability of tumorigenic cells.^[6,7] Therefore, DYRK1A as a novel target in EGFR-dependent glioblastoma represents a promising strategy for cancer therapy.

7-Azaindole DANDY (**1a**)^[8] is one of the most potent inhibitors of DYRK1A, and we recently reported^[7] the pharmacological evaluation of a series of 7-azaindole-based compounds against several kinases (DYRK1A, 1B, 2, and CLK1)

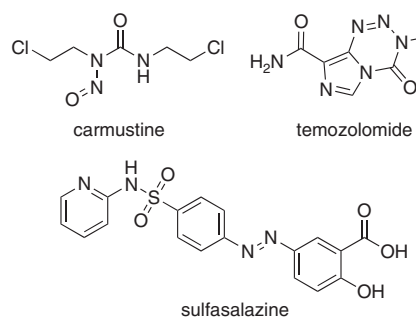
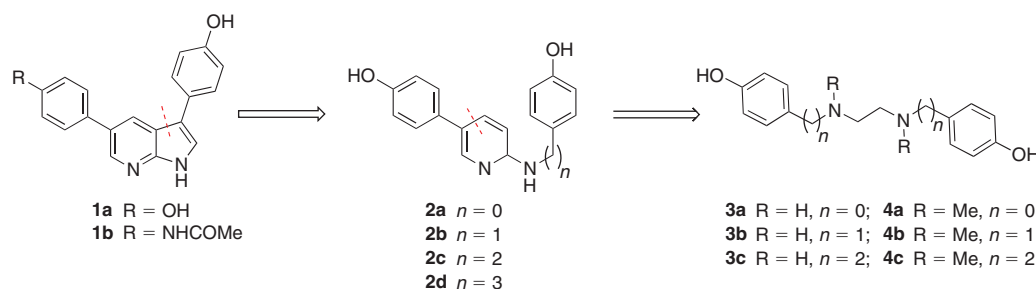


Fig. 1. Current compounds used for treating glioblastoma.

*Michael Kassiou is the recipient of the 2017 RACI Adrian Albert Award.



Scheme 1. Deconstruction of lead compound **1a** to investigate flexible analogues.

belonging to the CMGC family of kinases in glioblastoma. The chemical structures of the 7-azaindole series are related to the adenine core of adenosine triphosphate (ATP), and therefore act as ATP-competitive inhibitors, providing high target selectivity by the engagement of hydrogen bond donors and acceptors. However, the weakness of these inhibitors lies in their high lipophilicity resulting in wider distribution within the body and a higher risk of toxicity. Therefore, we sought to expand on these studies to investigate diverse skeletons with increased hydrophilicity while retaining the hydrogen-bonding characteristics of the lead compounds. To that end, we first examined lead compound **1a**, deconstructing it to the 5-membered ring giving rise to the 1-amino pyridine compound **2** with various linker lengths ($n=0$ to 3) (Scheme 1). This was then further deconstructed, opening the pyridine ring to produce the secondary or tertiary amine chain compound **3** or **4** respectively, and again examining various linker lengths ($n=0$ to 2). We then assessed these compounds in a DYRK1A inhibition assay and also a tumour and non-tumour cell-based viability assay.

Results and Discussion

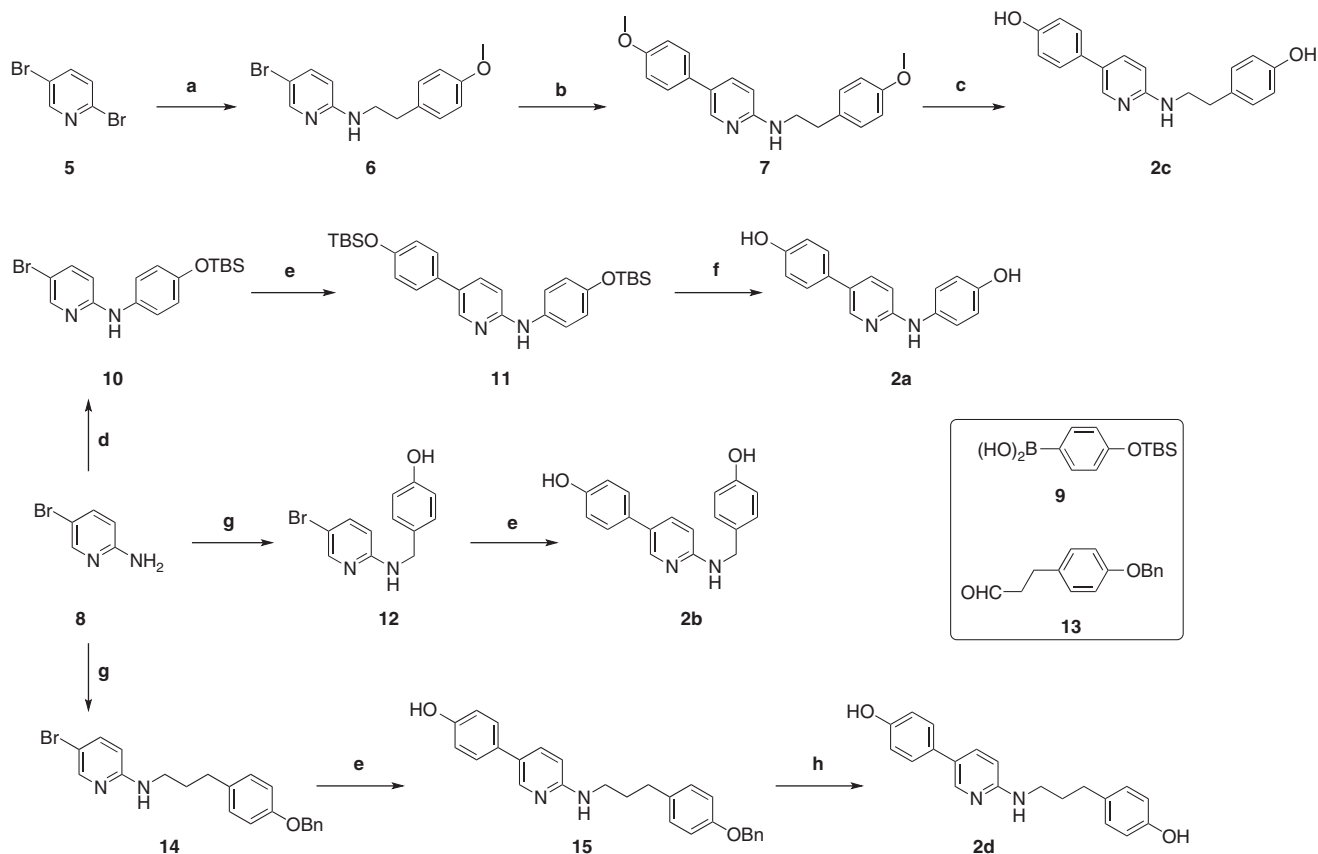
The pyridine diphenol **2c** was prepared from commercially available 2,5-dibromopyridine (**5**), which was treated with *p*-methoxyphenyletheneamine to give intermediate **6**,^[9] followed by a Suzuki cross-coupling reaction resulting in aryl-substituted pyridine **7** (Scheme 2). Subsequent demethylation by BBr_3 afforded the final compound **2c**. The synthetic routes to the remaining analogues of compound **2** were designed from the same starting material **8** (Scheme 2). The intermediate **10** was initially designed by following a similar synthetic route to that for the formation of intermediate **6**. Initial attempts employed a nucleophilic aromatic substitution under basic conditions to afford the corresponding secondary amine, but these were unsuccessful. Alternatively, a $\text{Cu}(\text{OAc})_2$ Chan–Lam coupling^[10] of **8** with *tert*-butyldimethylsilyl (TBS)-protected phenylboronic acid **9** in air produced **10** in moderate yield. A sequential Suzuki cross-coupling reaction, also with boronic acid **9**, was employed to afford compound **11**, which, following the deprotection of TBS groups,^[11] resulted in the desired compound **2a**. The route to compound **2b** from the same starting material **8** first employed a reductive amination with 4-hydroxybenzaldehyde and $\text{NaBH}(\text{OAc})_3$ in trifluoroethanol at room temperature.^[12] A subsequent Suzuki cross-coupling reaction afforded the desired compound **2b** in reasonable yield. Reductive amination of **8** with 3-(4-(benzyloxy)phenyl)propanal (**13**) following similar procedures previously mentioned gave intermediate **14**. A Suzuki coupling to give **15** and hydrolysis to remove the protecting group afforded the desired compound **2d**.

Compounds **3a** and **3c** could be synthesized^[13] from *p*-hydroxybenzyl amine **16a** or **16b** respectively and glyoxal to give the corresponding Schiff bases, followed by the reduction with NaBH_4 to give the secondary amines **3a** and **3c** (Scheme 3), whereas tertiary amines **4a** and **4c** could be easily obtained by reductive amination using 37% formaldehyde and NaBH_4 in EtOH. Similarly, condensation of *p*-hydroxybenzaldehyde (**17**) with ethylenediamine afforded the diimine intermediate, which, following reduction, gave **3b**. An additional reductive amination of **3b** produced tertiary amine **4b** in comparable yield.

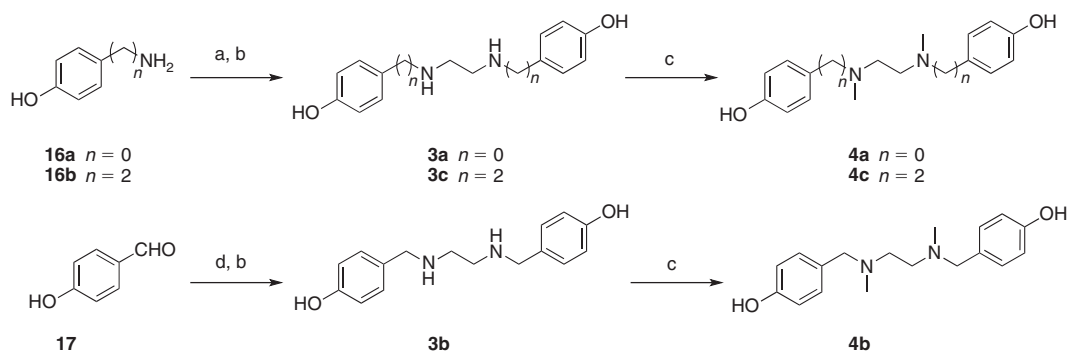
The potency of these analogues for DYRK1A inhibition was determined by performing a kinase assay in duplicate with Woodtide peptide as a substrate and an ATP concentration of 100 μM . The lead compound **1a** was confirmed to have inhibitory potency against DYRK1A, with a half maximal inhibitory concentration (IC_{50}) value of 14 nM and our improved acetamide **1b**^[7] showed an IC_{50} value of 6.6 nM (Table 1). We first assessed the pyrrole ring-opened 2-aminopyridine compounds **2a–d**. The diarylamine **2a** showed no inhibition at >1000 nM with a greater than 100-fold loss of potency in comparison with lead compound **1a** (Table 1). We assumed that the unreasonable distance and angles between the two phenols prevented inhibitory activity. Compounds **2b–d**, which avoided this problem by increasing the distance between the two phenols, were also tested, but showed similar results; IC_{50} values were increased to >1000 nM for all aminopyridine compounds (Table 1).

Despite these results, we expected that compounds **3a–c** and **4a–c**, where the pyridine ring was also disconnected, would show better inhibitory effects, which was rationalized in two ways. First, these compounds were now symmetrical, giving greater malleability within the binding pocket. Second, the two nitrogen atoms are essential for inhibition^[7] and by increasing the flexibility between these two atoms and not just the phenol groups, we anticipated that enhanced target interactions could be achieved. The hydrogen-bond donor and acceptor type and not just acceptor was also explored with compounds **3** and **4** respectively. Unfortunately, these rationalizations proved to be unfounded, as compounds **3a–c** did not improve inhibitory potency against DYRK1A. All IC_{50} values were shown to be >1000 nM (Table 1). These results were replicated with the methylated tertiary amines **4a–c**, with values also >1000 nM (Table 1).

Despite the lack of activity of these compounds towards DYRK1A, we explored their cytotoxicity against the established A172 glioblastoma cell line. In our investigation, lead compound **1a** showed cytotoxicity against the A172 cell line with half maximal effective concentration (EC_{50}) values of 3.4 μM , which is in line with results obtained with the improved



Scheme 2. Synthetic route to compounds **2a–d**. Reagents and conditions: (a) 2-(4-methoxyphenyl)ethan-1-amine (1.2 equiv.), K_2CO_3 (3.0 equiv.), DMF, $120^\circ C$, 8 h, 63%; (b) (4-methoxyphenyl)boronic acid (1.5 equiv.), $Pd(PPh_3)_4$ (2 mol-%), aq. K_2CO_3 (2 M, 2.0 equiv.), 1,4-dioxane, $90^\circ C$, 5 h, 90%; (c) BBr_3 (6.0 equiv.), CH_2Cl_2 , $0^\circ C$ to rt, 15 h, 59%; (d) **9** (1.2 equiv.), $Cu(OAc)_2$ (0.1 equiv.), MeOH, rt, 12 h, 60%; (e) **9** or (4-hydroxyphenyl)boronic acid (1.20 equiv.), $Pd(PPh_3)_4$ (2 mol-%), aq. K_2CO_3 (2 M, 2.0 equiv.), 1,4-dioxane, $90^\circ C$, 3 h, 70–80%; (f) TBAF (1.5 equiv.), THF, rt, 10 min, 95%; (g) **13** or 4-hydroxybenzaldehyde (1.0 equiv.), $NaBH(OAc)_3$ (1.5 equiv.), CF_3CH_2OH , rt, 12 h, 68–89%; (h) H_2 , Pd/C (10 wt-%), MeOH, rt, 2 h, 90%. TBAF, tetra-*n*-butylammonium fluoride; OTBS, *tert*-butyldimethylsilyl ether.



Scheme 3. Synthetic route to compounds **3a–c**, **4a–c**. Reagents and conditions: (a) glyoxal (40% in ethanol, 0.9 equiv.), ethanol, rt, 4 h; (b) $NaBH_4$ (1.0 equiv.), MeOH/ CH_2Cl_2 , 1:1 (v/v), $0^\circ C$ to rt, 30 min, 86–93% over two steps; (c) (1) formaldehyde (37%, 10.0 equiv.), ethanol, rt, 30 min; (2) $NaBH_4$ (1.0 equiv.), rt, 30 min, 88–90% over two steps; (d) ethylenediamine (0.5 equiv.), toluene, $110^\circ C$, 20 min.

DYRK1A inhibitor **1b** (Table 1). In comparison, analogue **2d**, which bears a three-carbon chain linker between the phenol amine and pyridine ring, showed moderate cytotoxic activity ($20.2 \mu M$) despite the total loss of DYRK1A inhibition, although analogues **2a–c** exhibited EC_{50} values of more than $50 \mu M$ (Table 1). More interestingly, secondary amine **3a** with disconnection of both the pyrrole and pyridine rings showed the best cytotoxicity against A172 cells, with an EC_{50} value of $2.4 \mu M$.

This means that although **3a** did not show any inhibition against DYRK1A, it exhibited more cytotoxicity than lead compound **1a**. When testing methylated tertiary amine **4a**, much weaker activity was observed, though moderate cytotoxicity was still present (EC_{50} $22.9 \mu M$). Secondary amines **3b–c** or tertiary amines **4b–c** with a longer distance between the amine and aromatic groups totally lost their cytotoxic behaviour in this study.

Table 1. DYRK1A inhibition assay versus cell viability assay of novel derivatives

Compound	Structures	DYRK1A IC ₅₀ [nM]	A172 EC ₅₀ [μM]
1a		14 ± 2 ^A	3.4
1b		6.6 ± 1.2 ^A	4.6 ± 0.2
2a		>1000	49.9 ± 0.5
2b		>1000	>50
2c		>1000	>50
2d		>1000	20.2 ± 0.8
3a		>1000	2.4 ± 0.2
4a		>1000	22.9 ± 2.8
3b		>1000	>50
4b		>1000	>50

(continued)

Table 1. (Continued)

Compound	Structures	DYRK1A IC ₅₀ [nM]	A172 EC ₅₀ [μM]
3c		>1000	>50
4c		>1000	>50

^ATaken from ref. [7].

Conclusion

In conclusion, we generated a library of 10 novel compounds and subjected them to inhibition assays against DYRK1A. Unfortunately, all the new compounds reported, **2a–d**, **3a–c**, and **4a–c**, displayed no inhibition of DYRK1A, confirming the importance of the azaindole motif. We can conclude that it is not just the positioning of two nitrogen atoms in a similar spatial arrangement that affords strong potency. Indeed, the importance of the aromatic skeleton with specific spatial arrangements of the two nitrogen atoms is confirmed. These data will be of use for future structure–activity relationship studies to further improve the selective inhibition of DYRK1A.

Additionally, an interesting finding of the present study is that although ring-opened compounds completely lost inhibitory activity against our initial target DYRK1A, some of them exhibit markedly potent cytotoxicity against glioblastoma cells. In particular, analogue **3a** with no inhibition against DYRK1A was cytotoxic against cancer cells at higher potencies than the lead compound **1a**, with an EC₅₀ value of 2.4 μM. Nevertheless, further investigations are necessary to explore the exact mechanism of how these compounds exhibit their glioblastoma cytotoxicity, and to analyse their effects in vivo.

Experimental

General Chemical Synthesis Details

Unless noted otherwise, commercially obtained reagents were used as purchased without further purification. Solvents for flash chromatography were distilled before use, or used as purchased for HPLC grade, with the eluent mixture reported as the volume/volume ratio (v/v). Flash chromatography was performed using Merck Kieselgel 60 (230–400 mesh) silica gel. Analytical thin-layer chromatography was performed using Merck aluminium-backed silica gel 60 F254 (0.2 mm) plates (Merck, Darmstadt, Germany), which were visualized using shortwave (254 nm) ultraviolet fluorescence. Melting points were measured with a rate of 6°C min⁻¹ and are uncorrected. Infrared absorption spectra are reported as vibrational frequency (cm⁻¹). Nuclear magnetic resonance spectra were recorded at 300 K using a 200, 300, 400 or 500-MHz spectrometer. The data are reported as chemical shift (δ, ppm) relative to the residual protonated solvent resonance, relative integral, multiplicity (s, singlet; br s, broad singlet; d, doublet; dd, doublet of doublets; t, triplet; m, multiplet, etc.), and coupling constants (*J*, Hz).

Low-resolution mass spectra (LRMS) were obtained from a ThermoQuest Finnigan LCQ Deca ion-trap mass spectrometer with electrospray ionization in positive (+ESI) mode. Data are expressed as observed mass (m/z), assignment (M = molecular ion) and relative intensity (%). High-resolution mass spectroscopy was performed on a Bruker Apex Qe 7T Fourier-transform ion cyclotron resonance mass spectrometer equipped with an Apollo II ESI dual source. Samples were run with syringe infusion at $150 \mu\text{L h}^{-1}$ on a Cole Palmer syringe pump into ESI. High-performance liquid chromatography (HPLC) analysis of organic purity was conducted on a Waters Alliance 2695 instrument using a SunFire™ C18 column ($5 \mu\text{m}$, $2.1 \times 150 \text{ mm}$) and detected using a Waters 2996 photodiode array (PDA) detector set at 254 nm. Separation was achieved using water (solvent A) and acetonitrile (solvent B) at flow rate of 0.2 mL min^{-1} and a gradient of 0 to 100 % B (Method A) or 0 to 80 % B (Method B) or 0 to 40 % B (Method C) over 30 min. HPLC data are reported as percentage purity and retention time (RT) in minutes.

General Procedure A for Suzuki Coupling Reaction

To a solution of aryl bromide (1.0 equiv.) in 1,4-dioxane (0.05 M) were added arylboronic acid (1.0 equiv.), aq. K_2CO_3 (2 M, 2.0 equiv.), and $\text{Pd}(\text{PPh}_3)_4$ (2 mol-%), and the reaction was heated to 90°C for 5 h under argon. The reaction mixture was cooled to room temperature, solvent was removed under reduced pressure, and the product then partitioned between water and ethyl acetate. The aqueous layer was extracted with ethyl acetate, and the combined organic layers were dried over MgSO_4 and concentrated under vacuum.

General Procedure B for Reductive Aminations^[12]

To a solution of 4-hydroxybenzaldehyde or **13** (1.0 equiv.) in 2,2,2-trifluoroethanol (0.04 M) was added 5-bromopyridin-2-amine **8** (1.0 equiv.), and the mixture was stirred at room temperature (rt). After 30 min, $\text{NaBH}(\text{OAc})_3$ (1.5 equiv.) was added and the mixture stirred for 12 h at rt. The solvent was removed under reduced pressure, and the residue was purified by flash chromatography to give the products.

General Procedure C for the Synthesis of Secondary Amines

Compounds were prepared according to the literature.^[14] To a solution of glyoxal (40 % in ethanol, 0.9 equiv.) in ethanol (0.10 M) was added amine **16a–b** (1.1 equiv.), and the mixture was stirred at rt for 4 h, filtered and washed with hexane, and dried under vacuum to get the yellow solid intermediate diimine without further purification. To a solution of the intermediate diimine in CH_2Cl_2 and methanol (1 : 1 v/v, 0.03 M) was added NaBH_4 (1.0 equiv.) at 0°C , and the mixture stirred at room temperature for 30 min. The solvent was removed under reduced pressure, and water (10 mL) was added, affording a white precipitate, which was filtered and washed with hexane, recrystallized in ethanol, and dried under vacuum to get products **3a** and **3c** respectively.

General Procedure D for Methylation of Secondary Amines to Tertiary Amines

To a solution of secondary amine-based diphenol (1.0 equiv.) in acetic acid (0.04 M) was added formaldehyde (37 % aqueous, 10.0 equiv.), and the mixture was stirred at room temperature. After 30 min, NaBH_4 (1.0 equiv.) was added and the mixture

was stirred for another 30 min. The solvent was removed under reduced pressure and the residue was taken up in $\text{Na}_2\text{CO}_3(\text{aq.})$ and extracted with ethyl acetate ($3 \times 15 \text{ mL}$), and the combined organic layers were dried over MgSO_4 and concentrated under vacuum.

5-Bromo-N-(4-methoxyphenethyl)pyridin-2-amine (6)

To a solution of 5-bromo-N-(4-methoxyphenethyl)pyridin-2-amine **5** (200 mg, 0.65 mmol) in DMF (15 mL) was added K_2CO_3 (270 mg, 1.95 mmol) and 2-(4-methoxyphenyl)ethan-1-amine (148 μL , 0.78 mmol), and the mixture was stirred at 120°C for 8 h. The mixture was quenched with water and extracted with ethyl acetate. The combined organic layers were dried over MgSO_4 and concentrated under vacuum. The residue was purified using flash chromatography (hexane/ethyl acetate 10 : 1 \rightarrow 4 : 1) to give the product as a brown solid (125 mg, 63 % yield). Mp. $154\text{--}156^\circ\text{C}$. R_f (hexane/ethyl acetate 2 : 1) 0.40. δ_{H} (500 MHz, CDCl_3) 8.09 (1H, dd, J 0.4, 2.4), 7.44 (1H, dd, J 2.4, 8.8), 7.12 (2H, ddd, J 2.0, 2.9, 8.6), 6.84 (2H, ddd, J 2.0, 2.9, 8.6), 6.25 (1H, dd, J 0.4, 8.8), 4.60 (1H, br s), 3.78 (3H, s), 3.48 (2H, dd, J 6.9, 12.8), 2.84 (2H, t, J 6.9). δ_{C} (125 MHz, CDCl_3) 158.4, 157.3, 148.8, 139.8, 131.0, 129.8, 114.2, 108.4, 107.0, 55.4, 43.6, 34.6. m/z (HRMS ESI+) 307.0443 and 309.0423; $[\text{M} + \text{H}]^+$ requires 307.0441 and 309.0420 for $\text{C}_{14}\text{H}_{15}\text{N}_2\text{OBr}$. ν_{max} (neat)/ cm^{-1} 3334, 2954, 2930, 2835, 1635, 1502, 1241, 1026, 816, 528.

N-(4-Methoxyphenethyl)-5-(4-methoxyphenyl)pyridin-2-amine (7)

This compound was prepared according to General Procedure A. The residue was purified by flash chromatography (hexane/ethyl acetate 3 : 1 \rightarrow 1 : 1) to give the product as an off-white solid (99 mg, 90 % yield). Mp $236\text{--}240^\circ\text{C}$. R_f (hexane/ethyl acetate 4 : 1) 0.40. δ_{H} (400 MHz, CDCl_3) 8.30 (1H, d, J 2.0), 7.61 (1H, dd, J 2.5, 8.6), 7.42 (2H, dd, J 2.1, 6.7), 7.16 (2H, d, J 8.6), 6.96 (2H, dd, J 2.1, 6.7), 6.86 (2H, dd, J 2.1, 6.7), 6.43 (1H, d, J 8.6), 4.57 (1H, t, J 5.6), 3.84 (3H, s), 3.80 (3H, s), 3.56 (2H, dd, J 6.9, 12.9), 2.89 (2H, t, J 6.9). δ_{C} (100 MHz, CDCl_3) 158.8, 158.4, 157.7, 146.1, 136.0, 131.3, 129.9, 127.3, 126.1, 114.5, 114.2, 106.8, 55.5, 55.4, 43.8, 34.9. m/z (HRMS ESI+) 357.1575; $[\text{M} + \text{Na}]^+$ requires 357.1573 for $\text{C}_{21}\text{H}_{22}\text{N}_2\text{O}_2$. ν_{max} (neat)/ cm^{-1} 3204, 2978, 2956, 1610, 1478, 1098, 876, 789.

4-(6-((4-Hydroxyphenethyl)amino)pyridin-3-yl)phenol (2c)

To a solution of **7** (1.0 equiv.) in dry CH_2Cl_2 (0.05 M) was added BBr_3 (1 M solution in CH_2Cl_2 , 6.0 equiv.) under nitrogen. The reaction mixture was stirred at room temperature for 15 h, then quenched at 0°C with MeOH and concentrated under vacuum. The residue was purified by flash chromatography ($\text{CH}_2\text{Cl}_2/\text{MeOH}$ 100 : 1 \rightarrow 40 : 1) to give the product as a white solid (54 mg, 59 % yield). Mp $156\text{--}158^\circ\text{C}$. R_f ($\text{CH}_2\text{Cl}_2/\text{MeOH}$ 20 : 1) 0.45. δ_{H} (500 MHz, $[\text{D}_6]\text{DMSO}$) 9.70 (1H, s), 9.23 (1H, s), 8.69 (1H, br s), 8.18 (1H, dd, J 2.1, 9.3), 8.01 (1H, s), 7.48 (2H, ddd, J 2.0, 2.9, 8.6), 7.13 (1H, s), 7.10 (2H, d, J 8.6), 6.87 (2H, ddd, J 2.0, 2.9, 8.6), 6.71 (2H, ddd, J 2.0, 2.9, 8.6), 3.55 (2H, dd, J 7.4, 11.5), 2.82 (2H, t, J 7.4). δ_{C} (125 MHz, $[\text{D}_6]\text{DMSO}$) 158.2, 156.4, 151.7, 141.8, 131.9, 130.2, 128.7, 127.8, 125.5, 125.2, 116.4, 115.6, 114.1, 43.9, 33.6. m/z (HRMS ESI+) 329.1262; $[\text{M} + \text{Na}]^+$ requires 329.1260 for $\text{C}_{19}\text{H}_{18}\text{N}_2\text{O}_2$. ν_{max} (neat)/ cm^{-1} 3513, 3256, 3009, 1662, 1514, 833. HPLC 98.4 % (Method A), RT 16.5 min.

4-((tert-Butyldimethylsilyloxy)phenyl)boronic Acid (9)

To a solution of 4-hydroxyphenylboronic acid (1.0 equiv., 5 mmol) in dry DMF (0.05 M) was added imidazole (5.0 equiv.) at rt, followed by the addition of TBSCl (3.5 equiv.). The reaction mixture was stirred at rt for 12 h; after completion monitored by TLC, the mixture was extracted with ethyl acetate (3 × 30 mL) and water (50 mL), and the organic layers were dried over MgSO₄ and concentrated under vacuum. The residue was purified by flash chromatography (hexane/ethyl acetate 10 : 1 → 3 : 1) to give the product as a white solid (2.27 g, 90 % yield). *R*_f (hexane/ethyl acetate 1 : 1) 0.30. δ_H (300 MHz, CDCl₃) 8.11 (2H, d, *J* 8.4), 6.96 (2H, d, *J* 8.4), 1.02 (9H, s), 0.26 (6H, s). δ_C (75 MHz, CDCl₃) 159.9, 137.6, 119.9, 111.0, 25.8, 18.4, −4.2. The spectroscopic data matched those reported in the literature.^[15]

5-Bromo-N-(4-((tert-butyldimethylsilyloxy)phenyl)pyridin-2-amine (10)

To a solution of 5-bromopyridin-2-amine **8** (1.0 equiv., 1 mmol) in MeOH (0.05 M) was added **9** (1.2 equiv., 1.2 mmol) at rt, followed by the addition of Cu(OAc)₂ (0.1 equiv., 0.1 mmol). The reaction mixture was stirred for 12 h under air at rt. After completion monitored by TLC, the metal solid was filtered through Celite®, and the solvent was removed under reduced pressure. The residue was purified by flash chromatography (hexane/ethyl acetate 10 : 1) to give the product as a white solid (227 mg, 60 % yield). Mp 131–132°C. *R*_f (hexane/ethyl acetate 10 : 1) 0.40. δ_H (400 MHz, CDCl₃) 8.16 (1H, d, *J* 2.0), 7.51 (1H, dd, *J* 2.0, 8.8), 7.14 (2H, dd, *J* 2.0, 6.4), 6.83 (2H, dd, *J* 2.0, 6.4), 6.60 (1H, d, *J* 8.8), 6.55 (1H, s), 0.99 (9H, s), 0.20 (6H, s). δ_C (100 MHz, CDCl₃) 155.8, 152.8, 148.4, 140.5, 133.0, 124.2, 121.0, 109.0, 108.4, 25.8, 18.4, −4.3. *m/z* (HRMS ESI+) 401.0659 and 403.0639; [M + Na]⁺ requires 401.0655 and 403.0635 for C₁₇H₂₃BrN₂O₂Si. *v*_{max} (neat)/cm^{−1} 3244, 2947, 2855, 1605, 1525, 1251, 904, 778.

N,5-Bis(4-((tert-butyldimethylsilyloxy)phenyl)pyridin-2-amine (11)

This compound was prepared according to General Procedure A. The residue was purified by flash chromatography (hexane/ethyl acetate 10 : 1 → 5 : 1) to give the product as a white solid (203 mg, 80 % yield). Mp 135–136°C. *R*_f (hexane/ethyl acetate 5 : 1) 0.45. δ_H (300 MHz, CDCl₃) 8.26 (1H, s), 7.71 (1H, d, *J* 9.0), 7.37–7.34 (3H, m), 7.18 (2H, d, *J* 8.1), 6.90 (2H, d, *J* 8.1), 6.86–6.79 (3H, m), 1.00 (18H, s), 0.22 (6H, s), 0.21 (6H, s). δ_C (75 MHz, CDCl₃) 155.6, 155.1, 153.0, 142.9, 137.8, 132.7, 130.5, 127.5, 127.4, 124.4, 121.1, 120.8, 108.3, 25.8 (two overlapping signals), 18.4 (two overlapping signals), −4.2 (two overlapping signals). *m/z* (HRMS ESI+) 507.2861; [M + H]⁺ requires 507.2858 for C₂₉H₄₂N₂O₂Si₂. *v*_{max} (neat)/cm^{−1} 3232, 2962, 2856, 1603, 1508, 1249, 911, 822, 775.

4-(6-((4-Hydroxyphenyl)amino)pyridin-3-yl)phenol (2a)

To a solution of **11** (1.0 equiv., 0.1 mmol) in dry THF (5 mL) was added tetra-*n*-butylammonium fluoride (TBAF) (1.5 equiv., 0.15 mmol) at rt dropwise, and the reaction mixture was stirred for 10 min under a nitrogen atmosphere and the solvent was removed under reduced pressure. The residue was washed with H₂O (10 mL) and extracted with ethyl acetate (3 × 10 mL), the organic layers were dried over MgSO₄ and concentrated under vacuum. The residue was purified by flash chromatography

(hexane/ethyl acetate 3 : 1 → 1 : 1) to give the product as a pale yellow solid (53 mg, 95 % yield). Mp 199–200°C. *R*_f (hexane/ethyl acetate 1 : 1) 0.30. δ_H (400 MHz, [D4]MeOD) 8.18 (1H, dd, *J* 0.8, 2.8), 7.70 (1H, dd, *J* 2.8, 8.8), 7.37 (2H, ddd, *J* 2.8, 4.8, 9.6), 7.21 (2H, ddd, *J* 3.2, 5.6, 10.0), 6.84 (2H, ddd, *J* 2.8, 4.8, 9.6), 6.78 (2H, ddd, *J* 3.2, 5.6, 10.0), 6.74 (1H, dd, *J* 0.8, 8.8). δ_C (100 MHz, [D4]MeOD) 157.9, 157.4, 154.5, 145.5, 137.3, 134.1, 130.8, 128.4, 128.1, 124.5, 116.8, 116.7, 110.1. *m/z* (HRMS ESI+) 279.1131; [M + H]⁺ requires 279.1128 for C₁₇H₁₄N₂O₂. *v*_{max} (neat)/cm^{−1} 3217, 2953, 1607, 1490, 1218, 815. HPLC >99.9 % (Method A), RT 16.2 min.

4-(((5-Bromopyridin-2-yl)amino)methyl)phenol (12)

This compound was prepared according to General Procedure B. The residue was purified by flash chromatography (hexane/ethyl acetate 5 : 1 → 3 : 1) to give the product as a white solid (190 mg, 68 % yield). Mp 125–128°C. *R*_f (hexane/ethyl acetate 4 : 1) 0.30. δ_H (400 MHz, [D4]MeOD) 7.98 (1H, d, *J* 2.4), 7.49 (1H, dd, *J* 2.4, 8.8), 7.17 (2H, dd, *J* 2.0, 6.8), 6.75 (2H, dd, *J* 2.0, 6.8), 6.48 (1H, d, *J* 8.8), 4.36 (2H, s). δ_C (100 MHz, [D4]MeOD) 159.0, 157.6, 148.5, 140.9, 131.3, 129.8, 116.2, 111.4, 106.9, 46.0. *m/z* (HRMS ESI+) 300.9950 and 302.9930; [M + Na]⁺ requires 300.9947 and 302.9926 for C₁₂H₁₁BrN₂O. *v*_{max} (neat)/cm^{−1} 3218, 1594, 1343, 815.

4-(6-((4-Hydroxybenzyl)amino)pyridin-3-yl)phenol (2b)

This compound was prepared according to General Procedure A. The residue was purified by flash chromatography (hexane/ethyl acetate 3 : 1 → 1 : 1) to give the product as a pale yellow solid (51 mg, 70 % yield). Mp 193–196°C. *R*_f (hexane/ethyl acetate 1 : 1) 0.35. δ_H (300 MHz, [D4]MeOD) 8.13 (1H, s), 7.65 (1H, d, *J* 8.7), 7.34 (2H, d, *J* 8.1), 7.20 (2H, d, *J* 8.1), 6.85 (2H, d, *J* 8.1), 6.76 (2H, d, *J* 8.1), 6.58 (1H, d, *J* 8.7), 4.41 (2H, s). δ_C (75 MHz, [D4]MeOD) 158.9, 157.7, 157.5, 145.2, 137.2, 131.6, 131.0, 129.7, 128.1, 127.1, 116.7, 116.2, 109.6, 46.3. *m/z* (HRMS ESI+) 607.2321; [M + Na]⁺ requires 607.2316 for (C₁₈H₁₆N₂O₂)₂. *v*_{max} (neat)/cm^{−1} 3211, 3025, 1613, 1508, 1247, 822, 529. HPLC >99.9 % (Method B), RT 16.2 min.

3-(4-(Benzyloxy)phenyl)propanal (13)

To a solution of 4-(3-hydroxypropyl)phenol (1.0 equiv., 1 mmol) in acetone (0.05 M) was added K₂CO₃ (1.5 equiv., 1.5 mmol), followed by the addition of benzyl bromide (1.2 equiv., 1.2 mmol) dropwise at rt, and the mixture was stirred at rt for 12 h. After completion, the solvent was removed under reduced pressure, and the residue was washed with H₂O (30 mL) and extracted with ethyl acetate (3 × 20 mL); the organic layers were dried over MgSO₄ and concentrated under vacuum. The residue was purified by flash chromatography (hexane/ethyl acetate 10 : 1 → 5 : 1) to give the product 3-(4-(benzyloxy)phenyl)propan-1-ol as a white solid (230 mg, 95 % yield). *R*_f (hexane/ethyl acetate 4 : 1) 0.30. δ_H (400 MHz, CDCl₃) 7.48–7.33 (5H, m), 7.15 (2H, ddd, *J* 2.8, 5.2, 9.6), 6.95 (2H, ddd, *J* 2.8, 5.2, 9.6), 5.06 (2H, s), 3.66 (2H, t, *J* 6.4), 2.70–2.66 (2H, m), 2.19 (1H, s), 1.92–1.85 (2H, m). δ_C (100 MHz, CDCl₃) 157.1, 137.3, 134.3, 129.4, 128.6, 127.9, 127.5, 114.9, 70.1, 62.1, 34.4, 31.2. The spectroscopic data matched those reported in the literature.^[16]

To a solution of 3-(4-(benzyloxy)phenyl)propan-1-ol (1.0 equiv., 0.5 mmol) in dry CH₂Cl₂ (10 mL) was added Dess–Martin periodinane (DMP, 1.5 equiv., 0.75 mmol), and the mixture was stirred at rt for 2 h. The mixture was quenched

with a mixture of saturated NaHCO₃ (2 mL) and Na₂S₂O₃ (2 mL), and the resulting mixture was extracted with CH₂Cl₂ (3 × 10 mL), and the organic layers were dried over MgSO₄ and concentrated under vacuum. The residue was purified by flash chromatography (hexane/ethyl acetate 10 : 1) to give the product **13** as a white solid (114 mg, 95 % yield). *R_f* (hexane/ethyl acetate 10 : 1) 0.50. δ_H (300 MHz, CDCl₃) 9.81 (1H, s), 7.44–7.32 (5H, m), 7.11 (2H, d, *J* 8.1), 6.91 (2H, d, *J* 8.1), 5.05 (2H, s), 2.91 (2H, t, *J* 7.2), 2.75 (2H, t, *J* 7.2). δ_C (75 MHz, CDCl₃) 201.9, 157.5, 137.2, 132.8, 129.4, 128.7, 128.1, 127.6, 115.1, 70.2, 45.6, 27.4. The spectroscopic data matched those reported in the literature.^[17]

N-(3-(4-(Benzyloxy)phenyl)propyl)-5-bromopyridin-2-amine (**14**)

This compound was prepared according to General Procedure B. The residue was purified by flash chromatography (hexane/ethyl acetate 10 : 1) to give the product as a white solid (353 mg, 89 % yield). Mp 97–98°C. *R_f* (hexane/ethyl acetate 10 : 1) 0.40. δ_H (400 MHz, CDCl₃) 8.09 (1H, d, *J* 2.4), 7.47–7.31 (6H, m), 7.10 (2H, ddd, *J* 2.8, 5.2, 9.6), 6.91 (2H, ddd, *J* 2.8, 5.2, 9.6), 6.23 (1H, d, *J* 8.8), 5.05 (2H, s), 4.65 (1H, br.s), 3.24 (2H, t, *J* 6.4), 2.66 (2H, t, *J* 7.6), 1.91 (2H, tt, *J* 7.6, 14.4). δ_C (100 MHz, CDCl₃) 157.5, 157.3, 148.7, 139.9, 137.3, 133.9, 129.4, 128.7, 128.0, 127.6, 115.0, 108.0, 106.8, 70.2, 41.9, 32.4, 31.2. *m/z* (HRMS ESI+) 397.0915 and 399.0894; [M + H]⁺ requires 397.0910 and 399.0890 for C₂₁H₂₁BrN₂O. *v*_{max} (neat)/cm⁻¹ 3247, 2937, 1586, 1243, 815, 726.

4-(6-((3-(4-(Benzyloxy)phenyl)propyl)amino)pyridin-3-yl)phenol (**15**)

This compound was prepared according to General Procedure A. The residue was purified by flash chromatography (hexane/ethyl acetate 10 : 1 → 3 : 1) to give the product as a pale yellow solid (154 mg, 75 % yield). Mp 138–140°C. *R_f* (hexane/ethyl acetate 6 : 1) 0.30. δ_H (300 MHz, CDCl₃) 8.26 (1H, s), 7.63 (1H, d, *J* 8.7), 7.44–7.34 (7H, m), 7.09 (2H, d, *J* 8.1), 6.93–6.88 (4H, m), 6.41 (1H, d, *J* 8.7), 5.03 (2H, s), 4.68 (1H, br.s), 3.30–3.28 (2H, m), 2.67 (2H, t, *J* 7.2), 1.93 (2H, tt, *J* 7.2, 13.8). δ_C (75 MHz, CDCl₃) 157.5, 157.3, 155.9, 145.3, 137.3, 136.6, 133.9, 130.5, 129.5, 128.7, 128.0, 127.6 (two overlapping signals), 126.3, 116.2, 115.0, 106.5, 70.2, 42.0, 32.4, 31.3. *m/z* (HRMS ESI+) 411.2071; [M + H]⁺ requires 411.2067 for C₂₇H₂₆N₂O₂. *v*_{max} (neat)/cm⁻¹ 3409, 3029, 2928, 2856, 1606, 1501, 1232, 811, 517.

4-(6-((3-(4-Hydroxyphenyl)propyl)amino)pyridin-3-yl)phenol (**2d**)

To a solution of **15** (1.0 equiv., 0.1 mmol) in MeOH (5 mL) was added Pd/C (10 wt-%, 5 mg) under a nitrogen atmosphere, and the mixture was stirred at room temperature for 2 h under 1 atm of H₂. After completion, the Pd/C was filtered through Celite®, and the solvent of the filtrate was removed under reduced pressure. The residue was purified by flash chromatography (hexane/ethyl acetate 1 : 1) to give the product as a pale yellow solid (69 mg, 90 % yield). Mp 217–219°C. *R_f* (hexane/ethyl acetate 1 : 1) 0.40. δ_H (400 MHz, [D6]DMSO) 9.37 (1H, br.s), 9.11 (1H, br.s), 8.18 (1H, d, *J* 2.4), 7.57 (1H, dd, *J* 2.4, 8.8), 7.34 (2H, dd, *J* 2.0, 6.4), 7.00 (2H, dd, *J* 2.0, 6.4), 6.79 (2H, dd, *J* 2.0, 6.4), 6.67 (2H, dd, *J* 2.0, 6.4), 6.52–6.48 (2H, m), 3.25–3.20 (2H, m), 2.54 (2H, t, *J* 7.6), 1.77 (2H, tt, *J* 7.6, 14.8). δ_C (100 MHz, [D6]DMSO) 157.7, 156.1, 155.2, 144.7, 134.5, 131.9, 129.1

(two overlapping signals), 126.5, 123.7, 115.7, 115.0, 107.9, 40.5, 31.9, 31.2. *m/z* (HRMS ESI+) 321.1601; [M + H]⁺ requires 321.1598 for C₂₀H₂₀N₂O₂. *v*_{max} (neat)/cm⁻¹ 3403, 3150, 2922, 2852, 1609, 1508, 1450, 1234, 813. HPLC 99.0 % (Method B), RT 18.3 min.

4,4'-(Ethane-1,2-diylbis(azanediyl))diphenol (**3a**)

This compound was prepared according to General procedure C to get the product as an off-white solid (220 mg, 90 % yield). Mp 170–172°C. *R_f* (CH₂Cl₂/MeOH 20 : 1) 0.35. δ_H (500 MHz, [D6]DMSO) 8.38 (2H, s), 6.54 (4H, d, *J* 8.8), 6.44 (4H, d, *J* 8.8), 4.90 (2H, s), 3.09 (4H, t, *J* 2.5). δ_C (125 MHz, [D6]DMSO) 148.3, 141.7, 115.7, 113.5, 43.4. *m/z* (HRMS ESI+) 267.1104; [M + Na]⁺ requires 267.1104 for C₁₄H₁₆N₂O₂. *v*_{max} (neat)/cm⁻¹ 3283, 3066, 2970, 1507, 641, 533. HPLC 96.5 % (Method A), RT 10.9 min.

4,4'-((Ethane-1,2-diylbis(azanediyl))bis(ethane-2,1-diyl))diphenol (**3c**)

This compound was prepared according to General procedure C to afford the product as an off-white solid (129 mg, 86 % yield). Mp 205–209°C. *R_f* (CH₂Cl₂/MeOH 20 : 1) 0.30. δ_H (500 MHz, [D6]DMSO) 6.96 (4H, d, *J* 8.1), 6.66 (4H, d, *J* 8.1), 2.65–2.62 (4H, m), 2.55–2.52 (8H, m), NH and OH signals not observed. δ_C (125 MHz, [D6]DMSO) 155.9, 130.9, 129.8, 115.5, 51.9, 49.4, 35.6. *m/z* (HRMS ESI+) 301.1910; [M + H]⁺ requires 301.1910 for C₁₈H₂₄N₂O₂. *v*_{max} (neat)/cm⁻¹ 3179, 3019, 2814, 1671, 1182, 1131. HPLC >99.9 % (Method C), RT 16.2 min.

4,4'-(Ethane-1,2-diylbis(methylazanediyl))diphenol (**4a**)

This compound was prepared according to General Procedure D. The residue was purified by flash chromatography (CH₂Cl₂/MeOH 100 : 1 → 80 : 1) to give the product as a white solid (60 mg, 88 % yield). Mp 174–176°C. *R_f* (CH₂Cl₂/MeOH 20 : 1) 0.45. δ_H (400 MHz, [D4]MeOD) 6.70–6.34 (8H, m), 3.33 (4H, s), 2.81 (6H, s), OH signals not observed. δ_C (100 MHz, [D4]MeOD) 150.6, 144.7, 116.9, 116.8, 52.4, 40.2. *m/z* (HRMS ESI+) 273.1597; [M + H]⁺ requires 273.1597 for C₁₆H₂₀N₂O₂. *v*_{max} (neat)/cm⁻¹ 3489, 3377, 3100, 1662, 1192, 545. HPLC 99.7 % (Method C), RT 16.7 min.

4,4'-((Ethane-1,2-diylbis(methylazanediyl))bis(ethane-2,1-diyl))diphenol (**4c**)

This compound was prepared according to General Procedure D. The residue was purified by flash chromatography (CH₂Cl₂/MeOH 100 : 1 → 80 : 1) to give the product as a pale brown solid (73 mg, 89 % yield). Mp 229–230°C. *R_f* (CH₂Cl₂/MeOH 20 : 1) 0.40. δ_H (400 MHz, [D6]DMSO) 9.07 (2H, br.s), 6.96 (4H, d, *J* 8.4), 6.62 (4H, d, *J* 8.4), 2.56–2.52 (4H, m), 2.48–2.43 (4H, m), 2.40 (4H, s), 2.17 (6H, s). δ_C (100 MHz, [D6]DMSO) 155.8, 131.0, 129.9, 115.4, 60.2, 55.4, 42.6, 32.6. *m/z* (HRMS ESI+) 329.2224; [M + H]⁺ requires 329.2223 for C₂₀H₂₈N₂O₂. *v*_{max} (neat)/cm⁻¹ 3201, 2939, 2622, 1513, 1200, 830, 659. HPLC 95.7 % (Method A), RT 12.3 min.

4,4'-((Ethane-1,2-diylbis(azanediyl))bis(methylene))diphenol (**3b**)

This compound was prepared according to the literature method.^[18] To a solution of ethylenediamine (55 μL, 0.82 mmol) in toluene (20 mL) was added 4-hydroxybenzaldehyde **17** (200 mg, 1.64 mmol), and the mixture was stirred at 110°C for

20 min, forming a yellow precipitate, which was filtered without further purification; the solid was dissolved in methanol (20 mL), followed by treatment with NaBH₄ (15.9 mg, 0.42 mmol) at 0°C, and heated at reflux for 20 min. The solvent was removed under reduced pressure. The mixture was quenched with NH₄Cl_(aq) and extracted with ethyl acetate (3 × 15 mL) and the combined organic layers were dried over MgSO₄ and concentrated under vacuum. The residue was purified by flash chromatography (CH₂Cl₂/MeOH 100:1 → 80:1) to give the product as off-white solid **3b** (207 mg, 93% yield). Mp 139–141°C. *R_f* (CH₂Cl₂/MeOH 20:1) 0.35. δ_H (500 MHz, [D₆]DMSO) 9.17 (2H, s), 7.07 (4H, d, *J* 8.4), 6.67 (4H, d, *J* 8.4), 3.52 (4H, s), 2.53 (4H, s). δ_C (125 MHz, [D₆]DMSO) 155.9, 131.2, 128.9, 114.7, 52.5, 48.2. *m/z* (HRMS ESI+) 273.1598; [M + H]⁺ requires 273.1597 for C₁₆H₂₀N₂O₂. *v*_{max} (neat)/cm⁻¹ 3254, 3018, 2856, 1611, 1512, 876. HPLC >99.9% (Method A), RT 10.8 min.

4,4'-((Ethane-1,2-diylbis(methylazanediyl))bis(methylene))diphenol (**4b**)

This compound was prepared according to General Procedure D. The residue was purified by flash chromatography (CH₂Cl₂/MeOH 100:1 → 80:1) to give the product as a white solid (67 mg, 90% yield). Mp 158–159°C. *R_f* (CH₂Cl₂/MeOH 20:1) 0.45. δ_H (500 MHz, [D₆]DMSO) 9.21 (2H, s), 7.03 (4H, d, *J* 8.3), 6.67 (4H, d, *J* 8.3), 3.32 (4H, s), 2.42 (4H, s), 2.06 (6H, s). δ_C (100 MHz, [D₄]MeOD) 158.0, 132.0, 129.3, 116.1, 62.8, 54.8, 42.7. *m/z* (HRMS ESI+) 301.1910; [M + H]⁺ requires 301.1910 for C₁₈H₂₄N₂O₂. *v*_{max} (neat)/cm⁻¹ 3269, 3009, 1671, 1126. HPLC >99.9% (Method C), RT 14.3 min.

Purification of His-DYRK1A

Human DYRK1A Kinase domain (126–490aa) with an *N*-terminal histidine tag was expressed in *Escherichia coli* BL21 (DE3) cells. A 10 mL overnight (O/N) culture (1 mL) containing 50 μg mL⁻¹ kanamycin and 34 μg mL⁻¹ chloramphenicol was used to inoculate 1 L of Luria–Bertani (LB) media supplemented with the same antibiotics. The culture was grown at 37°C until an optical density 600 (OD₆₀₀) of 0.5 was reached; the temperature was then reduced to 18°C. Expression was induced with the addition of 1 mM IPTG (isopropyl B-D-thiogalactoside) and incubated O/N at 18°C. The cells were harvested by centrifugation, 7459 g for 10 min, and resuspended in lysis buffer (50 mM HEPES pH 7.5, 500 mM NaCl, 5% glycerol, 5 mM imidazole, and 0.5 mM tris(2-carboxyethyl)phosphine (TCEP)). The cell pellet was lysed using an Emulsiflex C5 high-pressure homogenizer (Avestin) in the presence of protease inhibitors. The insoluble debris was removed by centrifugation at 10980 g for 30 min. The supernatant was bound to Ni-NTA resin (Ni²⁺-nitriloacetate, Qiagen) and washed with 30 column volumes (CV) of lysis buffer and 5 CV of wash buffer (50 mM HEPES pH 7.5, 500 mM NaCl, 5% glycerol, 25 mM imidazole, and 0.5 mM TCEP). The purified protein was finally eluted from the resin with 5 CV of elution buffer (50 mM HEPES pH 7.5, 500 mM NaCl, 5% glycerol, 250 mM imidazole, and 0.5 mM TCEP). The histidine tag was cleaved with the addition of tobacco etch virus (TEV) protease (1 mg mL⁻¹) and incubated at 4°C O/N. The eluted proteins were further purified by gel-filtration chromatography using an S200 16/60 column (GE Healthcare) in 25 mM HEPES pH 7.5, 500 mM NaCl, 5 mM dithiothreitol (DTT).

Kinase Inhibition Assay

Active DYRK1A was assayed in TRIS buffer (50 mM TRIS-HCl, pH 7.5) containing 0.1 mM egtazic acid (EGTA), 15 mM DTT, MgAc/ATP cocktail (0.5 mM HEPES pH 7.4; 10 mM Mg (CH₃COO)₂; 0.1 mM ATP), [γ-³²P]-ATP 100–300 cpm pmol⁻¹, and test compounds diluted in deionized water. As substrate, Woodtide (50 μM, Genscript) was used in the DYRK1A assay. The reaction was initiated with 1 ng μL⁻¹ DYRK1A. The reaction mixture was incubated at 30°C for 10 min. Reaction was stopped by pipetting 10 μL of the reaction mixture onto P81 paper (Reaction Biology) and washing with 0.75% w/v H₃PO₄ and acetone. P81 papers were transferred to sample bags containing Optiphase Supermix scintillation cocktail (PerkinElmer) and radioactivity (cpm) was measured with a MicroBeta Trilux 2 counter (PerkinElmer). Compounds were tested in duplicate at 1 and 10 μM for their ability to inhibit DYRK1A activity.

Supplementary Material

¹H and ¹³C NMR spectra of new compounds and HPLC chromatograms of final compounds are available on the Journal's website.

Conflicts of Interest

The authors declare no conflicts of interest.

Acknowledgements

This work was supported by the National Health & Medical Research Council of Australia (grant no. APP1106145).

References

- [1] (a) M. C. Chamberlain, *Cancer* **2010**, *116*, 3988. doi:10.1002/CNCR.25256
- (b) S. K. Singh, C. Hawkins, I. D. Clarke, J. A. Squire, J. Bayani, T. Hide, R. M. Henkelman, M. D. Cusimano, P. B. Dirks, *Nature* **2004**, *432*, 396. doi:10.1038/NATURE03128
- (c) R. Galli, E. Binda, U. Orfanelli, B. Cipelletti, A. Gritti, S. De Vitis, R. Fiocco, C. Foroni, F. Dimeco, A. Vecovio, *Cancer Res.* **2004**, *64*, 7011. doi:10.1158/0008-5472.CAN-04-1364
- [2] E. T. Wong, K. R. Hess, M. J. Gleason, K. A. Jaeckle, A. P. Kyritsis, M. D. Prados, V. A. Levin, W. K. A. Yung, *J. Clin. Oncol.* **1999**, *17*, 2572. doi:10.1200/JCO.1999.17.8.2572
- [3] M. D. Walker, E. Alexander, Jr, W. E. Hunt, C. S. MacCarty, M. S. Mahaley, Jr, J. Mealey, Jr, H. A. Norrell, G. Owens, J. Ransohoff, C. B. Wilson, E. A. Gehan, T. A. Strike, *J. Neurosurg.* **1978**, *49*, 333. doi:10.3171/JNS.1978.49.3.0333
- [4] R. Stupp, W. P. Mason, M. J. van den Bent, M. Weller, B. Fisher, M. J. B. Taphoorn, K. Belanger, A. A. Brandes, C. Marosi, U. Bogdahn, J. Curschmann, R. C. Janzer, S. K. Ludwin, T. Gorlia, A. Allgeier, D. Lacombe, J. G. Cairncross, E. Eisenhauer, R. O. Mirimanoff, *N. Engl. J. Med.* **2005**, *352*, 987. doi:10.1056/NEJM0A043330
- [5] R. S. Ignarro, G. Facchini, A. S. Vieira, D. R. De Melo, I. Lopes-Cendes, R. F. Castilho, F. Rogerio, *Mol. Cell. Biochem.* **2016**, *418*, 167. doi:10.1007/S11010-016-2742-X
- [6] N. Pozo, C. Zahonero, P. Fernandez, J. M. Linares, A. Ayuso, M. Hagiwara, A. Pérez, J. R. Ricoy, A. Hernández-Lain, J. M. Sepúlveda, P. Sánchez-Gómez, *J. Clin. Invest.* **2013**, *123*, 2475. doi:10.1172/JCI63623
- [7] Q. Zhou, A. F. Phoa, R. H. Abbassi, M. Hoque, T. A. Reekie, J. S. Font, R. M. Ryan, B. W. Stringer, B. W. Day, T. G. Johns, L. Munoz, M. Kassio, *J. Med. Chem.* **2017**, *60*, 2052. doi:10.1021/ACS.JMED.CHEM.6B01840
- [8] S. Gourdain, J. Dairou, C. Denhez, L. C. Bui, F. Rodrigues-Lima, N. Janel, J. M. Delabar, K. Cariou, R. H. Dodd, *J. Med. Chem.* **2013**, *56*, 9569. doi:10.1021/JM401049V

- [9] R. J. Ife, K. W. Catchpole, G. J. Durant, C. Robin Ganellin, C. A. Harvey, M. L. Meeson, D. A. A. Owen, M. E. Parsons, B. P. Slingsby, C. J. Theobald, *Eur. J. Med. Chem.* **1989**, *24*, 249. doi:10.1016/0223-5234(89)90006-8
- [10] D. N. Rao, S. Rasheed, S. Aravinda, R. A. Vishwakarma, P. Das, *RSC Adv.* **2013**, *3*, 11472. doi:10.1039/C3RA40735G
- [11] G. D. Kishore Kumar, A. Natarajan, *Tetrahedron Lett.* **2008**, *49*, 2103. doi:10.1016/j.tetlet.2008.01.135
- [12] M. Tajbakhsh, R. Hosseinzadeh, H. Alinezhad, S. Ghahari, A. Heydari, S. Khaksar, *Synthesis* **2011**, 490. doi:10.1055/S-0030-1258384
- [13] M. B. Abrams, B. L. Scott, R. T. Baker, *Organometallics* **2000**, *19*, 4944. doi:10.1021/OM000535I
- [14] H. Türkmen, B. Çetinkaya, *J. Organomet. Chem.* **2006**, *691*, 3749. doi:10.1016/J.JORGANCHEM.2006.05.020
- [15] M. A. van der Horst, T. P. Stalcup, S. Kaledhonkar, M. Kumauchi, M. Hara, A. Xie, K. J. Hellingwerf, W. D. Hoff, *J. Am. Chem. Soc.* **2009**, *131*, 17443. doi:10.1021/JA9057103
- [16] B. Chinnababu, S. P. Reddy, C. B. Rao, K. Rajesh, Y. Venkateswarlu, *Helv. Chim. Acta* **2010**, *93*, 1960. doi:10.1002/HLCA.200900478
- [17] C. G. Frost, B. C. Hartley, *J. Org. Chem.* **2009**, *74*, 3599. doi:10.1021/JO900390D
- [18] S.-F. Hsu, B. Plietker, *ChemCatChem* **2013**, *5*, 126. doi:10.1002/CCTC.201200590

REVIEW

Histone lysine demethylases and their functions in cancer

Jayden Sterling | Sharleen V. Menezes | Ramzi H. Abbassi | Lenka Munoz 

School of Medical Sciences and Charles Perkins Centre, Faculty of Medicine and Health, The University of Sydney, Sydney, New South Wales, Australia

Correspondence

Lenka Munoz, Charles Perkins Centre, Faculty of Medicine and Health, The University of Sydney, Sydney, NSW 2006, Australia.
Email: lenka.munoz@sydney.edu.au

Abstract

Histone lysine demethylases (KDMs) are enzymes that remove the methylation marks on lysines in nucleosomes' histone tails. These changes in methylation marks regulate gene transcription during both development and malignant transformation. Depending on which lysine residue is targeted, the effect of a given KDM on gene transcription can be either activating or repressing, and KDMs can regulate the expression of both oncogenes and tumour suppressors. Thus, the functions of KDMs can be regarded as both oncogenic and tumour suppressive, contingent on cell context and the enzyme isoform. Finally, KDMs also demethylate nonhistone proteins and have a variety of demethylase-independent functions. These epigenetic and other mechanisms that KDMs control make them important regulators of malignant tumours. Here, we present an overview of eight KDM subfamilies, their most-studied lysine targets and selected recent data on their roles in cancer stem cells, tumour aggressiveness and drug tolerance.

KEYWORDS

drug resistance, drug tolerance, epigenetics, histone lysine demethylase, histone methylation

Abbreviations: 2-OG, 2-oxoglutarate; AR, androgen receptor; ARID, AT-rich interacting domain; BET, bromodomain and extraterminal domain; CDKN1A, cyclin dependent kinase inhibitor 1A; DNA, deoxyribonucleic acid; DUSP3, dual-specificity protein phosphatase 3; E2F1, E2F transcription factor 1; EGFR, epidermal growth factor receptor; ERK, extracellular-signal-regulated kinase; ETS, erythroblast transformation specific; EZH2, enhancer of zeste homologue 2; FBXW7, F-Box and WD repeat domain containing 7; GATA, GATA-binding factor 1; GLI1, glioma-associated oncogene homologue 1; H3K4me3, histone 3 lysine 4 trimethylated; HIF1 α , hypoxia-inducible factor 1-alpha; Hox, homeobox; IDH1, isocitrate dehydrogenase 1; IGF1R, insulin-like growth factor binding protein 2; IL-8, interleukin 8; JAK2, Janus kinase 2; JmJc, Jumonji C; JNK, c-Jun N-terminal kinase; KDM, lysine demethylase; LOXL1, lysyl oxidase like 1; LRR, leucine-rich repeat; Meis, homeobox protein Meis1; MGMT, O-6-methylguanine-DNA methyltransferase; MLL1, mixed-lineage leukaemia protein 1; MMP9, matrix metalloproteinase 9; MSK1, mitogen- and stress-activated protein kinase 1; NF κ B, nuclear factor kappa-light-chain-enhancer of activated B cells; OGT, O-GlcNAc transferase; PD-1, programmed cell death protein 1; PDGFR, platelet-derived growth factor receptor; PHD, plant homeodomain; PHF5A, PHD finger protein 5A; PKA, protein kinase A; PRC1, protein regulator of cytokinesis 1; PTEN, phosphatase and tensin homologue; RCCD1, RCC1 domain-containing protein 1; RNA, ribonucleic acid; RNF8, ring finger protein 8; SASH1, SAM and SH3 domain containing 1; SCF, Skp, Cullin, F-box containing complex; SNAI2, snail family transcriptional repressor 2; STAT1/3, signal transducer and activator of transcription 1/3; SWI/SNF, SWItch/sucrose nonfermentable; SWIRM, Swi3p, Rsc8p and Moira; TLX, nuclear receptor subfamily 2 group E member 1; TOP2, topoisomerase-II; TRP, tetratricopeptide; TXNIP, thioredoxin-interacting protein; USP1, ubiquitin specific peptidase 1; Wnt, Wingless-related integration site; YY2, Yin and Yang 2.

1 | INTRODUCTION

Along with genetic abnormalities,¹ epigenetic modifications are critical in the pathogenesis of cancer. Epigenetic modifications include DNA methylation, which is the covalent addition of a methyl group to a cytosine base in DNA, and histone posttranslational modifications, which occur when DNA wraps around the core of two copies of the four histone proteins H2A, H2B, H3 and H4 in the nucleosome. These modifications lead to aberrant changes in gene expression that not only affect cancer progression but also determine the response of tumours to therapeutic modalities.

DNA methylation was the first epigenetic modification identified. DNA methylation impacts genomic stability and acts as a gene silencing mechanism.² Analyses of cancer cell methylomes have highlighted the critical role of DNA hypomethylation in the promoters of key oncogenic genes.³ The second type of epigenetic alteration is post-translational modification of histone N-terminal tails. Histone tails can be marked by phosphorylation, sumoylation, ubiquitination and—the two most studied—acetylation and methylation.

In acetylation, the addition of a negatively charged acetyl group to lysine residues on histone tails weakens the interaction between the histone and DNA. Functionally, histone acetylation is largely associated with active transcription. Thus, hyperacetylation occurring on proto-oncogenes activates gene expression, whereas hypoacetylation of tumour suppressors often causes these genes to be silenced.⁴

Histone methylation is the addition of methyl groups to the arginine and lysine residues on histone tails. Unlike the negative charge caused by acetylation, the methyl group does not provide additional charge and can cause both gene activation and repression. This is explained by the fact that methylation either loosens histone tails to allow access of transcription factors to DNA or, alternatively restricts access of transcription factors to DNA. Arginine methylation occurs on the histone H3 arginines R2, R8, R17, R26 and histone H4 arginine R3. Arginine residues can be monomethylated or dimethylated, with dimethylation occurring in either a symmetric (two separate nitrogen

atoms) or asymmetric (same nitrogen) manner. Functionally, arginine methylation has been associated mostly with the regulation of cell cycle.^{5,6}

The canonical lysine methylation sites are found on histone H3 lysines K4, K9, K27, K36, K56, K79 and on histone H4 lysine K20 (Figure 1). Each lysine can be monomethylated, dimethylated or trimethylated (me1, me2 and me3, respectively). Considering the substantial number of lysines that can be methylated, each with multiple methylation states, histone modifications regulate an array of biological processes (Figure 1). H3K4 methylation, for example, regulates stem cell differentiation and self-renewal, with H3K4me3 involved in activating genes for differentiation.⁷⁻⁹ H3K9 methylation is important for gene silencing during cell fate transitions, heterochromatin maintenance and induction of cellular senescence.¹⁰⁻¹² H3K27 methylation is similarly described as a silencing mark and is critical for the maintenance of gene repression, transcriptional elongation and the silencing

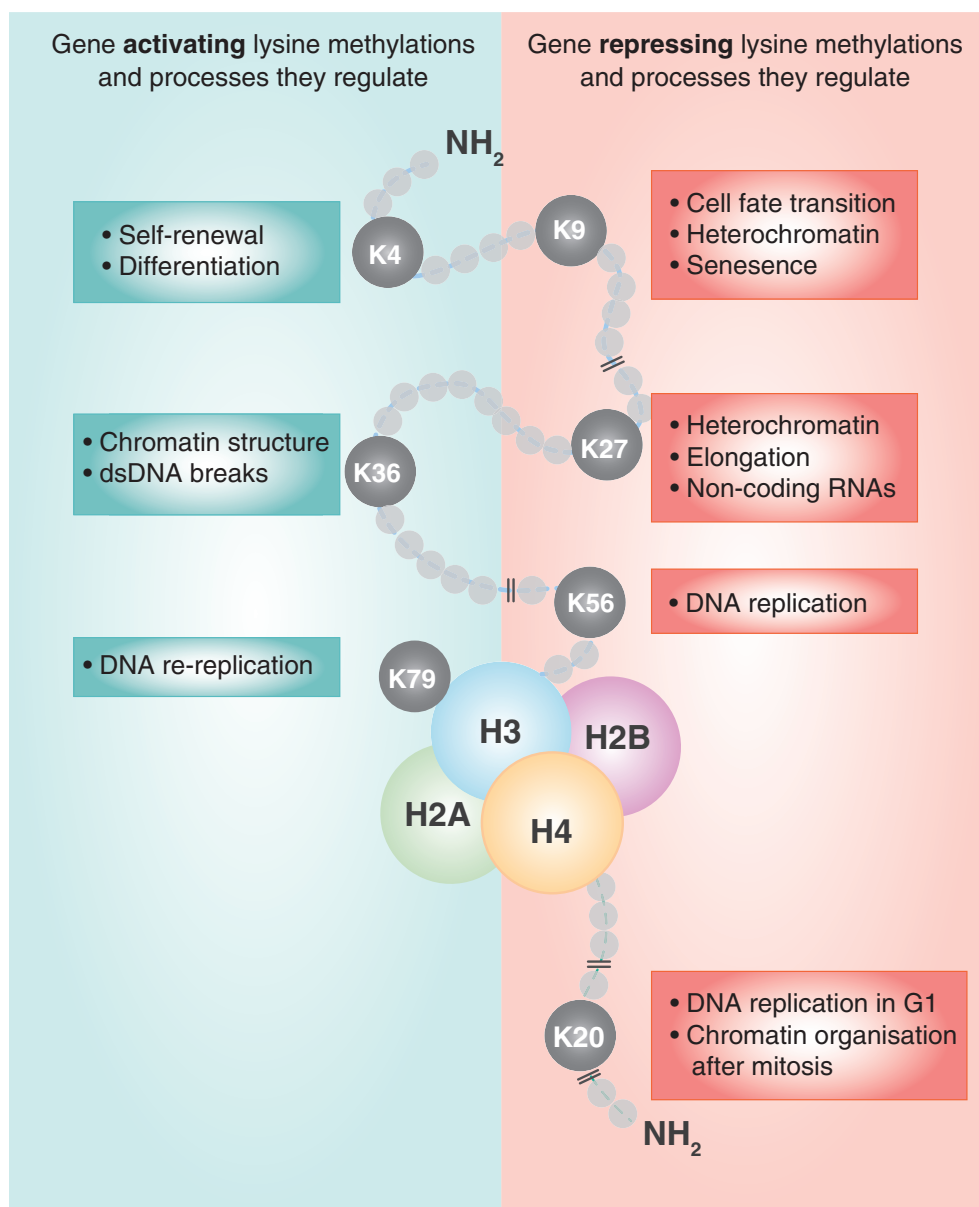


FIGURE 1 Canonical lysine methylation sites and examples of processes they regulate [Color figure can be viewed at wileyonlinelibrary.com]

TABLE 1 Overview of KDMs and their functions in cancer

	Synonyms	Targets	Links to cancer
KDM1A	LDS1, AOF2, KIAA0601	H3K4me2/me1, H3K9me2/me1	Acute myeloid leukaemia—maintains clonogenicity and inhibits differentiation ³⁶ Glioblastoma—inhibition degrades HIF1 α and induces senescence ⁴² Overexpressed in prostate, ⁴³ liver, ⁴⁴ breast, ⁴⁵ colorectal ⁴⁶ and lung tumours ⁴⁷
KDM1B	LDS2, AOF1, C6orf193	H3K4me2/me1	Breast cancer—knockdown reduces colony formation ³⁵ Glioblastoma—suppression maintains glioma-initiating cells in hypoxic environment ⁴⁸
KDM2A	CXXC8, FBL7, FBXL11, JHDM1A, KIAA1004	H3K36me2	Lung cancer—represses DUSP3 phosphatase, thereby activating ERK and JNK signalling, tumour growth and metastasis ⁶⁵
KDM2B	CXXC2, FBL10, FBXL10, JHDM1B, PCCX2	H3K4me3, H3K36me2	Glioblastoma—essential for proliferation of stem cells ⁶¹ Leukaemia—essential for self-renewal of stem cells ⁶²
KDM3A	JMJD1A, JHDM2A	H3K9me2/me1	Colorectal cancer—activates Wnt target genes, thereby enhancing self-renewal of stem cell ⁷³ Prostate cancer—regulates proliferation, survival and drug resistance ⁷⁶ Breast cancer—activates invasion, drug resistance and stemness ⁷⁸ Lung cancer—drives tolerance to taxane-platin therapy ¹⁴¹
KDM3B	JMJD1B, JHDM2B	H3K9me2/me1	Colorectal cancer—activates Wnt target genes, thereby enhancing self-renewal of stem cell ⁷³ Prostate cancer—activates genes needed for metabolism and proliferation ⁷⁹
KDM3C	JMJD1C, JHDM2C	H3K9me2/me1	Leukaemia—critical for the growth of stem cells, independent of demethylase activity ⁸⁰
KDM4A	JMJD2A, JHDM3A	H3K9me3/me2, H3K36me3/me2, H3K23me3	Leukaemia—redundantly promotes proliferation ⁸⁸ Breast cancer—knockout decreases tumour growth ⁹¹
KDM4B	JMJD2B, JHDM3B	H3K9me3/me2, H3K36me3/me2, H3K23me3	Leukaemia—redundantly promotes proliferation ⁸⁸ Gastric cancer—knockdown reduces IL-8, CXCL5 gene expression ⁹²
KDM4C	JMJD2C, JHDM3C	H3K9me3/me2, H3K36me3/me2	Leukaemia—redundantly promotes proliferation ⁸⁸ Glioblastoma—activates Wnt target genes ⁹³ Prostate cancer—knockdown reduces phosphorylation of proliferative kinases and increases expression of PTEN ⁸⁹
KDM4D	JMJD2D	H3K9me3/me2	Colorectal cancer—promotes tumour formation in mice ⁹⁵
KDM4E	JMJD2E	H3K9me3/me2	No function in cancer identified to date.
KDM5A	JARID1A, RBBP2	H3K4me3/me2	Breast cancer—decreases expression of tumour suppressors p16 and p27 ⁹⁹ Lung cancer—promotes proliferation by repressing NOTCH1/2 tumour suppressor target genes ¹⁰⁰ Lung cancer—promotes tolerance to EGFR inhibitors ^{138,139} Glioblastoma—controls resistance to standard-of-care temozolomide ¹⁴⁹
KDM5B	JARID1B	H3K4me3/me2	Leukaemia—downregulates <i>Hox/Meis</i> genes required for acute myeloid leukaemia pathogenesis ¹⁰² Melanoma—tumour suppressive role ¹⁰³ Melanoma—maintains slow-cycling stem cell population resistant to therapy ^{140,143} Myeloma—inhibition attenuates proliferation ¹⁰¹

(Continues)

TABLE 1 (Continued)

	Synonyms	Targets	Links to cancer
KDM5C	JARID1C	H3K4me3/me2	Breast cancer—inhibits migration, invasion and angiogenesis ¹⁰⁴ Renal cancer—tumour suppressive function, downregulation triggers genomic instability ¹⁰⁵
KDM5D	JARID1D	H3K4me3/2	Prostate cancer—represses invasive genes <i>MMP1</i> , <i>MMP2</i> , <i>MMP3</i> , <i>MMP7</i> and <i>SNAI2</i> ¹⁰⁶ Renal cancer—reduces cell viability ¹⁰⁷
KDM6A	UTX	H3K27me3/2	Breast cancer—knockdown inhibits proliferation, colony formation and migration ¹⁰⁹ Pancreatic cancer—knockout decreases expression of the tumour suppressor genes ¹¹⁰ Myeloma—depletion promotes tumorigenicity and confers sensitivity to EZH2 inhibition ¹¹¹ Lung cancer—deletion promotes tumour progression through an increase in EZH2/H3K27me3 ¹¹³ Acute lymphoblastic leukaemia—bona fide tumour suppressor ¹¹⁴ Pancreatic cancer—depletion induces metastasis in females ¹¹⁵ Suppresses myeloid leukemogenesis through noncatalytic functions ¹¹⁶ Glioblastoma—essential for stem cell transition to a drug-tolerant state ¹⁴⁴
KDM6B	JMJD3	H3K27me3/me2	Neuroblastoma—inhibits proliferation and increases differentiation of stem-like cells ¹¹⁷
KDM6C	UTY		Suppresses myeloid leukemogenesis through noncatalytic function, similar to KDM6A ¹¹⁶
KDM7A	JHDM1D, KDM7, KIAA1718	H3K9me2/me1, H3K27me2/me1, H4K20me1	Prostate cancer—knockdown attenuates proliferation of hormone-sensitive cancer cells ¹²¹ Glioblastoma—maintains viability of stem cells ⁹⁴
KDM7B	PHF8	H3K9me2/me1, H3K27me2/me1, H4K20me1	Laryngeal and hypopharyngeal squamous cell carcinoma—high expression correlates with increased chance of relapse and decreased survival rate ¹²²
KDM7C	PHF2	H3K9me2	Essential for progenitor self-renewal and cell cycle progression in neural progenitor cells ¹²⁰ Colon cancer—activates transcription of p53 target genes and p53-mediated cell death ¹¹⁹
KDM8 ^a	JMJD5	H3K36me2	Different tumours—inhibits cell proliferation ¹²³⁻¹²⁵

^aKDM8 demethylases activity remains elusive.

of long noncoding RNAs.¹³⁻¹⁵ H3K36 methylation is both a key player in controlling chromatin structure during transcription and integral to DNA double-strand break repair. H3K36 methylation initiates checkpoint activation and enables maintenance of chromatin structure at sites of breakage.¹⁶ H3K56 methylation represses chromatin state and regulates DNA replication.¹⁷ Demethylation of the H3K79 residue found in the globular domain maintains genomic stability as it associates with chromatin to prevent DNA re-replication.¹⁸ Finally, H4K20 methylation controls the chromatin compaction threshold by limiting DNA replication in the G₁ cell cycle phase and ensures normal chromatin organisation after mitosis.¹⁹

Lysine methylation is regulated by histone lysine methyltransferases and histone lysine demethylases (KDMs), which add

or remove methyl groups, respectively. Lysine methyltransferases have been recently reviewed in detail elsewhere.²⁰ Here we review the functions of KDMs in cancer (summarised in Table 1), the regulatory mechanisms underlying their increased expression in tumours and how they affect the efficacy of cancer drugs.

2 | HISTONE LYSINE DEMETHYLASES

There are eight KDM subfamilies (KDM1-8), which vary in terms of their structure and lysine targets. KDM1 contains a flavin adenine dinucleotide-dependent amine oxidase domain, which erases mono-methylation and dimethylation marks. The amino oxidase domain acts

by a hydride transfer on the ϵ -amine of lysine to form an unstable imine that spontaneously hydrolyses into formaldehyde.^{21,22} Because this imine product formation requires a lone pair of electrons in the nitrogen of the methyl lysine, KDM1 enzymes cannot demethylate trimethyl groups as the quaternary amines do not have a lone pair of electrons.²³

KDM2-8 subfamilies contain a catalytic Jumonji C (JmjC) domain and remove monomethylation, dimethylation and trimethylation marks on lysines.^{24,25} The demethylating activity of the JmjC domains requires Fe^{2+} , 2-oxoglutarate (2-OG) and oxygen to hydroxylate the methyl to hydroxymethyl, which is then released as formaldehyde. In addition to the JmjC catalytic domains, all KDM subfamilies contain additional N-terminal interaction elements referred to as JmjN, which provide structural integrity without participating in active site formation.^{26,27}

F-box, Leu-rich repeat (LRR) and tetratricopeptide (TRP) domains are all important for protein-protein interactions. Additionally, KDMs contain a wide variety of DNA and histone binding domains such as Swi3p, Rsc8p and Moira domain (SWIRM), AT-rich interacting domain (ARID), plant homeodomain (PHD), zinc fingers and Tudor domain. For example, KDM2 and KDM7 both have one PHD domain,^{28,29} whereas KDM5s contain two or three PHD domains, which are necessary for the binding to H3K4.³⁰ The N-terminal PHD domain binds to H3K4me1 and the C-terminal PHD domain binds to H3K4me3/me2.³¹ The PHD domain of KDM7, in contrast, is reported as nonessential for its catalytic activity.²⁹ Within the KDM family, only KDM4A-C contain a conserved double Tudor domain with slight variations, which create different lysine binding preferences between these three KDM4 isoforms.³² KDM4D and KDM4E are shortened versions of the KDM4 enzymes, not containing Tudor domains and likely using the variation within the JmjC domain for lysine recognition.³³ This suggests that the JmjC catalytic domain is also important for the KDMs' binding preferences. The lysine specificities of particular KDM subfamilies (Figure 2) and the connection of KDMs to various tumours are discussed below.

2.1 | KDM1

The first histone KDM identified was KDM1A as a part of the C-terminal binding protein 1 corepressor complex.³⁴ KDM1A demethylates H3K4me2/me1, and when complexed to an androgen receptor it demethylates H3K9me2/me1, leading to the monomethylated and unmethylated H3K4 and H3K9 (Figure 2).²³ The KDM1A mammalian homologue KDM1B demethylates only H3K4me2/me1. As methylation of H3K4 activates gene transcription, increased KDM1A/B expression results in specific gene repression.³⁵⁻³⁷ In contrast, KDM1A-dependent H3K9 demethylation triggers gene activation programs.^{38,39}

KDM1A is highly expressed in various cancers and, through its demethylase activity, mostly regulates the balance between self-renewal and differentiation of stem cells. In acute myeloid leukaemia cells, KDM1A maintains clonogenicity and inhibits differentiation

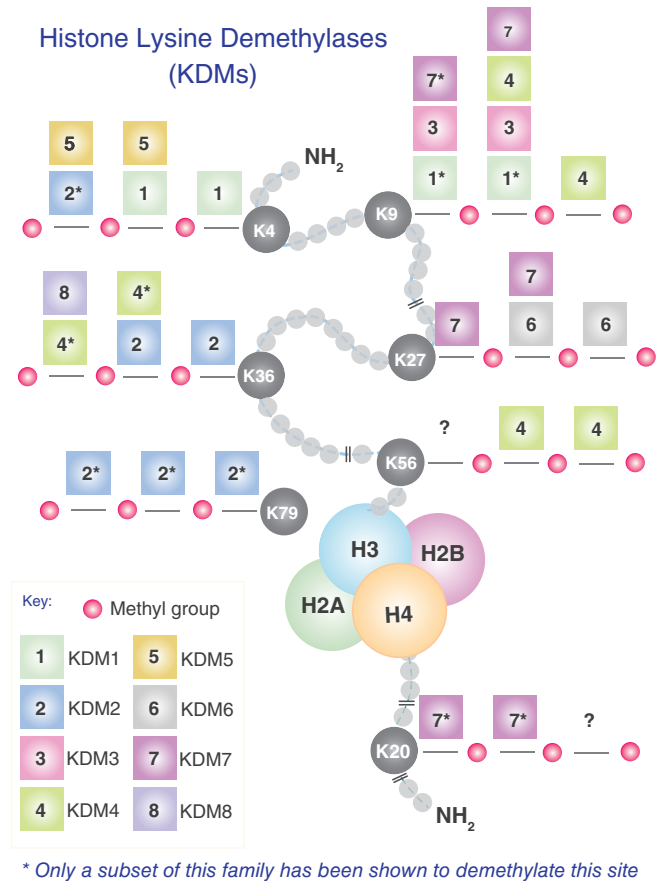


FIGURE 2 Histone lysine demethylases (KDM) and their targeted lysine residues [Color figure can be viewed at wileyonlinelibrary.com]

through H3K4 demethylation.³⁶ Similarly, differentiation of neural stem cells requires low KDM1A levels and an increase in H3K4 methylation. This results in the repression of the target genes of TLX,⁴⁰ an important nuclear receptor that regulates cell cycle progression by upregulating p21 and downregulating cyclin D1.⁴¹ KDM1A inhibition results in proteasome-mediated degradation of HIF1 α , which in turn is sufficient to induce senescence in glioblastoma cells.⁴² The overexpression and carcinogenic activities of KDM1A have been also reported in prostate,⁴³ liver,⁴⁴ breast,⁴⁵ colorectal⁴⁶ and lung cancers.⁴⁷

In contrast, KDM1B has not been found to be altered in many cancers. One study has reported that knockdown of KDM1B reduces breast cancer cell colony formation by increasing H3K4 methylation.³⁵ In glioblastoma, hypoxia-induced miR-215 is vital for adaptation of glioma-initiating cells to the hypoxic environment via suppression of KDM1B expression and associated modulation of glucose metabolism and angiogenesis.⁴⁸

In addition to histone demethylase activity, studies have shown that KDM1A also demethylates nonhistone proteins such as p53, E2F1 and HIF-1 α ⁴⁹⁻⁵¹ and exhibits demethylase-independent functions. For example, KDM1A is a pseudosubstrate for the tumour suppressor FBXW7, a crucial component of the ubiquitin ligase SCF complex. By binding to FBXW7, KDM1A promotes FBXW7 self-

ubiquitylation and degradation, thereby abrogating its function in tumour suppression.⁵² Intriguingly, the noncatalytic function of KDM1B contributes to repressive chromatin H3K9 methylation by forming a stable complex with the H3K9 methyltransferase G9a.⁵³ KDM1B has also been suggested to function as an E3 ubiquitin ligase, leading to the proteasomal degradation of O-GlcNAc transferase (OGT), an enzyme often increased in cancer.⁵⁴

2.2 | KDM2

The first documented JmjC demethylases were the KDM2A and KDM2B proteins.⁵⁵ KDM2A demethylates H3K36me2.⁵⁶ The specificity of KDM2B is currently contested, with some reporting demethylase activity at H3K4me3,^{57,58} and others demonstrating specific targeting of H3K36me2 (Figure 2).⁵⁹⁻⁶³ Nevertheless, both H3K36 and H3K4 methylations activate gene transcription and thus KDM2A/B generally repress genes.⁶⁴

Although much remains unknown about the exact functions of KDM2 enzymes, their overexpression in tumours suggests that KDM2 may be a drug target in certain cancers. KDM2A promotes progression of lung cancer by epigenetically enhancing ERK1/2 and JNK1/2 signalling. KDM2A-dependent H3K36 demethylation at the promoter of the dual-specificity protein phosphatase 3 (DUSP3) represses its expression, thus increasing ERK1/2 and JNK1/2 activities. This in turn promotes tumour growth and invasion to the lymph nodes.⁶⁵ In mouse embryonic fibroblasts, KDM2B knockdown induces senescence whereas KDM2B re-introduction restores proliferation by decreasing the tumour suppressor p15^{Ink4b} through H3K36me2 demethylation.⁵⁹ KDM2B is essential for leukaemia stem cell self-renewal⁶² and proliferation of glioblastoma stem cells.⁶¹ Knockdown of KDM2B in glioblastoma cells decreases the abundance of H3K36me2, reduces actively proliferating cells and causes DNA damage accumulation, implicating KDM2B in the maintenance of glioblastoma stem cells.

Apart from the demethylation of H3 tails, KDM2 also demethylates the nonhistone proteins NF- κ B and β -catenin^{66,67} and exhibits demethylase-independent roles. This includes recognition of CpG island, and recruitment of PRC1 to silence certain polycomb target genes in embryonic stem cells.⁶⁸ Furthermore, KDM2 proteins constrain gene expression from CpG island associated gene promoters by shaping RNA polymerase II occupancy.⁶⁹

2.3 | KDM3

KDM3A and its two human homologues KDM3B and KDM3C demethylate repressive H3K9me2 and H3K9me1 marks (Figure 2).⁷⁰ Several studies have reported that KDM3 catalytic activity extends beyond the demethylation of H3K9 and that KDM3 might also demethylate H4R3 and nonhistone targets.⁷¹ Given that H3K9me2/me1 are prominent marks of heterochromatin and inactive genes, removal of these marks by KDM3 is

expected to increase initiation of gene transcription. However, H3K9me1 is frequently found at active genes, and so targeting KDM3 proteins could potentially contribute to decreased transcription. As such, the net impact of KDM3-mediated H3K9 demethylation on gene transcription is dependent on the gene promoter, cell type or state of the cell.⁷¹

KDM3 enzymes are overexpressed in various tumours where they facilitate efficient tumour growth. In colorectal tumours, KDM3A/B profoundly alter the transcription of Wnt/ β -catenin target genes *c-Myc*, cyclin D1, *MMP9*; thereby enhancing self-renewal of colorectal cancer stem cells.^{72,73} They do so by reducing H3K9 methylation and indirectly increasing H3K4 methylation by recruiting the lysine methyltransferase MLL1. Interestingly, KDM3A is phosphorylated by Janus kinase 2 (JAK2). This phosphorylation enhances KDM3A binding to STAT3, where KDM3A-mediated H3K9me2 demethylation at the promoters of STAT3 target genes activates *c-Myc* transcription, thus increasing cell proliferation and motility.⁷⁴ In prostate cancer cells, KDM3A promotes recruitment of androgen receptor (AR) to the *c-Myc* gene enhancer and induces H3K9me3 demethylation, thereby promoting transcription of *c-Myc* mRNA and cell survival.⁷⁵ Other potential ways by which KDM3A might facilitate prostate carcinogenesis include recruitment of heterogeneous nuclear ribonucleoprotein F for the alternative splicing and generation of the androgen receptor splicing variant 7 (a constitutively active form of AR responsible for resistance to hormonal therapies).⁷⁶ In addition to promoting prostate cancer, KDM3A has been implicated as a potential therapeutic target in breast cancer where KDM3A is overexpressed and necessary for oestrogen receptor function.⁷⁷ KDM3A also induces pro-invasive genes by erasing repressive H3K9me3 marks and promotes chemoresistance by demethylating nonhistone protein p53.⁷⁸

Both KDM3B and KDM3C have also been reported to perform oncogenic functions. KDM3B promotes the recurrence of aggressive prostate cancer cells after androgen deprivation therapy through its H3K9me2 demethylase activity at the specific promoters of genes needed for metabolism and proliferation.⁷⁹ KDM3C appears to be critical for the growth of leukaemia stem cells where its overexpression upregulates several glycolytic enzymes. Notably, this metabolic function of KDM3C is independent of its demethylase activity as there are no changes in H3K9me2 levels of upregulated glycolytic genes.⁸⁰

Consistent with their epigenetic H3K9 demethylating activities, KDM3 proteins are predominantly localised within the nucleus of many cancer cells. Interestingly, KDM3 localisation is mechanosensitive, with KDM3 being cytoplasmic and downregulated on soft matrix.⁸¹ Others have reported that the catalytic activity of KDM3 proteins is not always required for many aspects of their function. For example, when KDM3A interacts with SWI/SNF chromatin remodelling complex, this scaffolding function does not require demethylase activity yet facilitates induction of gene transcription.⁸² A similar demethylase-independent scaffolding function has been proposed for the KDM3A-mediated stabilisation of the GLI1 transcription factor.⁸³

2.4 | KDM4

All five KDM4A-E enzymes demethylate H3K9me3/me2⁸⁴ and KDM4A-C also show demethylase activity at H3K36me3/2 (Figure 2).⁸⁵ Furthermore, KDM4A and KDM4B demethylate H3K23me3—a poorly understood lysine site found in spermato-cytes.³² Binding of KDM4A/B/C to H3K4me3 and H4K20me2/me3 has been reported without any demethylation specificities. Despite the fact that numerous lysine residues are targeted by KDM4, demethylation of the gene repressing H3K9me3/me2 and gene activating H3K36me3/me2 marks appears to be the most prominent function of KDM4.^{86,87} Thus, depending on the targeted lysine residue, the effect of KDM4 on transcription can be either activating or repressing.^{88,89}

Several studies demonstrate functional redundancy of KDM4 enzymes. While single knockout mice for KDM4A/B/C and double knockout mice for KDM4A/B and KDM4B/C are viable, KDM4A/C double- and KDM4A/B/C triple-knockout mice are embryonically lethal.⁹⁰ Further analysis has shown that KDM4A and KDM4C redundantly regulate histone via demethylation of H3K9me3 and H3K36me3 at highly similar transcriptional start sites.⁹⁰ Demethylation of H3K9me3 is required for transcriptional activation of the proliferative JAK-STAT pathway in leukaemia cells, but only the KDM4A/B/C triple knockout attenuates progression of acute myeloid leukaemia in mice.⁸⁸

In contrast, other cancer types depend solely on one member of the KDM4 subfamily. Single knockdown of KDM4A in breast cancer cells increases the H3K9me3 repressive mark at the EGFR promoter, resulting in decreased tumour growth, whereas knockdown of KDM4B/C/D has no effect.⁹¹ Antitumour efficacy of single KDM4B knockdown has been determined in chemokine IL-8-dependent gastric cancer. KDM4B demethylates H3K9me3/me2 at the promoter region of IL-8 to mediate IL-8 gene activation and gastric cancer progression.⁹² KDM4C knockdown in prostate cancer cells reduces the phosphorylation of several proliferative kinases while increasing the expression of the tumour suppressor PTEN, via epigenetic mechanisms associated with H3K9 and H3K36 demethylation.⁸⁹

KDM4C, but not KDM4A and KDM4B, are highly expressed in glioblastomas. Activation of Wnt in glioblastoma stabilises KDM4C protein which then promotes tumorigenesis by epigenetically activating Wnt target genes.⁹³ Further supporting the oncogenic role of KDM4C, glioblastoma stem cells contain low H3K9me3/me2 and H3K27me3/me2 levels compared to their differentiated counterparts.⁹⁴ KDM4D and H3K9me3 demethylation promotes colorectal tumour formation in mice through increasing levels of β -catenin, c-Myc and cyclin D1, which has been reversed with single KDM4D knockdown.⁹⁵ No studies to date have focused on the role of KDM4E in cancer and KDM4E has been considered a pseudogene.⁹⁶ Nevertheless, KDM4E is confirmed as a protein-encoding gene, with several studies briefly mentioning the KDM4E gene and/or protein.^{84,97,98}

2.5 | KDM5

Unlike other KDM subfamilies, which target several lysine residues, the KDM5 subfamily has catalytic activity only at gene activating H3K4me3/me2 marks (Figure 2). This suggests that KDM5A-D enzymes could be potential players in the downregulation of tumour suppressors as well as oncogenes. There is emerging evidence of pathological consequences of KDM5 deregulation in various types of cancer. In breast cancer, KDM5A-mediated H3K4me3 demethylation downregulates expression of genes encoding tumour suppressor proteins p16 and p27.⁹⁹ KDM5A also promotes proliferation of small cell lung cancer cells by repressing NOTCH1 and NOTCH2 tumour suppressors' target genes.¹⁰⁰ In further support of the oncogenic roles for KDM5A, potent and selective KDM5 inhibitors stops proliferation of myeloma cells.¹⁰¹

Leukaemia stem cells are maintained in a hyper-H3K4me3 and hypo-H3K79me2 state, and KDM5B inhibits their oncogenic potential by reducing H3K4me3/me2 levels on oncogenes such as *Hox/Meis*.¹⁰² Similarly, KDM5B/C under-expression in primary melanoma and breast cancer cells is consistent with a possible tumour suppressive function.^{103,104} Lower levels of KDM5C in renal cancer cells promote a transcriptionally active H3K4me3, triggering genomic instability and poor prognosis in patients.¹⁰⁵ In prostate cancer, KDM5D represses invasive genes *MMP1*, *MMP2*, *MMP3*, *MMP7* and *SNAI2* through the demethylation of H3K4me3 at their promoter regions. In support, KDM5D expression is low in metastatic prostate tumours compared to primary tumours.¹⁰⁶ Furthermore, loss of the entire Y-chromosome is common in clear cell renal carcinoma and results in lower expressions of KDM5D and KDM6C compared to tumours without a loss of the Y-chromosome. Ectopic expression of KDM5D in a renal cancer cells reduces their viability.¹⁰⁷ Together these studies imply a tumour suppressive role of KDM5 in a context-dependent manner.

2.6 | KDM6

KDM6A and KDM6B act on H3K27me3/me2 marks of gene repression (Figure 2). Thus, increased KDM6 expression generally leads to gene activation.¹⁰⁸ The roles of KDM6 enzymes in cancer appear context-dependent as evidence posits contradictory functions for these demethylases.

Loss of KDM6A in breast cancer cells decreases proliferation and migration. These effects are reversed when a catalytically active KDM6A is reintroduced, suggesting that KDM6A is responsible for these cancer hallmarks.¹⁰⁹ Controversially, numerous studies support the role of KDM6A as a tumour suppressor. For example, KDM6A-negative pancreatic ductal adenocarcinoma patients have worse overall survival compared to KDM6A-positive patients.¹¹⁰ This study further reports that KDM6A knockout decreases expression of the tumour suppressor genes *CDKN1A*, *LOXL1*, *SASH1*, *TXNIP*, *IGFBP2*, but also notes that these changes could be attributed to a decrease in H3K27 acetylation as opposed to an increase in H3K27me3 levels when KDM6A is knocked out.¹¹⁰

In multiple myeloma, loss of KDM6A promotes proliferation and confers sensitivity to EZH2 inhibition.¹¹¹ Similarly, KDM6A is frequently inactivated in urothelial bladder carcinoma cells, which are sensitive to EZH2 inhibition. In vivo, EZH2 inhibition causes regression of KDM6A-null bladder tumours.¹¹² The tumour suppressive function of KDM6A and its link to EZH2 are also critical to lung cancer progression. KDM6A deletion in vivo promotes lung cancer progression mainly through an increase in EZH2 and H3K27me3 levels. KDM6A-knockout lung cancer cells are sensitive to EZH2 inhibition, leading to significantly decreased proliferation and increased apoptosis.¹¹³

Likewise, KDM6A has been proposed to be a tumour suppressor in leukaemia and pancreatic cancers. KDM6A-knockdown results in significant acceleration of leukaemia onset in a NOTCH1-induced leukaemia mouse model.¹¹⁴ In K-Ras^{G12D} driven pancreatic cancer, KDM6A loss induces squamous-like metastatic tumours selectively in females through aberrant activation of super-enhancers regulating various oncogenes. Furthermore, KDM6A-deficient pancreatic cancer cells are sensitive to BET inhibitors, which reverses squamous differentiation and restrains tumour growth in vivo.¹¹⁵ Finally, KDM6A suppresses myeloid leukemogenesis through a noncatalytic function. KDM6A loss upregulates a transcriptional program driven by the ETS family of oncogenic transcription factors and downregulates a program of GATA-driven genes through loss of chromatin accessibility and local H3K27 acetylation.¹¹⁶

KDM6B has tumour suppressive roles and has been found to be downregulated in neuroblastoma stem-like cells. An overexpression of KDM6B inhibits proliferation and induces differentiation genes, suggesting that the demethylase activity of KDM6B is responsible for neuroblastoma differentiation.¹¹⁷

2.7 | KDM7

The KDM7 subfamily has catalytic activity at several lysines on histone tails. KDM7A and KDM7B predominantly target H3K9me2/me1, H3K27me2/me1 and H4K20me1,¹¹⁸ while KDM7C shows only H3K9me2 demethylase activity (Figure 2).^{119,120} H3K9 and H4K20 methylation are associated with gene silencing, while H3K27 methylation results in gene activation (Figure 1), which implies that KDM7 activity causes both gene activation and gene repression in a lysine-dependent context.

Very few studies have focused on the function of KDM7 proteins, but some of these publications have implicated KDM7 enzymes as drivers of tumorigenesis. Knockdown of KDM7A, and consequently decreased H3K27me2 levels in hormone-sensitive prostate cancer cells, downregulate androgen receptor signalling and cell proliferation.¹²¹ KDM7A maintains viability of glioblastoma stem cells by ensuring low H3K9 and H3K27 methylation.⁹⁴ Patients with laryngeal and hypopharyngeal squamous cell carcinoma showing high KDM7B expression and low H3K9me2/H3K27me2 levels have an increased chance of relapse.¹²² A study using neural progenitor cells found that KDM7C demethylates H3K9me2 at promoter regions of YY2 and

E2F4 genes, which are responsible for progenitor self-renewal and cell cycle progression.¹²⁰ In contrast, KDM7C has been found to be downregulated in colon and stomach cancers, where it acts as a tumour suppressor in association with p53. KDM7C demethylates H3K9me2 at p53 target gene *CDKN1A* and *HDM2* promoters, thereby activating transcription of p53 target genes and cell death.¹¹⁹

2.8 | KDM8

The newest member of the KDM family, the KDM8 protein, has many important biological roles. Several recent studies have identified overexpression of KDM8 being oncogenic in colon and breast cancer, providing evidence that loss of KDM8 compromises cancer cell proliferation.¹²³⁻¹²⁷ At the molecular level, the ability of KDM8 to regulate the cell cycle is linked to upregulation of cyclin A,¹²³ modulation of the expression of p53 and p21¹²⁸ and interaction with spindle microtubules.¹²⁹ Moreover, a centromere and DNA-binding protein RCCD1 augments KDM8 activity and the RCCD1-KDM8 complex controls cell cycle-regulated transcriptional repression and accurate mitotic division.¹³⁰

Despite its important pathological roles, the biochemical function of KDM8 remains elusive. Early studies identified KDM8 as a H3K36me2 demethylase, regulating cyclin A1 expression,¹²³ but this assignment has not been validated subsequently.^{131,132} High-resolution crystal structures of the KDM8 catalytic domain in complex with the co-factor 2-OG suggest that KDM8 was not a lysine demethylase and biochemical assays show no demethylase activity on any H3 or H4 residue.^{132,133} Other studies suggest that KDM8 may function as a dioxygenase,¹³¹ as well as an aminopeptidase mediating proteolytic cleavage of monomethylated histone tails to modulate chromatin conformation.^{134,135} Finally, KDM8 has been reported to function as a JmjC arginyl-hydroxylase, the first such catalytic activity identified for a human enzyme.¹³⁶ Taken together, these findings suggest that KDM8 may have some H3K36me2 demethylase activity in mammalian cells, but it is probably not a major demethylase at this site compared to the other H3K36 demethylases KDM2 or KDM4.

3 | KDMS AND CANCER THERAPY

In addition to directly regulating tumour progression (Table 1), excessive activity of KDMS is frequently implicated in the failure of cancer drugs. Changes in histone methylation are crucial for cell plasticity—a phenotypic switching process that cancer cells use to adopt cell states that are insensitive to drug-targeted pathways.¹³⁷ As the majority of cancer drugs target rapidly proliferating cells, a specific subpopulation of cancer stem cells, known as drug-tolerant persisters, uses various mechanisms of cell plasticity to convert to a reversible slow-proliferating state that counteracts antiproliferative therapies.^{138,139}

Increasing number of studies have found that this transition to a slow-cycling, drug-tolerant state, which facilitates acquisition of the drug resistant phenotype, is driven by specific KDMS.^{140,141} For

example, nonsmall cell lung cancer cells that are tolerant to taxane-platin treatment show increased expression of numerous *KDM* genes, with *KDM3A* being the most prominent and confirmed to be associated with poor patient survival. In support of elevated *KDM* activity, drug-tolerant cells show a global decrease in H3K9 and H3K27 methylation at the transcription start sites for specific genes. As these lung cancer cells transition to taxane-platin resistance, they also become more susceptible to *KDM* inhibitors.¹⁴¹

Notably, several studies implicate that *KDM5* plays a significant role in cell plasticity and drug tolerance.¹⁴² Lung cancer cells tolerant to epidermal growth factor receptor (EGFR) inhibitors show high expression of *KDM5A* and prominent H3K4me3/me2 demethylation. *KDM5A* knockdown prior to treatment with EGFR inhibitors reduces the number of drug-tolerant persisters.¹³⁸ Similarly, by blocking H3K4 demethylase activity, the *KDM5A* inhibitor CPI-455 reduces the number of lung cancer cells that are tolerant to the EGFR inhibitor erlotinib and melanoma cells that are tolerant to the B-Raf inhibitor vemurafenib.¹³⁹ A study of melanoma has reported high expression of *KDM5B* in the slow-growing cell subpopulation tolerant to various cancer drugs including cisplatin, vemurafenib, bortezomib, salinomycin and temozolomide. Importantly, *KDM5B* knockdown and consequently increased H3K4me3 prevents melanoma stem cells from shifting from a proliferative drug-sensitive state to a slow-proliferating drug-tolerant state, thereby sensitising tumours to vemurafenib and bortezomib treatments.^{140,143} These studies, together with those identifying *KDM5* as a tumour suppressor, provoke the intriguing hypothesis that tumour suppressors attenuate the efficacy of antiproliferative cancer drugs. Similarly, *KDM6A/B* is important for the survival of glioblastoma cells that are tolerant to the lethal doses of the PDGFR kinase inhibitor dasatinib. *KDM6A/B*-dependent H3K27me3 demethylation has been shown to be essential for a subpopulation of glioblastoma stem cells to transition to a slow-cycling Notch-dependent state that enables dasatinib-tolerance.¹⁴⁴

In addition to the regulation of cell plasticity and associated drug tolerance, several studies suggest different molecular mechanisms by which *KDMs* contribute to the failure of cancer drugs. One example is a study showing that combining *KDM1A* inhibitors with PD-1 antibody significantly suppresses growth and metastasis of triple-negative breast cancer tumours, which is mechanistically linked to increased T-cell recruitment via chemokine production.¹⁴⁵ Anthracyclines are an effective breast cancer chemotherapy that act in part through the inhibition of topoisomerase-II (TOP2) on accessible DNA. *KDM4B* has been shown to increase DNA accessibility for TOP2 binding, which increases anthracycline sensitivity.¹⁴⁶ The efficacy of the HER-targeting agent trastuzumab is improved with *KDM5* inhibitors in HER2-positive breast cancer cells.¹⁴⁷ Genetic deletion of *KDM5A/B* or inhibition of *KDM5* activity increases sensitivity to the anti-oestrogen drug fulvestrant in both hormone-sensitive and endocrine-resistant breast cancer cells.¹⁴⁸ In a study investigating MGMT-independent mechanisms of temozolomide resistance, *KDM5A* was found to be upregulated in temozolomide-resistant glioblastoma cells, with *KDM5A* inactivation restoring sensitivity to temozolomide.¹⁴⁹

4 | REGULATION OF *KDMs* EXPRESSION AND ACTIVITY

As discussed, *KDMs* not only play catalytically active roles in epigenetic gene regulation, but also possess various catalytically independent roles in cancer. While our understanding of *KDMs*' function is greater than the understanding of their regulation, it is clear that cancer cells have developed various methods of regulating their levels and activity.

Gain-of-function mutations are often a hallmark of an oncoprotein. The *KDM4C* gene was identified and cloned from the 9p24 amplified region of oesophageal cancer cells.¹⁵⁰ Both *KDM4C* and *KDM5A* genes have been found to be significantly amplified in breast cancers.^{151,152} The first reported histone demethylase found to be inactivated by mutation was *KDM6A*¹⁵³ and somatic inactivating mutations in *KDM6A* have been reported in several adult and paediatric malignancies^{154,155} However other *KDMs*, such as *KDM3* have a low mutation and amplification frequency in most tumour types,⁷¹ suggesting that the tumour-driving function of *KDMs* are more likely associated with deregulation of protein levels. For example, *KDM2A* is hypoxia-inducible at the transcriptional level as HIF-1 α is required for the recruitment of RNA polymerase II to the *KDM2A* promoter.⁵⁵ Further *KDMs* induced by hypoxia, some in a HIF-dependent manner, include *KDM3A*, *KDM4B/C*, *KDM5C* and *KDM6A*.^{156,157} Ubiquitination by SCF ubiquitin ligase complex controls the activity of *KDM4A* by targeting it for proteosomal degradation.^{158,159} *KDM4A* is also regulated by ubiquitination in response to DNA damage by the RNF8 and RNF168 complexes,¹⁶⁰ while deubiquitination by USP1 stabilises *KDM4A*. This deubiquitination leads to increased *KDM4*-promoted recruitment of androgen receptor to the *c-Myc* gene enhancer and prostate cancer cell proliferation.¹⁶¹

Posttranslational acetylation and phosphorylation further contribute to the regulation of *KDMs*' expression and activity. Acetylation of PHF5A increases *KDM3A* expression by regulating its pre-mRNA alternative splicing.¹⁶² Phosphorylation of *KDM7A* by PKA facilitates interaction with ARID5B and recruitment to target promoters, where it activates gene transcription via demethylation of H3K9me2.¹⁶³ In a similar manner, MSK1 phosphorylates *KDM3A*, which is then recruited by the transcription factor Stat1 to demethylate H3K9me2 and activate *KDM3A*-target genes.¹⁶⁴

Finally, *KDMs* rely on cofactors such as oxygen, 2-oxoglutarate and S-adenosyl methionine, some of which are key intermediates in metabolic processes. Thus, *KDM* activities are sensitive to the metabolic state of cells and their microenvironment. Interestingly, while hypoxia increases transcription and protein levels of certain *KDMs*, lower oxygen availability in the hypoxic cores of solid tumours leads to a substantial reduction in *KDM* catalytic activities. Aerobic glycolysis, a modified cellular metabolism specific to cancer cells that reduces 2-OG levels, could potentially inhibit *KDM* activity. In addition, the oncometabolite succinate and fumarate act as competitive inhibitors for 2-OG. Thus, loss-of-function mutations in succinate dehydrogenase or fumarate hydratase cause accumulation of succinate and fumarate, thereby potentially inhibiting catalytic activities of *KDMs*.

Neomorphic mutations in isocitrate dehydrogenase IDH1/2, a hallmark of low-grade gliomas,¹⁶⁵ lead to the production of another oncometabolite, 2-hydroxyglutarate, which also competes with 2-OG in the catalytic centre of KDMs. Altogether, metabolic changes in cancer cells alter KDM activities, which could be linked to tumourigenesis, especially if the inhibited KDM acts as a tumour suppressor. Whether these mechanisms of KDM regulation are relevant in any tumour type needs further evaluation in a context-dependent manner.

5 | CONCLUSION

Histone lysine methylation and demethylation are important mechanisms for regulating chromatin and thus all DNA-templated processes. Histone methylation-driven epigenetic control of gene expression is extremely complex due to the large number of lysine residues that can be methylated into three distinct states. Nevertheless, fuelled by discoveries from numerous laboratories across the globe, the scientific community has developed an understanding how histone methylation events contribute to cancer. Given their drugability, KDMs are particularly important targets in epigenetic drug discovery pipelines. While for some subfamilies, such as KDM5, significant progress has been made in delineating signalling pathways in different cancers and development of high-quality chemical probes and inhibitors, much remains unknown about other subfamilies, such as KDM7 and KDM8. Furthermore, targeting noncatalytic functions of KDMs will require chemical probes and inhibitors targeting protein-protein interactions, and such compounds are yet to be developed.

CONFLICT OF INTEREST

All authors declare no conflict of interest.

ORCID

Lenka Munoz  <https://orcid.org/0000-0002-7625-5646>

REFERENCES

- Bailey MH, Tokheim C, Porta-Pardo E, et al. Comprehensive characterization of cancer driver genes and mutations. *Cell*. 2018;173:371-385.
- Clark SJ, Argelaguet R, Kapourani CA, et al. scNMT-seq enables joint profiling of chromatin accessibility DNA methylation and transcription in single cells. *Nat Commun*. 2018;9:781.
- Casalino L, Verde P. Multifaceted roles of DNA methylation in neoplastic transformation, from tumor suppressors to EMT and metastasis. *Genes*. 2020;11:922.
- Audia JE, Campbell RM. Histone modifications and cancer. *Cold Spring Harb Perspect Biol*. 2016;8:a019521.
- Migliori V, Müller J, Phalke S, et al. Symmetric dimethylation of H3R2 is a newly identified histone mark that supports euchromatin maintenance. *Nat Struct Mol Biol*. 2012;19:136-144.
- Bouchard C, Sahu P, Meixner M, et al. Genomic location of PRMT6-dependent H3R2 methylation is linked to the transcriptional outcome of associated genes. *Cell Rep*. 2018;24:3339-3352.
- Lee JE, Wang C, Xu S, et al. H3K4 mono- and di-methyltransferase MLL4 is required for enhancer activation during cell differentiation. *Elife*. 2013;2:e01503.
- Wang C, Lee JE, Lai B, et al. Enhancer priming by H3K4 methyltransferase MLL4 controls cell fate transition. *Proc Natl Acad Sci USA*. 2016;113:11871-11876.
- Sze CC, Cao K, Collings CK, et al. Histone H3K4 methylation-dependent and -independent functions of Set1A/COMPASS in embryonic stem cell self-renewal and differentiation. *Genes Dev*. 2017;31:1732-1737.
- Liu N, Zhang Z, Wu H, et al. Recognition of H3K9 methylation by GLP is required for efficient establishment of H3K9 methylation, rapid target gene repression, and mouse viability. *Genes Dev*. 2015;29:379-393.
- Yu Y, Schleich K, Yue B, et al. Targeting the senescence-overriding cooperative activity of structurally unrelated H3K9 demethylases in melanoma. *Cancer Cell*. 2018;33:322-336.
- Shirai A, Kawaguchi T, Shimojo H, et al. Impact of nucleic acid and methylated H3K9 binding activities of Suv39h1 on its heterochromatin assembly. *Elife*. 2017;6:e25317.
- Ferrari KJ, Scelfo A, Jammula S, et al. Polycomb-dependent H3K27me1 and H3K27me2 regulate active transcription and enhancer fidelity. *Mol Cell*. 2014;53:49-62.
- Chen S, Ma J, Wu F, et al. The histone H3 Lys 27 demethylase JMJD3 regulates gene expression by impacting transcriptional elongation. *Genes Dev*. 2012;26:1364-1375.
- Wu SC, Kallin EM, Zhang Y. Role of H3K27 methylation in the regulation of lncRNA expression. *Cell Res*. 2010;20:1109-1116.
- Jha DK, Strahl BD. An RNA polymerase II-coupled function for histone H3K36 methylation in checkpoint activation and DSB repair. *Nat Commun*. 2014;5:3965.
- Yu Y, Song C, Zhang Q, et al. Histone H3 lysine 56 methylation regulates DNA replication through its interaction with PCNA. *Mol Cell*. 2012;46:7-17.
- Fu H, Maunakea AK, Martin MM, et al. Methylation of histone H3 on lysine 79 associates with a group of replication origins and helps limit DNA replication once per cell cycle. *PLoS Genet*. 2013;9:e1003542.
- Shoaib M, Walter D, Gillespie PJ, et al. Histone H4K20 methylation mediated chromatin compaction threshold ensures genome integrity by limiting DNA replication licensing. *Nat Commun*. 2018;9:3704.
- Husmann D, Gozani O. Histone lysine methyltransferases in biology and disease. *Nat Struct Mol Biol*. 2019;26:880-889.
- Gaweska H, Fitzpatrick PF. Structures and mechanism of the monoamine oxidase family. *Biomol Concepts*. 2011;2:365-377.
- Maes T, Mascaró C, Ortega A, et al. KDM1 histone lysine demethylases as targets for treatments of oncological and neurodegenerative disease. *Epigenomics*. 2015;7:609-626.
- Hosseini A, Minucci S. A comprehensive review of lysine-specific demethylase 1 and its roles in cancer. *Epigenomics*. 2017;9:1123-1142.
- Tsukada Y-i, Fang J, Erdjument-Bromage H, et al. Histone demethylation by a family of JmjC domain-containing proteins. *Nature*. 2006;439:811-816.
- Klose RJ, Kallin EM, Zhang Y. JmjC-domain-containing proteins and histone demethylation. *Nat Rev Genet*. 2006;7:715-727.
- Horton JR, Engstrom A, Zoeller EL, et al. Characterization of a linked jumonji domain of the KDM5/JARID1 family of histone H3 lysine 4 demethylases. *J Biol Chem*. 2016;291:2631-2646.
- Pilka ES, James T, Lisztwan JH. Structural definitions of Jumonji family demethylase selectivity. *Drug Discov Today*. 2015;20:743-749.
- Zheng Y, Hsu FN, Xu W, et al. A developmental genetic analysis of the lysine demethylase KDM2 mutations in *Drosophila melanogaster*. *Mech Dev*. 2014;133:36-53.

29. Tsukada Y, Ishitani T, Nakayama KI. KDM7 is a dual demethylase for histone H3 Lys 9 and Lys 27 and functions in brain development. *Genes Dev.* 2010;24:432-437.
30. Klein BJ, Piao L, Xi Y, et al. The histone-H3K4-specific demethylase KDM5B binds to its substrate and product through distinct PHD fingers. *Cell Rep.* 2014;6:325-335.
31. Liu X, Secombe J. The histone demethylase KDM5 activates gene expression by recognizing chromatin context through its PHD reader motif. *Cell Rep.* 2015;13:2219-2231.
32. Su Z, Wang F, Lee JH, et al. Reader domain specificity and lysine demethylase-4 family function. *Nat Commun.* 2016;7:13387.
33. Hillringhaus L, Yue WW, Rose NR, et al. Structural and evolutionary basis for the dual substrate selectivity of human KDM4 histone demethylase family. *J Biol Chem.* 2011;286:41616-41625.
34. Shi Y, Sawada J, Sui G, et al. Coordinated histone modifications mediated by a CtBP co-repressor complex. *Nature.* 2003;422:735-738.
35. Katz TA, Vasilatos SN, Harrington E, Oesterreich S, Davidson NE, Huang Y. Inhibition of histone demethylase, LSD2 (KDM1B), attenuates DNA methylation and increases sensitivity to DNMT inhibitor-induced apoptosis in breast cancer cells. *Breast Cancer Res Treat.* 2014;146:99-108.
36. Harris WJ, Huang X, Lynch JT, et al. The histone demethylase KDM1A sustains the oncogenic potential of MLL-AF9 leukemia stem cells. *Cancer Cell.* 2012;21:473-487.
37. Laurent B, Ruitu L, Murn J, et al. A specific LSD1/KDM1A isoform regulates neuronal differentiation through H3K9 demethylation. *Mol Cell.* 2015;57:957-970.
38. Hino S, Kohrogi K, Nakao M. Histone demethylase LSD1 controls the phenotypic plasticity of cancer cells. *Cancer Sci.* 2016;107:1187-1192.
39. Metzger E, Wissmann M, Yin N, et al. LSD1 demethylates repressive histone marks to promote androgen-receptor-dependent transcription. *Nature.* 2005;437:436-439.
40. Sun G, Alzayady K, Stewart R, et al. Histone demethylase LSD1 regulates neural stem cell proliferation. *Mol Cell Biol.* 2010;30:1997-2005.
41. Li W, Sun G, Yang S, Qu Q, Nakashima K, Shi Y. Nuclear receptor TLX regulates cell cycle progression in neural stem cells of the developing brain. *Mol Endocrinol.* 2008;22:56-64.
42. Saccà CD, Gorini F, Ambrosio S, et al. Inhibition of lysine-specific demethylase LSD1 induces senescence in glioblastoma cells through a HIF-1 α -dependent pathway. *Biochim Biophys Acta Gene Regul Mech.* 2019;1862:535-546.
43. Ellis L, Loda M. LSD1: a single target to combat lineage plasticity in lethal prostate cancer. *Proc Natl Acad Sci USA.* 2018;115:4530-4531.
44. Liu C, Liu L, Chen X, et al. LSD1 stimulates cancer-associated fibroblasts to drive notch3-dependent self-renewal of liver cancer stem-like cells. *Cancer Res.* 2018;78:938-949.
45. Cao C, Vasilatos SN, Bhargava R, et al. Functional interaction of histone deacetylase 5 (HDAC5) and lysine-specific demethylase 1 (LSD1) promotes breast cancer progression. *Oncogenesis.* 2017;36:133-145.
46. Hayami S, Kelly JD, Cho H-S, et al. Overexpression of LSD1 contributes to human carcinogenesis through chromatin regulation in various cancers. *Int J Cancer.* 2011;128:574-586.
47. Augert A, Eastwood E, Ibrahim AH, et al. Targeting NOTCH activation in small cell lung cancer through LSD1 inhibition. *Sci Signal.* 2019;12:eaau2922.
48. Hu J, Sun T, Wang H, et al. MiR-215 is induced post-transcriptionally via HIF-Drosha complex and mediates glioma-initiating cell adaptation to hypoxia by targeting KDM1B. *Cancer Cell.* 2016;29:49-60.
49. Huang J, Sengupta R, Espejo AB, et al. p53 is regulated by the lysine demethylase LSD1. *Nature.* 2007;449:105-108.
50. He Y, Zhao Y, Wang L, et al. LSD1 promotes S-phase entry and tumorigenesis via chromatin co-occupation with E2F1 and selective H3K9 demethylation. *Oncogene.* 2018;37:534-543.
51. Lee JY, Park JH, Choi HJ, et al. LSD1 demethylates HIF1 α to inhibit hydroxylation and ubiquitin-mediated degradation in tumor angiogenesis. *Oncogene.* 2017;36:5512-5521.
52. Lan H, Tan M, Zhang Q, et al. LSD1 destabilizes FBXW7 and abrogates FBXW7 functions independent of its demethylase activity. *Proc Natl Acad Sci USA.* 2019;116:12311-12320.
53. Fang R, Barbera AJ, Xu Y, et al. Human LSD2/KDM1b/AOF1 regulates gene transcription by modulating intragenic H3K4me2 methylation. *Mol Cell.* 2010;39:222-233.
54. Yang Y, Yin X, Yang H, Xu Y. Histone demethylase LSD2 acts as an E3 ubiquitin ligase and inhibits cancer cell growth through promoting proteasomal degradation of OGT. *Mol Cell.* 2015;58:47-59.
55. Batie M, Druker J, D'Ignazio L, Rocha S. KDM2 family members are regulated by HIF-1 in hypoxia. *Cell.* 2017;6:8.
56. Cao LL, Wei F, Du Y, et al. ATM-mediated KDM2A phosphorylation is required for the DNA damage repair. *Oncogene.* 2016;35:301-313.
57. Frescas D, Guardavaccaro D, Bassermann F, Koyama-Nasu R, Pagano M. JHDM1B/FBXL10 is a nucleolar protein that represses transcription of ribosomal RNA genes. *Nature.* 2007;450:309-313.
58. Janzer A, Stamm K, Becker A, Zimmer A, Buettner R, Kirfel J. The H3K4me3 histone demethylase Fbxl10 is a regulator of chemokine expression, cellular morphology, and the metabolome of fibroblasts. *J Biol Chem.* 2012;287:30984-30992.
59. He J, Kallin EM, Tsukada Y-i, Zhang Y. The H3K36 demethylase Jhd1b/Kdm2b regulates cell proliferation and senescence through p15Ink4b. *Nat Struct Mol Biol.* 2008;15:1169-1175.
60. Kurt IC, Sur I, Kaya E, et al. KDM2B, an H3K36-specific demethylase, regulates apoptotic response of GBM cells to TRAIL. *Cell Death Dis.* 2017;8:e2897.
61. Staberg M, Rasmussen RD, Michaelsen SR, et al. Targeting glioma stem-like cell survival and chemoresistance through inhibition of lysine-specific histone demethylase KDM2B. *Mol Oncol.* 2018;12:406-420.
62. He J, Nguyen AT, Zhang Y. KDM2b/JHDM1b, an H3K36me2-specific demethylase, is required for initiation and maintenance of acute myeloid leukemia. *Blood.* 2011;117:3869-3880.
63. He J, Shen L, Wan M, Taranova O, Wu H, Zhang Y. Kdm2b maintains murine embryonic stem cell status by recruiting PRC1 complex to CpG islands of developmental genes. *Nat Cell Biol.* 2013;15:373-384.
64. Chen JY, Luo CW, Lai YS, Wu CC, Hung WC. Lysine demethylase KDM2A inhibits TET2 to promote DNA methylation and silencing of tumor suppressor genes in breast cancer. *Oncogene.* 2017;36:e369.
65. Wagner KW, Alam H, Dhar SS, et al. KDM2A promotes lung tumorigenesis by epigenetically enhancing ERK1/2 signaling. *J Clin Invest.* 2013;123:5231-5246.
66. Lu L, Gao Y, Zhang Z, et al. Kdm2a/b lysine demethylases regulate canonical Wnt signaling by modulating the stability of nuclear β -catenin. *Dev Cell.* 2015;33:660-674.
67. Lu T, Jackson MW, Wang B, et al. Regulation of NF-kappaB by NSD1/FBXL11-dependent reversible lysine methylation of p65. *Proc Natl Acad Sci USA.* 2010;107:46-51.
68. Farcas AM, Blackledge NP, Sudbery I, et al. KDM2B links the Polycomb repressive complex 1 (PRC1) to recognition of CpG islands. *Elife.* 2012;1:e00205.
69. Turberfield AH, Kondo T, Nakayama M, et al. KDM2 proteins constrain transcription from CpG Island gene promoters independently of their histone demethylase activity. *Nucleic Acids Res.* 2019;47:9005-9023.
70. Becker JS, Nicetto D, Zaret KS. H3K9me3-dependent heterochromatin: barrier to cell fate changes. *Trends Genet.* 2016;32:29-41.

71. Sui Y, Gu R, Janknecht R. Crucial functions of the JMJD1/KDM3 epigenetic regulators in cancer. *Mol Cancer Res.* 2020. <https://doi.org/10.1158/1541-7786.MCR-20-0404>.
72. Li J, Yu B, Deng P, et al. KDM3 epigenetically controls tumorigenic potentials of human colorectal cancer stem cells through Wnt/ β -catenin signalling. *Nat Commun.* 2017;8:15146.
73. Peng K, Su G, Ji J, et al. Histone demethylase JMJD1A promotes colorectal cancer growth and metastasis by enhancing Wnt/ β -catenin signaling. *J Biol Chem.* 2018;293:10606-10619.
74. Kim H, Kim D, Choi SA, et al. KDM3A histone demethylase functions as an essential factor for activation of JAK2–STAT3 signaling pathway. *Proc Natl Acad Sci USA.* 2018;115:11766-11771.
75. Fan L, Peng G, Sahgal N, et al. Regulation of c-Myc expression by the histone demethylase JMJD1A is essential for prostate cancer cell growth and survival. *Oncogene.* 2016;35:2441-2452.
76. Fan L, Zhang F, Xu S, et al. Histone demethylase JMJD1A promotes alternative splicing of AR variant 7 (AR-V7) in prostate cancer cells. *Proc Natl Acad Sci USA.* 2018;115:E4584-E4593.
77. Wade MA, Jones D, Wilson L, et al. The histone demethylase enzyme KDM3A is a key estrogen receptor regulator in breast cancer. *Nucleic Acids Res.* 2015;43:196-207.
78. Ramadoss S, Guo G, Wang CY. Lysine demethylase KDM3A regulates breast cancer cell invasion and apoptosis by targeting histone and the non-histone protein p53. *Oncogene.* 2017;36:47-59.
79. Saraç H, Morova T, Pires E, et al. Systematic characterization of chromatin modifying enzymes identifies KDM3B as a critical regulator in castration resistant prostate cancer. *Oncogene.* 2020;39:2187-2201.
80. Lynch JR, Salik B, Connerty P, et al. JMJD1C-mediated metabolic dysregulation contributes to HOXA9-dependent leukemogenesis. *Leukemia.* 2019;33:1400-1410.
81. Kaukonen R, Mai A, Georgiadou M, et al. Normal stroma suppresses cancer cell proliferation via mechanosensitive regulation of JMJD1a-mediated transcription. *Nat Commun.* 2016;7:12237.
82. Abe Y, Rozqie R, Matsumura Y, et al. JMJD1A is a signal-sensing scaffold that regulates acute chromatin dynamics via SWI/SNF association for thermogenesis. *Nat Commun.* 2015;6:7052.
83. Schneider P, Miguel Bayo-Fina J, Singh R, et al. Identification of a novel Actin-dependent signal transducing module allows for the targeted degradation of GIL1. *Nat Commun.* 2015;6:8023.
84. Liu X, Wang Y, Gao Y, et al. H3K9 demethylase KDM4E is an epigenetic regulator for bovine embryonic development and a defective factor for nuclear reprogramming. *Development.* 2018;145:dev158261.
85. Berry WL, Janknecht R. KDM4/JMJD2 histone demethylases: epigenetic regulators in cancer cells. *Cancer Res.* 2013;73:2936-2942.
86. Deng P, Chen QM, Hong C, Wang CY. Histone methyltransferases and demethylases: regulators in balancing osteogenic and adipogenic differentiation of mesenchymal stem cells. *Int J Oral Sci.* 2015;7:197-204.
87. Bierhoff H, Dammert MA, Brocks D, Dambacher S, Schotta G, Grummt I. Quiescence-induced lncRNAs trigger H4K20 trimethylation and transcriptional silencing. *Mol Cell.* 2014;54:675-682.
88. Agger K, Miyagi S, Pedersen MT, Kooistra SM, Johansen JV, Helin K. Jmjd2/Kdm4 demethylases are required for expression of Il3ra and survival of acute myeloid leukemia cells. *Genes Dev.* 2016;30:1278-1288.
89. Lin C-Y, Wang B-J, Chen B-C, et al. Histone demethylase KDM4C stimulates the proliferation of prostate cancer cells via activation of AKT and c-Myc. *Cancers (Basel).* 2019;11:1785.
90. Pedersen MT, Kooistra SM, Radzishchanskaya A, et al. Continual removal of H3K9 promoter methylation by Jmjd2 demethylases is vital for ESC self-renewal and early development. *EMBO J.* 2016;35:1550-1564.
91. Metzger E, Stepputtis SS, Strietz J, et al. KDM4 inhibition targets breast cancer stem-like cells. *Cancer Res.* 2017;77:5900-5912.
92. Wu M-C, Cheng H-H, Yeh T-S, et al. KDM4B is a coactivator of c-Jun and involved in gastric carcinogenesis. *Cell Death Dis.* 2019;10:68.
93. Chen Y, Fang R, Yue C, et al. Wnt-induced stabilization of KDM4C is required for Wnt/ β -catenin target gene expression and glioblastoma tumorigenesis. *Cancer Res.* 2020;80:1049-1063.
94. Mallm J-P, Windisch P, Biran A, et al. Glioblastoma initiating cells are sensitive to histone demethylase inhibition due to epigenetic deregulation. *Int J Cancer.* 2020;146:1281-1292.
95. Peng K, Kou L, Yu L, et al. Histone demethylase JMJD2D interacts with β -catenin to induce transcription and activate colorectal cancer cell proliferation and tumor growth in mice. *Gastroenterology.* 2019;156:1112-1126.
96. Katoh M, Katoh M. Identification and characterization of JMJD2 family genes in silico. *Int J Oncol.* 2004;24:1623-1628.
97. Sanchez-Fernandez EM, Tarhonskaya H, Al-Qahtani K, et al. Investigations on the oxygen dependence of a 2-oxoglutarate histone demethylase. *Biochem J.* 2013;449:491-496.
98. Hendrickson PG, Doráis JA, Grow EJ, et al. Conserved roles for murine DUX and human DUX4 in activating cleavage stage genes and MERVL/HERVL retrotransposons. *Nat Genet.* 2017;49:925-934.
99. Yang G-J, Ko C-N, Zhong H-J, Leung C-H, Ma D-L. Structure-based discovery of a selective KDM5A inhibitor that exhibits anti-cancer activity via inducing cell cycle arrest and senescence in breast cancer cell lines. *Cancers (Basel).* 2019;11:92.
100. Oser MG, Sabet AH, Gao W, et al. The KDM5A/RBP2 histone demethylase represses NOTCH signaling to sustain neuroendocrine differentiation and promote small cell lung cancer tumorigenesis. *Genes Dev.* 2019;33:1718-1738.
101. Tumber A, Nuzzi A, Hookway ES, et al. Potent and selective KDM5 inhibitor stops cellular demethylation of h3k4me3 at transcription start sites and proliferation of MM1S myeloma cells. *Cell Chem Biol.* 2017;24:371-380.
102. Wong SH, Goode DL, Iwasaki M, et al. The H3K4-methyl epigenome regulates leukemia stem cell oncogenic potential. *Cancer Cell.* 2015;28:198-209.
103. Roesch A, Mueller AM, Stempf T, Moehle C, Landthaler M, Vogt T. RBP2-H1/JARID1B is a transcriptional regulator with a tumor suppressive potential in melanoma cells. *Int J Cancer.* 2008;122:1047-1057.
104. Shen H, Xu W, Guo R, et al. Suppression of enhancer overactivation by a RACK7-histone demethylase complex. *Cell.* 2016;165:331-342.
105. Rondinelli B, Rosano D, Antonini E, et al. Histone demethylase JARID1C inactivation triggers genomic instability in sporadic renal cancer. *J Clin Invest.* 2015;125:4625-4637.
106. Li N, Dhar SS, Chen TY, et al. JARID1D is a suppressor and prognostic marker of prostate cancer invasion and metastasis. *Cancer Res.* 2016;76:831-843.
107. Arseneault M, Monlong J, Vasudev NS, et al. Loss of chromosome Y leads to down regulation of KDM5D and KDM6C epigenetic modifiers in clear cell renal cell carcinoma. *Sci Rep.* 2017;7:44876.
108. Sengoku T, Yokoyama S. Structural basis for histone H3 Lys 27 demethylation by UTX/KDM6A. *Genes Dev.* 2011;25:2266-2277.
109. Kim J-H, Sharma A, Dhar SS, et al. UTX and MLL4 coordinately regulate transcriptional programs for cell proliferation and invasiveness in breast cancer cells. *Cancer Res.* 2014;74:1705-1717.
110. Watanabe S, Shimada S, Akiyama Y, et al. Loss of KDM6A characterizes a poor prognostic subtype of human pancreatic cancer and potentiates HDAC inhibitor lethality. *Int J Cancer.* 2019;145:192-205.

111. Ezponda T, Dupéré-Richer D, Will CM, et al. UTX/KDM6A loss enhances the malignant phenotype of multiple myeloma and sensitizes cells to EZH2 inhibition. *Cell Rep.* 2017;21:628-640.
112. Ler LD, Ghosh S, Chai X, et al. Loss of tumor suppressor KDM6A amplifies PRC2-regulated transcriptional repression in bladder cancer and can be targeted through inhibition of EZH2. *Sci Transl Med.* 2017;9:eaa18312.
113. Wu Q, Tian Y, Zhang J, et al. In vivo CRISPR screening unveils histone demethylase UTX as an important epigenetic regulator in lung tumorigenesis. *Proc Natl Acad Sci U S A.* 2018;115:E3978-E3986.
114. Van der Meulen J, Sanghvi V, Mavrakis K, et al. The H3K27me3 demethylase UTX is a gender-specific tumor suppressor in T-cell acute lymphoblastic leukemia. *Blood.* 2015;125:13-21.
115. Andricovich J, Perkalil S, Kai Y, Casasanta N, Peng W, Tzatsos A. Loss of KDM6A activates super-enhancers to induce gender-specific squamous-like pancreatic cancer and confers sensitivity to BET inhibitors. *Cancer Cell.* 2018;33:512-526.
116. Gozdecka M, Meduri E, Mazan M, et al. UTX-mediated enhancer and chromatin remodeling suppresses myeloid leukemogenesis through noncatalytic inverse regulation of ETS and GATA programs. *Nat Genet.* 2018;50:883-894.
117. Yang L, Zha Y, Ding J, et al. Histone demethylase KDM6B has an anti-tumorigenic function in neuroblastoma by promoting differentiation. *Oncogene.* 2019;8:3.
118. Park SY, Park J-W, Chun Y-S. Jumonji histone demethylases as emerging therapeutic targets. *Pharmacol Res.* 2016;105:146-151.
119. Lee KH, Park JW, Sung HS, et al. PHF2 histone demethylase acts as a tumor suppressor in association with p53 in cancer. *Oncogene.* 2015;34:2897-2909.
120. Pappa S, Padilla N, Iacobucci S, et al. PHF2 histone demethylase prevents DNA damage and genome instability by controlling cell cycle progression of neural progenitors. *Proc Natl Acad Sci USA.* 2019;116:19464-19473.
121. Lee K-H, Hong S, Kang M, et al. Histone demethylase KDM7A controls androgen receptor activity and tumor growth in prostate cancer. *Int J Cancer.* 2018;143:2849-2861.
122. Zhu G, Liu L, She L, et al. Elevated expression of histone demethylase PHF8 associates with adverse prognosis in patients of laryngeal and hypopharyngeal squamous cell carcinoma. *Epigenomics.* 2015;7:143-153.
123. Hsia DA, Tepper CG, Pochampalli MR, et al. KDM8, a H3K36me2 histone demethylase that acts in the cyclin A1 coding region to regulate cancer cell proliferation. *Proc Natl Acad Sci USA.* 2010;107:9671-9676.
124. Zhao Z, Sun C, Li F, Han J, Li X, Song Z. Overexpression of histone demethylase JMJD5 promotes metastasis and indicates a poor prognosis in breast cancer. *Int J Clin Exp Pathol.* 2015;8:10325-10334.
125. Wang HJ, Pochampalli M, Wang LY, et al. KDM8/JMJD5 as a dual coactivator of AR and PKM2 integrates AR/EZH2 network and tumor metabolism in CRPC. *Oncogene.* 2019;38:17-32.
126. Zhu H, Hu S, Baker J. JMJD5 regulates cell cycle and pluripotency in human embryonic stem cells. *Stem Cells.* 2014;32:2098-2110.
127. Ishimura A, Minehata K-i, Terashima M, Kondoh G, Hara T, Suzuki T. JMJD5, an H3K36me2 histone demethylase, modulates embryonic cell proliferation through the regulation of Cdkn1a expression. *Development.* 2012;139:749-759.
128. Huang X, Zhang S, Qi H, et al. JMJD5 interacts with p53 and negatively regulates p53 function in control of cell cycle and proliferation. *Biochim Biophys Acta.* 2015;1853:2286-2295.
129. He Z, Wu J, Su X, et al. JMJD5 (Jumonji domain-containing 5) associates with spindle microtubules and is required for proper mitosis. *J Biol Chem.* 2016;291:4684-4697.
130. Marcon E, Ni Z, Pu S, et al. Human-chromatin-related protein interactions identify a demethylase complex required for chromosome segregation. *Cell Rep.* 2014;8:297-310.
131. Youn MY, Yokoyama A, Fujiyama-Nakamura S, et al. JMJD5, a Jumonji C (JmjC) domain-containing protein, negatively regulates osteoclastogenesis by facilitating NFATc1 protein degradation. *J Biol Chem.* 2012;287:12994-13004.
132. Del Rizzo PA, Krishnan S, Trievel RC. Crystal structure and functional analysis of JMJD5 indicate an alternate specificity and function. *Mol Cell Biol.* 2012;32:4044-4052.
133. Wang H, Zhou X, Wu M, et al. Structure of the JmjC-domain-containing protein JMJD5. *Acta Crystallogr D.* 2013;69:1911-1920.
134. Liu H, Wang C, Lee S, et al. Clipping of arginine-methylated histone tails by JMJD5 and JMJD7. *Proc Natl Acad Sci USA.* 2017;114:E7717-E7726.
135. Shen J, Xiang X, Chen L, et al. JMJD5 cleaves monomethylated histone H3 N-tail under DNA damaging stress. *EMBO Rep.* 2017;18:2131-2143.
136. Wilkins SE, Islam MS, Gannon JM, et al. JMJD5 is a human arginyl C-3 hydroxylase. *Nat Commun.* 2018;9:1180.
137. Boumahdi S, de Sauvage FJ. The great escape: tumour cell plasticity in resistance to targeted therapy. *Nat Rev Drug Discov.* 2020;19:39-56.
138. Sharma SV, Lee DY, Li B, et al. A chromatin-mediated reversible drug-tolerant state in cancer cell subpopulations. *Cell.* 2010;141:69-80.
139. Vinogradova M, Gehling VS, Gustafson A, et al. An inhibitor of KDM5 demethylases reduces survival of drug-tolerant cancer cells. *Nat Chem Biol.* 2016;12:531-538.
140. Roesch A, Vultur A, Bogeski I, et al. Overcoming intrinsic multidrug resistance in melanoma by blocking the mitochondrial respiratory chain of slow-cycling JARID1B(high) cells. *Cancer Cell.* 2013;23:811-825.
141. Dalvi MP, Wang L, Zhong R, et al. Taxane-platin-resistant lung cancers co-develop hypersensitivity to jumonjiC demethylase inhibitors. *Cell Rep.* 2017;19:1669-1684.
142. Plch J, Hrabeta J, Eckschlager T. KDM5 demethylases and their role in cancer cell chemoresistance. *Int J Cancer.* 2019;144:221-231.
143. Liu X, Zhang S-M, McGeary MK, et al. KDM5B promotes drug resistance by regulating melanoma-propagating cell subpopulations. *Mol Cancer Ther.* 2019;18:706-717.
144. Liao BB, Sievers C, Donohue LK, et al. Adaptive chromatin remodeling drives glioblastoma stem cell plasticity and drug tolerance. *Cell Stem Cell.* 2017;20:233-246.
145. Qin Y, Vasilatos SN, Chen L, et al. Inhibition of histone lysine-specific demethylase 1 elicits breast tumor immunity and enhances antitumor efficacy of immune checkpoint blockade. *Oncogene.* 2019;38:390-405.
146. Seoane JA, Kirkland JG, Caswell-Jin JL, Crabtree GR, Curtis C. Chromatin regulators mediate anthracycline sensitivity in breast cancer. *Nat Med.* 2019;25:1721-1727.
147. Paroni G, Bolis M, Zanetti A, et al. HER2-positive breast-cancer cell lines are sensitive to KDM5 inhibition: definition of a gene-expression model for the selection of sensitive cases. *Oncogene.* 2019;38:2675-2689.
148. Hinohara K, Wu HJ, Vigneau S, et al. KDM5 histone demethylase activity links cellular transcriptomic heterogeneity to therapeutic resistance. *Cancer Cell.* 2019;35:330-332.
149. Banelli B, Carra E, Barbieri F, et al. The histone demethylase KDM5A is a key factor for the resistance to temozolomide in glioblastoma. *Cell Cycle.* 2015;14:3418-3429.
150. Yang ZQ, Imoto I, Fukuda Y, et al. Identification of a novel gene, GASC1, within an amplicon at 9p23-24 frequently detected in esophageal cancer cell lines. *Cancer Res.* 2000;60:4735-4739.
151. Liu G, Bollig-Fischer A, Kreike B, et al. Genomic amplification and oncogenic properties of the GASC1 histone demethylase gene in breast cancer. *Oncogene.* 2009;28:4491-4500.

152. Hou J, Wu J, Dombkowski A, et al. Genomic amplification and a role in drug-resistance for the KDM5A histone demethylase in breast cancer. *Am J Transl Res.* 2012;4:247-256.
153. Van Haften G, Dalgliesh GL, Davies H, et al. Somatic mutations of the histone H3K27 demethylase gene UTX in human cancer. *Nat Genet.* 2009;41:521-523.
154. Huether R, Dong L, Chen X, et al. The landscape of somatic mutations in epigenetic regulators across 1,000 paediatric cancer genomes. *Nat Commun.* 2014;5:3630.
155. Kandath C, McLellan MD, Vandin F, et al. Mutational landscape and significance across 12 major cancer types. *Nature.* 2013;502:333-339.
156. Krieg AJ, Rankin EB, Chan D, Razorenova O, Fernandez S, Giaccia AJ. Regulation of the histone demethylase JMJD1A by hypoxia-inducible factor 1 alpha enhances hypoxic gene expression and tumor growth. *Mol Cell Biol.* 2010;30:344-353.
157. Shmakova A, Batie M, Druker J, Rocha S. Chromatin and oxygen sensing in the context of JmJc histone demethylases. *Biochem J.* 2014;462:385-395.
158. Tan MK, Lim HJ, Harper JW. SCF(FBXO22) regulates histone H3 lysine 9 and 36 methylation levels by targeting histone demethylase KDM4A for ubiquitin-mediated proteasomal degradation. *Mol Cell Biol.* 2011;31:3687-3699.
159. Van Rechem C, Black JC, Abbas T, et al. The SKP1-Cul1-F-box and leucine-rich repeat protein 4 (SCF-FbxL4) ubiquitin ligase regulates lysine demethylase 4A (KDM4A)/Jumonji domain-containing 2A (JMJD2A) protein. *J Biol Chem.* 2011;286:30462-30470.
160. Mallette FA, Mattioli F, Cui G, et al. RNF8- and RNF168-dependent degradation of KDM4A/JMJD2A triggers 53BP1 recruitment to DNA damage sites. *EMBO J.* 2012;31:1865-1878.
161. Cui S-Z, Lei Z-Y, Guan T-P, et al. Targeting USP1-dependent KDM4A protein stability as a potential prostate cancer therapy. *Cancer Sci.* 2020;111:1567-1581.
162. Wang Z, Yang X, Liu C, et al. Acetylation of PHF5A modulates stress responses and colorectal carcinogenesis through alternative splicing-mediated upregulation of KDM3A. *Mol Cell.* 2019;74:1250-1263.
163. Baba A, Ohtake F, Okuno Y, et al. PKA-dependent regulation of the histone lysine demethylase complex PHF2-ARID5B. *Nat Cell Biol.* 2011;13:668-675.
164. Cheng MB, Zhang Y, Cao CY, Zhang WL, Zhang Y, Shen YF. Specific phosphorylation of histone demethylase KDM3A determines target gene expression in response to heat shock. *PLoS Biol.* 2014;12:e1002026.
165. Han S, Liu Y, Cai SJ, et al. IDH mutation in glioma: molecular mechanisms and potential therapeutic targets. *Br J Cancer.* 2020;122:1580-1589.

How to cite this article: Sterling J, Menezes SV, Abbassi RH, Munoz L. Histone lysine demethylases and their functions in cancer. *Int. J. Cancer.* 2020;1-14. <https://doi.org/10.1002/ijc.33375>

Chapter 8

Final Conclusions

CHAPTER 8. FINAL CONCLUSIONS

This body of work explored a critical unmet need for glioblastoma, the most fatal and common brain cancer. There is no effective treatment for glioblastoma; with a five-year survival rate less than 10%, the majority of patients succumb to the disease within two years.⁸ While survival rates for many cancers have significantly increased over 30 years, brain cancer survival has remained. Since glioblastoma occurs in people in the prime of their life, it shortens their lifespan by 12 years, on average – the highest average loss of life when compared with other forms of cancer, and is associated with the highest economic burden on patients and their families. Moreover, brain tumours kill more children than any other disease.⁴⁰⁴

Glioblastoma therapy is challenged by the presence of glioblastoma stem cells, which give rise to intertumour and intratumour heterogeneity. This heterogeneity leads to varying response to therapy between patients and across cells within a tumour. Moreover, drug design and development for brain-active drugs is impeded by the blood-brain barrier, which mitigates the efficacy of many successful drugs used for peripheral cancers, making brain cancers harder to treat (reviewed in **Chapter 1**).

8. 1. Drug tolerance versus drug resistance

The key focus of this dissertation is drug tolerance – a newly identified mechanism underlying tumour recurrence. Most of the research in understanding tumour recurrence has been on genetic drivers of drug resistance, including pre-existing mutations that give innate resistance (**Figure 8.1a**), amplification of genes encoding for drug efflux pumps or activation of alternative oncogenic pathways. Although useful, this one-directional view of resistance does not capture the phenotypic plasticity of cancer stem cells and their ability to adapt to stressful microenvironmental cues. Additionally, these mechanisms of resistance fail to explain the comparable drug sensitivity of some relapsed tumours when compared to their primary tumours.^{110, 143}

The notion of drug-tolerant persister cells was adapted from the field of microbiology. Shortly after the discovery of antibiotics in 1944, drug tolerance of persister bacteria was distinguished from innate drug resistance as a contributor to persistent infections.⁴⁰⁵ Likewise, drug-tolerant fungal cells have been reported to contribute to infection relapse.⁴⁰⁶ However, only recently have studies begun to show that non-mutational tolerance mechanisms are also stymieing cancer drugs.⁴⁰⁷ Our

understanding of drug-tolerant persister cells in cancer is limited to 44 publications (PubMed search for: “drug-tolerant persister” cell cancer, Dec 2020). Of these, only one study relates to glioblastoma tolerance to the kinase inhibitor dasatinib, which is relevant to only 10% of patients.¹⁰⁶

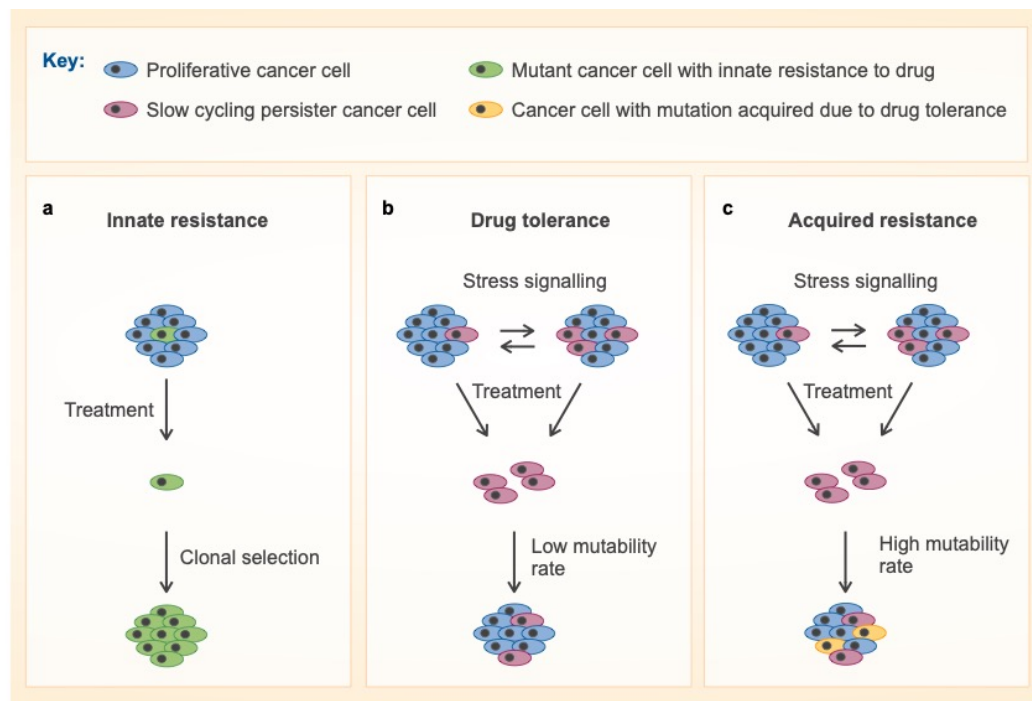


Figure 8.1 Mechanisms of cancer cell resistance to therapy.

(a) Conventional model of tumour recurrence as a result of clonal selection of cells with *de novo* mutations that make them resistant to a given treatment. (b) The drug tolerance model, consistent with the attractor state theory (Chapter 1), suggests the stochastic altering between fast- and slow-cycling (and drug-tolerant) cells, depending on the tumour microenvironment. For instance, cells in the perivascular niche will be mainly proliferative, while cells in the hypoxic and nutrient-deficient tumour core will contain more dormant and treatment-tolerating cells as a result of stress signalling. Upon treatment, tolerant cells persist and can re-establish the tumour once the drug is removed. (c) Depending on the mutability of drug-tolerant persisters, they can acquire rare mutations that make them resistant to therapy. Each model of resistance can contribute to tumour relapse, and the models are not mutually exclusive.

Drug tolerance is a conserved mechanism of survival across all domains of life and, in the context of cancer, is now believed to be the basis for tumour recurrence, even in the absence of mutations that provide innate resistance to any given drug. As shown in this thesis, DTPs regain their proliferative capacity upon drug holidays (Figure 8.1b).¹⁴³ Moreover, the dormant state can act as a precursor for rare mutations, giving rise to acquired resistance in emerging cell populations, depending on the mutability of DTPs (Figure 8.1c). For example, in colorectal cancer, DTPs emerging from treatment with the EGFR inhibitor cetuximab exhibited an up-regulation of error-prone DNA polymerases and concomitant down-regulation of mismatch repair and homologous DNA repair proteins, thereby increasing the mutability of these cells.⁴⁰⁸ Therefore, unlike innate

resistance, acquired resistance occurs in stages, beginning with a first line-of-defence tolerance mechanism that leads to a higher mutability and, under prolonged or repeated exposure to the drug, can give rise to acquired mutations (**Figure 8.1c**). Importantly, innate resistance, drug tolerance and acquired resistance can all contribute to tumour recurrence.⁴⁰⁷ Hence, understanding the mechanisms regulating drug tolerance and resistance will aid in targeting the entire tumour cell population – both the proliferative tumour cells and the tumour-initiating, dormant and drug-tolerant cancer stem cells.

Mutational resistance to microtubule-targeting agents has previously been reported. For example, mutations in β I-tubulin mediate resistance to paclitaxel in ovarian cancer. Elevated expression of β III-tubulin is associated with resistance in many tumour types.^{201, 245} However, only three other teams and we provide evidence of tolerance, and not innate resistance, to microtubule-targeting agents in cancer cells.^{1, 154, 155, 369}

We show that CMPD1 and the subclass of microtubule-targeting agents it represents are suitable drug candidates against glioblastoma.^{1, 214-216} We demonstrate for the first time that the sensitivity of cancer cells to microtubule-targeting agents is positively correlated with total tubulin levels. Glioblastoma cell lines expressing lower basal levels of tubulin were more tolerant to microtubule-targeting agents and yielded more drug-tolerant cells (**Figure 8.2**). These drug-tolerant cells were slow-cycling and recovered upon receiving drug holidays,¹ which is in agreement with previously published data (**Table 5.1, Table 8.1**). While tubulin levels are not the only determinant of drug-tolerant persister cell survival, our observation highlights the highly context-specific aspect of drug tolerance. First, the target concentration can dictate tolerance to the drug. Second, the target concentration, even of a target as ubiquitous as tubulin, varies significantly between patients (inter-patient heterogeneity). Third, both highly responsive and non-responsive tumours will possess a number of drug-tolerant persisters that can eventually recover and return to a proliferative state, *i.e.*, the more tolerant the cells are, the faster they recover. Nonetheless, the reversibility of the CMPD1-tolerant state in glioblastoma cells in our hands pointed to a transient epigenetic reprogramming.

8. 2. Targeting drug-tolerant glioblastoma cells

Epigenetic modulation during drug tolerance provides a landscape for a non-mutational phenotypic switch in cancer cells. In addition to the epigenetic changes reported in DTPs (**Table 5.1**), several studies report that DTPs increase their stemness and dormancy markers, slow down cell cycle progression and rely on lipid oxidation and oxidative

phosphorylation for survival. They also become dependent on pro-survival kinases (Table 8.1).^{371, 409, 410}

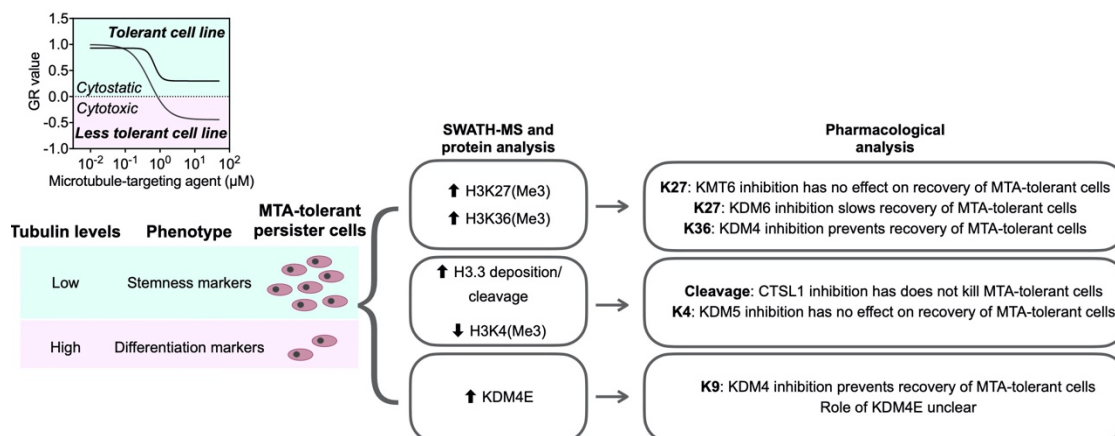


Figure 8.2 Summary of main findings.

Our large-scale proteomic analysis revealed a decrease in global histone H3 acetylation and an increase in global H3 methylation, consistent with a genetically repressed and dormant phenotype. On histone H3.1/3.2, we identified increases in H3K27 and H3K36 methylation (Figure 8.2). In normal development, K27 methylation causes repression of de-differentiation genes and K36 methylation activates differentiation genes. Moreover, K36 methylation negatively regulates K27 methylation.⁴¹¹ However, during oncogenic reprogramming, K27 methylation causes repression of differentiation genes while K36 methylation causes activation of de-differentiation genes. This deregulation of the dynamic interaction between these two lysine sites leads to pathological transcriptional changes that promote oncogenic reprogramming in acute lymphocytic leukaemia.³⁴⁷ Based on these findings and ours, the changes in methylation observed support the mounting evidence that drug-tolerant cells are less differentiated and more stem-like.

We also show that there is increased deposition of H3.3 in DTPs (Figure 8.2). Gain of function of H3.3 mutations can lead to epigenetic dysregulations that contribute to oncogenesis. Specifically, mutations in H3F3A and H3F3B, the genes encoding histone H3.3, are implicated in 11% of adult glioblastoma pathology and in 80% of paediatric glioblastomas. The most common mutation to histone H3.3 is a lysine to methionine mutation at residue 27 (K27M), which makes repressive lysine methylation impossible and leading to aberrant gene expression^{10, 12} Furthermore, the histone H3.3 variant deposition induces a pro-metastatic transcriptional reprogramming.³³² These findings implicate an increased aggressive trait in DTPs.

Additionally, we observed increased cleavage of H3.3 coupled with increased H3K4 demethylation in DTPs. Histone H3.3 cleavage, which was reported to drive a senescence programme in human fibroblasts,³³¹ has not been previously reported in drug tolerance. While inhibition of histone cleavage or H3K4 demethylases (KDM5) had no immediate effect on the surviving number of DTPs, inhibition of the H3.3-depositing protein complexes DAXX/ATRX or HUCA has been proposed as a novel therapeutic approach to inducing irreversible senescence and preventing tumour recurrence in glioblastoma.⁴¹² Further studies to elucidate the role of H3.3 in drug tolerance are warranted.

Further, we demonstrated a dependence of DTPs on KDM6, particularly in terms of recovery in drug-free media (**Figure 8.2**). This finding is in agreement with the study on glioblastoma tolerance to dasatinib.¹⁰⁶ However, it should be noted that treatment with the KDM5/6 inhibitor GSK-J4 failed to completely eradicate both dasatinib-tolerant and CMPD1-tolerant glioblastoma cells.

While we show that epigenetic changes are evident in drug-tolerant persisters, none of the drug combinations we tested succeeded at killing DTPs or preventing their regrowth completely, suggesting that tolerance of glioblastoma stem cells to microtubule-targeting agents may not be solely mediated through epigenetic reprogramming. Several other studies reported the dependence of DTPs on non-epigenetic enzymes (**Table 8.1**), highlighting the complexity of drug tolerance and treatment evasion.

DTPs are generally characterised by the activation of quiescence programs and increased expression of stem cell markers such as CD24, CD44 and CD133, resulting in dormant and slow-cycling cellular phenotypes.^{106, 144, 152} Breast cancer cells yielded DTPs in response to the standard-of-care treatment docetaxel both *in vitro* and *in vivo*. The surviving cell population exhibited a phenotypic switch towards expressing higher levels of CD44 and CD24. The increase of ligands CD44/CD24 in lipid rafts stimulated the activation of RTKs such as the c-Src family of kinases and, in turn, inhibited pro-apoptotic pathways. Inhibition of c-Src kinases with dasatinib had a toxic effect on DTPs but not parental cells, implying the reliance on these pathways for drug tolerance and not proliferation.¹⁵⁵

In some cancer types, DTPs depend on insulin-growth factor 1 receptor (IGF-1R) signalling for survival.¹⁴⁴ Moreover, aldehyde dehydrogenase (ALDH) enzymes are reported to increase in multiple DTP models.^{106, 144, 145, 155, 318, 370} The over-activation of ALDH is suggested to reduce the reactive oxygen species and protect DTPs from

oxidative stress.¹⁴⁵ Furthermore, DTPs become dependent on glutathione peroxidase 4 (GPX4), as it prevents the accumulation of reactive oxygen species-induced lipid peroxidation and hence, cell death by ferroptosis.¹⁵² Inhibition of IGF-1R, ALDH or GPX4 resulted in DTP cell death and prevented tumour regrowth.^{144, 145, 152} Inhibition of the mitochondrial ATP-synthase on which melanoma DTPs depend on for oxidative phosphorylation also results in cell death.¹⁵³

Table 8.1 Reported mechanisms of DTP survival in several cancers (addendum to Table 5.1).

DTP: Drug-Tolerant Persisters; GPX4: glutathione peroxidase 4; KDM: Histone lysine demethylase; ALDH: aldehyde dehydrogenase.

Drug	Cancer cell line	Epigenetic mechanism employed by DTPs	Phenotypic switch exhibited by DTPs	Intervention to suppress or eliminate DTPs	REF
Erlotinib	Lung	Not investigated	Dependence on lipid hydroperoxidase GPX4 for survival	GPX4 inhibition	152
	Lung	Not investigated	Increased stem cell markers, senescence program genes Decreased negative regulators of MAPK signalling	CDK4/12 inhibition	413, 414
Vemurafenib	Melanoma	Enrichment of KDM5B-high slow-cycling DTPs	Increased oxidative proteins	Mitochondrial ATP-synthase inhibition	153
	Melanoma	Not investigated	Dependence on GPX4 for survival	GPX4 inhibition	152
Crizotinib	Gastric	Not investigated	Increased ALDH Increased oxidative proteins	ALDH inhibition	145
5-fluorouracil	Gastric	Not investigated	Increased ALDH	mTOR inhibition	409
Lapatinib	Breast	Not investigated	Dependence on lipid hydroperoxidase GPX4 for survival	GPX4 inhibition	152
Docetaxel	Breast	Not investigated	Increased stem cell markers CD44 and CD24	c-Src inhibition	155

DTPs pose a significant threat to progression-free survival of patients. Proposed therapeutic strategies to eradicate DTPs include inducing irreversible cell senescence to prevent tumour recurrence or reawakening dormant cells to increase their susceptibility to antiproliferative drugs.⁴¹⁵ From a pharmacological perspective, DTPs can be targeted by inhibiting epigenetic enzymes that regulate gene expression, oxidative enzymes that protect cells from reactive oxygen species and upregulated pro-survival kinases upon which the cells depend (**Figure 8.3**).¹⁴³ However, changes in protein expression and activity during drug tolerance are highly dependent on the cancer type and drug used. Thus, DTPs need to be characterised for each cancer and each drug.

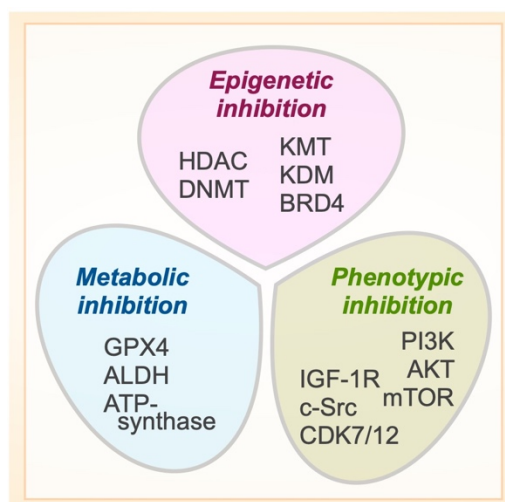


Figure 8.3 Pharmacological approaches to targeting drug-tolerant persister cells.

Cancer cells rely on epigenetic mechanisms that lead to the upregulation of oxidative phosphorylation proteins and pro-survival kinases. Several enzymes involved in the epigenetics, metabolism and survival of drug-tolerant persister offer novel druggable targets for cancer therapy.

In summary, drug tolerance is an intricate and multifaceted obstacle to complete tumour eradication. Our work demonstrates the complexity of drug tolerance in 2D glioblastoma cell models and provides insights into novel therapeutic avenues for targeting glioblastoma cells tolerant to microtubule-targeting agents. While explored the roles of KMTs and KDMs in these DTPs, the roles of other epigenetic enzymes like HDACs and non-epigenetic enzymes like GPX4 remain to be investigated.

8. 3. The role of KDM4 in glioblastoma

In addition to preceding findings, we discovered that the KDM4 inhibitor QC6352 drove both treatment-naïve and tolerance into an irreversible non-proliferative state (**Figure 8.2**). Thus far, only five studies reported functions of KDM4 in glioblastoma, which all support our findings.

Knockdowns of KDM4A promoted autophagy and apoptosis in glioblastoma cells by significantly increasing acidic vesicular organelles.⁴¹⁶ Glioma tissue was shown to have increased expression of KDM4A relative to normal brain tissue; furthermore, knockout of KDM4A prevented proliferation and colony formation in glioblastoma cell lines and reduced tumour mass *in vivo*.⁴¹⁷ The increased KDM4A expression was associated with strong activation of the AKT-PI3K-mTOR axis.⁴¹⁷ Moreover, a role of KDM4C was uncovered in Wnt/ β -catenin signalling, which induces expression of stemness and oncogenic target genes in glioblastoma. Wnt activation was shown to stabilise KDM4C, which in turn demethylated H3K9 by interacting with β -catenin to remove the gene-

repressing heterochromatin protein 1 (HP1) bound to histones and initiate transcription of target genes.⁴¹⁸ KDM4C expression was increased in glioblastoma, and the Wnt-KDM4C- β -catenin axis was shown to be critical for gliomagenesis.⁴¹⁸ Most recently, KDM4C was shown to be necessary for maintaining DNA repair and self-renewal in glioblastoma stem cells. Double-knockdown of KDM4C and KDM7A caused differentiation of glioblastoma stem cells and prevented their regrowth.⁴¹⁹

In addition, a G34R point mutation in histone H3.3 reported in paediatric glioblastoma was shown to inhibit KDM4A, KDM4B and KDM4C by preferentially binding to these enzymes and deactivating their demethylase activity. Ectopic expression of this point mutation in glioblastoma cells exerted the same epigenetic changes as triple knockout of KDM4A-C. These findings suggest that the H3.3-wildtype is necessary for KDM4 activity, although this link is yet to be delineated.⁴²⁰ No studies have investigated the roles of KDM4D and KDM4E in glioblastoma to date.

Based on the above studies and ours, KDM4 enzymes appear to be necessary for the maintenance of glioblastoma stem cell pluripotency and self-renewal capacity. However, due to the lack of orthogonal KDM4 inhibitors, KDM4 enzymes need to be further validated as targets in glioblastoma. Future studies in our laboratory will use novel inhibitors identified using the developed AlphaScreen assay (**Chapter 6**) and CRISPR-knockout to investigate the functions of KDM4 enzymes in glioblastoma further.

In conclusion, the work presented in this thesis has critically expanded our understanding of tolerance to microtubule-targeting agents in glioblastoma cells. While we were not able to completely eradicate DTPs, we uncovered several epigenetic changes with druggable targets that warrant further validation. Additionally, we uncovered a role for KDM4 in glioblastoma and provided an assay for the development of novel KDM4 inhibitors. KDM4 appears to be a promising target for the treatment of glioblastoma.

Chapter 9

References

CHAPTER 9. REFERENCES

1. Abbassi, R. H.; Recasens, A.; Indurthi, D. C.; Johns, T. G.; Stringer, B. W.; Day, B. W.; Munoz, L., Lower Tubulin Expression in Glioblastoma Stem Cells Attenuates Efficacy of Microtubule-Targeting Agents. *ACS Pharmacol Transl Sci* **2019**, *2* (6), 402-413.
2. Sterling, J.; Menezes, S. V.; Abbassi, R. H.; Munoz, L., Histone lysine demethylases and their functions in cancer. *Int J Cancer* **2020**.
3. Per, B., *The Central Nervous System*. 6 ed.; Oxford University Press: Oxford, UK, 2016.
4. Keith, L. L.; Karima, M.; Thomas, W. S., *Escourolle and Poirier's Manual of Basic Neuropathology*. Oxford University Press: Oxford, UK, 2014.
5. Zong, H.; Parada, L. F.; Baker, S. J., Cell of origin for malignant gliomas and its implication in therapeutic development. *Cold Spring Harb Perspect Biol* **2015**, *7* (5).
6. Ferlay, J.; Colombet, M.; Soerjomataram, I.; Mathers, C.; Parkin, D. M.; Pineros, M.; Znaor, A.; Bray, F., Estimating the global cancer incidence and mortality in 2018: GLOBOCAN sources and methods. *Int J Cancer* **2019**, *144* (8), 1941-1953.
7. Bray, F.; Ferlay, J.; Soerjomataram, I.; Siegel, R. L.; Torre, L. A.; Jemal, A., Global cancer statistics 2018: GLOBOCAN estimates of incidence and mortality worldwide for 36 cancers in 185 countries. *CA Cancer J Clin* **2018**, *68* (6), 394-424.
8. Ostrom, Q. T.; Gittleman, H.; Truitt, G.; Boscia, A.; Kruchko, C.; Barnholtz-Sloan, J. S., CBTRUS Statistical Report: Primary Brain and Other Central Nervous System Tumors Diagnosed in the United States in 2011-2015. *Neuro Oncol* **2018**, *20* (suppl_4), iv1-iv86.
9. Louis, D. N.; Ohgaki, H.; Wiestler, O. D.; Cavenee, W. K.; Burger, P. C.; Jouvet, A.; Scheithauer, B. W.; Kleihues, P., The 2007 WHO classification of tumours of the central nervous system. *Acta neuropathologica* **2007**, *114* (2), 97-109.
10. Louis, D. N.; Perry, A.; Reifenberger, G.; von Deimling, A.; Figarella-Branger, D.; Cavenee, W. K.; Ohgaki, H.; Wiestler, O. D.; Kleihues, P.; Ellison, D. W., The 2016 World Health Organization Classification of Tumors of the Central Nervous System: a summary. *Acta neuropathologica* **2016**, *131* (6), 803-20.
11. Eckel-Passow, J. E.; Lachance, D. H.; Molinaro, A. M.; Walsh, K. M.; Decker, P. A.; Sicotte, H.; Pekmezci, M.; Rice, T.; Kosel, M. L.; Smirnov, I. V.; Sarkar, G.; Caron, A. A.; Kollmeyer, T. M.; Praska, C. E.; Chada, A. R.; Halder, C.; Hansen, H. M.; McCoy, L. S.; Bracci, P. M.; Marshall, R.; Zheng, S.; Reis, G. F.; Pico, A. R.; O'Neill, B. P.; Buckner, J. C.; Giannini, C.; Huse, J. T.; Perry, A.; Tihan, T.; Berger, M. S.; Chang, S. M.; Prados, M. D.; Wiemels, J.; Wiencke, J. K.; Wrensch, M. R.; Jenkins, R. B., Glioma Groups Based on 1p/19q, IDH, and TERT Promoter Mutations in Tumors. *New England Journal of Medicine* **2015**, *372* (26), 2499-2508.
12. Molinaro, A. M.; Taylor, J. W.; Wiencke, J. K.; Wrensch, M. R., Genetic and molecular epidemiology of adult diffuse glioma. *Nature Reviews Neurology* **2019**, *15* (7), 405-417.
13. Brat, D. J.; Verhaak, R. G.; Aldape, K. D.; Yung, W. K.; Salama, S. R.; Cooper, L. A.; Rheinbay, E.; Miller, C. R.; Vitucci, M.; Morozova, O.; Robertson, A. G.; Noushmehr, H.; Laird, P. W.; Cherniack, A. D.; Akbani, R.; Huse, J. T.; Ciriello, G.; Poisson, L. M.; Barnholtz-Sloan, J. S.; Berger, M. S.; Brennan, C.; Colen, R. R.; Colman, H.; Flanders, A. E.; Giannini, C.; Grifford, M.; Iavarone, A.; Jain, R.; Joseph, I.; Kim, J.; Kasaian, K.; Mikkelsen, T.; Murray, B. A.; O'Neill, B. P.; Pachter, L.; Parsons, D. W.; Sougnez, C.; Sulman, E. P.; Vandenberg, S. R.; Van Meir, E. G.; von Deimling, A.; Zhang, H.; Crain, D.; Lau, K.; Mallery, D.; Morris, S.; Paulauskis, J.; Penny, R.; Shelton, T.; Sherman, M.; Yena, P.; Black, A.; Bowen, J.; Dicostanzo, K.; Gastier-Foster, J.; Leraas, K. M.; Lichtenberg, T. M.; Pierson, C. R.; Ramirez, N. C.; Taylor, C.; Weaver, S.; Wise, L.; Zmuda, E.; Davidsen, T.; Demchok, J. A.; Eley, G.; Ferguson, M. L.; Hutter, C. M.; Mills Shaw, K. R.; Ozenberger, B. A.; Sheth, M.; Sofia, H. J.; Tarnuzzer, R.; Wang, Z.; Yang, L.; Zenklusen, J. C.; Ayala, B.; Baboud, J.; Chudamani, S.; Jensen, M. A.; Liu, J.; Pihl, T.; Raman, R.; Wan, Y.; Wu, Y.; Ally, A.; Auman, J. T.; Balasundaram, M.; Balu, S.; Baylin, S. B.; Beroukhi, R.; Bootwalla, M. S.; Bowlby, R.; Bristow, C. A.; Brooks, D.; Butterfield, Y.; Carlsen, R.; Carter, S.; Chin, L.; Chu, A.; Chuah, E;

Cibulskis, K.; Clarke, A.; Coetzee, S. G.; Dhalla, N.; Fennell, T.; Fisher, S.; Gabriel, S.; Getz, G.; Gibbs, R.; Guin, R.; Hadjipanayis, A.; Hayes, D. N.; Hinoue, T.; Hoadley, K.; Holt, R. A.; Hoyle, A. P.; Jefferys, S. R.; Jones, S.; Jones, C. D.; Kucherlapati, R.; Lai, P. H.; Lander, E.; Lee, S.; Lichtenstein, L.; Ma, Y.; Maglinte, D. T.; Mahadeshwar, H. S.; Marra, M. A.; Mayo, M.; Meng, S.; Meyerson, M. L.; Mieczkowski, P. A.; Moore, R. A.; Mose, L. E.; Mungall, A. J.; Pantazi, A.; Parfenov, M.; Park, P. J.; Parker, J. S.; Perou, C. M.; Protopopov, A.; Ren, X.; Roach, J.; Sabedot, T. S.; Schein, J.; Schumacher, S. E.; Seidman, J. G.; Seth, S.; Shen, H.; Simons, J. V.; Sipahimalani, P.; Soloway, M. G.; Song, X.; Sun, H.; Tabak, B.; Tam, A.; Tan, D.; Tang, J.; Thiessen, N.; Triche, T., Jr.; Van Den Berg, D. J.; Veluvolu, U.; Waring, S.; Weisenberger, D. J.; Wilkerson, M. D.; Wong, T.; Wu, J.; Xi, L.; Xu, A. W.; Yang, L.; Zack, T. I.; Zhang, J.; Aksoy, B. A.; Arachchi, H.; Benz, C.; Bernard, B.; Carlin, D.; Cho, J.; DiCara, D.; Frazer, S.; Fuller, G. N.; Gao, J.; Gehlenborg, N.; Haussler, D.; Heiman, D. I.; Iype, L.; Jacobsen, A.; Ju, Z.; Katzman, S.; Kim, H.; Knijnenburg, T.; Kreisberg, R. B.; Lawrence, M. S.; Lee, W.; Leinonen, K.; Lin, P.; Ling, S.; Liu, W.; Liu, Y.; Liu, Y.; Lu, Y.; Mills, G.; Ng, S.; Noble, M. S.; Paull, E.; Rao, A.; Reynolds, S.; Saksena, G.; Sanborn, Z.; Sander, C.; Schultz, N.; Senbabaoglu, Y.; Shen, R.; Shmulevich, I.; Sinha, R.; Stuart, J.; Sumer, S. O.; Sun, Y.; Tasman, N.; Taylor, B. S.; Voet, D.; Weinhold, N.; Weinstein, J. N.; Yang, D.; Yoshihara, K.; Zheng, S.; Zhang, W.; Zou, L.; Abel, T.; Sadeghi, S.; Cohen, M. L.; Eschbacher, J.; Hattab, E. M.; Raghunathan, A.; Schniederjan, M. J.; Aziz, D.; Barnett, G.; Barrett, W.; Bigner, D. D.; Boice, L.; Brewer, C.; Calatozzolo, C.; Campos, B.; Carlotti, C. G., Jr.; Chan, T. A.; Cuppini, L.; Curley, E.; Cuzzubbo, S.; Devine, K.; DiMeco, F.; Duell, R.; Elder, J. B.; Fehrenbach, A.; Finocchiaro, G.; Friedman, W.; Fulop, J.; Gardner, J.; Hermes, B.; Herold-Mende, C.; Jungk, C.; Kendler, A.; Lehman, N. L.; Lipp, E.; Liu, O.; Mandt, R.; McGraw, M.; McLendon, R.; McPherson, C.; Neder, L.; Nguyen, P.; Noss, A.; Nunziata, R.; Ostrom, Q. T.; Palmer, C.; Perin, A.; Pollo, B.; Potapov, A.; Potapova, O.; Rathmell, W. K.; Rotin, D.; Scarpace, L.; Schilero, C.; Senecal, K.; Shimmel, K.; Shurkhay, V.; Sifri, S.; Singh, R.; Sloan, A. E.; Smolenski, K.; Staugaitis, S. M.; Steele, R.; Thorne, L.; Tirapelli, D. P.; Unterberg, A.; Vallurupalli, M.; Wang, Y.; Warnick, R.; Williams, F.; Wolinsky, Y.; Bell, S.; Rosenberg, M.; Stewart, C.; Huang, F.; Grimsby, J. L.; Radenbaugh, A. J.; Zhang, J., Comprehensive, Integrative Genomic Analysis of Diffuse Lower-Grade Gliomas. *N Engl J Med* **2015**, 372 (26), 2481-98.

14. Karsy, M.; Guan, J.; Cohen, A. L.; Jensen, R. L.; Colman, H., New Molecular Considerations for Glioma: IDH, ATRX, BRAF, TERT, H3 K27M. *Curr Neurol Neurosci Rep* **2017**, 17 (2), 19.
15. Yan, H.; Parsons, D. W.; Jin, G.; McLendon, R.; Rasheed, B. A.; Yuan, W.; Kos, I.; Batinic-Haberle, I.; Jones, S.; Riggins, G. J.; Friedman, H.; Friedman, A.; Reardon, D.; Herndon, J.; Kinzler, K. W.; Velculescu, V. E.; Vogelstein, B.; Bigner, D. D., IDH1 and IDH2 mutations in gliomas. *N Engl J Med* **2009**, 360 (8), 765-73.
16. Liu, J.; Zhang, X.; Yan, X.; Sun, M.; Fan, Y.; Huang, Y., Significance of TERT and ATRX mutations in glioma. *Oncol Lett* **2019**, 17 (1), 95-102.
17. Walsh, K. M.; Wiencke, J. K.; Lachance, D. H.; Wiemels, J. L.; Molinaro, A. M.; Eckel-Passow, J. E.; Jenkins, R. B.; Wrensch, M. R., Telomere maintenance and the etiology of adult glioma. *Neuro Oncol* **2015**, 17 (11), 1445-52.
18. Haycock, P. C.; Burgess, S.; Nounu, A.; Zheng, J.; Okoli, G. N.; Bowden, J.; Wade, K. H.; Timpson, N. J.; Evans, D. M.; Willeit, P.; Aviv, A.; Gaunt, T. R.; Hemani, G.; Mangino, M.; Ellis, H. P.; Kurian, K. M.; Pooley, K. A.; Eeles, R. A.; Lee, J. E.; Fang, S.; Chen, W. V.; Law, M. H.; Bowdler, L. M.; Iles, M. M.; Yang, Q.; Worrall, B. B.; Markus, H. S.; Hung, R. J.; Amos, C. I.; Spurdle, A. B.; Thompson, D. J.; O'Mara, T. A.; Wolpin, B.; Amundadottir, L.; Stolzenberg-Solomon, R.; Trichopoulou, A.; Onland-Moret, N. C.; Lund, E.; Duell, E. J.; Canzian, F.; Severi, G.; Overvad, K.; Gunter, M. J.; Tumino, R.; Svenson, U.; van Rij, A.; Baas, A. F.; Bown, M. J.; Samani, N. J.; van 't Hof, F. N. G.; Tromp, G.; Jones, G. T.; Kuivaniemi, H.; Elmore, J. R.; Johansson, M.; McKay, J.; Scelo, G.; Carreras-Torres, R.; Gaborieau, V.; Brennan, P.; Bracci, P. M.; Neale, R. E.; Olson, S. H.; Gallinger, S.; Li, D.; Petersen, G. M.; Risch, H. A.; Klein, A. P.; Han, J.; Abnet, C. C.; Freedman, N. D.; Taylor, P. R.; Maris, J. M.; Aben, K. K.; Kiemeny, L. A.; Vermeulen, S. H.; Wiencke, J. K.; Walsh, K. M.; Wrensch, M.; Rice, T.; Turnbull, C.; Litchfield, K.; Paternoster, L.; Standl, M.; Abecasis, G. R.; SanGiovanni, J. P.; Li, Y.; Mijatovic, V.; Sapkota, Y.; Low, S. K.; Zondervan, K. T.; Montgomery, G. W.; Nyholt, D. R.; van Heel, D. A.; Hunt, K.; Arking, D. E.; Ashar, F. N.; Sotoodehnia, N.; Woo, D.; Rosand, J.; Comeau, M. E.; Brown, W. M.; Silverman, E. K.; Hokanson, J. E.; Cho, M. H.; Hui, J.; Ferreira, M. A.; Thompson, P. J.; Morrison, A. C.; Felix, J. F.; Smith, N. L.; Christiano, A. M.; Petukhova, L.; Betz, R. C.; Fan, X.; Zhang, X.; Zhu, C.; Langefeld, C. D.; Thompson, S. D.; Wang, F.; Lin, X.; Schwartz, D. A.; Fingerlin, T.; Rotter, J. I.; Cotch, M. F.; Jensen, R. A.; Munz, M.; Dommisch, H.; Schaefer, A. S.; Han, F.; Ollila, H. M.; Hillary, R. P.; Albagha, O.; Ralston, S. H.; Zeng, C.; Zheng, W.; Shu, X. O.; Reis, A.; Uebe, S.; Huffmeier, U.; Kawamura, Y.; Otowa, T.; Sasaki, T.; Hibberd, M. L.; Davila, S.; Xie, G.; Siminovitch, K.; Bei, J. X.; Zeng, Y. X.; Forsti, A.

- Chen, B.; Landi, S.; Franke, A.; Fischer, A.; Ellinghaus, D.; Flores, C.; Noth, I.; Ma, S. F.; Foo, J. N.; Liu, J.; Kim, J. W.; Cox, D. G.; Delattre, O.; Mirabeau, O.; Skibola, C. F.; Tang, C. S.; Garcia-Barcelo, M.; Chang, K. P.; Su, W. H.; Chang, Y. S.; Martin, N. G.; Gordon, S.; Wade, T. D.; Lee, C.; Kubo, M.; Cha, P. C.; Nakamura, Y.; Levy, D.; Kimura, M.; Hwang, S. J.; Hunt, S.; Spector, T.; Soranzo, N.; Manichaikul, A. W.; Barr, R. G.; Kahali, B.; Speliotes, E.; Yerges-Armstrong, L. M.; Cheng, C. Y.; Jonas, J. B.; Wong, T. Y.; Fogh, I.; Lin, K.; Powell, J. F.; Rice, K.; Relton, C. L.; Martin, R. M.; Davey Smith, G., Association Between Telomere Length and Risk of Cancer and Non-Neoplastic Diseases: A Mendelian Randomization Study. *JAMA Oncol* **2017**, *3* (5), 636-651.
19. Pekmezci, M.; Rice, T.; Molinaro, A. M.; Walsh, K. M.; Decker, P. A.; Hansen, H.; Sicotte, H.; Kollmeyer, T. M.; McCoy, L. S.; Sarkar, G.; Perry, A.; Giannini, C.; Tihan, T.; Berger, M. S.; Wiemels, J. L.; Bracci, P. M.; Eckel-Passow, J. E.; Lachance, D. H.; Clarke, J.; Taylor, J. W.; Luks, T.; Wiencke, J. K.; Jenkins, R. B.; Wrensch, M. R., Adult infiltrating gliomas with WHO 2016 integrated diagnosis: additional prognostic roles of ATRX and TERT. *Acta neuropathologica* **2017**, *133* (6), 1001-1016.
 20. Ohgaki, H.; Kleihues, P., Population-Based Studies on Incidence, Survival Rates, and Genetic Alterations in Astrocytic and Oligodendroglial Gliomas. *Journal of Neuropathology & Experimental Neurology* **2005**, *64* (6), 479-489.
 21. Bettegowda, C.; Agrawal, N.; Jiao, Y.; Sausen, M.; Wood, L. D.; Hruban, R. H.; Rodriguez, F. J.; Cahill, D. P.; McLendon, R.; Riggins, G.; Velculescu, V. E.; Oba-Shinjo, S. M.; Marie, S. K.; Vogelstein, B.; Bigner, D.; Yan, H.; Papadopoulos, N.; Kinzler, K. W., Mutations in CIC and FUBP1 contribute to human oligodendroglioma. *Science* **2011**, *333* (6048), 1453-5.
 22. Halani, S. H.; Yousefi, S.; Velazquez Vega, J.; Rossi, M. R.; Zhao, Z.; Amrollahi, F.; Holder, C. A.; Baxter-Stoltzfus, A.; Eschbacher, J.; Griffith, B.; Olson, J. J.; Jiang, T.; Yates, J. R.; Eberhart, C. G.; Poisson, L. M.; Cooper, L. A. D.; Brat, D. J., Multi-faceted computational assessment of risk and progression in oligodendroglioma implicates NOTCH and PI3K pathways. *NPJ Precis Oncol* **2018**, *2*, 24.
 23. Tamimi, A. F.; Juweid, M., Epidemiology and outcome of glioblastoma. In *Glioblastoma*, Brisbane (AU), 2017.
 24. Aoki, K.; Nakamura, H.; Suzuki, H.; Matsuo, K.; Kataoka, K.; Shimamura, T.; Motomura, K.; Ohka, F.; Shiina, S.; Yamamoto, T.; Nagata, Y.; Yoshizato, T.; Mizoguchi, M.; Abe, T.; Momii, Y.; Muragaki, Y.; Watanabe, R.; Ito, I.; Sanada, M.; Yajima, H.; Morita, N.; Takeuchi, I.; Miyano, S.; Wakabayashi, T.; Ogawa, S.; Natsume, A., Prognostic relevance of genetic alterations in diffuse lower-grade gliomas. *Neuro Oncol* **2018**, *20* (1), 66-77.
 25. Stupp, R.; Mason, W. P.; van den Bent, M. J.; Weller, M.; Fisher, B.; Taphoorn, M. J. B.; Belanger, K.; Brandes, A. A.; Marosi, C.; Bogdahn, U.; Curschmann, J.; Janzer, R. C.; Ludwin, S. K.; Gorlia, T.; Allgeier, A.; Lacombe, D.; Cairncross, J. G.; Eisenhauer, E.; Mirimanoff, R. O., Radiotherapy plus Concomitant and Adjuvant Temozolomide for Glioblastoma. *New England Journal of Medicine* **2005**, *352* (10), 987-996.
 26. Yang, W.; Warrington, N. M.; Taylor, S. J.; Whitmire, P.; Carrasco, E.; Singleton, K. W.; Wu, N.; Lathia, J. D.; Berens, M. E.; Kim, A. H.; Barnholtz-Sloan, J. S.; Swanson, K. R.; Luo, J.; Rubin, J. B., Sex differences in GBM revealed by analysis of patient imaging, transcriptome, and survival data. *Sci Transl Med* **2019**, *11* (473).
 27. Sun, T.; Warrington, N. M.; Luo, J.; Brooks, M. D.; Dahiya, S.; Snyder, S. C.; Sengupta, R.; Rubin, J. B., Sexually dimorphic RB inactivation underlies mesenchymal glioblastoma prevalence in males. *J Clin Invest* **2014**, *124* (9), 4123-33.
 28. Ostrom, Q. T.; Cote, D. J.; Ascha, M.; Kruchko, C.; Barnholtz-Sloan, J. S., Adult Glioma Incidence and Survival by Race or Ethnicity in the United States From 2000 to 2014. *JAMA Oncol* **2018**, *4* (9), 1254-1262.
 29. Omuro, A.; DeAngelis, L. M., Glioblastoma and other malignant gliomas: a clinical review. *JAMA* **2013**, *310* (17), 1842-50.
 30. Labreche, K.; Kinnersley, B.; Berzero, G.; Di Stefano, A. L.; Rahimian, A.; Detrait, I.; Marie, Y.; Grenier-Boley, B.; Hoang-Xuan, K.; Delattre, J. Y.; Idbaih, A.; Houlston, R. S.; Sanson, M., Diffuse

gliomas classified by 1p/19q co-deletion, TERT promoter and IDH mutation status are associated with specific genetic risk loci. *Acta Neuropathol* **2018**, 135 (5), 743-755.

31. Rice, T.; Lachance, D. H.; Molinaro, A. M.; Eckel-Passow, J. E.; Walsh, K. M.; Barnholtz-Sloan, J.; Ostrom, Q. T.; Francis, S. S.; Wiemels, J.; Jenkins, R. B.; Wiencke, J. K.; Wrensch, M. R., Understanding inherited genetic risk of adult glioma - a review. *Neurooncol Pract* **2016**, 3 (1), 10-16.
32. Preston, D. L.; Ron, E.; Yonehara, S.; Kobuke, T.; Fujii, H.; Kishikawa, M.; Tokunaga, M.; Tokuoka, S.; Mabuchi, K., Tumors of the nervous system and pituitary gland associated with atomic bomb radiation exposure. *J Natl Cancer Inst* **2002**, 94 (20), 1555-63.
33. Neglia, J. P.; Robison, L. L.; Stovall, M.; Liu, Y.; Packer, R. J.; Hammond, S.; Yasui, Y.; Kasper, C. E.; Mertens, A. C.; Donaldson, S. S.; Meadows, A. T.; Inskip, P. D., New primary neoplasms of the central nervous system in survivors of childhood cancer: a report from the Childhood Cancer Survivor Study. *J Natl Cancer Inst* **2006**, 98 (21), 1528-37.
34. Pearce, M. S.; Salotti, J. A.; Little, M. P.; McHugh, K.; Lee, C.; Kim, K. P.; Howe, N. L.; Ronckers, C. M.; Rajaraman, P.; Sir Craft, A. W.; Parker, L.; Berrington de González, A., Radiation exposure from CT scans in childhood and subsequent risk of leukaemia and brain tumours: a retrospective cohort study. *Lancet* **2012**, 380 (9840), 499-505.
35. Linos, E.; Raine, T.; Alonso, A.; Michaud, D., Atopy and risk of brain tumors: a meta-analysis. *J Natl Cancer Inst* **2007**, 99 (20), 1544-50.
36. Ohgaki, H.; Kleihues, P., Genetic pathways to primary and secondary glioblastoma. *The American journal of pathology* **2007**, 170 (5), 1445-53.
37. Reitman, Z. J.; Yan, H., Isocitrate dehydrogenase 1 and 2 mutations in cancer: alterations at a crossroads of cellular metabolism. *J Natl Cancer Inst* **2010**, 102 (13), 932-41.
38. Turcan, S.; Rohle, D.; Goenka, A.; Walsh, L. A.; Fang, F.; Yilmaz, E.; Campos, C.; Fabius, A. W.; Lu, C.; Ward, P. S.; Thompson, C. B.; Kaufman, A.; Guryanova, O.; Levine, R.; Heguy, A.; Viale, A.; Morris, L. G.; Huse, J. T.; Mellinghoff, I. K.; Chan, T. A., IDH1 mutation is sufficient to establish the glioma hypermethylator phenotype. *Nature* **2012**, 483 (7390), 479-83.
39. Verhaak, R. G.; Hoadley, K. A.; Purdom, E.; Wang, V.; Qi, Y.; Wilkerson, M. D.; Miller, C. R.; Ding, L.; Golub, T.; Mesirov, J. P.; Alexe, G.; Lawrence, M.; O'Kelly, M.; Tamayo, P.; Weir, B. A.; Gabriel, S.; Winckler, W.; Gupta, S.; Jakkula, L.; Feiler, H. S.; Hodgson, J. G.; James, C. D.; Sarkaria, J. N.; Brennan, C.; Kahn, A.; Spellman, P. T.; Wilson, R. K.; Speed, T. P.; Gray, J. W.; Meyerson, M.; Getz, G.; Perou, C. M.; Hayes, D. N.; Cancer Genome Atlas Research, N., Integrated genomic analysis identifies clinically relevant subtypes of glioblastoma characterized by abnormalities in PDGFRA, IDH1, EGFR, and NF1. *Cancer Cell* **2010**, 17 (1), 98-110.
40. Cheng, L.; Wu, Q.; Guryanova, O. A.; Huang, Z.; Huang, Q.; Rich, J. N.; Bao, S., Elevated invasive potential of glioblastoma stem cells. *Biochem Biophys Res Commun* **2011**, 406 (4), 643-8.
41. Stupp, R.; Hegi, M. E.; Mason, W. P.; van den Bent, M. J.; Taphoorn, M. J.; Janzer, R. C.; Ludwin, S. K.; Allgeier, A.; Fisher, B.; Belanger, K.; Hau, P.; Brandes, A. A.; Gijtenbeek, J.; Marosi, C.; Vecht, C. J.; Mokhtari, K.; Wesseling, P.; Villa, S.; Eisenhauer, E.; Gorlia, T.; Weller, M.; Lacombe, D.; Cairncross, J. G.; Mirimanoff, R. O.; European Organisation for, R.; Treatment of Cancer Brain, T.; Radiation Oncology, G.; National Cancer Institute of Canada Clinical Trials, G., Effects of radiotherapy with concomitant and adjuvant temozolomide versus radiotherapy alone on survival in glioblastoma in a randomised phase III study: 5-year analysis of the EORTC-NCIC trial. *Lancet Oncol* **2009**, 10 (5), 459-66.
42. Stupp, R.; Taillibert, S.; Kanner, A.; Read, W.; Steinberg, D.; Lhermitte, B.; Toms, S.; Idbaih, A.; Ahluwalia, M. S.; Fink, K.; Di Meco, F.; Lieberman, F.; Zhu, J. J.; Stragliotto, G.; Tran, D.; Brem, S.; Hottinger, A.; Kirson, E. D.; Lavy-Shahaf, G.; Weinberg, U.; Kim, C. Y.; Paek, S. H.; Nicholas, G.; Bruna, J.; Hirte, H.; Weller, M.; Palti, Y.; Hegi, M. E.; Ram, Z., Effect of Tumor-Treating Fields Plus Maintenance Temozolomide vs Maintenance Temozolomide Alone on Survival in Patients With Glioblastoma: A Randomized Clinical Trial. *JAMA* **2017**, 318 (23), 2306-2316.
43. Branter, J.; Basu, S.; Smith, S., Tumour treating fields in a combinational therapeutic approach. *Oncotarget* **2018**, 9 (93), 36631-36644.

44. Hegi, M. E.; Diserens, A. C.; Gorlia, T.; Hamou, M. F.; de Tribolet, N.; Weller, M.; Kros, J. M.; Hainfellner, J. A.; Mason, W.; Mariani, L.; Bromberg, J. E.; Hau, P.; Mirimanoff, R. O.; Cairncross, J. G.; Janzer, R. C.; Stupp, R., MGMT gene silencing and benefit from temozolomide in glioblastoma. *N Engl J Med* **2005**, *352* (10), 997-1003.
45. Yang, P.; Zhang, W.; Wang, Y.; Peng, X.; Chen, B.; Qiu, X.; Li, G.; Li, S.; Wu, C.; Yao, K.; Li, W.; Yan, W.; Li, J.; You, Y.; Chen, C. C.; Jiang, T., IDH mutation and MGMT promoter methylation in glioblastoma: results of a prospective registry. *Oncotarget* **2015**, *6* (38), 40896-906.
46. Reifenberger, G.; Wirsching, H. G.; Knobbe-Thomsen, C. B.; Weller, M., Advances in the molecular genetics of gliomas - implications for classification and therapy. *Nat Rev Clin Oncol* **2017**, *14* (7), 434-452.
47. Leu, S.; von Felten, S.; Frank, S.; Vassella, E.; Vajtai, I.; Taylor, E.; Schulz, M.; Hutter, G.; Hench, J.; Schucht, P.; Boulay, J. L.; Mariani, L., IDH/MGMT-driven molecular classification of low-grade glioma is a strong predictor for long-term survival. *Neuro Oncol* **2013**, *15* (4), 469-79.
48. Weller, M.; Stupp, R.; Hegi, M. E.; van den Bent, M.; Tonn, J. C.; Sanson, M.; Wick, W.; Reifenberger, G., Personalized care in neuro-oncology coming of age: why we need MGMT and 1p/19q testing for malignant glioma patients in clinical practice. *Neuro Oncol* **2012**, *14* Suppl 4, iv100-8.
49. McLendon, R.; Friedman, A.; Bigner, D.; Van Meir, E. G.; Brat, D. J.; M. Mastrogiannis, G.; Olson, J. J.; Mikkelsen, T.; Lehman, N.; Aldape, K.; Alfred Yung, W. K.; Bogler, O.; Vandenberg, S.; Berger, M.; Prados, M.; Muzny, D.; Morgan, M.; Scherer, S.; Sabo, A.; Nazareth, L.; Lewis, L.; Hall, O.; Zhu, Y.; Ren, Y.; Alvi, O.; Yao, J.; Hawes, A.; Jhangiani, S.; Fowler, G.; San Lucas, A.; Kovar, C.; Cree, A.; Dinh, H.; Santibanez, J.; Joshi, V.; Gonzalez-Garay, M. L.; Miller, C. A.; Milosavljevic, A.; Donehower, L.; Wheeler, D. A.; Gibbs, R. A.; Cibulskis, K.; Sougnez, C.; Fennell, T.; Mahan, S.; Wilkinson, J.; Ziaugra, L.; Onofrio, R.; Bloom, T.; Nicol, R.; Ardlie, K.; Baldwin, J.; Gabriel, S.; Lander, E. S.; Ding, L.; Fulton, R. S.; McLellan, M. D.; Wallis, J.; Larson, D. E.; Shi, X.; Abbott, R.; Fulton, L.; Chen, K.; Koboldt, D. C.; Wendl, M. C.; Meyer, R.; Tang, Y.; Lin, L.; Osborne, J. R.; Dunford-Shore, B. H.; Miner, T. L.; Delehaanty, K.; Markovic, C.; Swift, G.; Courtney, W.; Pohl, C.; Abbott, S.; Hawkins, A.; Leong, S.; Haipek, C.; Schmidt, H.; Wiechert, M.; Vickery, T.; Scott, S.; Dooling, D. J.; Chinwalla, A.; Weinstock, G. M.; Mardis, E. R.; Wilson, R. K.; Getz, G.; Winckler, W.; Verhaak, R. G. W.; Lawrence, M. S.; O'Kelly, M.; Robinson, J.; Alexe, G.; Beroukhim, R.; Carter, S.; Chiang, D.; Gould, J.; Gupta, S.; Korn, J.; Mermel, C.; Mesirov, J.; Monti, S.; Nguyen, H.; Parkin, M.; Reich, M.; Stransky, N.; Weir, B. A.; Garraway, L.; Golub, T.; Meyerson, M.; Chin, L.; Protopopov, A.; Zhang, J.; Perna, I.; Aronson, S.; Sathiamoorthy, N.; Ren, G.; Yao, J.; Wiedemeyer, W. R.; Kim, H.; Won Kong, S.; Xiao, Y.; Kohane, I. S.; Seidman, J.; Park, P. J.; Kucherlapati, R.; Laird, P. W.; Cope, L.; Herman, J. G.; Weisenberger, D. J.; Pan, F.; Van Den Berg, D.; Van Neste, L.; Mi Yi, J.; Schuebel, K. E.; Baylin, S. B.; Absher, D. M.; Li, J. Z.; Southwick, A.; Brady, S.; Aggarwal, A.; Chung, T.; Sherlock, G.; Brooks, J. D.; Myers, R. M.; Spellman, P. T.; Purdom, E.; Jakkula, L. R.; Lapuk, A. V.; Marr, H.; Dorton, S.; Gi Choi, Y.; Han, J.; Ray, A.; Wang, V.; Durinck, S.; Robinson, M.; Wang, N. J.; Vranizan, K.; Peng, V.; Van Name, E.; Fontenay, G. V.; Ngai, J.; Conboy, J. G.; Parvin, B.; Feiler, H. S.; Speed, T. P.; Gray, J. W.; Brennan, C.; Socci, N. D.; Olshen, A.; Taylor, B. S.; Lash, A.; Schultz, N.; Reva, B.; Antipin, Y.; Stukalov, A.; Gross, B.; Cerami, E.; Qing Wang, W.; Qin, L.-X.; Seshan, V. E.; Villafania, L.; Cavatore, M.; Borsu, L.; Viale, A.; Gerald, W.; Sander, C.; Ladanyi, M.; Perou, C. M.; Neil Hayes, D.; Topal, M. D.; Hoadley, K. A.; Qi, Y.; Balu, S.; Shi, Y.; Wu, J.; Penny, R.; Bittner, M.; Shelton, T.; Lenkiewicz, E.; Morris, S.; Beasley, D.; Sanders, S.; Kahn, A.; Sfeir, R.; Chen, J.; Nassau, D.; Feng, L.; Hickey, E.; Zhang, J.; Weinstein, J. N.; Barker, A.; Gerhard, D. S.; Vockley, J.; Compton, C.; Vaught, J.; Fielding, P.; Ferguson, M. L.; Schaefer, C.; Madhavan, S.; Buetow, K. H.; Collins, F.; Good, P.; Guyer, M.; Ozenberger, B.; Peterson, J.; Thomson, E.; The Cancer Genome Atlas Research, N., Comprehensive genomic characterization defines human glioblastoma genes and core pathways. *Nature* **2008**, *455* (7216), 1061-1068.
50. Brennan, C. W.; Verhaak, R. G. W.; McKenna, A.; Campos, B.; Noushmehr, H.; Salama, S. R.; Zheng, S.; Chakravarty, D.; Sanborn, J. Z.; Berman, S. H.; Beroukhim, R.; Bernard, B.; Wu, C.-J.; Genovese, G.; Shmulevich, I.; Barnholtz-Sloan, J.; Zou, L.; Vegesna, R.; Shukla, S. A.; Ciriello, G.; Yung, W. K.; Zhang, W.; Sougnez, C.; Mikkelsen, T.; Aldape, K.; Bigner, D. D.; Van Meir, E. G.; Prados, M.; Sloan, A.; Black, K. L.; Eschbacher, J.; Finocchiaro, G.; Friedman, W.; Andrews, D. W.; Guha, A.; Iacocca, M.; O'Neill, B. P.; Foltz, G.; Myers, J.; Weisenberger, D. J.; Penny, R.; Kucherlapati, R.; Perou, C. M.; Hayes, D. N.; Gibbs, R.; Marra, M.; Mills, G. B.; Lander, E.; Spellman, P.; Wilson, R.; Sander, C.; Weinstein, J.; Meyerson, M.; Gabriel, S.; Laird, P. W.; Haussler, D.; Getz, G.; Chin, L., The Somatic Genomic Landscape of Glioblastoma. *Cell* **2013**, *155* (2), 462-477.

51. Hanahan, D.; Weinberg, R. A., Hallmarks of cancer: the next generation. *Cell* **2011**, *144* (5), 646-74.
52. Pearson, J. R. D.; Regad, T., Targeting cellular pathways in glioblastoma multiforme. *Signal Transduct Target Ther* **2017**, *2*, 17040.
53. Inda, M. M.; Bonavia, R.; Mukasa, A.; Narita, Y.; Sah, D. W.; Vandenberg, S.; Brennan, C.; Johns, T. G.; Bachoo, R.; Hadwiger, P.; Tan, P.; Depinho, R. A.; Cavenee, W.; Furnari, F., Tumor heterogeneity is an active process maintained by a mutant EGFR-induced cytokine circuit in glioblastoma. *Genes Dev* **2010**, *24* (16), 1731-45.
54. Heimberger, A. B.; Hlatky, R.; Suki, D.; Yang, D.; Weinberg, J.; Gilbert, M.; Sawaya, R.; Aldape, K., Prognostic effect of epidermal growth factor receptor and EGFRvIII in glioblastoma multiforme patients. *Clin Cancer Res* **2005**, *11* (4), 1462-6.
55. Bachoo, R. M.; Maher, E. A.; Ligon, K. L.; Sharpless, N. E.; Chan, S. S.; You, M. J.; Tang, Y.; DeFrances, J.; Stover, E.; Weissleder, R.; Rowitch, D. H.; Louis, D. N.; DePinho, R. A., Epidermal growth factor receptor and Ink4a/Arf: convergent mechanisms governing terminal differentiation and transformation along the neural stem cell to astrocyte axis. *Cancer Cell* **2002**, *1* (3), 269-77.
56. Zhu, H.; Acquaviva, J.; Ramachandran, P.; Boskovitz, A.; Woolfenden, S.; Pfannl, R.; Bronson, R. T.; Chen, J. W.; Weissleder, R.; Housman, D. E.; Charest, A., Oncogenic EGFR signaling cooperates with loss of tumor suppressor gene functions in gliomagenesis. *Proc Natl Acad Sci U S A* **2009**, *106* (8), 2712-6.
57. Mellinghoff, I. K.; Wang, M. Y.; Vivanco, I.; Haas-Kogan, D. A.; Zhu, S.; Dia, E. Q.; Lu, K. V.; Yoshimoto, K.; Huang, J. H.; Chute, D. J.; Riggs, B. L.; Horvath, S.; Liau, L. M.; Cavenee, W. K.; Rao, P. N.; Beroukhi, R.; Peck, T. C.; Lee, J. C.; Sellers, W. R.; Stokoe, D.; Prados, M.; Cloughesy, T. F.; Sawyers, C. L.; Mischel, P. S., Molecular determinants of the response of glioblastomas to EGFR kinase inhibitors. *N Engl J Med* **2005**, *353* (19), 2012-24.
58. Dunn, G. P.; Rinne, M. L.; Wykosky, J.; Genovese, G.; Quayle, S. N.; Dunn, I. F.; Agarwalla, P. K.; Chheda, M. G.; Campos, B.; Wang, A.; Brennan, C.; Ligon, K. L.; Furnari, F.; Cavenee, W. K.; Depinho, R. A.; Chin, L.; Hahn, W. C., Emerging insights into the molecular and cellular basis of glioblastoma. *Genes Dev* **2012**, *26* (8), 756-84.
59. Zhao, H. F.; Wang, J.; Shao, W.; Wu, C. P.; Chen, Z. P.; To, S. T.; Li, W. P., Recent advances in the use of PI3K inhibitors for glioblastoma multiforme: current preclinical and clinical development. *Mol Cancer* **2017**, *16* (1), 100.
60. Burkhart, D. L.; Sage, J., Cellular mechanisms of tumour suppression by the retinoblastoma gene. *Nat Rev Cancer* **2008**, *8* (9), 671-82.
61. Lane, D. P., Cancer. p53, guardian of the genome. *Nature* **1992**, *358* (6381), 15-6.
62. Vousden, K. H.; Lu, X., Live or let die: the cell's response to p53. *Nat Rev Cancer* **2002**, *2* (8), 594-604.
63. Kruse, J. P.; Gu, W., Modes of p53 regulation. *Cell* **2009**, *137* (4), 609-22.
64. Parsons, D. W.; Jones, S.; Zhang, X.; Lin, J. C.; Leary, R. J.; Angenendt, P.; Mankoo, P.; Carter, H.; Siu, I. M.; Gallia, G. L.; Olivi, A.; McLendon, R.; Rasheed, B. A.; Keir, S.; Nikolskaya, T.; Nikolsky, Y.; Busam, D. A.; Tekleab, H.; Diaz, L. A., Jr.; Hartigan, J.; Smith, D. R.; Strausberg, R. L.; Marie, S. K.; Shinjo, S. M.; Yan, H.; Riggins, G. J.; Bigner, D. D.; Karchin, R.; Papadopoulos, N.; Parmigiani, G.; Vogelstein, B.; Velculescu, V. E.; Kinzler, K. W., An integrated genomic analysis of human glioblastoma multiforme. *Science* **2008**, *321* (5897), 1807-12.
65. el-Deiry, W. S.; Tokino, T.; Velculescu, V. E.; Levy, D. B.; Parsons, R.; Trent, J. M.; Lin, D.; Mercer, W. E.; Kinzler, K. W.; Vogelstein, B., WAF1, a potential mediator of p53 tumor suppression. *Cell* **1993**, *75* (4), 817-25.
66. Toledo, F.; Wahl, G. M., MDM2 and MDM4: p53 regulators as targets in anticancer therapy. *Int J Biochem Cell Biol* **2007**, *39* (7-8), 1476-82.

67. Raizer, J. J.; Abrey, L. E.; Lassman, A. B.; Chang, S. M.; Lamborn, K. R.; Kuhn, J. G.; Yung, W. K.; Gilbert, M. R.; Aldape, K. A.; Wen, P. Y.; Fine, H. A.; Mehta, M.; Deangelis, L. M.; Lieberman, F.; Cloughesy, T. F.; Robins, H. I.; Dancey, J.; Prados, M. D.; North American Brain Tumor, C., A phase II trial of erlotinib in patients with recurrent malignant gliomas and nonprogressive glioblastoma multiforme postradiation therapy. *Neuro Oncol* **2010**, *12* (1), 95-103.
68. Prados, M. D.; Chang, S. M.; Butowski, N.; DeBoer, R.; Parvataneni, R.; Carliner, H.; Kabuubi, P.; Ayers-Ringler, J.; Rabbitt, J.; Page, M.; Fedoroff, A.; Sneed, P. K.; Berger, M. S.; McDermott, M. W.; Parsa, A. T.; Vandenberg, S.; James, C. D.; Lamborn, K. R.; Stokoe, D.; Haas-Kogan, D. A., Phase II study of erlotinib plus temozolomide during and after radiation therapy in patients with newly diagnosed glioblastoma multiforme or gliosarcoma. *J Clin Oncol* **2009**, *27* (4), 579-84.
69. Uhm, J. H.; Ballman, K. V.; Wu, W.; Giannini, C.; Krauss, J. C.; Buckner, J. C.; James, C. D.; Scheithauer, B. W.; Behrens, R. J.; Flynn, P. J.; Schaefer, P. L.; Dakhil, S. R.; Jaeckle, K. A., Phase II evaluation of gefitinib in patients with newly diagnosed Grade 4 astrocytoma: Mayo/North Central Cancer Treatment Group Study N0074. *Int J Radiat Oncol Biol Phys* **2011**, *80* (2), 347-53.
70. Reardon, D. A.; Nabors, L. B.; Mason, W. P.; Perry, J. R.; Shapiro, W.; Kavan, P.; Mathieu, D.; Phuphanich, S.; Cseh, A.; Fu, Y.; Cong, J.; Wind, S.; Eisenstat, D. D.; Group, B. I. T.; the Canadian Brain Tumour, C., Phase I/randomized phase II study of afatinib, an irreversible ErbB family blocker, with or without protracted temozolomide in adults with recurrent glioblastoma. *Neuro Oncol* **2015**, *17* (3), 430-9.
71. Neyns, B.; Sadones, J.; Joosens, E.; Bouttens, F.; Verbeke, L.; Baurain, J. F.; D'Hondt, L.; Strauven, T.; Chaskis, C.; In't Veld, P.; Michotte, A.; De Greve, J., Stratified phase II trial of cetuximab in patients with recurrent high-grade glioma. *Ann Oncol* **2009**, *20* (9), 1596-1603.
72. Yang, S. B.; Gao, K. D.; Jiang, T.; Cheng, S. J.; Li, W. B., Bevacizumab combined with chemotherapy for glioblastoma: a meta-analysis of randomized controlled trials. *Oncotarget* **2017**, *8* (34), 57337-57344.
73. Raymond, E.; Brandes, A. A.; Dittrich, C.; Fumoleau, P.; Coudert, B.; Clement, P. M.; Frenay, M.; Rampling, R.; Stupp, R.; Kros, J. M.; Heinrich, M. C.; Gorlia, T.; Lacombe, D.; van den Bent, M. J.; European Organisation for, R.; Treatment of Cancer Brain Tumor Group, S., Phase II study of imatinib in patients with recurrent gliomas of various histologies: a European Organisation for Research and Treatment of Cancer Brain Tumor Group Study. *J Clin Oncol* **2008**, *26* (28), 4659-65.
74. Dresemann, G.; Weller, M.; Rosenthal, M. A.; Wedding, U.; Wagner, W.; Engel, E.; Heinrich, B.; Mayer-Steinacker, R.; Karup-Hansen, A.; Fluge, O.; Nowak, A.; Mehdorn, M.; Schleyer, E.; Krex, D.; Olver, I. N.; Steinbach, J. P.; Hosius, C.; Sieder, C.; Sorenson, G.; Parker, R.; Nikolova, Z., Imatinib in combination with hydroxyurea versus hydroxyurea alone as oral therapy in patients with progressive pretreated glioblastoma resistant to standard dose temozolomide. *J Neurooncol* **2010**, *96* (3), 393-402.
75. Grisanti, S.; Ferrari, V. D.; Buglione, M.; Agazzi, G. M.; Liserre, R.; Poliani, L.; Buttolo, L.; Gipponi, S.; Pedersini, R.; Consoli, F.; Panciani, P.; Roca, E.; Spena, G.; Triggiani, L.; Berruti, A.; Gruppo Neuro-Oncologico, B., Second line treatment of recurrent glioblastoma with sunitinib: results of a phase II study and systematic review of literature. *J Neurosurg Sci* **2019**, *63* (4), 458-467.
76. Lassman, A. B.; Pugh, S. L.; Gilbert, M. R.; Aldape, K. D.; Geinoz, S.; Beumer, J. H.; Christner, S. M.; Komaki, R.; DeAngelis, L. M.; Gaur, R.; Youssef, E.; Wagner, H.; Won, M.; Mehta, M. P., Phase 2 trial of dasatinib in target-selected patients with recurrent glioblastoma (RTOG 0627). *Neuro Oncol* **2015**, *17* (7), 992-8.
77. Laack, N. N.; Galanis, E.; Anderson, S. K.; Leinweber, C.; Buckner, J. C.; Giannini, C.; Geoffroy, F. J.; Johnson, D. R.; Lesser, G. J.; Jaeckle, K. A.; Sarkaria, J. N., Randomized, placebo-controlled, phase II study of dasatinib with standard chemo-radiotherapy for newly diagnosed glioblastoma (GBM), NCCTG N0877 (Alliance). *Journal of Clinical Oncology* **2015**, *33* (15_suppl), 2013-2013.
78. Wen, P. Y.; Drappatz, J.; de Groot, J.; Prados, M. D.; Reardon, D. A.; Schiff, D.; Chamberlain, M.; Mikkelsen, T.; Desjardins, A.; Holland, J.; Ping, J.; Weitzman, R.; Cloughesy, T. F., Phase II study of cabozantinib in patients with progressive glioblastoma: subset analysis of patients naive to antiangiogenic therapy. *Neuro Oncol* **2018**, *20* (2), 249-258.

79. Wen, P. Y.; Touat, M.; Alexander, B. M.; Mellinghoff, I. K.; Ramkissoon, S.; McCluskey, C. S.; Pelton, K.; Haidar, S.; Basu, S. S.; Gaffey, S. C.; Brown, L. E.; Martinez-Ledesma, J. E.; Wu, S.; Kim, J.; Wei, W.; Park, M. A.; Huse, J. T.; Kuhn, J. G.; Rinne, M. L.; Colman, H.; Agar, N. Y. R.; Omuro, A. M.; DeAngelis, L. M.; Gilbert, M. R.; de Groot, J. F.; Cloughesy, T. F.; Chi, A. S.; Roberts, T. M.; Zhao, J. J.; Lee, E. Q.; Nayak, L.; Heath, J. R.; Horky, L. L.; Batchelor, T. T.; Beroukhi, R.; Chang, S. M.; Ligon, A. H.; Dunn, I. F.; Koul, D.; Young, G. S.; Prados, M. D.; Reardon, D. A.; Yung, W. K. A.; Ligon, K. L., Buparlisib in Patients With Recurrent Glioblastoma Harboring Phosphatidylinositol 3-Kinase Pathway Activation: An Open-Label, Multicenter, Multi-Arm, Phase II Trial. *J Clin Oncol* **2019**, *37* (9), 741-750.
80. Halatsch, M. E.; Gehrke, E. E.; Vougioukas, V. I.; Botefur, I. C.; F, A. B.; Efferth, T.; Gebhart, E.; Domhof, S.; Schmidt, U.; Buchfelder, M., Inverse correlation of epidermal growth factor receptor messenger RNA induction and suppression of anchorage-independent growth by OSI-774, an epidermal growth factor receptor tyrosine kinase inhibitor, in glioblastoma multiforme cell lines. *J Neurosurg* **2004**, *100* (3), 523-33.
81. Parker, J. J.; Dionne, K. R.; Massarwa, R.; Klaassen, M.; Foreman, N. K.; Niswander, L.; Canoll, P.; Kleinschmidt-Demasters, B. K.; Waziri, A., Gefitinib selectively inhibits tumor cell migration in EGFR-amplified human glioblastoma. *Neuro Oncol* **2013**, *15* (8), 1048-57.
82. Griffiero, F.; Daga, A.; Marubbi, D.; Capra, M. C.; Melotti, A.; Pattarozzi, A.; Gatti, M.; Bajetto, A.; Porcile, C.; Barbieri, F.; Favoni, R. E.; Lo Casto, M.; Zona, G.; Spaziante, R.; Florio, T.; Corte, G., Different response of human glioma tumor-initiating cells to epidermal growth factor receptor kinase inhibitors. *J Biol Chem* **2009**, *284* (11), 7138-48.
83. Goodwin, C. R.; Rath, P.; Oyinlade, O.; Lopez, H.; Mughal, S.; Xia, S.; Li, Y.; Kaur, H.; Zhou, X.; Ahmed, A. K.; Ho, S.; Olivi, A.; Lal, B., Crizotinib and erlotinib inhibits growth of c-Met(+)/EGFRvIII(+) primary human glioblastoma xenografts. *Clin Neurol Neurosurg* **2018**, *171*, 26-33.
84. Sarkaria, J. N.; Yang, L.; Grogan, P. T.; Kitange, G. J.; Carlson, B. L.; Schroeder, M. A.; Galanis, E.; Giannini, C.; Wu, W.; Dinca, E. B.; James, C. D., Identification of molecular characteristics correlated with glioblastoma sensitivity to EGFR kinase inhibition through use of an intracranial xenograft test panel. *Mol Cancer Ther* **2007**, *6* (3), 1167-74.
85. Vengoji, R.; Macha, M. A.; Nimmakayala, R. K.; Rachagani, S.; Siddiqui, J. A.; Mallya, K.; Gorantla, S.; Jain, M.; Ponnusamy, M. P.; Batra, S. K.; Shonka, N., Afatinib and Temozolomide combination inhibits tumorigenesis by targeting EGFRvIII-cMet signaling in glioblastoma cells. *J Exp Clin Cancer Res* **2019**, *38* (1), 266.
86. Eller, J. L.; Longo, S. L.; Kyle, M. M.; Bassano, D.; Hicklin, D. J.; Canute, G. W., Anti-epidermal growth factor receptor monoclonal antibody cetuximab augments radiation effects in glioblastoma multiforme in vitro and in vivo. *Neurosurgery* **2005**, *56* (1), 155-62; discussion 162.
87. Song, J.; Xue, Y. Q.; Zhao, M. M.; Xu, P., Effectiveness of lomustine and bevacizumab in progressive glioblastoma: a meta-analysis. *Onco Targets Ther* **2018**, *11*, 3435-3439.
88. Wick, W.; Gorlia, T.; Bendszus, M.; Taphoorn, M.; Sahn, F.; Harting, I.; Brandes, A. A.; Taal, W.; Domont, J.; Idbaih, A.; Campone, M.; Clement, P. M.; Stupp, R.; Fabbro, M.; Le Rhun, E.; Dubois, F.; Weller, M.; von Deimling, A.; Golfinopoulos, V.; Bromberg, J. C.; Platten, M.; Klein, M.; van den Bent, M. J., Lomustine and Bevacizumab in Progressive Glioblastoma. *N Engl J Med* **2017**, *377* (20), 1954-1963.
89. DeLay, M.; Jahangiri, A.; Carbonell, W. S.; Hu, Y. L.; Tsao, S.; Tom, M. W.; Paquette, J.; Tokuyasu, T. A.; Aghi, M. K., Microarray analysis verifies two distinct phenotypes of glioblastomas resistant to antiangiogenic therapy. *Clin Cancer Res* **2012**, *18* (10), 2930-42.
90. Russell, J. S.; Brady, K.; Burgan, W. E.; Cerra, M. A.; Oswald, K. A.; Camphausen, K.; Tofilon, P. J., Gleevec-mediated inhibition of Rad51 expression and enhancement of tumor cell radiosensitivity. *Cancer Res* **2003**, *63* (21), 7377-83.
91. Geng, L.; Shinohara, E. T.; Kim, D.; Tan, J.; Osusky, K.; Shyr, Y.; Hallahan, D. E., STI571 (Gleevec) improves tumor growth delay and survival in irradiated mouse models of glioblastoma. *Int J Radiat Oncol Biol Phys* **2006**, *64* (1), 263-71.

92. de Bouvard, S.; Herlin, P.; Christensen, J. G.; Lemoisson, E.; Gauduchon, P.; Raymond, E.; Guillamo, J. S., Antiangiogenic and anti-invasive effects of sunitinib on experimental human glioblastoma. *Neuro Oncol* **2007**, *9* (4), 412-23.
93. D'Amico, R.; Lei, L.; Kennedy, B. C.; Sisti, J.; Ebiana, V.; Crisman, C.; Christensen, J. G.; Gil, O.; Rosenfeld, S. S.; Canoll, P.; Bruce, J. N., The addition of Sunitinib to radiation delays tumor growth in a murine model of glioblastoma. *Neurol Res* **2012**, *34* (3), 252-61.
94. Hainsworth, J. D.; Ervin, T.; Friedman, E.; Priego, V.; Murphy, P. B.; Clark, B. L.; Lamar, R. E., Concurrent radiotherapy and temozolomide followed by temozolomide and sorafenib in the first-line treatment of patients with glioblastoma multiforme. *Cancer* **2010**, *116* (15), 3663-9.
95. Ahluwalia, M. S.; de Groot, J.; Liu, W. M.; Gladson, C. L., Targeting SRC in glioblastoma tumors and brain metastases: rationale and preclinical studies. *Cancer Lett* **2010**, *298* (2), 139-49.
96. Navis, A. C.; Bourgonje, A.; Wesseling, P.; Wright, A.; Hendriks, W.; Verrijp, K.; van der Laak, J. A.; Heerschap, A.; Leenders, W. P., Effects of dual targeting of tumor cells and stroma in human glioblastoma xenografts with a tyrosine kinase inhibitor against c-MET and VEGFR2. *PLoS One* **2013**, *8* (3), e58262.
97. Burger, M. T.; Pecchi, S.; Wagman, A.; Ni, Z. J.; Knapp, M.; Hendrickson, T.; Atallah, G.; Pfister, K.; Zhang, Y.; Bartulis, S.; Frazier, K.; Ng, S.; Smith, A.; Verhagen, J.; Haznedar, J.; Huh, K.; Iwanowicz, E.; Xin, X.; Menezes, D.; Merritt, H.; Lee, I.; Wiesmann, M.; Kaufman, S.; Crawford, K.; Chin, M.; Bussiere, D.; Shoemaker, K.; Zaror, I.; Maira, S. M.; Voliva, C. F., Identification of NVP-BKM120 as a Potent, Selective, Orally Bioavailable Class I PI3 Kinase Inhibitor for Treating Cancer. *ACS Med Chem Lett* **2011**, *2* (10), 774-9.
98. Koul, D.; Fu, J.; Shen, R.; LaFortune, T. A.; Wang, S.; Tiao, N.; Kim, Y. W.; Liu, J. L.; Ramnarian, D.; Yuan, Y.; Garcia-Echeverria, C.; Maira, S. M.; Yung, W. K., Antitumor activity of NVP-BKM120-a selective pan class I PI3 kinase inhibitor showed differential forms of cell death based on p53 status of glioma cells. *Clin Cancer Res* **2012**, *18* (1), 184-95.
99. Koul, D.; Shen, R.; Kim, Y. W.; Kondo, Y.; Lu, Y.; Bankson, J.; Ronen, S. M.; Kirkpatrick, D. L.; Powis, G.; Yung, W. K., Cellular and in vivo activity of a novel PI3K inhibitor, PX-866, against human glioblastoma. *Neuro Oncol* **2010**, *12* (6), 559-69.
100. Gwak, H. S.; Shingu, T.; Chumbalkar, V.; Hwang, Y. H.; DeJournett, R.; Latha, K.; Koul, D.; Alfred Yung, W. K.; Powis, G.; Farrell, N. P.; Bogler, O., Combined action of the dinuclear platinum compound BBR3610 with the PI3-K inhibitor PX-866 in glioblastoma. *Int J Cancer* **2011**, *128* (4), 787-96.
101. Pitz, M. W.; Eisenhauer, E. A.; MacNeil, M. V.; Thiessen, B.; Easaw, J. C.; Macdonald, D. R.; Eisenstat, D. D.; Kakumanu, A. S.; Salim, M.; Chalchal, H.; Squire, J.; Tsao, M. S.; Kamel-Reid, S.; Banerji, S.; Tu, D.; Powers, J.; Hausman, D. F.; Mason, W. P., Phase II study of PX-866 in recurrent glioblastoma. *Neuro Oncol* **2015**, *17* (9), 1270-4.
102. Huang, L.; Fu, L., Mechanisms of resistance to EGFR tyrosine kinase inhibitors. *Acta Pharm Sin B* **2015**, *5* (5), 390-401.
103. Schrock, A. B.; Zhu, V. W.; Hsieh, W. S.; Madison, R.; Creelan, B.; Silberberg, J.; Costin, D.; Bharne, A.; Bonta, I.; Bosemani, T.; Nikolinakos, P.; Ross, J. S.; Miller, V. A.; Ali, S. M.; Klempner, S. J.; Ou, S. I., Receptor Tyrosine Kinase Fusions and BRAF Kinase Fusions are Rare but Actionable Resistance Mechanisms to EGFR Tyrosine Kinase Inhibitors. *J Thorac Oncol* **2018**, *13* (9), 1312-1323.
104. Xu, H.; Shen, J.; Xiang, J.; Li, H.; Li, B.; Zhang, T.; Zhang, L.; Mao, X.; Jian, H.; Shu, Y., Characterization of acquired receptor tyrosine-kinase fusions as mechanisms of resistance to EGFR tyrosine-kinase inhibitors. *Cancer Manag Res* **2019**, *11*, 6343-6351.
105. Westphal, M.; Maire, C. L.; Lamszus, K., EGFR as a Target for Glioblastoma Treatment: An Unfulfilled Promise. *CNS Drugs* **2017**, *31* (9), 723-735.
106. Liau, B. B.; Sievers, C.; Donohue, L. K.; Gillespie, S. M.; Flavahan, W. A.; Miller, T. E.; Venteicher, A. S.; Hebert, C. H.; Carey, C. D.; Rodig, S. J.; Shareef, S. J.; Najm, F. J.; van Galen, P.; Wakimoto, H.; Cahill, D. P.; Rich, J. N.; Aster, J. C.; Suva, M. L.; Patel, A. P.; Bernstein, B. E., Adaptive Chromatin

- Remodeling Drives Glioblastoma Stem Cell Plasticity and Drug Tolerance. *Cell Stem Cell* **2017**, *20* (2), 233-246 e7.
107. Cloughesy, T. F.; Cavenee, W. K.; Mischel, P. S., Glioblastoma: from molecular pathology to targeted treatment. *Annu Rev Pathol* **2014**, *9*, 1-25.
 108. Bonavia, R.; Inda, M. M.; Cavenee, W. K.; Furnari, F. B., Heterogeneity maintenance in glioblastoma: a social network. *Cancer Res* **2011**, *71* (12), 4055-60.
 109. Pucciarelli, D.; Lengger, N.; Takacova, M.; Csaderova, L.; Bartosova, M.; Breiteneder, H.; Pastorekova, S.; Hafner, C., Hypoxia increases the heterogeneity of melanoma cell populations and affects the response to vemurafenib. *Mol Med Rep* **2016**, *13* (4), 3281-8.
 110. Prager, B. C.; Bhargava, S.; Mahadev, V.; Hubert, C. G.; Rich, J. N., Glioblastoma Stem Cells: Driving Resilience through Chaos. *Trends Cancer* **2020**, *6* (3), 223-235.
 111. Phillips, H. S.; Kharbanda, S.; Chen, R.; Forrest, W. F.; Soriano, R. H.; Wu, T. D.; Misra, A.; Nigro, J. M.; Colman, H.; Soroceanu, L.; Williams, P. M.; Modrusan, Z.; Feuerstein, B. G.; Aldape, K., Molecular subclasses of high-grade glioma predict prognosis, delineate a pattern of disease progression, and resemble stages in neurogenesis. *Cancer Cell* **2006**, *9* (3), 157-73.
 112. Brennan, C.; Momota, H.; Hambardzumyan, D.; Ozawa, T.; Tandon, A.; Pedraza, A.; Holland, E., Glioblastoma subclasses can be defined by activity among signal transduction pathways and associated genomic alterations. *PLoS One* **2009**, *4* (11), e7752.
 113. Shi, Q.; Qin, L.; Wei, W.; Geng, F.; Fan, R.; Shin, Y. S.; Guo, D.; Hood, L.; Mischel, P. S.; Heath, J. R., Single-cell proteomic chip for profiling intracellular signaling pathways in single tumor cells. *Proc Natl Acad Sci U S A* **2012**, *109* (2), 419-24.
 114. Sottoriva, A.; Spiteri, I.; Piccirillo, S. G.; Touloumis, A.; Collins, V. P.; Marioni, J. C.; Curtis, C.; Watts, C.; Tavare, S., Intratumor heterogeneity in human glioblastoma reflects cancer evolutionary dynamics. *Proc Natl Acad Sci U S A* **2013**, *110* (10), 4009-14.
 115. Mukherjee, B.; McEllin, B.; Camacho, C. V.; Tomimatsu, N.; Sirasanagandala, S.; Nannepaga, S.; Hatanpaa, K. J.; Mickey, B.; Madden, C.; Maher, E.; Boothman, D. A.; Furnari, F.; Cavenee, W. K.; Bachoo, R. M.; Burma, S., EGFRvIII and DNA double-strand break repair: a molecular mechanism for radioresistance in glioblastoma. *Cancer Res* **2009**, *69* (10), 4252-9.
 116. Broekman, M. L.; Maas, S. L. N.; Abels, E. R.; Mempel, T. R.; Krichevsky, A. M.; Breakefield, X. O., Multidimensional communication in the microenvirons of glioblastoma. *Nat Rev Neurol* **2018**, *14* (8), 482-495.
 117. Dirkse, A.; Golebiewska, A.; Buder, T.; Nazarov, P. V.; Muller, A.; Poovathingal, S.; Brons, N. H. C.; Leite, S.; Sauvageot, N.; Sarkisjan, D.; Seyfrid, M.; Fritah, S.; Stieber, D.; Michelucci, A.; Hertel, F.; Herold-Mende, C.; Azuaje, F.; Skupin, A.; Bjerkvig, R.; Deutsch, A.; Voss-Bohme, A.; Niclou, S. P., Stem cell-associated heterogeneity in Glioblastoma results from intrinsic tumor plasticity shaped by the microenvironment. *Nat Commun* **2019**, *10* (1), 1787.
 118. Gimple, R. C.; Bhargava, S.; Dixit, D.; Rich, J. N., Glioblastoma stem cells: lessons from the tumor hierarchy in a lethal cancer. *Genes Dev* **2019**, *33* (11-12), 591-609.
 119. Singh, S. K.; Hawkins, C.; Clarke, I. D.; Squire, J. A.; Bayani, J.; Hide, T.; Henkelman, R. M.; Cusimano, M. D.; Dirks, P. B., Identification of human brain tumour initiating cells. *Nature* **2004**, *432* (7015), 396-401.
 120. Lee, J.; Kotliarova, S.; Kotliarov, Y.; Li, A.; Su, Q.; Donin, N. M.; Pastorino, S.; Purow, B. W.; Christopher, N.; Zhang, W.; Park, J. K.; Fine, H. A., Tumor stem cells derived from glioblastomas cultured in bFGF and EGF more closely mirror the phenotype and genotype of primary tumors than do serum-cultured cell lines. *Cancer Cell* **2006**, *9* (5), 391-403.
 121. Matarredona, E. R.; Pastor, A. M., Neural Stem Cells of the Subventricular Zone as the Origin of Human Glioblastoma Stem Cells. Therapeutic Implications. *Front Oncol* **2019**, *9*, 779.
 122. Sundar, S. J.; Hsieh, J. K.; Manjila, S.; Lathia, J. D.; Sloan, A., The role of cancer stem cells in glioblastoma. *Neurosurg Focus* **2014**, *37* (6), E6.

123. Lathia, J. D.; Hitomi, M.; Gallagher, J.; Gadani, S. P.; Adkins, J.; VasANJI, A.; Liu, L.; Eyler, C. E.; Heddleston, J. M.; Wu, Q.; Minhas, S.; Soeda, A.; Hoepfner, D. J.; Ravin, R.; McKay, R. D.; McLendon, R. E.; Corbeil, D.; Chenn, A.; Hjelmeland, A. B.; Park, D. M.; Rich, J. N., Distribution of CD133 reveals glioma stem cells self-renew through symmetric and asymmetric cell divisions. *Cell Death Dis* **2011**, *2*, e200.
124. Cheng, L.; Huang, Z.; Zhou, W.; Wu, Q.; Donnola, S.; Liu, J. K.; Fang, X.; Sloan, A. E.; Mao, Y.; Lathia, J. D.; Min, W.; McLendon, R. E.; Rich, J. N.; Bao, S., Glioblastoma stem cells generate vascular pericytes to support vessel function and tumor growth. *Cell* **2013**, *153* (1), 139-52.
125. Bao, S.; Wu, Q.; Sathornsumetee, S.; Hao, Y.; Li, Z.; Hjelmeland, A. B.; Shi, Q.; McLendon, R. E.; Bigner, D. D.; Rich, J. N., Stem cell-like glioma cells promote tumor angiogenesis through vascular endothelial growth factor. *Cancer Res* **2006**, *66* (16), 7843-8.
126. Wakimoto, H.; Kesari, S.; Farrell, C. J.; Curry, W. T., Jr.; Zaupa, C.; Aghi, M.; Kuroda, T.; Stemmer-Rachamimov, A.; Shah, K.; Liu, T. C.; Jeyaretna, D. S.; Debasitis, J.; Pruszkak, J.; Martuza, R. L.; Rabkin, S. D., Human glioblastoma-derived cancer stem cells: establishment of invasive glioma models and treatment with oncolytic herpes simplex virus vectors. *Cancer Res* **2009**, *69* (8), 3472-81.
127. Liu, G.; Yuan, X.; Zeng, Z.; Tunic, P.; Ng, H.; Abdulkadir, I. R.; Lu, L.; Irvin, D.; Black, K. L.; Yu, J. S., Analysis of gene expression and chemoresistance of CD133+ cancer stem cells in glioblastoma. *Mol Cancer* **2006**, *5*, 67.
128. Chen, J.; Li, Y.; Yu, T. S.; McKay, R. M.; Burns, D. K.; Kernie, S. G.; Parada, L. F., A restricted cell population propagates glioblastoma growth after chemotherapy. *Nature* **2012**, *488* (7412), 522-6.
129. Bao, S.; Wu, Q.; McLendon, R. E.; Hao, Y.; Shi, Q.; Hjelmeland, A. B.; Dewhirst, M. W.; Bigner, D. D.; Rich, J. N., Glioma stem cells promote radioresistance by preferential activation of the DNA damage response. *Nature* **2006**, *444* (7120), 756-60.
130. Furusawa, C.; Kaneko, K., Chaotic expression dynamics implies pluripotency: when theory and experiment meet. *Biol Direct* **2009**, *4*, 17.
131. Sachdeva, R.; Wu, M.; Johnson, K.; Kim, H.; Celebre, A.; Shahzad, U.; Graham, M. S.; Kessler, J. A.; Chuang, J. H.; Karamchandani, J.; Bredel, M.; Verhaak, R.; Das, S., BMP signaling mediates glioma stem cell quiescence and confers treatment resistance in glioblastoma. *Sci Rep* **2019**, *9* (1), 14569.
132. Hambardzumyan, D.; Bergers, G., Glioblastoma: Defining Tumor Niches. *Trends Cancer* **2015**, *1* (4), 252-265.
133. Zhu, T. S.; Costello, M. A.; Talsma, C. E.; Flack, C. G.; Crowley, J. G.; Hamm, L. L.; He, X.; Hervey-Jumper, S. L.; Heth, J. A.; Muraszko, K. M.; DiMeco, F.; Vescovi, A. L.; Fan, X., Endothelial cells create a stem cell niche in glioblastoma by providing NOTCH ligands that nurture self-renewal of cancer stem-like cells. *Cancer Res* **2011**, *71* (18), 6061-72.
134. Brooks, M. D.; Sengupta, R.; Snyder, S. C.; Rubin, J. B., Hitting Them Where They Live: Targeting the Glioblastoma Perivascular Stem Cell Niche. *Curr Pathobiol Rep* **2013**, *1* (2), 101-110.
135. Jain, R. K.; di Tomaso, E.; Duda, D. G.; Loeffler, J. S.; Sorensen, A. G.; Batchelor, T. T., Angiogenesis in brain tumours. *Nat Rev Neurosci* **2007**, *8* (8), 610-22.
136. Semenza, G. L., HIF-1 mediates metabolic responses to intratumoral hypoxia and oncogenic mutations. *J Clin Invest* **2013**, *123* (9), 3664-71.
137. Forsythe, J. A.; Jiang, B. H.; Iyer, N. V.; Agani, F.; Leung, S. W.; Koos, R. D.; Semenza, G. L., Activation of vascular endothelial growth factor gene transcription by hypoxia-inducible factor 1. *Mol Cell Biol* **1996**, *16* (9), 4604-13.
138. Seidel, S.; Garvalov, B. K.; Wirta, V.; von Stechow, L.; Schanzer, A.; Meletis, K.; Wolter, M.; Sommerlad, D.; Henze, A. T.; Nister, M.; Reifenberger, G.; Lundeberg, J.; Frisen, J.; Acker, T., A hypoxic niche regulates glioblastoma stem cells through hypoxia inducible factor 2 alpha. *Brain* **2010**, *133* (Pt 4), 983-95.

139. Covello, K. L.; Kehler, J.; Yu, H.; Gordan, J. D.; Arsham, A. M.; Hu, C. J.; Labosky, P. A.; Simon, M. C.; Keith, B., HIF-2alpha regulates Oct-4: effects of hypoxia on stem cell function, embryonic development, and tumor growth. *Genes Dev* **2006**, *20* (5), 557-70.
140. Rockwell, S.; Dobrucki, I. T.; Kim, E. Y.; Marrison, S. T.; Vu, V. T., Hypoxia and radiation therapy: past history, ongoing research, and future promise. *Curr Mol Med* **2009**, *9* (4), 442-58.
141. Molina, J. R.; Hayashi, Y.; Stephens, C.; Georgescu, M. M., Invasive glioblastoma cells acquire stemness and increased Akt activation. *Neoplasia* **2010**, *12* (6), 453-63.
142. Ortensi, B.; Setti, M.; Osti, D.; Pelicci, G., Cancer stem cell contribution to glioblastoma invasiveness. *Stem Cell Res Ther* **2013**, *4* (1), 18.
143. Recasens, A.; Munoz, L., Targeting Cancer Cell Dormancy. *Trends in Pharmacological Sciences* **2019**, *40* (2), 128-141.
144. Sharma, S. V.; Lee, D. Y.; Li, B.; Quinlan, M. P.; Takahashi, F.; Maheswaran, S.; McDermott, U.; Azizian, N.; Zou, L.; Fischbach, M. A.; Wong, K. K.; Brandstetter, K.; Wittner, B.; Ramaswamy, S.; Classon, M.; Settleman, J., A chromatin-mediated reversible drug-tolerant state in cancer cell subpopulations. *Cell* **2010**, *141* (1), 69-80.
145. Raha, D.; Wilson, T. R.; Peng, J.; Peterson, D.; Yue, P.; Evangelista, M.; Wilson, C.; Merchant, M.; Settleman, J., The cancer stem cell marker aldehyde dehydrogenase is required to maintain a drug-tolerant tumor cell subpopulation. *Cancer Res* **2014**, *74* (13), 3579-90.
146. Hoang-Minh, L. B.; Siebzehnrubl, F. A.; Yang, C.; Suzuki-Hatano, S.; Dajac, K.; Loche, T.; Andrews, N.; Schmoll Massari, M.; Patel, J.; Amin, K.; Vuong, A.; Jimenez-Pascual, A.; Kubilis, P.; Garrett, T. J.; Moneypenny, C.; Pacak, C. A.; Huang, J.; Sayour, E. J.; Mitchell, D. A.; Sarkisian, M. R.; Reynolds, B. A.; Deleyrolle, L. P., Infiltrative and drug-resistant slow-cycling cells support metabolic heterogeneity in glioblastoma. *EMBO J* **2018**, *37* (23).
147. Bhat, K. P. L.; Balasubramaniyan, V.; Vaillant, B.; Ezhilarasan, R.; Hummelink, K.; Hollingsworth, F.; Wani, K.; Heathcock, L.; James, J. D.; Goodman, L. D.; Conroy, S.; Long, L.; Lelic, N.; Wang, S.; Gumin, J.; Raj, D.; Kodama, Y.; Raghunathan, A.; Olar, A.; Joshi, K.; Pelloski, C. E.; Heimberger, A.; Kim, S. H.; Cahill, D. P.; Rao, G.; Den Dunnen, W. F. A.; Boddeke, H.; Phillips, H. S.; Nakano, I.; Lang, F. F.; Colman, H.; Sulman, E. P.; Aldape, K., Mesenchymal differentiation mediated by NF-kappaB promotes radiation resistance in glioblastoma. *Cancer Cell* **2013**, *24* (3), 331-46.
148. Tong, L.; Yi, L.; Liu, P.; Abeysekera, I. R.; Hai, L.; Li, T.; Tao, Z.; Ma, H.; Xie, Y.; Huang, Y.; Yu, S.; Li, J.; Yuan, F.; Yang, X., Tumour cell dormancy as a contributor to the reduced survival of GBM patients who received standard therapy. *Oncol Rep* **2018**, *40* (1), 463-471.
149. Park, S. Y.; Nam, J. S., The force awakens: metastatic dormant cancer cells. *Exp Mol Med* **2020**, *52* (4), 569-581.
150. Jin, X.; Kim, L. J. Y.; Wu, Q.; Wallace, L. C.; Prager, B. C.; Sanvornanart, T.; Gimple, R. C.; Wang, X.; Mack, S. C.; Miller, T. E.; Huang, P.; Valentim, C. L.; Zhou, Q. G.; Barnholtz-Sloan, J. S.; Bao, S.; Sloan, A. E.; Rich, J. N., Targeting glioma stem cells through combined BMI1 and EZH2 inhibition. *Nat Med* **2017**, *23* (11), 1352-1361.
151. Levin-Reisman, I.; Ronin, I.; Gefen, O.; Braniss, I.; Shoshani, N.; Balaban, N. Q., Antibiotic tolerance facilitates the evolution of resistance. *Science* **2017**, *355* (6327), 826-830.
152. Hangauer, M. J.; Viswanathan, V. S.; Ryan, M. J.; Bole, D.; Eaton, J. K.; Matov, A.; Galeas, J.; Dhruv, H. D.; Berens, M. E.; Schreiber, S. L.; McCormick, F.; McManus, M. T., Drug-tolerant persister cancer cells are vulnerable to GPX4 inhibition. *Nature* **2017**, *551* (7679), 247-250.
153. Roesch, A.; Vultur, A.; Bogeski, I.; Wang, H.; Zimmermann, K. M.; Speicher, D.; Korb, C.; Laschke, M. W.; Gimotty, P. A.; Philipp, S. E.; Krause, E.; Patzold, S.; Villanueva, J.; Krepler, C.; Fukunaga-Kalabis, M.; Hoth, M.; Bastian, B. C.; Vogt, T.; Herlyn, M., Overcoming intrinsic multidrug resistance in melanoma by blocking the mitochondrial respiratory chain of slow-cycling JARID1B(high) cells. *Cancer Cell* **2013**, *23* (6), 811-25.
154. Dalvi, M. P.; Wang, L.; Zhong, R.; Kollipara, R. K.; Park, H.; Bayo, J.; Yenerall, P.; Zhou, Y.; Timmons, B. C.; Rodriguez-Canales, J.; Behrens, C.; Mino, B.; Villalobos, P.; Parra, E. R.; Suraokar,

- M.; Pataer, A.; Swisher, S. G.; Kalthor, N.; Bhanu, N. V.; Garcia, B. A.; Heymach, J. V.; Coombes, K.; Xie, Y.; Girard, L.; Gazdar, A. F.; Kittler, R.; Wistuba, I. I.; Minna, J. D.; Martinez, E. D., Taxane-Platin-Resistant Lung Cancers Co-develop Hypersensitivity to JumoniC Demethylase Inhibitors. *Cell Reports* **2017**, *19* (8), 1669-1684.
155. Goldman, A.; Majumder, B.; Dhawan, A.; Ravi, S.; Goldman, D.; Kohandel, M.; Majumder, P. K.; Sengupta, S., Temporally sequenced anticancer drugs overcome adaptive resistance by targeting a vulnerable chemotherapy-induced phenotypic transition. *Nature Communications* **2015**, *6*, 6139.
156. Arvanitis, C. D.; Ferraro, G. B.; Jain, R. K., The blood-brain barrier and blood-tumour barrier in brain tumours and metastases. *Nat Rev Cancer* **2020**, *20* (1), 26-41.
157. van Tellingen, O.; Yetkin-Arik, B.; de Gooijer, M. C.; Wesseling, P.; Wurdinger, T.; de Vries, H. E., Overcoming the blood-brain tumor barrier for effective glioblastoma treatment. *Drug Resist Updat* **2015**, *19*, 1-12.
158. Calinescu, A. A.; Castro, M. G., Microtubule targeting agents in glioma. *Transl Cancer Res* **2016**, *5* (Suppl 1), S54-S60.
159. Malhotra, V.; Perry, M. C., Classical chemotherapy: mechanisms, toxicities and the therapeutic window. *Cancer Biol Ther* **2003**, *2* (4 Suppl 1), S2-4.
160. Jordan, M. A.; Wilson, L., Microtubules as a target for anticancer drugs. *Nature Reviews Cancer* **2004**, *4* (4), 253-265.
161. Rankovic, Z., CNS Physicochemical Property Space Shaped by a Diverse Set of Molecules with Experimentally Determined Exposure in the Mouse Brain. *Journal of Medicinal Chemistry* **2017**, *60* (14), 5943-5954.
162. Schatten, H., Brief Overview of the Cytoskeleton. In *The Cytoskeleton in Health and Disease*, Schatten, H., Ed. Springer New York: New York, NY, 2015; pp 3-7.
163. Dumontet, C.; Jordan, M. A., Microtubule-binding agents: a dynamic field of cancer therapeutics. *Nat Rev Drug Discov* **2010**, *9* (10), 790-803.
164. Pasquier, E.; Kavallaris, M., Microtubules: a dynamic target in cancer therapy. *IUBMB Life* **2008**, *60* (3), 165-70.
165. Toya, M.; Takeichi, M., Organization of Non-centrosomal Microtubules in Epithelial Cells. *Cell Struct Funct* **2016**, *41* (2), 127-135.
166. Tovey, C. A.; Conduit, P. T., Microtubule nucleation by gamma-tubulin complexes and beyond. *Essays Biochem* **2018**, *62* (6), 765-780.
167. Kollman, J. M.; Polka, J. K.; Zelter, A.; Davis, T. N.; Agard, D. A., Microtubule nucleating gamma-TuSC assembles structures with 13-fold microtubule-like symmetry. *Nature* **2010**, *466* (7308), 879-82.
168. Desai, A.; Mitchison, T. J., Microtubule polymerization dynamics. *Annu Rev Cell Dev Biol* **1997**, *13*, 83-117.
169. Steinmetz, M. O.; Prota, A. E., Microtubule-Targeting Agents: Strategies To Hijack the Cytoskeleton. *Trends in Cell Biology* **2018**, *28* (10), 776-792.
170. Nogales, E.; Zhang, R., Visualizing microtubule structural transitions and interactions with associated proteins. *Curr Opin Struct Biol* **2016**, *37*, 90-6.
171. Howard, J.; Hyman, A. A., Dynamics and mechanics of the microtubule plus end. *Nature* **2003**, *422* (6933), 753-8.
172. Hirokawa, N.; Noda, Y.; Tanaka, Y.; Niwa, S., Kinesin superfamily motor proteins and intracellular transport. *Nat Rev Mol Cell Biol* **2009**, *10* (10), 682-96.

173. Roberts, A. J.; Kon, T.; Knight, P. J.; Sutoh, K.; Burgess, S. A., Functions and mechanics of dynein motor proteins. *Nat Rev Mol Cell Biol* **2013**, *14* (11), 713-26.
174. Akhmanova, A.; Steinmetz, M. O., Control of microtubule organization and dynamics: two ends in the limelight. *Nat Rev Mol Cell Biol* **2015**, *16* (12), 711-26.
175. Brouhard, G. J.; Rice, L. M., The contribution of alphabeta-tubulin curvature to microtubule dynamics. *J Cell Biol* **2014**, *207* (3), 323-34.
176. Dimitrov, A.; Quesnoit, M.; Moutel, S.; Cantaloube, I.; Pous, C.; Perez, F., Detection of GTP-tubulin conformation in vivo reveals a role for GTP remnants in microtubule rescues. *Science* **2008**, *322* (5906), 1353-6.
177. Rodionov, V. I.; Borisy, G. G., Microtubule treadmill in vivo. *Science* **1997**, *275* (5297), 215-8.
178. Arpag, G.; Lawrence, E. J.; Farmer, V. J.; Hall, S. L.; Zanic, M., Collective effects of XMAP215, EB1, CLASP2, and MCAK lead to robust microtubule treadmill. *Proc Natl Acad Sci U S A* **2020**, *117* (23), 12847-12855.
179. Jordan, M. A.; Toso, R. J.; Thrower, D.; Wilson, L., Mechanism of mitotic block and inhibition of cell proliferation by taxol at low concentrations. *Proc Natl Acad Sci U S A* **1993**, *90* (20), 9552-6.
180. Prota, A. E.; Bargsten, K.; Zurwerra, D.; Field, J. J.; Diaz, J. F.; Altmann, K. H.; Steinmetz, M. O., Molecular mechanism of action of microtubule-stabilizing anticancer agents. *Science* **2013**, *339* (6119), 587-90.
181. Prota, A. E.; Bargsten, K.; Northcote, P. T.; Marsh, M.; Altmann, K. H.; Miller, J. H.; Diaz, J. F.; Steinmetz, M. O., Structural basis of microtubule stabilization by laulimalide and peloruside A. *Angew Chem Int Ed Engl* **2014**, *53* (6), 1621-5.
182. Massarotti, A.; Coluccia, A.; Silvestri, R.; Sorba, G.; Brancale, A., The tubulin colchicine domain: a molecular modeling perspective. *ChemMedChem* **2012**, *7* (1), 33-42.
183. Prota, A. E.; Setter, J.; Waight, A. B.; Bargsten, K.; Murga, J.; Diaz, J. F.; Steinmetz, M. O., Pironetin Binds Covalently to alphaCys316 and Perturbs a Major Loop and Helix of alpha-Tubulin to Inhibit Microtubule Formation. *J Mol Biol* **2016**, *428* (15), 2981-8.
184. Gigant, B.; Wang, C.; Ravelli, R. B.; Roussi, F.; Steinmetz, M. O.; Curmi, P. A.; Sobel, A.; Knossow, M., Structural basis for the regulation of tubulin by vinblastine. *Nature* **2005**, *435* (7041), 519-22.
185. Prota, A. E.; Bargsten, K.; Diaz, J. F.; Marsh, M.; Cuevas, C.; Liniger, M.; Neuhaus, C.; Andreu, J. M.; Altmann, K. H.; Steinmetz, M. O., A new tubulin-binding site and pharmacophore for microtubule-destabilizing anticancer drugs. *Proc Natl Acad Sci U S A* **2014**, *111* (38), 13817-21.
186. Miltenburg, N. C.; Boogerd, W., Chemotherapy-induced neuropathy: A comprehensive survey. *Cancer Treat Rev* **2014**, *40* (7), 872-82.
187. Choy, H., Taxanes in combined modality therapy for solid tumors. *Crit Rev Oncol Hematol* **2001**, *37* (3), 237-47.
188. Engels, F. K.; Sparreboom, A.; Mathot, R. A.; Verweij, J., Potential for improvement of docetaxel-based chemotherapy: a pharmacological review. *Br J Cancer* **2005**, *93* (2), 173-7.
189. Ploussard, G.; Terry, S.; Maille, P.; Allory, Y.; Sirab, N.; Kheuang, L.; Soyeux, P.; Nicolaiew, N.; Coppolani, E.; Paule, B.; Salomon, L.; Culine, S.; Buttyan, R.; Vacherot, F.; de la Taille, A., Class III beta-tubulin expression predicts prostate tumor aggressiveness and patient response to docetaxel-based chemotherapy. *Cancer Res* **2010**, *70* (22), 9253-64.
190. Puhalla, S.; Brufsky, A., Ixabepilone: a new chemotherapeutic option for refractory metastatic breast cancer. *Biologics* **2008**, *2* (3), 505-15.
191. McMeekin, S.; Dizon, D.; Barter, J.; Scambia, G.; Manzyuk, L.; Lisyanskaya, A.; Oaknin, A.; Ringuette, S.; Mukhopadhyay, P.; Rosenberg, J.; Vergote, I., Phase III randomized trial of second-line ixabepilone versus paclitaxel or doxorubicin in women with advanced endometrial cancer. *Gynecol Oncol* **2015**, *138* (1), 18-23.

192. Kwok, K. K.; Vincent, E. C.; Gibson, J. N., 36 - Antineoplastic Drugs. In *Pharmacology and Therapeutics for Dentistry (Seventh Edition)*, Dowd, F. J.; Johnson, B. S.; Mariotti, A. J., Eds. Mosby: 2017; pp 530-562.
193. Martino, E.; Casamassima, G.; Castiglione, S.; Cellupica, E.; Pantalone, S.; Papagni, F.; Rui, M.; Siciliano, A. M.; Collina, S., Vinca alkaloids and analogues as anti-cancer agents: Looking back, peering ahead. *Bioorg Med Chem Lett* **2018**, 28 (17), 2816-2826.
194. Gregory, R. K.; Smith, I. E., Vinorelbine--a clinical review. *Br J Cancer* **2000**, 82 (12), 1907-13.
195. Bonfil, R. D.; Russo, D. M.; Binda, M. M.; Delgado, F. M.; Vincenti, M., Higher antitumor activity of vinflunine than vinorelbine against an orthotopic murine model of transitional cell carcinoma of the bladder. *Urol Oncol* **2002**, 7 (4), 159-66.
196. Twelves, C.; Cortes, J.; Vahdat, L. T.; Wanders, J.; Akerele, C.; Kaufman, P. A., Phase III trials of eribulin mesylate (E7389) in extensively pretreated patients with locally recurrent or metastatic breast cancer. *Clin Breast Cancer* **2010**, 10 (2), 160-3.
197. Schoffski, P.; Chawla, S.; Maki, R. G.; Italiano, A.; Gelderblom, H.; Choy, E.; Grignani, G.; Camargo, V.; Bauer, S.; Rha, S. Y.; Blay, J. Y.; Hohenberger, P.; D'Adamo, D.; Guo, M.; Chmielowski, B.; Le Cesne, A.; Demetri, G. D.; Patel, S. R., Eribulin versus dacarbazine in previously treated patients with advanced liposarcoma or leiomyosarcoma: a randomised, open-label, multicentre, phase 3 trial. *Lancet* **2016**, 387 (10028), 1629-37.
198. Geraud, A.; Xu, H. P.; Beuzebec, P.; Kirova, Y. M., Preliminary experience of the concurrent use of radiosurgery and T-DM1 for brain metastases in HER2-positive metastatic breast cancer. *J Neurooncol* **2017**, 131 (1), 69-72.
199. Barok, M.; Joensuu, H.; Isola, J., Trastuzumab emtansine: mechanisms of action and drug resistance. *Breast Cancer Res* **2014**, 16 (2), 209.
200. Verma, S.; Miles, D.; Gianni, L.; Krop, I. E.; Welslau, M.; Baselga, J.; Pegram, M.; Oh, D. Y.; Dieras, V.; Guardino, E.; Fang, L.; Lu, M. W.; Olsen, S.; Blackwell, K.; Group, E. S., Trastuzumab emtansine for HER2-positive advanced breast cancer. *N Engl J Med* **2012**, 367 (19), 1783-91.
201. Kavallaris, M., Microtubules and resistance to tubulin-binding agents. *Nat Rev Cancer* **2010**, 10 (3), 194-204.
202. Xiang, Q.; Zhen, Z.; Deng, D. Y.; Wang, J.; Chen, Y.; Li, J.; Zhang, Y.; Wang, F.; Chen, N.; Chen, H.; Chen, Y., Tivantinib induces G2/M arrest and apoptosis by disrupting tubulin polymerization in hepatocellular carcinoma. *J Exp Clin Cancer Res* **2015**, 34, 118.
203. Rimassa, L.; Assenat, E.; Peck-Radosavljevic, M.; Pracht, M.; Zagonel, V.; Mathurin, P.; Rota Caremoli, E.; Porta, C.; Daniele, B.; Bolondi, L.; Mazzaferro, V.; Harris, W.; Damjanov, N.; Pastorelli, D.; Reig, M.; Knox, J.; Negri, F.; Trojan, J.; Lopez Lopez, C.; Personeni, N.; Decaens, T.; Dupuy, M.; Sieghart, W.; Abbadessa, G.; Schwartz, B.; Lamar, M.; Goldberg, T.; Shuster, D.; Santoro, A.; Bruix, J., Tivantinib for second-line treatment of MET-high, advanced hepatocellular carcinoma (METIV-HCC): a final analysis of a phase 3, randomised, placebo-controlled study. *Lancet Oncol* **2018**, 19 (5), 682-693.
204. Santoro, A.; Rimassa, L.; Borbath, I.; Daniele, B.; Salvagni, S.; Van Laethem, J. L.; Van Vlierberghe, H.; Trojan, J.; Kolligs, F. T.; Weiss, A.; Miles, S.; Gasbarrini, A.; Lencioni, M.; Cicalese, L.; Sherman, M.; Gridelli, C.; Buggisch, P.; Gerken, G.; Schmid, R. M.; Boni, C.; Personeni, N.; Hassoun, Z.; Abbadessa, G.; Schwartz, B.; Von Roemeling, R.; Lamar, M. E.; Chen, Y.; Porta, C., Tivantinib for second-line treatment of advanced hepatocellular carcinoma: a randomised, placebo-controlled phase 2 study. *Lancet Oncol* **2013**, 14 (1), 55-63.
205. Senese, S.; Lo, Y. C.; Huang, D.; Zangle, T. A.; Gholkar, A. A.; Robert, L.; Homet, B.; Ribas, A.; Summers, M. K.; Teitell, M. A.; Damoiseaux, R.; Torres, J. Z., Chemical dissection of the cell cycle: probes for cell biology and anti-cancer drug development. *Cell Death & Disease* **2014**, 5 (10), e1462.
206. Prabhu, S.; Harris, F.; Lea, R.; Snape, T. J., Small-molecule clinical trial candidates for the treatment of glioma. *Drug Discovery Today* **2014**, 19 (9), 1298-1308.

207. Paller, C. J.; Antonarakis, E. S., Cabazitaxel: a novel second-line treatment for metastatic castration-resistant prostate cancer. *Drug Des Devel Ther* **2011**, *5*, 117-24.
208. Oehler, C.; Frei, K.; Rushing, E. J.; McSheehy, P. M.; Weber, D.; Allegrini, P. R.; Weniger, D.; Lutolf, U. M.; Knuth, A.; Yonekawa, Y.; Barath, K.; Brogini-Tenzer, A.; Pruschy, M.; Hofer, S., Patupilone (epothilone B) for recurrent glioblastoma: clinical outcome and translational analysis of a single-institution phase I/II trial. *Oncology* **2012**, *83* (1), 1-9.
209. Hoffmann, J.; Fichtner, I.; Lemm, M.; Lienau, P.; Hess-Stumpp, H.; Rotgeri, A.; Hofmann, B.; Klar, U., Sagopilone crosses the blood-brain barrier in vivo to inhibit brain tumor growth and metastases. *Neuro Oncol* **2009**, *11* (2), 158-66.
210. Stupp, R.; Tosoni, A.; Bromberg, J. E. C.; Hau, P.; Campone, M.; Gijtenbeek, J.; Frenay, M.; Breimer, L.; Wiesinger, H.; Allgeier, A.; van den Bent, M. J.; Bogdahn, U.; van der Graaf, W.; Yun, H. J.; Gorlia, T.; Lacombe, D.; Brandes, A. A., Sagopilone (ZK-EPO, ZK 219477) for recurrent glioblastoma. A phase II multicenter trial by the European Organisation for Research and Treatment of Cancer (EORTC) Brain Tumor Group. *Ann Oncol* **2011**, *22* (9), 2144-2149.
211. Engdahl, A. J.; Torres, E. A.; Lock, S. E.; Engdahl, T. B.; Mertz, P. S.; Streu, C. N., Synthesis, Characterization, and Bioactivity of the Photoisomerizable Tubulin Polymerization Inhibitor azo-Combretastatin A4. *Org Lett* **2015**, *17* (18), 4546-9.
212. Grossmann, K. F.; Colman, H.; Akerley, W. A.; Glantz, M.; Matsuoko, Y.; Beelen, A. P.; Yu, M.; De Groot, J. F.; Aiken, R. D.; Olson, J. J.; Evans, B. A.; Jensen, R. L., Phase I trial of verubulin (MPC-6827) plus carboplatin in patients with relapsed glioblastoma multiforme. *J Neurooncol* **2012**, *110* (2), 257-64.
213. Kim, L. J.; Chamberlain, M. C.; Zhu, J.; Raizer, J. J.; Grimm, S. A.; Phuphanich, S.; Fadul, C. E.; Rosenfeld, S.; Balch, A. H.; Pope, C. C.; Brulotte, M.; Beelen, A. A. P.; Recht, L. D., Phase II study of verubulin (MPC-6827) for the treatment of subjects with recurrent glioblastoma naïve to treatment with bevacizumab. *Journal of Clinical Oncology* **2011**, *29* (15_suppl), 2088-2088.
214. Gurgis, F.; Åkerfeldt, M. C.; Heng, B.; Wong, C.; Adams, S.; Guillemin, G. J.; Johns, T. G.; Chircop, M.; Munoz, L., Cytotoxic activity of the MK2 inhibitor CMPD1 in glioblastoma cells is independent of MK2. *Cell Death Discovery* **2015**, *1*, 15028.
215. Dobber, A.; Phoa, A. F.; Abbassi, R. H.; Stringer, B. W.; Day, B. W.; Johns, T. G.; Abadleh, M.; Peifer, C.; Munoz, L., Development and Biological Evaluation of a Photoactivatable Small Molecule Microtubule-Targeting Agent. *ACS Med Chem Lett* **2017**, *8* (4), 395-400.
216. Phoa, A. F.; Browne, S.; Gurgis, F. M. S.; Åkerfeldt, M. C.; Döbber, A.; Renn, C.; Peifer, C.; Stringer, B. W.; Day, B. W.; Wong, C.; Chircop, M.; Johns, T. G.; Kassiou, M.; Munoz, L., Pharmacology of novel small-molecule tubulin inhibitors in glioblastoma cells with enhanced EGFR signalling. *Biochemical Pharmacology* **2015**, *98* (4), 587-601.
217. Janke, C.; Magiera, M. M., The tubulin code and its role in controlling microtubule properties and functions. *Nat Rev Mol Cell Biol* **2020**, *21* (6), 307-326.
218. Parker, A. L.; Teo, W. S.; McCarrroll, J. A.; Kavallaris, M., An Emerging Role for Tubulin Isoforms in Modulating Cancer Biology and Chemotherapy Resistance. *Int J Mol Sci* **2017**, *18* (7), 1434.
219. Gadadhar, S.; Bodakuntla, S.; Natarajan, K.; Janke, C., The tubulin code at a glance. *Journal of Cell Science* **2017**, *130* (8), 1347.
220. Luduena, R. F., Are tubulin isoforms functionally significant. *Mol Biol Cell* **1993**, *4* (5), 445-57.
221. Strassel, C.; Magiera, M. M.; Dupuis, A.; Batzenschlager, M.; Hovasse, A.; Pleines, I.; Gueguen, P.; Eckly, A.; Moog, S.; Mallo, L.; Kimmerlin, Q.; Chappaz, S.; Strub, J. M.; Kathiresan, N.; de la Salle, H.; Van Dorsselaer, A.; Ferec, C.; Py, J. Y.; Gachet, C.; Schaeffer-Reiss, C.; Kile, B. T.; Janke, C.; Lanza, F., An essential role for alpha4A-tubulin in platelet biogenesis. *Life Sci Alliance* **2019**, *2* (1).
222. Schwer, H. D.; Lecine, P.; Tiwari, S.; Italiano, J. E., Jr.; Hartwig, J. H.; Shivdasani, R. A., A lineage-restricted and divergent beta-tubulin isoform is essential for the biogenesis, structure and function of blood platelets. *Curr Biol* **2001**, *11* (8), 579-86.

223. Ti, S. C.; Alushin, G. M.; Kapoor, T. M., Human beta-Tubulin Isoforms Can Regulate Microtubule Protofilament Number and Stability. *Dev Cell* **2018**, 47 (2), 175-190 e5.
224. Pamula, M. C.; Ti, S. C.; Kapoor, T. M., The structured core of human beta tubulin confers isotype-specific polymerization properties. *J Cell Biol* **2016**, 213 (4), 425-33.
225. Denoulet, P.; Edde, B.; Gros, F., Differential expression of several neurospecific beta-tubulin mRNAs in the mouse brain during development. *Gene* **1986**, 50 (1-3), 289-97.
226. Poirier, K.; Keays, D. A.; Francis, F.; Saillour, Y.; Bahi, N.; Manouvrier, S.; Fallet-Bianco, C.; Pasquier, L.; Toutain, A.; Tuy, F. P.; Bienvenu, T.; Joriot, S.; Odent, S.; Ville, D.; Desguerre, I.; Goldenberg, A.; Moutard, M. L.; Fryns, J. P.; van Esch, H.; Harvey, R. J.; Siebold, C.; Flint, J.; Beldjord, C.; Chelly, J., Large spectrum of lissencephaly and pachygyria phenotypes resulting from de novo missense mutations in tubulin alpha 1A (TUBA1A). *Hum Mutat* **2007**, 28 (11), 1055-64.
227. Lu, C.; Zhang, J.; He, S.; Wan, C.; Shan, A.; Wang, Y.; Yu, L.; Liu, G.; Chen, K.; Shi, J.; Zhang, Y.; Ni, R., Increased alpha-tubulin1b expression indicates poor prognosis and resistance to chemotherapy in hepatocellular carcinoma. *Dig Dis Sci* **2013**, 58 (9), 2713-20.
228. Blenk, S.; Engelmann, J. C.; Pinkert, S.; Weniger, M.; Schultz, J.; Rosenwald, A.; Muller-Hermelink, H. K.; Muller, T.; Dandekar, T., Explorative data analysis of MCL reveals gene expression networks implicated in survival and prognosis supported by explorative CGH analysis. *BMC Cancer* **2008**, 8, 106.
229. Petrukhin, K. E.; Speer, M. C.; Cayanis, E.; Bonaldo, M. F.; Tantravahi, U.; Soares, M. B.; Fischer, S. G.; Warburton, D.; Gilliam, T. C.; Ott, J., A microsatellite genetic linkage map of human chromosome 13. *Genomics* **1993**, 15 (1), 76-85.
230. Uhlen, M.; Fagerberg, L.; Hallstrom, B. M.; Lindskog, C.; Oksvold, P.; Mardinoglu, A.; Sivertsson, A.; Kampf, C.; Sjostedt, E.; Asplund, A.; Olsson, I.; Edlund, K.; Lundberg, E.; Navani, S.; Szgyarto, C. A.; Odeberg, J.; Djureinovic, D.; Takanen, J. O.; Hober, S.; Alm, T.; Edqvist, P. H.; Berling, H.; Tegel, H.; Mulder, J.; Rockberg, J.; Nilsson, P.; Schwenk, J. M.; Hamsten, M.; von Feilitzen, K.; Forsberg, M.; Persson, L.; Johansson, F.; Zwaehlen, M.; von Heijne, G.; Nielsen, J.; Ponten, F., Proteomics. Tissue-based map of the human proteome. *Science* **2015**, 347 (6220), 1260419.
231. Stanchi, F.; Corso, V.; Scannapieco, P.; Ievolella, C.; Negrisola, E.; Tiso, N.; Lanfranchi, G.; Valle, G., TUBA8: A new tissue-specific isoform of alpha-tubulin that is highly conserved in human and mouse. *Biochem Biophys Res Commun* **2000**, 270 (3), 1111-8.
232. Leandro-Garcia, L. J.; Leskela, S.; Landa, I.; Montero-Conde, C.; Lopez-Jimenez, E.; Leton, R.; Cascon, A.; Robledo, M.; Rodriguez-Antona, C., Tumoral and tissue-specific expression of the major human beta-tubulin isoforms. *Cytoskeleton (Hoboken)* **2010**, 67 (4), 214-23.
233. Kavallaris, M.; Kuo, D. Y.; Burkhart, C. A.; Regl, D. L.; Norris, M. D.; Haber, M.; Horwitz, S. B., Taxol-resistant epithelial ovarian tumors are associated with altered expression of specific beta-tubulin isoforms. *J Clin Invest* **1997**, 100 (5), 1282-93.
234. Hasegawa, S.; Miyoshi, Y.; Egawa, C.; Ishitobi, M.; Tamaki, Y.; Monden, M.; Noguchi, S., Mutational analysis of the class I beta-tubulin gene in human breast cancer. *Int J Cancer* **2002**, 101 (1), 46-51.
235. Ohishi, Y.; Oda, Y.; Basaki, Y.; Kobayashi, H.; Wake, N.; Kuwano, M.; Tsuneyoshi, M., Expression of beta-tubulin isoforms in human primary ovarian carcinoma. *Gynecol Oncol* **2007**, 105 (3), 586-92.
236. Bernard-Marty, C.; Treilleux, I.; Dumontet, C.; Cardoso, F.; Fellous, A.; Gancberg, D.; Bissery, M. C.; Paesmans, M.; Larsimont, D.; Piccart, M. J.; Di Leo, A., Microtubule-associated parameters as predictive markers of docetaxel activity in advanced breast cancer patients: results of a pilot study. *Clin Breast Cancer* **2002**, 3 (5), 341-5.
237. Hasegawa, S.; Miyoshi, Y.; Egawa, C.; Ishitobi, M.; Taguchi, T.; Tamaki, Y.; Monden, M.; Noguchi, S., Prediction of response to docetaxel by quantitative analysis of class I and III beta-tubulin isoform mRNA expression in human breast cancers. *Clin Cancer Res* **2003**, 9 (8), 2992-7.
238. Paradiso, A.; Mangia, A.; Chiriatti, A.; Tommasi, S.; Zito, A.; Latorre, A.; Schittulli, F.; Lorusso, V., Biomarkers predictive for clinical efficacy of taxol-based chemotherapy in advanced breast cancer. *Ann Oncol* **2005**, 16 Suppl 4, iv14-19.

239. Gan, P. P.; McCarroll, J. A.; Byrne, F. L.; Garner, J.; Kavallaris, M., Specific beta-tubulin isotypes can functionally enhance or diminish epothilone B sensitivity in non-small cell lung cancer cells. *PLoS One* **2011**, *6* (6), e21717.
240. Hwang, J. E.; Hong, J. Y.; Kim, K.; Kim, S. H.; Choi, W. Y.; Kim, M. J.; Jung, S. H.; Shim, H. J.; Bae, W. K.; Hwang, E. C.; Lee, K. H.; Lee, J. H.; Cho, S. H.; Chung, I. J., Class III beta-tubulin is a predictive marker for taxane-based chemotherapy in recurrent and metastatic gastric cancer. *BMC Cancer* **2013**, *13*, 431.
241. Roque, D. M.; Bellone, S.; English, D. P.; Buza, N.; Cocco, E.; Gasparrini, S.; Bortolomai, I.; Ratner, E.; Silasi, D. A.; Azodi, M.; Rutherford, T. J.; Schwartz, P. E.; Santin, A. D., Tubulin-beta-III overexpression by uterine serous carcinomas is a marker for poor overall survival after platinum/taxane chemotherapy and sensitivity to epothilones. *Cancer* **2013**, *119* (14), 2582-92.
242. Smiyun, G.; Azarenko, O.; Miller, H.; Rifkind, A.; LaPointe, N. E.; Wilson, L.; Jordan, M. A., betaIII-tubulin enhances efficacy of cabazitaxel as compared with docetaxel. *Cancer Chemother Pharmacol* **2017**, *80* (1), 151-164.
243. Shalli, K.; Brown, I.; Heys, S. D.; Schofield, A. C., Alterations of beta-tubulin isotypes in breast cancer cells resistant to docetaxel. *FASEB J* **2005**, *19* (10), 1299-301.
244. Gan, P. P.; Kavallaris, M., Tubulin-targeted drug action: functional significance of class II and class IVb beta-tubulin in vinca alkaloid sensitivity. *Cancer Res* **2008**, *68* (23), 9817-24.
245. McCarroll, J. A.; Sharbeen, G.; Liu, J.; Youkhana, J.; Goldstein, D.; McCarthy, N.; Limbri, L. F.; Dischl, D.; Ceyhan, G. O.; Erkan, M.; Johns, A. L.; Biankin, A. V.; Kavallaris, M.; Phillips, P. A., betaIII-tubulin: a novel mediator of chemoresistance and metastases in pancreatic cancer. *Oncotarget* **2015**, *6* (4), 2235-49.
246. Cucchiarelli, V.; Hiser, L.; Smith, H.; Frankfurter, A.; Spano, A.; Correia, J. J.; Lobert, S., Beta-tubulin isotype classes II and V expression patterns in nonsmall cell lung carcinomas. *Cell Motil Cytoskeleton* **2008**, *65* (8), 675-85.
247. Christoph, D. C.; Kasper, S.; Gauler, T. C.; Loesch, C.; Engelhard, M.; Theegarten, D.; Poettgen, C.; Hepp, R.; Peglow, A.; Loewendick, H.; Welter, S.; Stamatis, G.; Hirsch, F. R.; Schuler, M.; Eberhardt, W. E.; Wohlschlaeger, J., betaV-tubulin expression is associated with outcome following taxane-based chemotherapy in non-small cell lung cancer. *Br J Cancer* **2012**, *107* (5), 823-30.
248. Mathew, D.; Wang, Y.; Van Arsdale, A.; Horwitz, S. B.; McDaid, H., Expression of betaV-Tubulin in Secretory Cells of the Fallopian Tube Epithelium Marks Cellular Atypia. *Int J Gynecol Cancer* **2018**, *28* (2), 363-370.
249. Chao, S. K.; Wang, Y.; Verdier-Pinard, P.; Yang, C. P.; Liu, L.; Rodriguez-Gabin, A.; McDaid, H. M.; Horwitz, S. B., Characterization of a human betaV-tubulin antibody and expression of this isotype in normal and malignant human tissue. *Cytoskeleton (Hoboken)* **2012**, *69* (8), 566-76.
250. Feng, R.; Sang, Q.; Kuang, Y.; Sun, X.; Yan, Z.; Zhang, S.; Shi, J.; Tian, G.; Luchniak, A.; Fukuda, Y.; Li, B.; Yu, M.; Chen, J.; Xu, Y.; Guo, L.; Qu, R.; Wang, X.; Sun, Z.; Liu, M.; Shi, H.; Wang, H.; Feng, Y.; Shao, R.; Chai, R.; Li, Q.; Xing, Q.; Zhang, R.; Nogales, E.; Jin, L.; He, L.; Gupta, M. L., Jr.; Cowan, N. J.; Wang, L., Mutations in TUBB8 and Human Oocyte Meiotic Arrest. *N Engl J Med* **2016**, *374* (3), 223-32.
251. Joe, P. A.; Banerjee, A.; Luduena, R. F., The roles of cys124 and ser239 in the functional properties of human betaIII tubulin. *Cell Motil Cytoskeleton* **2008**, *65* (6), 476-86.
252. Katsetos, C. D.; Del Valle, L.; Geddes, J. F.; Assimakopoulou, M.; Legido, A.; Boyd, J. C.; Balin, B.; Parikh, N. A.; Maraziotis, T.; de Chadarevian, J. P.; Varakis, J. N.; Matsas, R.; Spano, A.; Frankfurter, A.; Herman, M. M.; Khalili, K., Aberrant localization of the neuronal class III beta-tubulin in astrocytomas. *Arch Pathol Lab Med* **2001**, *125* (5), 613-24.
253. Levallet, G.; Bergot, E.; Antoine, M.; Creveuil, C.; Santos, A. O.; Beau-Faller, M.; de Fraipont, F.; Brambilla, E.; Levallet, J.; Morin, F.; Westeel, V.; Wislez, M.; Quoix, E.; Debieuvre, D.; Dubois, F.; Rouquette, I.; Pujol, J. L.; Moro-Sibilot, D.; Camonis, J.; Zalcman, G.; Intergroupe Francophone de Cancerologie, T., High TUBB3 expression, an independent prognostic marker in patients with early

- non-small cell lung cancer treated by preoperative chemotherapy, is regulated by K-Ras signaling pathway. *Mol Cancer Ther* **2012**, *11* (5), 1203-13.
254. McCarroll, J. A.; Gan, P. P.; Erlich, R. B.; Liu, M.; Dwarthe, T.; Sagnella, S. S.; Akerfeldt, M. C.; Yang, L.; Parker, A. L.; Chang, M. H.; Shum, M. S.; Byrne, F. L.; Kavallaris, M., TUBB3/betaIII-tubulin acts through the PTEN/AKT signaling axis to promote tumorigenesis and anoikis resistance in non-small cell lung cancer. *Cancer Res* **2015**, *75* (2), 415-25.
 255. Xiao, M.; Tang, Y.; Chen, W. W.; Wang, Y. L.; Yang, L.; Li, X.; Song, G. L.; Kuang, J., Tubb3 regulation by the Erk and Akt signaling pathways: a mechanism involved in the effect of arginine ADP-ribosyltransferase 1 (Art1) on apoptosis of colon carcinoma CT26 cells. *Tumour Biol* **2016**, *37* (2), 2353-63.
 256. Derry, W. B.; Wilson, L.; Khan, I. A.; Luduena, R. F.; Jordan, M. A., Taxol differentially modulates the dynamics of microtubules assembled from unfractionated and purified beta-tubulin isoforms. *Biochemistry* **1997**, *36* (12), 3554-62.
 257. Rai, A.; Kapoor, S.; Naaz, A.; Kumar Santra, M.; Panda, D., Enhanced stability of microtubules contributes in the development of colchicine resistance in MCF-7 cells. *Biochem Pharmacol* **2017**, *132*, 38-47.
 258. Kanakkanthara, A.; Northcote, P. T.; Miller, J. H., betaII-tubulin and betaIII-tubulin mediate sensitivity to peloruside A and laulimalide, but not paclitaxel or vinblastine, in human ovarian carcinoma cells. *Mol Cancer Ther* **2012**, *11* (2), 393-404.
 259. Wehenkel, A.; Janke, C., Towards elucidating the tubulin code. *Nat Cell Biol* **2014**, *16* (4), 303-5.
 260. Portran, D.; Schaedel, L.; Xu, Z.; Thery, M.; Nachury, M. V., Tubulin acetylation protects long-lived microtubules against mechanical ageing. *Nat Cell Biol* **2017**, *19* (4), 391-398.
 261. Kim, G. W.; Li, L.; Ghorbani, M.; You, L.; Yang, X. J., Mice lacking alpha-tubulin acetyltransferase 1 are viable but display alpha-tubulin acetylation deficiency and dentate gyrus distortion. *J Biol Chem* **2016**, *291* (48), 25279.
 262. Zhang, Y.; Kwon, S.; Yamaguchi, T.; Cubizolles, F.; Rousseaux, S.; Kneissel, M.; Cao, C.; Li, N.; Cheng, H. L.; Chua, K.; Lombard, D.; Mizeracki, A.; Matthias, G.; Alt, F. W.; Khochbin, S.; Matthias, P., Mice lacking histone deacetylase 6 have hyperacetylated tubulin but are viable and develop normally. *Mol Cell Biol* **2008**, *28* (5), 1688-701.
 263. North, B. J.; Marshall, B. L.; Borra, M. T.; Denu, J. M.; Verdin, E., The human Sir2 ortholog, SIRT2, is an NAD⁺-dependent tubulin deacetylase. *Mol Cell* **2003**, *11* (2), 437-44.
 264. Xu, Z.; Schaedel, L.; Portran, D.; Aguilar, A.; Gaillard, J.; Marinkovich, M. P.; Thery, M.; Nachury, M. V., Microtubules acquire resistance from mechanical breakage through intraluminal acetylation. *Science* **2017**, *356* (6335), 328-332.
 265. Fourest-Lieuvin, A.; Peris, L.; Gache, V.; Garcia-Saez, I.; Juillan-Binard, C.; Lantiez, V.; Job, D., Microtubule regulation in mitosis: tubulin phosphorylation by the cyclin-dependent kinase Cdk1. *Mol Biol Cell* **2006**, *17* (3), 1041-50.
 266. Ori-McKenney, K. M.; McKenney, R. J.; Huang, H. H.; Li, T.; Meltzer, S.; Jan, L. Y.; Vale, R. D.; Wiita, A. P.; Jan, Y. N., Phosphorylation of beta-Tubulin by the Down Syndrome Kinase, Minibrain/DYRK1a, Regulates Microtubule Dynamics and Dendrite Morphogenesis. *Neuron* **2016**, *90* (3), 551-63.
 267. Chu, C. W.; Hou, F.; Zhang, J.; Phu, L.; Loktev, A. V.; Kirkpatrick, D. S.; Jackson, P. K.; Zhao, Y.; Zou, H., A novel acetylation of beta-tubulin by San modulates microtubule polymerization via down-regulating tubulin incorporation. *Mol Biol Cell* **2011**, *22* (4), 448-56.
 268. Aillaud, C.; Bosc, C.; Peris, L.; Bosson, A.; Heemeryck, P.; Van Dijk, J.; Le Friec, J.; Boulan, B.; Vossier, F.; Sanman, L. E.; Syed, S.; Amara, N.; Coute, Y.; Lafanechere, L.; Denarier, E.; Delphin, C.; Pelletier, L.; Humbert, S.; Bogyo, M.; Andrieux, A.; Rogowski, K.; Moutin, M. J., Vasohibins/SVBP are tubulin carboxypeptidases (TCPs) that regulate neuron differentiation. *Science* **2017**, *358* (6369), 1448-1453.

269. Nieuwenhuis, J.; Adamopoulos, A.; Bleijerveld, O. B.; Mazouzi, A.; Stickel, E.; Celie, P.; Altelaar, M.; Knipscheer, P.; Perrakis, A.; Blomen, V. A.; Brummelkamp, T. R., Vasohibins encode tubulin detyrosinating activity. *Science* **2017**, *358* (6369), 1453-1456.
270. Ersfeld, K.; Wehland, J.; Plessmann, U.; Dodemont, H.; Gerke, V.; Weber, K., Characterization of the tubulin-tyrosine ligase. *J Cell Biol* **1993**, *120* (3), 725-32.
271. Paturle, L.; Wehland, J.; Margolis, R. L.; Job, D., Complete separation of tyrosinated, detyrosinated, and nontyrosinatable brain tubulin subpopulations using affinity chromatography. *Biochemistry* **1989**, *28* (6), 2698-704.
272. Aillaud, C.; Bosc, C.; Saoudi, Y.; Denarier, E.; Peris, L.; Sago, L.; Taulet, N.; Cieren, A.; Tort, O.; Magiera, M. M.; Janke, C.; Redeker, V.; Andrieux, A.; Moutin, M. J., Evidence for new C-terminally truncated variants of alpha- and beta-tubulins. *Mol Biol Cell* **2016**, *27* (4), 640-53.
273. Wang, Q.; Crevenna, A. H.; Kunze, I.; Mizuno, N., Structural basis for the extended CAP-Gly domains of p150(glued) binding to microtubules and the implication for tubulin dynamics. *Proc Natl Acad Sci U S A* **2014**, *111* (31), 11347-52.
274. Peris, L.; Wagenbach, M.; Lafanechere, L.; Brocard, J.; Moore, A. T.; Kozielski, F.; Job, D.; Wordeman, L.; Andrieux, A., Motor-dependent microtubule disassembly driven by tubulin tyrosination. *J Cell Biol* **2009**, *185* (7), 1159-66.
275. Bonnet, C.; Denarier, E.; Bosc, C.; Lazereg, S.; Denoulet, P.; Larcher, J. C., Interaction of STOP with neuronal tubulin is independent of polyglutamylolation. *Biochem Biophys Res Commun* **2002**, *297* (4), 787-93.
276. Janke, C.; Rogowski, K.; Wloga, D.; Regnard, C.; Kajava, A. V.; Strub, J. M.; Temurak, N.; van Dijk, J.; Boucher, D.; van Dorselaer, A.; Suryavanshi, S.; Gaertig, J.; Edde, B., Tubulin polyglutamylase enzymes are members of the TTL domain protein family. *Science* **2005**, *308* (5729), 1758-62.
277. Ikegami, K.; Mukai, M.; Tsuchida, J.; Heier, R. L.; Macgregor, G. R.; Setou, M., TTL7 is a mammalian beta-tubulin polyglutamylase required for growth of MAP2-positive neurites. *J Biol Chem* **2006**, *281* (41), 30707-16.
278. Kimura, Y.; Kurabe, N.; Ikegami, K.; Tsutsumi, K.; Konishi, Y.; Kaplan, O. I.; Kunitomo, H.; Iino, Y.; Blacque, O. E.; Setou, M., Identification of tubulin deglutamylase among *Caenorhabditis elegans* and mammalian cytosolic carboxypeptidases (CCPs). *J Biol Chem* **2010**, *285* (30), 22936-41.
279. Tort, O.; Tanco, S.; Rocha, C.; Bieche, I.; Seixas, C.; Bosc, C.; Andrieux, A.; Moutin, M. J.; Aviles, F. X.; Lorenzo, J.; Janke, C., The cytosolic carboxypeptidases CCP2 and CCP3 catalyze posttranslational removal of acidic amino acids. *Mol Biol Cell* **2014**, *25* (19), 3017-27.
280. Rogowski, K.; van Dijk, J.; Magiera, M. M.; Bosc, C.; Deloulme, J. C.; Bosson, A.; Peris, L.; Gold, N. D.; Lacroix, B.; Bosch Grau, M.; Bec, N.; Larroque, C.; Desagher, S.; Holzer, M.; Andrieux, A.; Moutin, M. J.; Janke, C., A family of protein-deglutamylating enzymes associated with neurodegeneration. *Cell* **2010**, *143* (4), 564-78.
281. Lacroix, B.; van Dijk, J.; Gold, N. D.; Guizetti, J.; Aldrian-Herrada, G.; Rogowski, K.; Gerlich, D. W.; Janke, C., Tubulin polyglutamylation stimulates spastin-mediated microtubule severing. *J Cell Biol* **2010**, *189* (6), 945-54.
282. Valenstein, M. L.; Roll-Mecak, A., Graded Control of Microtubule Severing by Tubulin Glutamylation. *Cell* **2016**, *164* (5), 911-21.
283. Sirajuddin, M.; Rice, L. M.; Vale, R. D., Regulation of microtubule motors by tubulin isotypes and post-translational modifications. *Nat Cell Biol* **2014**, *16* (4), 335-44.
284. Jordan, M. A.; Thrower, D.; Wilson, L., Effects of vinblastine, podophyllotoxin and nocodazole on mitotic spindles. Implications for the role of microtubule dynamics in mitosis. *J Cell Sci* **1992**, *102* (Pt 3), 401-16.

285. Zhang, Z.; Yamashita, H.; Toyama, T.; Sugiura, H.; Omoto, Y.; Ando, Y.; Mita, K.; Hamaguchi, M.; Hayashi, S.; Iwase, H., HDAC6 expression is correlated with better survival in breast cancer. *Clin Cancer Res* **2004**, *10* (20), 6962-8.
286. Lafanechere, L.; Courtay-Cahen, C.; Kawakami, T.; Jacrot, M.; Rudiger, M.; Wehland, J.; Job, D.; Margolis, R. L., Suppression of tubulin tyrosine ligase during tumor growth. *J Cell Sci* **1998**, *111* (Pt 2), 171-81.
287. Zhang, B.; Wu, Z.; Xie, W.; Tian, D.; Chen, F.; Qin, C.; Du, Z.; Tang, G.; Gao, Q.; Qiu, X.; Wu, C.; Tian, J.; Hu, H., The expression of vasohibin-1 and its prognostic significance in bladder cancer. *Exp Ther Med* **2017**, *14* (4), 3477-3484.
288. Sangrajrang, S.; Fellous, A., Taxol resistance. *Chemotherapy* **2000**, *46* (5), 327-34.
289. Soucek, K.; Kamaid, A.; Phung, A. D.; Kubala, L.; Bulinski, J. C.; Harper, R. W.; Eiserich, J. P., Normal and prostate cancer cells display distinct molecular profiles of alpha-tubulin posttranslational modifications. *Prostate* **2006**, *66* (9), 954-65.
290. Mialhe, A.; Lafanechère, L.; Treilleux, I.; Peloux, N.; Dumontet, C.; Brémond, A.; Panh, M. H.; Payan, R.; Wehland, J.; Margolis, R. L.; Job, D., Tubulin detyrosination is a frequent occurrence in breast cancers of poor prognosis. *Cancer Res* **2001**, *61* (13), 5024-7.
291. Whipple, R. A.; Matrone, M. A.; Cho, E. H.; Balzer, E. M.; Vitolo, M. I.; Yoon, J. R.; Ioffe, O. B.; Tuttle, K. C.; Yang, J.; Martin, S. S., Epithelial-to-mesenchymal transition promotes tubulin detyrosination and microtentacles that enhance endothelial engagement. *Cancer Res* **2010**, *70* (20), 8127-37.
292. Kato, C.; Miyazaki, K.; Nakagawa, A.; Ohira, M.; Nakamura, Y.; Ozaki, T.; Imai, T.; Nakagawara, A., Low expression of human tubulin tyrosine ligase and suppressed tubulin tyrosination/detyrosination cycle are associated with impaired neuronal differentiation in neuroblastomas with poor prognosis. *Int J Cancer* **2004**, *112* (3), 365-75.
293. Hoque, M.; Abbassi, R. H.; Froio, D.; Man, J.; Johns, T. G.; Stringer, B. W.; Day, B. W.; Pajic, M.; Kassiou, M.; Munoz, L., Changes in cell morphology guide identification of tubulin as the off-target for protein kinase inhibitors. *Pharmacol Res* **2018**, *134*, 166-178.
294. Abbassi, R.; Johns, T. G.; Kassiou, M.; Munoz, L., DYRK1A in neurodegeneration and cancer: Molecular basis and clinical implications. *Pharmacol Ther* **2015**, *151*, 87-98.
295. Zhou, Q.; Phoa, A. F.; Abbassi, R. H.; Hoque, M.; Reekie, T. A.; Font, J. S.; Ryan, R. M.; Stringer, B. W.; Day, B. W.; Johns, T. G.; Munoz, L.; Kassiou, M., Structural Optimization and Pharmacological Evaluation of Inhibitors Targeting Dual-Specificity Tyrosine Phosphorylation-Regulated Kinases (DYRK) and CDC-like kinases (CLK) in Glioblastoma. *J Med Chem* **2017**, *60* (5), 2052-2070.
296. Zhou, Q.; Reekie, T. A.; Abbassi, R. H.; Indurthi Venkata, D.; Font, J. S.; Ryan, R. M.; Munoz, L.; Kassiou, M., Synthesis and in vitro evaluation of diverse heterocyclic diphenolic compounds as inhibitors of DYRK1A. *Bioorg Med Chem* **2018**, *26* (22), 5852-5869.
297. Zhou, Q.; Reekie, T. A.; Abbassi, R. H.; Venkata, D. I.; Font, J. S.; Ryan, R. M.; Rendina, L. M.; Munoz, L.; Kassiou, M., Flexible Analogues of Azaindole DYRK1A Inhibitors Elicit Cytotoxicity in Glioblastoma Cells. *Australian Journal of Chemistry* **2018**, *71* (10), 789-797.
298. Hafner, M.; Niepel, M.; Chung, M.; Sorger, P. K., Growth rate inhibition metrics correct for confounders in measuring sensitivity to cancer drugs. *Nature Methods* **2016**, *13*, 521.
299. Hafner, M.; Niepel, M.; Sorger, P. K., Alternative drug sensitivity metrics improve preclinical cancer pharmacogenomics. *Nature biotechnology* **2017**, *35* (6), 500-502.
300. Goldman, A.; Harper, S.; Speicher, D. W., Detection of Proteins on Blot Membranes. *Curr Protoc Protein Sci* **2016**, *86*, 10.8.1-10.8.11.
301. Chou, T. C., Drug combination studies and their synergy quantification using the Chou-Talalay method. *Cancer Res* **2010**, *70* (2), 440-6.

302. Lin, S.; Garcia, B. A., Chapter One - Examining Histone Posttranslational Modification Patterns by High-Resolution Mass Spectrometry. In *Methods in Enzymology*, Wu, C.; Allis, C. D., Eds. Academic Press: 2012; Vol. 512, pp 3-28.
303. MacLean, B.; Tomazela, D. M.; Shulman, N.; Chambers, M.; Finney, G. L.; Frewen, B.; Kern, R.; Tabb, D. L.; Liebler, D. C.; MacCoss, M. J., Skyline: an open source document editor for creating and analyzing targeted proteomics experiments. *Bioinformatics* **2010**, *26* (7), 966-8.
304. Frewen, B.; MacCoss, M. J., Using BiblioSpec for Creating and Searching Tandem MS Peptide Libraries. *Current Protocols in Bioinformatics* **2007**, *20* (1), 13.7.1-13.7.12.
305. Johnson, W. E.; Li, C.; Rabinovic, A., Adjusting batch effects in microarray expression data using empirical Bayes methods. *Biostatistics* **2007**, *8* (1), 118-27.
306. Tonge, P. J., Drug-Target Kinetics in Drug Discovery. *ACS Chem Neurosci* **2018**, *9* (1), 29-39.
307. Zink, L. M.; Hake, S. B., Histone variants: nuclear function and disease. *Curr Opin Genet Dev* **2016**, *37*, 82-89.
308. Rasmussen, K. D.; Helin, K., Role of TET enzymes in DNA methylation, development, and cancer. *Genes Dev* **2016**, *30* (7), 733-50.
309. Pfeifer, G. P., Defining Driver DNA Methylation Changes in Human Cancer. *Int J Mol Sci* **2018**, *19* (4).
310. Prakash, K.; Fournier, D., Histone Code and Higher-Order Chromatin Folding: A Hypothesis. *Genom Comput Biol* **2017**, *3* (2).
311. Gruszka, D. T.; Xie, S.; Kimura, H.; Yardimci, H., Single-molecule imaging reveals control of parental histone recycling by free histones during DNA replication. *Sci Adv* **2020**, *6* (38).
312. Henikoff, S., Nucleosome destabilization in the epigenetic regulation of gene expression. *Nat Rev Genet* **2008**, *9* (1), 15-26.
313. Goldberg, A. D.; Banaszynski, L. A.; Noh, K. M.; Lewis, P. W.; Elsaesser, S. J.; Stadler, S.; Dewell, S.; Law, M.; Guo, X.; Li, X.; Wen, D.; Chappier, A.; DeKever, R. C.; Miller, J. C.; Lee, Y. L.; Boydston, E. A.; Holmes, M. C.; Gregory, P. D.; Grealia, J. M.; Rafii, S.; Yang, C.; Scambler, P. J.; Garrick, D.; Gibbons, R. J.; Higgs, D. R.; Cristea, I. M.; Urnov, F. D.; Zheng, D.; Allis, C. D., Distinct factors control histone variant H3.3 localization at specific genomic regions. *Cell* **2010**, *140* (5), 678-91.
314. Lewis, P. W.; Elsaesser, S. J.; Noh, K. M.; Stadler, S. C.; Allis, C. D., Daxx is an H3.3-specific histone chaperone and cooperates with ATRX in replication-independent chromatin assembly at telomeres. *Proc Natl Acad Sci U S A* **2010**, *107* (32), 14075-80.
315. Rai, T. S.; Puri, A.; McBryan, T.; Hoffman, J.; Tang, Y.; Pchelintsev, N. A.; van Tuyn, J.; Marmorstein, R.; Schultz, D. C.; Adams, P. D., Human CABIN1 is a functional member of the human HIRA/UBN1/ASF1a histone H3.3 chaperone complex. *Mol Cell Biol* **2011**, *31* (19), 4107-18.
316. Pan, D.; Walstein, K.; Take, A.; Bier, D.; Kaiser, N.; Musacchio, A., Mechanism of centromere recruitment of the CENP-A chaperone HJURP and its implications for centromere licensing. *Nat Commun* **2019**, *10* (1), 4046.
317. Bannister, A. J.; Kouzarides, T., Regulation of chromatin by histone modifications. *Cell Res* **2011**, *21* (3), 381-95.
318. Vinogradova, M.; Gehling, V. S.; Gustafson, A.; Arora, S.; Tindell, C. A.; Wilson, C.; Williamson, K. E.; Guler, G. D.; Gangurde, P.; Manieri, W.; Busby, J.; Flynn, E. M.; Lan, F.; Kim, H. J.; Odate, S.; Cochran, A. G.; Liu, Y.; Wongchenko, M.; Yang, Y.; Cheung, T. K.; Maile, T. M.; Lau, T.; Costa, M.; Hegde, G. V.; Jackson, E.; Pitti, R.; Arnott, D.; Bailey, C.; Bellon, S.; Cummings, R. T.; Albrecht, B. K.; Harmange, J. C.; Kiefer, J. R.; Trojer, P.; Classon, M., An inhibitor of KDM5 demethylases reduces survival of drug-tolerant cancer cells. *Nat Chem Biol* **2016**, *12* (7), 531-8.
319. Guler, G. D.; Tindell, C. A.; Pitti, R.; Wilson, C.; Nichols, K.; KaiWai Cheung, T.; Kim, H. J.; Wongchenko, M.; Yan, Y.; Haley, B.; Cuellar, T.; Webster, J.; Alag, N.; Hegde, G.; Jackson, E.

- Nance, T. L.; Giresi, P. G.; Chen, K. B.; Liu, J.; Jhunjhunwala, S.; Settleman, J.; Stephan, J. P.; Arnott, D.; Classon, M., Repression of Stress-Induced LINE-1 Expression Protects Cancer Cell Subpopulations from Lethal Drug Exposure. *Cancer Cell* **2017**, *32* (2), 221-237 e13.
320. Collins, B. C.; Hunter, C. L.; Liu, Y.; Schilling, B.; Rosenberger, G.; Bader, S. L.; Chan, D. W.; Gibson, B. W.; Gingras, A. C.; Held, J. M.; Hirayama-Kurogi, M.; Hou, G.; Krisp, C.; Larsen, B.; Lin, L.; Liu, S.; Molloy, M. P.; Moritz, R. L.; Ohtsuki, S.; Schlapbach, R.; Selevsek, N.; Thomas, S. N.; Tzeng, S. C.; Zhang, H.; Aebersold, R., Multi-laboratory assessment of reproducibility, qualitative and quantitative performance of SWATH-mass spectrometry. *Nat Commun* **2017**, *8* (1), 291.
321. Krautkramer, K. A.; Reiter, L.; Denu, J. M.; Dowell, J. A., Quantification of SAHA-Dependent Changes in Histone Modifications Using Data-Independent Acquisition Mass Spectrometry. *J Proteome Res* **2015**, *14* (8), 3252-62.
322. Fuchs, S. M.; Krajewski, K.; Baker, R. W.; Miller, V. L.; Strahl, B. D., Influence of combinatorial histone modifications on antibody and effector protein recognition. *Curr Biol* **2011**, *21* (1), 53-8.
323. Hattori, T.; Taft, J. M.; Swist, K. M.; Luo, H.; Witt, H.; Slattery, M.; Koide, A.; Ruthenburg, A. J.; Krajewski, K.; Strahl, B. D.; White, K. P.; Farnham, P. J.; Zhao, Y.; Koide, S., Recombinant antibodies to histone post-translational modifications. *Nat Methods* **2013**, *10* (10), 992-5.
324. Peach, S. E.; Rudomin, E. L.; Udeshi, N. D.; Carr, S. A.; Jaffe, J. D., Quantitative assessment of chromatin immunoprecipitation grade antibodies directed against histone modifications reveals patterns of co-occurring marks on histone protein molecules. *Mol Cell Proteomics* **2012**, *11* (5), 128-37.
325. Nishikori, S.; Hattori, T.; Fuchs, S. M.; Yasui, N.; Wojcik, J.; Koide, A.; Strahl, B. D.; Koide, S., Broad ranges of affinity and specificity of anti-histone antibodies revealed by a quantitative peptide immunoprecipitation assay. *J Mol Biol* **2012**, *424* (5), 391-9.
326. Ludwig, C.; Gillet, L.; Rosenberger, G.; Amon, S.; Collins, B. C.; Aebersold, R., Data-independent acquisition-based SWATH-MS for quantitative proteomics: a tutorial. *Mol Syst Biol* **2018**, *14* (8), e8126.
327. Law, K. P.; Lim, Y. P., Recent advances in mass spectrometry: data independent analysis and hyper reaction monitoring. *Expert Rev Proteomics* **2013**, *10* (6), 551-66.
328. Hafner, M.; Heiser, L. M.; Williams, E. H.; Niepel, M.; Wang, N. J.; Korkola, J. E.; Gray, J. W.; Sorger, P. K., Quantification of sensitivity and resistance of breast cancer cell lines to anti-cancer drugs using GR metrics. *Scientific Data* **2017**, *4*, 170166.
329. Azevedo, H.; Pessoa, G. C.; de Luna Vitorino, F. N.; Nsengimana, J.; Newton-Bishop, J.; Reis, E. M.; da Cunha, J. P. C.; Jasiulionis, M. G., Gene co-expression and histone modification signatures are associated with melanoma progression, epithelial-to-mesenchymal transition, and metastasis. *Clin Epigenetics* **2020**, *12* (1), 127.
330. Gonzales-Cope, M.; Sidoli, S.; Bhanu, N. V.; Won, K. J.; Garcia, B. A., Histone H4 acetylation and the epigenetic reader Brd4 are critical regulators of pluripotency in embryonic stem cells. *BMC Genomics* **2016**, *17*, 95.
331. Duarte, L. F.; Young, A. R.; Wang, Z.; Wu, H. A.; Panda, T.; Kou, Y.; Kapoor, A.; Hasson, D.; Mills, N. R.; Ma'ayan, A.; Narita, M.; Bernstein, E., Histone H3.3 and its proteolytically processed form drive a cellular senescence programme. *Nat Commun* **2014**, *5*, 5210.
332. Gomes, A. P.; Ilter, D.; Low, V.; Rosenzweig, A.; Shen, Z. J.; Schild, T.; Rivas, M. A.; Er, E. E.; McNally, D. R.; Mutvei, A. P.; Han, J.; Ou, Y. H.; Cavaliere, P.; Mullarky, E.; Nagiec, M.; Shin, S.; Yoon, S. O.; Dephoure, N.; Massague, J.; Melnick, A. M.; Cantley, L. C.; Tyler, J. K.; Blenis, J., Dynamic Incorporation of Histone H3 Variants into Chromatin Is Essential for Acquisition of Aggressive Traits and Metastatic Colonization. *Cancer Cell* **2019**, *36* (4), 402-417 e13.
333. Lesch, B. J.; Page, D. C., Poised chromatin in the mammalian germ line. *Development* **2014**, *141* (19), 3619-26.
334. Gallo, M.; Coutinho, F. J.; Vanner, R. J.; Gayden, T.; Mack, S. C.; Murison, A.; Remke, M.; Li, R.; Takayama, N.; Desai, K.; Lee, L.; Lan, X.; Park, N. I.; Baryte-Lovejoy, D.; Smil, D.; Sturm, D.;

- Kushida, M. M.; Head, R.; Cusimano, M. D.; Bernstein, M.; Clarke, I. D.; Dick, J. E.; Pfister, S. M.; Rich, J. N.; Arrowsmith, C. H.; Taylor, M. D.; Jabado, N.; Bazett-Jones, D. P.; Lupien, M.; Dirks, P. B., MLL5 Orchestrates a Cancer Self-Renewal State by Repressing the Histone Variant H3.3 and Globally Reorganizing Chromatin. *Cancer Cell* **2015**, *28* (6), 715-729.
335. Maya Miles, D.; Penate, X.; Sanmartin Olmo, T.; Jourquin, F.; Munoz Centeno, M. C.; Mendoza, M.; Simon, M. N.; Chavez, S.; Geli, V., High levels of histones promote whole-genome-duplications and trigger a Swe1 (WEE1)-dependent phosphorylation of Cdc28(CDK1). *Elife* **2018**, *7*.
336. Feser, J.; Truong, D.; Das, C.; Carson, J. J.; Kieft, J.; Harkness, T.; Tyler, J. K., Elevated histone expression promotes life span extension. *Mol Cell* **2010**, *39* (5), 724-35.
337. Karnavas, T.; Pintonello, L.; Agresti, A.; Bianchi, M. E., Histone content increases in differentiating embryonic stem cells. *Front Physiol* **2014**, *5*, 330.
338. Hyun, K.; Jeon, J.; Park, K.; Kim, J., Writing, erasing and reading histone lysine methylations. *Exp Mol Med* **2017**, *49* (4), e324.
339. Qian, C.; Zhou, M. M., SET domain protein lysine methyltransferases: Structure, specificity and catalysis. *Cell Mol Life Sci* **2006**, *63* (23), 2755-63.
340. Falandry, C.; Fourel, G.; Galy, V.; Ristriani, T.; Horard, B.; Bensimon, E.; Salles, G.; Gilson, E.; Magdinier, F., CLLD8/KMT1F is a lysine methyltransferase that is important for chromosome segregation. *J Biol Chem* **2010**, *285* (26), 20234-41.
341. Yu, Y.; Song, C.; Zhang, Q.; DiMaggio, P. A.; Garcia, B. A.; York, A.; Carey, M. F.; Grunstein, M., Histone H3 lysine 56 methylation regulates DNA replication through its interaction with PCNA. *Mol Cell* **2012**, *46* (1), 7-17.
342. Rao, R. C.; Dou, Y., Hijacked in cancer: the KMT2 (MLL) family of methyltransferases. *Nat Rev Cancer* **2015**, *15* (6), 334-46.
343. Gregory, G. D.; Vakoc, C. R.; Rozovskaia, T.; Zheng, X.; Patel, S.; Nakamura, T.; Canaani, E.; Blobel, G. A., Mammalian ASH1L is a histone methyltransferase that occupies the transcribed region of active genes. *Mol Cell Biol* **2007**, *27* (24), 8466-79.
344. An, S.; Yeo, K. J.; Jeon, Y. H.; Song, J. J., Crystal structure of the human histone methyltransferase ASH1L catalytic domain and its implications for the regulatory mechanism. *J Biol Chem* **2011**, *286* (10), 8369-74.
345. Kumar, A.; Kumari, N.; Nallabelli, N.; Prasad, R., Pathogenic and Therapeutic Role of H3K4 Family of Methylases and Demethylases in Cancers. *Indian J Clin Biochem* **2019**, *34* (2), 123-132.
346. Nguyen, A. T.; Zhang, Y., The diverse functions of Dot1 and H3K79 methylation. *Genes Dev* **2011**, *25* (13), 1345-58.
347. Husmann, D.; Gozani, O., Histone lysine methyltransferases in biology and disease. *Nat Struct Mol Biol* **2019**, *26* (10), 880-889.
348. Yang, X.; Li, F.; Konze, K. D.; Meslamani, J.; Ma, A.; Brown, P. J.; Zhou, M. M.; Arrowsmith, C. H.; Kaniskan, H. U.; Vedadi, M.; Jin, J., Structure-Activity Relationship Studies for Enhancer of Zeste Homologue 2 (EZH2) and Enhancer of Zeste Homologue 1 (EZH1) Inhibitors. *J Med Chem* **2016**, *59* (16), 7617-33.
349. van Mierlo, G.; Veenstra, G. J. C.; Vermeulen, M.; Marks, H., The Complexity of PRC2 Subcomplexes. *Trends Cell Biol* **2019**, *29* (8), 660-671.
350. Xiao, B.; Jing, C.; Wilson, J. R.; Walker, P. A.; Vasisht, N.; Kelly, G.; Howell, S.; Taylor, I. A.; Blackburn, G. M.; Gamblin, S. J., Structure and catalytic mechanism of the human histone methyltransferase SET7/9. *Nature* **2003**, *421* (6923), 652-6.
351. Di Zazzo, E.; De Rosa, C.; Abbondanza, C.; Moncharmont, B., PRDM Proteins: Molecular Mechanisms in Signal Transduction and Transcriptional Regulation. *Biology (Basel)* **2013**, *2* (1), 107-41.

352. Black, J. C.; Van Rechem, C.; Whetstine, J. R., Histone lysine methylation dynamics: establishment, regulation, and biological impact. *Mol Cell* **2012**, *48* (4), 491-507.
353. Gaweska, H.; Fitzpatrick, P. F., Structures and Mechanism of the Monoamine Oxidase Family. *Biomol Concepts* **2011**, *2* (5), 365-377.
354. Hosseini, A.; Minucci, S., A comprehensive review of lysine-specific demethylase 1 and its roles in cancer. *Epigenomics* **2017**, *9* (8), 1123-1142.
355. Cao, L. L.; Wei, F.; Du, Y.; Song, B.; Wang, D.; Shen, C.; Lu, X.; Cao, Z.; Yang, Q.; Gao, Y.; Wang, L.; Zhao, Y.; Wang, H.; Yang, Y.; Zhu, W. G., ATM-mediated KDM2A phosphorylation is required for the DNA damage repair. *Oncogene* **2016**, *35* (3), 301-13.
356. Frescas, D.; Guardavaccaro, D.; Bassermann, F.; Koyama-Nasu, R.; Pagano, M., JHDM1B/FBXL10 is a nucleolar protein that represses transcription of ribosomal RNA genes. *Nature* **2007**, *450* (7167), 309-13.
357. Kang, J. Y.; Kim, J. Y.; Kim, K. B.; Park, J. W.; Cho, H.; Hahm, J. Y.; Chae, Y. C.; Kim, D.; Kook, H.; Rhee, S.; Ha, N. C.; Seo, S. B., KDM2B is a histone H3K79 demethylase and induces transcriptional repression via sirtuin-1-mediated chromatin silencing. *FASEB J* **2018**, *32* (10), 5737-5750.
358. Becker, J. S.; Nicetto, D.; Zaret, K. S., H3K9me3-Dependent Heterochromatin: Barrier to Cell Fate Changes. *Trends Genet* **2016**, *32* (1), 29-41.
359. Abe, Y.; Rozqie, R.; Matsumura, Y.; Kawamura, T.; Nakaki, R.; Tsurutani, Y.; Tanimura-Inagaki, K.; Shiono, A.; Magoori, K.; Nakamura, K.; Ogi, S.; Kajimura, S.; Kimura, H.; Tanaka, T.; Fukami, K.; Osborne, T. F.; Kodama, T.; Aburatani, H.; Inagaki, T.; Sakai, J., JMJD1A is a signal-sensing scaffold that regulates acute chromatin dynamics via SWI/SNF association for thermogenesis. *Nat Commun* **2015**, *6*, 7052.
360. Labbe, R. M.; Holowatyj, A.; Yang, Z. Q., Histone lysine demethylase (KDM) subfamily 4: structures, functions and therapeutic potential. *Am J Transl Res* **2013**, *6* (1), 1-15.
361. Gray, S. G.; Iglesias, A. H.; Lizcano, F.; Villanueva, R.; Camelo, S.; Jingu, H.; Teh, B. T.; Koibuchi, N.; Chin, W. W.; Kokkotou, E.; Dangond, F., Functional characterization of JMJD2A, a histone deacetylase- and retinoblastoma-binding protein. *J Biol Chem* **2005**, *280* (31), 28507-18.
362. Klose, R. J.; Kallin, E. M.; Zhang, Y., JmjC-domain-containing proteins and histone demethylation. *Nat Rev Genet* **2006**, *7* (9), 715-27.
363. Ponnaluri, V. K.; Vavilala, D. T.; Putty, S.; Gutheil, W. G.; Mukherji, M., Identification of non-histone substrates for JMJD2A-C histone demethylases. *Biochem Biophys Res Commun* **2009**, *390* (2), 280-4.
364. Kawazu, M.; Saso, K.; Tong, K. I.; McQuire, T.; Goto, K.; Son, D. O.; Wakeham, A.; Miyagishi, M.; Mak, T. W.; Okada, H., Histone demethylase JMJD2B functions as a co-factor of estrogen receptor in breast cancer proliferation and mammary gland development. *PLoS One* **2011**, *6* (3), e17830.
365. Plch, J.; Hrabeta, J.; Eckschlager, T., KDM5 demethylases and their role in cancer cell chemoresistance. *Int J Cancer* **2019**, *144* (2), 221-231.
366. Tran, N.; Broun, A.; Ge, K., Lysine Demethylase KDM6A in Differentiation, Development, and Cancer. *Mol Cell Biol* **2020**, *40* (20).
367. Tsukada, Y.; Ishitani, T.; Nakayama, K. I., KDM7 is a dual demethylase for histone H3 Lys 9 and Lys 27 and functions in brain development. *Genes Dev* **2010**, *24* (5), 432-7.
368. Roesch, A.; Fukunaga-Kalabis, M.; Schmidt, E. C.; Zabierowski, S. E.; Brafford, P. A.; Vultur, A.; Basu, D.; Gimotty, P.; Vogt, T.; Herlyn, M., A temporarily distinct subpopulation of slow-cycling melanoma cells is required for continuous tumor growth. *Cell* **2010**, *141* (4), 583-94.
369. Deblois, G.; Tonekaboni, S. A. M.; Grillo, G.; Martinez, C.; Kao, Y. I.; Tai, F.; Ettayebi, I.; Fortier, A. M.; Savage, P.; Fedor, A. N.; Liu, X.; Guilhamon, P.; Lima-Fernandes, E.; Murison, A.; Kuasne, H.; Ba-Alawi, W.; Cescon, D. W.; Arrowsmith, C. H.; De Carvalho, D. D.; Haibe-Kains, B.; Locasale,

- J. W.; Park, M.; Lupien, M., Epigenetic Switch-Induced Viral Mimicry Evasion in Chemotherapy-Resistant Breast Cancer. *Cancer Discov* **2020**, *10* (9), 1312-1329.
370. Wang, Y.; Cardenas, H.; Fang, F.; Condello, S.; Taverna, P.; Segar, M.; Liu, Y.; Nephew, K. P.; Matei, D., Epigenetic targeting of ovarian cancer stem cells. *Cancer Res* **2014**, *74* (17), 4922-36.
371. Risom, T.; Langer, E. M.; Chapman, M. P.; Rantala, J.; Fields, A. J.; Boniface, C.; Alvarez, M. J.; Kendersky, N. D.; Pelz, C. R.; Johnson-Camacho, K.; Dobrolecki, L. E.; Chin, K.; Aswani, A. J.; Wang, N. J.; Califano, A.; Lewis, M. T.; Tomlin, C. J.; Spellman, P. T.; Adey, A.; Gray, J. W.; Sears, R. C., Differentiation-state plasticity is a targetable resistance mechanism in basal-like breast cancer. *Nat Commun* **2018**, *9* (1), 3815.
372. Bojang, P., Jr.; Ramos, K. S., The promise and failures of epigenetic therapies for cancer treatment. *Cancer Treat Rev* **2014**, *40* (1), 153-69.
373. Asklund, T.; Kvarnbrink, S.; Holmlund, C.; Wibom, C.; Bergenheim, T.; Henriksson, R.; Hedman, H., Synergistic killing of glioblastoma stem-like cells by bortezomib and HDAC inhibitors. *Anticancer Res* **2012**, *32* (7), 2407-13.
374. Friday, B. B.; Anderson, S. K.; Buckner, J.; Yu, C.; Giannini, C.; Geoffroy, F.; Schwerkoske, J.; Mazurczak, M.; Gross, H.; Pajon, E.; Jaeckle, K.; Galanis, E., Phase II trial of vorinostat in combination with bortezomib in recurrent glioblastoma: a north central cancer treatment group study. *Neuro Oncol* **2012**, *14* (2), 215-21.
375. Konze, K. D.; Ma, A.; Li, F.; Barsyte-Lovejoy, D.; Parton, T.; Macnevin, C. J.; Liu, F.; Gao, C.; Huang, X. P.; Kuznetsova, E.; Rougie, M.; Jiang, A.; Pattenden, S. G.; Norris, J. L.; James, L. I.; Roth, B. L.; Brown, P. J.; Frye, S. V.; Arrowsmith, C. H.; Hahn, K. M.; Wang, G. G.; Vedadi, M.; Jin, J., An orally bioavailable chemical probe of the Lysine Methyltransferases EZH2 and EZH1. *ACS Chem Biol* **2013**, *8* (6), 1324-34.
376. Kruidenier, L.; Chung, C. W.; Cheng, Z.; Liddle, J.; Che, K.; Joberty, G.; Bantscheff, M.; Bountra, C.; Bridges, A.; Diallo, H.; Eberhard, D.; Hutchinson, S.; Jones, E.; Katso, R.; Leveridge, M.; Mander, P. K.; Mosley, J.; Ramirez-Molina, C.; Rowland, P.; Schofield, C. J.; Sheppard, R. J.; Smith, J. E.; Swales, C.; Tanner, R.; Thomas, P.; Tumber, A.; Drewes, G.; Oppermann, U.; Patel, D. J.; Lee, K.; Wilson, D. M., A selective jumonji H3K27 demethylase inhibitor modulates the proinflammatory macrophage response. *Nature* **2012**, *488* (7411), 404-8.
377. Cottone, L.; Hookway, E. S.; Cribbs, A.; Wells, G.; Lombard, P.; Ligammari, L.; Tumber, A.; Tirabosco, R.; Amary, F.; Szommer, T.; Johansson, C.; Brennan, P. E.; Pillay, N.; Oppermann, U.; Flanagan, A. M., Epigenetic inactivation of oncogenic brachyury (TBXT) by H3K27 histone demethylase controls chordoma cell survival. *bioRxiv* **2018**, 432005.
378. Monaghan, L.; Massett, M. E.; Bunschoten, R. P.; Hoose, A.; Pirvan, P. A.; Liskamp, R. M. J.; Jorgensen, H. G.; Huang, X., The Emerging Role of H3K9me3 as a Potential Therapeutic Target in Acute Myeloid Leukemia. *Front Oncol* **2019**, *9*, 705.
379. Schiller, R.; Scozzafava, G.; Tumber, A.; Wickens, J. R.; Bush, J. T.; Rai, G.; Lejeune, C.; Choi, H.; Yeh, T. L.; Chan, M. C.; Mott, B. T.; McCullagh, J. S.; Maloney, D. J.; Schofield, C. J.; Kawamura, A., A cell-permeable ester derivative of the JmjC histone demethylase inhibitor IOX1. *ChemMedChem* **2014**, *9* (3), 566-71.
380. Chen, Y. K.; Bonaldi, T.; Cuomo, A.; Del Rosario, J. R.; Hosfield, D. J.; Kanouni, T.; Kao, S. C.; Lai, C.; Lobo, N. A.; Matuszkiewicz, J.; McGeehan, A.; O'Connell, S. M.; Shi, L.; Stafford, J. A.; Stansfield, R. K.; Veal, J. M.; Weiss, M. S.; Yuen, N. Y.; Wallace, M. B., Design of KDM4 Inhibitors with Antiproliferative Effects in Cancer Models. *ACS Med Chem Lett* **2017**, *8* (8), 869-874.
381. McCabe, M. T.; Ott, H. M.; Ganji, G.; Korenchuk, S.; Thompson, C.; Van Aller, G. S.; Liu, Y.; Graves, A. P.; Della Pietra, A., 3rd; Diaz, E.; LaFrance, L. V.; Mellinger, M.; Duquenne, C.; Tian, X.; Kruger, R. G.; McHugh, C. F.; Brandt, M.; Miller, W. H.; Dhanak, D.; Verma, S. K.; Tummino, P. J.; Creasy, C. L., EZH2 inhibition as a therapeutic strategy for lymphoma with EZH2-activating mutations. *Nature* **2012**, *492* (7427), 108-12.
382. Bradley, W. D.; Arora, S.; Busby, J.; Balasubramanian, S.; Gehling, V. S.; Nasveschuk, C. G.; Vaswani, R. G.; Yuan, C. C.; Hatton, C.; Zhao, F.; Williamson, K. E.; Iyer, P.; Mendez, J.; Campbell, R.; Cantone, N.; Garapaty-Rao, S.; Audia, J. E.; Cook, A. S.; Dakin, L. A.; Albrecht, B. K.;

- Harmange, J. C.; Daniels, D. L.; Cummings, R. T.; Bryant, B. M.; Normant, E.; Trojer, P., EZH2 inhibitor efficacy in non-Hodgkin's lymphoma does not require suppression of H3K27 monomethylation. *Chem Biol* **2014**, *21* (11), 1463-75.
383. Vaswani, R. G.; Gehling, V. S.; Dakin, L. A.; Cook, A. S.; Nasveschuk, C. G.; Duplessis, M.; Iyer, P.; Balasubramanian, S.; Zhao, F.; Good, A. C.; Campbell, R.; Lee, C.; Cantone, N.; Cummings, R. T.; Normant, E.; Bellon, S. F.; Albrecht, B. K.; Harmange, J. C.; Trojer, P.; Audia, J. E.; Zhang, Y.; Justin, N.; Chen, S.; Wilson, J. R.; Gamblin, S. J., Identification of (R)-N-((4-Methoxy-6-methyl-2-oxo-1,2-dihydropyridin-3-yl)methyl)-2-methyl-1-(1-(1-(2,2,2-trifluoroethyl)piperidin-4-yl)ethyl)-1H-indole-3-carboxamide (CPI-1205), a Potent and Selective Inhibitor of Histone Methyltransferase EZH2, Suitable for Phase I Clinical Trials for B-Cell Lymphomas. *J Med Chem* **2016**, *59* (21), 9928-9941.
384. Knutson, S. K.; Warholic, N. M.; Wigle, T. J.; Klaus, C. R.; Allain, C. J.; Raimondi, A.; Porter Scott, M.; Chesworth, R.; Moyer, M. P.; Copeland, R. A.; Richon, V. M.; Pollock, R. M.; Kuntz, K. W.; Keilhack, H., Durable tumor regression in genetically altered malignant rhabdoid tumors by inhibition of methyltransferase EZH2. *Proc Natl Acad Sci U S A* **2013**, *110* (19), 7922-7.
385. Kanherkar, R. R.; Bhatia-Dey, N.; Csoka, A. B., Epigenetics across the human lifespan. *Front Cell Dev Biol* **2014**, *2*, 49.
386. Menard, R.; Carmona, E.; Takebe, S.; Dufour, E.; Plouffe, C.; Mason, P.; Mort, J. S., Autocatalytic processing of recombinant human procathepsin L. Contribution of both intermolecular and unimolecular events in the processing of procathepsin L in vitro. *J Biol Chem* **1998**, *273* (8), 4478-84.
387. Ravindran Menon, D.; Hammerlindl, H.; Torrano, J.; Schaidler, H.; Fujita, M., Epigenetics and metabolism at the crossroads of stress-induced plasticity, stemness and therapeutic resistance in cancer. *Theranostics* **2020**, *10* (14), 6261-6277.
388. Kuo, C. Y.; Ann, D. K., When fats commit crimes: fatty acid metabolism, cancer stemness and therapeutic resistance. *Cancer Commun (Lond)* **2018**, *38* (1), 47.
389. Schapira, M., Chemical Inhibition of Protein Methyltransferases. *Cell Chem Biol* **2016**, *23* (9), 1067-1076.
390. Kawamura, A.; Tumber, A.; Rose, N. R.; King, O. N.; Daniel, M.; Oppermann, U.; Heightman, T. D.; Schofield, C., Development of homogeneous luminescence assays for histone demethylase catalysis and binding. *Anal Biochem* **2010**, *404* (1), 86-93.
391. Lin, H.; Li, Q.; Li, Q.; Zhu, J.; Gu, K.; Jiang, X.; Hu, Q.; Feng, F.; Qu, W.; Chen, Y.; Sun, H., Small molecule KDM4s inhibitors as anti-cancer agents. *J Enzyme Inhib Med Chem* **2018**, *33* (1), 777-793.
392. Pedersen, M. T.; Helin, K., Histone demethylases in development and disease. *Trends Cell Biol* **2010**, *20* (11), 662-71.
393. Chen, Z.; Zang, J.; Whetstone, J.; Hong, X.; Davrazou, F.; Kutateladze, T. G.; Simpson, M.; Mao, Q.; Pan, C. H.; Dai, S.; Hagman, J.; Hansen, K.; Shi, Y.; Zhang, G., Structural insights into histone demethylation by JMJD2 family members. *Cell* **2006**, *125* (4), 691-702.
394. Luo, W.; Chang, R.; Zhong, J.; Pandey, A.; Semenza, G. L., Histone demethylase JMJD2C is a coactivator for hypoxia-inducible factor 1 that is required for breast cancer progression. *Proc Natl Acad Sci U S A* **2012**, *109* (49), E3367-76.
395. Thines, C. C.; England, K. S.; Kawamura, A.; Chowdhury, R.; Schofield, C. J.; Hopkinson, R. J., Targeting histone lysine demethylases - progress, challenges, and the future. *Biochim Biophys Acta* **2014**, *1839* (12), 1416-32.
396. Rose, N. R.; Ng, S. S.; Mecinovic, J.; Lienard, B. M.; Bello, S. H.; Sun, Z.; McDonough, M. A.; Oppermann, U.; Schofield, C. J., Inhibitor scaffolds for 2-oxoglutarate-dependent histone lysine demethylases. *J Med Chem* **2008**, *51* (22), 7053-6.
397. Hopkinson, R. J.; Tumber, A.; Yapp, C.; Chowdhury, R.; Aik, W.; Che, K. H.; Li, X. S.; Kristensen, J. B. L.; King, O. N. F.; Chan, M. C.; Yeoh, K. K.; Choi, H.; Walport, L. J.; Thines, C. C.; Bush, J. T.; Lejeune, C.; Rydzik, A. M.; Rose, N. R.; Bagg, E. A.; McDonough, M. A.; Krojer, T.; Yue, W. W.; Ng, S. S.; Olsen, L.; Brennan, P. E.; Oppermann, U.; Muller-Knapp, S.; Klose, R. J.; Ratcliffe,

- P. J.; Schofield, C. J.; Kawamura, A., 5-Carboxy-8-hydroxyquinoline is a Broad Spectrum 2-Oxoglutarate Oxygenase Inhibitor which Causes Iron Translocation. *Chem Sci* **2013**, *4* (8), 3110-3117.
398. Rai, G.; Kawamura, A.; Tumber, A.; Liang, Y.; Vogel, J. L.; Arbuckle, J. H.; Rose, N. R.; Dexheimer, T. S.; Foley, T. L.; King, O. N.; Quinn, A.; Mott, B. T.; Schofield, C. J.; Oppermann, U.; Jadhav, A.; Simeonov, A.; Kristie, T. M.; Maloney, D. J., Discovery of ML324, a JMJD2 demethylase inhibitor with demonstrated antiviral activity. In *Probe Reports from the NIH Molecular Libraries Program*, Bethesda (MD), 2010.
399. Kenny, P. W., The nature of ligand efficiency. *Journal of Cheminformatics* **2019**, *11* (1), 8.
400. Yasgar, A.; Jadhav, A.; Simeonov, A.; Coussens, N. P., AlphaScreen-Based Assays: Ultra-High-Throughput Screening for Small-Molecule Inhibitors of Challenging Enzymes and Protein-Protein Interactions. *Methods Mol Biol* **2016**, *1439*, 77-98.
401. Jammi, N. V.; Whitby, L. R.; Beal, P. A., Small molecule inhibitors of the RNA-dependent protein kinase. *Biochem Biophys Res Commun* **2003**, *308* (1), 50-7.
402. Bavetsias, V.; Lanigan, R. M.; Ruda, G. F.; Atrash, B.; McLaughlin, M. G.; Tumber, A.; Mok, N. Y.; Le Bihan, Y. V.; Dempster, S.; Boxall, K. J.; Jeganathan, F.; Hatch, S. B.; Savitsky, P.; Velupillai, S.; Krojer, T.; England, K. S.; Sejberg, J.; Thai, C.; Donovan, A.; Pal, A.; Scozzafava, G.; Bennett, J. M.; Kawamura, A.; Johansson, C.; Szykowska, A.; Gileadi, C.; Burgess-Brown, N. A.; von Delft, F.; Oppermann, U.; Walters, Z.; Shipley, J.; Raynaud, F. I.; Westaway, S. M.; Prinjha, R. K.; Fedorov, O.; Burke, R.; Schofield, C. J.; Westwood, I. M.; Bountra, C.; Muller, S.; van Montfort, R. L.; Brennan, P. E.; Blagg, J., 8-Substituted Pyrido[3,4-d]pyrimidin-4(3H)-one Derivatives As Potent, Cell Permeable, KDM4 (JMJD2) and KDM5 (JARID1) Histone Lysine Demethylase Inhibitors. *J Med Chem* **2016**, *59* (4), 1388-409.
403. Dahlin, J. L.; Nissink, J. W. M.; Strasser, J. M.; Francis, S.; Higgins, L.; Zhou, H.; Zhang, Z.; Walters, M. A., PAINS in the Assay: Chemical Mechanisms of Assay Interference and Promiscuous Enzymatic Inhibition Observed during a Sulfhydryl-Scavenging HTS. *Journal of Medicinal Chemistry* **2015**, *58* (5), 2091-2113.
404. Haider, S. A.; Asmaro, K.; Kalkanis, S. N.; Lee, I. Y.; Bazydlo, M.; Nerenz, D. R.; Salloum, R. G.; Snyder, J.; Walbert, T., The economic impact of glioma survivorship: The cost of care from a patient perspective. *Neurology* **2020**, *95* (11), e1575-e1581.
405. Brauner, A.; Fridman, O.; Gefen, O.; Balaban, N. Q., Distinguishing between resistance, tolerance and persistence to antibiotic treatment. *Nat Rev Microbiol* **2016**, *14* (5), 320-30.
406. Berman, J.; Krysan, D. J., Drug resistance and tolerance in fungi. *Nat Rev Microbiol* **2020**, *18* (6), 319-331.
407. Vallette, F. M.; Olivier, C.; Lezot, F.; Oliver, L.; Cochonneau, D.; Lalier, L.; Cartron, P. F.; Heymann, D., Dormant, quiescent, tolerant and persister cells: Four synonyms for the same target in cancer. *Biochem Pharmacol* **2019**, *162*, 169-176.
408. Russo, M.; Crisafulli, G.; Sogari, A.; Reilly, N. M.; Arena, S.; Lamba, S.; Bartolini, A.; Amodio, V.; Magri, A.; Novara, L.; Sarotto, I.; Nagel, Z. D.; Pietti, C. G.; Amatu, A.; Sartore-Bianchi, A.; Siena, S.; Bertotti, A.; Trusolino, L.; Corigliano, M.; Gherardi, M.; Lagomarsino, M. C.; Di Nicolantonio, F.; Bardelli, A., Adaptive mutability of colorectal cancers in response to targeted therapies. *Science* **2019**, *366* (6472), 1473-1480.
409. Kawakami, R.; Mashima, T.; Kawata, N.; Kumagai, K.; Migita, T.; Sano, T.; Mizunuma, N.; Yamaguchi, K.; Seimiya, H., ALDH1A3-mTOR axis as a therapeutic target for anticancer drug-tolerant persister cells in gastric cancer. *Cancer Sci* **2020**, *111* (3), 962-973.
410. Tetsu, O.; Phuchareon, J.; Eisele, D. W.; Hangauer, M. J.; McCormick, F., AKT inactivation causes persistent drug tolerance to EGFR inhibitors. *Pharmacol Res* **2015**, *102*, 132-7.
411. Zheng, Y.; Sweet, S. M.; Popovic, R.; Martinez-Garcia, E.; Tipton, J. D.; Thomas, P. M.; Licht, J. D.; Kelleher, N. L., Total kinetic analysis reveals how combinatorial methylation patterns are established on lysines 27 and 36 of histone H3. *Proc Natl Acad Sci U S A* **2012**, *109* (34), 13549-54.

412. Fan, H. C.; Chen, C. M.; Chi, C. S.; Tsai, J. D.; Chiang, K. L.; Chang, Y. K.; Lin, S. Z.; Harn, H. J., Targeting Telomerase and ATRX/DAXX Inducing Tumor Senescence and Apoptosis in the Malignant Glioma. *Int J Mol Sci* **2019**, *20* (1).
413. Rusan, M.; Li, K.; Li, Y.; Christensen, C. L.; Abraham, B. J.; Kwiatkowski, N.; Buczkowski, K. A.; Bockorny, B.; Chen, T.; Li, S.; Rhee, K.; Zhang, H.; Chen, W.; Terai, H.; Tavares, T.; Leggett, A. L.; Li, T.; Wang, Y.; Zhang, T.; Kim, T. J.; Hong, S. H.; Poudel-Neupane, N.; Silkes, M.; Mudianto, T.; Tan, L.; Shimamura, T.; Meyerson, M.; Bass, A. J.; Watanabe, H.; Gray, N. S.; Young, R. A.; Wong, K. K.; Hammerman, P. S., Suppression of Adaptive Responses to Targeted Cancer Therapy by Transcriptional Repression. *Cancer Discov* **2018**, *8* (1), 59-73.
414. Terai, H.; Kitajima, S.; Potter, D. S.; Matsui, Y.; Quiceno, L. G.; Chen, T.; Kim, T. J.; Rusan, M.; Thai, T. C.; Piccioni, F.; Donovan, K. A.; Kwiatkowski, N.; Hinohara, K.; Wei, G.; Gray, N. S.; Fischer, E. S.; Wong, K. K.; Shimamura, T.; Letai, A.; Hammerman, P. S.; Barbie, D. A., ER Stress Signaling Promotes the Survival of Cancer "Persister Cells" Tolerant to EGFR Tyrosine Kinase Inhibitors. *Cancer Res* **2018**, *78* (4), 1044-1057.
415. Shaffer, S. M.; Dunagin, M. C.; Torborg, S. R.; Torre, E. A.; Emert, B.; Krepler, C.; Beqiri, M.; Sproesser, K.; Brafford, P. A.; Xiao, M.; Eggan, E.; Anastopoulos, I. N.; Vargas-Garcia, C. A.; Singh, A.; Nathanson, K. L.; Herlyn, M.; Raj, A., Rare cell variability and drug-induced reprogramming as a mode of cancer drug resistance. *Nature* **2017**, *546* (7658), 431-435.
416. Wang, B.; Fan, X.; Ma, C.; Lei, H.; Long, Q.; Chai, Y., Downregulation of KDM4A Suppresses the Survival of Glioma Cells by Promoting Autophagy. *J Mol Neurosci* **2016**, *60* (2), 137-44.
417. Li, M.; Cheng, J.; Ma, Y.; Guo, H.; Shu, H.; Huang, H.; Kuang, Y.; Yang, T., The histone demethylase JMJD2A promotes glioma cell growth via targeting Akt-mTOR signaling. *Cancer Cell Int* **2020**, *20*, 101.
418. Chen, Y.; Fang, R.; Yue, C.; Chang, G.; Li, P.; Guo, Q.; Wang, J.; Zhou, A.; Zhang, S.; Fuller, G. N.; Shi, X.; Huang, S., Wnt-Induced Stabilization of KDM4C Is Required for Wnt/beta-Catenin Target Gene Expression and Glioblastoma Tumorigenesis. *Cancer Res* **2020**, *80* (5), 1049-1063.
419. Mallm, J. P.; Windisch, P.; Biran, A.; Gal, Z.; Schumacher, S.; Glass, R.; Herold-Mende, C.; Meshorer, E.; Barbus, M.; Rippe, K., Glioblastoma initiating cells are sensitive to histone demethylase inhibition due to epigenetic deregulation. *Int J Cancer* **2020**, *146* (5), 1281-1292.
420. Voon, H. P. J.; Udugama, M.; Lin, W.; Hii, L.; Law, R. H. P.; Steer, D. L.; Das, P. P.; Mann, J. R.; Wong, L. H., Inhibition of a K9/K36 demethylase by an H3.3 point mutation found in paediatric glioblastoma. *Nat Commun* **2018**, *9* (1), 3142.